CONF-8909163--Vol.2

Volume 2

CONF-8909163

5th SYMPOSIUM ON CONTAINMENT OF UNDERGROUND NUCLEAR EXPLOSIONS



September 19-21, 1989

Mission Research Corp.
Santa Barbara, CA

DISTRIBUTION OF THIS DOCUMENT IS UNLIMITED

DISCLAIMER

This report was prepared as an account of work sponsored by an agency of the United States Government. Neither the United States Government nor any agency thereof, nor any of their employees, makes any warranty, express or implied, or assumes any legal liability or responsibility for the accuracy, completeness, or usefulness of any information, apparatus, product, or process disclosed, or represents that its use would not infringe privately owned rights. Reference herein to any specific commercial product, process, or service by trade name, trademark, manufacturer, or otherwise does not necessarily constitute or imply its endorsement, recommendation, or favoring by the United States Government or any agency thereof. The views and opinions of authors expressed herein do not necessarily state or reflect those of the United States Government or any agency thereof.

DISCLAIMER

Portions of this document may be illegible in electronic image products. Images are produced from the best available original document.

DISCLAIMER

This document was prepared as an account of work sponsored by an agency of the United States Government. Neither the United States Government nor the University of California nor any of their employees, makes any warranty, express or implied, or assumes any legal liability or responsibility for the accuracy, completeness, or usefulness of any information, apparatus, product, or process disclosed, or represents that its use would not infringe privately owned rights. Reference herein to any specific commercial products, process, or service by trade name, trademark, manufacturer, or otherwise, does not necessarily constitute or imply its endorsement, recommendation, or favoring by the United States Government or the University of California. The views and opinions of authors expressed herein do not necessarily state or reflect those of the United States Government thereof, and shall not be used for advertising or product endorsement purposes.

Work performed under the auspices of the U.S. Department of Energy by Lawrence Livermore National Laboratory under Contract W-7405-Eng-48.

Proceedings of the Fifth Symposium on Containment of Underground Nuclear Explosions—Volume 2

Mission Research Corp. Santa Barbara, Calif. September 19–21, 1989

CONF-8909163--Vol.2

DE91 002817

Clifford W. Olsen, Scientific Editor
Julie A. Carter, Publication Editor

MASTER

DISTRIBUTION OF THIS DOCUMENT IS UNLIMITED

Preface and Acknowledgements

This is Volume 2 of two unclassified volumes of the Proceedings of the Fifth Symposium on Containment of Underground Nuclear Explosions. The symposium, held September 19–21, 1989, was a meeting of workers at all levels in the containment community. Papers on containment and related geological, geophysical, engineering, chemical, and computational topics were included.

We express our sincere thanks to personnel at Mission Research Corporation (MRC) of Santa Barbara, California, for hosting the Symposium, and we give special thanks to Mary Sourmany of MRC for her splendid cooperation in providing fine facilities. We would also like to thank Robert Nelson, Deputy Manager of the U.S. DOE Nevada Operations Office for his welcoming remarks and Gylan Allen for his most interesting opening address on the Joint Verification Experiment in the Soviet Union. Special thanks are also due to S-Cubed (a division of Maxwell Laboratories, Inc.) and FSN (formerly Fenix & Scisson, Inc.) for underwriting the Tuesday evening social. Finally, we give our sincere thanks to Rochelle Hostetter, Marie Kaye, Kathleen Smith, Richard Navarro, and Dennis Quinn for their invaluable support.

The program committee wishes to thank all presenters and attendees for their support, along with special thanks to the session chairpersons: Margaret Baldwin, Harry Covington, Sanders Dolce, John Kalinowski, Mark Mathews, Len Reed, Norton Rimer, Byron Ristvet, Bruce Trent, and Vern Wheeler.

The Program Committee

Les Hill, Sandia
Jack House, Los Alamos
Cliff Olsen, LLNL
Paul Orkild, USGS
Roger Thompson, DNA

Organizers

Jack House, Los Alamos
Cliff Olsen, LLNL

Symposium Attendees

ADNEY, Kenneth J, U.S. Department of Energy, P.O. Box A, Germantown, MD 20874
ALLEN, Gylan C., U.S. Department of Energy, P.O. Box 98518, Las Vegas, NV 89193-8518
APP, Frederick, Los Alamos National Laboratory, Los Alamos, NM 87545
ATTIA, Armand, Lawrence Livermore National Laboratory, Livermore, CA 94550
BABCOCK, Beverly, Lawrence Livermore National Laboratory, Livermore, CA 94550
BALDWIN, Margaret, Fenix & Scisson, Inc., P.O. Box 768, Mercury, NV 89023
BARBER, James, Fenix & Scisson, Inc., P.O. Box 768, Mercury, NV 89023
BARRETT, William H., Sandia National Laboratories, Albuquerque, NM 87185
BEGLEY, Harold A., Holmes and Narver, Inc., P.O. Box 14340, Las Vegas, NV 89114-4340
BENNETT, Max J., Fenix & Scisson, Inc., P.O. Box 768, Mercury, NV 89023
BERGSTRESSER, Thomas, Sandia National Laboratories, Albuquerque, NM 87185
BRODERICK, Nicholas, EG&G/EM, P.O. Box 9051, Pleasanton, CA 94566
BROWNLEE, Robert R., Los Alamos National Laboratory, Los Alamos, NM 87545
BRUESCH, Grant T., Fenix & Scisson, Inc., P.O. Box 768, Mercury, NV 89023
BRUNISH, Wendee M., Los Alamos National Laboratory, Los Alamos, NM 87545
BURCHETT, Olden L., Sandia National Laboratories, Albuquerque, NM 87185
BURKHARD, Norman R., Lawrence Livermore National Laboratory, Livermore, CA 94550
BUSKIRK, Ernest P., Holmes and Narver, Inc., P.O. Box 14340, Las Vegas, NV 89114-4340
CARLSON, Richard C., Lawrence Livermore National Laboratory, Livermore, CA 94550
CAROTHERS, James E., Lawrence Livermore National Laboratory, Livermore, CA 94550
CHABAI, Albert J., Sandia National Laboratories, Albuquerque, NM 87185
CHIU, Robert Y., Sandia National Laboratories, Albuquerque, NM 87185
COFFEY, Timothy J., Fenix & Scisson, Inc., P.O. Box 768, Mercury, NV 89023
COLE, James C., U. S. Geological Survey, 1527 Cole Blvd., Golden, CO 80401
CONAWAY, John G., Los Alamos National Laboratory, Los Alamos, NM 87545
COOK, C. Wayne, Sandia National Laboratories, Albuquerque, NM 87185
CORNELL, Ray H., Lawrence Livermore National Laboratory, Livermore, CA 94550
COVINGTON, Harry H., U. S. Geological Survey, 1527 Cole Blvd., Golden, CO 80401
COVINGTON, Jerry N., Fenix & Scisson, Inc., P.O. Box 768, Mercury, NV 89023
DALVIT-DUNN, Sandra, Science & Engineering Associates, Santa Fe, NM 87504
DAVIS, Patricia, Holmes and Narver, Inc., P.O. Box 14340, Las Vegas, NV 89114-4340
DEMUTH, Ruth B., Los Alamos National Laboratory, Los Alamos, NM 87545
DEUPREE, Robert G., Los Alamos National Laboratory, Los Alamos, NM 87545
DEVAULT, Guillaume P., Los Alamos National Laboratory, Los Alamos, NM 87545
DISMUKES, Charles R., S-CUBED, P.O. Box 1620, La Jolla, CA 92038
DOLCE, Sanders R., Sandia National Laboratories, Albuquerque, NM 87185
DONITHAN, James D., Lawrence Livermore National Lab., P.O. Box 45, Mercury, NV 89023
DOUGLAS, Carl W., Fenix & Scisson, Inc., P.O. Box 768, Mercury, NV 89023
DRELLACK, Jr., Sigmund L., Fenix & Scisson, Inc., P.O. Box 768, Mercury, NV 89023
DUDA, Leonard, Sandia National Laboratories, Albuquerque, NM 87185
DUFF, Russell E., S-CUBED, P.O. Box 1620, La Jolla, CA 92038
EDWARDS, Thomas O., EG&G/EM, P.O. Box 9051, Pleasanton, CA 94566
ELLE, Donald R., U. S. Department of Energy, Las Vegas, NV 89193-8518
ELLIS, Mona J., S-CUBED, P.O. Box 1620, La Jolla, CA 92038
FARTHING, Larry E., EG&G/EM, Las Vegas, Nevada 89125
FELSKE, Donald J., Lawrence Livermore National Lab., P.O. Box 45, Mercury, NV 89023
FENSKE, Paul R., Desert Research Institute, Reno, NV 89507
FICKAS, Jr., Ernest T., GEO-Centers, Inc., Albuquerque, NM 87106
FISHER, Sandra K., Lawrence Livermore National Laboratory, Livermore, CA 94550
FOGEL, Martin B., Science Applications International Corporation, San Diego, CA 92121

Symposium Attendees

GABRIEL, Lawrence J., Defense Nuclear Agency, P.O. Box 208, Mercury, NV 89023
GERETY, Michael T., Los Alamos National Laboratory, Los Alamos, NM 87545
GLENN, Lewis A., Lawrence Livermore National Laboratory, Livermore, CA 94550
GLOVER, Dale P., Defense Intelligence Agency/DT, Washington, D. C. 20340
GOLDWIRE, Henry C., Lawrence Livermore National Laboratory, Livermore, CA 94550
GOODIN, Stephen W., Defense Nuclear Agency, P.O. Box 208, Mercury, NV 89023
GREEN, Sidney, Terra Tek, 420 Wakara Way, Salt Lake City, UT 84108
GRIFFITHS, Stewart K., Sandia National Laboratories, Livermore, CA 94550
HARRIS-WEST, Barbara L., Defense Nuclear Agency, P.O. Box 208, Mercury, NV 89023
HARTER, Bernadette V., Lawrence Livermore National Laboratory, Livermore, CA 94550
HATCH, Jr., Melton A., EG&G/EM, P.O. Box 9051, Pleasanton, CA 94566
HAWKINS, Ward L., Los Alamos National Laboratory, Los Alamos, NM 87545
HEARST, Joseph R, Lawrence Livermore National Laboratory, Livermore, CA 94550
HERMAN, Cheryl L., U. S. Department of Energy, Las Vegas, NV 89193-8518
HIGGINBOTHAM, Michael L., S-CUBED, P.O. Box 1620, La Jolla, CA 92038
HIGGINS, Gary H., Consultant, P.O. Box 1991, Woodland, CA 95695
HILL, Leslie R., Sandia National Laboratories, Albuquerque, NM 87185
HOPKINS, Steven P., Fenix & Scisson, Inc., P.O. Box 768, Mercury, NV 89023
HOSTETTER, Rochelle A., Lawrence Livermore National Laboratory, Livermore, CA 94550
HOUSE, Jack W., Los Alamos National Laboratory, Los Alamos, NM 87545
HUDSON, Billy C., Lawrence Livermore National Laboratory, Livermore, CA 94550
JACOBSON, Roger L., Desert Research Institute, Reno, NV 89507
JENKINS, Evan C., U. S. Geological Survey, Golden, CO 80401
KALINOWSKI, John A., EG&G/EM, P.O. Box 9051, Pleasanton, CA 94566
KAYE, Marie, Los Alamos National Laboratory, Los Alamos, NM 87545
KELLER, Diana Hollis, S-CUBED, P.O. Box 1620, La Jolla, CA 92038
KILB, Deborah L., Science Applications International Corporation, San Diego, CA 92121
KLUK, Emily C., Los Alamos National Laboratory, Los Alamos, NM 87545
KRIER, Donathon J., Los Alamos National Laboratory, Los Alamos, NM 87545
KUNKLE, Thomas D., Los Alamos National Laboratory, Los Alamos, NM 87545
LADELFE, Carol M., Los Alamos National Laboratory, Los Alamos, NM 87545
LARSON, Donald B., Lawrence Livermore National Laboratory, Livermore, CA 94550
LEEDOM, Stephen H., U. S. Department of Energy, Las Vegas, NV 89193-8518
LOWRY, William E., Science & Engineering Associates, Santa Fe, NM 87504
MACLEOD, Gorden A., Fenix & Scisson, Inc., P.O. Box 768, Mercury, NV 89023
MARTIN, Wes, Terra Tek, 420 Wakara Way, Salt Lake City, UT 84108
MARUSAK, Nancy L., Los Alamos National Laboratory, Los Alamos, NM 87545
MATHEWS, Mark A., Los Alamos National Laboratory, Los Alamos, NM 87545
MCHURON, David C., EG&G/EM, P.O. Box 9051, Pleasanton, CA 94566
MCKAGUE, H. Lawrence, Lawrence Livermore National Laboratory, Livermore, CA 94550
MCKINNIS, William B., Lawrence Livermore National Lab., P.O. Box 45, Mercury, NV 89023
MERCIER, John A., Lawrence Livermore National Laboratory, Livermore, CA 94550
MILLETT, Melvyn R., Lawrence Livermore National Lab. P.O. Box 45, Mercury, NV 89023
MINOR, Scott A., U. S. Geological Survey, 1527 Cole Blvd., Golden, CO 80401
MOELLER, Albert E., EG&G/EM, Las Vegas, Nevada 89125
MOSS, William C., Lawrence Livermore National Laboratory, Livermore, CA 94550
NAVARETTE, Donna L., Teck Reps, Inc., Albuquerque, NM 87110-6390
NAVARRO, Richard, U. S. Department of Energy, Las Vegas, NV 89193-8518
NELSON, Robert M., U. S. Department of Energy, Las Vegas, NV 89193-8518
NEWMARK, Robin L., Lawrence Livermore National Laboratory, Livermore, CA 94550

Symposium Attendees

NILSON, Robert H., S-CUBED, P.O. Box 1620, La Jolla, CA 92038
NOYES, Roger P., EG&G/EM, Las Vegas, Nevada 89125
O'BRIEN, Margaret B., Fenix & Scisson, Inc., P.O. Box 768, Mercury, NV 89023
O'LAUGHLIN, Clay L., Holmes and Narver, Inc., P.O. Box 14340, Las Vegas, NV 89114-4340
OLSEN, Clifford W., Lawrence Livermore National Laboratory, Livermore, CA 94550
ORKILD, Paul P., U. S. Geological Survey, 1527 Cole Blvd., Golden, CO 80401
ORTIZ, Cynthia, U. S. Department of Energy, P.O. Box 98518, Las Vegas, NV 89193-8518
PASSOW, Richard A., Maj. Defense Intelligence Agency/DT, Washington, D. C. 20340
PATCH, Dan F., Science Applications International Corporation, San Diego, CA 92121
PAWLOSKI, Gayle A., Lawrence Livermore National Laboratory, Livermore, CA 94550
PETERSON, Edward W., S-CUBED, P.O. Box 1620, La Jolla, CA 92038
PLANNER, Harry N., Los Alamos National Laboratory, Los Alamos, NM 87545
PLIMPTON, James D., Sandia National Laboratories, Albuquerque, Albuquerque, NM 87185
PRATUCH, Steven M., Lawrence Livermore National Laboratory, Livermore, CA 94550
PROFFER, William J., S-CUBED, P.O. Box 1620, La Jolla, CA 92038
RAMBO, John T., Lawrence Livermore National Laboratory, Livermore, CA 94550
RAYBURN, Christopher J., Fenix & Scisson, Inc., P.O. Box 768, Mercury, NV 89023
REED, Leonard L., S-CUBED, P.O. Box 1620, La Jolla, CA 92038
REED, Melvin E., EG&G/EM, Las Vegas, Nevada 89125
RIMER, Norton, S-CUBED, P.O. Box 1620, La Jolla, CA 92038
RISTVET, Byron L., Defense Nuclear Agency, P.O. Box 98539, Las Vegas, NV 89193-8539
RONSHAUGEN, Stephen C., U. S. Department of Energy, Las Vegas, NV 89193-8518
ROTTLER, J. Steven, Sandia National Laboratories, Albuquerque, Albuquerque, NM 87185
SALAZAR, Roberto S., EG&G/EM, Pleasanton, CA 94566
SANDMAN, Rachel A., S-CUBED, P.O. Box 1620, La Jolla, CA 92038
SAUNDERS, B. Roy, Los Alamos National Laboratory, Los Alamos, NM 87545
SAWYER, David, U. S. Geological Survey, 1527 Cole Blvd., Golden, CO 80401
SCOTT, William B., U.S. Geological Survey, Water Resources Division, Las Vegas, NV 89109
SHEAR, Rodney C., Sandia National Laboratories, Albuquerque, Albuquerque, NM 87185
SHKOLLER, Boris, S-CUBED, P.O. Box 1620, La Jolla, CA 92038
SMITH, Carl W., Fenix & Scisson, Inc., P.O. Box 768, Mercury, NV 89023
SMITH, Charles F., Lawrence Livermore National Laboratory, Livermore, CA 94550
SMITH, Kathleen M., Lawrence Livermore National Laboratory, Livermore, CA 94550
STEWART, Lana M., Holmes and Narver, Inc., P.O. Box 14340, Las Vegas, NV 89114-4340
STUBBS, Theodore F., EG&G/EM, Pleasanton, CA 94566
SWIFT, Robert P., Lawrence Livermore National Laboratory, Livermore, CA 94550
TATE, Paula J., Lawrence Livermore National Laboratory, Livermore, CA 94550
THOMPSON, Peter H., Fenix & Scisson, Inc., P.O. Box 768, Mercury, NV 89023
THOMPSON, Roger C., Defense Nuclear Agency, P.O. Box 98539, Las Vegas, NV 89193-8539
THOMPSON, Samuel L., Fenix & Scisson, Inc., P.O. Box 768, Mercury, NV 89023
TORRES, Gary, Terra Tek, 420 Wakara Way, Salt Lake City, UT 84108
TOWNSEND, Dean R., Fenix & Scisson, Inc., P.O. Box 768, Mercury, NV 89023
TRAVIS, Bryan J., Los Alamos National Laboratory, Los Alamos, NM 87545
TRENT, Bruce C., Los Alamos National Laboratory, Los Alamos, NM 87545
TRUDEAU, Douglas A., U.S. Geological Survey, Water Resources Division, Las Vegas, NV 89109
TWENHOFEL, William S., Consultant, 820 Estes St., Lakewood, CO 80215
VALK, Theodore C., Lawrence Livermore National Laboratory, Livermore, CA 94550
VOLLMER, Donald W., Lawrence Livermore National Laboratory, Livermore, CA 94550
WAGONER, Jeffrey L., Lawrence Livermore National Laboratory, Livermore, CA 94550
WALSH, Robert C., Science & Engineering Associates, Santa Fe, NM 87504

Symposium Attendees

WARREN, Richard G., Los Alamos National Laboratory, Los Alamos, NM 87545
WEISS, Jonathon D., Sandia National Laboratories, Albuquerque, Albuquerque, NM 87185
WHEELER, Vernon E., Lawrence Livermore National Laboratory, Livermore, CA 94550
WILLIAMS, Van S., U. S. Geological Survey, 1527 Cole Blvd., Golden, CO 80401
WOODWARD, Ervin C. Jr., Lawrence Livermore National Laboratory, Livermore, CA 94550
YATES, David R., S-CUBED, P.O. Box 1620, La Jolla, CA 92038

Contents

Volume 1

Stress Measurements

A - 1 **In Situ Stress Measurements Made in Conjunction with the MIGHTY OAK and MISSION GHOST Nuclear Events**
M. J. Baldwin, D. R. Townsend, S. P. Hopkins, T. J. Coffey, J. W. LaComb 3

A - 2 **In Situ "Stress Relief" Measurements and Initial Analysis from a Mine-By in U12p-Tunnel**
B. L. Harris-West, M. B. Fogel 40

A - 4 **Gage Inclusion Experiments**
C. W. Smith 41

LOS Pipe Topics

B - 4 **Development of the Steel/Aluminum Composite Gate for the Modified Auxiliary Closure**
J. C. Weydert, R. Y. Chiu, M. D. Bennett 61

B - 6 **Plasma Flow in PINEX Diagnostic LOS Pipes and a Novel Flow Reduction Scheme**
L. L. Reed, D. J. Hollis 72

Tunnel and Cavity Events

C - 1 **MIGHTY OAK Containment Review**
B. Hudson, E. Peterson, R. Brownlee, A. Chabai, G. Higgins, J. LaComb 107

C - 2 **Containment Design Review for Standard Yield Line-of-Sight Tests**
E. W. Peterson 119

C - 4 **Energy Transfer in a Containment Vessel**
B. Walsh, N. K. Ruiz 138

C - 6 **Success-Tree Methods for Assuring Reliable Containment**
B. Walsh, B. H. Wheeler 160

Stemming and Gas Flow

D - 1 **Stemming Performance of Four Similar Experiments**
B. C. Trent, N. L. Marusak 177

D - 2 **An Optimization Approach to Stemming Design**
B. J. Travis, B. C. Trent 193

D - 3 **The Effect of Cavity Gas Pressure and Porous Flow on Stemming Performance**
B. Hudson, B. Trent 211

D - 4 **Gas-Flow Acceptance of a Fractured Permeable Medium**
R. H. Nilson 231

D - 5 **Containment of Cavity Gas in Fractured or Rubblized Emplacement Media**
N. R. Burkhard, J. R Hearst, E. W. Peterson, R. H. Nilson, K. H. Lie 253

D - 6 **More About Breathing on the Mesa**
E. C. Woodward 281

Hydrofracture and Material Properties

E - 1 **The Application of a Dynamic Hydrofracture Model to the Containment of the MISTY ECHO Cavity Event**
N. Rimer, E. Halda 287

E - 2 **Containment Implications of Inelastic Rock Deformation Occurring During Hydrofracture Growth**
R. H. Nilson, N. Rimer, E. Halda 313

E - 3 **Choking Limitations on the Speed of Gas-Driven Fractures**
S. K. Griffiths, R. H. Nilson 335

E - 4 **Dynamic Properties of DSRM-2 Grout**
M. Fogel 355

E - 5 **Characterization of Shock Conditioned Tuff**
G. Torres, S. J. Green, V. J. Tester, J. W. LaComb 368

E - 6 **In Situ Permeability Measurements, and Gas Flow Calculations and Measurements for the LEDOUX Event**
B. Lowry, S. Dalvit Dunn 384

Volume 2

Ground Motion and Stress

F - 1 **Application of an Effective Stress Model to Underground Nuclear Explosions**
R. P. Swift, A. V. Attia 3

F - 2 **Residual Stresses Calculated Using an Effective Stress Model**
A. V. Attia, R. P. Swift 14

F - 3 **Sensitivity of the Residual Stress Field to Variation of the Strengths for a Weak Layer Overlaying a Strong Working Point Layer**
H. D. Glenn, J. T. Rambo 22

F - 5 **Ground Motion in a Multilayered Media: Calculated and Experimental Results from the HARDIN Event**
V. E. Wheeler, J. T. Rambo 51

F - 6 **Prediction of Ground Motion Based on Working Point Medium and Overburden Lithology**
W. M. Brunish, T. D. Kunkle 65

Event Modeling and Cavity Phenomena

G - 1 **Modeling of the BANDICOOT Event**
F. N. App, W. M. Brunish 69

G - 3 **Modeling of the HEARTS Event**
F. N. App, W. M. Brunish, C. L. Edwards 70

G - 4 **Modeling of MERLIN Alluvium**
W. M. Brunish, F. N. App 96

G - 5 **Recent Nuclear Cavity Pressure Measurements**
B. Hudson, T. Stubbs, R. Nilson, E. Peterson 133

Hydrology and Mineralogy

H - 1 **Hydrologic Testing in Exploratory Drill Hole UE4T, Yucca Flat, the Nevada Test Site**
W. L. Hawkins, D. A. Trudeau, T. M. Mahevc 141

H - 3 **In-Situ Equivalent CO_2 Estimates Using a Neutron-Induced Gamma-Ray Spectroscopy Logging System**
J. R. Hearst, J. G. Conaway, M. A. Mathews, J. W. Barber 160

H - 5 **Occurrence, Distribution and Measurement of Carbonate in the Alluvium of Southern Yucca Flat, Nevada Test Site**
S. L. Drellack, Jr., P. H. Thompson, C. J. Rayburn 186

H - 7 **Bound Water Corrections to Epithermal-Neutron-Derived Water Contents**
N. R. Burkhard, J. R Hearst 206

Geophysics and Material Properties

I - 1 **Physical Properties in LLNL Yucca Flat Areas: the Rock Pile Concept**
N. R. Burkhard 223

I - 2 **Carbonate Rock Emplacement Sites at the Nevada Test Site**
A. H. Cogbill, M. T. Gerety, F. N. App, W. L. Hawkins 274

I - 3 **An Expert System for Assisting in Geologic Site Characterization**
N. L. Marusak, K. P. Berkbigler, G. J. Papcun 297

I - 4 **A Study of the Difference Between Gravimetric and Gamma-Gamma Density Near the Surface in Northern Yucca Flat**
J. R Hearst, N. R. Burkhard 310

I - 5 **Distortion of Geophysical Logs Near Bed Boundaries and in Complex Lithologies**
J. G. Conaway 337

I - 6 **Computerized Tomography as a Geoscience Tool**
G. Torres, V. J. Tester, J. Sharer, S. J. Green, J. W. LaComb 355

I - 7 **A Statistical Analysis of Grain Density Measurements from Cuttings and Percussion Gun Samples**
G. A. Pawloski 372

Geologic Structure and Related Topics

J - 1 **Revised Volcanic Stratigraphy of the Southwestern Nevada Volcanic Field**
R. G. Warren, D. A. Sawyer, H. R. Covington 387

J - 2 **Geology of the U-1a.01 Horizontal Drift Complex, Southwestern Yucca Flat, Nevada Test Site**
S. L. Drellack, Jr., P. H. Thompson, C. J. Rayburn 388

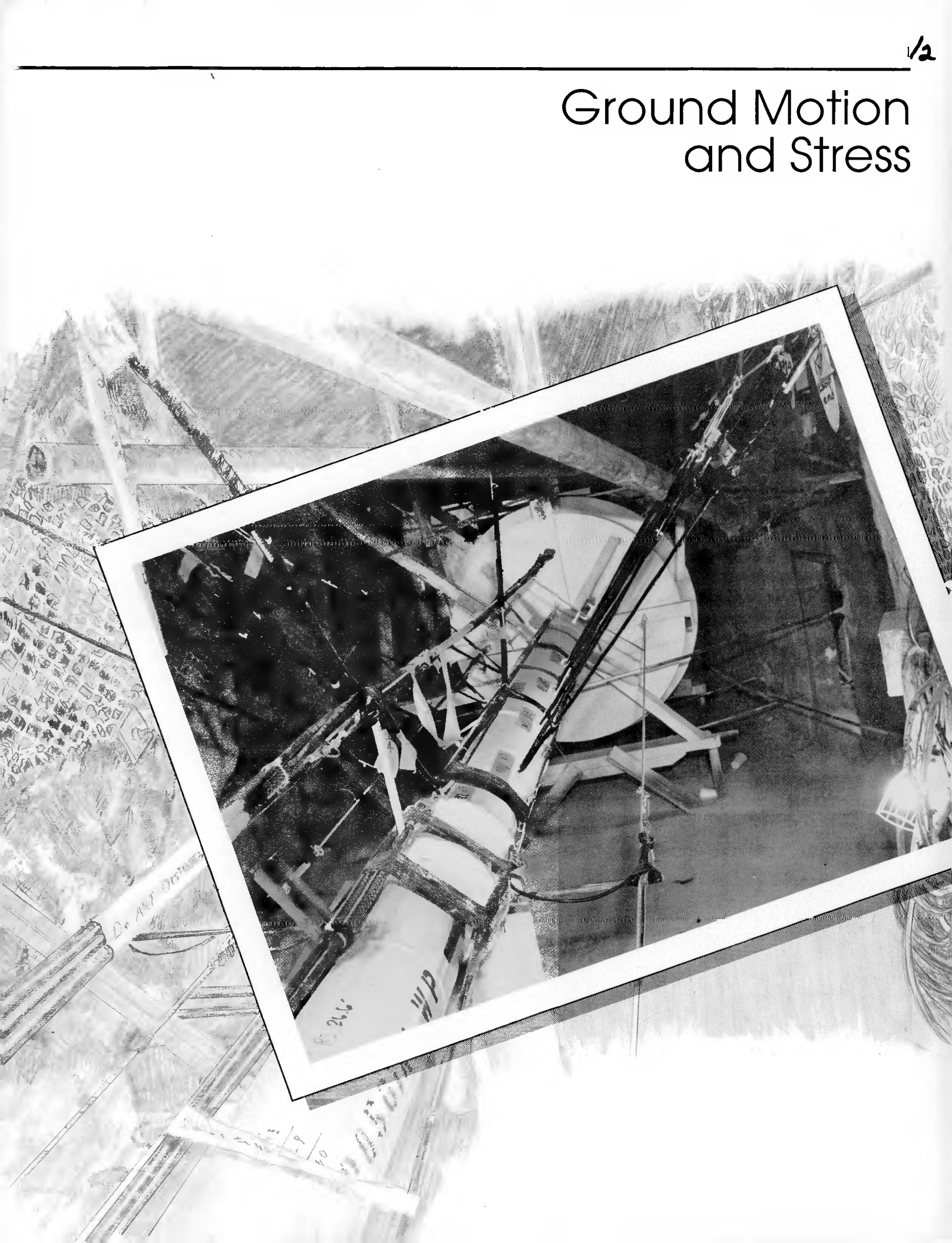
J - 3 **The Delamar Fracture Zone: Recognition of Unmapped Zones of Weakness on Pahute Mesa, Nevada Test Site**
H. R. Covington 405

J - 4 **Paleomagnetic Evaluation of the Yucca-Frenchman Flexure, Southern Nevada**
M. R. Hudson 417

J - 5 **Structural Relations Within the Paleozoic Basement of the Mine Mountain Block; Implications for Interpretation of Gravity Data in Yucca Flat, Nevada Test Site**
J. C. Cole, R. R. Wahl, M. R. Hudson 431

J - 6 **Paleostress Investigation Near Rainier Mesa, Nevada Test Site**
S. A. Minor 457

Ground Motion and Stress



APPLICATION OF AN EFFECTIVE STRESS MODEL TO UNDERGROUND NUCLEAR EXPLOSIONS

Robert P. Swift and Armand M. Attia

Lawrence Livermore National Laboratory
P.O. Box 808, L-200, Livermore, CA 94550

Most numerical simulations for assessing the containment of underground nuclear explosions are based on "total stress" constitutive models, where the porous rock-fluid material is represented as a homogeneous mixture using a single equation of state. However, many work point regions are at or near a state of total saturation, hence, a possibility exists that pore pressure can have an effect on containment behavior. To examine the importance of water and its interaction with a porous rock matrix, an "effective stress" constitutive model has been developed and implemented into the finite element code DYNA2D. In this model, the constituents of a rock-fluid mixture are represented with separate equations of state and combined with an effective stress response law to account for the interaction of the porous matrix with its contained fluid. Numerical simulations of an underground nuclear explosion in a uniform carbonate geology are performed with the effective stress model and compared to that obtained from a total stress representation. The results show that the interaction of fluid and rock accounted for in the effective stress model significantly alters the residual stress field and tensile damage region from the classical conditions given by a total stress model.

1. INTRODUCTION

This paper examines containment phenomena for an underground nuclear explosion in saturated carbonate rock using an "Effective Stress constitutive Model" (ESM) and makes comparison with the behavior obtained from the more standard approach using a "Total Stress Constitutive Model" (TSM). Most numerical simulation assessments of containment behavior are based on the TSM approach, where the porous rock-fluid composite is treated as a homogeneous mixture with a single equation of state.[1] However, in geologies that have large amounts of water and are at or near total saturation, the pore pressure in the rock matrix produced by the explosion can have a significant influence on containment behavior. To examine this influence, the ESM uses separate equations of state to represent the rock and fluid constituents and combines them with an effective stress response law to describe the solid-fluid interaction of the saturated porous matrix.[2]

Numerical simulations using the ESM and TSM were conducted with the finite element code DYNA2D.[3] Results indicate that the residual stress field and tensile damage regions obtained with the ESM are considerably altered from the more classical conditions obtained with the TSM. In Section 2, the ESM is described and applied to laboratory strain path data, representative of spherical shock wave response, obtained on samples of Salem limestone.[4] The TSM is also described and it was fit to mimic the undrained response given by the ESM to facilitate a realistic comparison of phenomena. The calculations are described and the differences obtained with the two models are discussed in Section 3. In Section 4, we summarize the containment related aspects of the differences observed and make recommendations for further assessment.

2. MODEL DESCRIPTION AND APPLICATIONS

The ESM describes a solid skeletal material containing flaws configured as preexisting, isotropic pores and anisotropic, stress induced tensile cracks that are fluid filled. It is assumed that pressure equilibrium of the fluid exists between the two types of flaws and if the volume of the pores and cracks exceeds that accommodating a fully saturated state the pore pressure is assumed to be zero. For the present application zero relative motion between the solid and fluid constituents is assumed (i.e., undrained behavior). A complete discussion of the ESM is given in Rev. 2. A brief description of the ESM features is given below.

2.1 Volumetric Response

Conservation of mass for the solid and fluid provides a kinematic relation ship for strains and porosity in the form

$$d\varphi = \varphi(1-\varphi)(d\varepsilon_f - d\varepsilon_s) \tag{1}$$

where φ, ε_f, and ε_s are the total porosity, fluid volume strain and solid volume strain, respectively. The volumetric portions of the constituent response laws describe the compressibility of the solid grains and the fluid in terms of the bulk moduli K_s and K_f as

$$d\sigma_s = K_s d\varepsilon_s \qquad \text{and} \qquad d\sigma_f = K_f d\varepsilon_f \tag{2}$$

where σ_s and σ_f are the mean stresses in the solid and fluid. Note that the bulk moduli can be nonlinear and dependent functionals of the loading history. The mean effective stress, σ_e, is defined in terms of the mean solid stress and fluid stress as

$$\sigma_e = (1-\varphi)(\sigma_s - \sigma_f). \tag{3}$$

The effective stress law is given in the form

$$d\sigma_e = K\left(d\varepsilon - \frac{d\sigma_f}{K_s}\right) \tag{4}$$

where K is the drained bulk modulus o f the matrix skeleton and ε is the total volume strain.

The total mean stress, σ, is related to the fluid and solid pressure by

$$\sigma = (1-\varphi)\sigma_s + \varphi\sigma_f. \tag{5}$$

The TSM representation of the porous rock-fluid composite treats it as a single homogeneous continuum having an averaged response based on the fraction of each constituent.[1] No explicit interaction of the rock matrix with the fluid is accounted, hence the volumetric behavior is given by a single equation of state in the form

$$d\sigma = K_u d\varepsilon \tag{6}$$

where K_u is, in the present case, the undrained bulk modulus as predicted by the ESM.

2.2 Failure Models

Inelastic behavior is accounted for by separating the total strain increment into elastic and inelastic parts. For a given strain increment, $d\varepsilon_{ij}$, the corresponding effective stress increment is

$$\left(d\sigma_{ij}\right)_e = G_{jkl}\left(d\varepsilon_{kl} - \frac{d\sigma_f}{K_s}\delta_{kl}\right) - \left(d\sigma_{ij}^S\right)_e - \left(d\sigma_{ij}^T\right)_e \qquad (7)$$

where the fourth order tensor, G, represents bulk and shear moduli, and $d\sigma_{ij}^S$ and $d\sigma_{ij}^T$ represent shear failure and tensile failure corrections to the trial elastic state. These corrections are provided by a flow rule and one or more constraint surfaces $F(\sigma_{ij}) = 0$.[5] If the potential surface of the flow rule $H(\sigma_{ij}) = F(\sigma_{ij})$ the process is associative and behavior such as shear coupled compaction and dilatancy can be accommodated. If these surfaces are not the same, the failure process is non-associative and the above stress tensor adjustments are independent of volume change.

The presence of fluid in porous rock reduces the yield strength and pore pressure can cause the matrix to fail in tension. For the ESM, shear yielding is represented by a dry pressure dependent surface, $F\left(\sigma_e, \sqrt{J_2}\right) = 0$, where J_2 is is the second deviatoric stress invariant. The use of σ_e accounts for pore pressure effects in the model. For the TSM, the total mean stress, σ, is used in place of σ_e and the undrained or wet yield surface predicted by the ESM is used. Tensile failure is based on an anisotropic model[6] and occurs when one or more of the principal stresses $(\sigma_e)i \geq T$, where T is the specified tensile strength. As in shear failure, the total stress replaces the effective stress for the TSM.

Because associative shear failure and tensile failure cause changes in the volumetric response from that of the trial state, the void space produced by these processes enter into the total porosity. The adjustments to porosity, pore pressure, and solid pressure are determined from Eq. (1-3) along with $\left(d\sigma_{ij}^S\right)_e$ and $\left(d\sigma_{ij}^T\right)_e$ determined from the failure algorithms.

2.3 Salem Limestone Fit

The ESM was applied to Salem limestone using drained data obtained for strain paths typical for spherical shockwaves.[4] The ESM fit to drained uniaxial strain behavior is shown in Figures 1 and 2. The predicted undrained response for uniaxial strain given by the ESM is compared to undrained data for totally saturated limestone in Figure 3. The hysteretic behavior observed is caused by the compaction of the saturated pore structure and its non-recoverability, which results in higher pore pressure and lower total stress for a given total strain during unloading.

The drained "dry" shear failure surface obtained from triaxial compression data is shown in Figure 4, along with the wet (fully saturated) shear failure surface predicted by the ESM. The TSM was fit to this wet yield surface and to the predicted undrained stress-strain response in Figure 3. However, the TSM treats the volumetric behavior as being reversible and does not account for the compaction associated with the fully saturated undrained response. Tables 1

and 2 give the material parameters for Salem limestone that are used in the ESM and TSM, respectively.

Table 1

Material Parameters used in ESM

Solid Density (g/cc	2.722
Dry Density (g/cc)	2.398
Total Porosity	0.135
Saturation	1.000
Water Content by Weight	0.054
Poisson's Ratio	0.250
Tensile strength (bars)	3.500

Table 2

Material Parameters used in TSM

Bulk Density (g/cc)	2.394
Air Filled Porosity	0.000
Poisson's Ratio	0.340
Tensile Strength (bars)	3.500

3. CALCULATIONS

Calculations to examine containment phenomena in saturated porous carbonate rock were performed using the explicit finite-element code DYNA2D.[3] The computational configuration, in cylindrical axisemmetric geometry, shown in Figure 5, indicates the outer boundary conditions. The nuclear explosion source condition driving the calculation is cavity pressure as a function of cavity volume as shown in Figure 6. This source condition, representing the cavity expansion for 160 KT, was obtained from a one dimensional spherical symmetric simulation where the energy was deposited in a one-meter radius of the carbonate rock. For the current simulations, the source was located at a depth-of-burial of 600 meters with an initial cavity radius of 30 meters and initial cavity pressure of 100 Kbar. The calculations were carried out for a duration of 1 second.

3.1 Residual Stresses

The residual stress field surrounding the cavity is one measure of assessing containment. it is associated with the growth and rebound of the cavity region and its onset coincides with the reversal of the cavity region flow field. A residual stress field thickness of two to three cavity radii for the in-plane circumferential and the out-of-plane hoop stresses that sufficiently exceed the cavity pressure is indicative of successful containment of cavity gases at early time (i.e., on the order of seconds). The residual out-of-plane hoop stresses given at 1 second for the ESM and the TSM are shown in Figures 7 and 8, respectively. Both models show residual stresses higher (i.e., dotted region) than the cavity pressure, of 310 bars for the ESM case and 490 bars for the TSM case, surrounding the cavity. In both cases the residual thickness in the upper cavity region is less than that in the bottom region, typical of the effect of overburden stress. The ESM shows overall a much broader region exceeding the cavity pressure. The in-plane circumferential residual stress fields are shown in Figures 9 and 10 for the ESM and the TSM. This component is considerably degraded in the upper cavity region for both models, again with the ESM giving a broader residual region exceeding the cavity pressure. The degradation of the in-plane stresses in the upper cavity region is associated with the arrival of the rarefaction wave from the free surface. These stresses are much more sensitive to the rarefaction wave influence than the hoop stresses are. They can be significantly reduced if the rarefaction wave arrives with sufficient strength in the cavity region near the time of onset for cavity rebound.[7]

Although the residual stress region for the ESM shown in Figures 7 and 9 appear to be quite thick, a good portion of the stress in this region is totally composed of pore pressure, as shown in Figure 11. A liquified region exists around the cavity caused by tensile failure of the porous matrix resulting in all effective stresses vanishing (e.g. a region devoid of shear stress). The

pore pressure in the liquified region at 1 second is equal to or slightly above the cavity pressure, giving rise to an "effective cavity" that extends out from 1.5 to 2.0 cavity radii of the cavity itself. This is also evident in Figure 12 which shows residual shear stress around the cavity, This localized loss of shear strength in the liquified region surrounding the cavity causes the actual cavity to be larger and the corresponding cavity pressure to be lower for the ESM case.

Figures 13 and 14 compare, in the horizontal direction, the out-of-plane hoop and the in-plane circumferential stresses, respectively, predicted at one second by the ESM and the TSM. Also shown is the pore pressure predicted by the ESM. Note, an effect of the tensile induced liquified region causes the residual stress field exceeding cavity pressure to be shifted outward for the ESM case. Even though the cavity pressure is considerably lower for the ESM case, the resulting residual stresses exceed the cavity pressure by more and are boarder in extent than their counterparts predicted by the TSM. For the ESM case, the dip in pore pressure and in-plane circumferential residual stress at a range of 160 to 200 meters, outside the liquified region, is a result of opened in-plane radial fractures. No fracturing has occurred in this region for the TSM case and the lower than cavity pressure in-plane circumferential stress is a result of the influence of the surface rarefaction wave.

3.2 Tensile Damage

Tensile damage regions resulting from the explosion are shown in Figures 15 and 16 for the ESM and TSM, respectively, and exhibit considerable differences. As noted above, a pulverized liquified region, 1.5 to 2 cavity radii thick, surrounds the cavity in the ESM case, whereas no such damage region exists for the TSM case. Both models show damage in the surface region which results from interaction of surface with the outgoing ground shock and the returning rarefaction wave. The damage associated with the ESM is considerably more extensive and pervades to deeper depths than that for the TSM. In fact, for this saturated media some tensile damage is evident all the way from the highly damaged cavity region out to the surface for the ESM case. This is a result of the relative ease for tensile failure to occur in the ESM in comparison to the TSM. The ESM provides a stiff unloading path for matrix material and a soft one for the water. Hence, during shock unloading the coupling effective response law, Eq. (4), allows for the effective stresses to go into tension inducing tensile failure even when the fluid (i.e., water) is still in a compressive state of stress. This feature is not accounted for in the TSM where tensile failure can occur only when a total stress component goes into a state of tension.

4. SUMMARY AND RECOMMENDATIONS

The ESM and the TSM have been applied to a simulation of a 160 KT explosion, 600 meters below the surface in a saturated porous carbonate geology. The early containment phenomenology (i.e., on the order of a second or so) given by the ESM is significantly different from that described by the TSM. The differences attributed to the coupling interaction features between the solid rock matrix and water in the ESM are the following:

1) A stronger and thicker residual stress field is obtained with the ESM.

2) A liquified tensile failure damage region surrounds the cavity in the ESM case with pore pressure nearly the same as the cavity pressure and shifts the residual stress field outward on the order of 1.5 to 2 cavity radii. This is in contrast with the residual stress buildup given by the TSM which is adjacent to cavity with no tensile damage.

3) Lack of shear stress in the liquified region causes the actual cavity to be larger and cavity pressure to be smaller for the ESM case.

4) Considerably more tensile damage is evident with the ESM where pore pressure induced tensile failure occurs from the cavity region out to the surface spall region.

The results given here are for a hypothetical totally saturated media having a porosity of 13.5 percent. Further work is required to determine if the differences between the ESM and TSM approaches are as severe for more realistic geologies and partially saturated conditions. Never the less, it is felt that the ESM is a more physical realistic model and that tests near or below the water table should be assessed with such a model accounting for the influence of pore pressure. In addition, it is recommended that the ESM be checked with shock wave response data from experiments on saturated or nearly saturated rocks or soils.[8,9]

5. REFERENCES

1. T.R. Butkovich, A Technique for Generating Pressure-Volume Relationships and Failure Envelopes for Rocks, UCRL-51441, November, 1973.

2. R. P. Swift and D. E. Burton, Numerical Modeling of the Mechanics of Nonlinear Porous Media Under Dynamic Loading, UCRL-53568, July, 1984.

3. J.O. Hallquist, User's Manual for DYNA-2D, and Explicit Two-Dimensional Hydrodynamic Finite Element Code with Interactive Rezoning and Graphical Display, UCID-18756, Rev. 3, February, 1987.

4. S. Blouin and D. Chitty, Private Communication, Applied Research Associates, Inc. (South Royalton, VT, 1988).

5. R. Hill, Mathematical Theory of Plasticity, Oxford Press, London, 1950.

6. D. Burton et al., Anisotropic Creation and Closure of Tension Induced Fractures, UCRL-79578, June, 1977.

7. R. P. Swift, J. T. Rambo and J. B. Bryan, The Role of Calculations to Define Containment Phenomenology in Complex Geology, UCRL-92437, October, 1985.

8. D. S. Drumheller, Stress-Wave Calculations of Two Containment Experiments, Proc. Third Symposium on Containment of Underground Nuclear Explosions, Sept. 9-13, 1985, Vol 2, p. 268.

9. S. A. Miller and A. L. Florence, Results of Spherical Wave Experiments in Saturated Indiana Limestone, DNA Report, to be published.

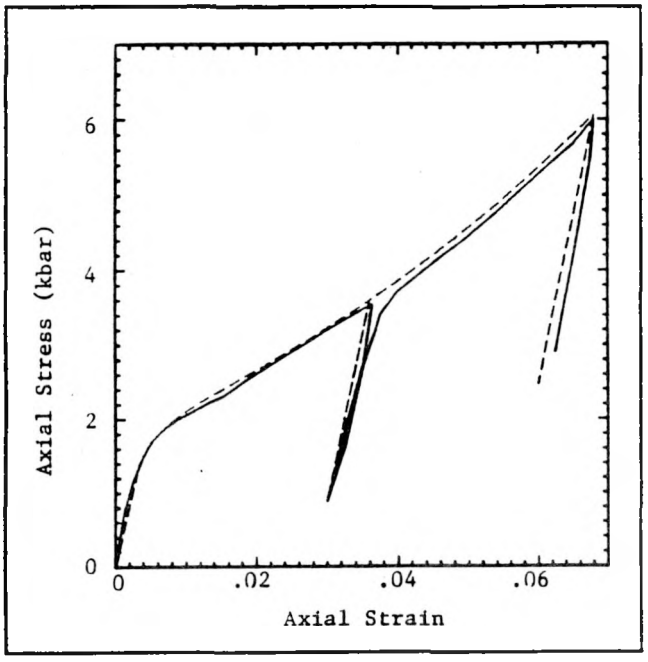


Figure 1: Drained Uniaxial Strain Response for Salem Limestone. Solid - data Ref. 4, Dash - ESM.

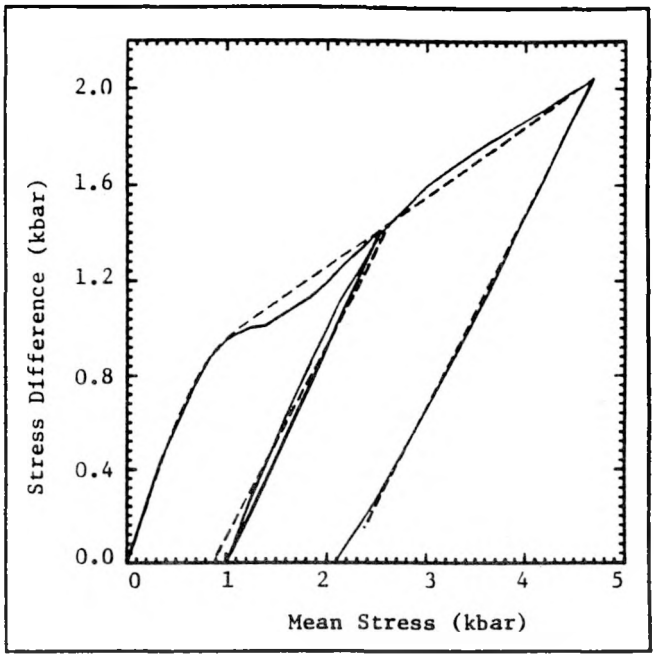


Figure 2: Drained Uniaxial Strain Response for Salem Limestone. Solid - data Ref. 4, Dash - ESM.

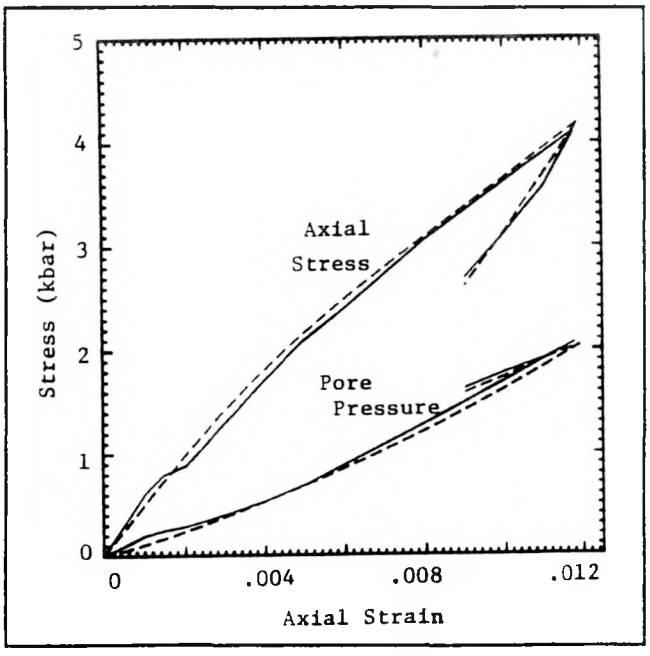


Figure 3: Undrained Uniaxial Strain Response for Salem Limestone. Solid - Data from Ref. 4, Dash - ESM.

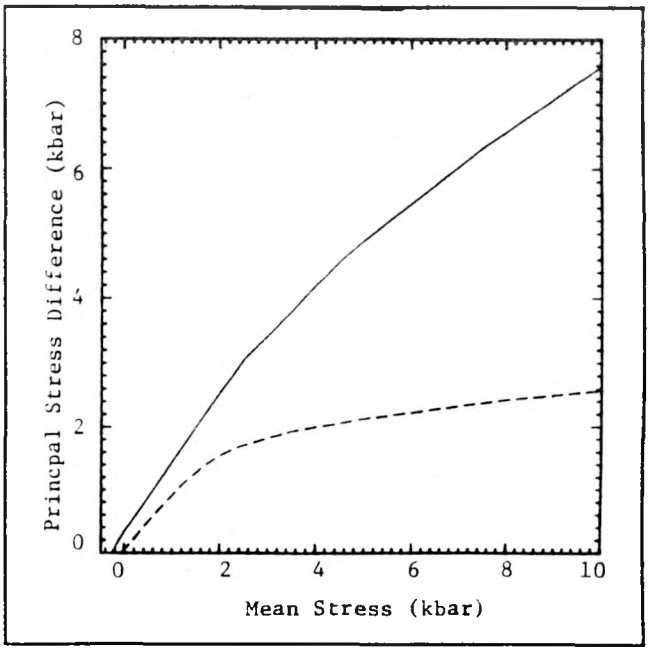


Figure 4: Shear Failure Surfaces for Salem Limestone. Solid-Drained data from Ref. 4, Dash-Undrained Predicted by ESM.

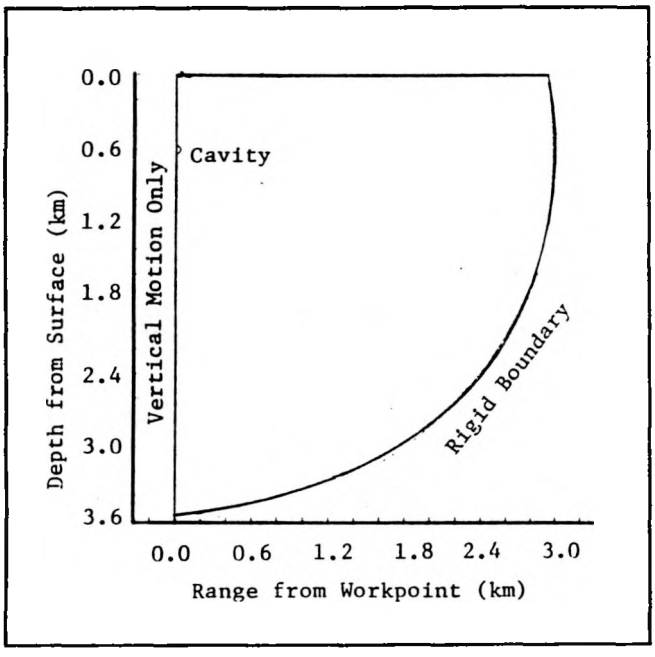


Figure 5: Computational Configuration

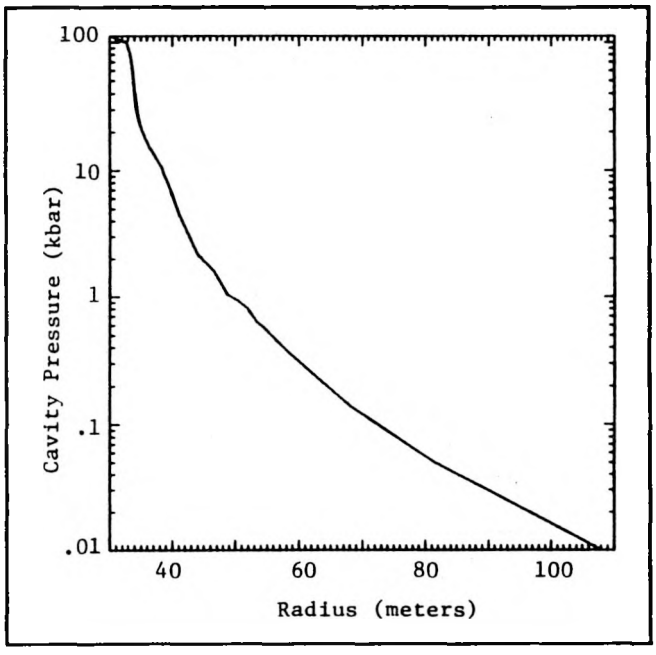


Figure 6: Pressure-Radius Boundary Condition for Cavity

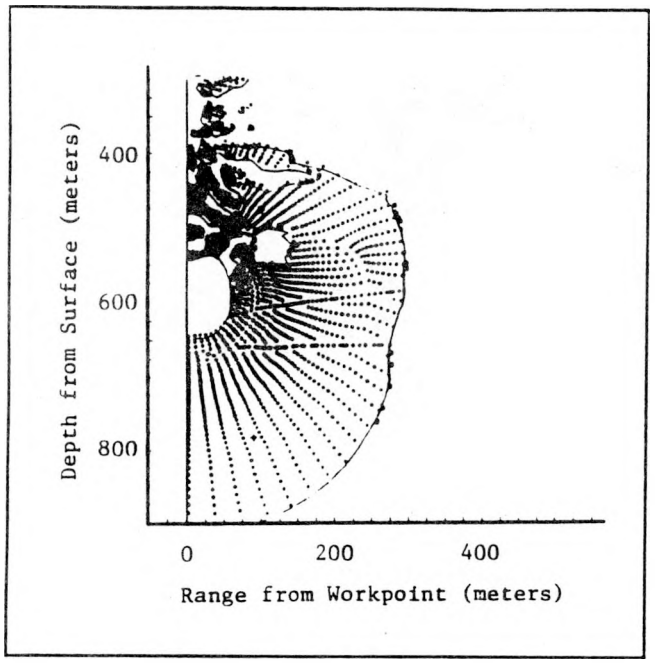


Figure 7: ESM Calculation for Region (shown dotted) where Residual Out-of-Plane Hoop Stress Exceeds Cavity Pressure.

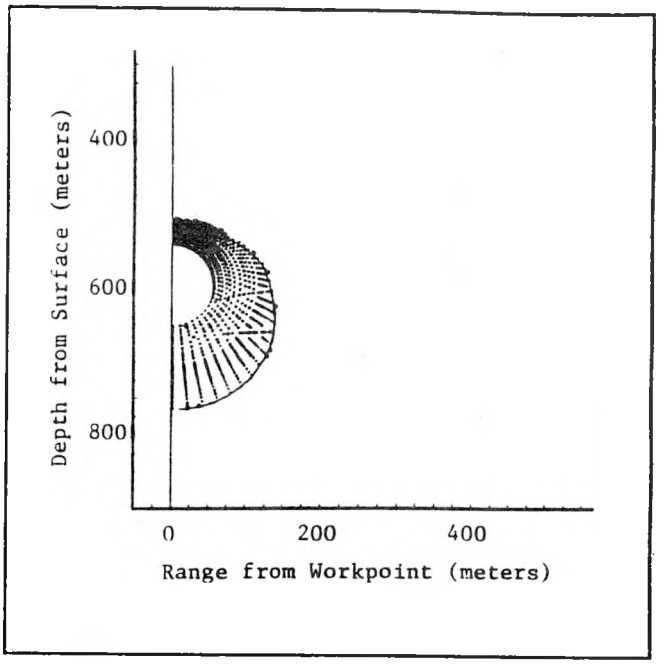


Figure 8: TSM Calculation for Region (shown dotted) where Residual Out-of-Plane Hoop Stress Exceeds Cavity Pressure.

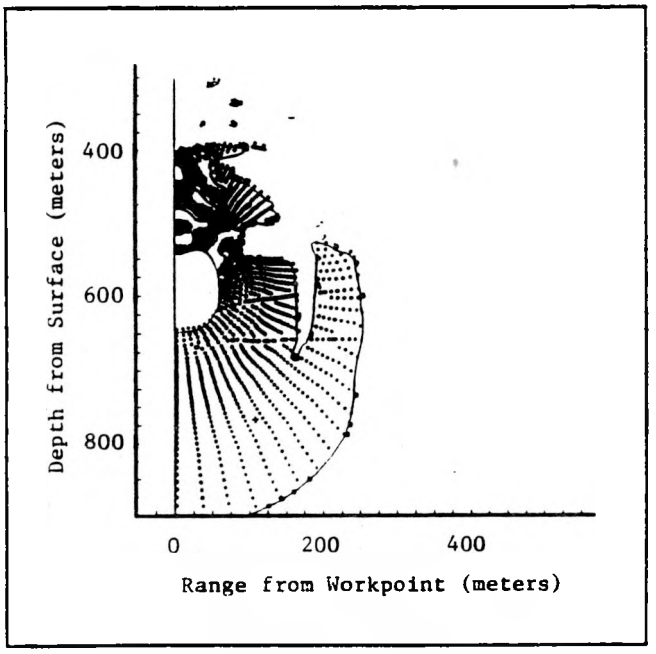


Figure 9: ESM Calculation for Region (shown dotted) where Residual In-Plane Circumferential Stress Exceeds Cavity Pressure.

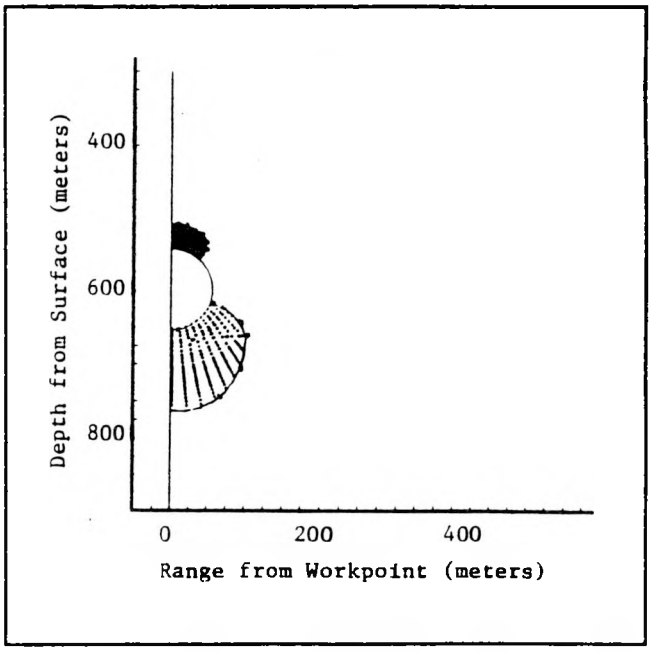


Figure 10: TSM Calculation for Region (Shown Dotted) where Residual In-Plane Circumferential Stress Exceeds Cavity Pressure.

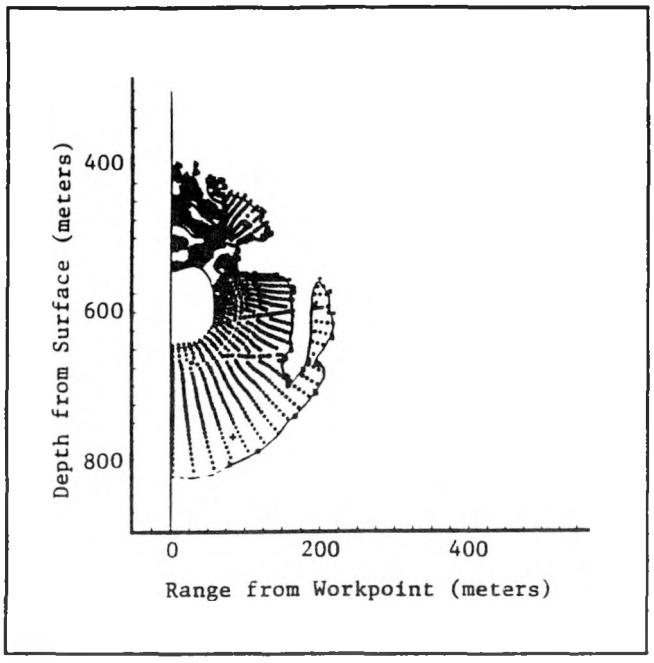


Figure 11: ESM Calculation for Region (shown dotted) Where Water Alone Accounts for Pressure.

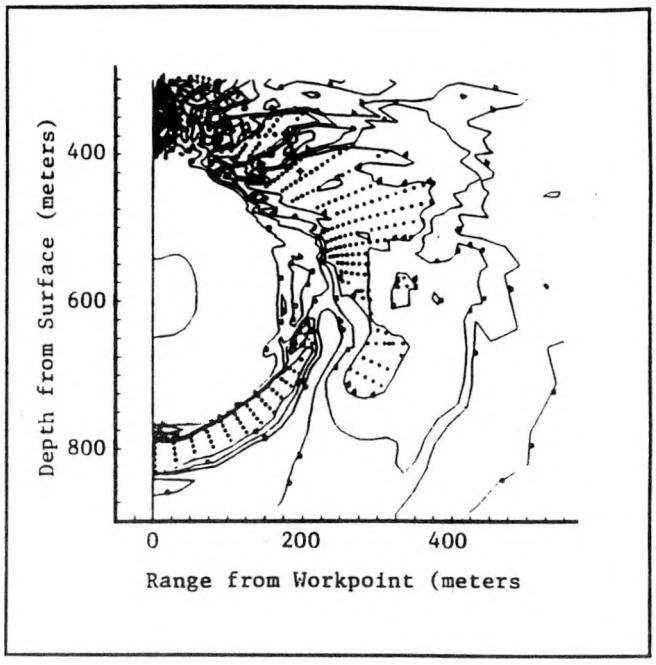


Figure 12: ESM Calculation for Regions of Shear Stress Above Cavity Pressure (dotted) and Below Cavity Pressure (clear).

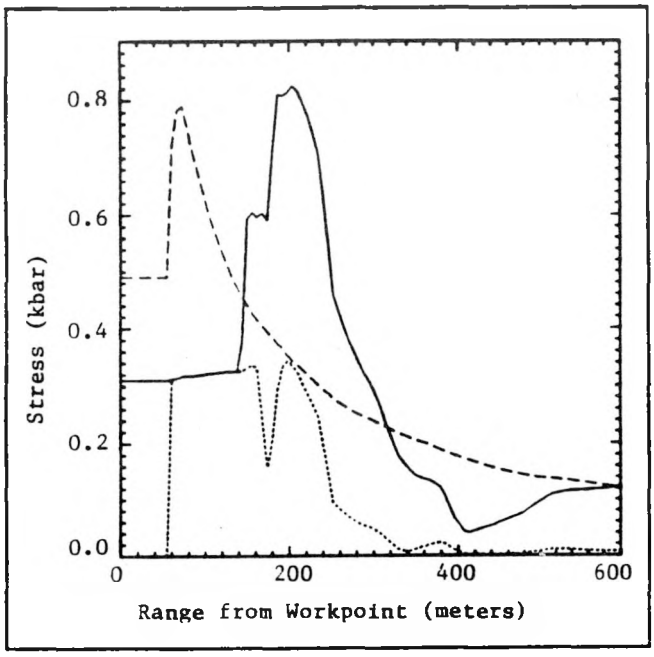


Figure 13: Comparison of Out-of-Plane Hoop Stress in Horizontal Direction. Solid ESM case, Lg. Dash TSM Case, Sm. Dash ESM Pore Pressure.

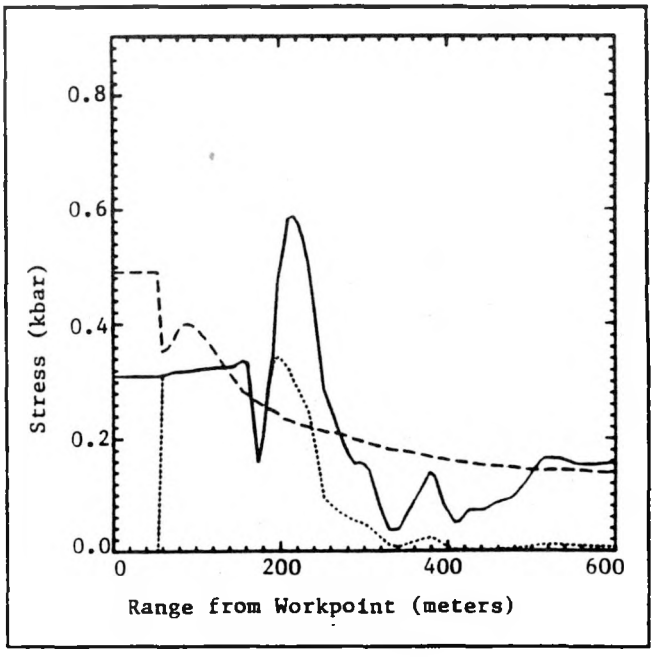


Figure 14: Comparison of In-Plane Circumferential Stress in Horizontal Direction. Solid ESM Case, Lg. Dash TSM Case, and Sm. Dash ESM Pore Pressure.

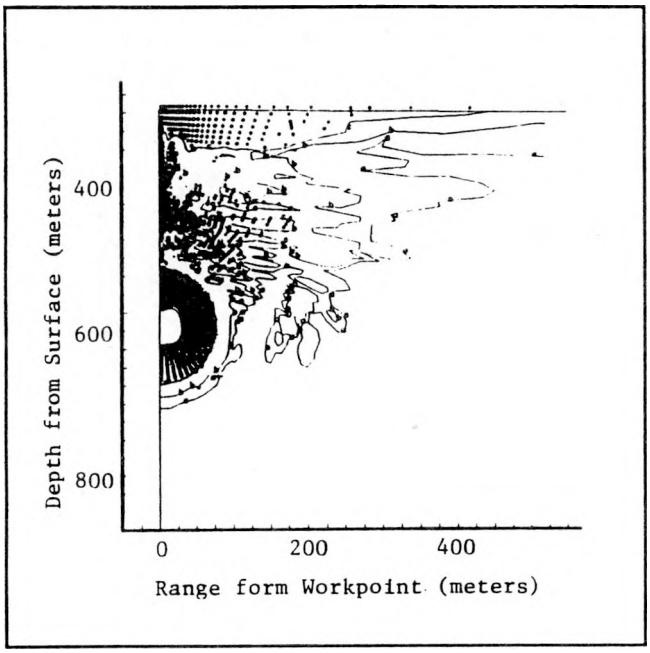


Figure 15: ESM Calculation Showing Tensile Damage with Liquified Regions (shown dotted).

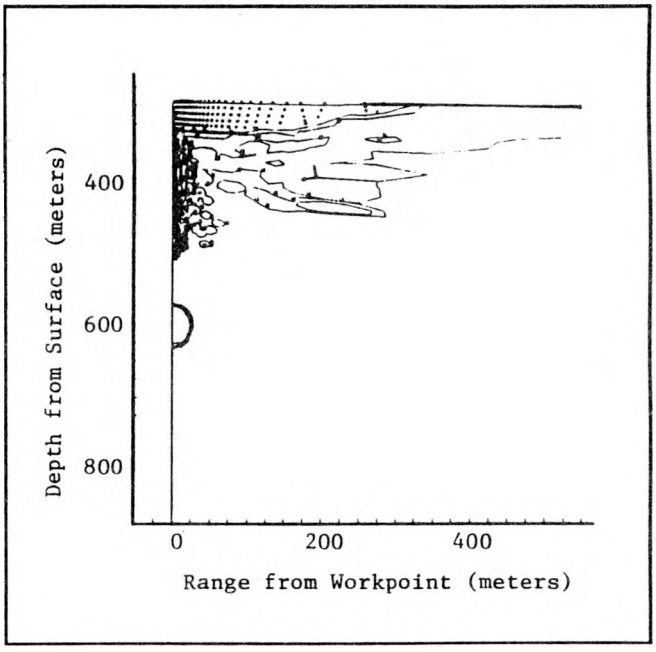


Figure 16: TSM Calculation Showing Pulverized Tensile Damage Region (shown dotted).

RESIDUAL STRESSES CALCULATED USING AN EFFECTIVE STRESS MODEL

A. V. ATTIA and R. P. SWIFT

Lawrence Livermore National Laboratory
P.O. Box 808, L-200, Livermore, CA 94550

ABSTRACT

The effect of water content in saturated porous rocks is of interest in assessing the transient rock response to underground nuclear explosions. The interaction of the water-filled pores with the rock matrix is represented in an "effective stress" constitutive model. Separate equations of state are used for the rock and the water. The effective stress governs the failure response of the rock. Effect of water drainage is assumed to be negligible during early transient response to shock loading of interest. For comparison, a simpler constitutive model is also described. This model represents the saturated porous rock as a homogeneous mixture, using a single equation of state. The associated total homogeneous stress governs the failure response. These models have been incorporated into the 2D explicit finite-element code DYNA-2D. Stress fields around the explosively generated cavity are calculated for a particular event using the "Effective Stress" and the "Total (homogeneous) Stress" models, and results are discussed.

1. INTRODUCTION.

The goal of this work is to evaluate the role of fluid-solid interaction (FSI) in containment phenomena. In an earlier paper[1] , we have described the role of fluid-solid interaction in modeling a small-scale containment experiment, in which a saturated rock matching grout was loaded with a confined high explosive charge.[2] Fluid-solid interaction was introduced through an "Effective Stress Model" (ESM), in which separate equations of state are used to represent the compressibilities of the solid and the water. When a single equation of state is used to represent the solid and water as a homogeneous mixture, the ESM reduces to a "Total (homogeneous) Stress Model" (TSM), in which there is no fluid-solid interaction.

In this paper, we describe the effect of fluid-solid interaction on a full-scale underground explosion for a highly porous (36.7%), fully-saturated rock, similar to the type found in the Barnwell workpoint area. In Section 2, we describe the material region boundary conditions and the cavity driving pressure. The material properties are discussed in Section 3. In Section 4, we compare calculated residual stress fields obtained with and without fluid-solid interaction. In Section 5, we summarize the main impact of FSI on Containment response.

2. STATEMENT OF THE PROBLEM.

We wish to find the residual stress field due to a nuclear explosion 600 meters below the surface. Two calculations will be described: one using ESM (which considers FSI), and one using TSM (which does not consider FSI).

The calculations are performed using the explicit finite-element code DYNA-2D[3], in 2D cylindrically symmetric geometry. Figure 1 shows the computational configuration in the vertical plane. Points on the ground surface are free to move in the the horizontal or vertical directions. Along the axis of symmetry, points are restricted to move vertically only. Along the remaining outer periphery, no motion is allowed at all.

The nuclear explosion itself is represented as follows. A one-dimensional spherically symmetric simulation of the explosion is performed by depositing energy equivalent to the yield of the event into a small region of the rock. As the rock vaporizes, a cavity forms, giving pressure and radius as functions of time. The resulting pressure-radius relation, shown in Figure 2, is then applied as the driving boundary condition at the cavity interior surface, located on the axis of symmetry at 600 m depth, in Figure 1. The initial cavity radius is approximately 30 m, and the initial cavity pressure is thus seen to be about 100 kbar.

3. MATERIAL PROPERTIES.

Tables 1 and 2 show material parameters based on a rock similar to that found in the Barnwell[4] workpoint area.

Table 1

Material Parameters used in ESM	
Solid Density (g/cc)	2.500
Bulk Dry Density (g/cc)	1.583
Total Porosity	0.367
Saturation	1.000
Water Content by Weight	0.188
Poisson's Ratio	0.153

Table 2

Material Parameters used in TSM	
Solid-Water Density (g/cc)	1.950
Air-filled Porosity	0.000
Poisson's Ratio	0.256

Dry shear strength data[4] (50 m above the workpoint) was extrapolated from a mean stress of 2 kbars to 100 kbars, the maximum cavity pressure, using a hyperbolic fit, suggested by Butkovich: [5]

$$Y = (p-p_o)/[A + (p-p_o)/Y^*]$$

where Y is the difference between the maximum and minimum principal stresses, p is the average stress; we chose A = 0.46, p_o = -62.5 bars and Y^* = 11 kbars for best fit to the available data. Figure 3 shows the resulting dry shear strength curve.

Dry compaction data[4] for the 36.7% (drained) porous rock was extrapolated from 6 kbars to 100 kbars, using a logarithmic fit, also suggested by Butkovich.[5] Figure 4 shows the resulting dry compaction characteristics, for the porous material and the fully compacted solid.

Wet shear strength (Fig. 3) and wet compaction (Fig. 4), used as input for the TSM, were predicted from the saturated behavior, using the ESM. There is very little difference between loading and unloading curves for the homogeneous fully saturated material.

Poisson's ratio for the dry rock was determined from measured dry compaction p-V data, giving the elastic bulk modulus, and from measured dilational sound speed.

Poisson's ratio for the wet rock was determined from the linear elastic uniaxial strain response calculated using the ESM with the above dry data as input.

4. RESULTS.

Residual stress fields calculated 1 second after the explosion will now be discussed. Figures 5 and 6 show the in-plane hoop stress fields calculated with and without FSI, respectively. In the dotted region, the stress exceeds the cavity pressure at 1 second, which is 300 bars for both calculations. Neither model predicts a complete residual stress field which exceeds the cavity pressure all around the cavity. However, a broader residual stress field is predicted with the ESM than with the TSM. The out-of-plane hoop stress fields (shown in Figures 7 and 8) show similar differences between the predictions of the models.

To gain a better understanding of this broader residual stress field predicted with FSI, we turn to Figure 9, which shows a region all around the cavity where the total pressure is just the pore water pressure; i.e., the effective pressure vanishes. Consequently, the ESM model predicts no shear strength[1] in this region. Thus, there is a liquefied region which extends more than one cavity radius beyond the cavity itself. This is shown more clearly, in the horizontal direction, in Figure 10. Beyond the cavity itself (at a radius of 60 m), the liquefied region extends approximately 1.5 cavity radii,

Figure 11 shows the large difference between the two models in a horizontal profile of in-plane hoop stress. With FSI, the ESM gives a stress field which extends the cavity pressure and then rises sharply. Without FSI, the TSM shows a radially outward stress field which decreases sharply below the cavity pressure.

Figure 12 shows the difference between the maximum and minimum principal stresses. With FSI, the ESM thus shows no shear stress in the liquefied region, as expected. Beyond this region, the shear stress rises sharply. Without FSI, the TSM shows some shear stress in the region where the ESM predicts liquefaction. Furthermore, the TSM predicts a shear stress which never exceeds the value predicted by the ESM.

These results were obtained using the same geometric configuration and boundary conditions. The two models (ESM and TSM) differ fundamentally[1] in the role of pore water pressure. In the ESM, the compaction of fully-saturated pores reduces the effective pressure, and thus the shear strength. In the TSM, the shear strength depends on the pressure in the homogeneous solid-water mixture; thus, there can be no reduction in shear strength due to pore pressure alone. Consequently, the TSM cannot predict liquefaction, unlike the ESM. Thus, the TSM predicts that the material still shows some shear strength, where the ESM shows that the material has no shear strength at all.

On the other hand, beyond the liquefied region, as the pore water pressure decreases (See Figure 10), the ESM now predicts the material to have a much greater shear strength than the TSM, as can be seen from Figure 12. Now, at sufficiently high pressures, Figure 3 shows that the dry shear strength is certainly higher than the wet (homogeneous) shear strength. This is true even at pressures as low as 300 bars. This explains the large difference in shear strength between the ESM and TSM predictions, just outside the liquefied region.

Another important difference between the ESM and TSM relates to the role of the solid grain pressure. In the TSM, there is only one pressure which is common to the solid and the water, in the homogeneous mixture. In the ESM, the solid pressure can exceed the water pressure, giving rise to the effective pressure[1]. Thus, the ESM predicts greater strength than the TSM, both volumetrically, through the effective pressure, and deviatorically, through the greater dry shear strength. This explains the larger in-plane hoop stress predicted by the ESM than by the TSM (Figure 11).

5. CONCLUSIONS.

Fluid-solid interaction plays an important role in calculating the residual stress field in the containment of underground nuclear explosions performed in saturated tuffs. By considering fluid-solid interaction, we find:

1) a broader and stronger residual stress field that exceeds the cavity pressure,

2) a liquefied region around the cavity,

3) a stronger residual shear stress beyond the liquefied region.

Further work is indicated to verify the phenomena predicted, when fluid-solid interaction is considered. One candidate experiment being considered is the ONETON[6] experiment, which was performed in 33% porous ashfall tuff, 98.2% saturated. Experimental data is available for hoop stress, radial stress, and particle velocity.

6. ACKNOWLEDGEMENTS.

We are grateful to J.T. Rambo and W. Durham for their assistance in making available the experimental data for material properties. Work performed under the auspices of the U.S. Department of Energy by the Lawrence Livermore National Laboratory under Contract W-7405-ENG-48.

7. REFERENCES.

1. A. V. Attia, Numerical Simulation of Shock Response of Fluid-Filled Porous Rocks, Proc. Amer. Phys. Soc. Top. Conf. on Shock Waves in Condensed Matter, Albuquerque, New Mexico, 14-17 August 1989, in press.

2. J. C. Cizek and A.L. Florence, Laboratory Investigation of Containment of Underground Explosions, Defense Nuclear Agency, DNA-TR-82-83, December 1982.

3. J.O. Hallquist, User's Manual for DYNA-2D, an Explicit Two-Dimensional Hydrodynamic Finite Element Code with Interactive Rezoning and Graphical Display, UCID-18756, Rev. 3, February 1987.

4. W. Durham, Barnwell and Nash Rock Mechanics Tests: Samples Preparation and Experimental Procedures, LLNL Internal Memorandum, September 5, 1989.

5. T. R. Butkovich, A Technique for Generating Pressure-Volume Relationships and Failure Envelopes for Rocks, UCRL-51441, November, 1973.

6. D.S. Drumheller, Stress-Wave Calculations of Two Containment Experiments, Proc. Third Symposium on Containment of Underground Nuclear Explosions, Sept 9-13 1985, Vol. 2, p.268.

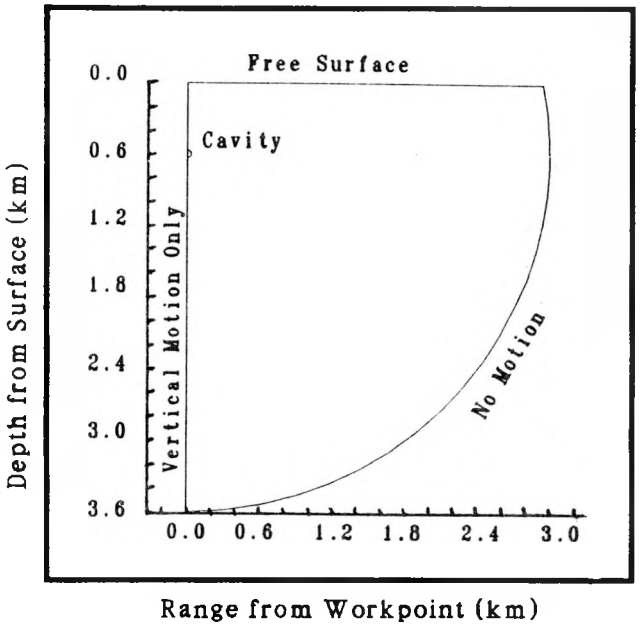


Figure 1: Computational Configuration With Boundary Conditions

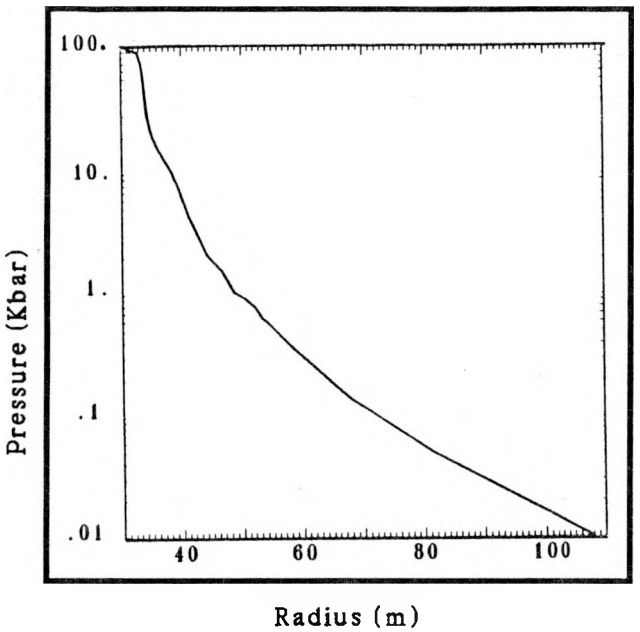


Figure 2: Exploding Cavity Pressure-Radius Relation

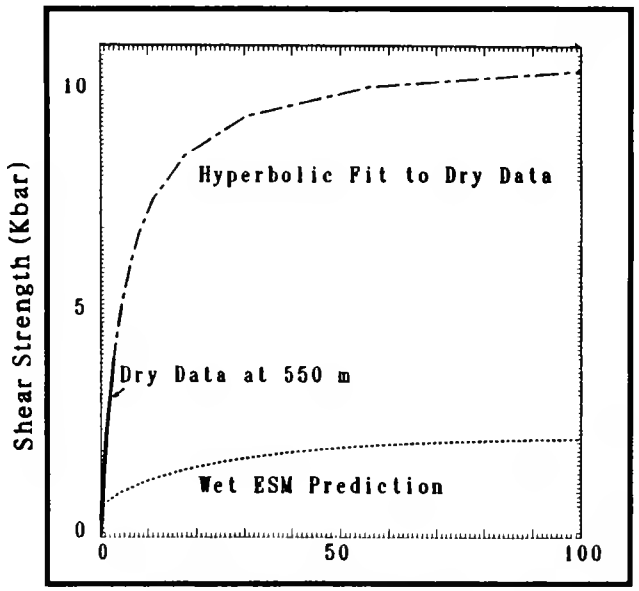


Figure 3: Shear Strengths For Workpoint Material

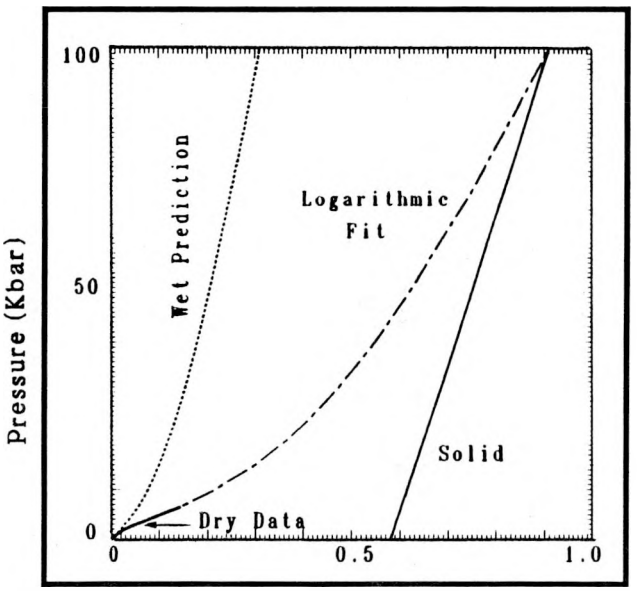


Figure 4: Compaction Characteristics

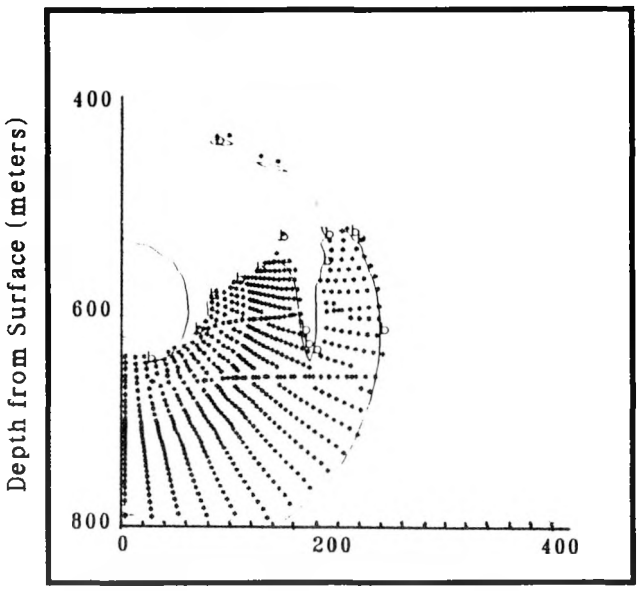


Figure 5: ESM Calculation for Region (shown dotted) Where Residual In-Plane Hoop Stress Exceeds Cavity Pressure

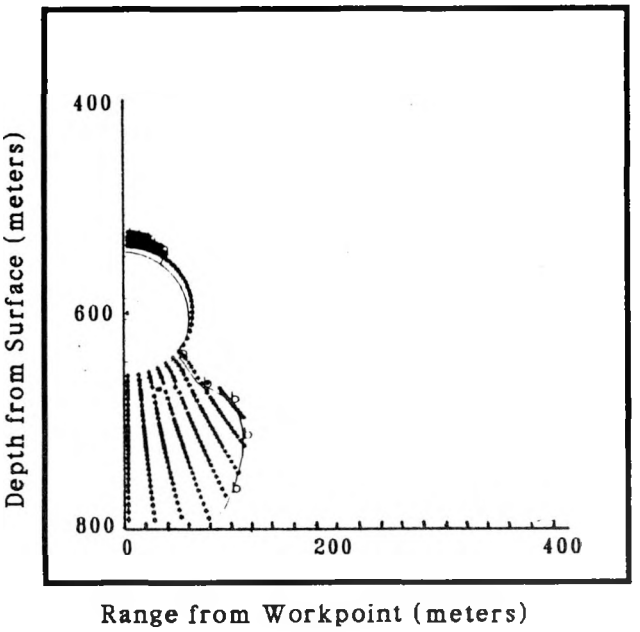


Figure 6: TSM Calculation for Region (shown dotted) Where Residual In-Plane Hoop Stress Exceeds Cavity Pressure

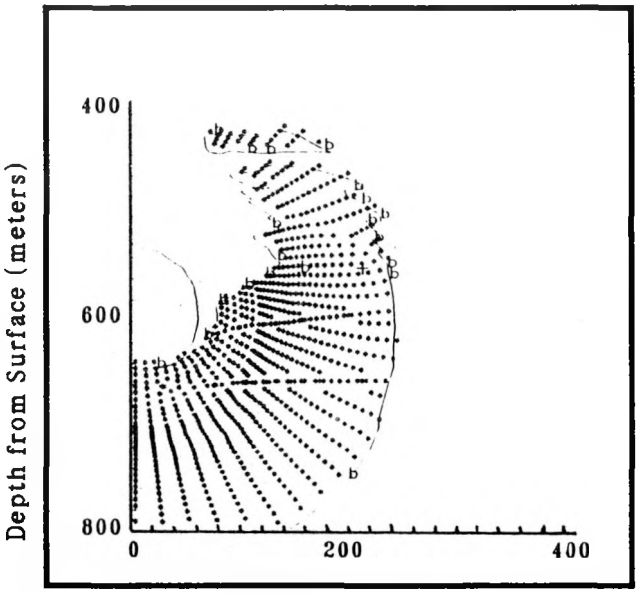


Figure 7: ESM Calculation for Region (shown dotted) Where Residual Out-of-Plane Hoop Stress Exceeds Cavity Pressure

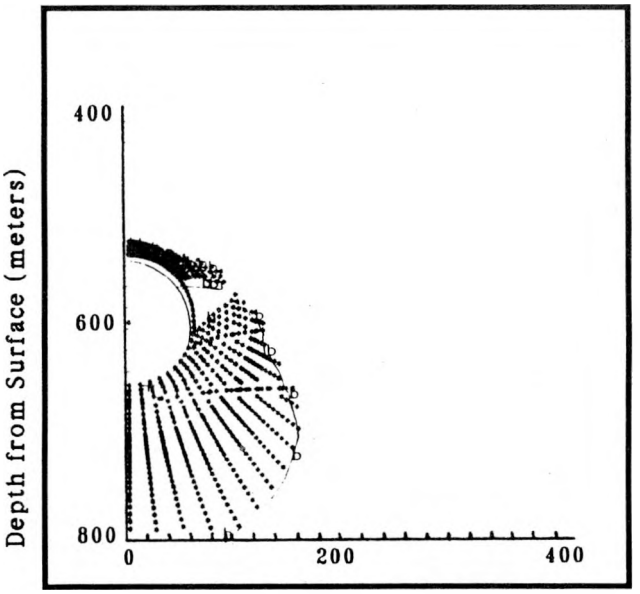


Figure 8: TSM Calculation for Region (shown dotted) Where Residual Out-of-Plane Hoop Stress Exceeds Cavity Pressure

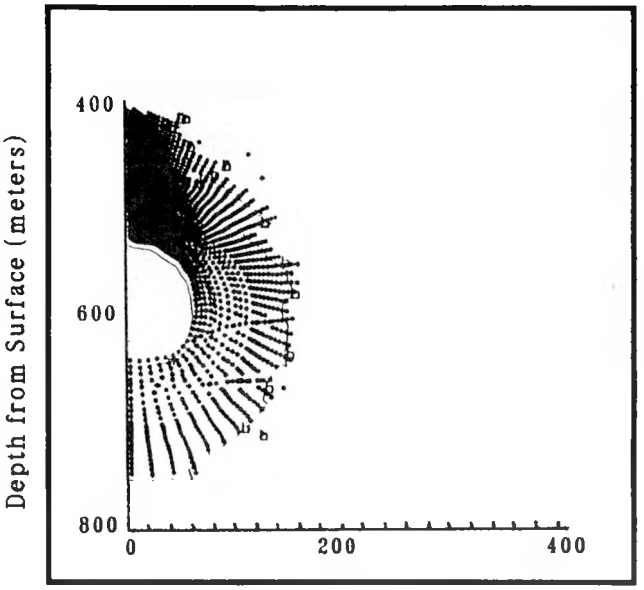


Figure 9: ESM Calculation for Region (shown dotted) Where Water Alone Accounts for Pressure

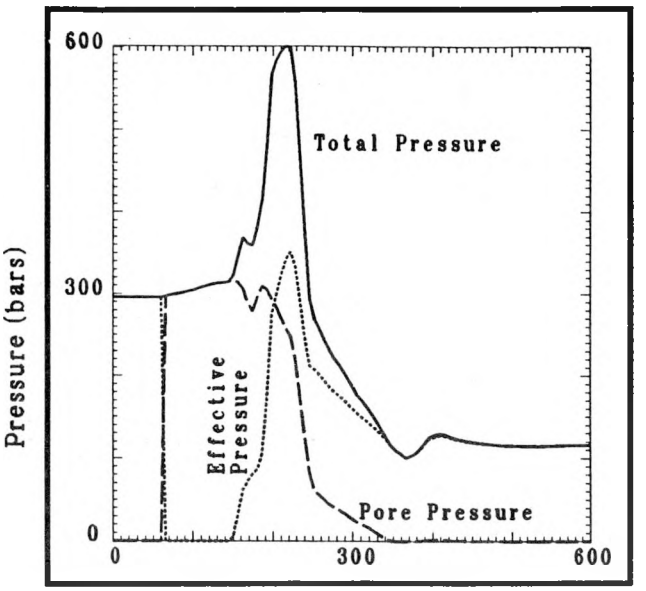


Figure 10: Horizontal Residual Pressure Profiles Calculated by ESM at Workpoint Level

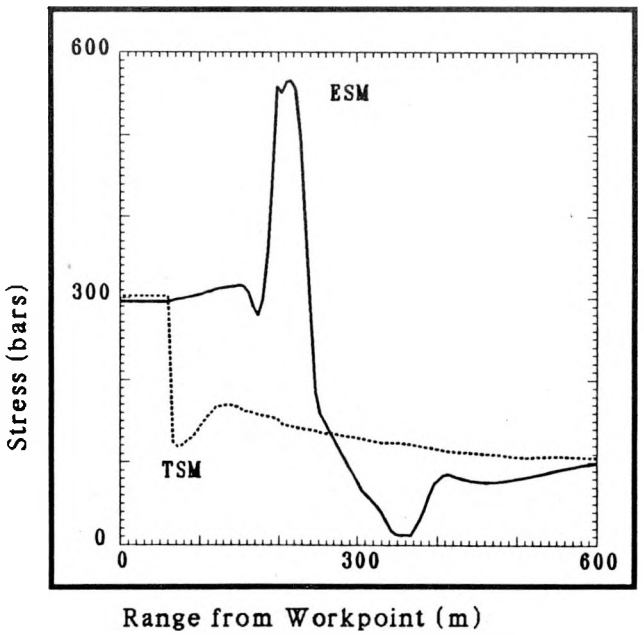


Figure 11: Horizontal Residual Profile of In-Plane Hoop Stress at Workpoint Level

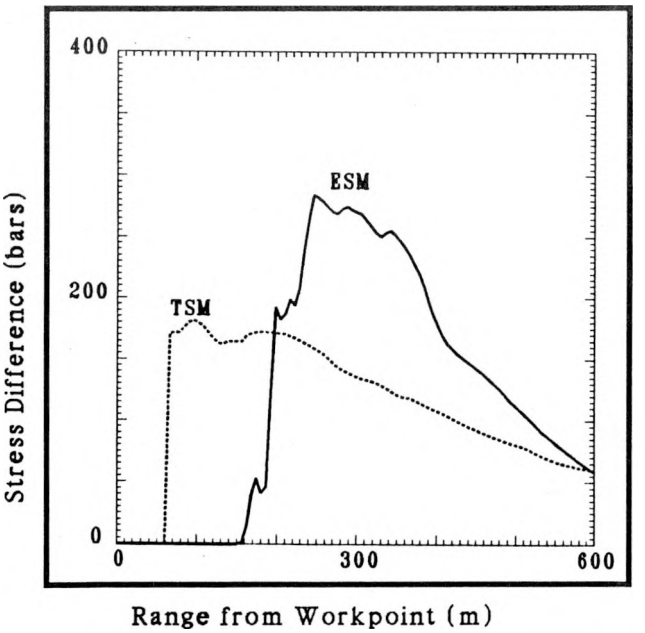


Figure 12: Horizontal Residual Profile of Difference between Maximum and Minimum Principal Stresses at Workpoint Level

SENSITIVITY OF THE RESIDUAL STRESS FIELD TO VARIATION OF THE STRENGTHS FOR A WEAK LAYER OVERLAYING A STRONG WORKING POINT LAYER*

H. D. Glenn and J. T. Rambo

ABSTRACT

A parameter study using the two-dimensional TENSOR code examines the sensitivity of the residual stress field around the cavity created by an underground nuclear explosion when the shear strengths were varied for: a strong layer containing the WP and a weaker overlaying layer. The baseline calculation used materials similar to those encountered in Area 20 of the Nevada Test Site (NTS). To provide a quantitative basis for comparing the effect of the calculated residual stress fields, a product factor is introduced that combines the magnitude and thickness of the residual stress field relative to cavity size and pressure. This product factor is useful in parameter studies for comparing levels of residual stress field, and is a supplement to other judgment factors which are considered in calculational site evaluations for containment purpose. Calculational results indicate generally stronger hoop stress along the horizontal than the vertical direction. This reflects the fact the weaker material above the cavity tends to degrade hoop stress in that direction. The magnitude of the hoop stress above the cavity generally increases as the strength of the upper material increases from 2 to 20 MPa. However, the magnitude of the hoop stress decreases, when the strength of working point material increases from 17 to 68 MPa. This is due to the smaller cavity radius and higher resulting cavity pressure in combination with a characteristic lower residual stress in the weak upper material.

---

*Work performed under the auspices of the U. S. Department of Energy by the Lawrence Livermore National Laboratory under Contract W-7405-Eng-48.

INTRODUCTION

Previous numerical simulation studies of underground nuclear explosions have identified the surrounding media shear strengths as the predominant factor controlling the cavity radius and subsequent formation of the residual tangential stress field surrounding the final cavity.[1-5] The strength of the rock within one to four cavity radii controls cavity growth and ultimate magnitude of the residual tangential stress field around the cavity. The presence of a strong residual stress region surrounding the cavity is an explanation of the excellent containment history in preventing the escape of cavity gas through the geologic structure for hundreds of underground nuclear tests conducted at the Nevada Test Site (NTS).

Presently, numerical simulations of scheduled underground nuclear events primarily depend upon correlating different layers to similar layers of previous events for which strength estimates were made. For about 10% of recent events calculated, laboratory strength tests on borehole cores or sidewall samples have been conducted to provide estimates of media response to shock propagations. However, there always exists differences in the physical properties (e.g., density, saturation, etc.) in such correlation between layers on different events to question the validity of such assumptions. The primary objective of the present parameter study was to make changes in the assumed material shear strengths of the two layers in the vicinity of the WP to provide a quantitative basis to judge the sensitivity to shear strength of the resultant tangential stress field surrounding the cavity.

The next section describes the TENSOR two-dimensional finite difference code, and an example geologic cross-section used in the parameter study. It also includes a description of the material models used in the numerical calculations. In the following section the calculational results will be presented. The last section provides a summary of this parameter study.

COMPUTATIONAL MODEL

This parameter study was conducted using the two-dimensional version of the TENSOR code.[6,7] The TENSOR code utilizes finite difference equations of continuum mechanics to simulate stress-wave propagation induced by an explosive source. The rock constitutive models in the codes, for the different geologic layers, take in account: rock vaporization and melting, pore collapse, ductile and brittle failure, and tensile failure with crack opening and closure. Confidence in TENSOR simulation studies has been achieved by comparing calculational results with experimental results for a broad range of high-explosive[8,9] and nuclear explosive[10-12] tests over the last couple of decades.

The following parameter study was conducted for a working point (WP) at a depth of 644.7-m in hole U20ar at NTS. This location corresponds to one of the alternate WP's chosen to examine the sensitivity of the tangential stress field surrounding the final cavity when we lowered the WP location from a weak to an underlying strong layer for a specific site.[13] This configuration was chosen because it has been calculationally shown[5] that, for certain material strengths, a weak residual stress field has been observed. This study[13] was based on an early version of the site characterization[14] illustrated in Figure 1 and Table 1. Figure 2 shows the numerical model used by TENSOR to simulate the shock phenomenology following the nuclear explosion. The numerical model chosen used the Z-axis (vertical) through the emplacement hole as the axis of symmetry to reduce the problem to a two-dimensional cylindrical geometry. This represents a reasonable assumption since the geologic layers are horizontal. In addition, zoning was provided to model the stemming in the emplacement hole for all the calculations conducted for the parameter study.

The parameter study consisted in varying only the material strengths for two layers in the vicinity of the WP. The layers of interest are the saturated Rhyolite layer in which the WP is located and the Tuff layer immediately above the Rhyolite. The layer strengths used are typical of Rhyolites and Tuffs. Table 2 presents the values assigned in the

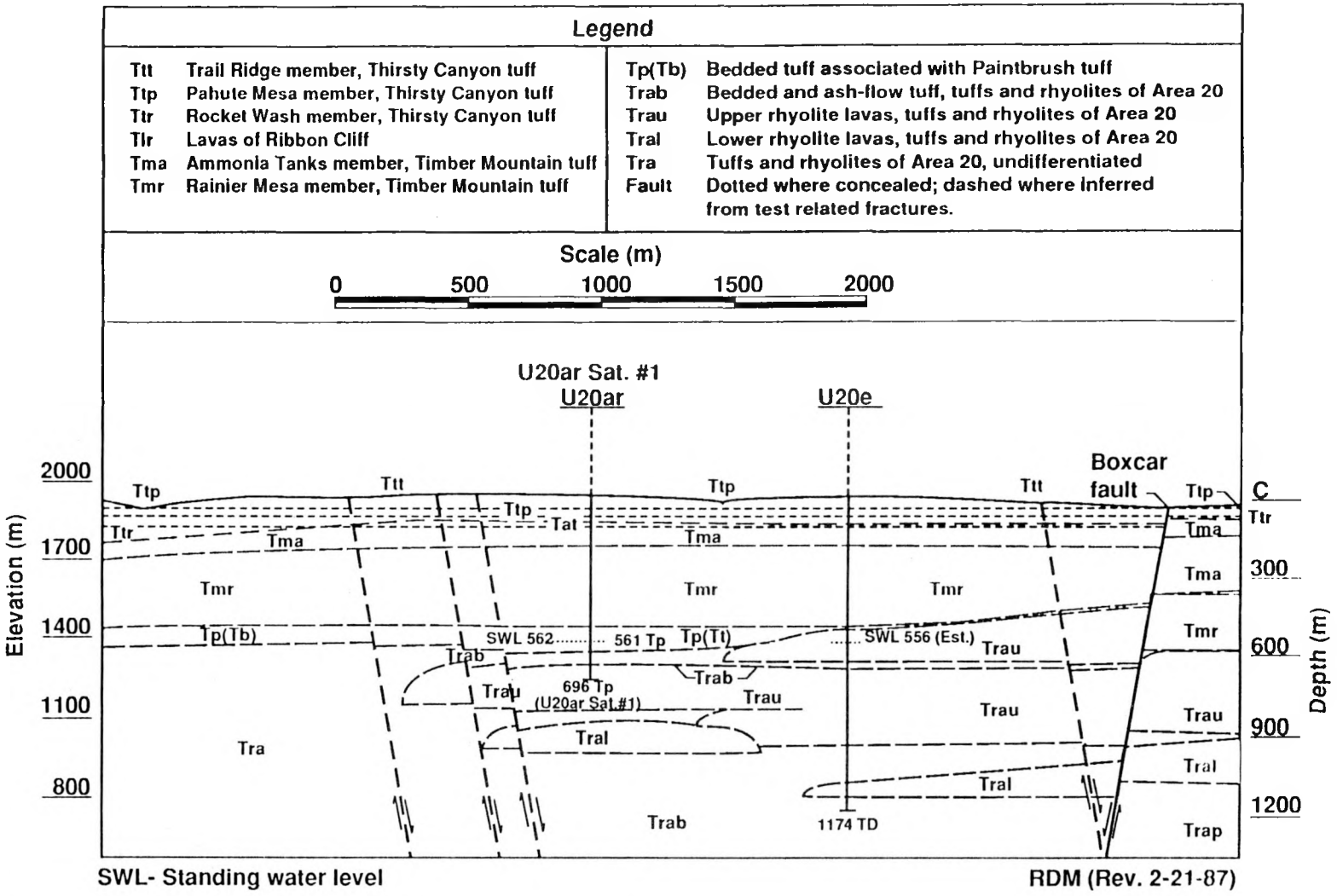


Figure 1. Geologic cross section through U20ar

Table 1.

Averaged material and strength properties for U20ar.

Material #	Depth Metres	Range Metres	H_2O^m Wt%	$\rho_o{}^m$ Mg/m^3	$\rho_g{}^m$ Mg/m^3	ϕ %	S %	ψ %	Poisson's Ratio	Velocity^m m/sec	P_T MPa	Max. Shear St. MPa	Unconfined Compressive Strength (MPa)
Ttt	0	644.7	7.1	2.01	2.59	28.0	51.1	13.7	.25	1129	21.4	21.4	12.84
57	20	624.7											
Tma, Tb	20	624.7	12.3	1.48	2.61	51.0	36.5	32.5	.2	1198	4.34	16.7	3.26
56	140	504.7											
Lower Tma	140	504.7	7.59	1.89	2.59	32.6	44.0	18.2	.25	2013	14.6	28.1	8.76
55	170	474.7											
Tb	170	474.7	18.9	1.54	2.57	51.4	56.7	22.3	.2	1607	6.4	10.2	4.8
54	200	444.7											
Upper Tmr	200	444.7	3.8	2.17	2.58	19.7	45.9	10.7	.27	2680	138.0	700.0	68.0
53	400	244.7											
Lower Tmr, Vlt	400	244.7	3.6	2.28	2.55	15.1	59.6	6.3	.27	3868	190.0^m	700.0	93.0^m
52	460	184.7											
Tb	460	184.7	17.5	1.64	2.44	44.6	64.2	16.0	.2	1864	6.0	336.9	0.0^m
51	563.9	80.8											
Saturated Rhyolite	563.9	80.8	5.79	2.22	2.40	12.8	100.	0.0	.30	2856	138.0^m	700.0	68.0^m
60	6000	5888.7											

^{m}Measured

Where: ρ_o = bulk density, ρ_g = grain density, ϕ = total porosity, ψ = gas porosity and P_T = elastic limit.

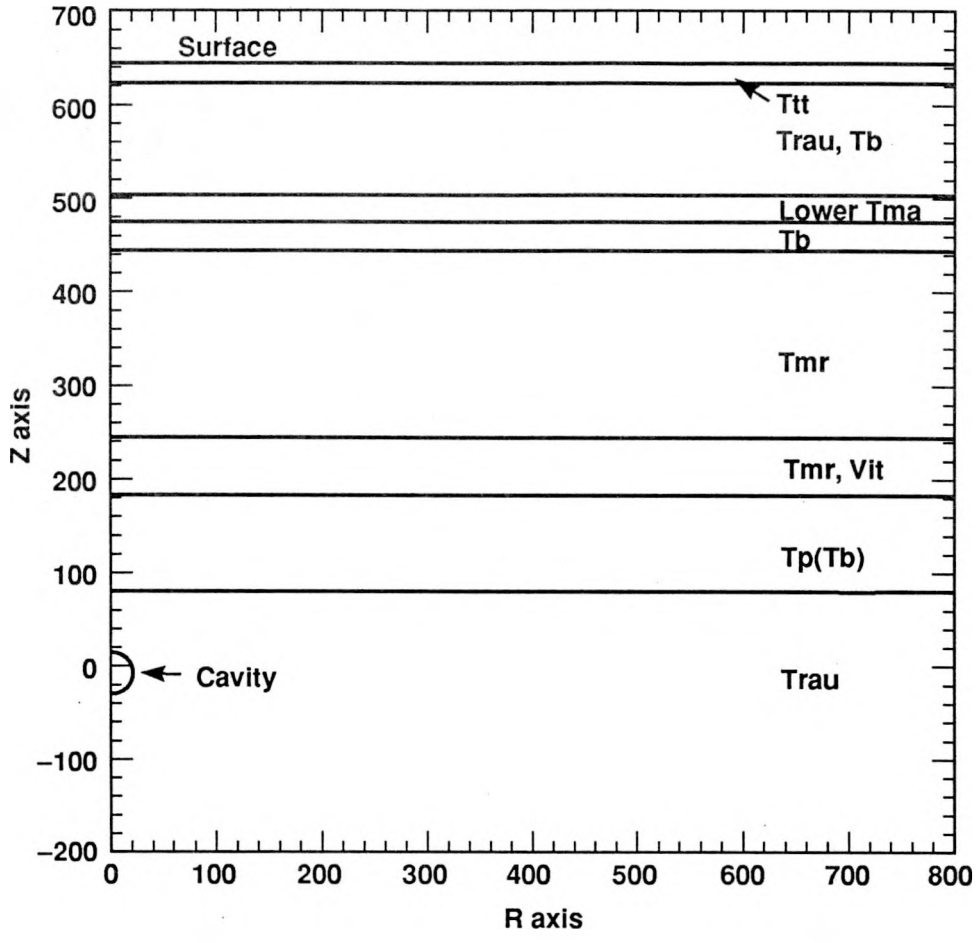


Figure 2. Idealized geologic cross-section at U20ar for numerical modeling with TENSOR.

Table 2.

TENSOR simulation study showing strength parameters varied for the Tuff and Rhyolite layers identified in Table 1 as Materials 51 and 60, respectively.

Problem ID	Layer	τ_{uc} (MPa)	τ_m (MPa)	P_T (MPa)	G_{por} (%)
	RHYOLITE	17	175	34.5	0
AJHPA	TUFF	2	8	3	16
AJHA1	TUFF	5	20	7.5	16
AJHPD	TUFF	20	80	30	16
	RHYOLITE	34	350	69	0
AJHPE	TUFF	2	8	3	16
AJHE1	TUFF	5	20	7.5	16
AJHE2	TUFF	10	40	15	16
AJHPG	TUFF	20	80	30	16
	RHYOLITE	51	525	103.5	0
AJHH1	TUFF	2	8	3	16
AJHH2	TUFF	5	20	7.5	16
AJHH3	TUFF	10	40	15	16
AJHH4	TUFF	20	80	30	16
	RHYOLITE	68	700	138	0
AJHPI	TUFF	2	8	3	16
AJHI1	TUFF	5	20	7.5	16
AJHI2	TUFF	10	40	15	16
AJHPK	TUFF	20	80	30	16
AJHK1	TUFF	30	120	45	16

16 parametric calculations to the unconfined shear strength (τ_{uc}), the maximum shear strength (τ_m), and the elastic limit (P_T). The Rhyolite was assumed to be saturated (i.e., ψ set to zero), and the Tuff was assumed to have a constant value of 16% gas-filled porosity (ψ). The tensile strength for Tuff was set to zero while the corresponding values for Rhyolite were based on an earlier study done with JORUM Rhyolites.[15] The brittle-ductile failure points were determined assuming a slope of 0.5 for tau versus mean pressure from the origin for both the Tuff and Rhyolite damage models.[16] The values for τ_m correspond to a pressure of 100 GPA. The fact that τ_m exceeds τ_{uc} by a factor of four results in a small constant positive slope for the shear strength curves between the brittle-ductile failure points and corresponding τ_m values at a pressure of 100 GPa. The range of shear strengths (2 to 30 MPa) used for the Tuff parameter study is a reasonable range for NTS Tuffs[2] and brackets the measured value[17] of 18 MPa for material from this layer. An example of specific values used for material strengths are given in Appendix A.

CALCULATIONAL RESULTS

For the orientation of the reader, we present a brief chronological description of the dynamic phenomenology following an underground nuclear explosion. We will then present only those results of the present calculational study that highlight features interesting from the standpoint of evaluating the residual hoop stresses around the cavity.

General Phenomenology

The energy (W) released by a nuclear explosion vaporizes the geologic medium in the vicinity of the WP. If 11.72 MJ/Kg (2800 cal/gm) is assumed[18] to be the energy required to totally vaporize a geologic medium composed of SiO_2-H_2O mixtures, then the vaporization radius for a medium with an in situ density of approximately 2.1 Mg/m^3 will be 2.0 $m/kt^{1/3}$. In typical geologic media the cavity expansion achieves its full size of 11 to 16 $m/kt^{1/3}$ within a scaled time of 60 to 100 $ms/kt^{1/3}$.

Initially, the shock pressures in the vaporized rock are sufficient to produce a melt region followed by a region of crushed and/or fractured rock that extends for three to five cavity radii. Beyond the close-in fracture region the shock amplitude decays below the elastic limit of the geologic media and the shock propagates elastically at sonic velocities.

As the spherically divergent shock wave crosses geologic layers, the impedance differences result in shear, compressive, or tensile waves being propagated back toward the WP. That portion of the spherical wave propagating in the direction of the surface may produce significant ground motion generally decreasing in magnitude with increasing horizontal distance from surface ground zero (SGZ). This mounding effect can generate radial cracking due to divergence of the medium near the surface. In addition, the incident compressive wave when reflected from the surface will induce tangential cracking, i.e., spall,[19] as it propagates as a tensile wave back toward the WP. The above two shock phenomena may generate a highly fractured region that extends to a considerable depth below the surface. The total depth depends upon the duration and magnitude of the radially divergent shock wave.[19]

During the above processes, the region around the cavity has rebounded and depending on the shear strengths, may form a strong tangential stress field around the cavity to confine the cavity gases. If the tangential stresses above the cavity are strong enough, they will withstand the returning tensile wave from the surface and other subsurface layers. The above scenario can essentially be applied to any underground explosion, and detailed analyses of the shock phenomenology have been used in the past to explain the calculated residual tangential stress field surrounding the cavity.[1,4,20] However, due to the large number (16) of TENSOR calculations performed in this parameter study (Table 2), a detailed analysis of each problem is not feasible. Instead, we have adopted the approach of accepting the residual tangential field at 800 ms as being representative of the final configuration (i.e., we assume dynamic motions after this time would not significantly alter the results).

Analysis of the Residual Stress Fields

Isometric plots of Neg T_3 (out of plane hoop stress) for the 16 calculations at 800 ms are given in Appendix B. Reference to Appendix B during the course of the following analysis will provide the reader with a three-dimensional picture to aid in a broader understanding. Although the isometric plots provide a clear qualitative perspective of the sensitivity of residual stress field around the cavity to varying strengths of the Rhyolite and Tuff layers, they are not very amenable to quantitative analysis. The Neg TTAN (in plane hoop stress) isometric plots are not shown, but were in essential agreement with the Neg T_3 isometric plots for region above the cavity.

To provide a basis for a more quantitative analysis, we have obtained the stress field along three separate plot axes starting from the WP. The first axis starts at the WP and extends horizontally into the Rhyolite layer. The second axis extends from the WP to the surface at an angle of 88° with respect to the horizontal plane. For sake of brevity we will denote this axis as "vertical", although in reality it is 2° off the vertical and in the media above the cavity. To highlight weakness of the residual stress field, the third axis is at one metre radius, but parallel with the vertical symmetry axis through the WP, extends vertically through the emplacement hole from the WP depth, and passes through the stemming materials to the surface. Again, for brevity, we will denote this axis as the stemming axis. Each of these axes constitute the abscissa of a two dimensional plot with the values of Neg T_3 as the ordinate.

Before proceeding further, consider a generic plot of an idealized residual stress field to establish some useful nomenclature. Figure 3 illustrates a classic hoop stress[1,11] along some arbitrary radial axis extending from the WP. In this idealized case the hoop stress exceeds the cavity pressure (C_p) out to a distance of two cavity radii (R_c). This was the second of the original five criteria[1] cited for a "strong" tangential stress field around the cavity at late times (i.e., following the end of the dynamic phase[11,20]). The peak tangential stress (σ_T) shown in Figure 3 has twice

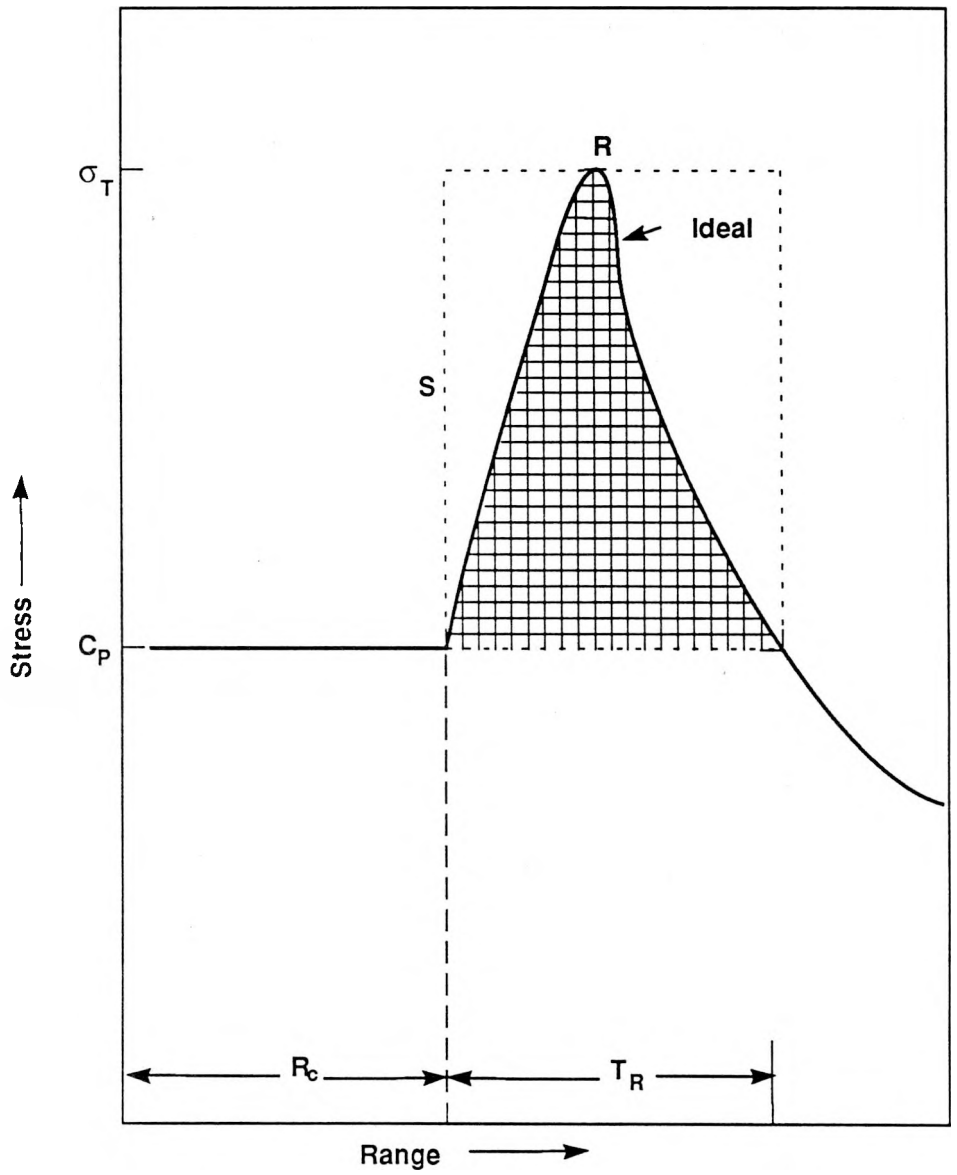


Figure 3. An idealized stress state surrounding the cavity. (C_P is cavity pressure; σ_T is peak tangential stress; R_C is cavity radius; and T_R is thickness of stress region exceeding cavity pressure.)

the magnitude of C_p. This is an arbitrary choice at this time and is primarily based on a very conservative stance that future studies may definitely lower. If we define the following ratios for the ordinate (S) and abscissa (R) as follows:

$$S = \frac{\sigma_T - C_p}{C_p} \tag{1}$$

and

$$R = \frac{T_R}{R_c} . \tag{2}$$

Then for the ideal residual stress conditions we have imposed in Figure 3, the product (P) of these two ratios is

$$P = S \bullet R = 1. \tag{3}$$

In the S and R space defined by the dotted lines in Fig. 3, we can see that the shaded area under the residual stress curve that exceeds C_p corresponds closer to a value of 0.5 than above value of one shown in Equation (3). Generally speaking the residual stress fields in the final analysis of the 16 parameter calculations will have shapes with areas that equal or exceed the shaded area (i.e., >0.5) shown in Fig. 3 for the ideal stress profile in S and R space. Thus to provide a reasonable approach for application we will arbitrarily relax the requirement set in Fig. 3 to where $P \geq 0.5$ should still provide a adequate residual stress field for containment of cavity gases. This choice is partially based on the desire to develop a more practical method and avoid the arduous task of determining the area under the residual stress field that exceeds the cavity pressure for each profile obtained in S and R space.

With establishment of the above nomenclature we can proceed with the analysis of the calculational results for the 16 parameter TENSOR calculations by examining the corresponding product (Eq. (3)) for the horizontal (P_H), vertical (P_V), and stemming (P_S) axes for Neg T_3. Figures 4, 5, and 6 present these results versus the Tuff unconfined compressive strength (τ_{UC}), where the values plotted for τ_{UC} are given in Table 2. The

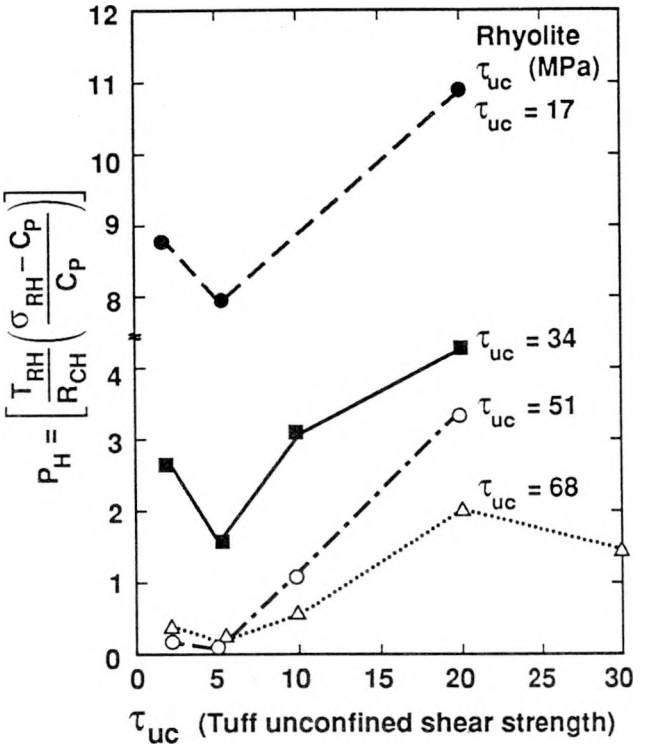


Figure 4. Horizontal product factor (P_H) versus τ_{uc} for tuff.

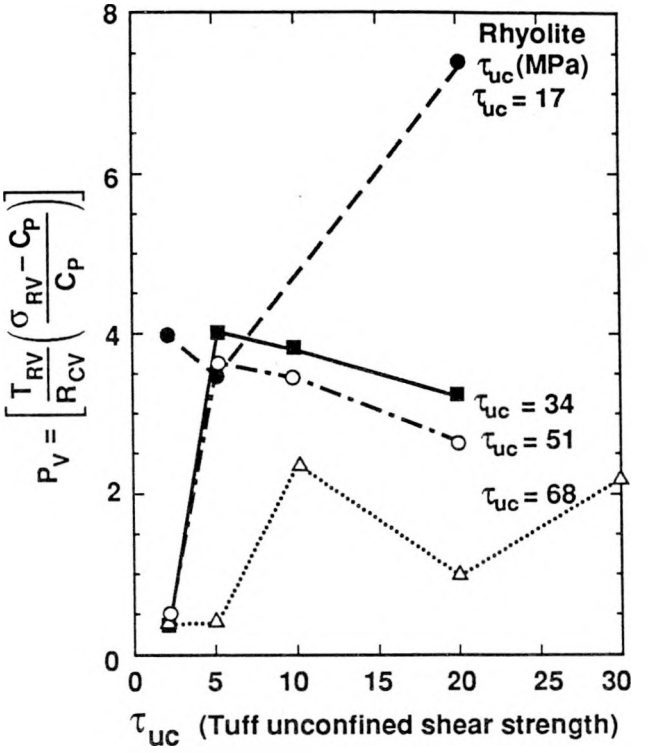


Figure 5. Vertical product factor (P_V) versus τ_{uc} for tuff.

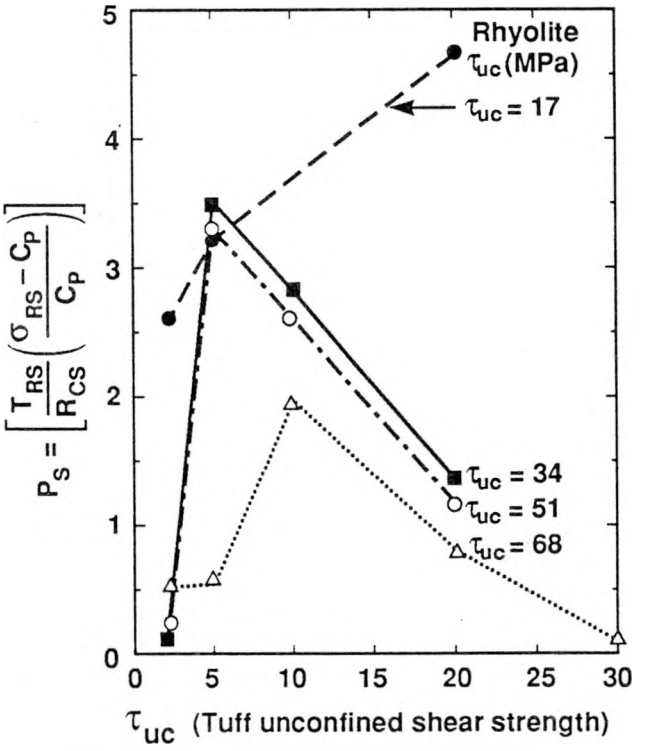


Figure 6. Stemming product factor (P_S) versus τ_{uc} for tuff.

four curves in each figure correspond to Rhyolite τ_{uc} values of 17, 34, 51 and 68 MPa (Table 2). In comparing results for the three figures, note that the ordinate scale decreases significantly in going from horizontal (P_H) to the vertical and stemming product factors (P_V, P_S). This reflects the fact the 16% air filled porosity and generally weaker Tuff tends to degrade the residual hoop stress above the cavity. Except for an unexplained dip at 5 MPa, the value of P_H increases as τ_{uc} increases from 5- to 20-MPa indicating stronger hoop stresses in the Rhyolite. Except for the weakest Rhyolite the value of P_V and P_S seem to peak in the 5- to 10-MPa range. Based on the above results the criteria that $P \geq 0.5$ appears to be satisfied except for the weakest (τ_{uc} = 2 MPa) or strongest (τ_{uc} = 30 MPa) Tuff shear strengths. An explanation of the exceptions cited would require a detailed dynamic analysis to explain the residual stress field at 800 ms and is beyond the scope of this paper.

The values for P_V and P_S are misleading for several of the points plotted in Figs. 5 and 6. The major difficulty with the values calculated for P_V and P_S is illustrated with Fig. 7 as an example. The peak of the residual stress field occurs in the Rhyolite region with the remaining portion of the stress field in the Tuff layer only slightly greater than C_p. The Rhyolite in this example is a fairly strong material which undergoes significant shear and tensile fracture because of high shock pressures and large displacements close to the cavity and tensile failure from rarefaction off the weak high gas porosity Tuff layer. The fact the Rhyolite becomes highly fractured is going to result in a highly permeable medium[21] above the cavity such that the subsequent rebound and buildup of hoop stresses will not greatly decrease the induced high permeability in the Rhyolite above the cavity. To correct P_V and P_S for this effect we reanalyzed the results for all 16 calculations to only include those portions of the residual hoop stress in the Tuff layers or stemming material above the Rhyolite. The corrected product factors for the Tuff layers are relabeled P_{tv} and P_{ts} for the vertical and stemming axes, respectively. The results of this reanalysis are shown in Figs. 8 and 9.

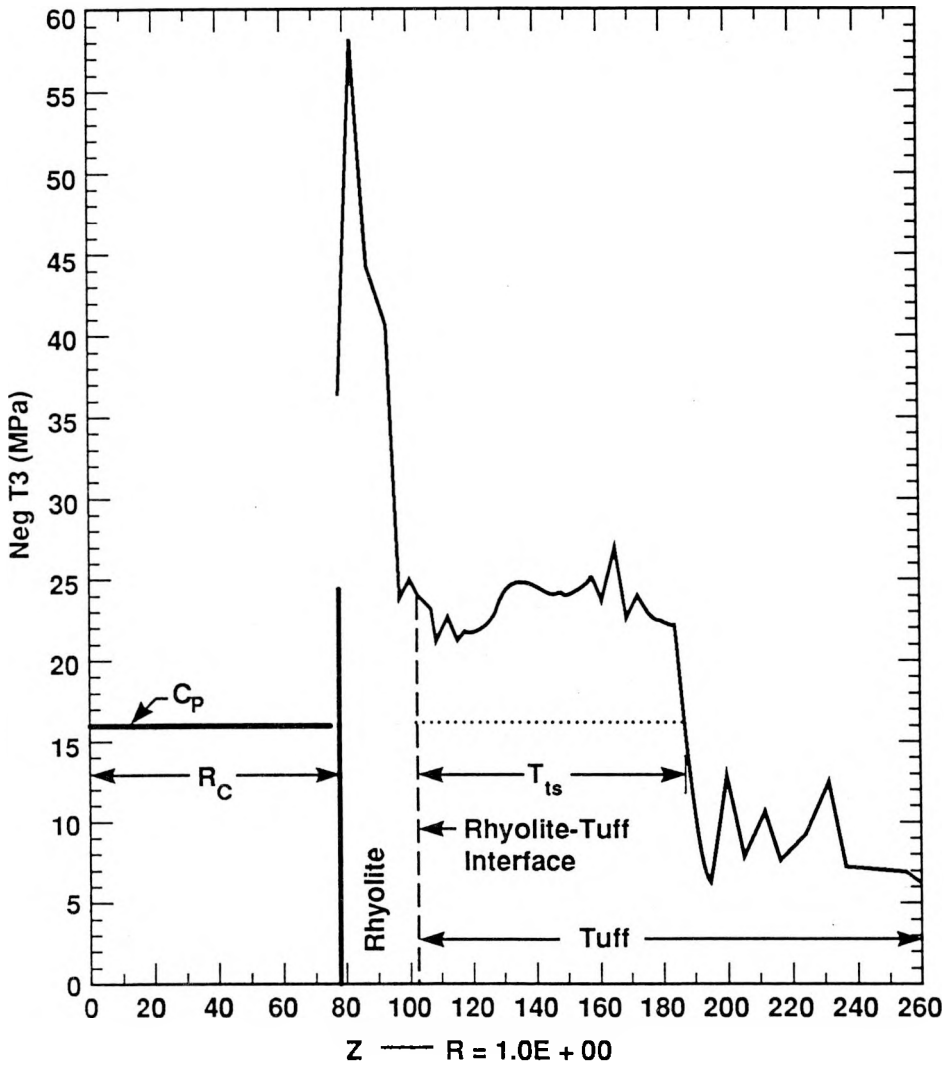


Figure 7. Hoop stress versus distance above WP. The high hoop stress region in the rhyolite omitted from consideration as a barrier for confining cavity gases.

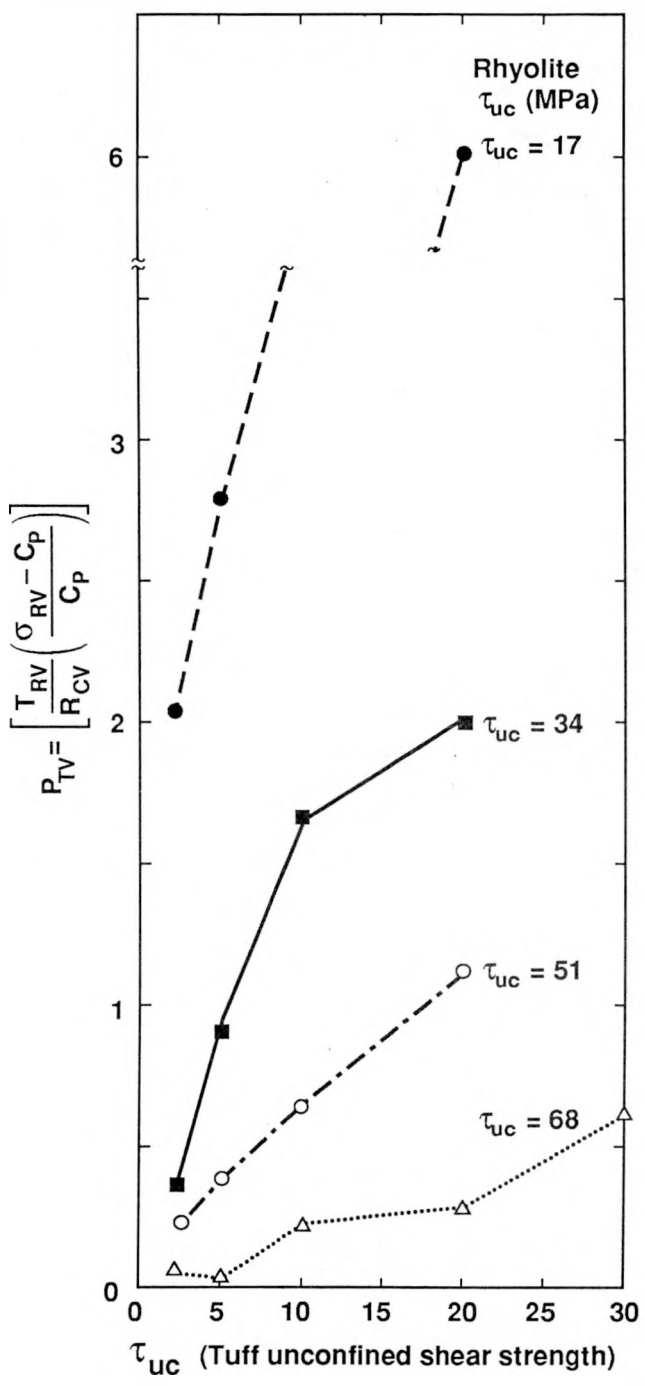


Figure 8. Vertical product factor versus τ_{uc} for tuff for that portion of residual hoop stress in tuff layers above cavity.

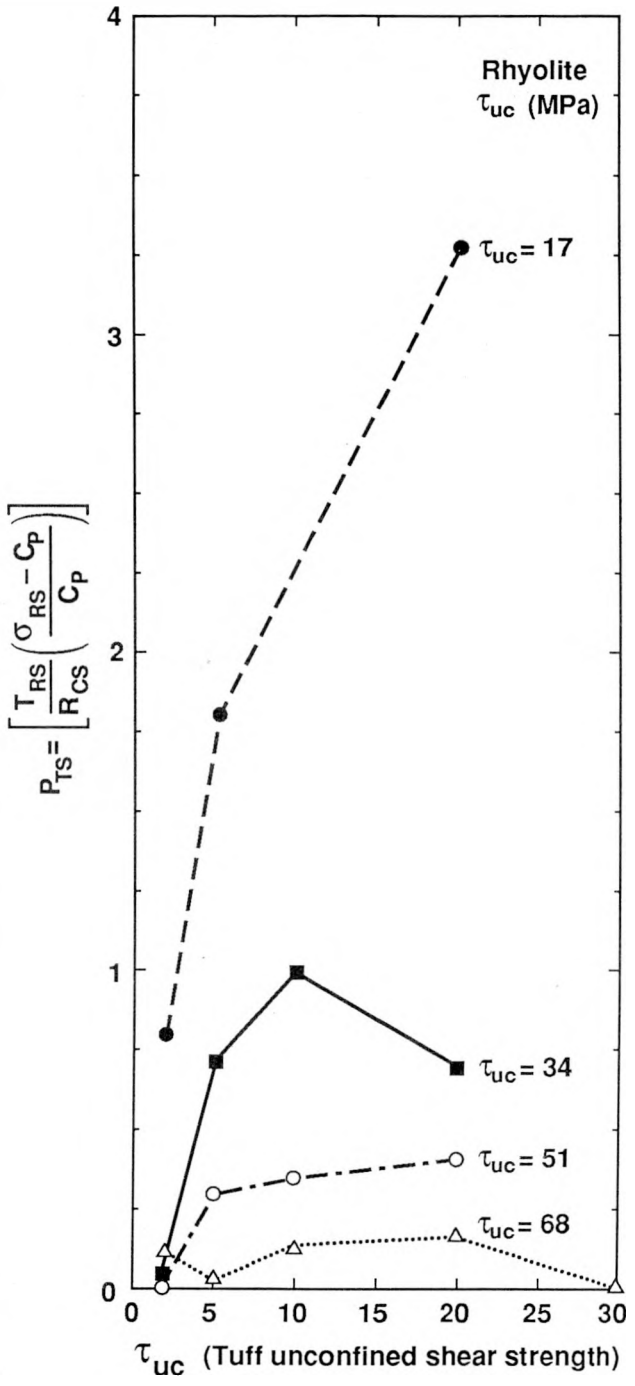


Figure 9. Stemming product factor versus τ_{uc} for tuff for that portion of residual hoop stress in tuff layers above cavity.

The general patterns for P_{tv} and P_{ts} are consistent with previous results for P_v and P_s. Degradation of the residual hoop stress occurs with increasing shear strength of the Rhyolite. With a few exceptions the residual hoop stress appears to increase with increasing shear strength of the Tuff layer above the WP. Based on the criteria that $P \geq 0.5$ only the weakest Rhyolite would be acceptable for τ_{uc} = 2 MPa in the Tuff layer. Furthermore, taking both P_{tv} and P_{ts} into account would indicate the two strongest Rhyolites (τ_{uc} = 51 and 68 MPa) fail to provide an acceptable residual stress field above the cavity. The remaining calculational results provide acceptable values for P_{tv} and P_{ts}. In summary, only 6 of the 16 calculations would be deemed acceptable based on the criteria that $P \geq 0.5$ along the two axes considered.

In the calculational results discussed above, the value P_{ts} was consistently lower than the value for P_{tv}. However, design of the stemming for the emplacement hole has evolved over several decades. This aspect of containment being the weak link has been significantly reduced by the placement of: fines layers, cable gas blocks and fanouts, gypsum and coal tar epoxy plugs. That is, the emplacement hole is a hole in the geologic fabric that can be tailored by stemming procedures to significantly reduce its threat to containment. Taken in this context, the values for P_{tv} (Fig. 8) might be a more realistic choice to compare with the criteria $P \geq 0.5$ mentioned above. From this standpoint 9 of the 16 calculations exceed the residual stress criterion. However, it should be recognized that the residual stress field in the Tuff adjacent to the emplacement hole should be analyzed in conjunction with the stemming plan to determine whether the peak hoop stresses occur at the locations where fines or plugs exist to enhance the containment features for each nuclear event.

SUMMARY

This parameter study was conducted using the two-dimensional version of the TENSOR code to examine the sensitivity of the residual stress field around the cavity when the strengths were varied for a strong Rhyolite and weaker Tuff layer near the WP. The geologic cross-section chosen was a variation to one used in a numerical simulation for a past

nuclear event. In the new geologic configuration there were material strengths chosen that would show residual stresses less than cavity pressure. The WP was located in a saturated Rhyolite layer and the unconfined shear strength (τ_{uc}) was varied from 17 to 68 MPa. Immediately above the Rhyolite was a relatively weak Tuff layer with 16% gas porosity for which τ_{uc} was varied from 2 to 30 MPa. The strengths for the above layers in some cases were based on laboratory measurements of samples from the emplacement hole and a nearby hole and the P-Mu GEN code. Since the geologic layering was horizontal, a cylindrical geometry was used in the numerical model. A total of 16 TENSOR calculations were performed.

To provide a quantitative basis for evaluating the residual stress field around the cavity, we selected three axes that extended radially from the WP. The first axis extended horizontally into the Rhyolite layer. The second axis was 2° off vertical and extending primarily through the geologic media, but for brevity was labeled the vertical axis. The third axis was parallel with the center of the emplacement hole, but offset 1 m and called stemming axis. Each axis forms the abscissa of a plot with Neg T_3 (out of plane hoop stress) as the ordinate. The results of the calculations at 800 ms were graphically portrayed for each of the parameter calculations. From these graphs the ratios of thickness of Neg T_3 (in the media that exceeded cavity pressure) to cavity radius were obtained. Then the ratios of the peak Neg T_3 (that exceeded cavity pressure) to the cavity pressure were obtained. The product of these two ratios was labeled as the product factor (P) with appropriate subscripts corresponding to each of these axes. Essentially these values of P provided a measure of the quality of the residual stress field related to the cavity gas pressure. A calculational criteria of $P \geq 0.5$ was arbitrarily suggested as a bound for a "good" residual stress field around the cavity for containment of cavity gases.

The calculation results indicate that generally a stronger hoop stress exists along the horizontal axis (Rhyolite) than the vertical (Rhyolite and Tuffs) and stemming axes. This reflects the fact that the weaker Tuffs above the cavity tend to degrade the hoop stresses since large hoop stresses cannot form in weak materials. Generally the magnitude of the

hoop stresses increase as the strength for Tuff increases for the layer above the Rhyolite. However, the magnitude of hoop stress decreases with increasing strengths in the Rhyolite because of smaller cavity and less rebound. Based on our criteria of $P \geq 0.5$ only 6 of the 16 TENSOR calculations indicate acceptable hoop stress for "good" containment. These results were controlled by the hoop stresses in the emplacement hole (stemming axis results).

Stemming procedures (fines layers, cable gas blocks and fanouts, gypsum and coal tax epoxy plugs) have significantly reduced the emplacement hole as an area for containment concern. Alternatively, if the geology above the WP is a concern then a more realistic choice is the calculational results for the vertical axis. A review of the calculational results for this vertical axis indicate 9 of the 16 calculations exceed the residual stress criterion of $P \geq 0.5$.

ACKNOWLEDGMENTS

The authors gratefully acknowledge Joseph Hearst for his advice and support, Francois Heuze for his critical review, Miriam Lohmann for production assistance, Robin Newmark for council on the geology, and Lydia Grabowski for her careful typing of this report.

REFERENCES

1. R. W. Terhune, H. D. Glenn, D. E. Burton, and J. T. Rambo, "Containment Analysis for the Simultaneous Detonation of Two Nuclear Explosives", Lawrence Livermore National Laboratory, Rept. UCRL-52268 (1977).

2. R. W. Terhune and H. D. Glenn, "Estimate of Earth Media Shear Strength at the Nevada Test Site", Lawrence Livermore National Laboratory, Rept. UCRL-52358 (1977).

3. N. Rimer, "A Relationship Between Material Properties, Residual Stresses, and Cavity Radius Due to a Nuclear Explosion", Systems, Science, and Software, Rept. SSS-R-77-3339 (1977).

4. H. D. Glenn, J. T. Rambo, and R. W. Terhune, "Calculational Examination of the BANEBERRY Event - Addendum", Lawrence Livermore National Laboratory, Rept. UCRL-53164 (1981).

5. J. T. Rambo, "Geologic and Material Property Combinations that Adversely Influence Residual Stress in 2-D Dynamic Containment Calculations", Fourth Symposium on Containment of Underground Nuclear Explosions, U.S. Air Force Academy, Colorado Springs, CO., CONF-870961, Vol. 1, p. 196, Sept. 21-24, 1987.

6. G. Maenchen and S. Sack, "The TENSOR Code", Lawrence Livermore National Laboratory, Rept. UCRL-7316 (1963).

7. D. E. Burton, L. A. Lettis, Jr., J. B. Bryan, and N. R. Frary, "Physics and Numerics of the TENSOR Code", Lawrence Livermore National Laboratory, Rept. UCID-19428 (1982).

8. D. E. Burton, C. M. Snell, and J. B. Bryan, "Computer Design of High Explosive Experiments to Simulate Subsurface Nuclear Detonations", Lawrence Livermore National Laboratory, Rept. UCRL-75190 (1975).

9. H. D. Glenn and J. M. Thomsen, "Computer Simulation of a High Explosive Cratering Experiment in a Complex Multilayered Geology", Lawrence Livermore National Laboratory, Rept. UCRL-78155 (1986).

10. J. T. Cherry and F. L. Petersen, "Numerical Simulations of Stress Wave Propagation from Underground Nuclear Explosions", Lawrence Livermore National Laboratory, Rept. UCRL-72216 (1970).

11. R. W. Terhune, H. D. Glenn, D. E. Burton, H. L. McKague, and J. T. Rambo, "Calculational Examination of the Baneberry Event", Lawrence Livermore National Laboratory, Rept. UCRL-52365 (1977).

12. D. E. Burton, R. P. Swift, J. B. Bryan, and H. D. Glenn, "Subsidence in the Craters of Nuclear Tests at the Pacific Proving Grounds", Lawrence Livermore National Laboratory, Rept. UCRL-91583 (1984).

13. J. T. Rambo and N. Rimer, "Containment Calculations for a Weak Working Point Region Between Hard Rock Layers", Fourth Symposium on Containment of Underground Nuclear Explosions, U.S. Air Force Academy, Colorado Springs, CO., CONF-870961, Vol. 3, p. 59, Sept. 21-24, 1987.

14. R. Newmark and R. McArthur, "U20ar Site Characteristics Report", Earth Sciences Department, Lawrence Livermore National Laboratory, Internal Rept. CP 86-39 (1986).

15. H. C. Heard and H. Washington, "Mechanical Properties of SCHOONER and JORUM Rocks", Lawrence Livermore National Laboratory, Internal Memorandum PMD-329 (1968).

16. R. W. Terhune, Lawrence Livermore National Laboratory, Livermore, CA, private communication (1988).

17. G. Anderson and A. Kusubov, "Second Interim Report on Strength Measurements on Material from Hole U20ar, 500.6 m Depth", Lawrence Livermore National Laboratory, Internal Memorandum (1986).

18. T. R. Butkovich, "The Gas Equation of State for Natural Materials", Lawrence Livermore National Laboratory, Rept. UCRL-14729 (1976).

19. H. D. Glenn, "Spall Study in One Dimension", Lawrence Livermore National Laboratory, Rept. UCID-17144 (1976).

20. R. W. Terhune, "Analysis of Burial Depth Criteria for Containment", Lawrence Livermore National Laboratory, Rept. UCRL-52395 (1978).

21. H. L. McKague, Lawrence Livermore National Laboratory, Livermore, CA, private communication (1988).

22. T. R. Butkovich, "A Technique for Generating Pressure-Volume Relationships and Failure Envelopes for Rocks", Lawrence Livermore National Laboratory, Rept. UCRL-51441 (1973).

APPENDIX A

The geology for U20ar was presented in Fig. 1 and the corresponding numerical model in Fig. 2. Information pertinent to the numerical model was summarized in Table 1. Material properties were not varied for the eight layers used in the numerical studies. The strength properties of the top six layers were also held constant. Ranges for the strength properties of the lowest two layers are shown in Table 1 with the specific strengths used for each problem given in Table 2. The values for weight percentage water, bulk density (ρ_O), grain density (ρ_g) and elastic limit (P_T) are used as input to a rock mechanics code (P-Mu GEN)[22] to provide compressibility and failure envelopes for the top six layers. The P-Mu code also provides the compressibility input for the lower two layers, but the failure envelopes for the Tuff and Rhyolite are based on the values given in Table 2. Figure A1 illustrates the failure curves used for the Tuff layer as example.

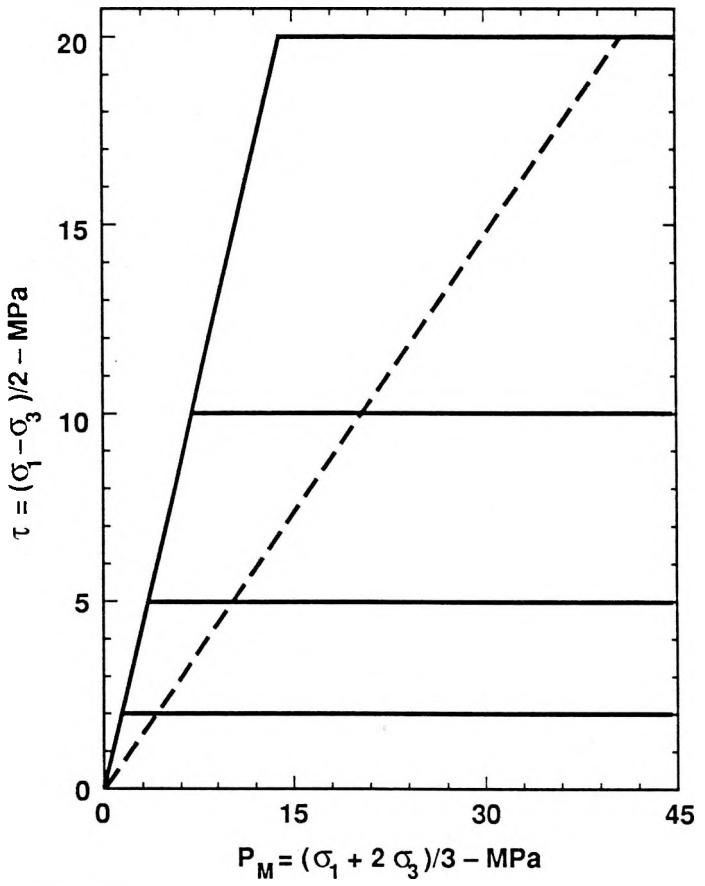


Figure A1. Shear strength envelopes for tuff used in parameter study.

APPENDIX B

This appendix presents isometric plots of the hoop stress (Neg T_3) fields at 800 ms for all 16 parameter calculations using the two-dimensional version of TENSOR. After 800 ms the dynamic motion should have negligible effect on the residual tangential configuration. In these figures, the R and Z axis form an isometric plane and the magnitude of the hoop stress is given by the vertical axis. To accentuate details of the residual stress field around the cavity, the Z-axis extends from 100 m below and 250 m above the WP, while the R-axis extends from the vertical axis through the emplacement hole to 350 m horizontally. The vertical axis is keyed to the maximum hoop stress in the region to further highlight details of the cavity pressure and stress region around the cavity. Comparing plots for different strengths may require a mental scaling to achieve a true relationship for the differences in the residual stress fields that were obtained.

An exhaustive discussion of all 16 figures is not practical. Although these figures were not used to obtain the quantitative results presented in the text they can be used to correlate those results to obtain a better three-dimensional perspective to the interrelationship of the three axes analysis. To facilitate that correlation we will provide a brief description of specific features pertinent to the earlier analysis.

Cavity growth is enhanced in the upward direction by the weak Tuff layer. However, both the cavity radii and asymmetry are reduced as strengths are increased for the Tuff and Rhyolite. The Tuff layer is overlain at 184.7 m above the WP by a strong Rainier Mesa Tuff. The presence of this strong layer is evident by the weak residual hoop stresses (when τ_{uc} = 2 MPa) between the Rhyolite and Rainier Mesa Tuff. As we increase the strength of the Tuff the residual stresses in this region increase to where the distinction between the Tuff layers disappear. The magnitude of the residual hoop stresses in the stemming can be seen along the Z-axis. Compaction of stemming material in the emplacement hole results from failure of the surrounding geologic media during passage of

the ground shock and not from shock propagation coming up the stemming in the emplacement hole. After passage of the ground shock, the geologic media rebounds, locking in the residual stresses. As the strengths of the Rhyolite and Tuff increase less failure around the emplacement hole occurs and subsequently less compaction of the stemming. This effect can be observed in the plots along the Z-axis and the earlier analysis conducted in the text.

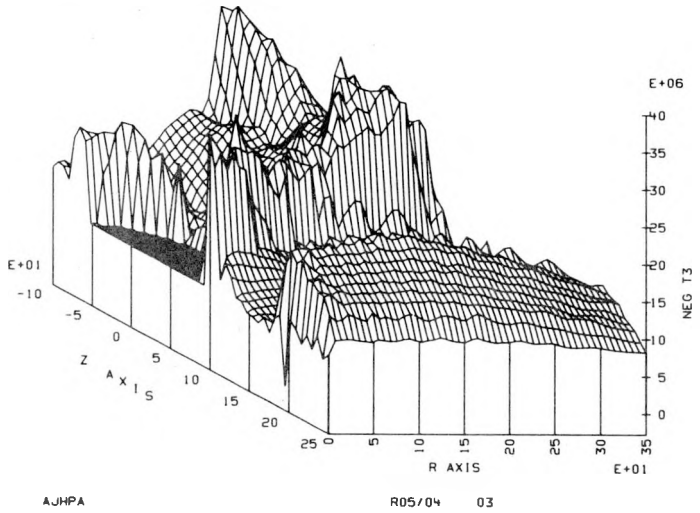


Figure B1. AJPHA–RHY τ_{uc} = 17 MPa
Tuff τ_{uc} = 2 MPa

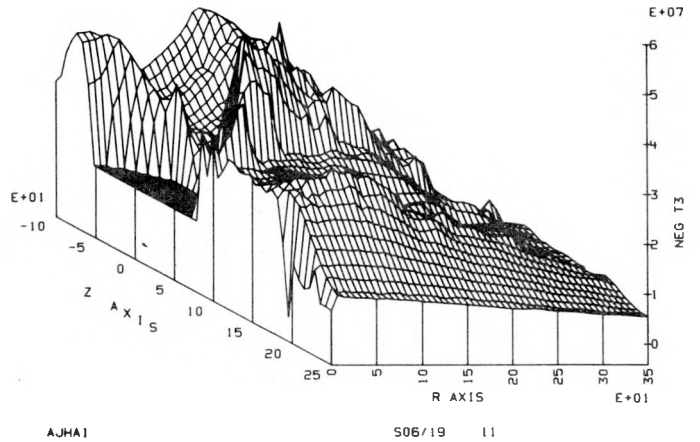


Figure B2. AJHA1–RHY τ_{uc} = 17 MPa
Tuff τ_{uc}= 5 MPa

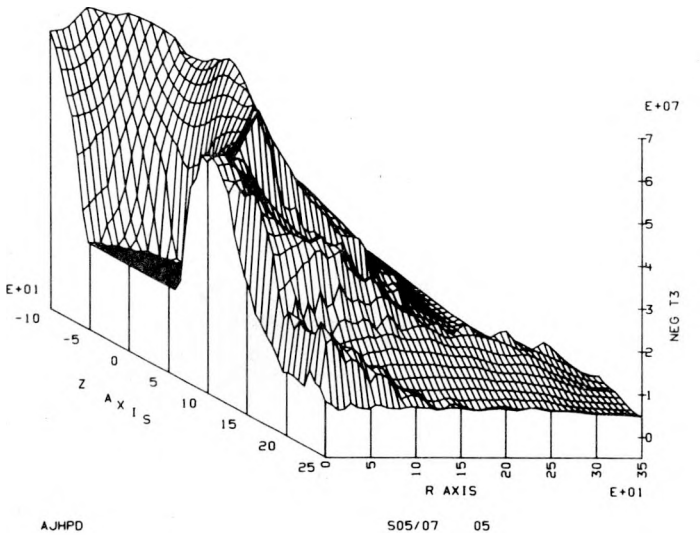


Figure B3. AJHPD–RHY τ_{uc}= 17 MPa
Tuff τ_{uc} = 20 MPa

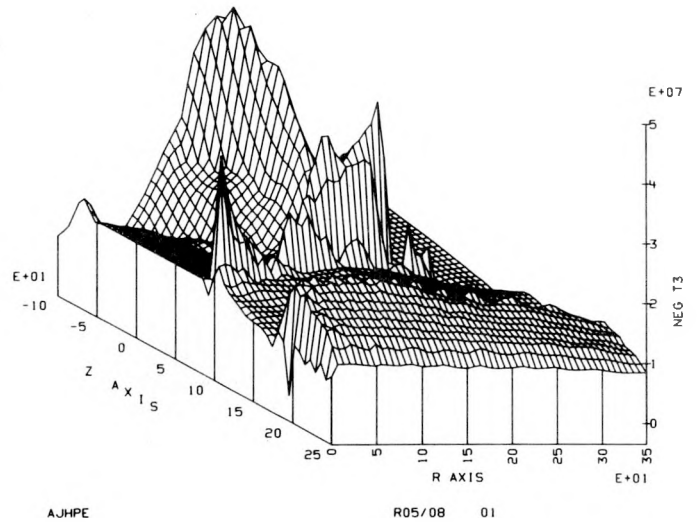


Figure B4. AJHPE–RHY τ_{uc}= 34 MPa
Tuff τ_{uc} = 2 MPa

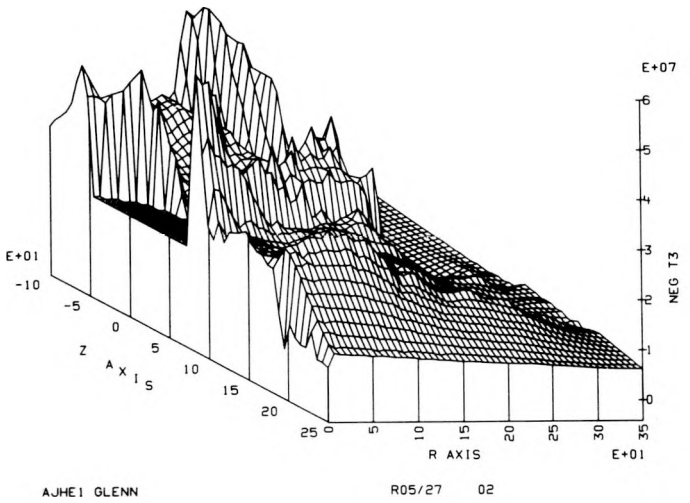


Figure B5. AJHE1–RHY τ_{uc} = 34 MPa
Tuff τ τ = 5 MPa

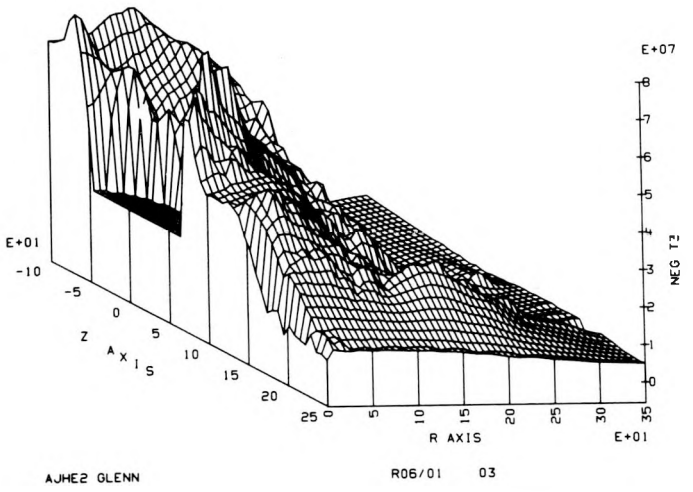


Figure B6. AJHE2–RHY τ_{uc} = 34 MPa
Tuff τ_{uc} = 10 MPa

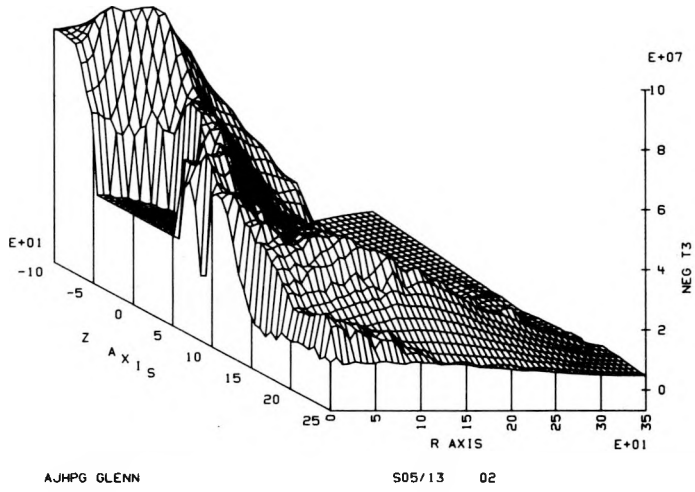


Figure B7. AJHPG–RHY τ_{uc} = 34 MPa
Tuff τ $_{uc}$ 20 MPa

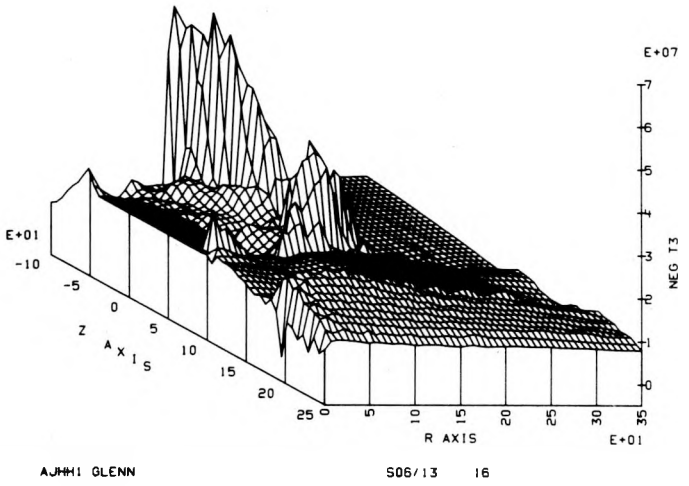


Figure B8. AJHH1–RHY τ_{uc} = 51 MPa
Tuff τ_{uc} = 2 MPa

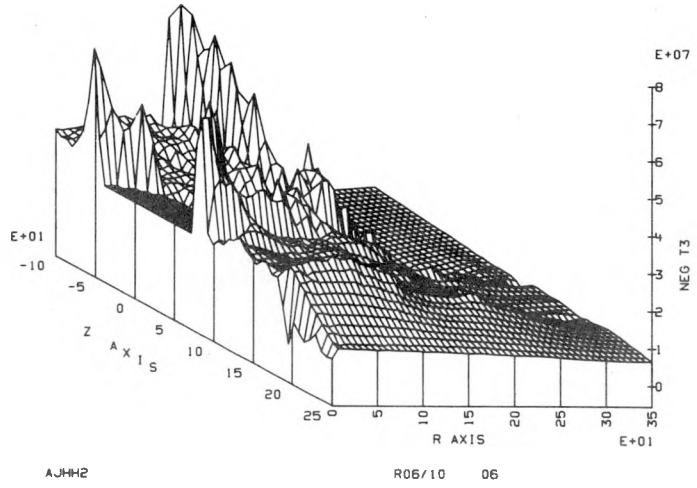


Figure B9. AJHH2–RHY τ_{uc} = 51 MPa
Tuff τ_{uc} = 5 MPa

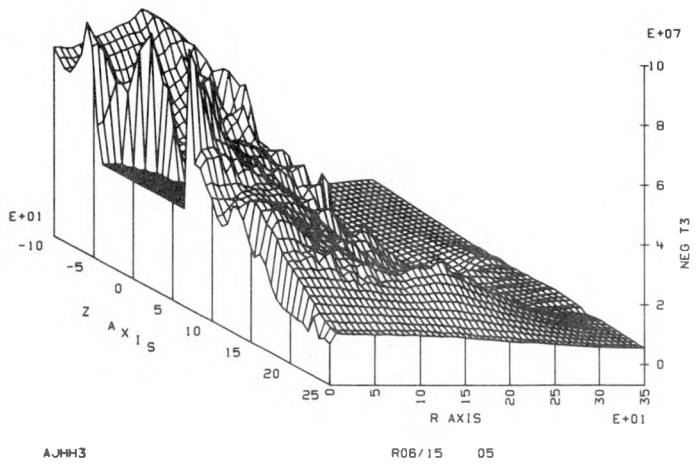


Figure B10. AJHH3–RHY τ_{uc} = 51 MPa
Tuff τ_{uc} = 10 MPa

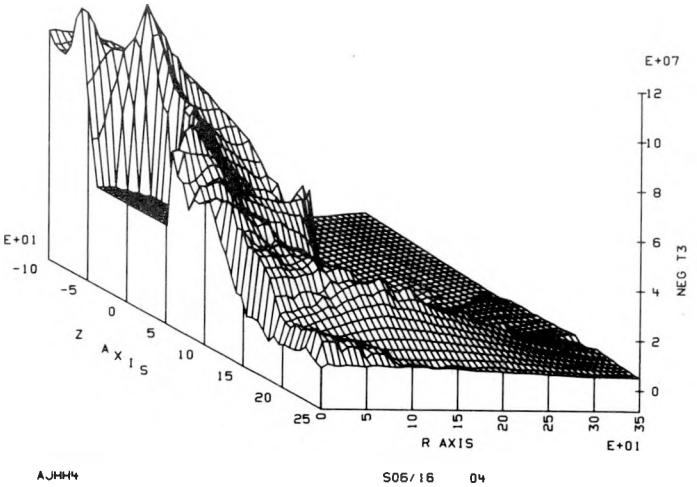


Figure B11. AJHH4–RHY τ_{uc} = 51 MPa
Tuff τ_{uc} = 20 MPa

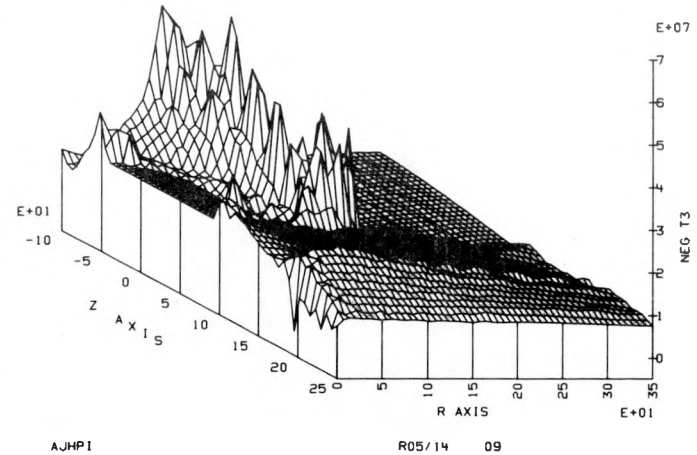


Figure B12. AJHP1–RHY τ_{uc} = 68 MPa
Tuff τ_{uc} = 2 MPa

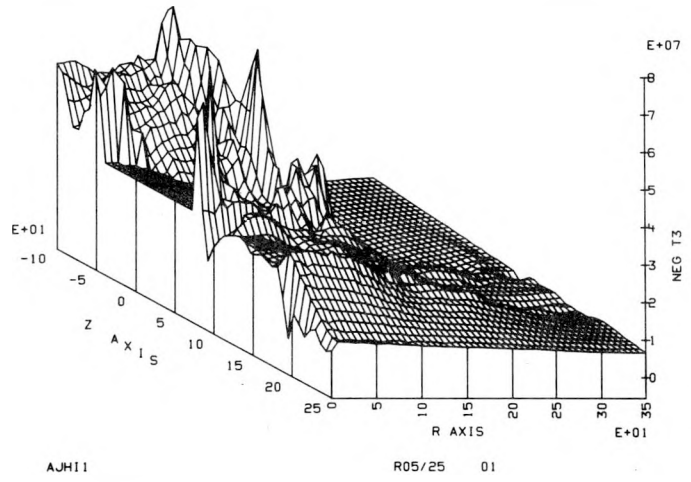


Figure B13. AJHI1–RHY τ_{uc} = 68 MPa
Tuff τ_{uc} = 5 MPa

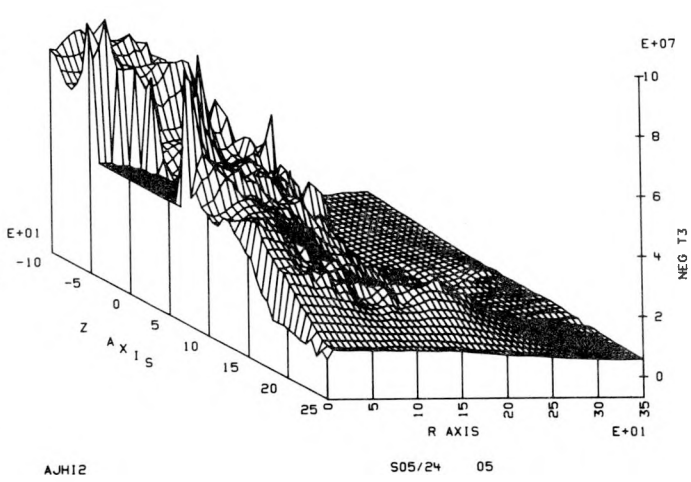


Figure B14. AJHI2–RHY τ_{uc} = 68 MPa
Tuff τ_{uc} = 10 MPa

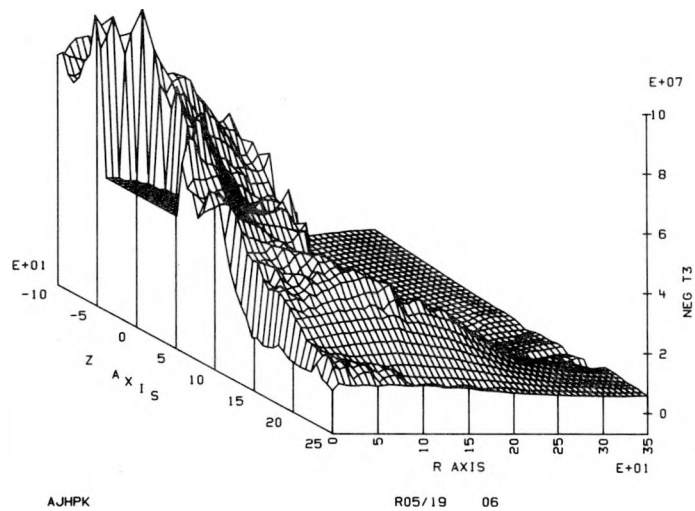


Figure B15. AJHPK–RHY τ_{uc} = 68 MPa
Tuff τ_{uc} = 20 MPa

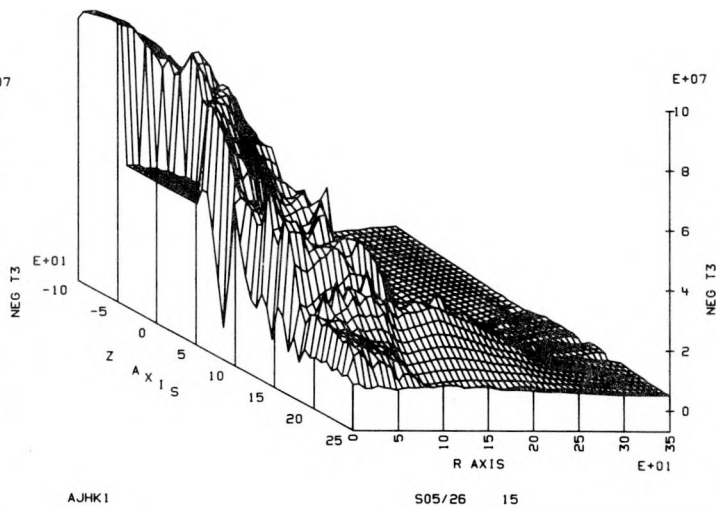


Figure B16. AJHK1–RHY τ_{uc} = 68 MPa
Tuff τ_{uc} = 30 MPa

Ground Motion in a Multilayered Media: Calculated and Experimental Results from the HARDIN Event

V. E. Wheeler and J. T. Rambo
Lawrence Livermore National Laboratory
P.O. Box 808
Livermore, CA 94550

Abstract

HARDIN was fired on Pahute Mesa. The overburden was formed of intermixed layers of bedded and ashflow tuffs with a single layer of lava. As a continuation of our efforts to test calculational models used to predict the effects of underground nuclear explosions, HARDIN was instrumented with ground motion stations both in a satellite hole and the emplacement hole as well as the surface. Pre-shot and post-shot numerical simulations of HARDIN were performed using the 2-D Tensor code. Presented here are the comparisons between the calculational results using pre-shot material models and the measured data.

Introduction

HARDIN was fired on Pahute Mesa in hole U20av at a depth of 625 m. This event was of special interest to Containment because of a lava flow and dike located to the east of the emplacement hole. Pre-shot calculations were run as part of the containment analysis of HARDIN and a satellite hole (drilled for other purposes) was instrumented for ground motion measurements.

Event Site

The HARDIN emplacement hole is located in the south-eastern portion of Area 20 as shown on the accompanying map (Figure 1). The geologic structure for this site is shown in Figure 2; an east-west cross section which crosses the major structures. The symbols used to denote the units on the cross section are defined in Table 1. The shot point was located in a bedded tuff associated with the Paintbrush Tuff. Within the bedded tuff and to the east of U20av is a lava flow and the dike which fed it. Debris from the edge of the lava flow extends through the emplacement hole. Overlying the bedded tuff of the shot point region are the Timber Mountain Tuffs and Thirsty Canyon Tuffs. Summary plots of the geophysical logs from the emplacement hole and from an exploratory hole, UE20av drilled 100 m N60°E of U20av, are shown in Figures 3 and 4. The complete geologic description of HARDIN site is given in Reference 1, from which all the above figures and tables were taken.

Experimental Geometry

The satellite hole, U20av Sat #1, was drilled 12.5 m from the emplacement hole. Seven ground motion canisters were installed in the satellite hole along with a surface ground zero station. All stations contained at least a vertical

accelerometer and a vertical velocity gage. The layout of the instrumentation along with a density log and the lithology is shown in Figure 5. Two stations were located in the bedded tuff below the Rainier Mesa Tuff. Three stations were spaced through the Rainier Mesa Tuff and two stations were located between the top of the Rainier Mesa Tuff and the surface.

Calculations

Prior to the execution of HARDIN, two calculations of the effects of the explosion were run using the LLNL TENSOR code (Reference 2). The calculations were conservative in that where there was a choice in material properties for a unit, the choice was made in the direction that would provide the greatest danger to containment. The calculations were designed to specifically assess the effect of the reflection of the stress wave off the base of the Rainier Mesa Tuff and the nearby rhyolitic dike on the containment cage. Thus the Rainier Mesa Tuff was considered to be a very strong unit while the bedded tuff below the Rainier Mesa was considered to be a weak unit. One calculation used the geology as shown to the east of U20av, which included the dike and lava flow, and the other used the geology as shown to west, which essentially eliminated the dike and flow from the calculation. The locations of the models used are shown in Figure 6. The physical properties used in these calculations are given in Table 2. After HARDIN was fired the same two calculations were rerun using the TENSOR code and the measured yield. The models and the physical properties used in all four calculations were the same, the only difference being the use of the measured yield in the post-shot calculations.

Results

The comparison of the calculated particle velocity wave at each ground motion station and the measured particle velocity are shown in Figures 7. The dashed curve is the measured data. The dotted curve is the pre-shot calculation and the solid curve is the post-shot calculation. The signals from the deepest ground motion station (Station 41) were lost on the the rise of the outgoing stress wave and the signal from 21UV, located in the emplacement hole, has been substituted for 41UV. Comparison of records from the emplacement hole and satellite hole at greater ranges, shows this to be a valid substitution. The next three stations (42, 43, and 44) were lost when spall broke the signal cables between 400 and 500 ms but still provide sufficient data for comparison with calculation. The remaining stations survived the explosion. The pre-shot calculation is included in these figures to show the difference the yield used in the calculation makes in the calculated wave form and to judge the adequacy of the calculation in defining the destructive effects of reflections off the base of the Rainier Mesa Tuffs on the containment cage. The proper comparison to make for comparing calculations with measurements, is between the measured data and the post-shot calculation (the solid curve) in which the measured device yield was used.

Comparison of experimental results with calculations

Referring to Figure 7 the most noticeable feature in the measured data is the lack of a significant time delay between the arrival of the precursor and the main shock wave while the calculations show a distinct time delay between the two waves. This is attributed to a model with a low elastic limit or having greater compressibility than the in situ materials.

The closest measurement to the shot point was from 21UV which is shown with the calculations at a radial distance of 185 m. The reflection of the peak of the stress wave off the base of the Rainier Mesa Tuff arrives at this station at approximately 190 ms, well before the loss of the gage at about 235 ms. The east calculation, which included the lava flow, shows good agreement with the measured data. The wave shape is in very good agreement and the calculated peak velocity is only about 20% low. Some less agreement is shown at 235 m (42UV) between the east calculation and the measurement. As this location is only 30 m below the Rainier Mesa Tuff, the sharp boundary required by the calculation rather than the graded boundary as seen in the log summary (Figure 3) is probably showing its effect. The stronger agreement of measurements with the east calculation than with the west calculation indicates that the lava flow to the east is controlling the ground motion, at least up to the Rainier Mesa Tuff. The next three stations (305 m, 365 m, and 420 m radial range) are in the Rainier Mesa Tuff. The amplitude of the calculated motion has been greatly attenuated in relation to the measurement by the conservative choice of material properties for both the Rainier Mesa Tuff and the Paintbrush Tuff below it. The agreement in wave form from the east calculation is degenerating while the wave form from the west calculation is showing better agreement with measurement. At the 420 m range the calculated motion shows a strong secondary peak, almost twice the initial peak in the west calculation, which from the calculated stress history is a tensile wave. The measured data at this range also shows a wave at approximately the same time but a factor of 20 lower in amplitude. The timing is such that this second peak should include the reflection of the main stress wave from the surface. At a range of 490 m, 55 m above the Rainier Mesa Tuff, the wave form of the west calculation shows moderate agreement. Above 490 m, at 555 m and the surface, agreement in both wave form and amplitude is poor.

Conclusions

An inherent limitation of digital computers is the large amount of preparation time and computer memory required to describe a physical system. Thus the model used to describe the HARDIN site is a compromise between the abilities of the computer and the actual site. The physical properties are averaged over a geologic unit and the interfaces are step functions. The logs of the hole show large variations of physical properties within units as well as gradational boundaries. The TENSOR code is a two dimensional code while the measurements are three dimensional thus measuring something of an average of the two calculations. The gages also respond to the local geology as well as the gross features. As the local geology varies in both the vertical and horizontal

directions, individual measurements may also be suspect. Thus we should not expect calculation and measurement to agree in detail and they don't.

The reasonable agreement between east calculation and measurement below the Rainier Mesa Tuff indicates that the purpose of the pre-shot calculations was most likely met. Above the base of the Rainier Mesa Tuff, the low amplitude given by the calculation is a reflection of the conservative physical properties assigned to the Paintbrush and Rainier Mesa Tuffs. The better agreement in waveform shifting from the east to the west calculation above the base of the Rainier Mesa Tuff is disconcerting. A probable explanation is that as the strong lava flows lies to the east of the hole, refraction of the shock wave at the Rainier Mesa-Paintbrush boundary removes the effect of the lava flow from the vertically traveling shock wave leaving the major components of the shock wave those which have traveled through the tuffs and debris rather than the lava.

The use of these calculations to determine the adequacy of the containment cage for HARDIN was appropriate. The calculations overstated the damage to the containment cage as the calculations were designed to do. The calculations understated the effects above the base of the Rainier Mesa Tuff and thus any conclusions about the effects of the shock wave on the emplacement hole stemming features and hardware or spall depth and fracturing of the medium would be under estimated.

There is more that we can learn from the data taken at HARDIN for future modeling. We did not cover in this paper iterations of the model with the data as suggested by observations of the data.

Calculations are an important guide in the containment evaluation of an event. But as these comparisons show, considerable care must be exercised in the use and interpretation of a particular calculation.

References

1 S. Clark and D. McArthur, "U20av Site Characteristics Report", Lawrence Livermore National Laboratory, CP 86-55, December 12, 1986.

2 D. E. Burton, L. A. Lettis Jr., J. B. Bryan, and N. R. Frary, "Physics and Numerics of the TENSOR Code", Lawrence Livermore National Laboratory, Rept. UCID-19428 (1982)

Acknowledgements

This work was performed under the auspices of the U.S. Department of Energy by Lawrence Livermore National Laboratory under contract No. W-7405-Eng-48. The work was supported by the LLNL Nuclear Test Containment Program.

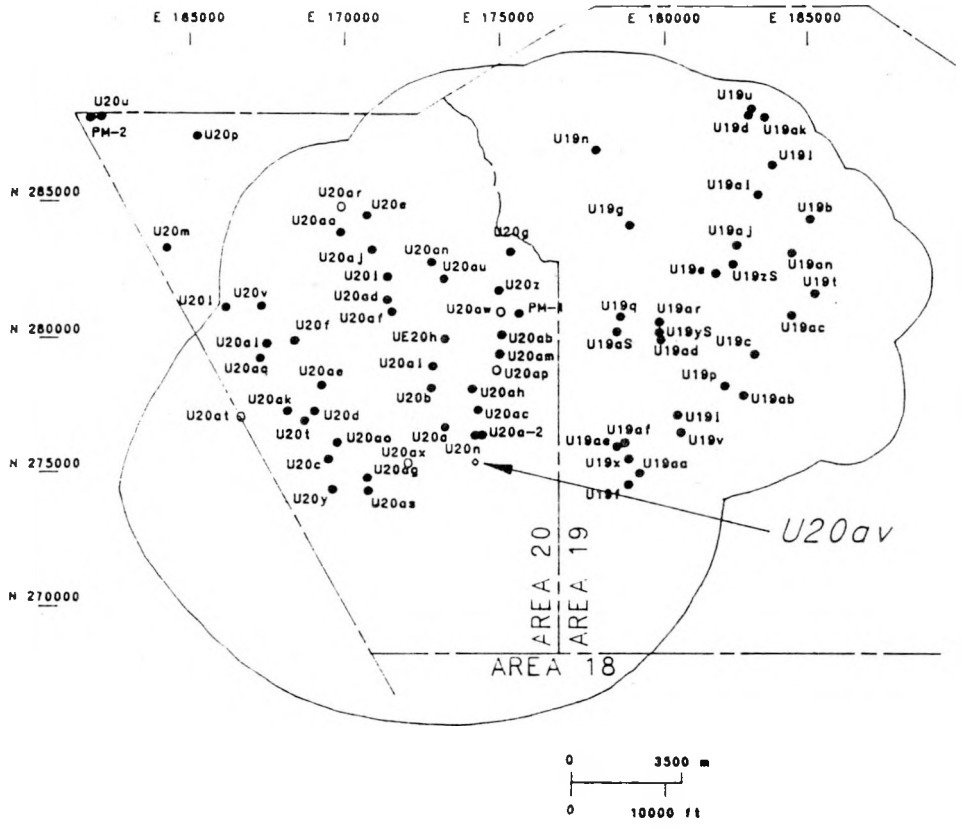


Figure1

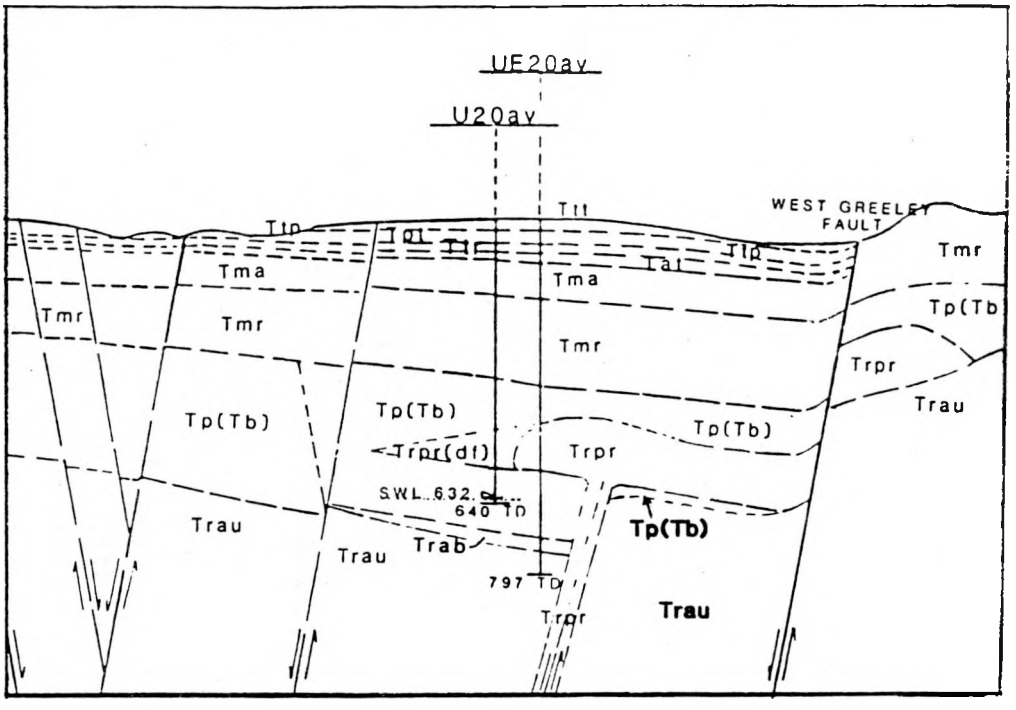


Figure 2

Table 1

IDENTIFICATION OF UNITS USED IN THE GEOLOGIC MAP AND CROSS SECTION, U20av

QUATERNARY

Qac--Alluvium and colluvium

TERTIARY

Ttt	Trail Ridge Member; Thirsty Canyon Tuff
Ttp	Pahute Mesa Member; Thirsty Canyon Tuff
Ttr	Rocket Wash Member; Thirsty Canyon Tuff
Tat	Bedded tuff related to Thirsty Canyon and Timber Mountain Tuffs
Tma	Ammonia Tanks Member; Timber Mountain Tuff
Tmr	Rainier Mesa Member, Timber Mountain Tuff
Tp(Tb)	Bedded Tuff associated with the Paintbrush Tuff
Trpr	Quartz-rich Rhyolite lava of the Scrugham Peak Quadrangle
Trpr (ds)	Quartz-rich Rhyolite lava debris flow of the Scrugham Peak Quadrangle
Trpq	Quartz-bearing Rhyolite lava of the Scrugham Peak Quadrangle
Trpb	Biotite rhyolite lava of the Scrugham Peak Quadrangle
Trau	Upper Rhyolite lavas, Tuffs and Rhyolites of Area 20
Trab	Bedded and ash-flow tuffs, tuffs and rhyolites of Area 20
Tra	Tuffs and rhyolites of Area 20, undifferentiated
Fault	Dotted where concealed; dashed where inferred from test related fractures. Bar and ball on down thrown side. Offsets are in cm.

Table 2

Material and Strength Properties for U20av - HARDIN

Vertical Material No.	Depth m	Range m	H_2O wt%	p_0 Mg/m^3	p_g Mg/m^3	ϕ %	S %	ψ %	Poisson's Ratio	Velocity m/s	P_t MPa	Maximum* Shear Strength MPa	Unconfined* Compressive Strength MPa
58 Ttb	0-50	575-625	7.3	2.00	2.59	26.2	52.7	12.8	0.25	1186	20.0	29.2	12.0
57 Tma Ttr	50-190	435-575	16.2	1.57	2.56	49.3	52.2	23.6	0.20	1566	6.12	12.2	4.59
56 Tmr	190-360	265-435	4.2	2.19	2.54	18.9	57.1	10.3	0.25	2235	58.2	58.2	34.9
55 Tp	360-470	155-265	15.8	1.81	2.50	38.9	73.7	10.2	0.25	2257	3.0	12.0	1.8
54 Trpr	470-500	125-155	7.5	2.22	2.49	17.9	92.2	1.4	0.27	2701	20.0	35.0	11.1
53 Trpr Debris	500-518	107-115	8.9	1.86	2.48	31.7	52.1	15.2	0.25	2653	4.9	100.0	2.95
52 Trpr bottom	518-550	75-107	12.9	1.94	2.50	32.5	77.3	7.4	0.25	2309	4.9	100.0	2.95
51 Tp WP	550-635	-10-75	20.4	1.87	2.55	41.3	92.0	3.4	0.30	3001	7.4	25.0	5.55
Material below standing water level													
81 Tp Sat	635-757	-10 to -132	16.26	1.92	2.46	41.3	100.0	0.0	0.30	3001	7.4	25.0	5.55
82 Trau Sat	757-4625	-132 to -4000	39.5	1.95	2.46	39.5	100.0	0.0	0.30	3001	20.0	35.0	11.1
83 Dike Closest Approach	572-1550	2.5 167.4-231	2.4	2.49	6.0	100.0	0.0	0.273868		138.0	700.0	68.0	

* Strength Values are one half the stress difference

ϕ is Total Porosity
S is Saturation
ψ is Gas Porosity

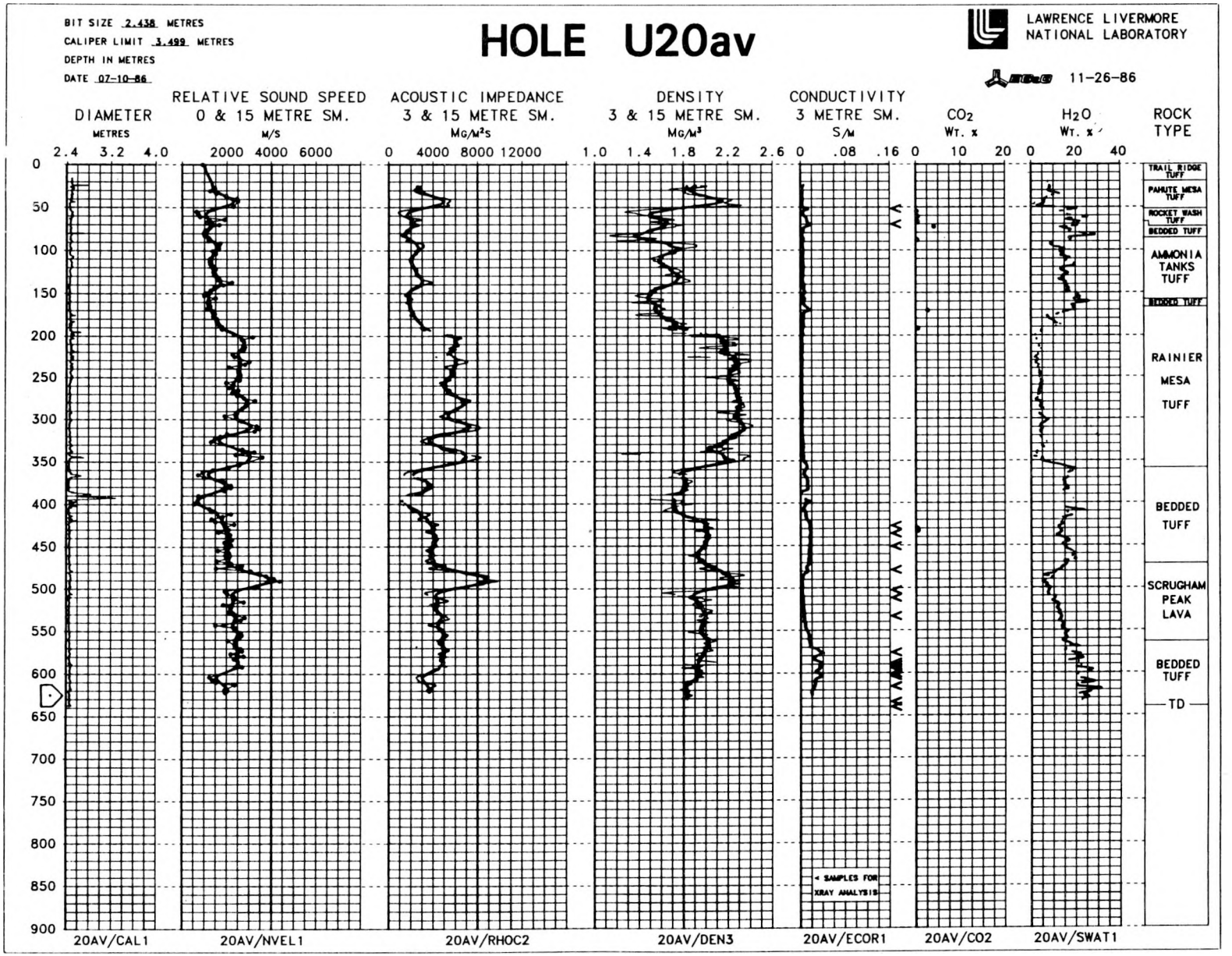

BIT SIZE 2.438 METRES
CALIPER LIMIT 3.499 METRES
DEPTH IN METRES
DATE 07-10-86
HOLE U20av
LAWRENCE LIVERMORE NATIONAL LABORATORY
11-26-86
DIAMETER
METRES
2.4 3.2 4.0
RELATIVE SOUND SPEED
0 & 15 METRE SM.
M/S
2000 4000 6000
ACOUSTIC IMPEDANCE
3 & 15 METRE SM.
MG/M²S
0 4000 8000 12000
DENSITY
3 & 15 METRE SM.
MG/M³
1.0 1.4 1.8 2.2 2.6
CONDUCTIVITY
3 METRE SM.
S/M
0 .08 .16
CO2
WT. %
0 10 20
H2O
WT. %
0 20 40
ROCK TYPE
0 50 100 150 200 250 300 350 400 450 500 550 600 650 700 750 800 850 900
TRAIL RIDGE TUFF
PAHUTE MESA TUFF
ROCKET WASH TUFF
BEDDED TUFF
AMMONIA TANKS TUFF
BEDDED TUFF
RAINIER MESA TUFF
BEDDED TUFF
SCRUGHAM PEAK LAVA
BEDDED TUFF
TD
< SAMPLES FOR XRAY ANALYSIS
20AV/CAL1
20AV/NVEL1
20AV/RHOC2
20AV/DEN3
20AV/ECOR1
20AV/CO2
20AV/SWAT1

Figure 3

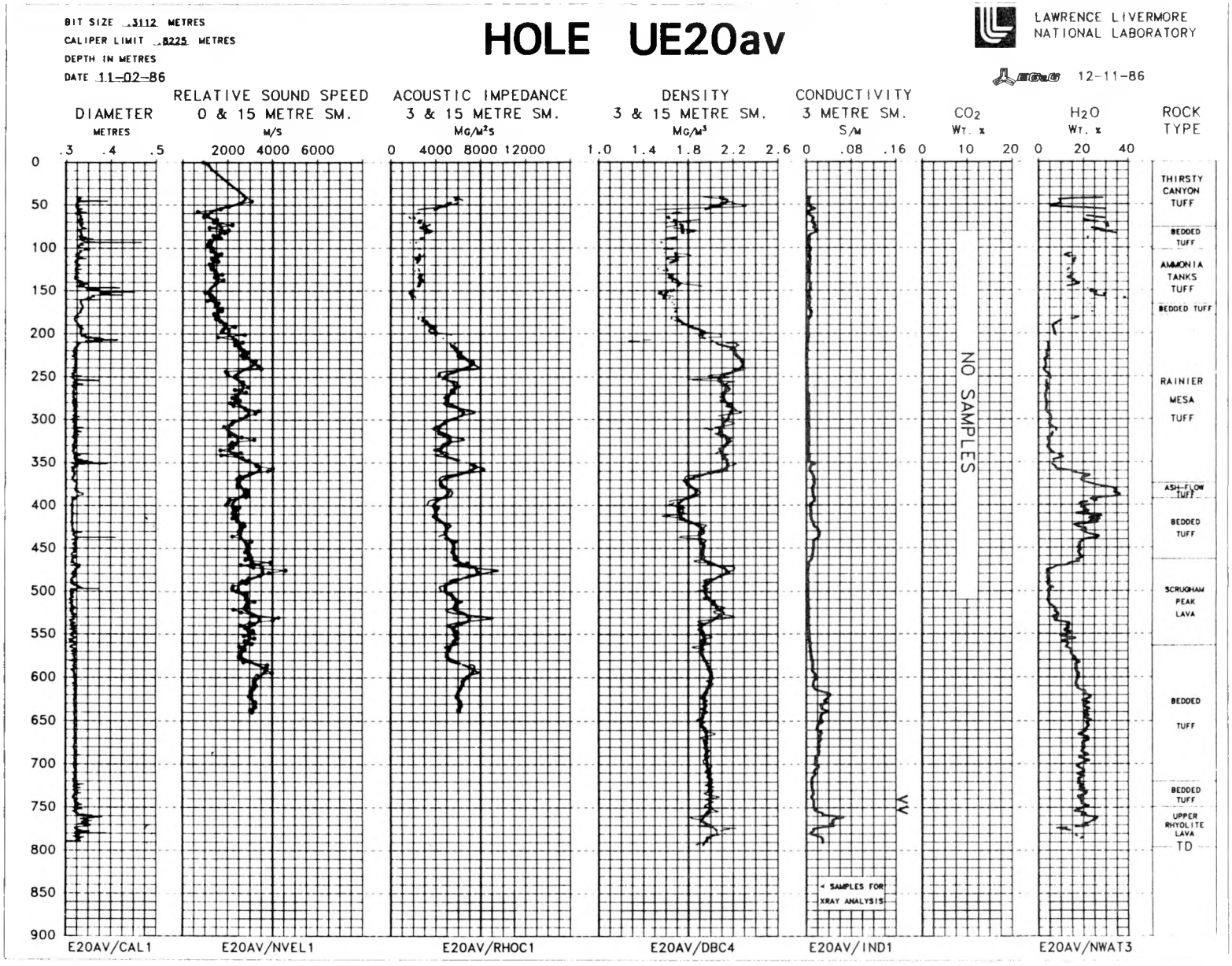

HOLE UE20av
BIT SIZE .3112 METRES
CALIPER LIMIT .8225 METRES
DEPTH IN METRES
DATE 11-02-86
LAWRENCE LIVERMORE NATIONAL LABORATORY
12-11-86
DIAMETER METRES .3 .4 .5
RELATIVE SOUND SPEED 0 & 15 METRE SM. M/S 2000 4000 6000
ACOUSTIC IMPEDANCE 3 & 15 METRE SM. MG/M²S 0 4000 8000 12000
DENSITY 3 & 15 METRE SM. MG/M³ 1.0 1.4 1.8 2.2 2.6
CONDUCTIVITY 3 METRE SM. S/M 0 .08 .16
CO2 WT. % 0 10 20
H2O WT. % 0 20 40
ROCK TYPE
0 50 100 150 200 250 300 350 400 450 500 550 600 650 700 750 800 850 900
NO SAMPLES
THIRSTY CANYON TUFF
BEDDED TUFF
AMMONIA TANKS TUFF
BEDDED TUFF
RAINIER MESA TUFF
ASH-FLOW TUFF
BEDDED TUFF
SCRUGHAM PEAK LAVA
BEDDED TUFF
BEDDED TUFF
UPPER RHYOLITE LAVA
TD
< SAMPLES FOR XRAY ANALYSIS
E20AV/CAL1
E20AV/NVEL1
E20AV/RHOC1
E20AV/DBC4
E20AV/IND1
E20AV/NWAT3

Figure 4

HARDIN Ground Motion Measurements

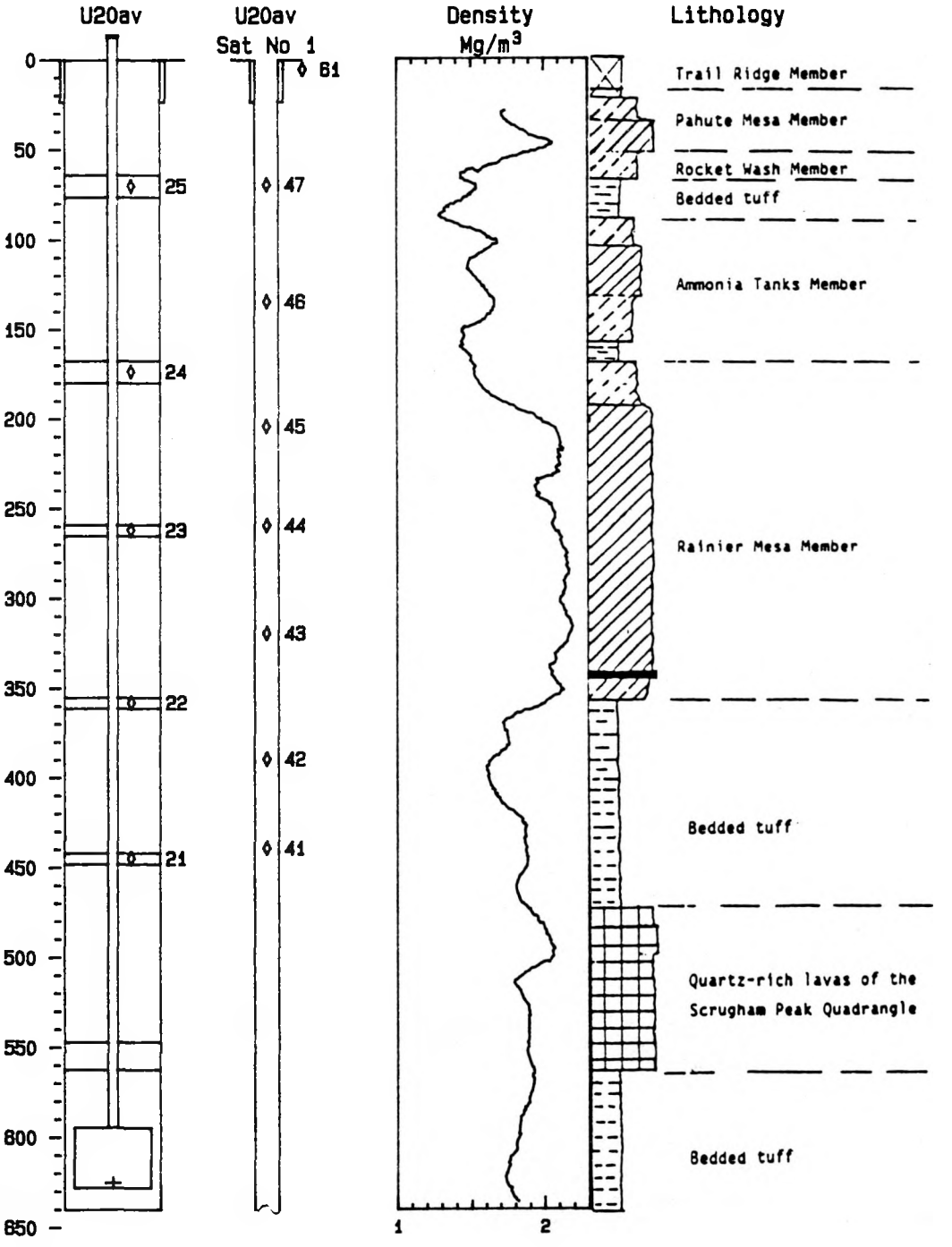


Figure 5

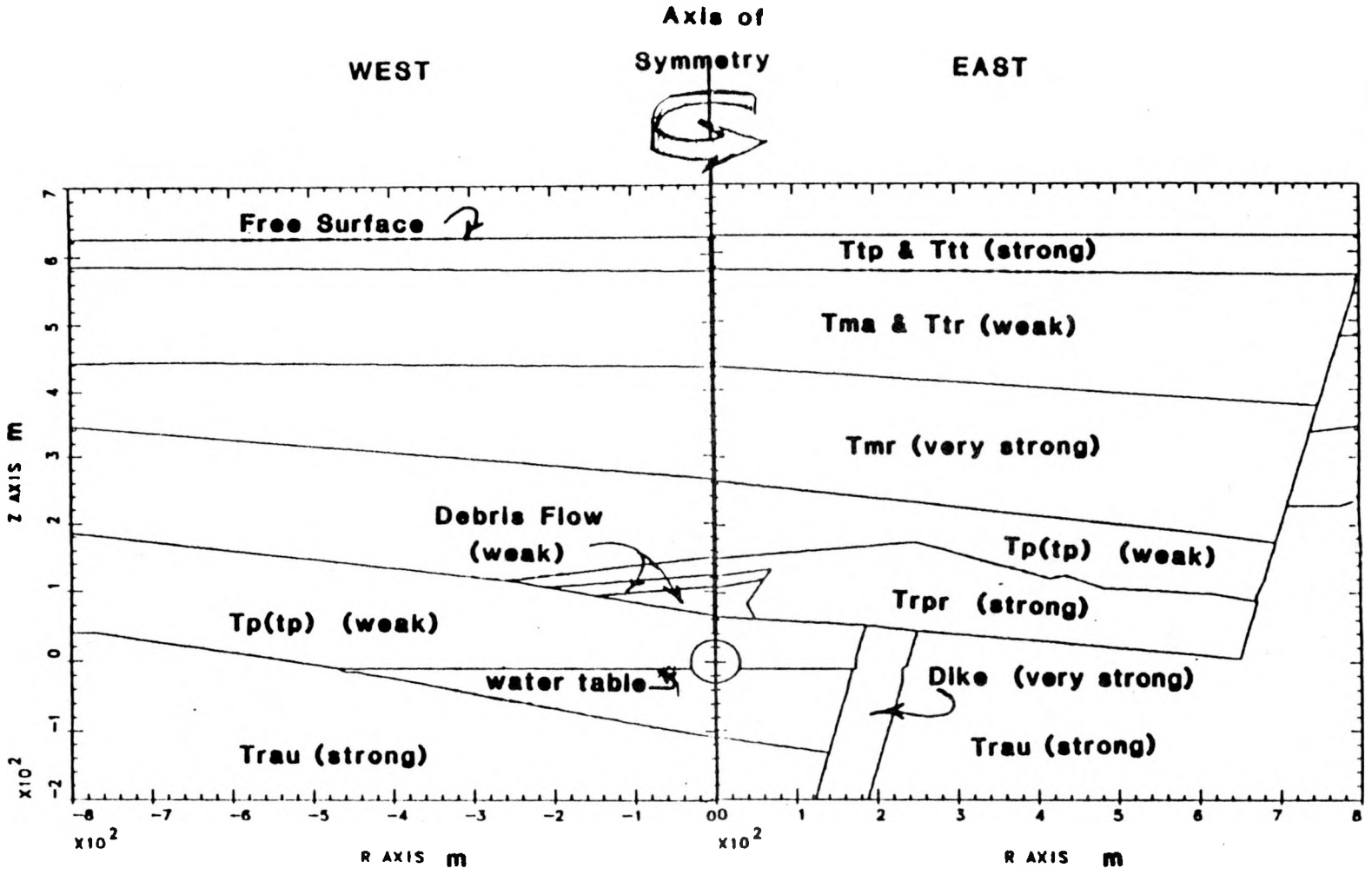

Axis of
Symmetry
WEST
EAST
Free Surface
Ttp & Ttt (strong)
Tma & Ttr (weak)
Tmr (very strong)
Debris Flow
(weak)
Tp(tp) (weak)
Trpr (strong)
Tp(tp) (weak)
water table
Dike (very strong)
Trau (strong)
Trau (strong)
Z AXIS m
X10 2
R AXIS m
X10 2
R AXIS m

Figure 6

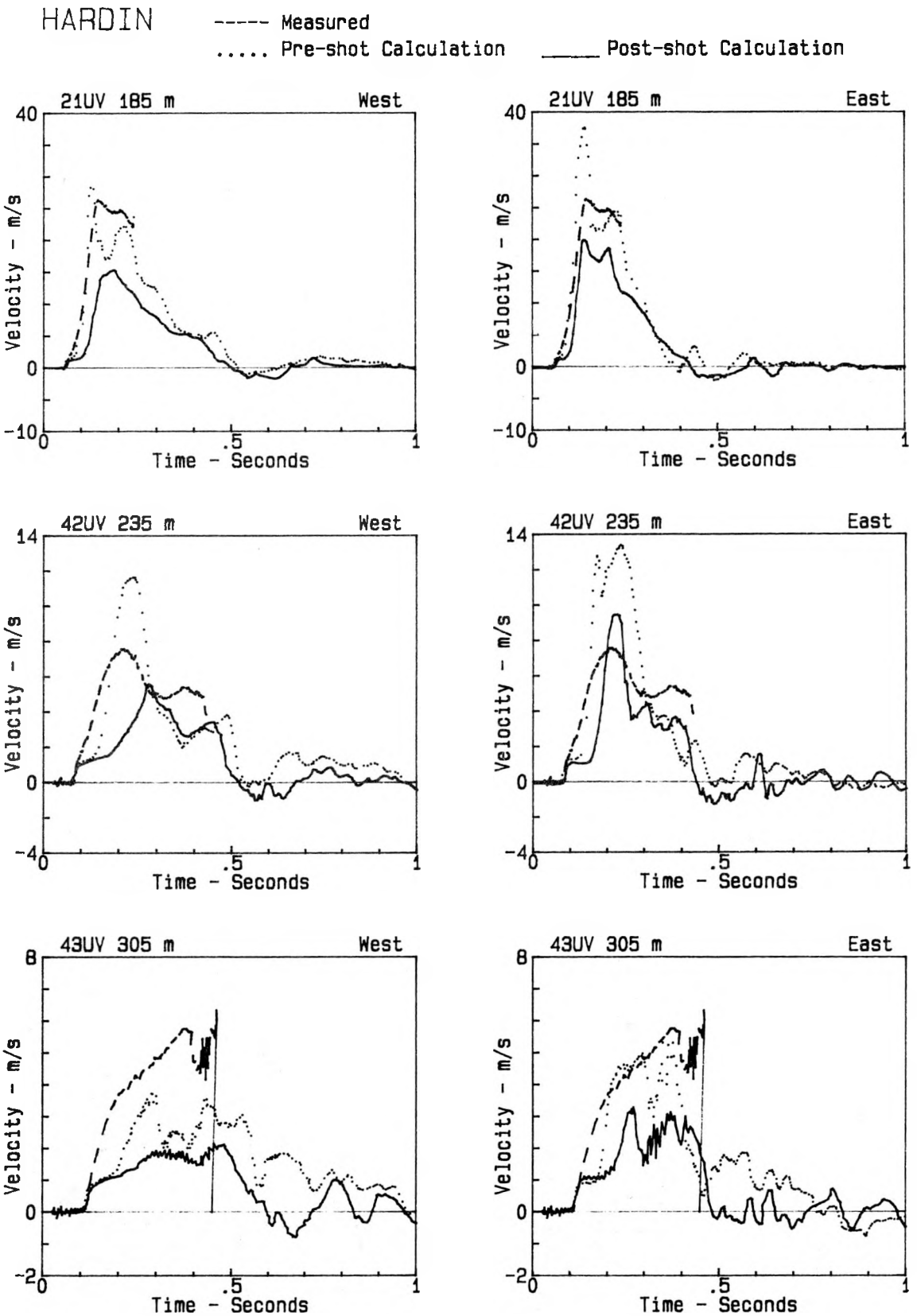

HARDIN
----- Measured
..... Pre-shot Calculation
_____ Post-shot Calculation
21UV 185 m
West
21UV 185 m
East
42UV 235 m
West
42UV 235 m
East
43UV 305 m
West
43UV 305 m
East
Velocity - m/s
Time - Seconds
40
0
-10
14
-4
8
-2
.5
1

Figure 7

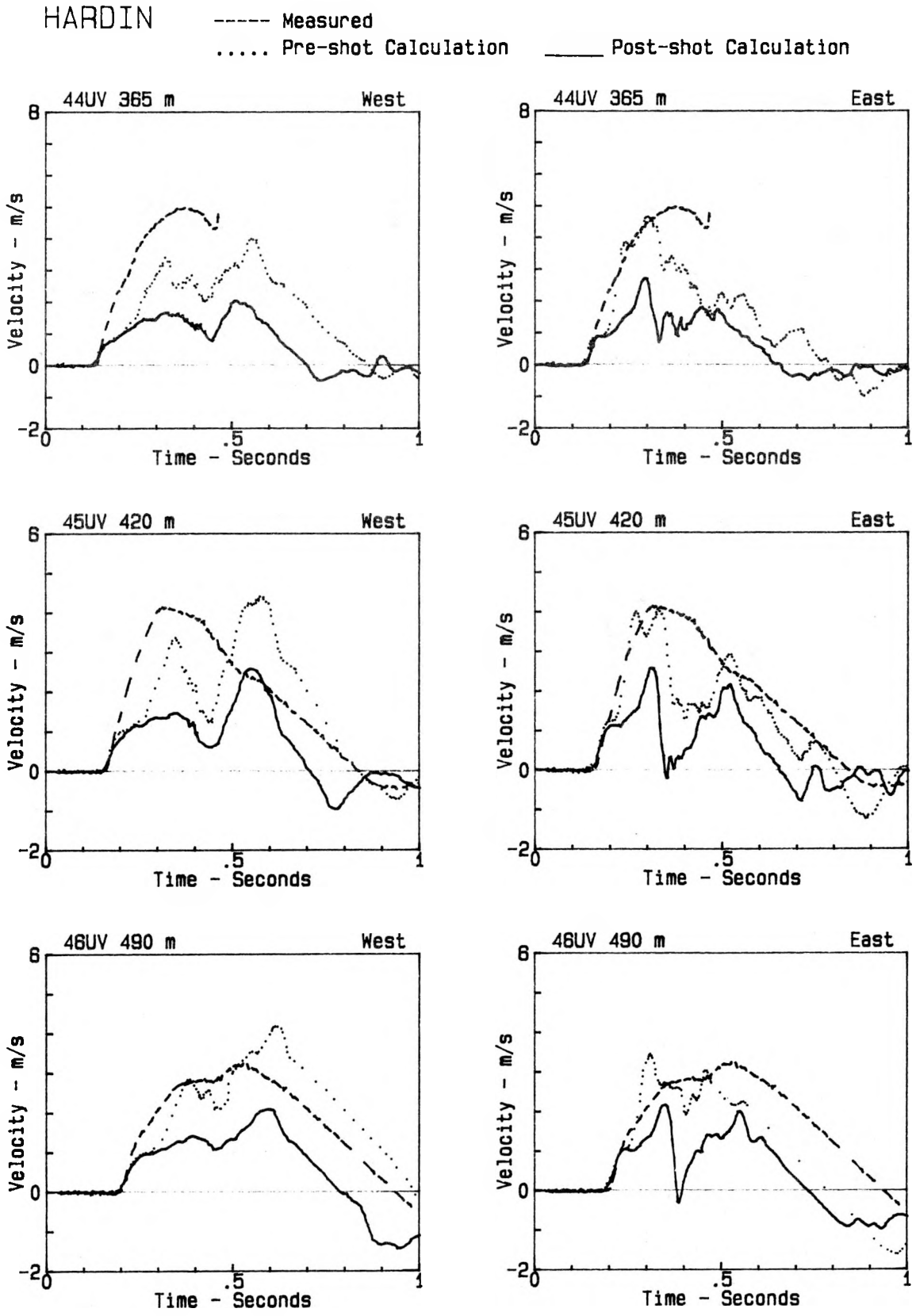


Figure 7 continued

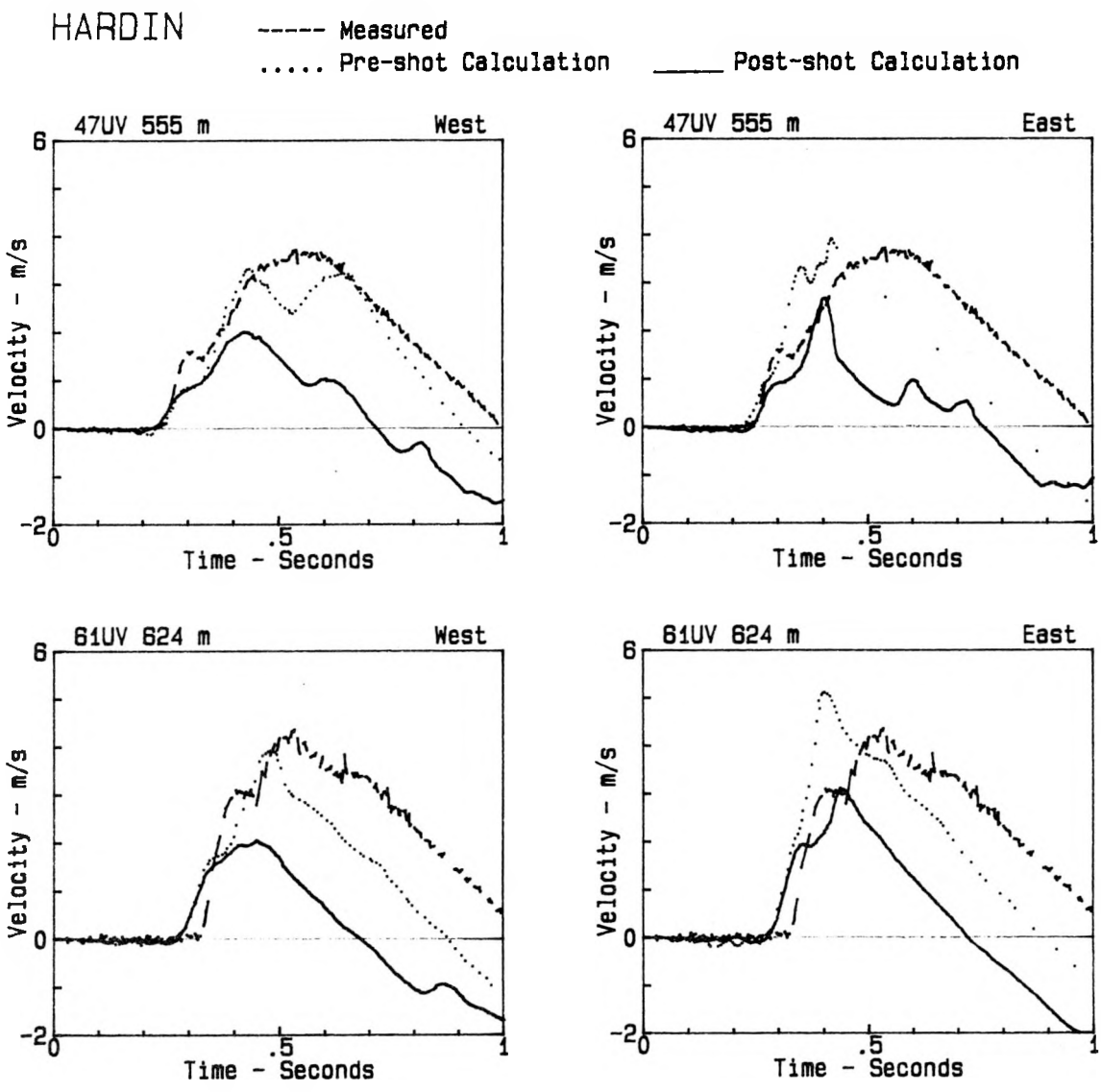


Figure 7 continued

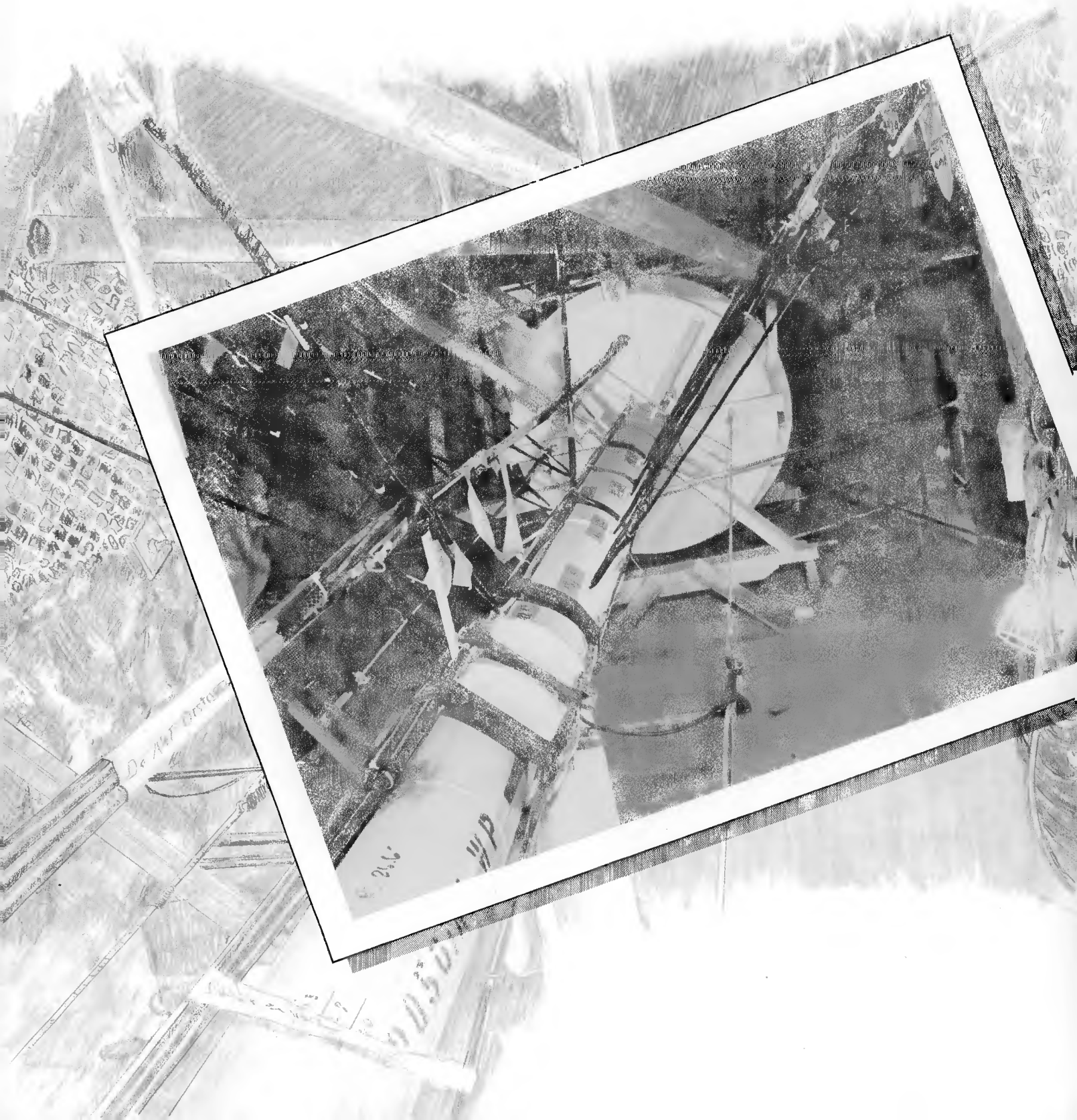
ABSTRACT

PREDICTION OF GROUND MOTION BASED ON WORKING POINT MEDIUM AND OVERBURDEN LITHOLOGY

W.M. Burnish and T.D. Kunkle,
Los Alamos National Laboratory,
P.O. Box 1663, Los Alamos, NM 87545

The two factors that have the clearest effect on ground motion are the scaled depth of burial (SDOB) and the working point (WP) medium. In particular, the saturation of the WP medium seems to have a large effect on the magnitude of the surface motion. Events with working points in saturated tuff have peak velocities a factor of 2 or more higher than events in unsaturated tuff. However, events with working points just above the static water level, i.e., in wet but not fully saturated material, sometimes behave like shots in an unsaturated medium and sometimes like shots fired below the water table. Events in saturated tuff with SDOB less than 135 $m/kt^{1/3}$ often display a "focusing" effect, having unusually high velocities at surface ground zero that drop off sharply with increased range. Events in unsaturated tuff do not exhibit this behavior, at least not at the SDOB at which we normally operate. This paper investigates what other parameters may affect the ground motion, such as density, water content, and lithology, and whether we can establish better rules for predicting near-field ground motion at the Nevada Test Site.

Event Modeling and Cavity Phenomena



ABSTRACT

MODELING OF THE BANDICOOT EVENT

F.N. App and W.M. Burnish,
Los Alamos National Laboratory,
P.O. Box 1663, Los Alamos, NM 87545

Using stress-wave calculations with realistic material response properties for alluvium derived from the nearby Merlin Event (U3ct) site, we have attempted to shed some light on the conditions that led to the dynamic venting that occurred with execution of the Bandicoot Event (U3bj). Bandicoot is one of the more spectacular examples of an event that should have been contained at its official scaled depth of burial; therefore, its failure has strongly influenced siting criteria for events in alluvium. Until this time, the event has defied modeling because of an inadequate understanding of the response properties of alluvium to ground shock. However, recent advances in modeling alluvium now make such an endeavor meaningful and practical.

The study is limited to the calculation of stress and does not address the issue of hydrofracture in the weak stress field about and above the Bandicoot cavity. Nor does it address the influence of the Area 3 fault that traverses surface ground zero. The emphasis of the study is on depth of spall, its influence on the state of residual stress about the Bandicoot cavity, and how this interaction could lead to conditions suitable to the formation of a dynamic vent path. The study also addresses the controversial issue of "actual" Bandicoot yield.

MODELLING OF THE HEARTS EVENT

Fred N. App
Wendee M. Brunish
C. L. Edwards

Los Alamos National Laboratory

ABSTRACT

The ability to calculate stress wave propagation in layered media is relevant to both containment and verification. This study uses HEARTS (U4n) as the subject event for such a calculational exercise. HEARTS is chosen because it is located within a well understood area of the test site known as the "Tuff Pile" that has the requisite layered stratigraphy and because there is considerable free field motion data available from a nearby satellite hole for verifying our calculated results. The main emphasis is on developing material response models to fit available data, and in the process improve our understanding of the physical mechanisms that shape the observed waveforms. Additionally, two calculations were made of the nearby LOWBALL and CREWLINE events to compare the calculated late-time residual stress fields with the measured micro-earthquake activity associated with those events. Most of the study is performed using a special Los Alamos version of the SNLA TOODY stress code.

We are able to achieve good agreement with most HEARTS motion measurements using fairly uncomplicated material response descriptions. Measured waveforms from near surface ground zero are the most difficult to replicate. There is excellent agreement with measured waveforms away from surface ground zero. We find that the surface ground zero and near surface waveforms are most strongly influenced by the properties we assign the alluvium and the working point tuff. Intervening materials are not as important. There is good correlation between measured post-shot microquake activity and the calculated residual stress fields for both LOWBALL and CREWLINE.

I. INTRODUCTION

The ability to calculate stress wave propagation in layered media is relevant to both containment and verification. We describe a series of two-dimensional calculations that relate to the influence of rock properties and geologic layering on 1) the state of residual stress following an

underground nuclear explosion, 2) the seismic source function for underground test verification and 3) surface ground motion. The main emphasis is on developing material response models to fit available data, and in the process to improve our understanding of the physical mechanisms that shape the observed motion waveforms. The HEARTS (U4n) event is chosen because it is located within a well understood area of the test site known as the "Tuff Pile" that has the requisite layered stratigraphy and because there is a large body of strong motion data available for the event, including both free field (from a nearby satellite/instrument hole) and free surface data, to guide us in the development of our models. Also, the nearby CREWLINE (U7ap ~1040 m NE) and LOWBALL (U7av ~1295 m SW) events were conducted in the same structural block and highly stratified environment, and each of these had measurements of postshot micro-earthquakes (microquakes) that we believe relate to the development of the late time residual stress field (Edwards, et. al, 1983). CREWLINE and LOWBALL were calculated using the same material response models that were used for HEARTS, and the resulting patterns of residual stress are compared to the observed patterns of microquake activity. This provides yet another means for verifying our models.

II. APPROACH

All calculations used in the analysis were performed using a Los Alamos modified version of the SNLA TOODY stress code. As it is configured at Los Alamos, this code is especially well suited to parameter/sensitivity studies due to the flexibility of its analytical equation of state for rock and its special method for automatically rezoning through the cavity, reducing computer execution times (and costs) to a minimum. Some calculations were made with the SHALE stress wave code for benchmarking and comparing to the TOODY calculations. SHALE currently is being brought on-line at Los Alamos for containment and verification studies. The SHALE results are not reported here.

There is a companion study on the MERLIN (U3ct) event being done by the authors in parallel with this work on the HEARTS event (Brunish and App, 1989). The emphasis of the MERLIN study is on response of alluvium (only) to ground shock from an underground test. Calculations and conclusions from that study are being reported separately, but some of the results of that effort did influence the work on HEARTS.

Figure 1 is a generic east-west geologic cross section of the area near HEARTS, CREWLINE and LOWBALL, with approximate locations of each of the three events projected onto the line of section. The waveform analysis was done only for HEARTS because it is the only event of the three with free-field, satellite hole ground motion measurements. The microquake, residual stress comparisons were done only for CREWLINE and LOWBALL because they are the events with interpreted and reported microquake locations. All three events were conducted beneath the

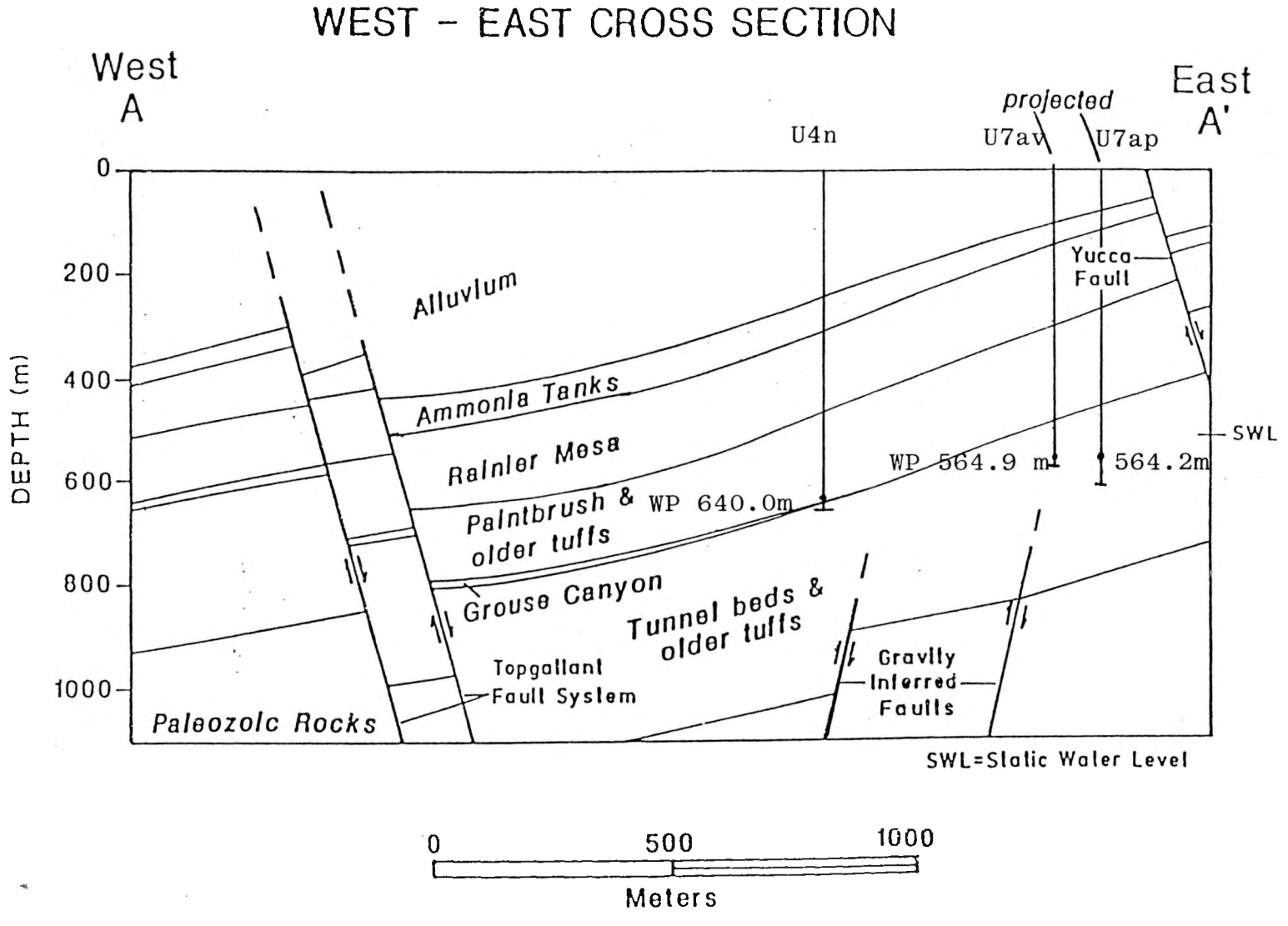


Figure 1. Typical geologic cross section across the "Tuff Pile". Shows projected locations of holes U4n (HEARTS), U7av (LOWBALL) and U7ap (CREWLINE) and the approximate positions ot the WP's within the stratigraphic section.

water table. The area lithology is comprised of a layered sequence of tuffs, ranging from very strong (140 MPa uniaxial strength) to weak (~6 MPa uniaxial strength), overlain by a thick alluvial section. Physical properties for each lithologic unit were taken from the "Tuff Pile" averages (App and Marusak, 1983). Initially, mechanical properties used in the models were from measurements on Yucca Flat core, primarily from holes Ue7f, Ue4g#2 and Ue4b, all located within the boundaries of the "Tuff Pile". Adjustments to the mechanical response models were made as the calculations progressed.

III. LITHOLOGY AND STATION LOCATIONS

Figure 2 shows the initial computational mesh for HEARTS on which the locations of measurement stations and layering are superposed. The model is two-dimensional with axial symmetry about the vertical axis. Locations of measurement stations are identified as Sta 1-8, which are subsurface stations in satellite hole Ue4f, and GM 1-12, located on the ground surface. Because we are limited in the calculations to a 2-D representation, we model the stratigraphy as flat lying, whereas in fact the beds have substantial dip (approximately 10 degrees - refer to Figure 1). Also, there is a 9 m offset in the Tmr between U4n and Ue4f, suggesting the presence of a fault between the two holes at Tmr depth. We have attempted to assess the effect of these departures from two-dimensionality in the study.

The WP is within a sequence of bedded, zeolitized Wahmonie tuffs and Pre-Rainier, Post-Wahmonie tuffs sometimes (inaccurately) referred to as Paintbrush Tuff (Tp). For the most part, they are beneath the water table at U4n so they have little or no gas filled porosity. This sequence of tuffs have similar physical, and as far as we know, mechanical properties, so for purposes of calculations we combine them as one unit under the Paintbrush designation. The unconfined compressive strength (maximum stress difference under a condition of applied uniaxial stress) of these rocks is about 13 MPa, as determined from mechanical measurements on undamaged core. Maximum strength is about 30 MPa.

The top of the zeolitized Tunnel Beds Tuff is located 15 m beneath the WP. We generally assign an unconfined strength of 16 MPa and maximum strength of 50 MPa to these rocks. The Paleozoic (Pz) Dolomite is at a depth of about 1070 m, 430 m below the WP. The assigned unconfined strength is 60 MPa accompanied by a very large increase in strength with confinement.

The Rainier Mesa Tuff (Tmr) above the WP is highly variable in its properties, and in the calculations has been subdivided into 4 sections. The lowermost (Tmrl) is a non-welded, partially zeolitized ashflow tuff that is known to be weak and friable. We believe it is almost saturated with water despite being above the water table. Its unconfined compressive strength is about 6 MPa and the maximum strength is 20 MPa. Station 8 is within this layer. The welded,

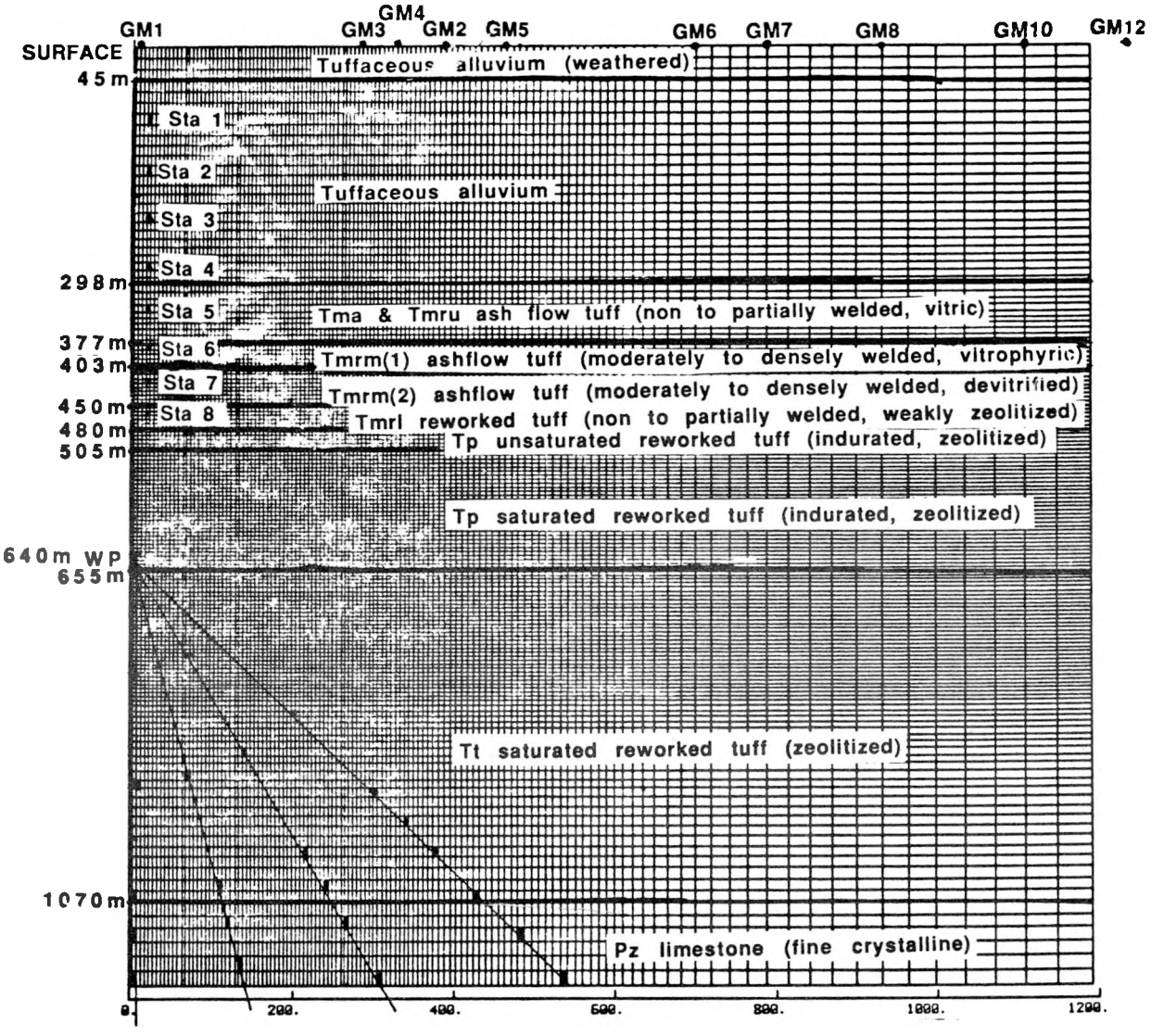


Figure 2. Computational mesh (partial) used for most 2-D calculations. Shows layering and locations of ground motion stations. The unidentified points along radials down from the WP are output edit points for the calculations that are not discussed in this paper. The full mesh extends 2000 m down and to the right.

middle portion extends from 377 to 450 m depth and is designated as Tmrm(1) and Tmrm(2). This is a very strong unit with measured (on core) unconfined strengths as high as 140 MPa. The relative positions of Tmrm(1) and Tmrm(2) within the Tmrm and the strength and stiffness of each are among the parameters varied as part of the study. Station 7 is located within what is described as a "moderately" welded portion of this unit. Station 6 also is in moderately welded Tmrm but it is located just beneath a vitrophyre near the top of the unit. Above this very strong layer is another weak, friable ashflow unit designated as Tmru, which is in turn overlain by the slightly more competent, bedded Ammonia Tanks member of the Rainier Mesa Tuff (Tma). We modeled these two units as a single layer, assigning it an unconfined strength of 9 MPa and a maximum strength of 25 MPa. The combined Tmru-Tma is the first unit up from the WP that has a substantial amount of easily crushed gas filled porosity (about 20%). Station 5 is within this unit.

Tuffaceous alluvium extends from the top of the Tma at 298 m to the surface. The mechanical properties of this alluvium are not well known and they were treated as parameters to be adjusted in the waveform analysis. The gas filled porosity of the alluvium is 16%. Stations 1 through 4 are located in the alluvium.

IV. MOTION MEASUREMENTS

The satellite, or instrument, hole (Ue4f) is located 24 m N-NE of the U4n HEARTS emplacement hole. Accelerometers in the satellite hole were emplaced in grout and measured vertical motion only. At the surface motion array, all three components of motion were measured except at GM1 (SGZ), where only the vertical component was measured. Figures 3, 4 and 5 show the measured waveforms at all recording stations from 0 to 3 seconds. Not included are the y-component (horizontal - tangent to SGZ) measurements along the ground surface. In general, the y-component is very small until spall closure, at which time it shows substantial amplitude at some of the stations. From this standpoint, our assumption of 2-D, axial symmetry is entirely adequate until spall closure.

Along the satellite hole (Figure 3), all plots are scaled from -10 to +30 m/s to show the attenuation of amplitude with distance and material type as the wave propagates toward the surface. The gage at Station 8 was lost before it reached its peak and in order to keep a good plot scale for the shallower stations, the Station 8 measurement is truncated. The Station 8 gage had reached 55 m/s when it failed. It is just a steep rise, with no discernible structure. All of the three deepest stations have very steep rises to their peak amplitudes, in keeping with the low rock compressibilities at these locations. The rise is considerably slower at Station 5 where apparently some crush of the initial 20% gas porosity occurs. The front end of the wave becomes much broader in the alluvium. Somewhere between Stations 4 and 3 the amplitude decays to the point

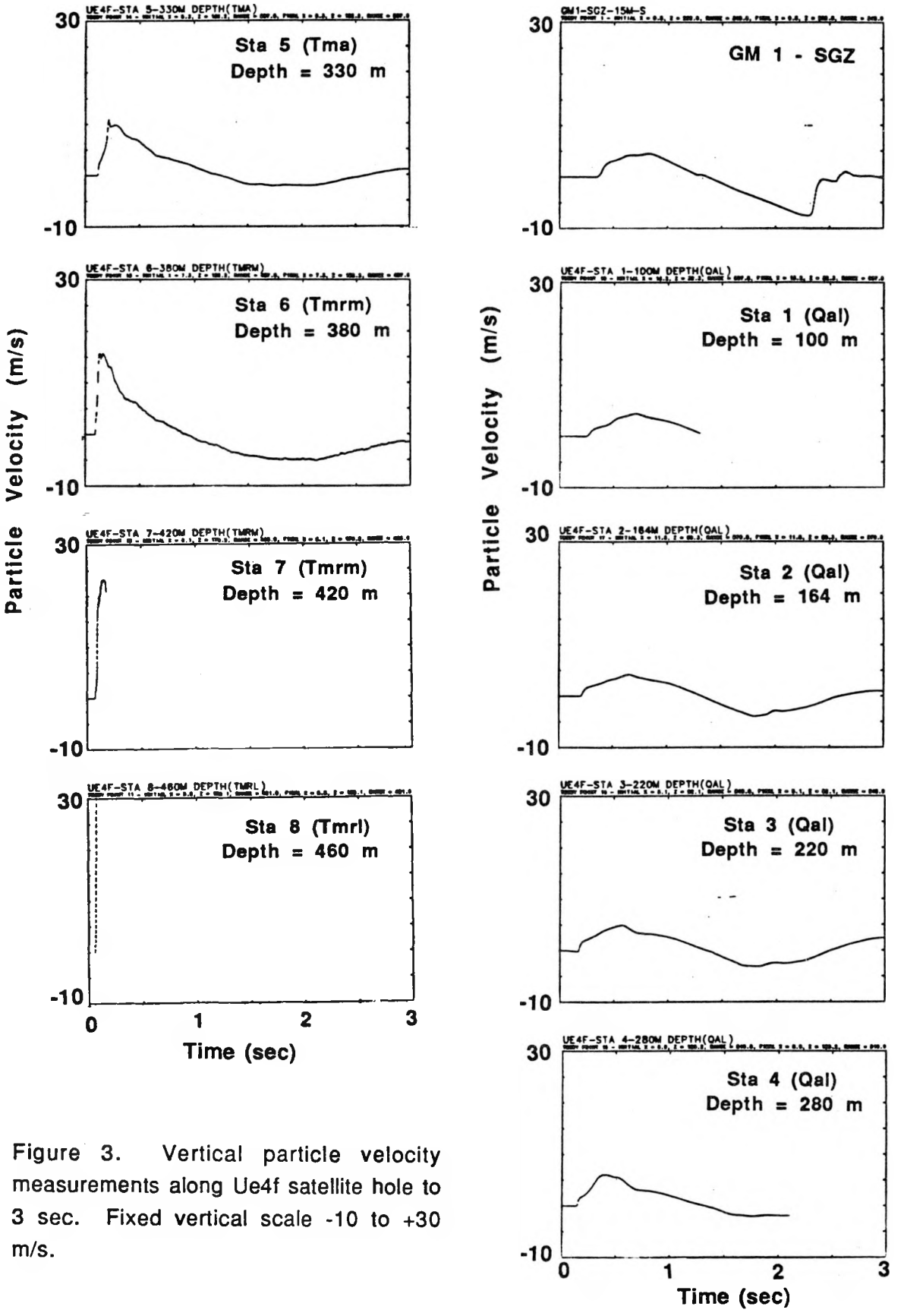


Figure 3. Vertical particle velocity measurements along Ue4f satellite hole to 3 sec. Fixed vertical scale -10 to +30 m/s.

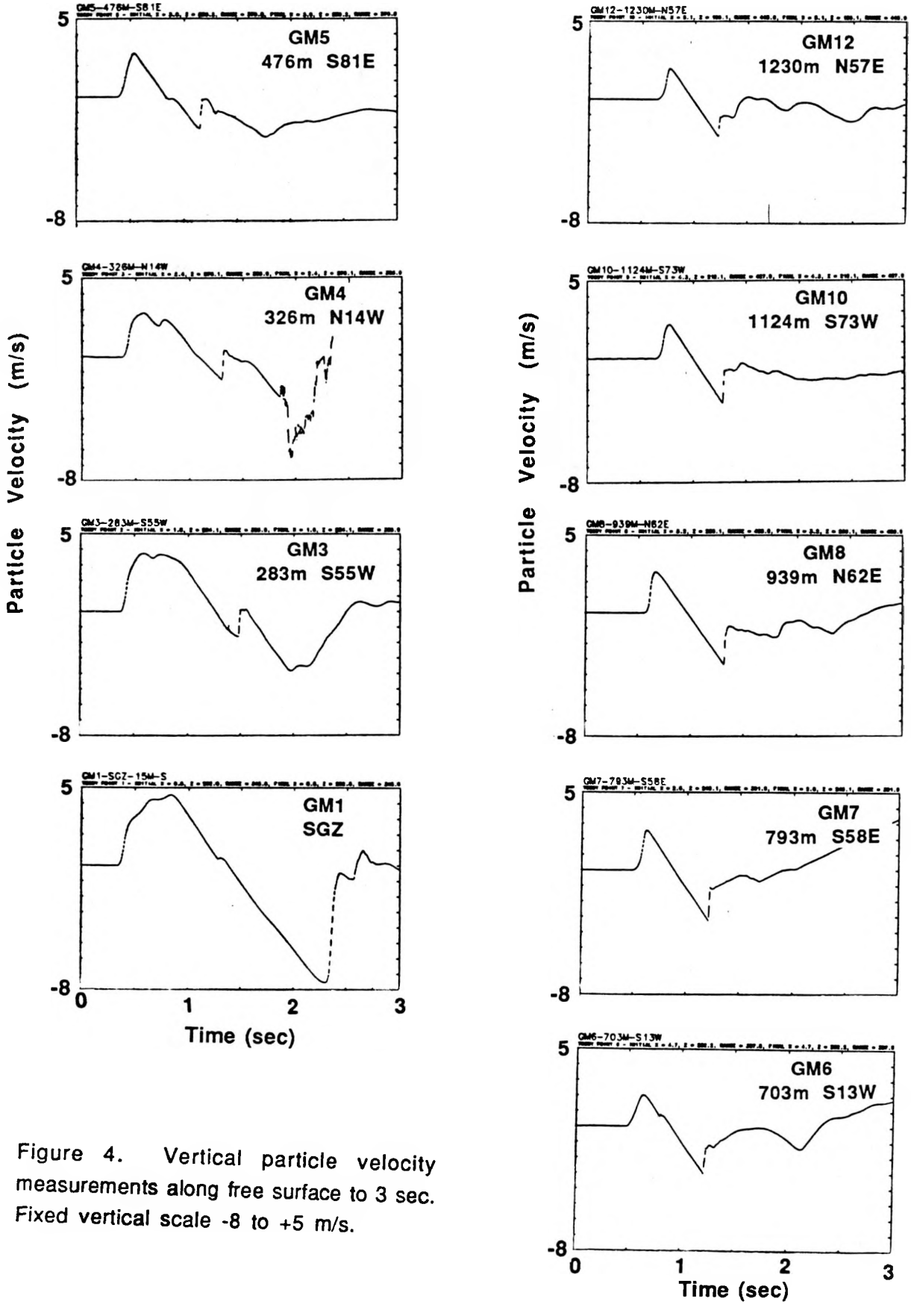


Figure 4. Vertical particle velocity measurements along free surface to 3 sec. Fixed vertical scale -8 to +5 m/s.

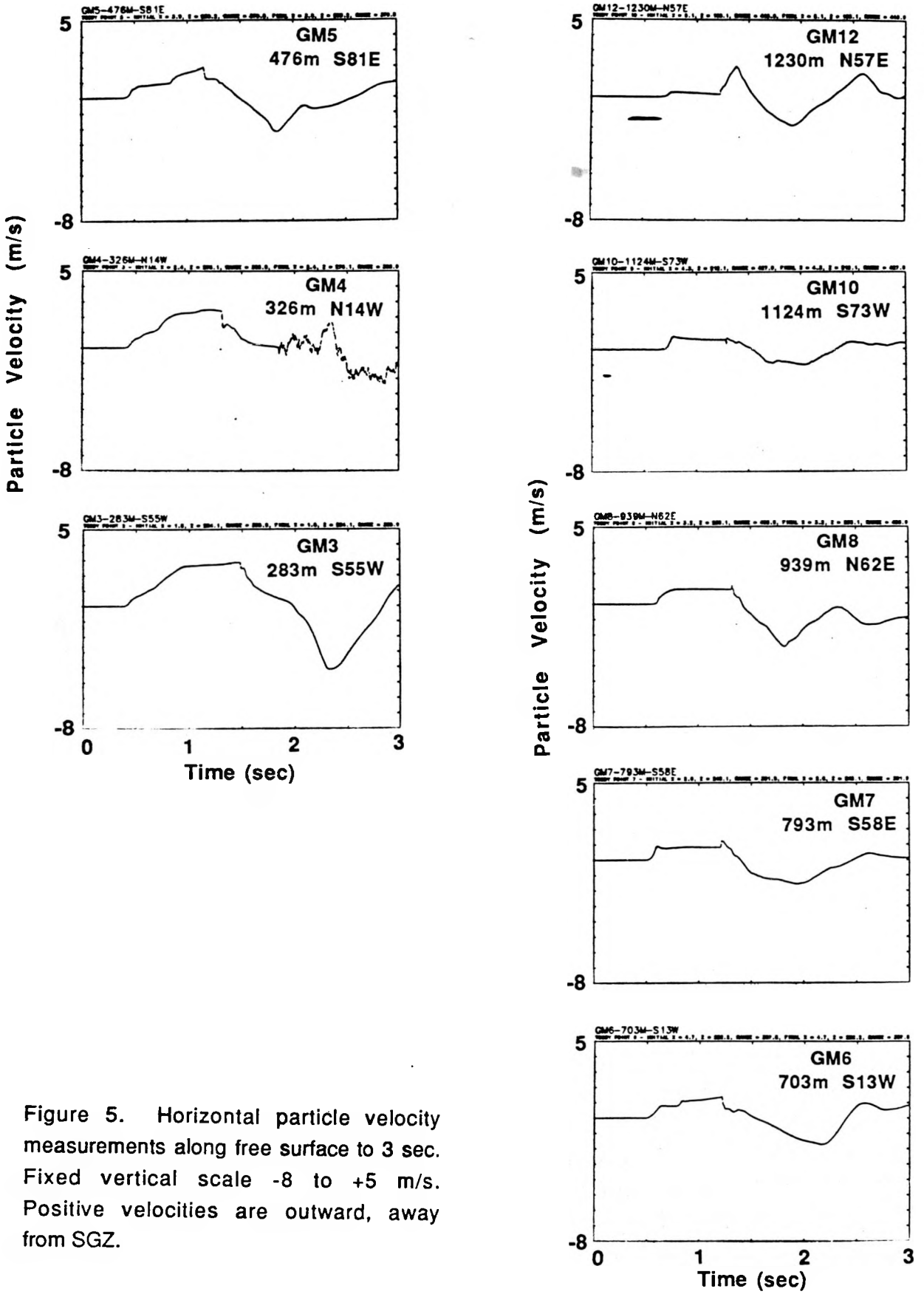


Figure 5. Horizontal particle velocity measurements along free surface to 3 sec. Fixed vertical scale -8 to +5 m/s. Positive velocities are outward, away from SGZ.

where pore crush no longer occurs, i.e., the elastic radius. Station 3 has a rise time to peak amplitude of about 400 ms, followed by a very gradual decay. There is no significant additional broadening after Station 3. This very long wavelength causes free surface spall to be delayed until after 800 ms. A very broad positive velocity phase with delayed spall is a frequently observed characteristic of free surface motion for events conducted beneath the water table with overlying alluvium. It generally is not true of tuff events conducted above the water table with overlying alluvium.

Along the free surface (Figures 4 and 5), and with increasing distance from SGZ, the characteristic shape of the waveform changes from the broad pulse mentioned above to one that has the characteristic "N" shape of surface motions observed for events at hard rock sites, and to a lesser degree, events conducted in tuff above the water table. Horizontal motion is initially outward, followed by an inward acceleration at spall closure. The lone exception to this is the farthest station 1230 m from SGZ (GM12). It appears that spall closure is outward at that point, either because of its distance or because it is located on the other side of the Yucca Fault (see Figure 1). This is the only station located east of that fault. It is noted that Station GM2 is omitted from this and all other figures showing surface motion. The data from that station does not add substantially to the discussion and we needed to eliminate one station to conserve space in the figures.

Complete response histories, including particle velocities, were calculated and plotted at each measurement station. We took the approach of adjusting the material mechanical properties, sometimes accompanied by changes in the material response equation of state subroutine, until we achieved an acceptable match to the measured waveforms. The presence of distinct layers of widely varying properties makes the problem of waveform matching more difficult, but it also provides an opportunity for studying the manner in which layering perturbs a propagating stress wave.

V. RESULTS OF WAVEFORM MATCHING

Approximately 50 2-D HEARTS calculations were performed during the course of the study. Many of these were special purpose sensitivity studies. It is not the purpose of this paper to discuss in detail the effect of each model used in all calculations, but rather to summarize the general results of all calculations using two selected examples that we feel are representative of our efforts to date. These are identified as Problems HE71 and HE86. There is no "best calculation", meaning there is no single calculation that replicates to our complete satisfaction the observed waveforms at all stations. We do believe the calculations performed thus far have provided us with some valuable insight into the physical mechanisms responsible for the observed response.

The mesh and layering for HE71 are as shown in Figure 2. The mesh for HE86 is similar to that for HE71 except that zones are of uniform size to the surface, without the gradation to larger zones as the surface is approached. The layering is slightly different for HE86. The stratigraphic section in the Tmr units is 10 m higher and there are some differences in how the Tmrm unit is subdivided. The layering for HE86 is consistent with that encountered at hole Ue4f, the satellite/instrument hole. The layering for HE71, and shown in Figure 2, is for the U4n HEARTS emplacement hole. These differences are relatively minor, but we feel the HE86 layering is an improvement over HE71 because instrument station edit points are more accurately located relative to the lithologic boundaries.

The main difference between the two calculations is the manner in which we treated the rock near the WP. In HE86, we used a rather standard approach in which the Tt, Tp and Tmrl were given little or no gas porosity and we assumed that the rock experienced moderate "damage" with accumulated, inelastic shear strain. We allowed the shear strength to drop to about one-half its virgin, undamaged strength at 10 percent strain, with no further damage beyond that.

In Problem HE71, we used a technique that links shear failure to the onset of pore crush. The shear failure surface is adjusted at execution time to be coincident with the state of shear at the initiation of crush. All rocks beneath the water table were given a minute amount of gas porosity (0.5 percent) with a threshold crush pressure of 10 MPa. The effect of this "linkage" is to severely weaken the rock near the WP. We achieved essentially the same result in other, unreported calculations simply by allowing more damage to occur with accumulated strain. We do not mean to imply, through our reporting of this particular calculation, that the shear/crush linkage technique is a preferred technique for material modelling.

PROBLEM HE86.

Figure 6 is a comparison of the HE86 calculated waveforms with the satellite hole measurements. Following is a station-by-station description and interpretation of those waveforms.

Stations 8, 7, 6 and 5 - Tuff. In order to match the short rise times and amplitudes at these deeper stations, we found it necessary to have nearly saturated materials to the base of the Tmrm at 450 m depth. The U.S.G.S estimated depth is 500 m, but the exact depth to the saturated zone is not well determined in this area. A gas porosity of only 2 percent in the interval between 500 m and 450 m results in a well developed precursor that is not evident in the measurements. The calculated peak amplitude at Station 7, near the middle of the welded Tmrm, appears to be about right - perhaps slightly low. This measurement terminated just after the peak velocity was reached. At Station 6, located near the top of the Tmrm, the calculated peak amplitude is about 50 percent higher than the measured value, and is in fact about 5 percent higher than the

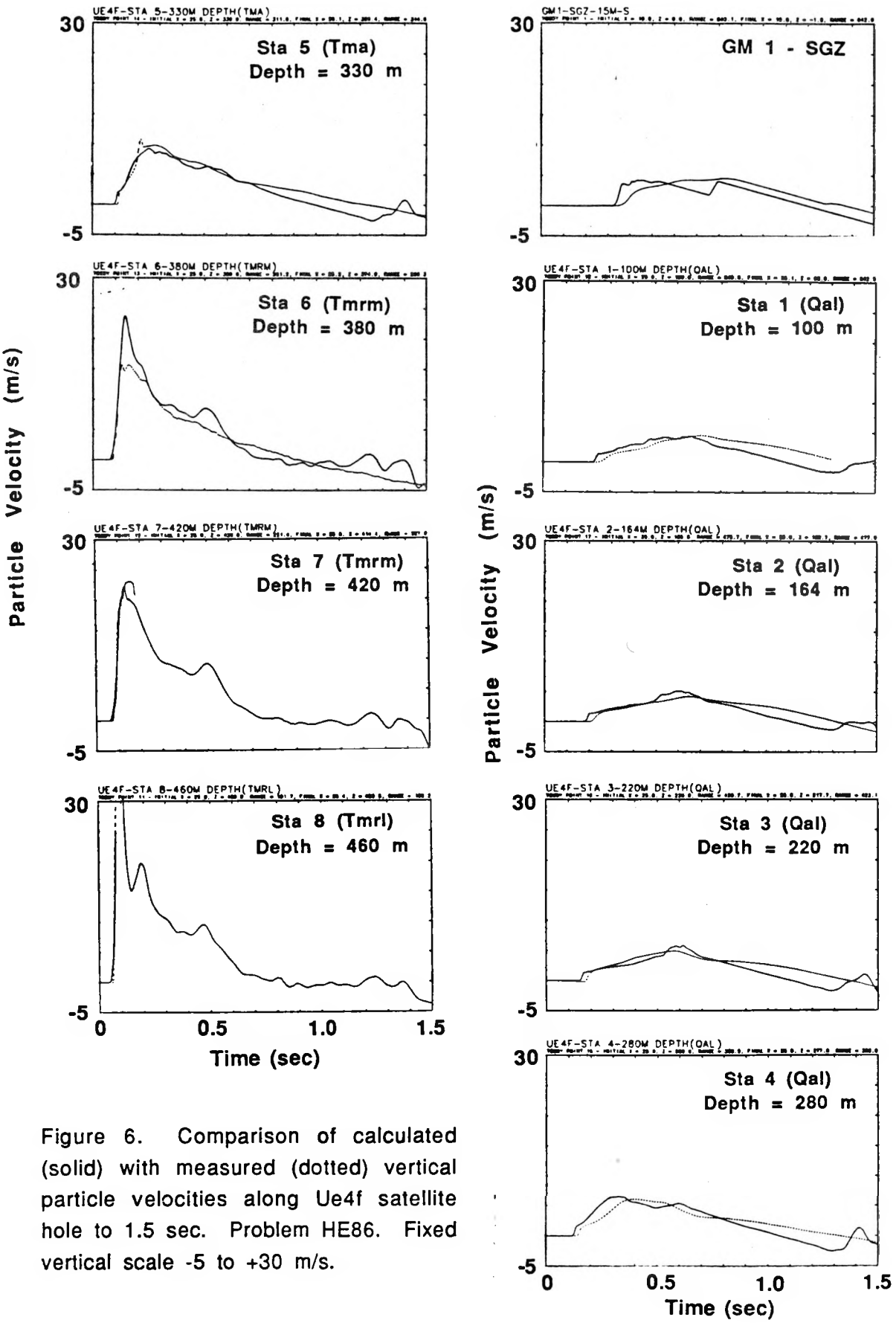


Figure 6. Comparison of calculated (solid) with measured (dotted) vertical particle velocities along Ue4f satellite hole to 1.5 sec. Problem HE86. Fixed vertical scale -5 to +30 m/s.

calculated value at Station 7. In the calculation, the jump in particle velocity is caused by the reflected rarefaction returning from the Tmrm/Tmru-Tma interface. We believe we are using reasonably correct models for both the Tmrm and the Tmru-Tma. The sharp rise and lack of a well developed precursor at Stations 7 and 6 supports our contention that the Tmrm is strong and relatively incompressible. Very little gas porosity is being crushed from this rock. At Station 5, in the Tma-Tmru, a marked increase in risetime indicates that this layer is quite compressible, in keeping with our expectations. We tried to find the reason for the apparent discrepancy between the measurement and calculation. We modelled the vitrophyre just above Station 6 as very strong and stiff to see if that would mute the influence of the stress relief wave. Also, we ran a special calculation with the interface dipping 20 degrees from horizontal, consistent with the observed offset between U4n and the satellite hole. Neither of these approaches had a significant impact on the calculated Station 6 response. One can postulate that the structure responsible for the 9 m offset at the Tmrm between U4n and Ue4f is responding in such a way as to cause a local reduction of the vertical component of velocity at Station 6. However, it is difficult to examine such a possibility under our current limitation to two dimensions. Despite the too large amplitude at Station 6, the calculated waveform at Station 5 in the Tmru-Tma agrees well with that station's measurement.

Stations 4, 3, 2 and 1 - Alluvium. At Station 4 there is a marked change in the character of the waveform. The measured risetime increases from about 100 ms at Station 5 to over 200 ms at Station 4. In the calculation, we capture some, but not all, of this increase. At Station 3 we calculate a 450 ms rise to the peak, slightly greater than measured. The calculated transition point from crush to no crush behavior occurs between Stations 4 and 3 in both the calculations and measurements. However, apparently there is a difference in the ranges at which this occurs. We know from our work on MERLIN alluvium that the amplitude and wave shape near the transition point is very sensitive to the exact range at which the transition occurs. The fact that our calculated rise time to the peak at Station 4 is a bit short is not of concern to us. At the shallower stations, the calculations continue to have about the same, correct rise to peak amplitude, but the drop off in amplitude at the tail of the wave is too severe. The strength of the rarefaction from the free surface is too great, or to put it another way, there is not enough energy in the trailing portion of the outgoing wave to mitigate and delay the spallation caused by the surface rarefaction.

An important feature to note is the positive (upward) velocity excursion in the tuff (Stations 8, 7, 6 and 5) that occurs between 0.4 to 0.6 sec, in the trailing, "rarefaction" part of the wave. This is associated with an elastic phase that accompanies a change in principle stress direction from one of maximum stress in the direction of wave propagation to transverse to the direction of propagation. It is a rebound phenomena related to cavity growth and rebound. We believe we see a similar feature in the measured waveform at about the same time, but it is not as prominent as in the calculation. In the calculation, it forms at depth (in the Tp) and propagates upward at

the elastic wave speed. Because it is an elastic wave, its amplitude decay is much less than that of the initial shock and it dominates the waveform at the shallower stations, contributing to the "peaked" appearance of the wave at Stations 3 and above. It manifests itself at the free surface by further delaying the onset of spall at stations close to SGZ. If we are correct in believing that we are modelling a behavior similar to what is actually occurring, then this is a significant development. It means that the propagating wave contains information on cavity growth that is visible and possibly interpretable at stations far removed from the WP, and perhaps even at the free surface. Equally important, the wave contains information on the response properties of rocks near the WP after they have been shock damaged. We believe we see the same behavior in the MERLIN data, which implies that the possibilities are not limited to events conducted in the high water environment of HEARTS.

PROBLEM HE71

This is our most successful attempt at matching the near surface waveforms. We forced shear failure to occur at the onset of pore crush, thus markedly reducing the shear strength of all rocks between the WP and the base of the Tmrm. Figure 7 is a comparison of Problem HE71 with the satellite hole measurements, In this calculation the depth interval from 500 m to 450 m was modelled with 2 percent gas porosity. The weaker WP materials resulted in an initially higher amplitude wave in the WP materials, and we needed to include some gas porosity in order to reduce the peak amplitudes to that of the measurements at Stations 7 and 6. There is an obvious, well developed precursor at Stations 8 through 5 that is not evident in the data (which was the original argument for not including much gas porosity). A subtle, but important, effect is that the deep, late-time elastic rebound mentioned in connection with HE86 above, is less pronounced, more gradual, resulting in a waveform at shallower stations that are a little more like the measurements. Spall, and the "first" spall closure, appears to be less severe.

Figures 8 and 9 show the vertical and horizontal surface motions respectively. At SGZ (GM1), we are getting some, but not enough, of the broadening and delayed spall that occurs in the data. The same is true at GM3, 283 m from SGZ. Farther away from SGZ, the agreement becomes progressively better with both the vertical and horizontal calculated waveforms in excellent agreement with the data. Additionally, we are capturing, in a qualitative sense, the intermediate spall closures indicated by the data.

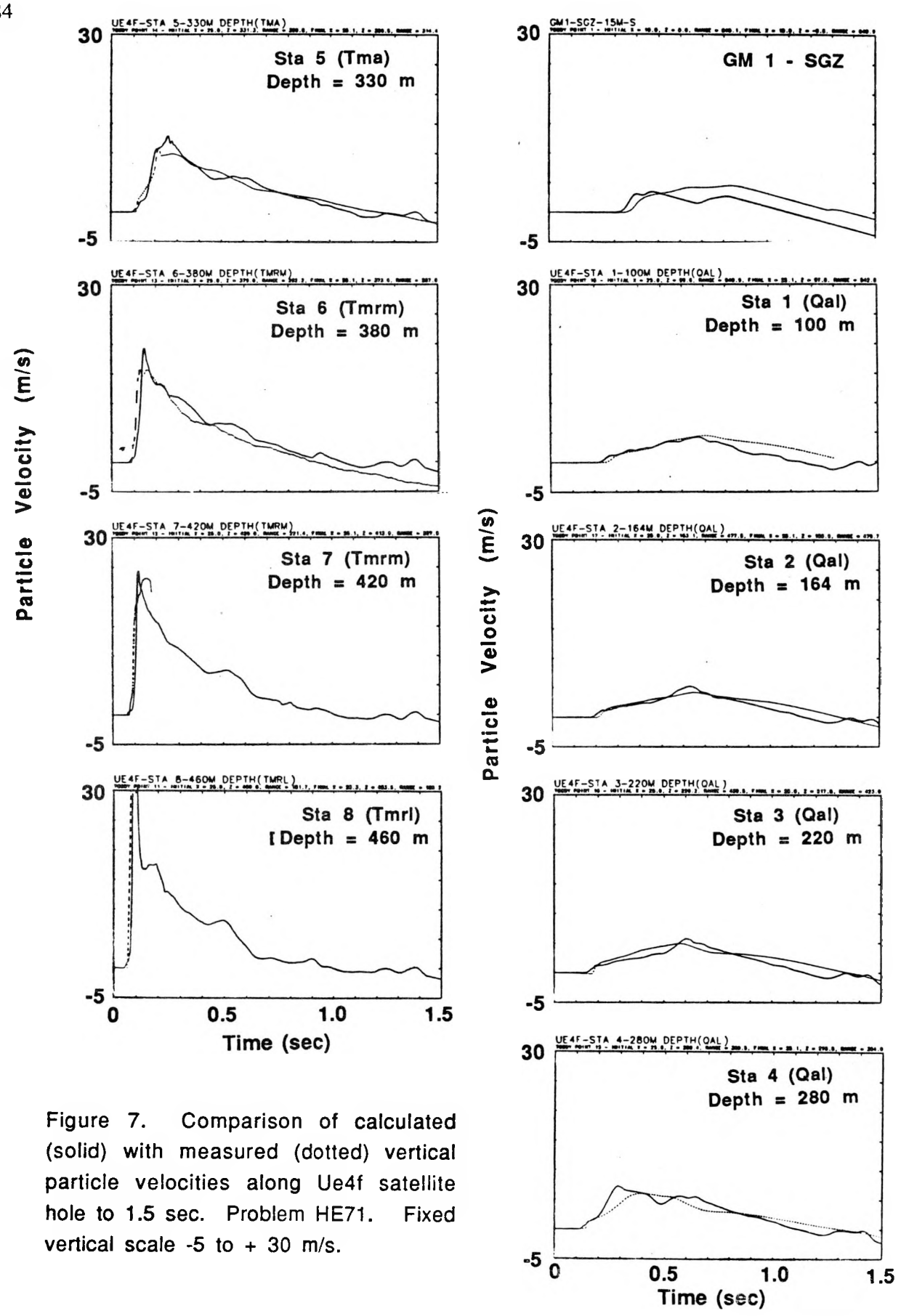


Figure 7. Comparison of calculated (solid) with measured (dotted) vertical particle velocities along Ue4f satellite hole to 1.5 sec. Problem HE71. Fixed vertical scale -5 to + 30 m/s.

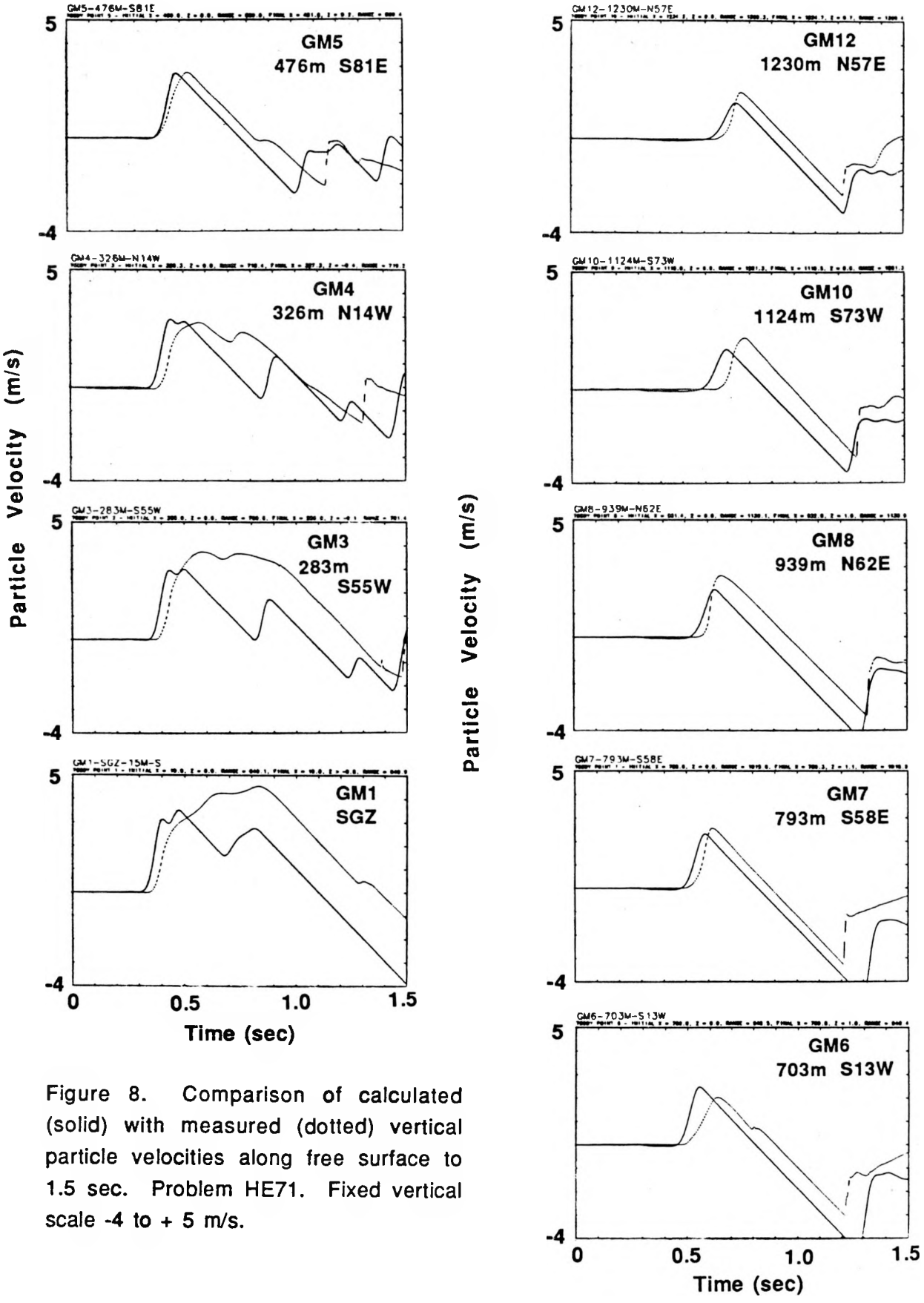


Figure 8. Comparison of calculated (solid) with measured (dotted) vertical particle velocities along free surface to 1.5 sec. Problem HE71. Fixed vertical scale -4 to + 5 m/s.

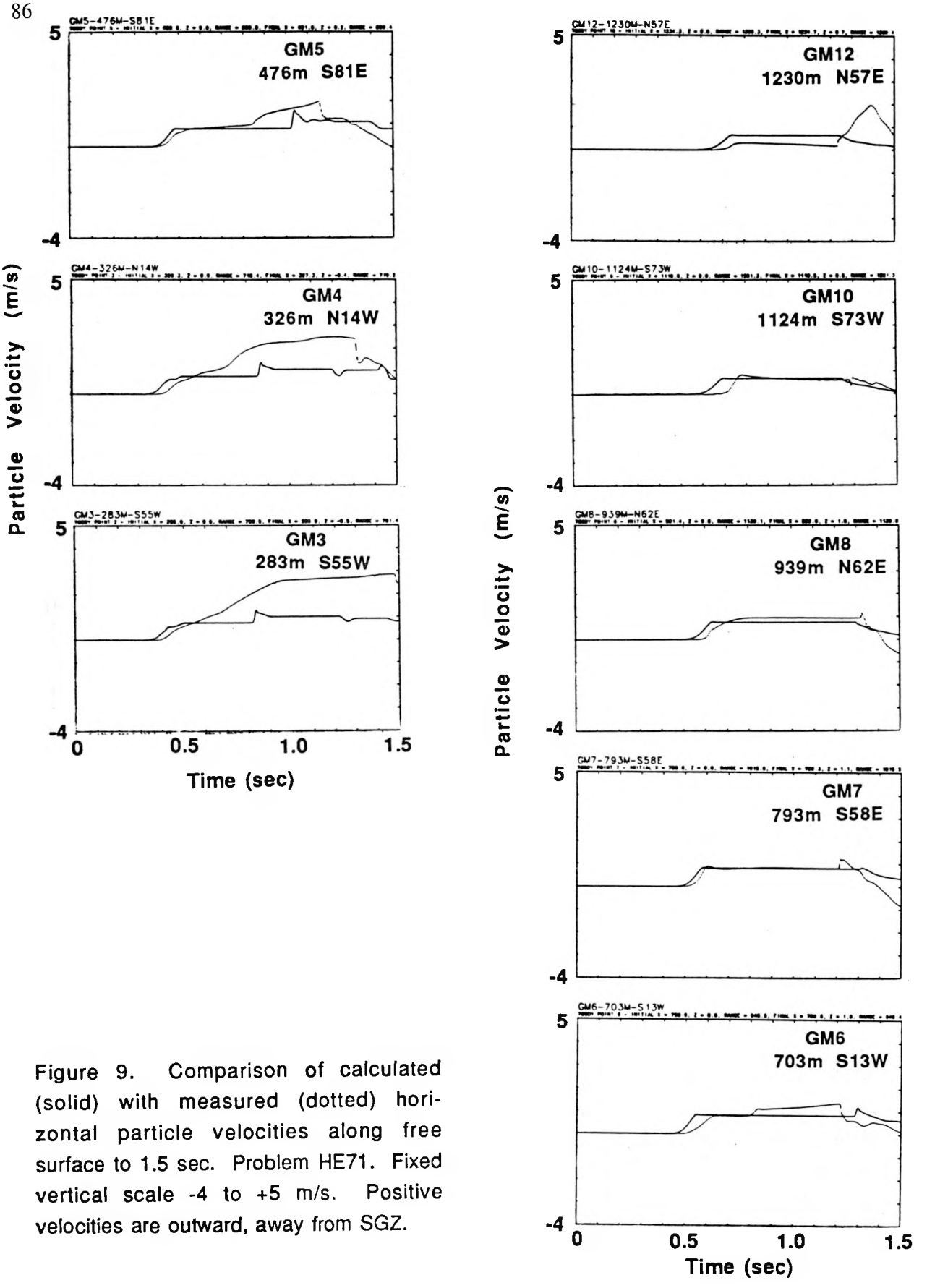


Figure 9. Comparison of calculated (solid) with measured (dotted) horizontal particle velocities along free surface to 1.5 sec. Problem HE71. Fixed vertical scale -4 to +5 m/s. Positive velocities are outward, away from SGZ.

Figures 10 and 11 show the surface motions for a slightly different version of Problem HE71, the only differences being that the alluvium and the Tmru-Tma are slightly less compressible and the alluvium is modelled as initially very weak in shear, as opposed to having it weaken with accumulated damage (the virgin failure envelope is the same as the fully damaged envelope for the case just discussed). This has a surprising effect. There is improved agreement (increased amplitude, broader waveform) at SGZ (GM1) and GM3, but the amplitudes at the farther out stations are too low. Also, the ratio of horizontal to vertical velocity, which was quite good in HE71, now is too small. What we thought were minor changes significantly increased the focusing of energy toward surface ground zero.

A problem that we have not yet resolved is reconciling the rock strengths we apparently need to achieve waveform agreement with the strength required for agreement with cavity radius measurements. To this point in the study, we have largely ignored cavity radius considerations, preferring to let the waveforms dictate the strength models used. In each of the calculations presented here, the cavity radius is 20% larger than measured for HEARTS.

VI. RESULTS OF MICROQUAKE ANALYSIS

The calculations of LOWBALL and CREWLINE were made using the same material response models for the deep tuffs (Tmr, Tp, Tt) and Pz as were employed in the HEARTS HE86 calculation. Figures 12a and 12b show the calculated hoop stress component (horizontal, tangential to the cavity) of residual stress for each event at 900 ms. By 900 ms all significant motion in the vicinity of the cavity has ceased and the calculated stresses are in equilibrium with the pressurized cavity. After this early phase of cavity growth and stabilization, the slower process of cavity decay and readjustment of the stress field occurs. From observations of late-time seismic activity in the vicinity of an underground test, it appears that the stress readjustments are accompanied by small magnitude microquakes. For LOWBALL and CREWLINE, the hypocenters of these microquakes have been determined and are correlated with the calculated residual stresses. For both events, the microquake data represents the total useable activity recorded in the time frame between strong ground shock passage and cavity collapse.

The calculated residual stress field for LOWBALL (Figure 12a) is typical for events without severe layering or other complications near the cavity. It shows the usual reduction of stress above the WP due to less initial overburden and the degrading influence of surface and other layer rarefactions from above. Below the WP, the nearest layer interface of any significance is the Tt/Pz contact (about 330 m beneath the WP). There is a slight perturbation to the stress field near the Pz, but nothing of any great consequence. Peak stress in the tuff near the Pz is about 2 to 3 MPa higher than if the Pz had not been present. The peak of the cavity's residual stress

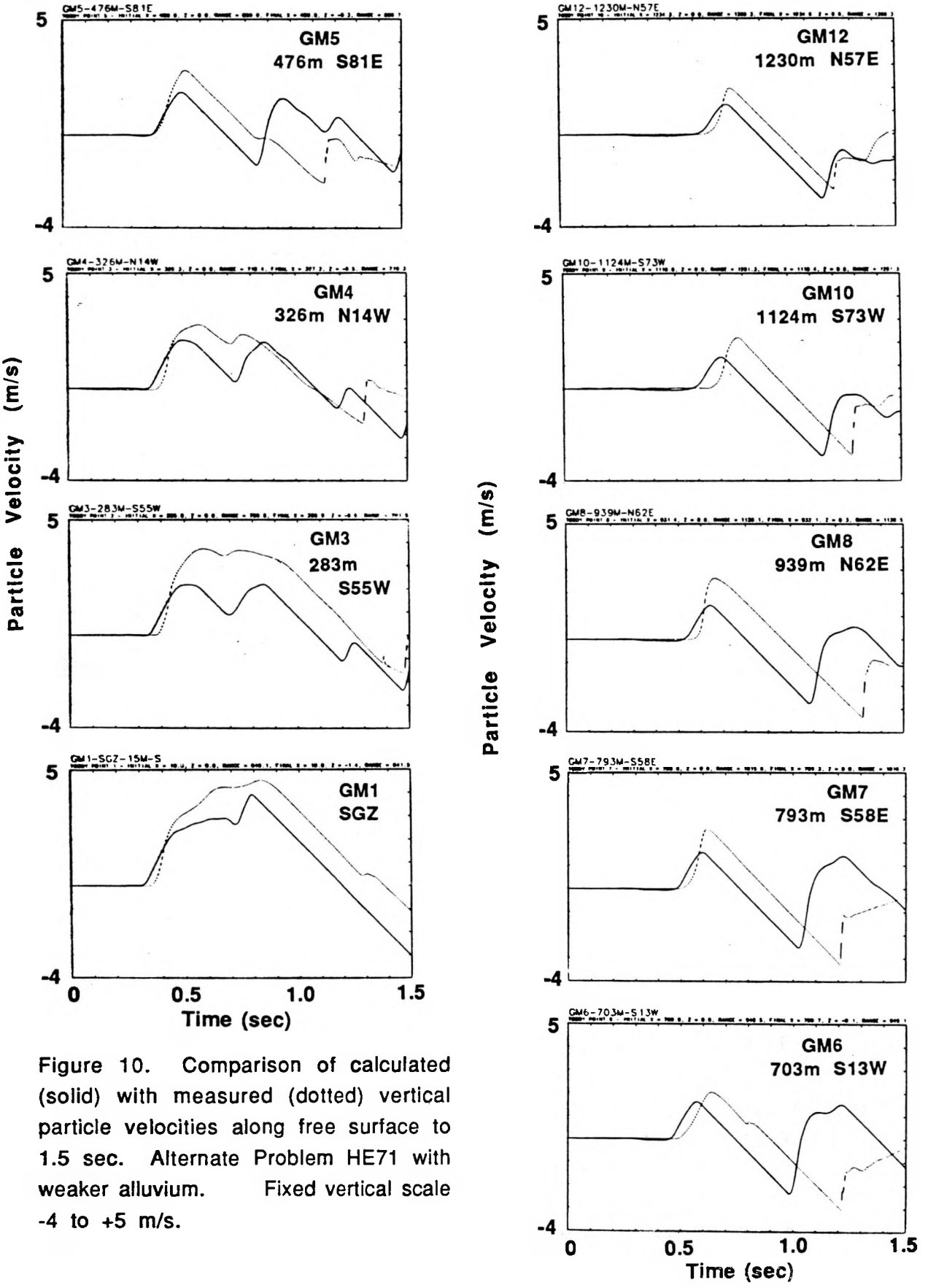


Figure 10. Comparison of calculated (solid) with measured (dotted) vertical particle velocities along free surface to 1.5 sec. Alternate Problem HE71 with weaker alluvium. Fixed vertical scale -4 to +5 m/s.

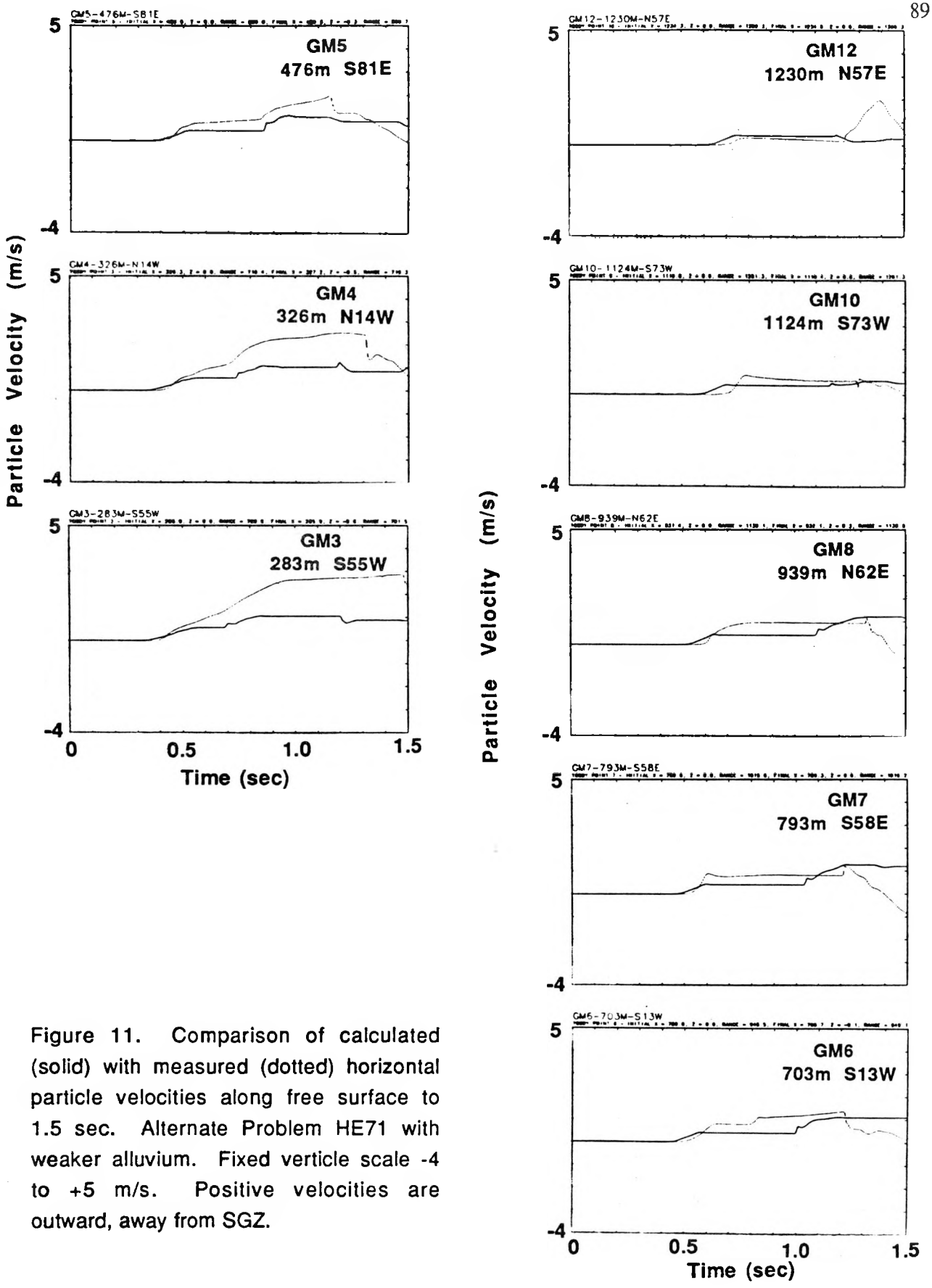


Figure 11. Comparison of calculated (solid) with measured (dotted) horizontal particle velocities along free surface to 1.5 sec. Alternate Problem HE71 with weaker alluvium. Fixed verticle scale -4 to +5 m/s. Positive velocities are outward, away from SGZ.

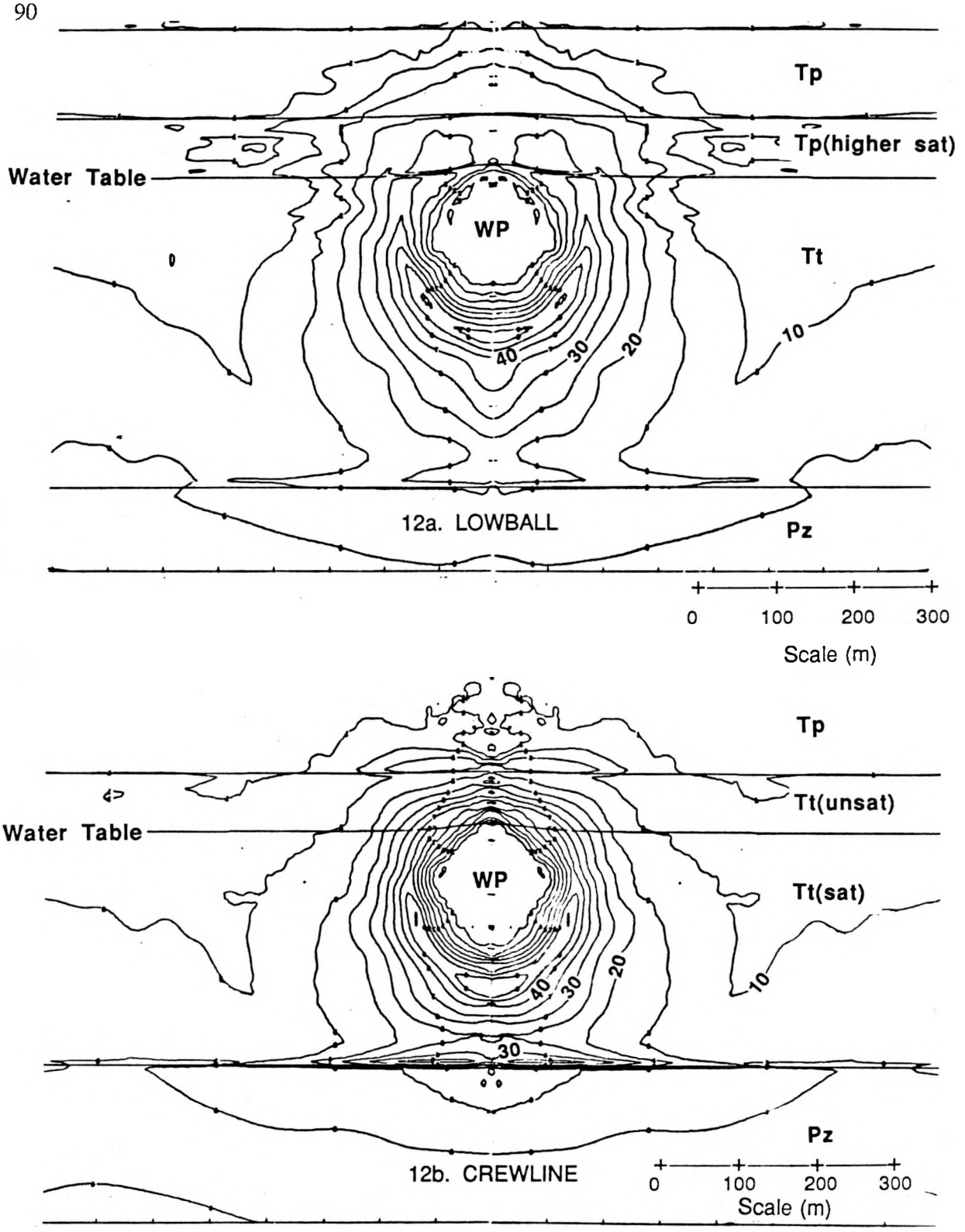


Figure 12. Contour plots of hoop component (horizontal - out of plane of plot) of residual stress at 900 ms for LOWBALL and CREWLINE calculations. Contours are at 5 MPa intervals. Shows compressive residual field about each cavity. For CREWLINE, shows second region of enhanced stress in the tuff at Tt/Pz contact. Similar, but much less stress enhancement at Tt/Pz contact for LOWBALL. Outline of cavity not shown.

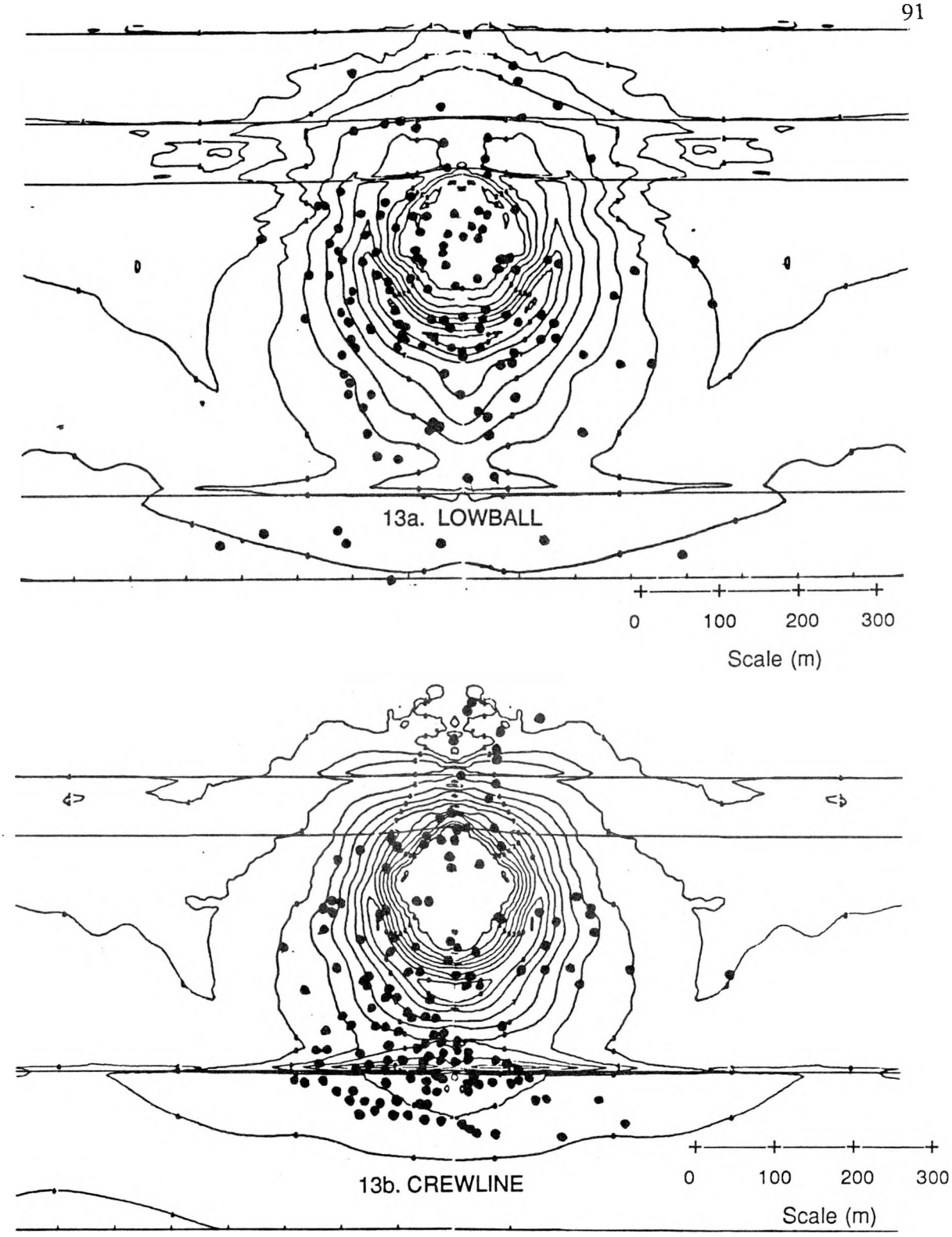


Figure 13. Contour plots of hoop component of residual stress at 900 ms for LOWBALL and CREWLINE with hypocenters of microquakes superposed. Stress contours are at 5 MPa intervals. The microquakes are three-dimensional, projected onto the two-dimensional plane of the plot. Good correlation between microquake hypocenters and regions of elevated residual stress.

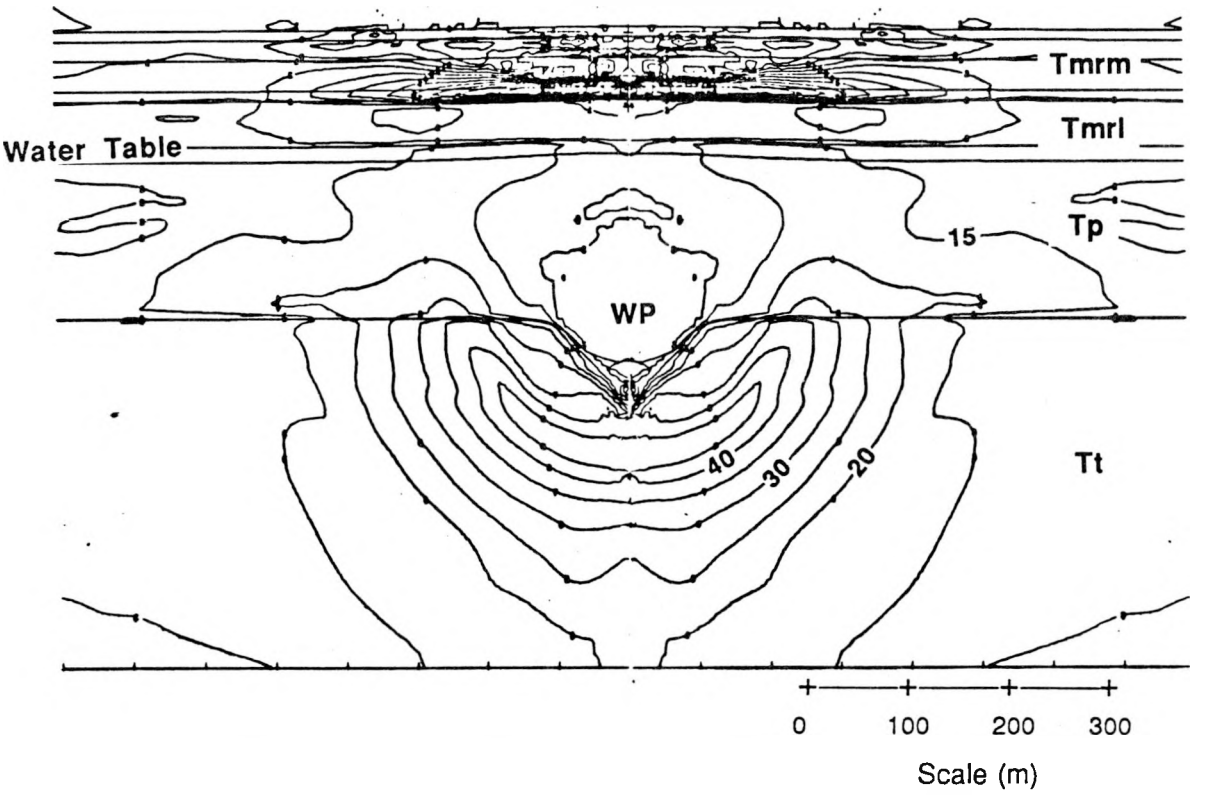


Figure 14. Contour plots of hoop component of residual stress at 900 ms for HEARTS calculation. Stress contours are at 5 MPa intervals. Shows well developed residual stress field beneath WP. Poorly developed in Tp above and to side of WP. Strong stress gradients in welded Tmrm above WP.

field is about 130 m radius from the original WP. Figure 13a shows the microquake hypercenters superposed on the same stress contour plot. There appears to be a definite correlation between the density of microquake source locations and the gradient (distance between contours) of the residual stress field. There are more in the hemisphere beneath the cavity than above, consistent with the pattern of stress and stress gradient.

The calculated residual stress field for CREWLINE (Figure 12b) is more complicated than that for LOWBALL. In this case, the Pz is located just 235 m from the WP, close enough to cause the formation of a second, highly compressive residual stress field at the Tt/Pz interface, extending out about 200 m along the interface. About the cavity, and out to a radius of about 110 m, there is formed the normal pattern of residual stress associated with cavity growth and rebound. The elevated stress near the Pz is what is unusual, and this is due to the additional plastic flow in the tuff that occurred next to the relatively immovable Pz. In the calculation, the Pz itself did not fail in shear, but it did undergo some tension near the interface. Figure 13b has the CREWLINE microquake hypocenters superposed on the calculated stress field. Again we have good correlation between microquake activity and the calculated stresses. There is the usual distribution about the cavity plus a concentration of microquakes near the Pz interface where the second concentration of stress occurs.

Figure 14 is a similar hoop stress contour plot for HEARTS. The Pz is too far below the WP to show up on this plot. The microquakes for HEARTS were measured but not processed, so we do not yet have hypocenter locations. If the stress gradient is the key (which seems reasonable), we would expect most of the usual activity beneath the cavity with some additional, concentrated activity near and within the welded Tmrm.

VII. CONCLUSIONS AND FUTURE WORK

In the HEARTS waveform analysis, we believe we are not too far from being able to replicate all waveforms at all stations in a single calculation. We believe the keys to broadening the wave, an essential ingredient in reproducing the observations at the free surface, is through the handling of shear deformation and failure in the deep tuffs below 450 m, in combination with modelling the alluvium as very weak material. Using calculations, we may be able to back out the late time, mechanical response properties of the WP rocks. We believe there is enough information in the propagating waveform to do this. With regard to the WP tuffs, there are other approaches in equation-of-state development we intend to pursue. One promising candidate is the effective stress model now being developed and tested in the Los Alamos SHALE code.

In some manner we must reconcile the need for using low strengths near the WP to achieve the desired broadening of the wave, with the need for higher strength for agreement with final cavity radius measurements. There is no suggestion from cavity radius measurements that rocks beneath the water table are severely weakened following ground shock. Perhaps we are being misled by "cavity radius" measurements.

We have found that surface motions are not particularly sensitive to details of how we model the "mid-range" tuff units (Tmrm, Tmru-Tma). Modelling of the alluvium is important in controlling the amount of "focusing" of energy toward SGZ and the change in character of the free surface waveforms from SGZ to distant stations. Also, surface waveforms at stations well removed from SGZ are less sensitive to the material models used than are the waveforms at stations in the near field, either on the surface or subsurface. This observation was not particularly obvious from the examples shown here, but it was strongly indicated by the calculations taken as a whole.

There is good correlation between post-shot microquake activity and the stress gradients attending the residual stress field. This reassures us that our material response models are reasonably correct, at least for Tunnel Beds Tuff. We calculated an enhancement of residual stress in a location next to the Pz where concentrated microquake activity was observed (CREWLINE). This result, coupled with lack of stress enhancement next to the Pz, and absence of micro-earthquake activity, in a case where the distance to the Pz was just a bit greater (LOWBALL), suggests that our models for damaged rock are reasonably correct. The range to which shear failure occurs, and a residual stress field subsequently forms, is very sensitive to the shear strength.

In future work, once we have improved our "damage" models to the point where they give good waveform agreement at all stations, we will revisit CREWLINE and LOWBALL to determine if the newer models provide the same good correlation with the microquakes. A complete, correct response model should allow one to replicate not just the dynamic, strong motion measurements but should result in a correct state of residual stress after all strong motion has ceased. The microquakes provide us with at least some check on this latter requirement.

The most important result of this study, and that of the companion study on MERLIN alluvium, is that we have gained some additional insight into which response mechanisms are important in shaping the waveforms. We know better where the problems are and where the physical response modelling needs to be improved. The HEARTS study, and others like it, will continue with the ongoing goal of establishing and improving our level of confidence in containment and test ban/treaty verification calculations.

VIII. ACKNOWLEDGEMENTS

The authors wish to thank Jack House, Nuclear Test Containment Program Manager, for providing the resources in support the HEARTS, and the companion MERLIN, research efforts. This work is supported by the United States Department of Energy.

IX. REFERENCES

Edwards, C. L., Harper, M. D., Weaver, T. A., Cash, D. J., Ray, J. M. and Homuth, E. F., 1983, Microquake Activity Associated with Underground Nuclear Testing at the Nevada Test Site, Los Alamos Report LA-8552-MS.

Brunish, W. M. and App, F. N., Modelling of MERLIN Alluvium, in publication, Proceedings of the Fifth Symposium on Containment of Underground Nuclear Explosions, September 18-22, 1989, Santa Barbara, CA, C. W. Olsen, editor, Lawrence Livermore National Laboratory.

App, F. N. and Marusak, N. L., A Justification for the Projection of Material Properties within a Portion of Los Alamos Test Areas 1, 3, 4 and 6, unpublished Los Alamos Report ESS-CPO-83-22.

MODELLING OF MERLIN ALLUVIUM

Wendee M. Brunish
Fred N. App

Los Alamos National Laboratory

ABSTRACT

We have attempted to see what we could learn about the material response of alluvium by modelling the observed ground motion waveforms from the MERLIN event. We took this phenomenological approach because there is an extreme paucity of mechanical measurement data on alluvium, due to the fact that it is poorly consolidated and sample preparation is very difficult. The MERLIN event has one of the most extensive ground motion arrays for any NTS event, and the data appear to be of uniformly high quality. The MERLIN working point was in alluvium, and the site is homogenous and uncomplicated. In addition, some mechanical measurements do exist that were performed on "reconstituted" samples obtained from a nearby exploratory hole. These measurements offer guidance on how to model the strength and compressibility of the alluvium.

Our results show that this alluvium is indeed very weak material. We modelled it with an unconfined strength of less than 0.1 MPa and a maximum strength of 10 MPa. The crush initiation pressure we used was 1.2 MPa followed by a highly compressible crush interval to 30 MPa. These parameters are consistent with the mechanical measurements and gave us good agreement with the velocity data. In order to get satisfactory agreement with the waveforms, we found that we had to modify the computer code to allow more shear strain during crush than is normally provided in a "constant shear modulus" treatment. Also, we allowed for the effect of damage on shear strength by reducing the shear failure surface with increased failure-associated shear strain. Overall, we were able to produce calculations that were in excellent agreement with the data. Other effects that we investigated include anisotropy of in-situ stress and linkage of volumetric and shear strain. We feel that we have developed material models that accurately reflect the response properties of alluvium, and tell us something about the in-situ behavior of alluvium.

I. INTRODUCTION

We have attempted to see what we could learn about the material response of alluvium by modelling the observed ground motion waveforms from the MERLIN event. We took this phenomenological approach because there is an extreme paucity of mechanical measurement data on alluvium, due to the fact that it is poorly consolidated and sample preparation is very difficult. The MERLIN event has one of the most extensive ground motion arrays for any NTS event (see Figure 1), including two nearby satellite holes with vertical arrays of gages, a horizontal array at working point (WP) depth (in a series of satellite holes at progressively further ranges), as well as the surface motion array which extended out to a range of 762 m from surface ground zero (SGZ). The MERLIN event was conducted in hole U3ct at a depth-of-burial (DOB) of 296 m on February 16, 1965 and had an announced yield of 10 kilotons. The data appear to be of uniformly high quality, and only the closest in station failed due to ground shock before the peak velocity was reached (Perret, 1971).

MERLIN has several other advantages that make it a good candidate for modelling. The WP was in alluvium and the entire overburden consists of alluvium, There is no indication of any significant changes in the physical properties with depth. (The sound speed does appear to vary with depth, but there does not seem to be any related density or porosity variation). There is also no nearby structure or material interface in the horizontal or upward directions. The tuff contact is more than 50 m below the WP, and does not affect the vertical or surface arrays, although it may influence the wave forms along the horizontal WP level array. For the most part, we can treat the alluvium as a homogeneous material in all directions. We have modelled the sound speed variations as mentioned above. A further reason for choosing MERLIN is that some mechanical measurements do exist that were performed on "reconstituted" samples obtained from Ue3ct (Bonner et. al., 1972). These measurements offer some initial guidance on how to model the strength and compressibility of the alluvium.

Possible future applications of this work include modelling of past containment failures in alluvium (e.g. BANDICOOT), prediction of ground motion and modelling of the seismic source function for verification.

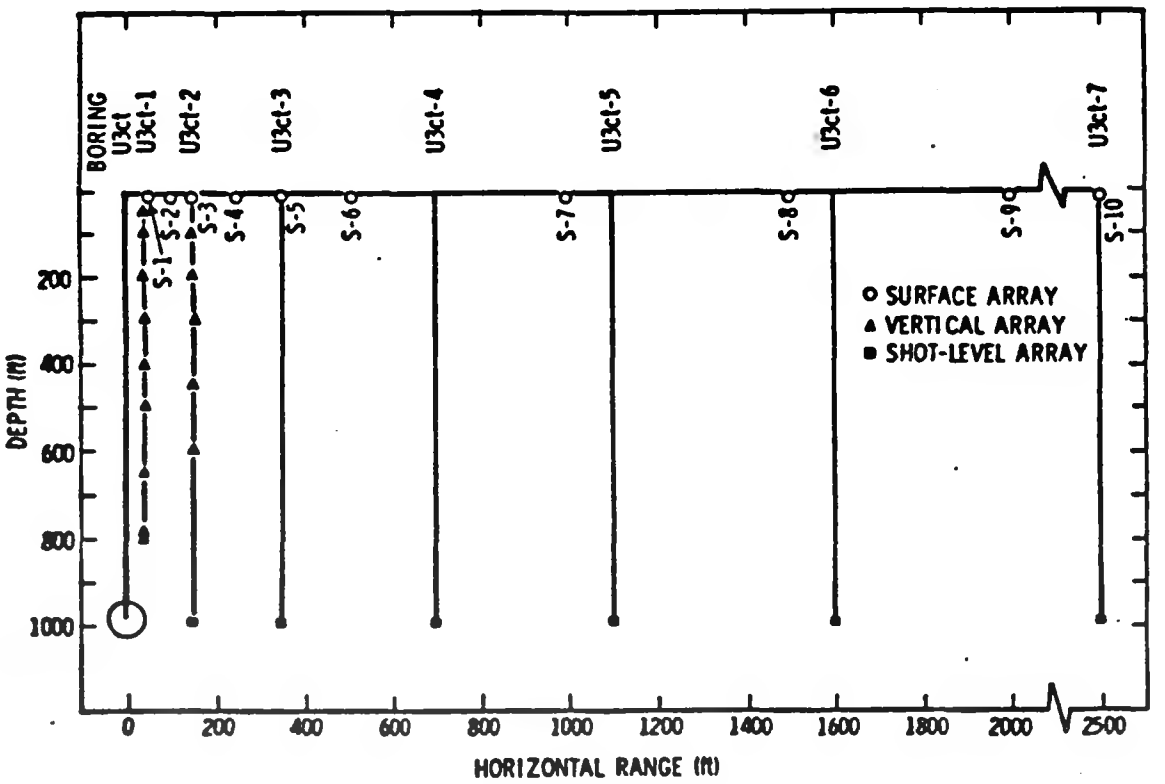


Figure 1. The MERLIN ground motion array. Open circles represent the surface array, filled triangles represent the gages in vertical satellite holes, and the filled squares are the horizontal array at working point depth. Reproduced from Perret (1971).

II. APPROACH - MATERIAL MODELS AND EQUATION OF STATE

Our approach was to use as many material properties as were available to us as a starting point, then to run a series of one-dimensional parameter/sensitivity studies using waveform matching to the MERLIN measurements, adjusting our response model and properties as seemed appropriate. We followed this phase with two-dimensional calculations that used the 1-D derived properties, and further refined the models from there. All calculations were run with a Los Alamos modified version of the SNLA TOODY stress wave code. As it is configured at Los Alamos, this code is exceptionally well suited to parameter/sensitivity studies due to the flexibility of its analytical equation of state for rock and its special method for automatically rezoning through the cavity, reducing computer execution time and cost to a minimum.

For the physical properties input we used the available velocity data, log data from a nearby hole, and the laboratory mechanical measurements on reconstituted core. The bulk density and water content were based on geophysical logs run in the nearby hole U3kx, and the values we used were 1.710 Mg/m^3 and 10.9 weight percent, respectively. They revealed that the alluvium was very homogeneous, so we adopted a single value for all of the alluvium. We used the mechanical measurements to determine appropriate starting values for the threshold crush pressure, P_e, the fully crushed pressure, P_s, the unconfined compressive strength, and the maximum confined strength. The pressure at which the pores begin to crush out (i.e. large specific volume increase for a small pressure increase; see Figure 2) can be seen to be quite a bit less than 10 MPa (100 bars). The pressure at which most of the air filled voids have been crushed out (i.e. very little specific volume increase with large pressure increase; see Figure 3) appears to be at about 20 to 30 MPa for most of the samples. Figure 4 shows the "failure" surfaces for several different samples. These samples have virtually no unconfined strength. The confined strength of the samples is obviously a very strong function of water content and ranges from less than 1 MPa (fully saturated) to over 10 MPa (dry).

The final values we arrived at through the waveform analysis, and that we feel best represent the in-situ condition of the MERLIN alluvium, are all consistent with the mechanical test data. For the calculations presented here, the mechanical properties are as follows. For the threshold crush pressure we have adopted a value of 1.2 MPa, and for the "fully crushed" pressure we have used a value of 30 MPa. We have modelled this material with 0.01 MPa unconfined strength and we have given the material a maximum confined compressive strength of 10 MPa, which is consistent with the data for a water content of 10-15%. A tuff layer, located 50 m below the working point, was modelled not as tuff but rather as a higher sound speed alluvium.

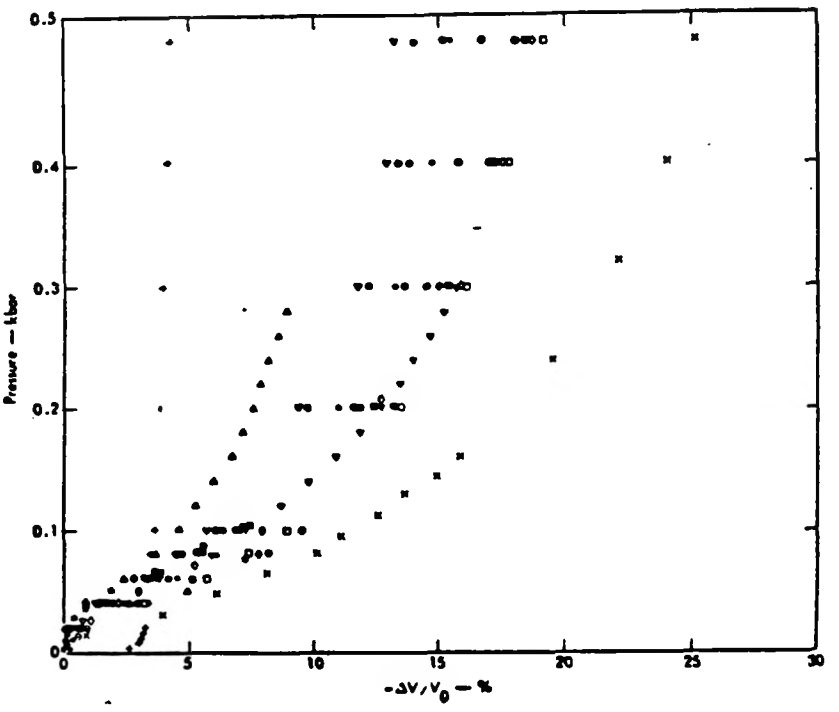


Figure 2. Pressure-volume curves for low-pressure uniaxial tests on MERLIN laboratory samples. The different symbols represent different samples which differ mainly in degree of saturation. Reproduced from Bonner et. al. (1972).

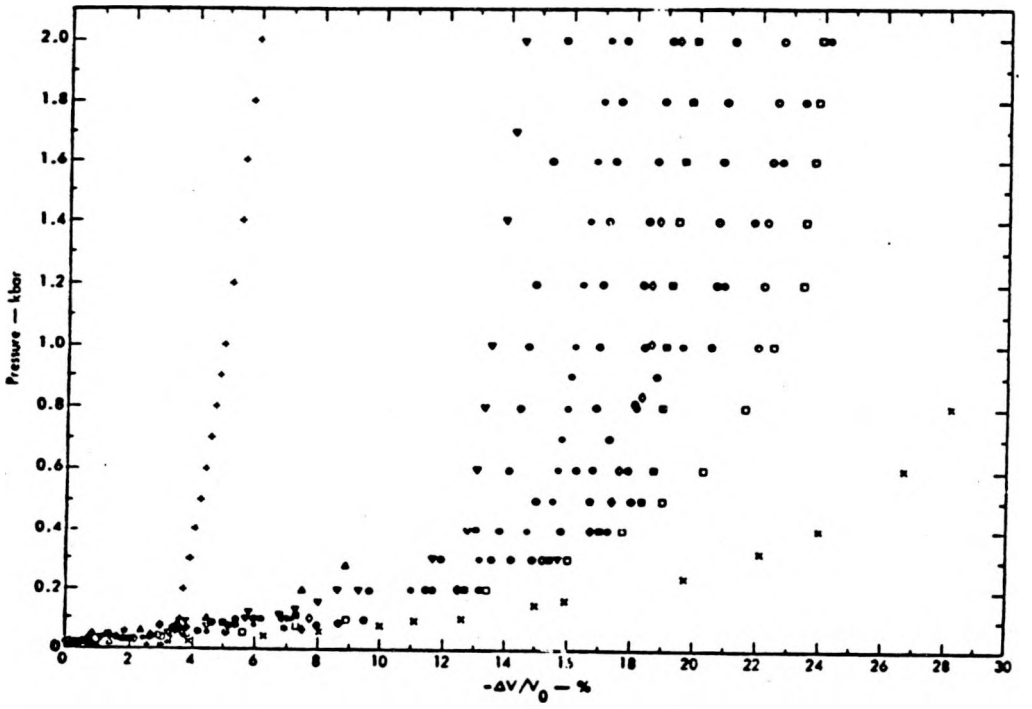


Figure 3. Pressure-volume curves for high-pressure uniaxial tests on MERLIN laboratory samples. The different symbols represent different samples which differ mainly in degree of saturation. Reproduced from Bonner et. al. (1972).

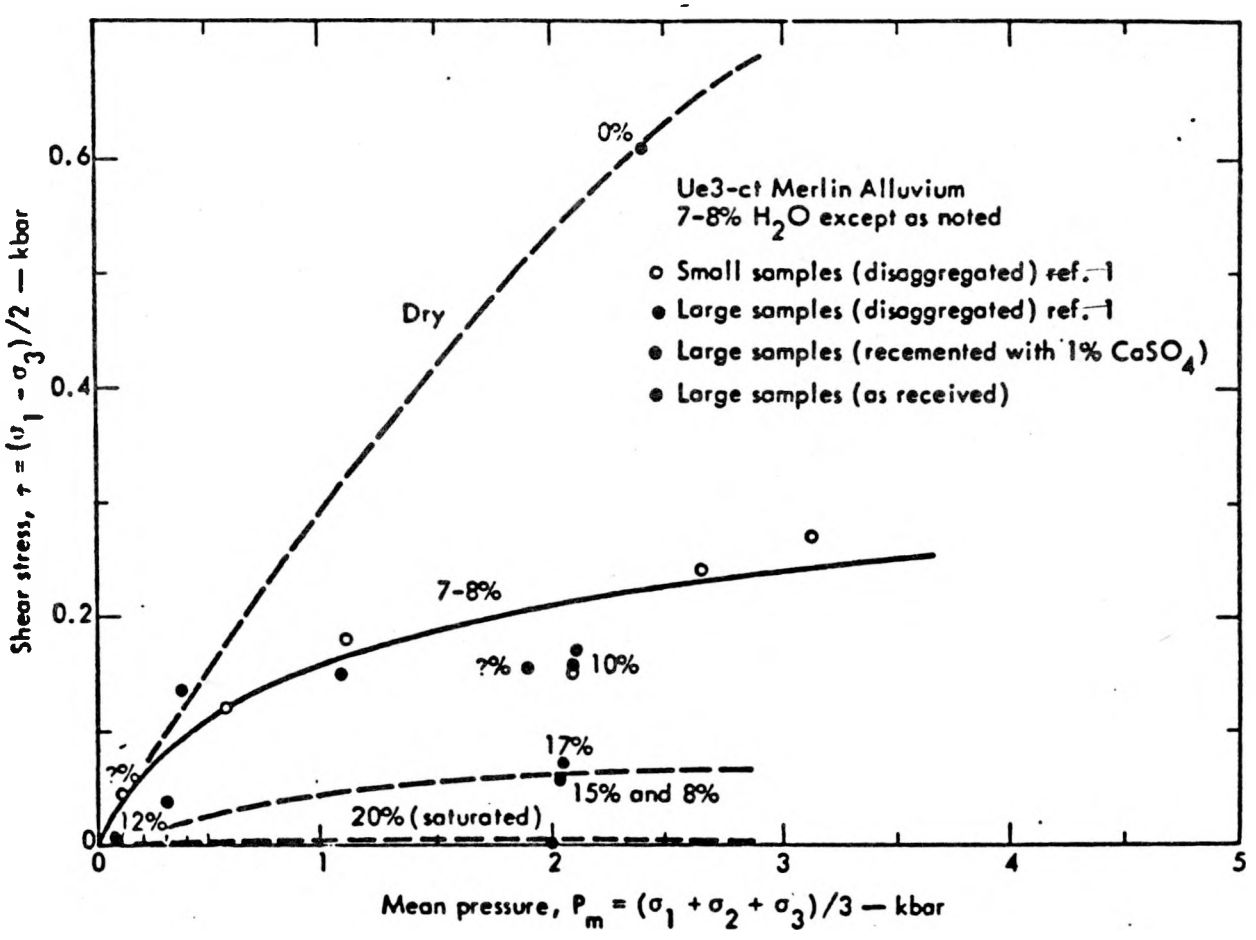


Figure 4. Failure surfaces for MERLIN laboratory samples. The different symbols represent varying degrees of saturation as shown in the legend. Reproduced from Bonner et. al. (1972).

Refractions from it may influence the waveforms at the more distant horizontal stations. In addition, we have modelled a "weathered" surface layer (about 30 m deep), the existence of which is evidenced in geophone surveys and various reflection seismic surveys at the NTS. We gave it a very low sound speed in keeping with geophone data.

The equation of state (EOS) routine was modified to allow more control over the shear modulus behavior during crush. The equation-of-state model we are currently using is a hybrid "variable shear modulus" and elastic-plastic model that employs a shear failure envelope and, when the material is not undergoing shear failure, a means for varying the shear modulus as a function of both compression and the compressive state (elastic, porous crush, fully crushed or unload). This provides a fairly simple and straightforward linkage between shear and volumetric behavior. Also, there is an optional provision for linkage between shear failure and the initiation of pore crush. Also as an option, we allow for weakening (or strengthening) the material with either accumulated damage (currently defined as the total failure-associated shear strain) or the peak stress seen by the material. The exact shape of the pressure-volume relationship can be easily adjusted, an important parameter in adjusting the shape and rise time of the leading portion of the wave. We can allow for nonisotropic in-situ stress as long as the two horizontal components of stress are equal.

Most of the parameter studies were done using a one-dimensional, spherically symmetric representation of the MERLIN site to save time and computer funds. Comparisons of the one-dimensional and two-dimensional results revealed that they agreed well overall. The surface rarefaction was unrealistically strong in the one-dimensional case due to the convergent geometry. Also the effects of refraction and anisotropic overburden could not be modelled in one dimension. We also did some tests of zone size effects and they were not significant. When we used smaller zones, the arrival times were somewhat later (in better agreement with the data) and the effective "elastic radius" (distance to the transition from plastic to primarily elastic behavior) was changed slightly, but other effects were minimal. Most of the 2-D calculations were done with 4 m rectangular zones. For the waveform comparisons throughout this report, dashed lines represent the measurements and solid lines represent the calculated waveforms.

III. ONE-DIMENSIONAL STUDY

Figure 5 shows a subset of the velocity waveforms reported by Perret (1971). It is the data set used in comparing 1-D calculational results with measurements and it contains most of the features of waveforms of interest to us. The data was hand digitized from very small figures in

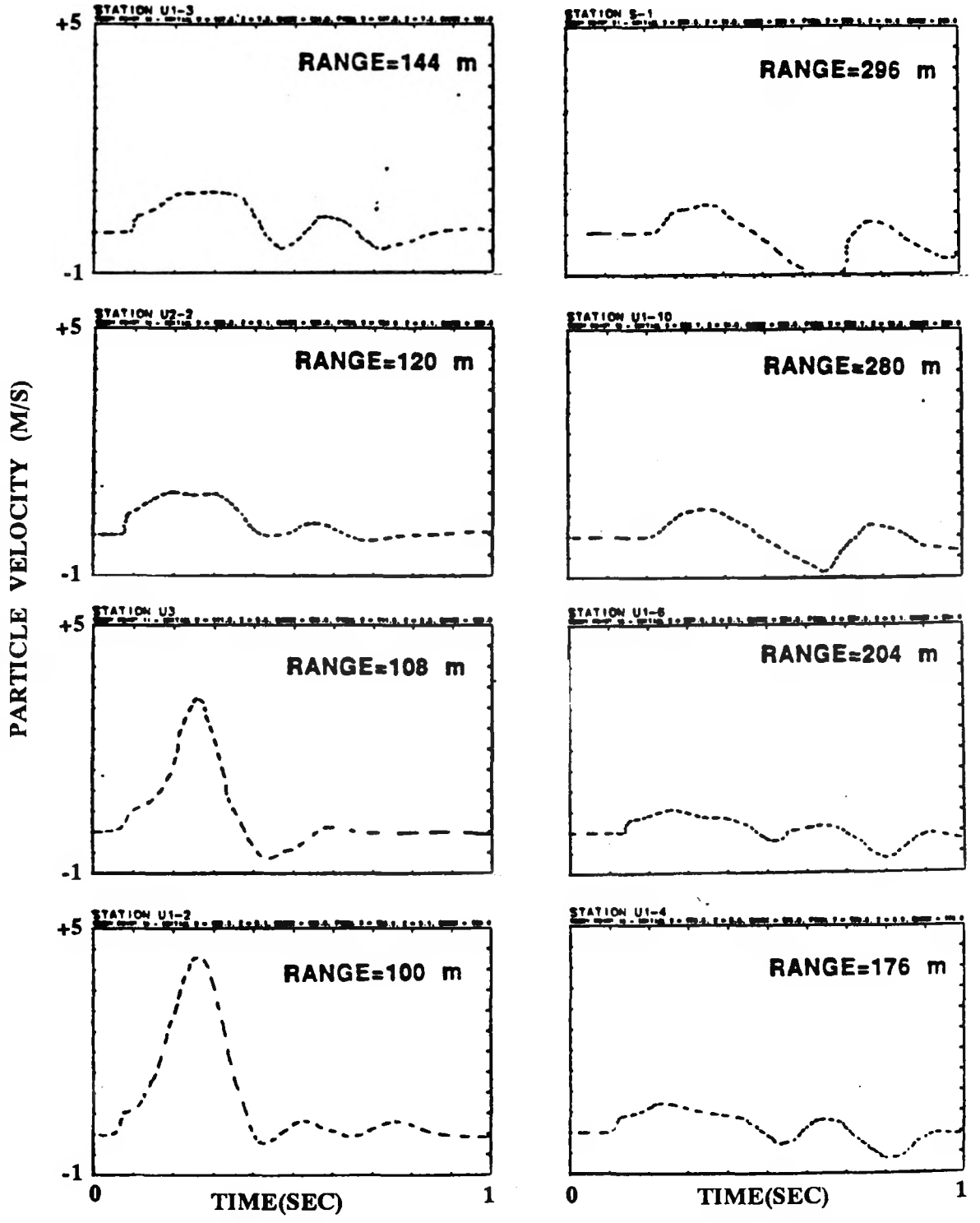


Figure 5. The experimental ground motion data at various ranges to 1 sec. Particle velocity at fixed scale -1 to +5 m/s. Stations U1-2, U1-3, U1-4, U1-6 and U1-10 are from the first vertical array. Station U2-2 is from the second vertical satellite hole. Station U3 is from the horizontal array and station S-1 is the SGZ station. Data is digitized from Perret (1971).

Perret's report. There are some anomalies in the waveforms, introduced during the digitization process, that are not indicative of the quality of the original MERLIN data set. However Figure 5 does accurately portray the most important characteristics of the explosion produced wavelet as it propagates to successively greater ranges from the WP.

Proceeding from bottom to top and then from left to right in Figure 5, each frame shows the data from a gage at successively greater range. Frames 1, 3, and 4 through 7 represent vertical gages. Frame 2 shows the data from one of the gages at working point depth, and frame 8 shows the surface ground zero station. At the close-in stations (range < 120 m), the waveform is sharply peaked. The elastic precursor is clearly visible but there is no other noticeable structure. The peak amplitude is about 4.5 m/s. At further out stations (range $\geq$ 120 m), the waveform has a broad double peak. The elastic precursor amplitude is still about 1 m/s, but the amplitude of the plastic peak has dropped to about 1 m/s. Clearly there is a great deal of attenuation in the plastic wave. Once the plastic wave decays to the amplitude of the elastic precursor, there are no further changes of substance in the waveshape except for effects from the free surface. At the ground surface, we see "spall", but it occurs at an acceleration of about 7 m/s^2, rather than 9.8 m/s^2 (-1g). Our experience shows that very weak material "spalls" differently than stronger material.

Figure 6 shows a comparison of our current "best" 1-D calculation (hereinafter referred to as the 1-D baseline calculation) with the observed waveforms. There is good waveform agreement at all ranges. We successfully capture the large attenuation at the close-in stations, the transition from non-linear to primarily linear elastic wave propagation at about 120 m and the increase in amplitude and spall signature as we approach the free surface. The transition to the double peak structure between 100 and 120 m range is most striking and we replicated this behavior by allowing pore crush to be accompanied by a decrease in the shear modulus.

Figures 7 and 8 show in greater detail the evolution of the wave from primarily plastic (inelastic) to elastic response. All waveforms in Figure 7 are at the same scale to show the marked amplitude attenuation over a relatively short distance. The plot scales of Figure 8 are scaled to the amplitudes of the individual waveforms to show more detail at the lower amplitude stations. Following is a description of the response of the alluvium as inferred from the calculations. We note that the response model used in this calculation is but one of a number of models tried during the course of the study. A very important requirement in replicating the observed transitional behaviour is a decrease in resistance to shear (shear modulus) during pore crush. The shear modulus was decreased by a factor of about 30 from its elastic value.

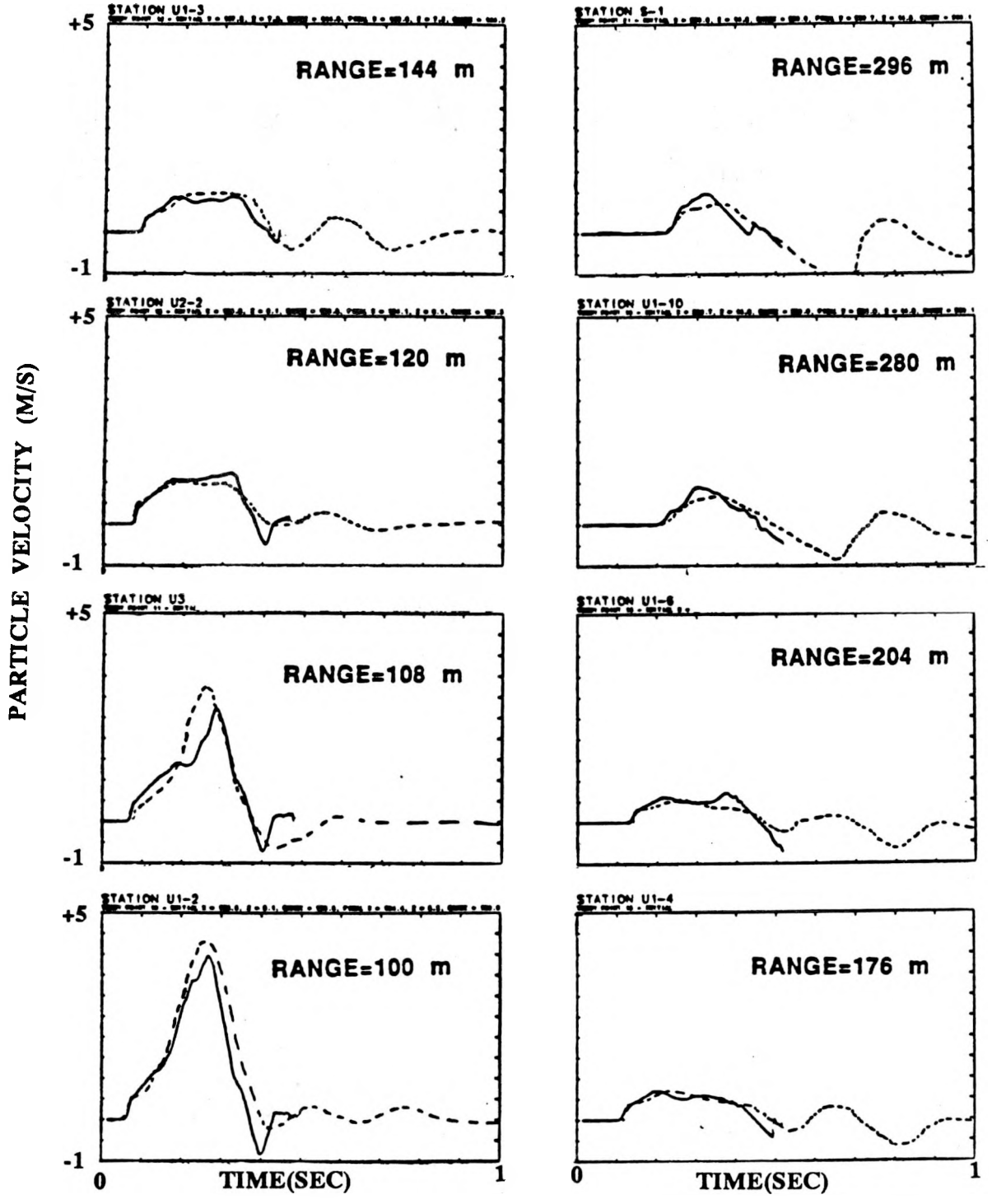


Figure 6. Comparison of the 1-D baseline calculation (solid) with the measurements (dashed) at various ranges. Particle velocity at fixed scale -1 to +5 m/s. Time scale 0 to 1 sec.

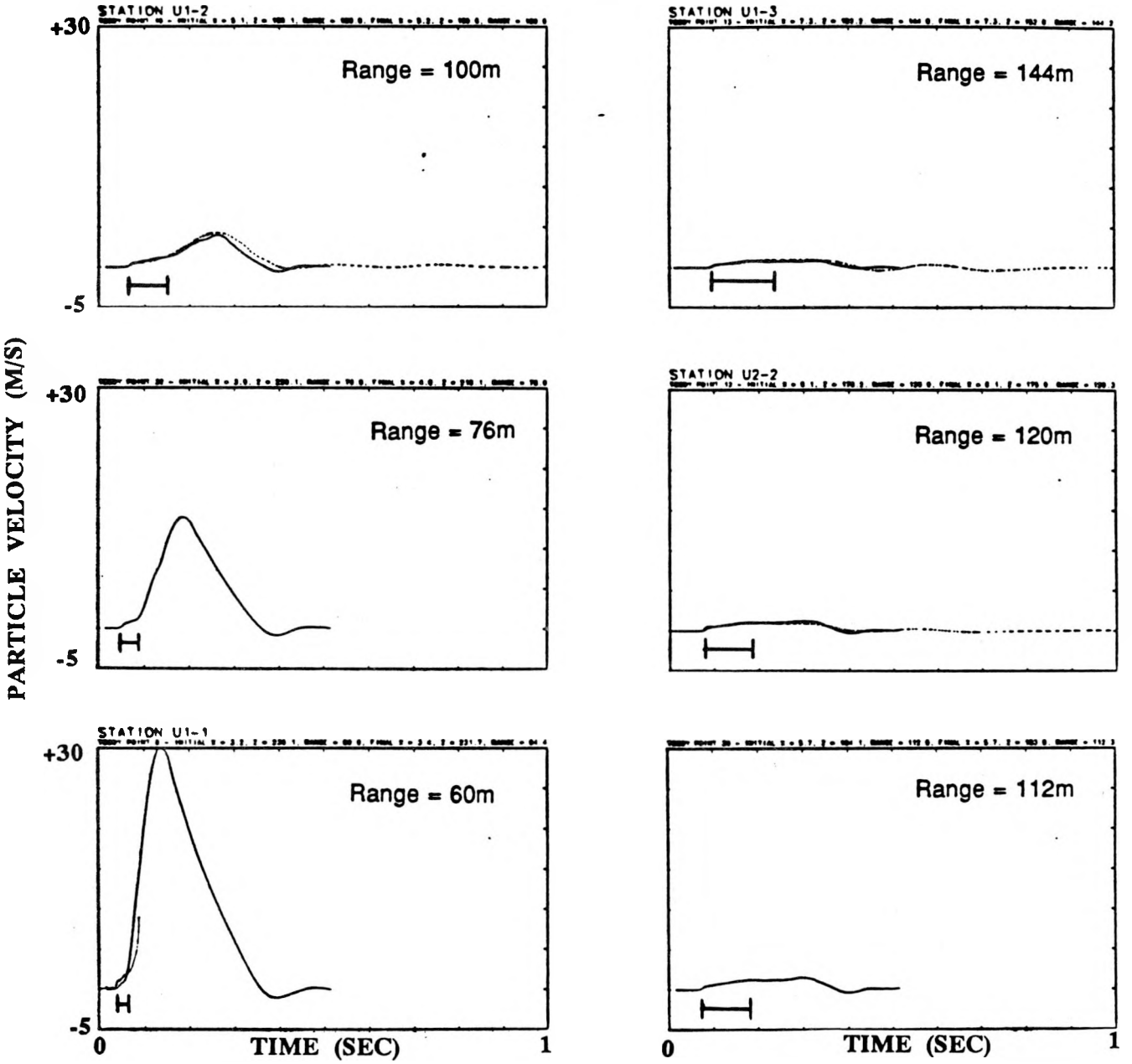


Figure 7. Evolution of waveform from 60 m to 144 m range for 1-D baseline calculation. Vertical particle velocity with fixed scale -5 m/s to 30 m/s. Time scale from 0 to 1 sec. Large attenuation due to pore crush. Horizontal bars are drawn coincident with the elastic precursor. Gage at U1-1 terminated early. No measurements at 76 m and 112 m ranges.

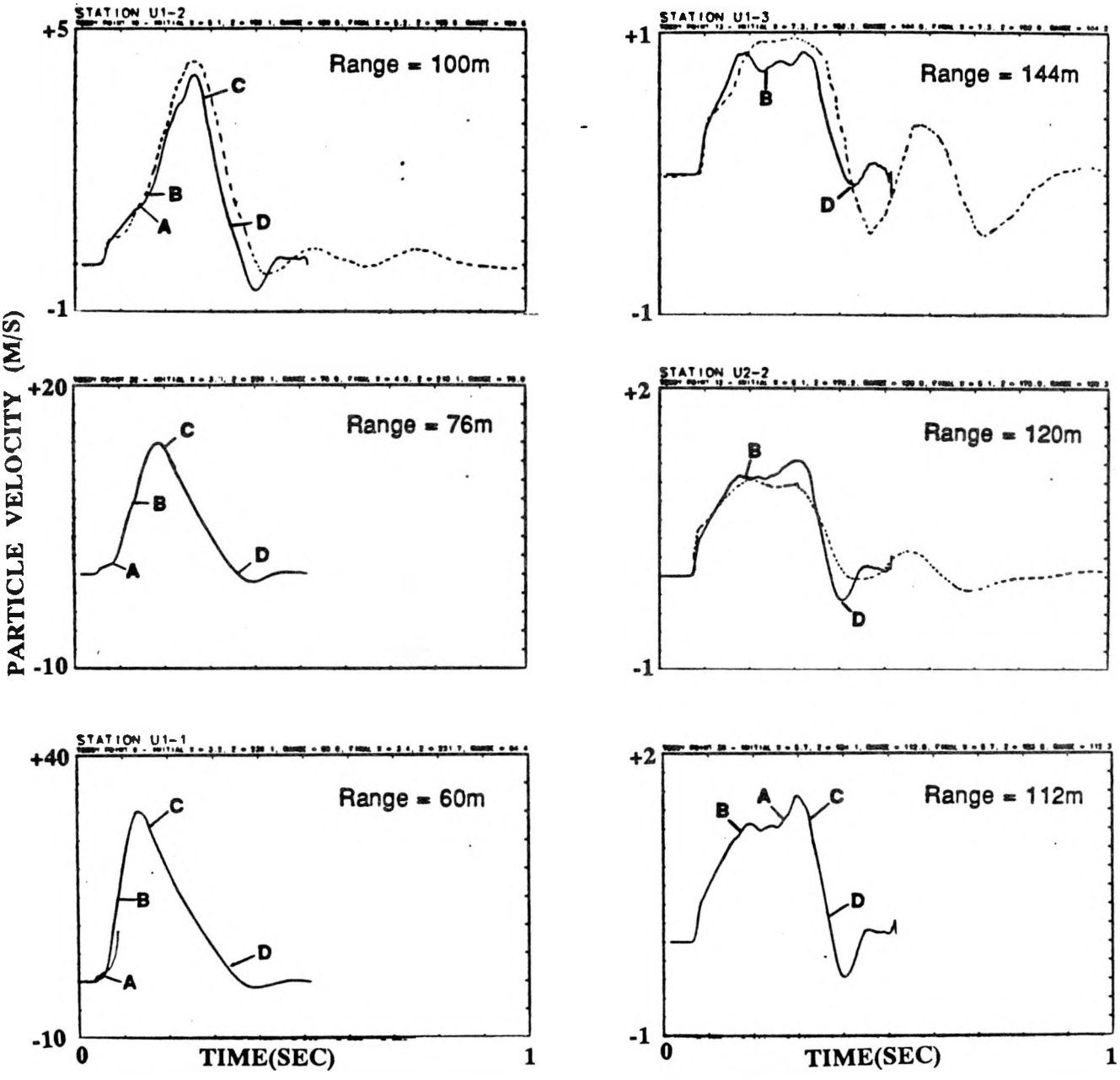


Figure 8. Evolution of waveform from 60 m to 144 m range for 1-D baseline calculation. Vertical particle velocity. Plot scales adjusted to wave amplitudes. Time scale from 0 to 1 sec. A = initiation of crush. B = initiation of shear failure. C = end of crush. D = end of shear failure. No crush at Stations U2-2 or U1-3.

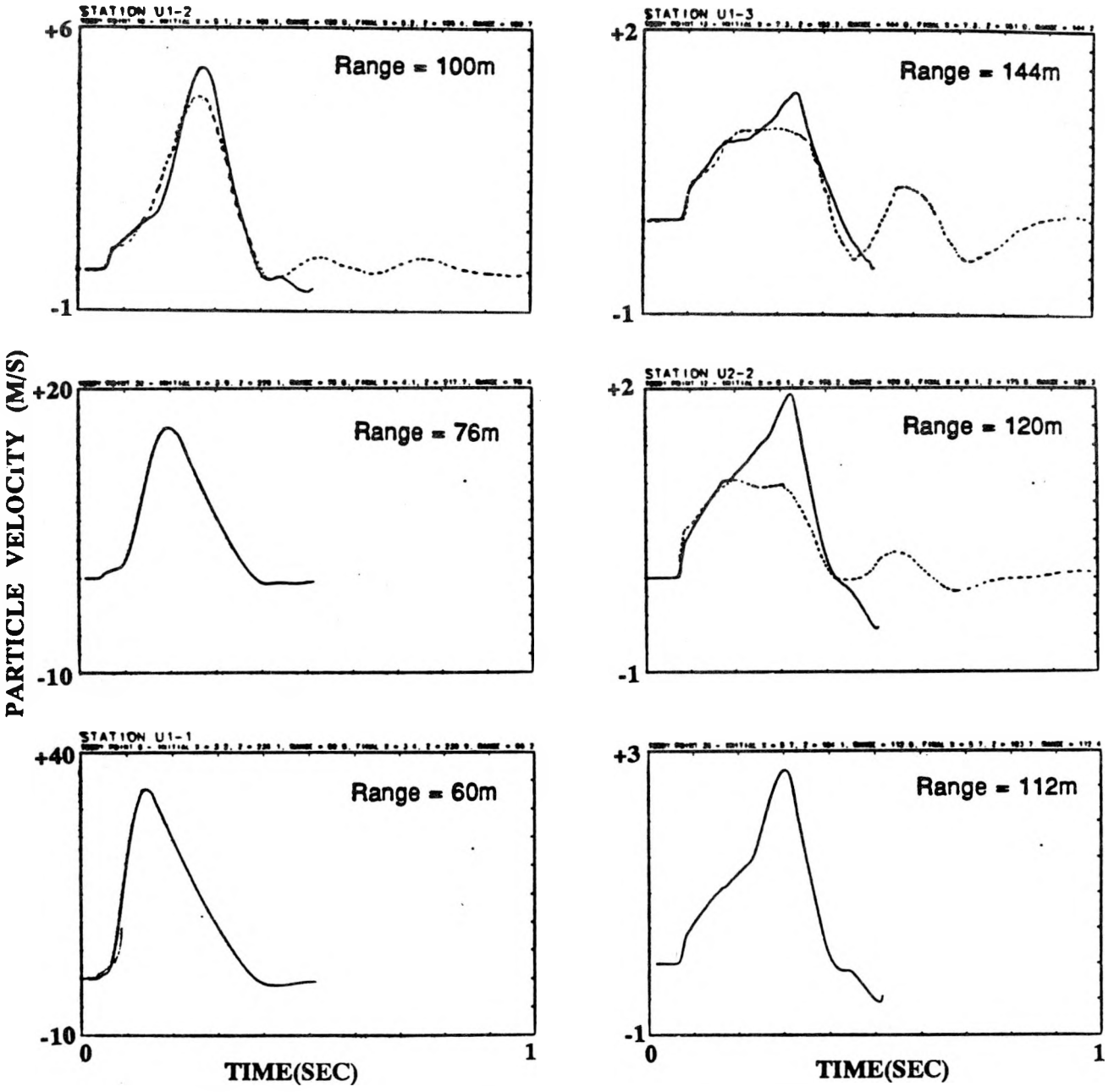


Figure 9. Evolution of waveform from 60 m to 144 m range - 1-D crush/shear linkage calculation. Vertical particle velocity. Plot scales adjusted to wave amplitudes. Time scale from 0 to 1 sec. Linkage results in a smoother waveform.

Figure 7 shows the large decrease in peak amplitude and the elongation of the elastic precursor (purely elastic response) with range. Figure 8 shows in more detail the R^{-1} amplitude decay at the front end of the precursor (spherical divergence), causing the failure point to move successively further back on the waveform. This process "stretches out" the elastic precursor until the stress no longer is high enough to collapse pores, i.e., the "elastic radius" is reached. This is how the front end of the wave attains its characteristic shape. After this, the only additional changes to the shape of the waveform are caused by additional shear failure in the trailing part of the wave, and effects from the free surface. The value used for the elastic shear modulus is critical in achieving the correct shape on the precursor and therefore to the shape of the front end of the elastic wave. A nearly constant value of about 3000 MPa appears to work well. The small inflections on the front end of the wave are not observed in the data. These inflections are due to the onset of shear failure and the fact that there is not a smooth transition from elastic shearing to shear failure in the model. The inflections are as small as they are because we do reduce the shear modulus during crush. In reality, the transition from elastic to inelastic response probably involves coincident crush and shear failure. We note that in the calculations, once away from the close-in, strong shock region, the stress path in loading prior to failure is not one of uniaxial strain. Consequently, prior to a calculation it is difficult to adjust equation-of-state input parameters to achieve the desired coincident crush/shear failure. Figure 9 shows the waveforms that result using a model that forces shear failure to be coincident with crush. Shear failure surfaces are calculated, during code execution, to be consistent with the calculated (and observed) precursors. We refer to this as our "linkage" model. Note that the rises to peak amplitude now are smooth and much more like the measurements. However, there is poorer agreement at later times due to excessive shear failure.

Now we will look at the effects of other parameters on the calculated waveforms. In each case, all parameters are the same as in the baseline case except for the parameter being examined. All calculations except one are made using the variable shear modulus treatment discussed above. The comparisons are made at stations U1-2 and U1-3, the stations that best demonstrate the transition from inelastic to elastic behavior.

The effect of increasing the threshold crush pressure (P_e) by a factor of two is shown in Figure 10. The elastic precursor amplitude is too high and the amount of crush that occurs before shear failure is excessive as compared to the baseline calculation. If we decrease the fully crushed pressure (see Figure 11), the amplitudes are severely reduced.

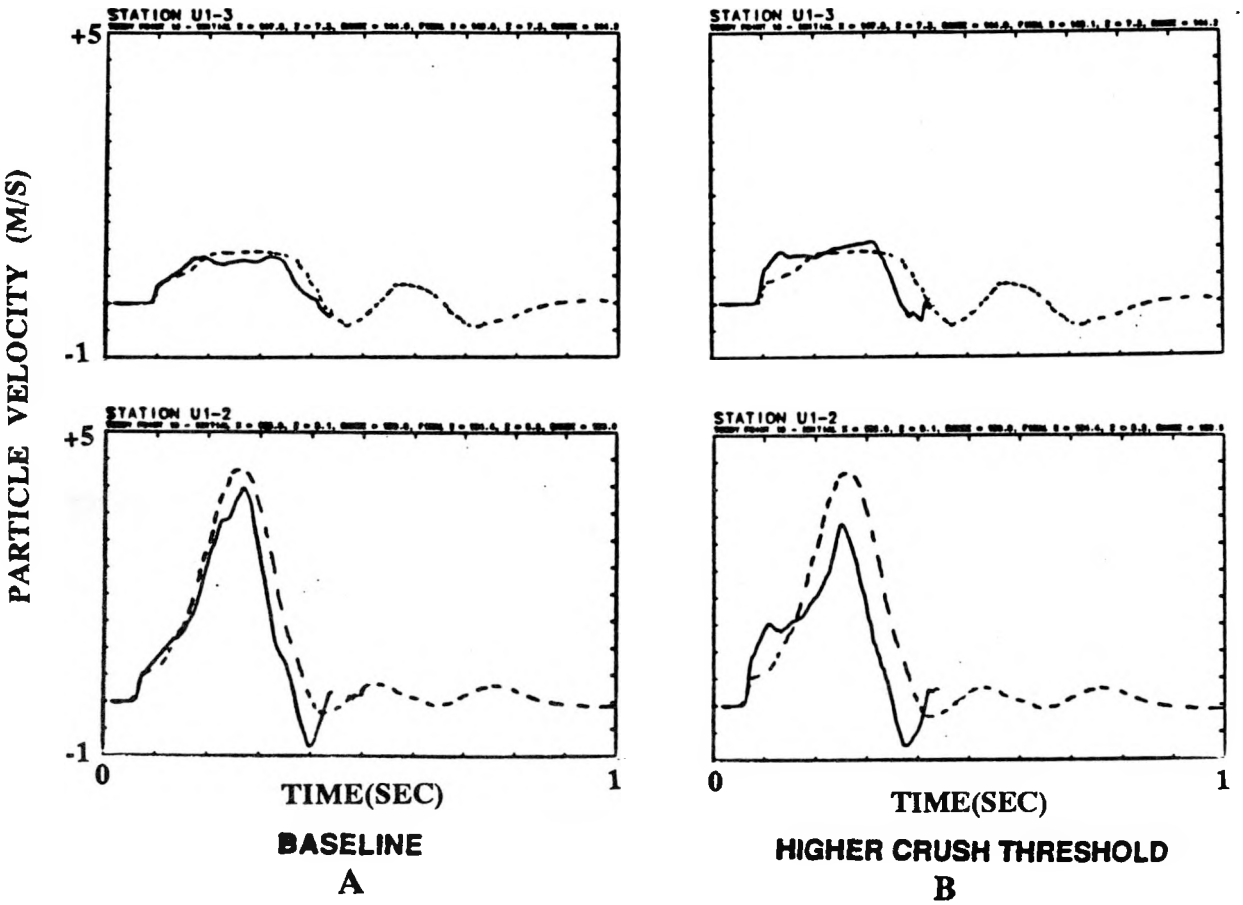


Figure 10. Effect of crush initiation pressure on particle velocity waveforms at Stations U1-2 and U1-3. Time scale 0 to 1 sec. Vertical scales fixed -1 to +5 m/s. A) 1-D baseline calculation with crush threshold pressure of 1.2 MPa. B) Same as baseline but using higher crush threshold pressure of 2.4 MPa.

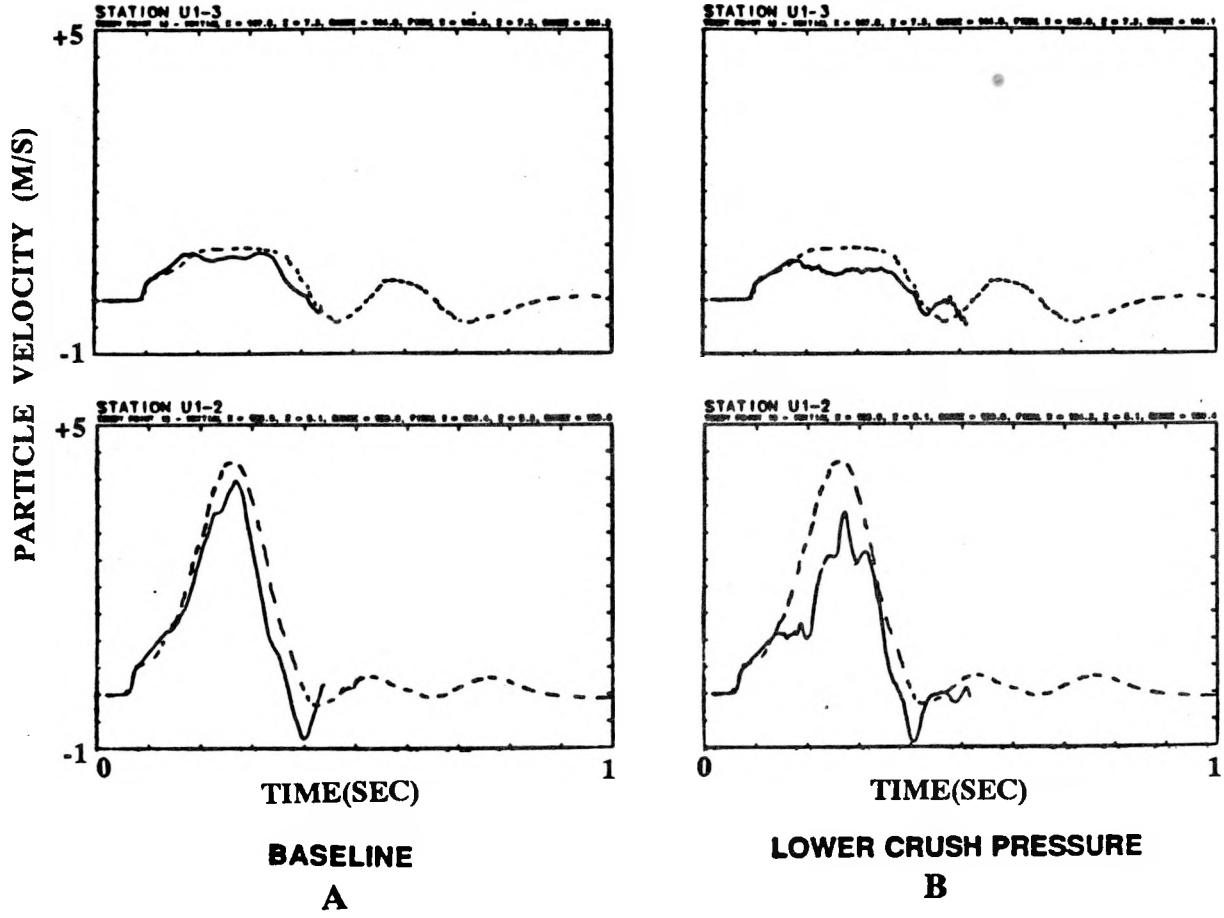


Figure 11. Effect of pore "full crush pressure" on waveforms at Stations U1-2 and U1-3. Time scale 0 to 1 sec. Vertical scales fixed -1 to +5 m/s. A) 1-D baseline calculation using crush pressure of 30 MPa . B) Same as baseline but using lower crush pressure of 15 MPa.

In Figure 12 we show the effect of changing the shape of the crush curve (i.e. the material resistance to crush just after crush initiation). If we make the material more compressible at the initiation of crush, the front end of the wave becomes broad and flattened. If the material is stiffened, the peak of the plastic wave occurs too early.

The constant shear modulus (or "constant Poisson's ratio") models do not allow sufficient shear deformation during crush, resulting in a broad and flattened front end (see Figure 13) and shear failure occurs too late.

The effects of changing the shape of the failure surface are fairly easy to predict. Decreasing the strength of the material causes the plastic amplitude to increase (and occur somewhat earlier), while increasing the material strength decreases the peak amplitude (see Figure 14). Similarly, the effects of damage are fairly predictable (see Figure 15). When no damage is included, the arrival and rise times are correct but the peak occurs too early and the waveform is not broad enough. Too much damage results in a later, higher amplitude peak, and broader waveform.

IV. TWO-DIMENSIONAL STUDY

Figure 16 shows the relevant portion of the computational mesh used for most 2-D calculations, with the editing/measurement stations superposed on the mesh. Four meter, rectangular zones are used throughout the region near the WP and to the surface, with a gradational increase in zone size horizontally out and downward. For economy, all 2-D parameter/sensitivity studies were conducted using this mesh. A single fine zoned calculation (not reported) was made to assure us that zone size was not having a detrimental effect on our results and conclusions.

Figures 17 through 22 show the waveform comparisons at all measurement/edit stations for a single calculation. The alluvium material properties/model used are those described earlier for the 1-D baseline calculation, therefore this calculation is referred to as the 2-D baseline. Figures 17 through 22 are the 2-D analog to the 1-D results of Figures 6 through 8. Because we need not be concerned about the effect of a converging rarefaction from the free surface inherent in the 1-D treatment, we carried the calculation out to 1 second problem time. Figures 17 and 18 show good agreement with the 1-D calculation and measured waveforms for the first 500 ms. The calculated waveform is a bit narrower due to refraction (focusing) effects not present in 1-D. Following is a more detailed description of the upward propagating wave.

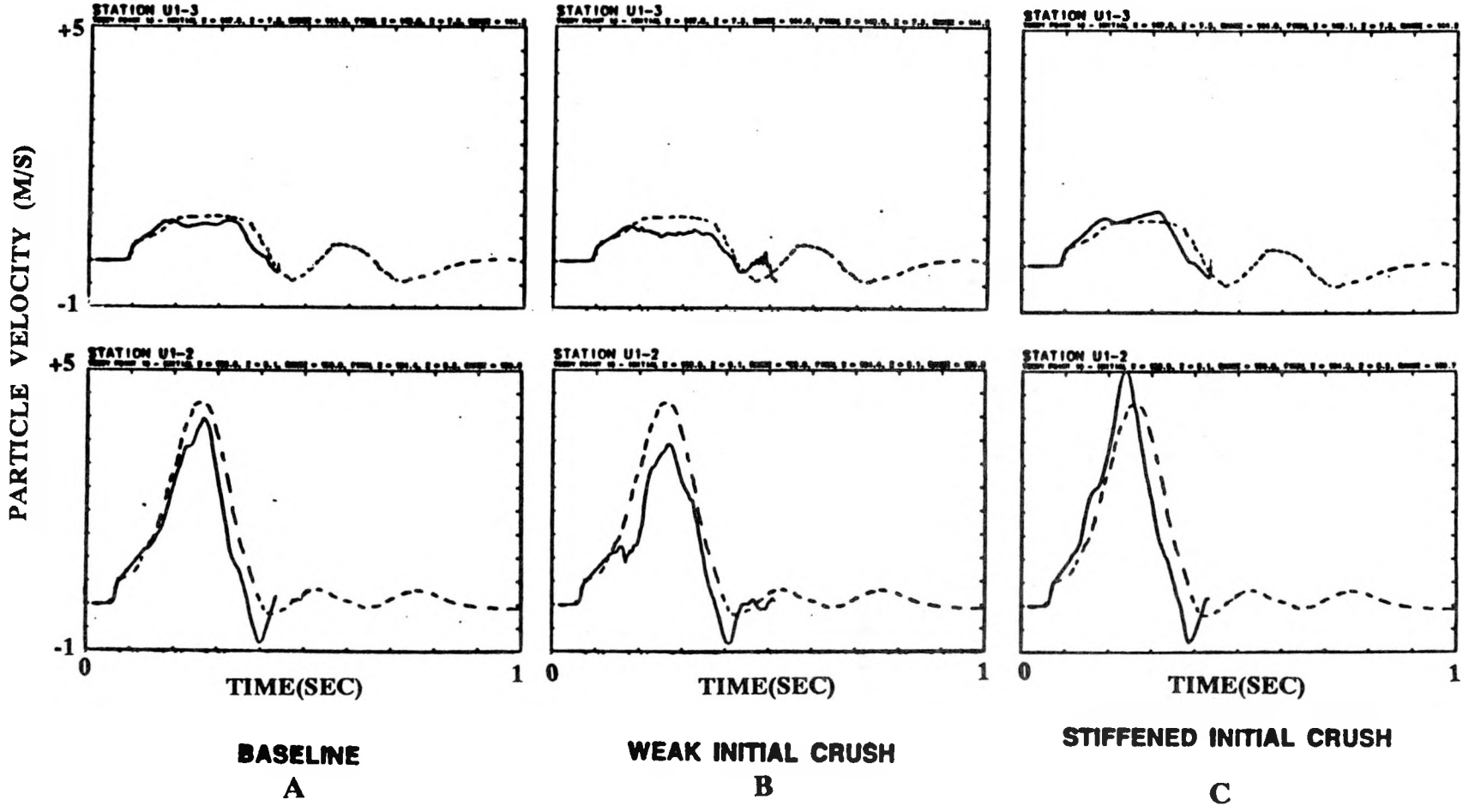


Figure 12. Effect of initial shape of crush loading curve on waveforms at Stations U1-2 and U1-3. Time scale 0 to 1 sec. Vertical scales fixed -1 to +5 m/s. A) 1-D baseline calculation. B) Same as baseline but shape of the crush loading curve is changed to crush more easily at low stress. C) Same as baseline but shape of loading curve is changed to crush less easily at low stress.

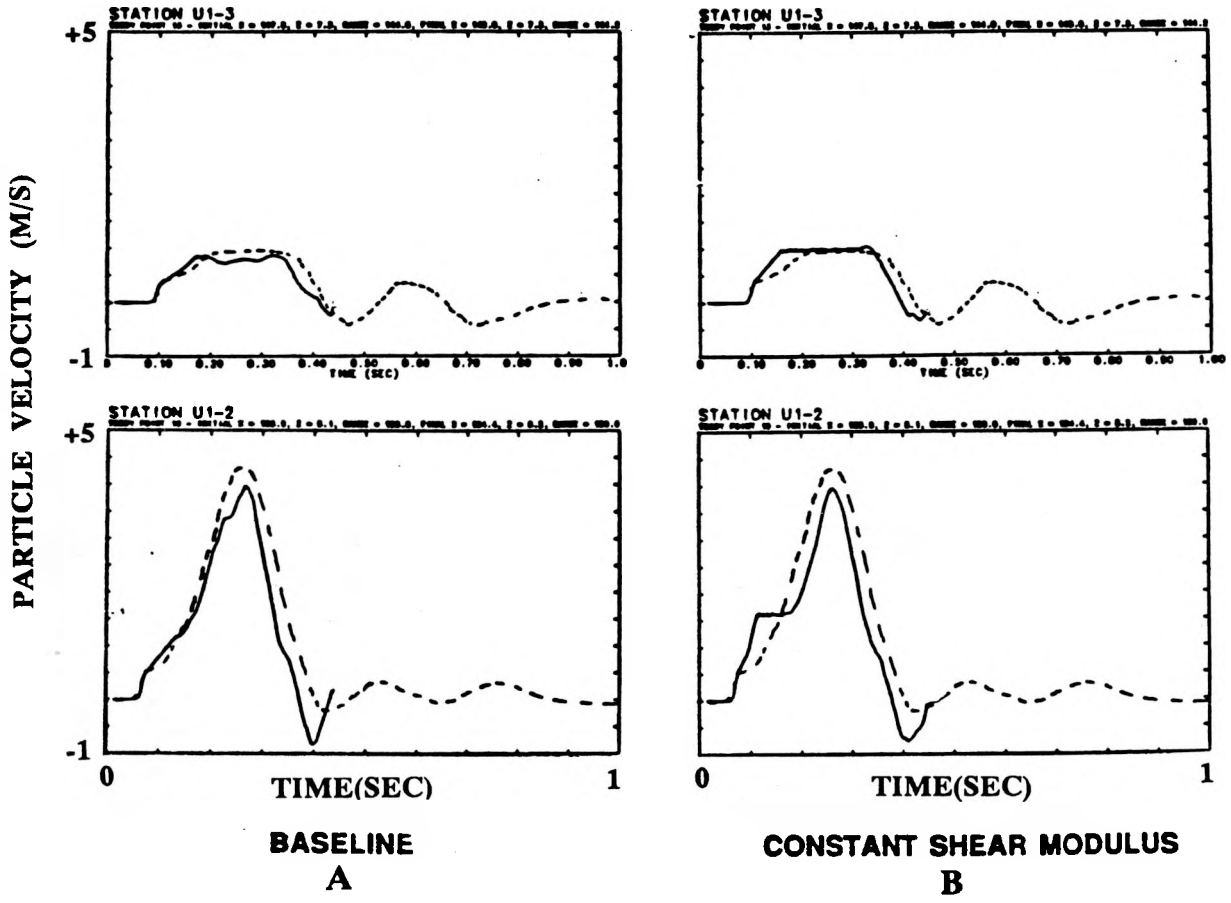


Figure 13. Effect of shear modulus treatment during crush (in absence of shear failure) on particle velocity waveforms at Stations U1-2 and U1-3. Time scale 0 to 1 sec. Vertical scales fixed -1 to +5 m/s. A) 1-D baseline calculation using reduced shear modulus during crush. B) Same as baseline but using constant shear modulus during crush.

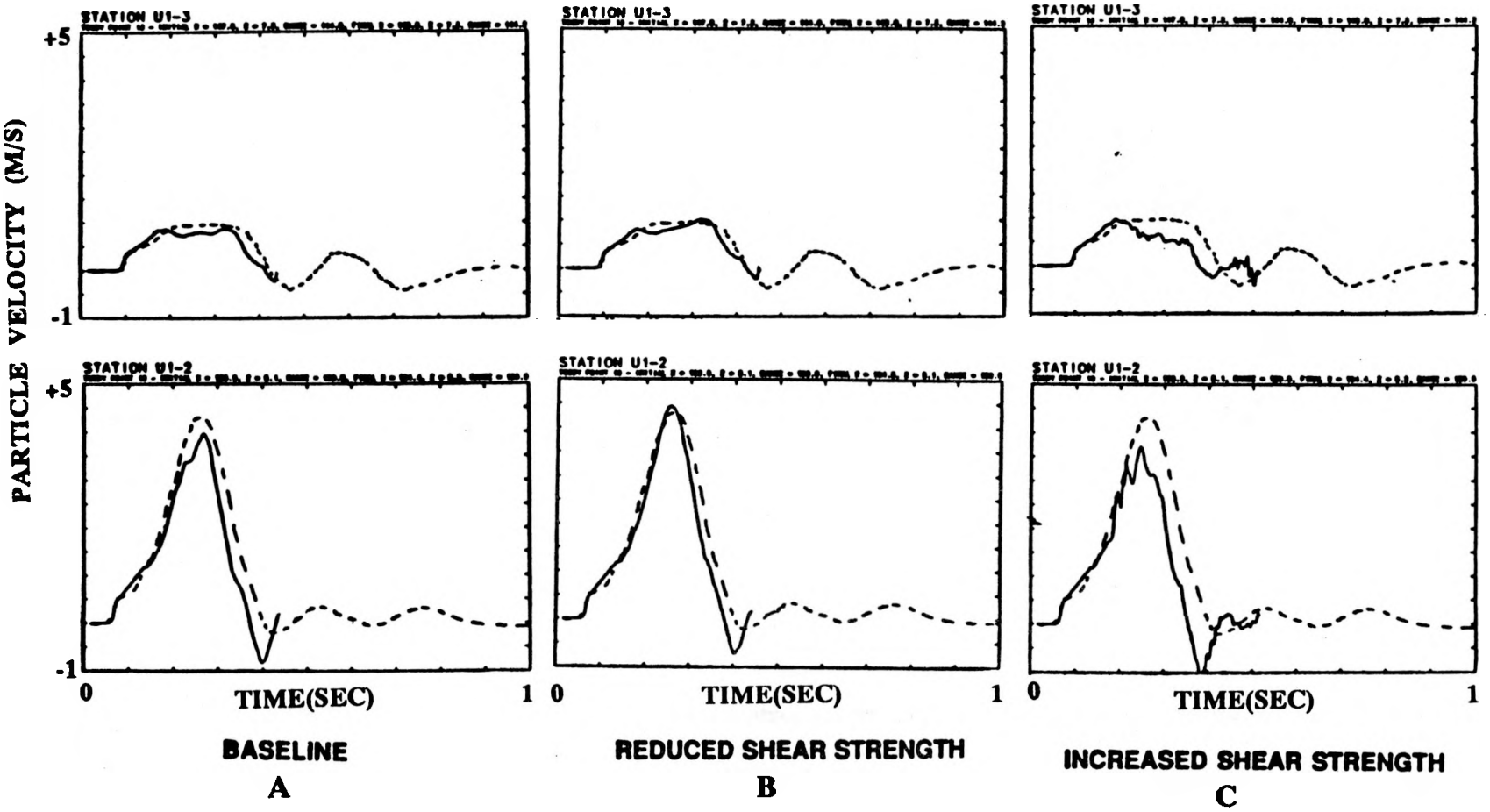


Figure 14. Effect of shear strength on particle velocity waveforms at Stations U1-2 and U1-3. Time scale 0 to 1 sec. Vertical scales fixed -1 to +5 m/s. A) 1-D baseline calculation (undamaged stress difference at 5.0 MPa confining pressure = 6.3 MPa). B) Same as baseline but with lower shear strength (undamaged stress difference at 5.0 MPa confining pressure = 5.6 MPa). C) Same as baseline but using higher shear strength (undamaged stress difference at 5.0 MPa confining pressure = 8.2 MPa).

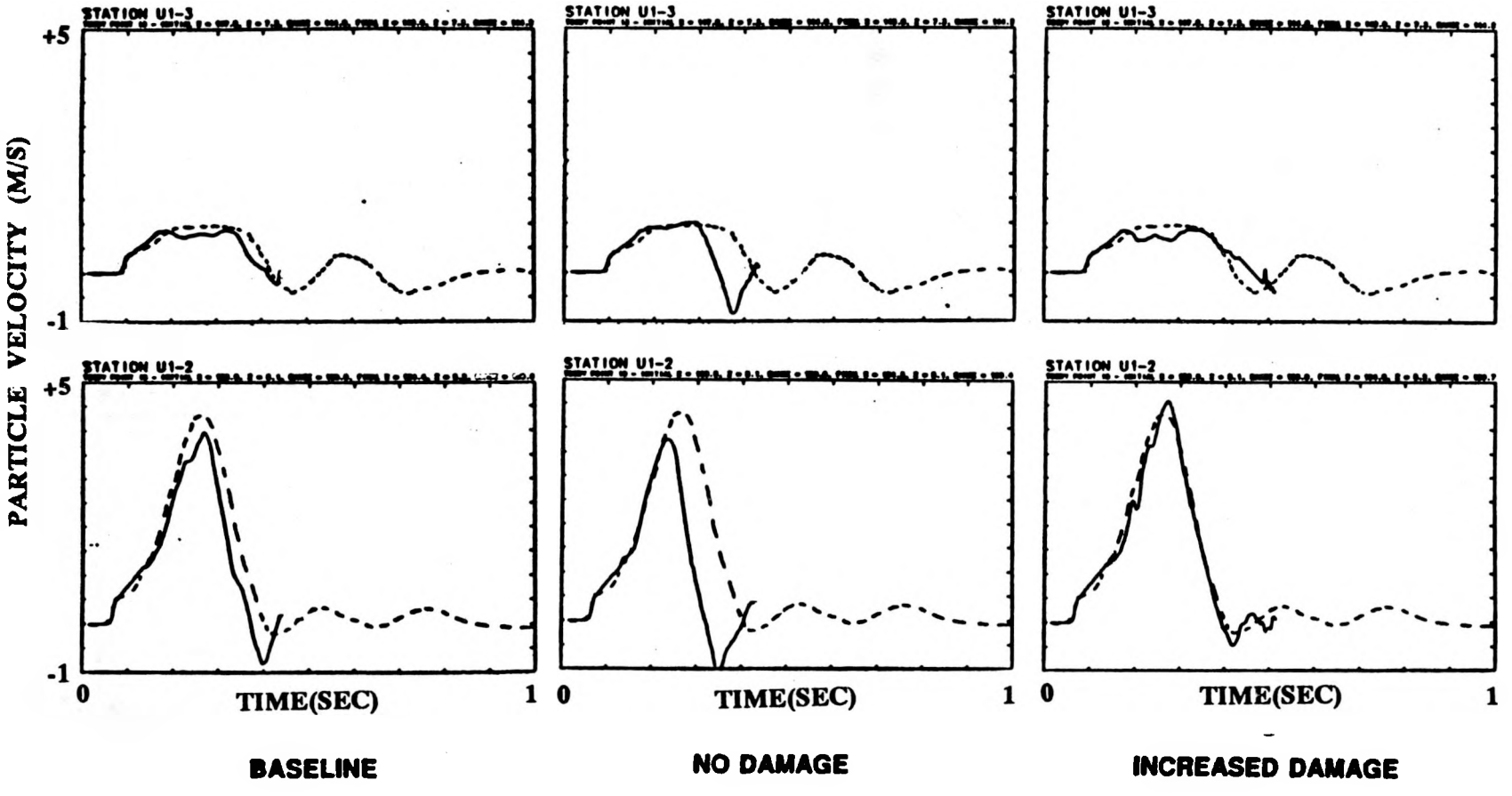


Figure 15. Effect of damage on particle velocity waveforms at Stations U1-2 and U1-3. Time scale 0 to 1 sec. Vertical scales fixed -1 to +5 m/s. A) 1-D baseline calculation (fully damaged stress difference at 5.0 MPa confining pressure = 3.8 MPa). B) Same as baseline but without damage. C) Same as baseline but using increased damage (fully damaged stress difference at 5.0 MPa confining pressure decreased to 3.1 MPa).

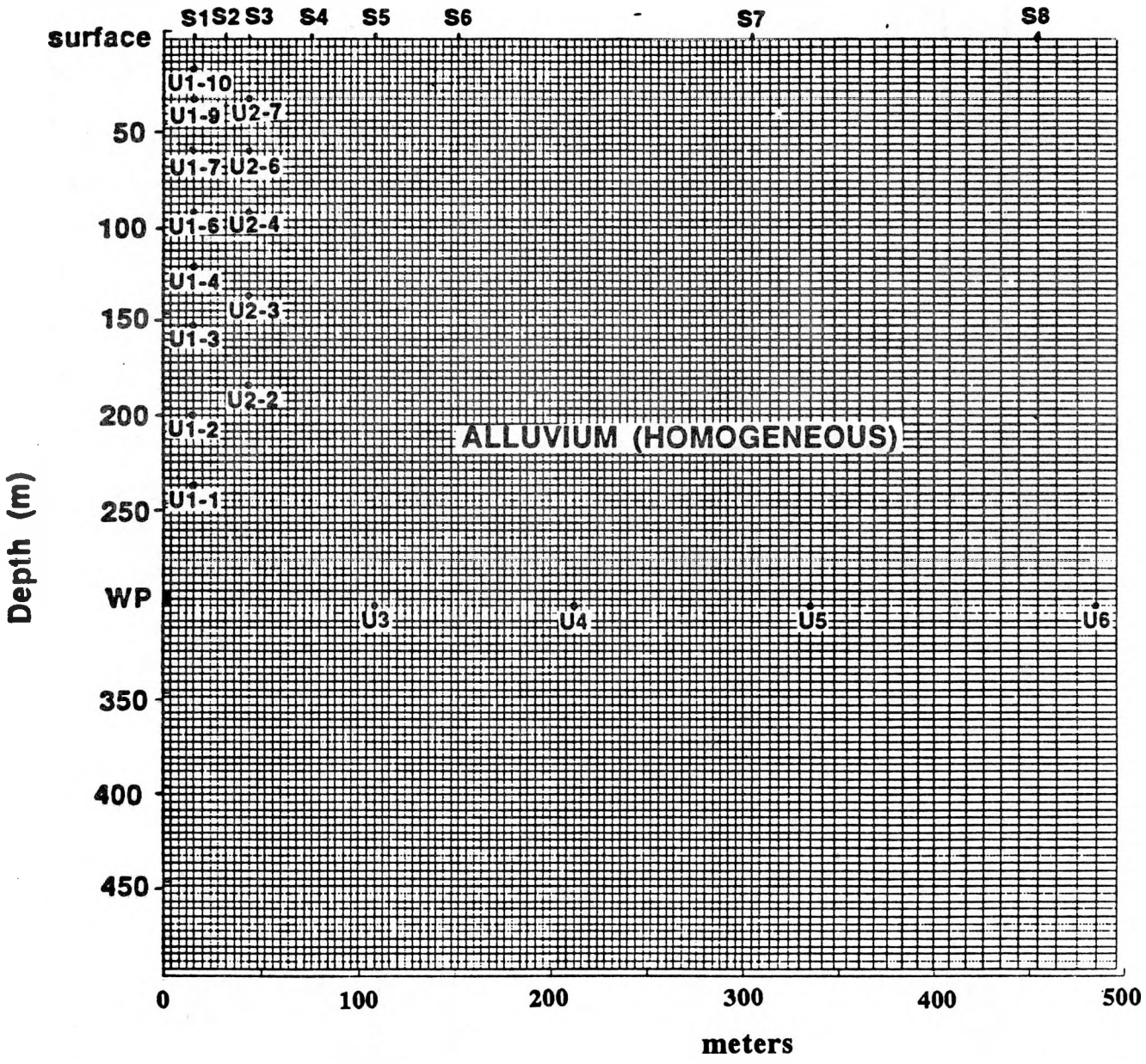


Figure 16. Portion of two-dimensional mesh (coarse zoned) showing the locations of MERLIN instrument stations. Stations S9 (605 m from SGZ), S10 (767 m from SGZ) and U7 (767 m from WP) are off the plot to the right. Mesh outer boundaries are at 1396 m, downward and to the right.

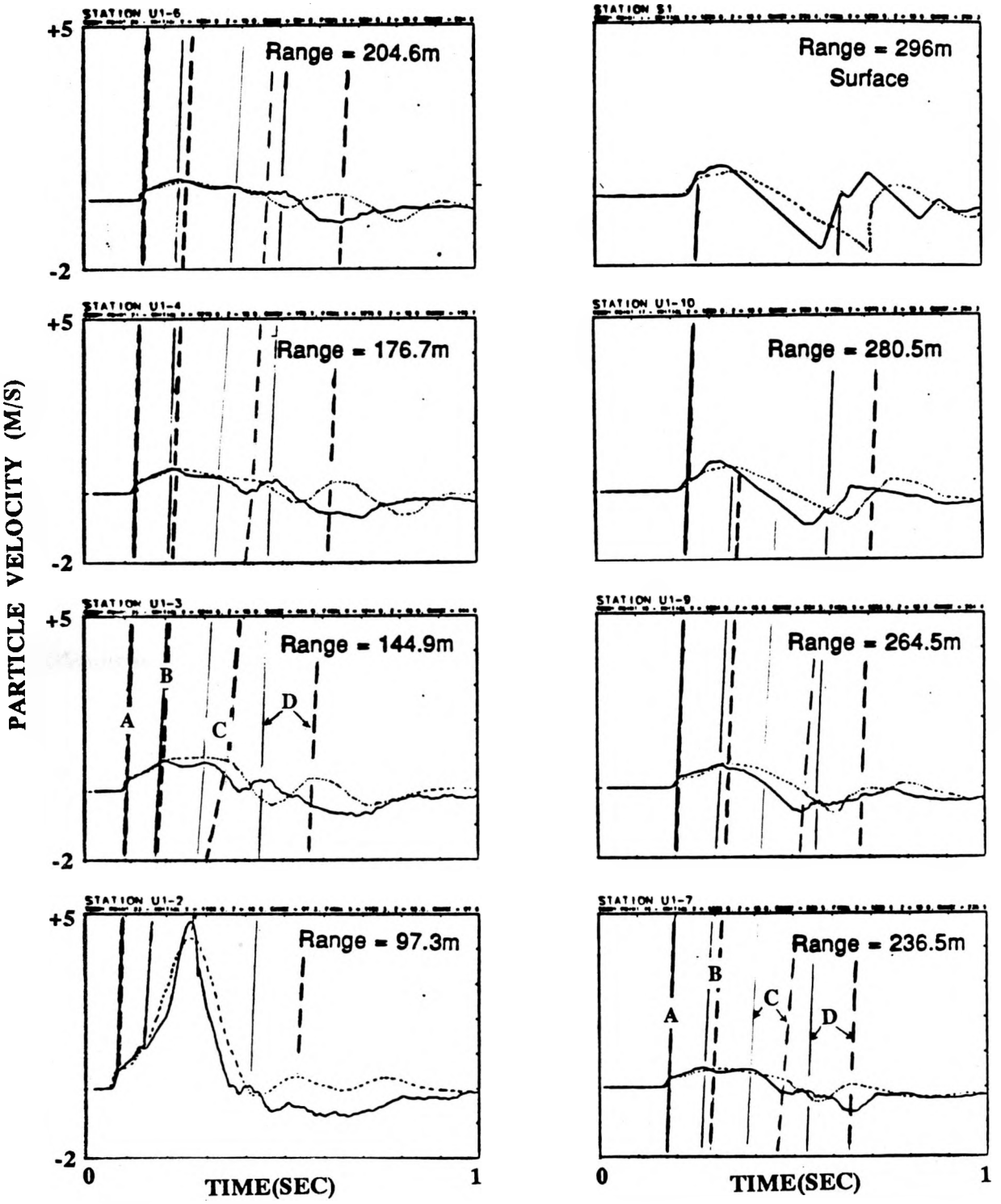


Figure 17. Comparison of 2-D baseline calculation (solid) with measurements (dashed) along U1 satellite hole to 1 sec. Vertical particle velocity at fixed scale -2 to +5 m/s. Measurements are digitized from Perret (1971). Straight lines and letter designations identify and connect the various phase arrivals for calculation (solid) and measurements (dashed). See text for more description.

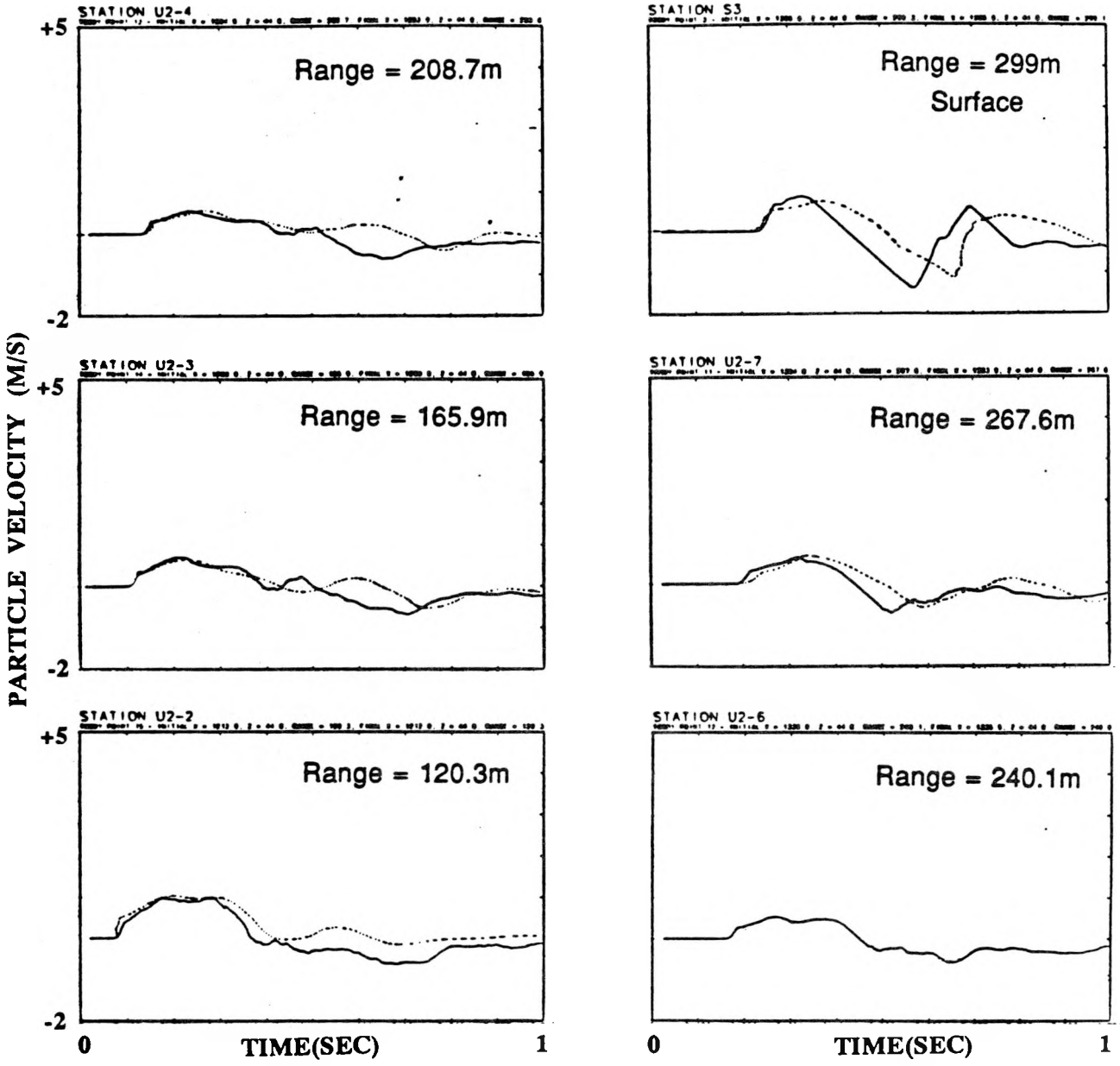


Figure 18. Comparison of 2-D baseline calculation (solid) with measurements (dashed) along U2 satellite hole to 1 sec. Vertical particle velocity at fixed scale -2 to +5 m/s. Measurements are digitized from Perret (1971).

In Figure 17, the various phases of the upward traveling wave are connected by lines - solid lines for the calculation, dashed lines for the measurements. The lines identified as "A" mark the "toe" of the elastic precursor, which is the same for both the calculation and measurements. "B" identifies the point at which pore crush first occurs. Here too there is good agreement between the calculation and measurements. "C" marks the peak of the plastic wave. We are capturing some, but not all, of the broadening that occurs in the measurements in this particular 2-D calculation. The 1-D "baseline" calculation (Figure 6) captured more of this broadening and some small adjustments need to be made to bring the 2-D results into better agreement in this regard. However, in general, both the 1-D and 2-D calculations replicate very well the considerable change in waveform shape, and the marked attenuation, that occurs between stations U1-2 and U1-3. Solid line "D" identifies a rebound phase that occurs in the calculation that is related to cavity rebound. There is a similar, but later and longer period, phase in the data which may or may not be directly related to MERLIN cavity rebound. In the calculation, this late time response is controlled primarily by the residual strength and shear properties of the alluvium after passage of the main stress wave. At Station U1-2, the material goes elastic in the time interval 320 to 450 ms, followed by some additional shear failure from 450 to 650 ms, that has the calculated "rebound" out of phase with the measurement. Obviously more work needs to be done on the response of "shock-damaged" alluvium. With the exception of the "late time" behavior, we appear to be capturing all of the important response characteristics of the alluvium in the vertically upward direction.

Figures 19 and 20 show waveform comparisons along the WP level horizontal array. Figure 19 is fixed scale to show the substantial attenuation observed in both calculations and measurements. Figure 20 has variable scaling to show detail at each station. At first glance, the agreement is not as good as in the vertical arrays. At Station U3, the calculated peak amplitude is about one-half of what it should be. What has happened is that we have missed the transition point from inelastic to elastic response by about 6 meters. The unidentified edit point (for which there is no measurement station) in the lower left of Figure 19 is located just 7 meters closer to the MERLIN WP than the actual "as built" location of Station U3. At this point, the calculated amplitude is slightly higher than the U3 measurement. We believe there is some slight anisotropy present that currently is not being modeled. The far stations (U4 - U7) are well out into the elastic region and the amplitudes are very small. These particle motions may be affected by refractions off deeper, higher velocity tuff layers. This possibility was mentioned by Perret in Reference 1. More work needs to be done in order to match the waveforms at these stations.

Figures 21 and 22 show the surface motion array. In Figure 21, the slightly narrower calculated waveform noted earlier for the subsurface stations is reflected in the surface motions. Taking

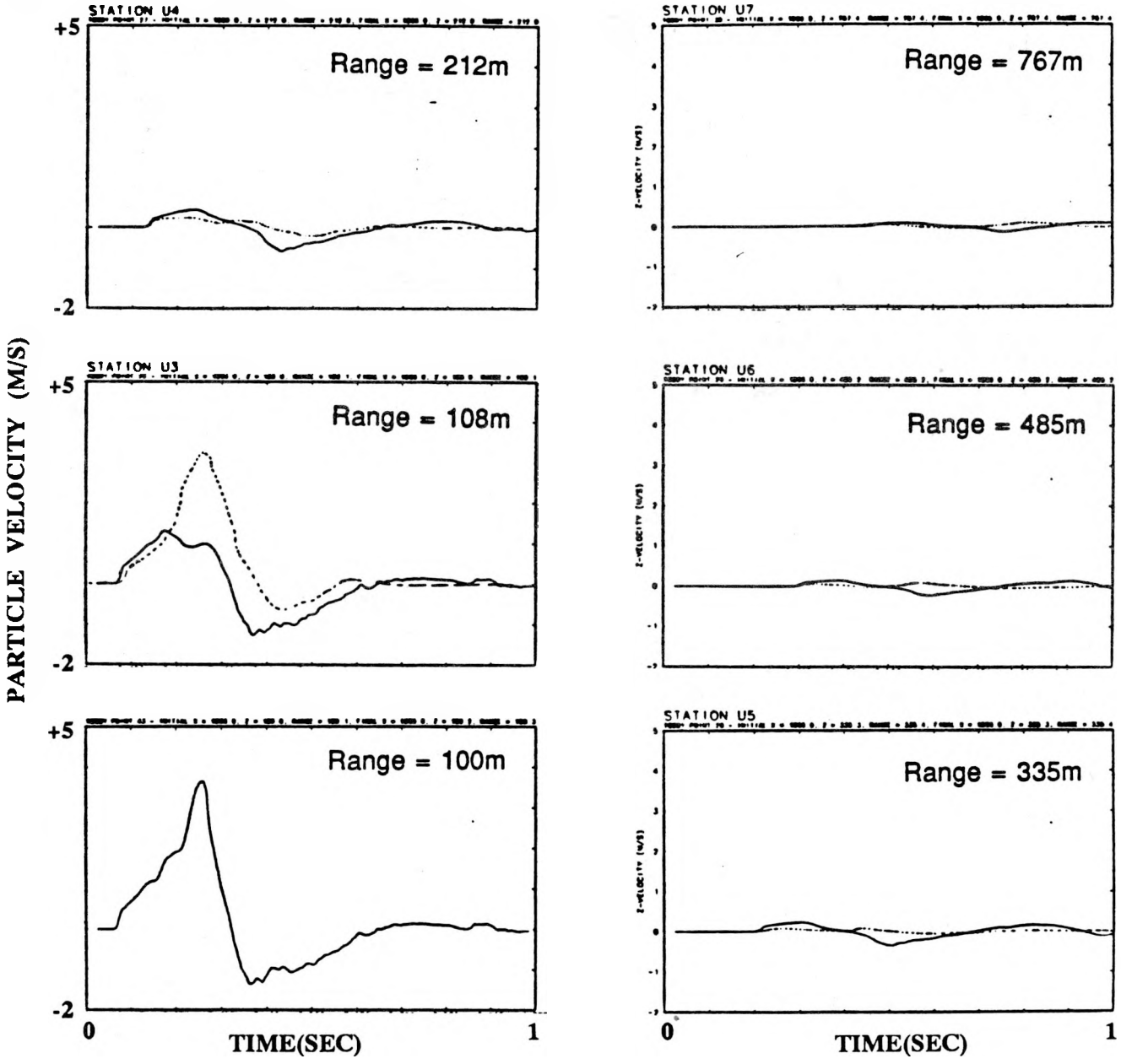


Figure 19. Comparison of 2-D baseline calculation (solid) with measurements (dashed) along WP level array (satellite holes U3, U4, U5, U6 and U7) to 1 sec. Horizontal particle velocity at fixed scale -2 to +5 m/s. Measurements are digitized from Perret (1971). There is no measurement at range = 100 m.

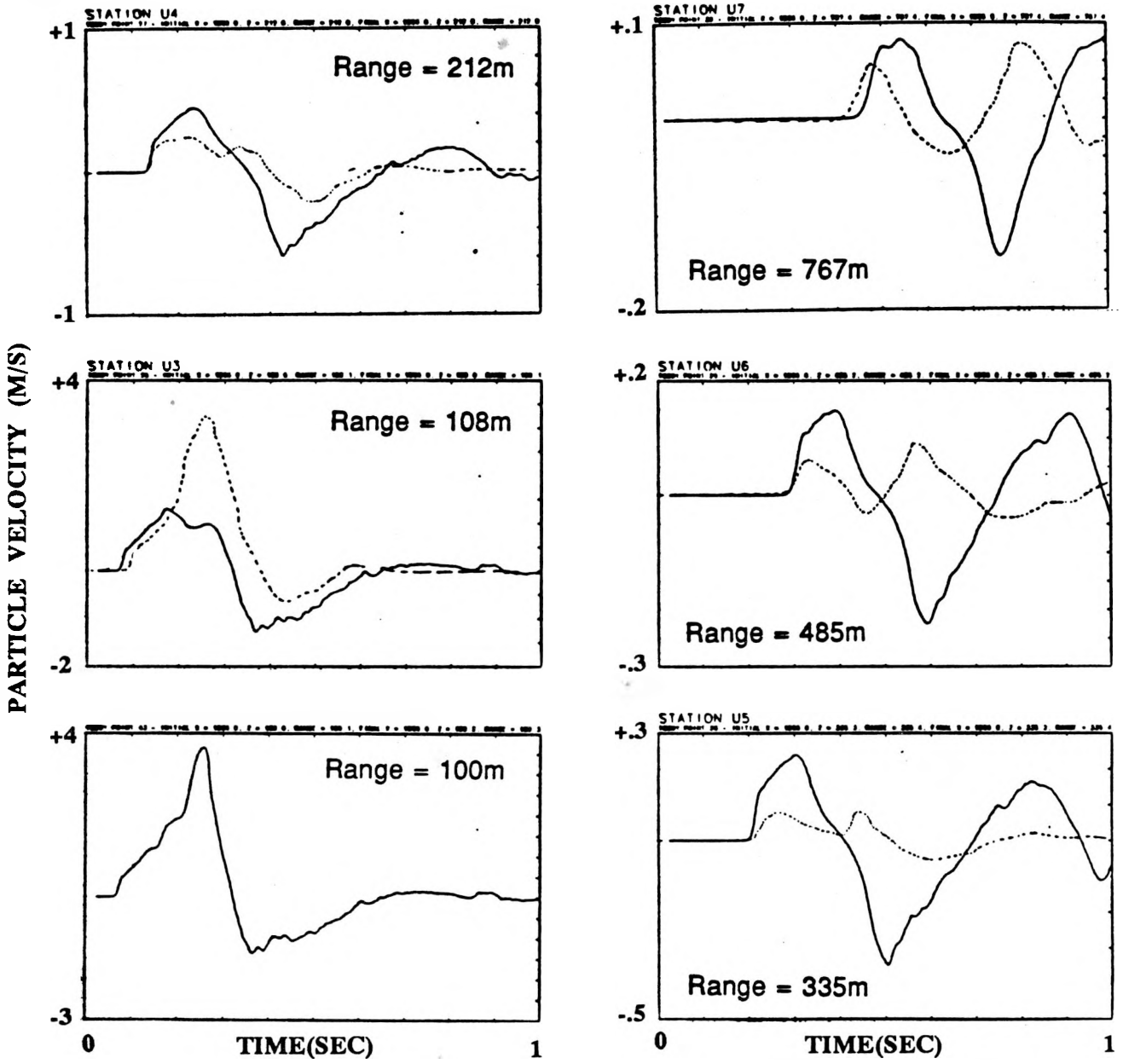


Figure 20. Comparison of 2-D baseline calculation (solid) with measurements (dashed) along WP level array to 1 sec. Horizontal particle velocity in m/s at various scales to show detail at outer gages. There is no measurement at range = 100 m.

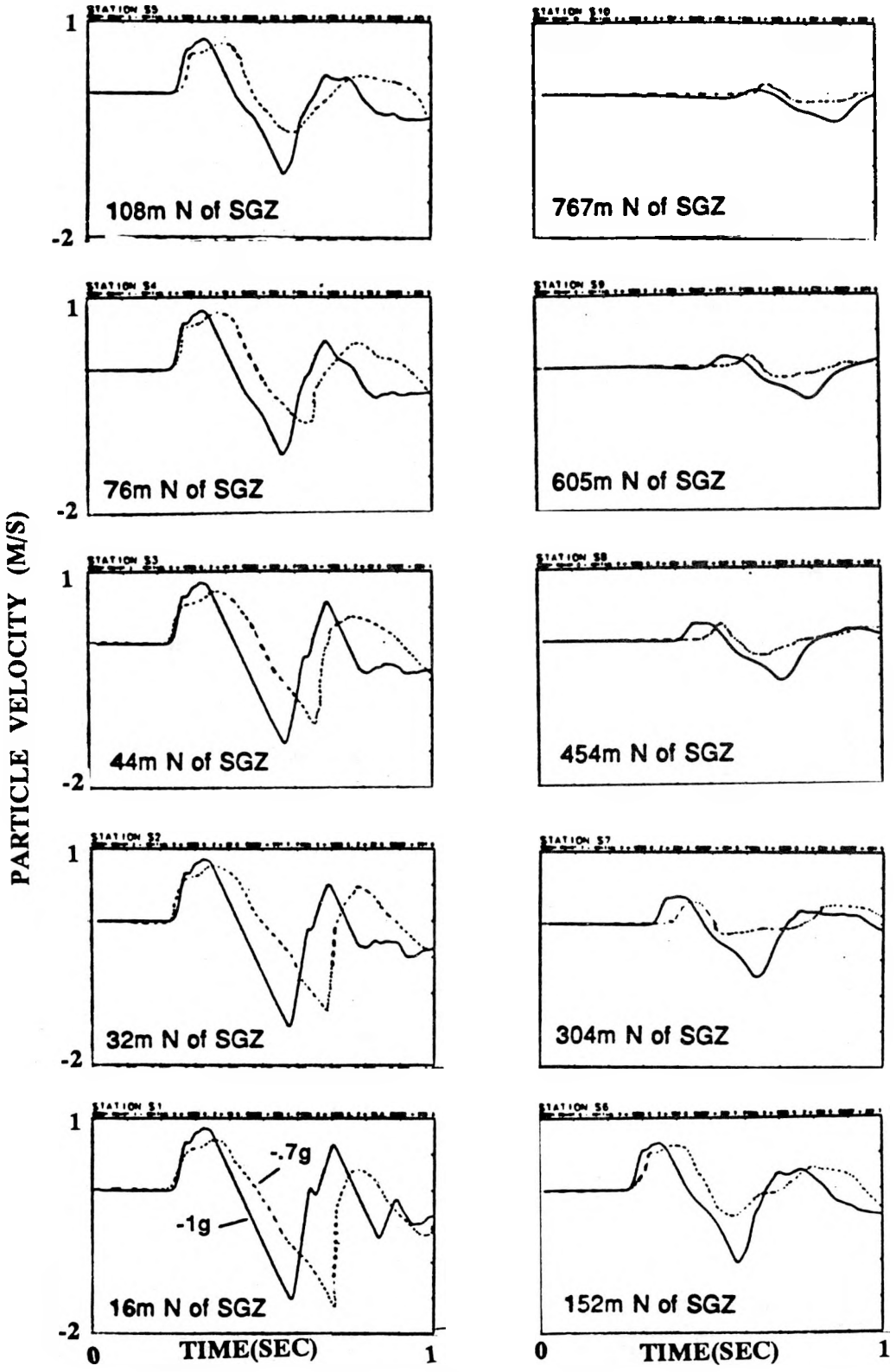


Figure 21. Comparison of 2-D baseline calculation (solid) with measurements (dashed) along ground surface to 1 sec. Vertical free surface velocity at fixed scale -2 to +1 m/s. Measurements are digitized from Perret (1971).

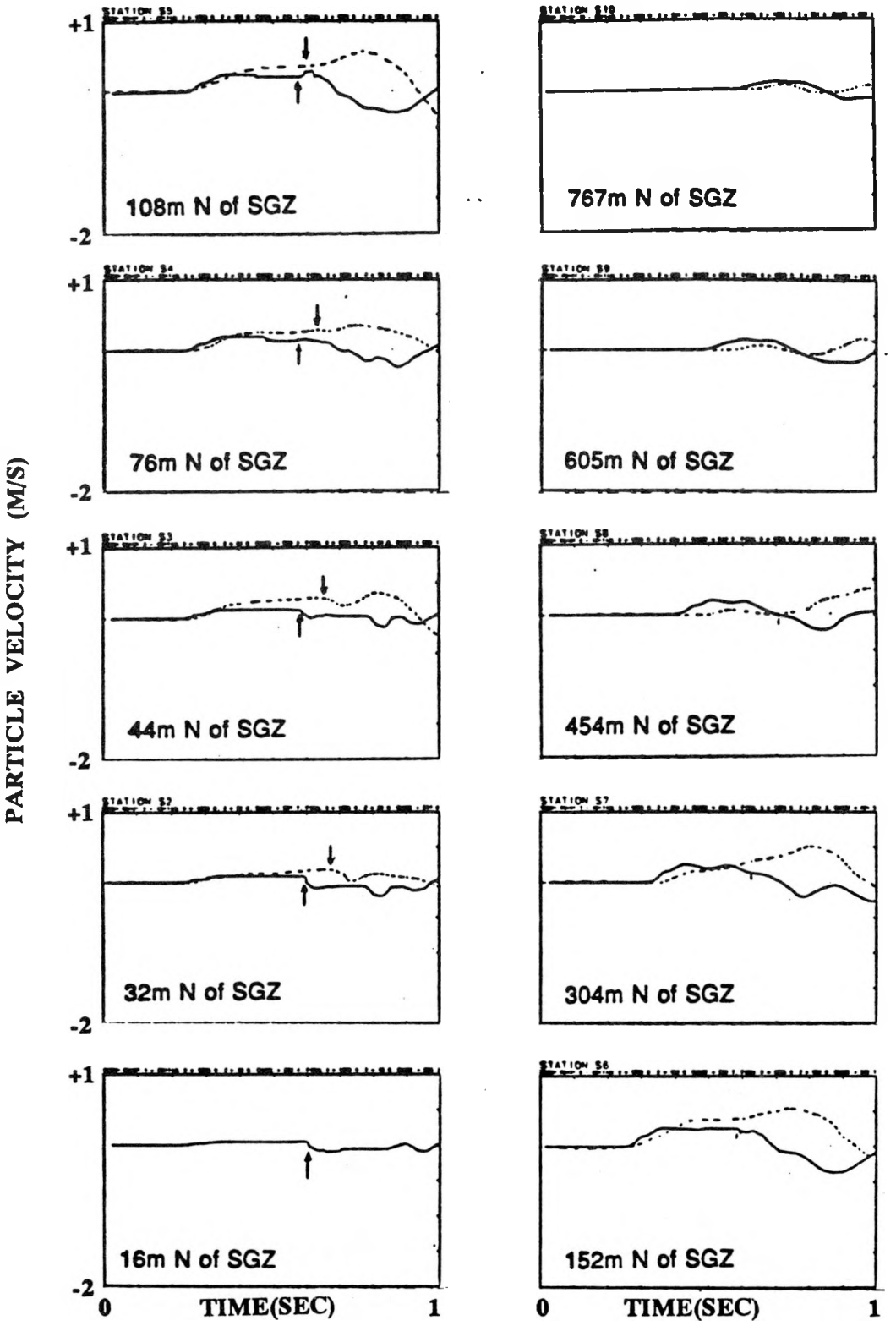


Figure 22. Comparison of 2-D baseline calculation (solid) with measurements (dashed) along ground surface to 1 sec. Horizontal free surface velocity at fixed scale -2 to +1 m/s. Measurements are digitized from Perret (1971). Arrows point to spall closure.

this into account, the agreement between calculated and measured waveforms is excellent. We capture the peak amplitudes, the spall closures and the decrease in amplitude with range from SGZ very well. The calculated spall is a bit stronger than the measurements suggest. Calculations at Stations S1 through S3 have calculated spall accelerations of 9.8 m/s^2 (-1g). The measurements show about -7.0 m/s^2 (-.7g). Farther out the calculated spall accelerations (average) also are less than -1g. Clearly the surface material at MERLIN did not spall in the classical sense of material parting completely and going into ballistic trajectory (a less than -1g "spall" acceleration is generally observed for tests conducted in NTS-Area 3 alluvium). This behavior was replicated in certain other of our calculations (not reported) and the controlling mechanism was incomplete or discontinuous tensile failure of the near surface materials. In those calculations, the broadness of the outgoing waveform and the very low shear strength of the material were responsible for the phenomena.

The agreement with the horizontal velocity measurements (Figure 22) is almost equally good, with one exception. We observe the same initial outward (away from SGZ) motion, with the correct amplitude. The one difference is the direction of motion when spall closure occurs. In the calculations, there is a change in the direction of motion (to inward - toward SGZ) when spall closure occurs. In the measurements, motion continues outward after "spall" closure (but not by much). This small difference may be remedied when we provide a material model that broadens the outgoing wave. We believe we are very close to replicating all facets of the MERLIN surface motion.

Figure 23 is a comparison of waveforms along satellite hole U1 using the aforementioned "linkage" model. The properties and model employed are identical to that used in the 1-D calculation described in conjunction with Figure 9. The model actually works better in the 2-D case than in 1-D for replicating the positive velocity portion of the waveform. The waveform is broader and more in agreement with the data than in the previously described 2-D calculation. Note that at SGZ, the reverse slope of the waveform (spall) is tending toward less than -1g, as observed in the measurement. The remarkable aspect of the improvement is that the code is generating a shear failure surface for each computational zone based only on the state of shear at the point of crush initiation (and on a user defined "failure surface shape definition"). As mentioned earlier, the appropriate failure surface cannot be defined ahead of time because the stress path during the initial elastic response is unknown - it is not purely uniaxial strain loading.

The model, as it is currently constructed, appears to break down during the release phase. The material is too weak after the compressive wave passes and there is a "collapse" of material back toward the MERLIN calculated cavity (see U1-2 and U1-3, Figure 23). Currently we are not

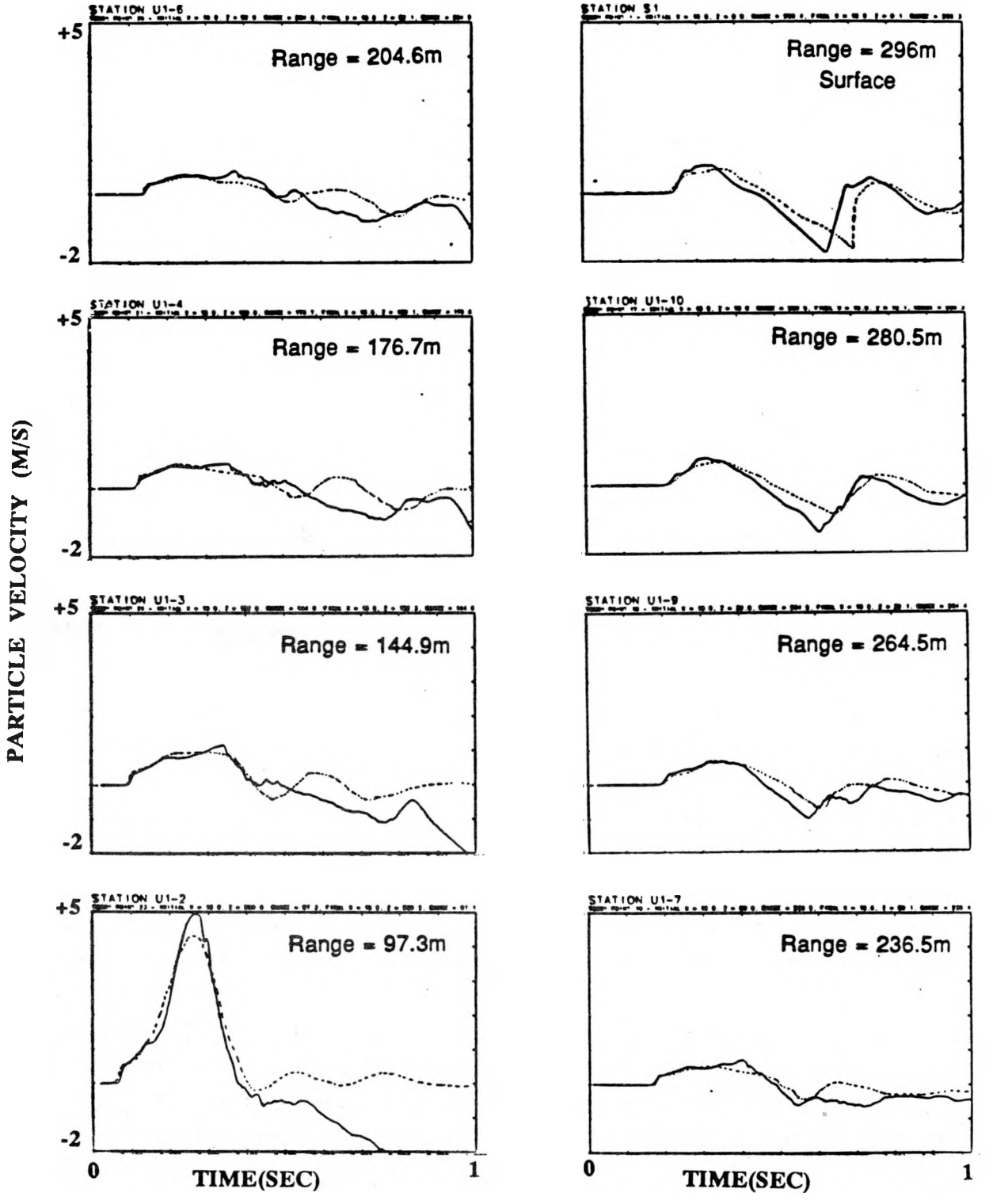


Figure 23. Comparison of 2-D crush/shear linkage calculation (solid) with measurements (dashed) along satellite hole U-1 to 1 sec. Vertical particle velocity at fixed scale -2 to +5 m/s.

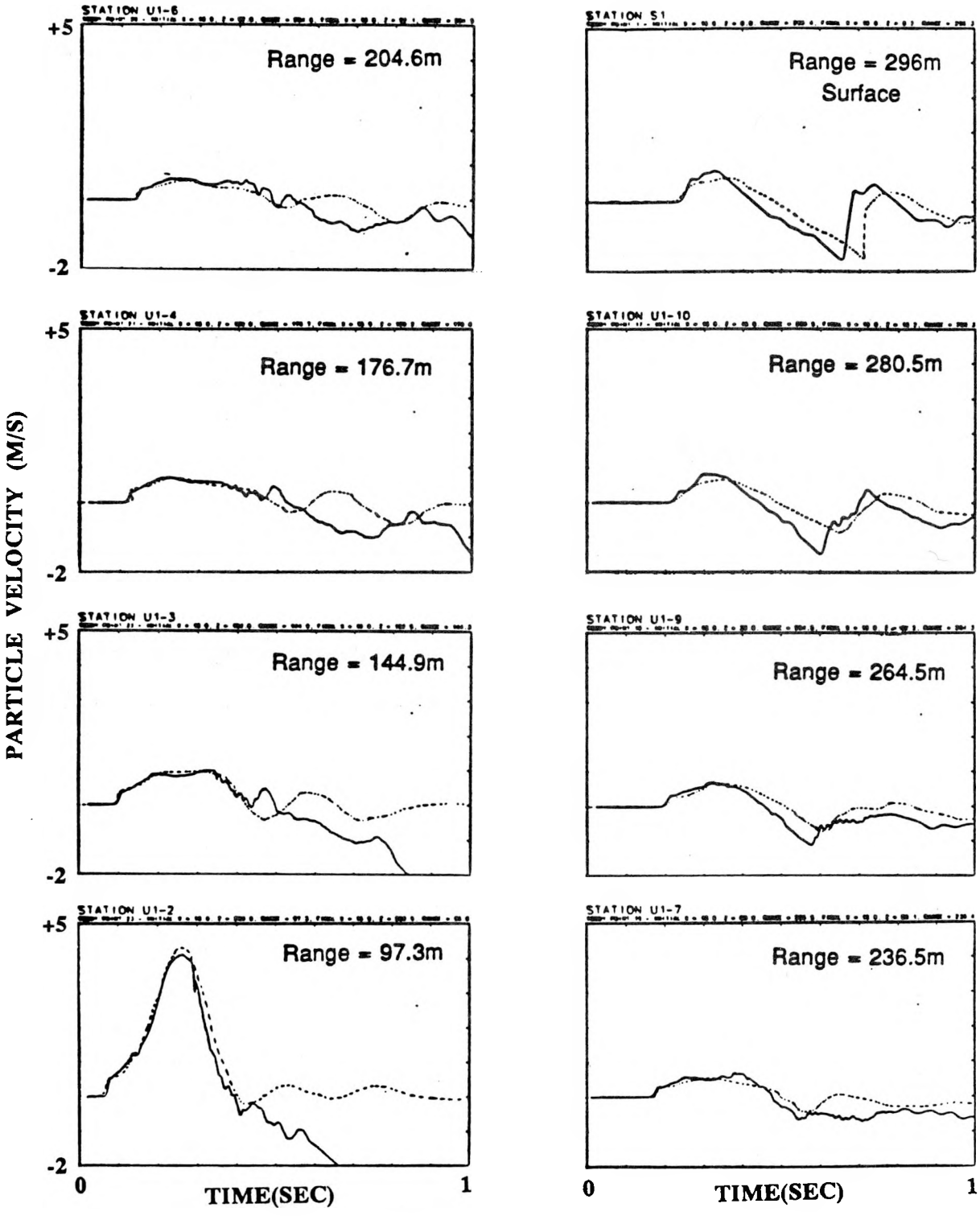


Figure 24. Comparison of 2-D "increased damage" calculation (solid) with measurements (dashed) along satellite hole U-1 to 1 sec. Vertical particle velocity at fixed scale -2 to +5 m/s.

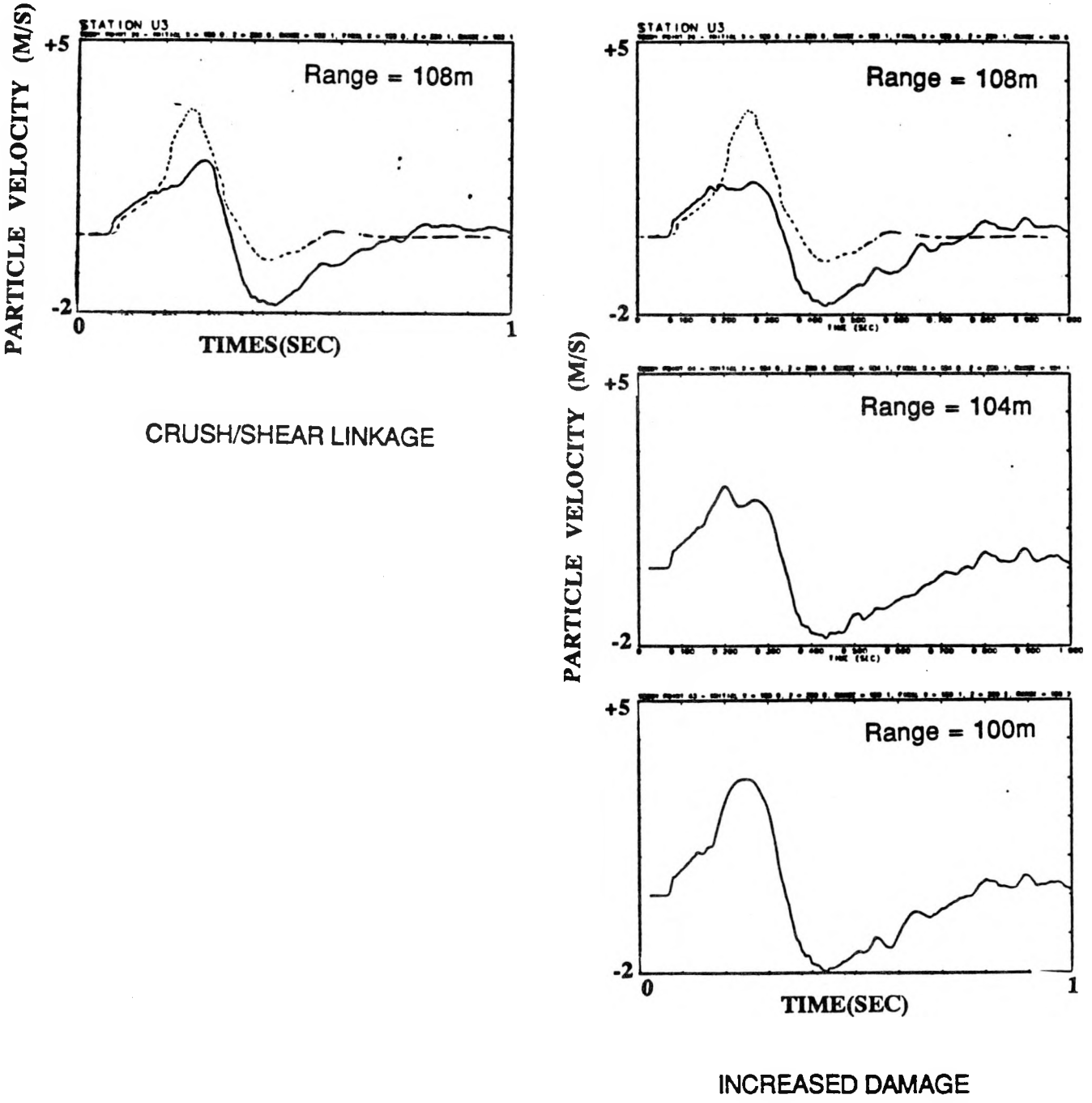


Figure 25. Comparison at Station U3 between "crush/shear linkage" and "increased damage" 2-D calculations to 1 sec. Horizontal particle velocity at fixed scale -2 to +5 m/s. There are no measurements at the 100 m and 104 m ranges.

sure if this is a problem with the material model or cavity gas equation of state. We strongly suspect the former. There is the possibility that the alluvium is stronger in extension (tangential stress greater than the radial component - the state of stress at U1-2 and U1-3 at late times) than in compression (radial stress greater than tangential - the state of stress during passage of the outgoing compressive wave). We intend to investigate this possibility.

Figure 24 is a comparison of waveforms for a calculation that includes increased "damage" (reduction of shear strength with accumulated shear strain) but no crush/shear failure "linkage". The results are similar to the "linkage" calculation. The waveform is broader, more in agreement with the data. Again, the reverse slope of the waveform (spall) is tending toward less than -1g, as observed in the measurement. But also there is the "collapse" of material toward the cavity similar to the "linkage" case.

Figure 25 is a comparison at the U3 station for the latter two discussed calculations (crush/shear linkage and increased shear damage). In both of these cases, there is a slight improvement over the waveform shown in Figure 20. The inelastic-elastic transition range is nearer what it should be, based on the U3 measurement. At all measurement stations, it appears that the latter treatments give improved results if one ignores the late time failure and collapse toward the cavity.

Figure 26 is a "hoop stress" contour plot showing the final state of residual stress for the first 2-D calculation discussed. It shows that the residual stress field, sometimes referred to as the "stress cage" or "containment cage", is very weak under the assumptions of the model. This is consistent with our observations that events in alluvium appear to be "leaky". However, this result must be strongly qualified. Our poorest agreement with the measurements is at the deep stations at late times, when this stress field is forming. The strength of the alluvium in resisting cavity growth and late-time rebound is crucial to the formation of the containment cage.

V. CONCLUSIONS

We find that there are some properties of alluvium that are strongly constrained by the data. Small variations (factors of two) lead to drastic changes in the waveform character. These parameters include the crush initiation pressure, fully crushed pressure and shape of the loading curve. Other factors can be used in unison to achieve satisfactory agreement with a variety of combinations. These include the failure envelope in conjunction with damage. To achieve good agreement at stations over a large range we find that it is necessary to provide more control over

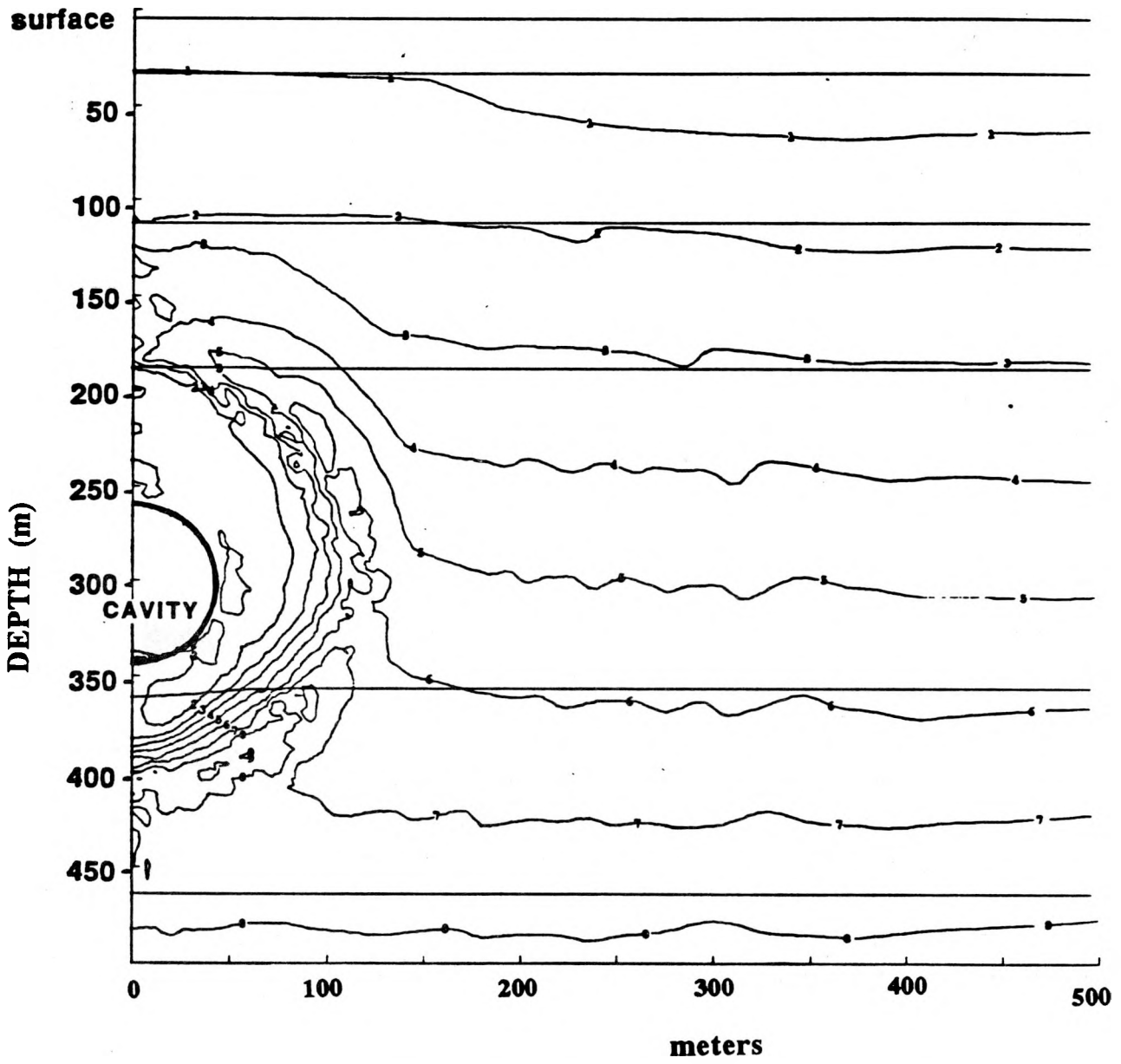


Figure 26. Contour plot of hoop stress (horizontal, out-of-plane of plot) for 2-D baseline calculation at 1 sec problem time. Contours are labeled in MPa. Cavity pressure = 1.6 MPa.

shear behavior than is allowed by the more conventional treatment of separating the effects of shear and volumetric behavior within the EOS. The "effective" shear modulus must be reduced during pore crush. There are other EOS treatments that incorporate this behavior, the Weidlinger "Cap Model" being one. We have developed two computationally convenient schemes for implementing this, each with its own benefits and drawbacks.

We are currently achieving good agreement at stations in all directions and at all the ranges covered, but there is room for improvement. We feel we understand the behavior that is determining the shape of the waveforms. There is some further work to be done to better model and understand the results. Further work is planned in the development of a damage model that provides improved agreement at late time (> 500 ms). Also, there are some indications that some anisotropic shear behavior should be incorporated into the model. We have indications from calculations that include anisotropic in-situ stress (not reported) that indicate a considerable sensitivity to this parameter. We hope that with further work we can shed some light on the actual state of in-situ stress in Area 3. We intend to investigate more thoroughly the crush/shear "linkage" model to determine if it is a reasonable treatment for the response of alluvium.

We feel that the results of this study provide a good basis for developing a more physics based EOS for alluvium. That is the real goal of this work and additional effort in this direction may result in a true predictive capability for modelling underground explosions. But even at our current state of development, we feel that we are able to do a credible job of analyzing low yield events in porous alluvium using computer stress wave modelling as a tool. This class of events constitutes a large percentage of the U.S. underground tests that historically have been the most difficult to contain.

VI. ACKNOWLEDGEMENTS

The authors wish to thank Jack House, Nuclear Test Containment Program Manager, for providing the resources in support the MERLIN, and the companion HEARTS, research efforts. This work is supported by the United States Department of Energy

VI. REFERENCES

Perret, W. R., 1971, Free-Field Motion from a Nuclear Explosion in Alluvium: MERLIN Event, Sandia National Laboratory Report SC-RR-69-334.

Bonner, B. P., Abey, A. E., Heard, H. C., and Schock, R. N., 1972, High Pressure Mechanical Properties of MERLIN Alluvium, Lawrence Livermore National Laboratory Report UCRL-51252.

Recent Nuclear Cavity Pressure Measurements

B. Hudson
Lawrence Livermore National Laboratory
Livermore, CA 94550

T. Stubbs
EG&G Energy Measurements, Inc.
Pleasanton, CA 94566

R. Nilson, E. Peterson
S-Cubed
La Jolla, CA 92037

An underground nuclear test is typically conducted in an emplacement hole hundreds of metres deep that has been back-filled with sand, gravel,and concrete plugs. These plugs, which vary in thickness and strength, serve not only to prevent radioactive material from reaching the surface but also, ideally, to constrain it to a region near the explosion cavity. When we determine the appropriate depth of burial (DOB) for a device, we have to make it shallow enough to be economical but deep enough to reasonably ensure containment given the expected yield of the device and the particular geology of the hole. To do this, we have developed sophisticated computer models that consider each site's geologic structure and physical properties to predict explosion effects such as ground motion, confining stresses around the cavity, and cavity pressure. However, to be able to assess the performance and relative accuracy of these computational models, we must develop a data base of the measured values for each of these effects that can be compared with predictions.

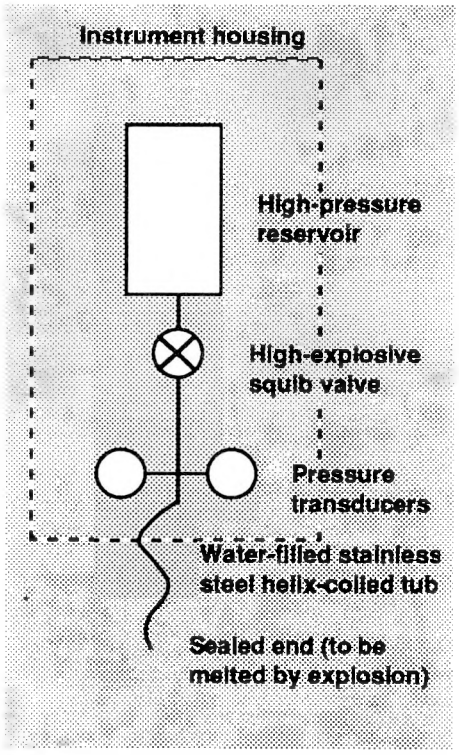


Figure 1. Schematic diagram of the apparatus (one of three) used for measuring cavity pressure on the CORNUCOPIA Event.

Over the past 25 years, many attempts have been made to measure a cavity pressure history. Unfortunately, few attempts have succeeded in giving even partial pressure histories. Furthermore, it has been difficult to establish the validity of data from supposedly successful measurements. In the mid-1980s, we devised a new scheme based on the results of past attempts and phenomenological observations from reentry studies of events detonated in tunnels under Rainier Mesa at NTS. This new scheme was designed to optimize chances of maintaining pressure communication with a nuclear cavity. The essential elements of the new design included a fluid-filled, helically coiled capillary tube and a reservoir containing high pressures (up to 12,000 psi) for blowing the fluid from the tubing after cavity formation (see Fig. 1). Three separate but identical systems were fielded on the CORNUCOPIA Event at Yucca Flat in 1986[1]. Figure 2 shows a plot of the three resulting pressure traces. The agreement between channels was extremely good, giving a believable pressure record that

extended from zero time through cavity collapse. A similar measurement set was fielded on a Defense Nuclear Agency (DNA) tunnel event (MISSION GHOST) under Rainier Mesa in 1987[2]. Figure 3 shows the two complete data sets in a log-log format. Although the absolute levels are quite different, these data suggested three separate stages of cavity pressure decay. The absolute differences in the traces of the two events are not particularly surprising because there were significant differences in material properties, geologic structure, and yield, each of which is believed to play a role in developing the initial pressure. Following a study of CORNUCOPIA, we concluded that pressure decay could be described in terms of three stages[1]:

- Stage I - Initial pressure is either much lower than predicted or hydrofractures allow the initial cavity pressure to drop to a level controlled by non-event-related confining stresses within a very short time (about 50 s on CORNUCOPIA).
- Stage II - The addition of mass combined with additional hydrofractures maintains a nearly constant pressure for a relatively long period (about one hour on CORNUCOPIA) while the temperature drops to near the melting point of rock (about 1400 k)
- Stage III - Heat conduction and Darcian flow out of the cavity cause a monotonic pressure decay until collapse.

Although our conclusions concerning the last two stages seemed fairly well based in theory, we were not as comfortable with our conclusions concerning the first stage, as a result of the uncertainty in time required by the high pressure (7000-11,000 psi) to remove the fluid from the capillary tubing. This time was impossible to calibrate because we do not know the exact configuration of the tubing after detonation. In an attempt to obviate this difficulty, we fielded a modified measurement set on the RHYOLITE Event in Yucca Flat in 1988[3]. This configuration differed from the previous ones in that it did not have a pressure reservoir for blowing out the fluid. Figure 4 contains the pressure data from this event. Although there is now an uncertainty of up to about 100 psi because of the fluid in the tubes, we believe that the RHYOLITE data are representative of cavity pressure from after about 2 s.

The RHYOLITE data suggest that the pressure histories determined from CORNUCOPIA and MISSION GHOST are not representative of cavity pressure during the period called Stage I and that the beginning of the relatively constant Stage II is probably representative of the initial cavity pressure, which is controlled by cavity growth, prompt-shock-induced mixing of material, and the possible occurrence of hydrofracture. If these interpretations are correct, there is a qualitative difference between CORNUCOPIA, which had an initial pressure of less than half the overburden, and the more recent MISSION GHOST and RHYOLITE events, which had initial pressures considerably greater than overburden pressure. More data are needed to determine whether this difference is indicative of measurement or modeling difficulties.

Current plans include fielding of similar measurement set on one DNA and one LLNL event.

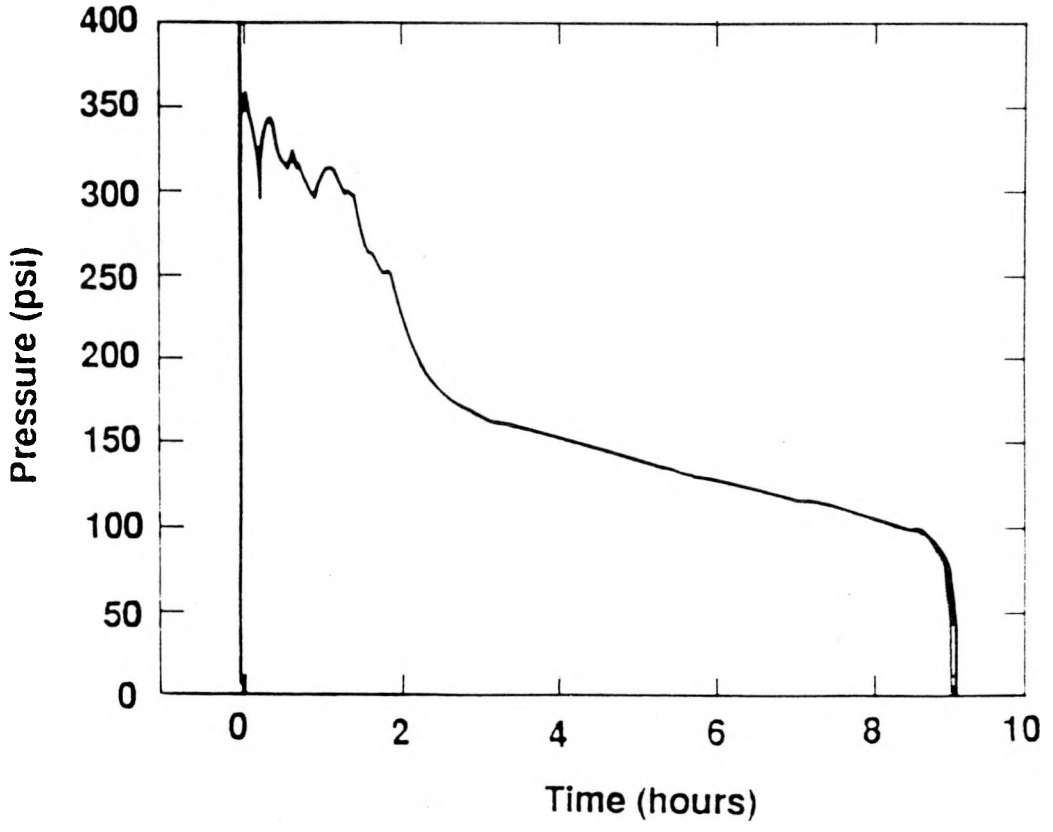


Figure 2. Plot of three pressure traces, which gives a complete pressure history of the CORNUCOPIA Event cavity from the explosion to cavity collapse about nine hours later. Agreement between the three traces is extremely good. High pressure was applied to the fluid in the helix tubes about 2 s before detonation. The increased rate of pressure drop in the minutes before collapse strongly suggests that reduced cavity pressure brought on, rather than resulted from, cavity collapse.

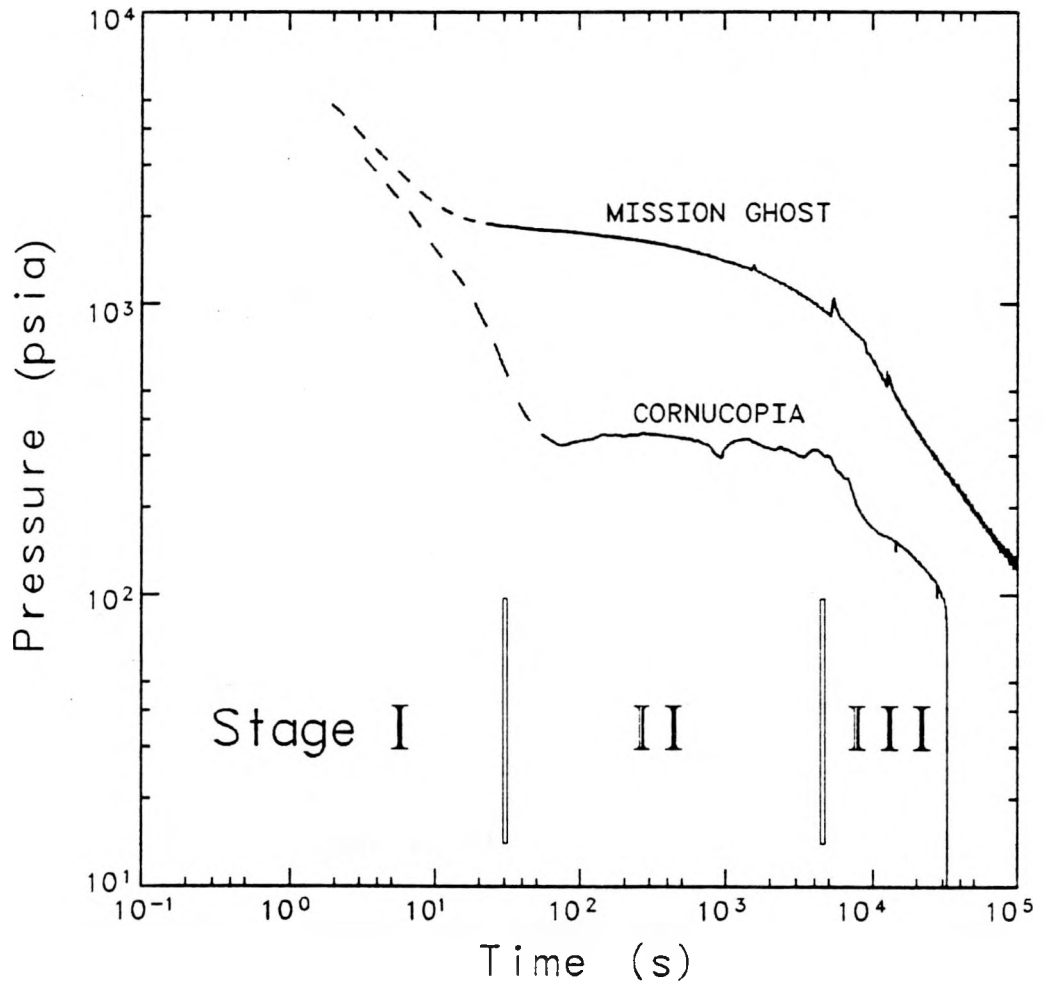


Figure 3. The MISSION GHOST cavity pressure appears to have distinct stages of decay, similar to those of CORNUCOPIA. The pressure histories suspected of being the result of fluid "blow-out" are shown as dashed lines.

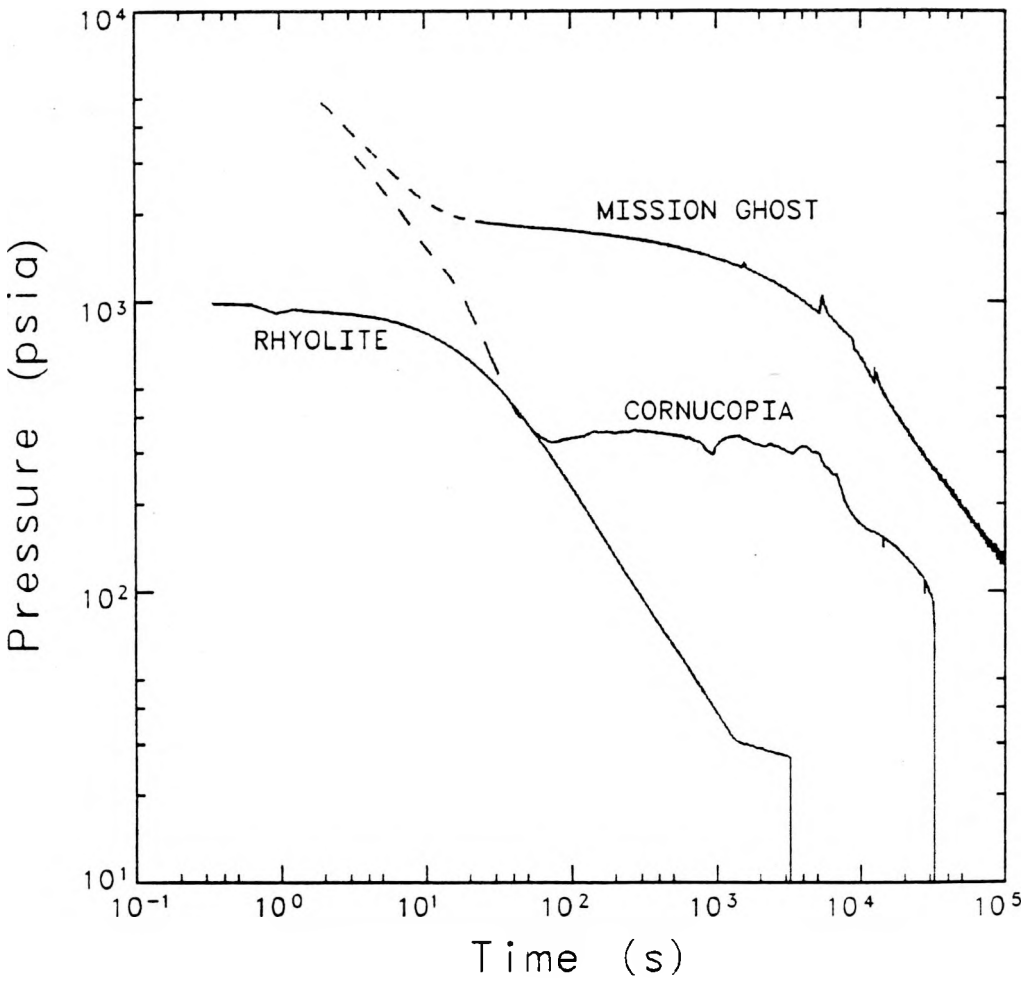


Figure 4. Pressure data from the RHYOLITE Event are believed to be representative of cavity pressure from less than 2 s on, suggesting that the "plateaus" seen on CORNUCOPIA and MISSION GHOST are the initial starting pressures, while the pre-plateau pressures (dashed lines) are artifacts of the fluid removal process.

---

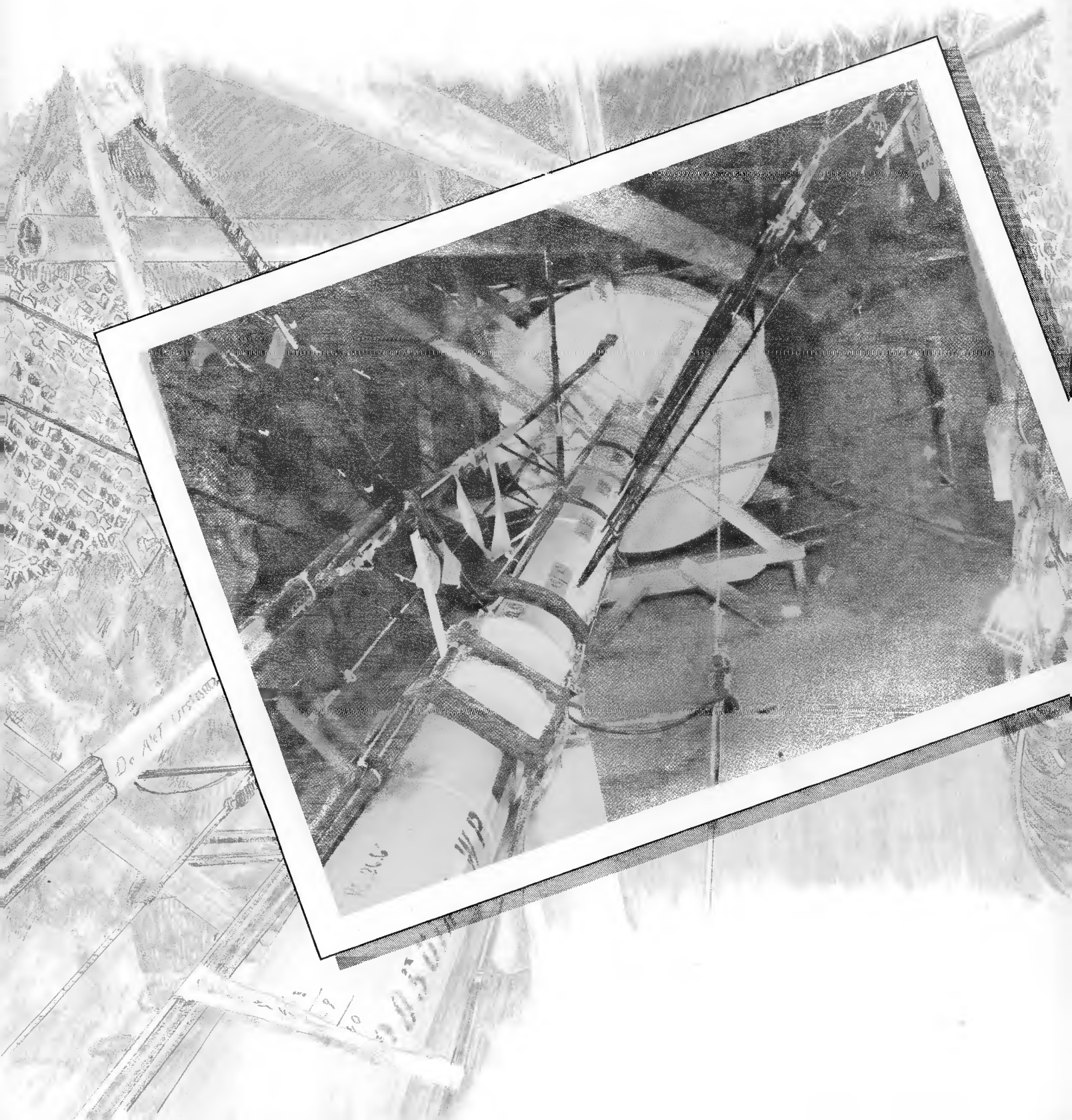
[1] B. C. Hudson, C. Cordill, L. Starrh, J. Kalinowski, T. Stubbs, C. Keller, E. Peterson, R. Nilson, *CORNUCOPIA Cavity Pressure Measurements*, Lawrence Livermore National Laboratory, Livermore, Calif. UCRL-96354 (1987)

[2] C. Sisemore, B. C. Hudson, C. Cordill, and C. Smith, *Cavity Pressure Measurements and Gas Sampling for MISSION GHOST*, LAWRENCE Livermore NATIONAL LABORATORY, Livermore, CALIF., UCID-21295 (1987).

[3] B. C. Hudson, T. Stubbs, C. Cordill, and C. Sisemore, *RHYOLITE Containment Data report* Lawrence Livermore National Laboratory, Livermore, Calif., MISC.-4642

Work performed under the auspices of the U.S. Department of Energy by the Lawrence Livermore National Laboratory under Contract W-7405-Eng-48.

Hydrology and Mineralogy



HYDROLOGIC TESTING IN EXPLORATORY DRILL HOLE UE4T, YUCCA FLAT, THE NEVADA TEST SITE

Ward L. Hawkins, Los Alamos National Laboratory, Los Alamos, NM 87545
Douglas A. Trudeau, U.S. Geological Survey/WRD, 1500 E. Tropicana Ave., Suite 201, Las Vegas, NV 89109
Todd M. Mihevc, Desert Research Institute, P. O. Box 60220, Reno, NV 89512

ABSTRACT

Ue4t is a 0.25-m diameter hole drilled in early 1987 to a total depth of 736 m in the central portion of Yucca Flat. The water level in this uncased hole rose to a depth of 268 m below land surface datum (LSD); however, the estimated depth to the water table is 506 m. Elevated fluid levels are responsible for emplacement hole construction problems and may affect radionuclide migration. Straddle packer testing was conducted in Ue4t during January, February and May of 1989 to determine the vertical hydraulic gradient, the magnitude of formation fluid pressures and to define the water table.

Results from the hydrologic testing indicate that there is a general upward hydraulic gradient in hole Ue4t because the lowest formation pressure (287 psia) was measured between the surface and a depth of 542 m below LSD, while the highest formation pressure (755 psia) was measured between 629 m and the bottom of the hole. The general upward pressure gradient is not evident between 542 m and 629 m below LSD as the formation pressures in this interval are between 501 psia and 571 psia.

Testing to determine the location of the water table in Ue4t was unsuccessful due to communication around the packers. Pressure buildup below the bottom packer set at 525 m caused hydrofracture around the packers. Similar hydrofracture occurred during the straddle packer testing of the interval between the 597 m and 607 m.

INTRODUCTION

Los Alamos National Laboratory, the U.S. Geological Survey (USGS), and the Desert Research Institute (DRI), with support from the Hydrology and Radionuclide Migration Program of the Nevada Operations Office of the U.S. Department of Energy, have been investigating the hydrogeology of a portion of Yucca Flat at the Nevada Test Site, where underground nuclear tests have been conducted in tuffs below the water table (Fig. 1). Most of the data available for this area was obtained for the geologic site characterizations used in containment evaluations. Exploratory hole Ue4t, however, was drilled specifically for hydrology and radionuclide migration studies.

Nineteen underground nuclear explosions have been detonated within a 1500 m radius of Ue4t, Ue4t (Fig. 2). The effect on local hydrogeology from nuclear detonations has been observed since the early 1960's (Garber, 1963; Hale et al., 1963). More recently, in Ue4t and several other drill holes near tests conducted below the water table, fluid levels in excess of 300 m above the expected

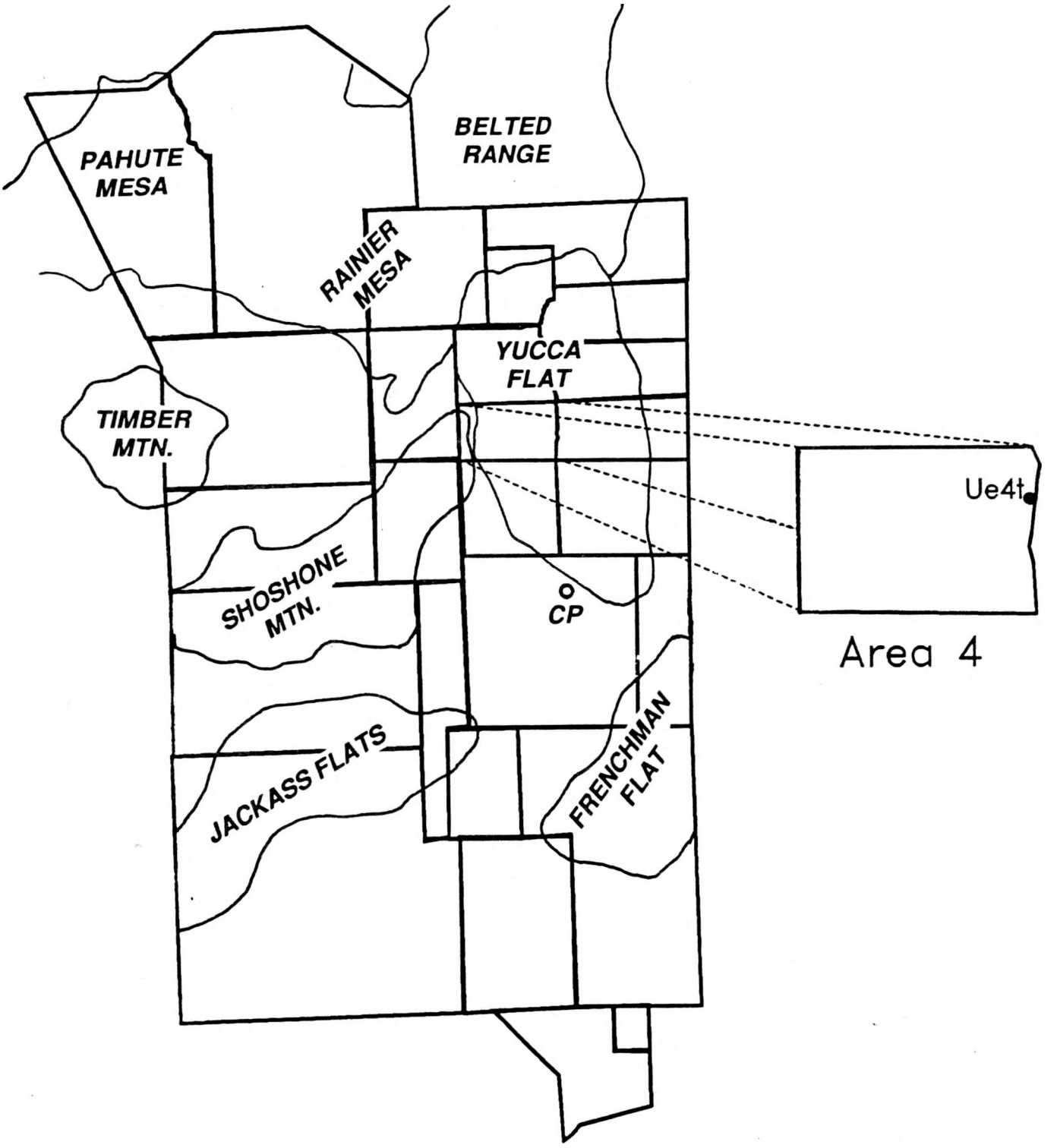


Fig. 1. Location of Ue4t within the Nevada Test Site.

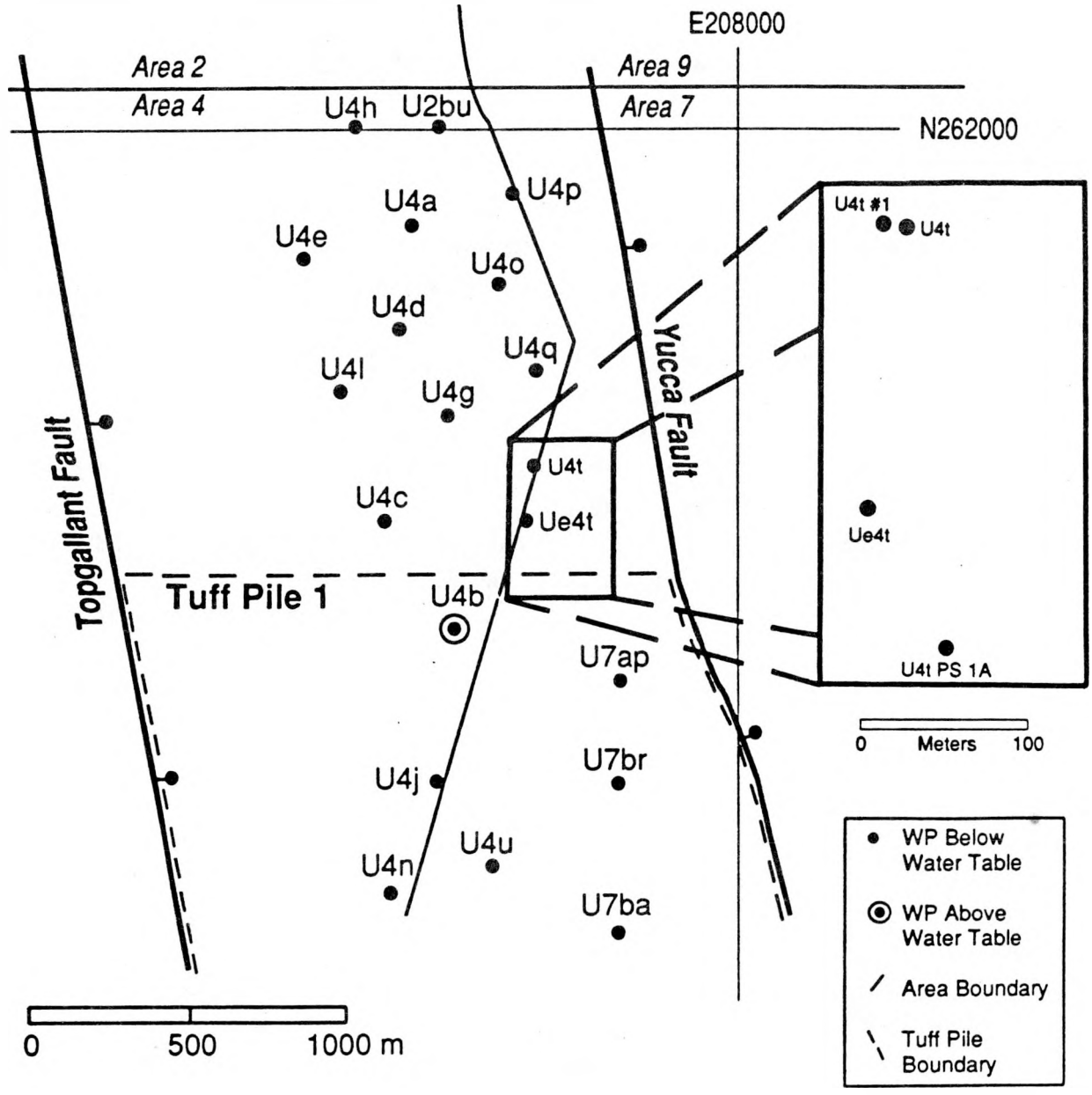


Fig. 2. Expended emplacement sites near Ue4t.

water table have been measured (Hawkins et al., 1987). The nature and occurrence of these elevated fluid levels is being investigated to avoid emplacement hole construction problems and to assist in the study of radionuclide migration.

This report presents results of straddle packer testing conducted in Ue4t to determine the vertical hydraulic gradient, the magnitude of formation fluid pressures, and the depth to the water table. Hydrologic information will contribute to understanding of groundwater conditions in Yucca Flat and the effect of underground testing on the hydrologic system; it will also aid the emplacement design of future tests.

BACKGROUND

U4t was a 3.05-m diameter emplacement hole drilled to a total depth (TD) of 615.7 m on May 28, 1985. It was lined from 441 - 601 m with a 1.88-m diameter steel liner for an estimated water table depth of 506 m. During the month following insertion of the liner, slowly rising fluid levels were detected. After dewatering of the liner, video inspection revealed a collapsed section of liner with a leak about 5.5 m above the hemispherical liner bottom. No fluid was seen entering the liner from above. To permit the use of the hole as an emplacement site, a 1.68-m diameter liner was cemented inside the original liner from a depth of 426 - 599 m. The fluid level in U4t had not stabilized before the installation of the second liner. A ton of sodium bromide was mixed with the stemming material at the bottom of the hole as a groundwater tracer for hydrologic and radionuclide migration studies. The tracer has not been detected in any drill holes.

Twelve meters to the west of U4t, satellite hole U4t #1 was drilled in April of 1986 (Fig. 2). Two months after the completion of this 0.31-m diameter, 640 m deep, uncased hole, the depth to fluid was 323 m. The fluid level stabilized after another two months at a depth of 315 m, or 191 m above the predicted static water level of 506 m (Doty and Thordardson, 1983) and over 100 m above the U4t liner top. During a borehole video inspection, fluid was observed seeping into U4t at a depth of 387.4 m. This fluid is believed to have come from the satellite hole because five days later, after the fluid was removed from the satellite hole, the seepage in U4t ceased.

Drilling commenced on Ue4t in January of 1987, two months after the execution of the GASCON event in U4t. It was drilled 168 m south, and 15 m west of U4t (Fig. 2). The 0.25-m diameter hole was rotary drilled in three phases using air-foam to a TD of 736 m. Fluid levels were monitored following dewatering after each phase of drilling (Fig. 3). Data gathered during this operation indicate the presence of pressurized zones, as the depth to fluid decreased with drilled depth (Hawkins et al., 1987). Tags following phase one drilling were insufficient for projection of a stabilized fluid level; however, the stabilized phase two fluid level was at a depth of approximately 320 m. The phase three fluid level seems to have stabilized at a depth of about 265 m.

Several fluid level monitoring programs have been conducted in Ue4t. The USGS installed a pressure transducer in Ue4t in the fall of 1987 to determine the normal water level fluctuation. These continuous water level measurements show that the level fluctuates, with corresponding changes in

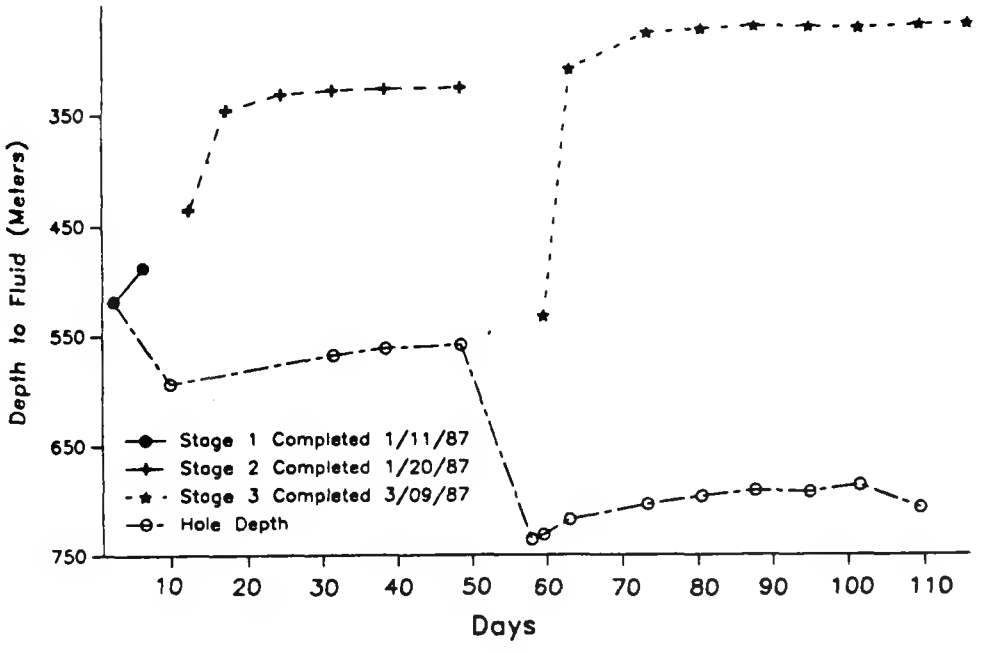


Fig. 3. Fluid levels during staged drilling of Ue4t.

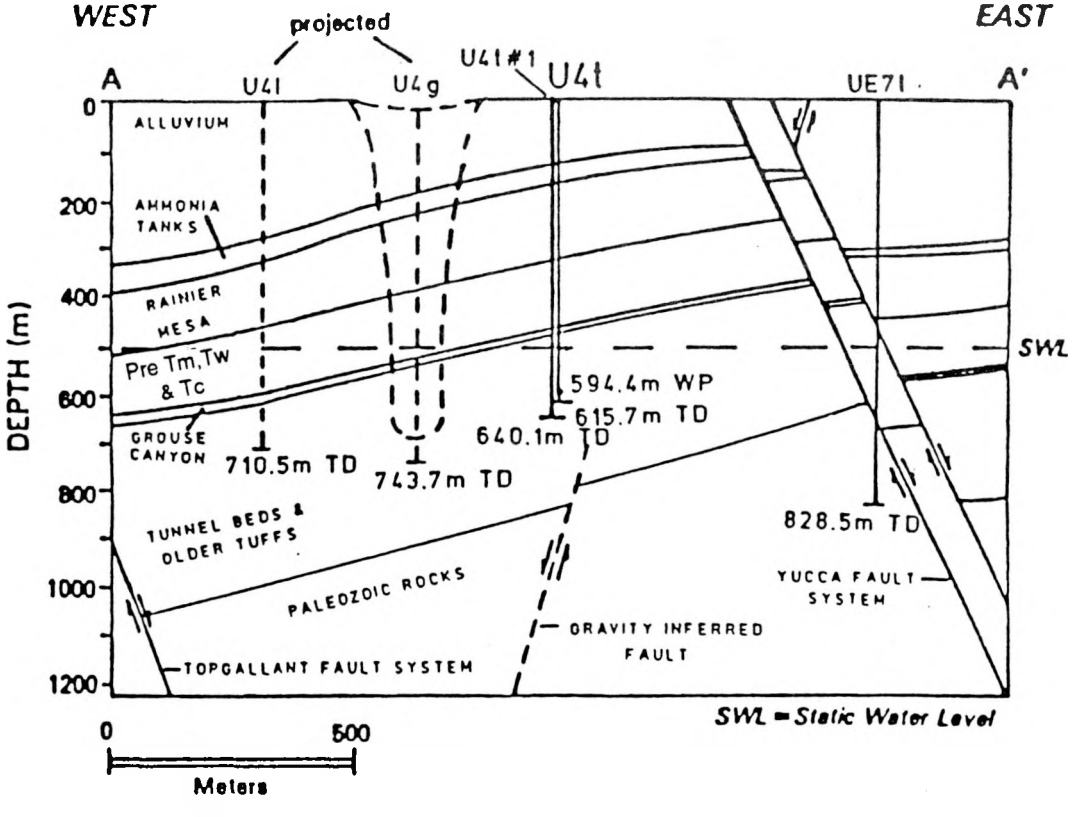


Fig. 4. Geologic cross section through U4t, 170 m north of Ue4t.

the atmospheric pressure, about 1.5 m. Analysis of temperature logs from Ue4t suggests fluid is entering the hole at depth, flowing up the hole, and exiting at several shallower depths (Conaway, 1987). No elevated levels of tritium or fission products have been detected in Ue4t.

Post-shot hole U4t PS 1A was drilled immediately following the GASCON event to recover radiochemical samples from the cavity region and gas samples from the chimney. Its surface location is 253 m south-southeast of U4t and 137 m south and 47.5 m east of Ue4t (Fig. 2). On October 4, 1988, DRI installed a pressure transducer and barometer in the post-shot hole. The transducer is at a depth of 520 m along the length of this approximately 23 degree angle hole in the gas sampling tubing. Pressure data are being continuously recorded.

GEOLOGIC SETTING

The geologic setting for hole Ue4t has been extensively investigated. It is in the center of Yucca Flat, a typical Basin and Range structural basin filled with Tertiary volcanics and alluvium. Ue4t is located in a north-south trending structural block between two east-dipping normal faults (Fig. 4). To the east at a surface distance of 350 m is the Yucca Fault with approximately 250 m of displacement at the Paleozoic (Pz) surface. The Topgallant fault more than 1300 m to the west of the hole also has a large vertical offset. The maximum dip of the beds in this area is consistently measured at approximately 17 degrees to the west. No faults were detected in the Ue4t hole.

Ue4t is just north of an area known as Tuff Pile 1 because of its predictable physical properties (F. App, written comm.). Stratigraphy at the Ue4t site is as expected for this portion of Yucca Flat (Drellack, 1988). The Pz rocks are at an estimated depth of 815 m. Overlying the Pz rocks are approximately 364 m of ash-flow, air-fall and bedded tuff with minor tuffaceous sandstone of the Tunnel Beds and older tuffs. A 6-m thick section of the Grouse Canyon Member of the Belted Range Tuff, an air-fall tuff, overlies the Tunnel Beds. Bedded tuffs from a depth of 317 m to a depth of 445 m are the pre-Timber Mountain, Wahmonie and Crater Flat stratigraphic units. Above the bedded tuffs is the non- to densely-welded ash-flow tuff of the Rainier Mesa Member of the Timber Mountain Tuff (Tmr) from a depth of 169 - 317 m. The Ammonia Tanks Member of the Timber Mountain Tuff (Tma), a non- to partially-welded ash-flow tuff, is directly below the tuffaceous alluvium from 131 - 161 m depth. Between the Tmr and the Tma is 8 m of bedded tuff. All the units are at least moderately zeolitized below a depth of 308 m. The water table is predicted to be at a depth of 506 m.

HYDROLOGIC SETTING

The principal hydrologic units in the vicinity of Ue4t are the Paleozoic lower carbonate aquifer and the Cenozoic tuff confining unit. Ue4t did not penetrate the lower carbonate aquifer but it is predicted to be at a depth of 815 m below the surface. The lower carbonate aquifer is a complex group of formations composed predominantly of limestone and dolomite with minor amounts of

siltstone and quartzite. Groundwater flow in this regional aquifer is mainly controlled by fractures (Winograd and Thordardson, 1975).

The Cenozoic hydrologic units consist of the tuff confining unit, the tuff aquifer, and the alluvial aquifer. Permeability of the tuffs is quite variable. The tuff units below the predicted water table at Ue4t are considered to be the tuff confining unit. The controlling feature in these units is the presence of zeolite or clay minerals (Winograd and Thordarson, 1975). Groundwater in the tuff confining unit in Yucca Flat is generally semi-perched with respect to the carbonate aquifer, because there is a downward gradient from the tuffs to the carbonate aquifer. Based on water level measurements in nearby holes, the water table at Ue4t is predicted to be at a depth of 506 m (Doty and Thordardson, 1983).

Analysis of temperature logs indicates the possibility of fluid entering the hole at depth and exiting the borehole at six shallower depths (Conaway, 1987). The known high pressures at depth in Ue4t probably results in a "pumping" phenomenon with fluid traveling up the borehole and exiting through permeable, normally unsaturated tuff units higher in the hole.

PACKER TESTING OPERATIONS

Straddle packer testing operations at Ue4t were designed to obtain hydrologic data for specific intervals by measuring formation fluid pressures (Garber and Koopman, 1968). The interval below the estimated water table, approximately 506 m below land surface datum (LSD), was the primary zone of interest. Water levels were determined by straddling different intervals in the hole with the testing assembly and measuring the pressure increase. Pressure measurements were converted to water levels to determine the distribution of water levels with depth. Hydrologic testing was accomplished from January 23 through February 14, 1989.

The hydrologic testing assembly (Fig. 5) consisted of, from top to bottom: a transducer carrier; safety joint; the upper packer, which includes the J-tool for setting the packers; a wireline operated sliding sleeve port centered in the interval between the packers; the lower packer; and the bottom plug unit. The plug was also handled with a wireline. The hydrologic testing tool was run in drill hole UE4t on 73 - mm diameter tubing. Tubing was also used for spacing between the packers.

Four pressure and temperature gauges were used for most of the testing. The gauges were calibrated between 0 - 2500 pounds per square inch, absolute (psia) and between 0 - 150 degrees Fahrenheit (^{o}F) with an accuracy of 1 psia and 1^{o}F. Three pressure transducers were installed in the transducer carrier on the testing assembly, and one transducer was hung, using a logging cable within the 73 - mm diameter tubing. One of the three gauges in the transducer carrier was connected to the interval below the bottom packer and another was connected to the interval between the packers by 6.35 - mm diameter stainless steel tubing running through the packer elements. The third gauge in the transducer carrier monitored the interval above the top packer. Gauges in the transducer carrier were connected to the surface recording equipment by double armored, 4 - conductor cable

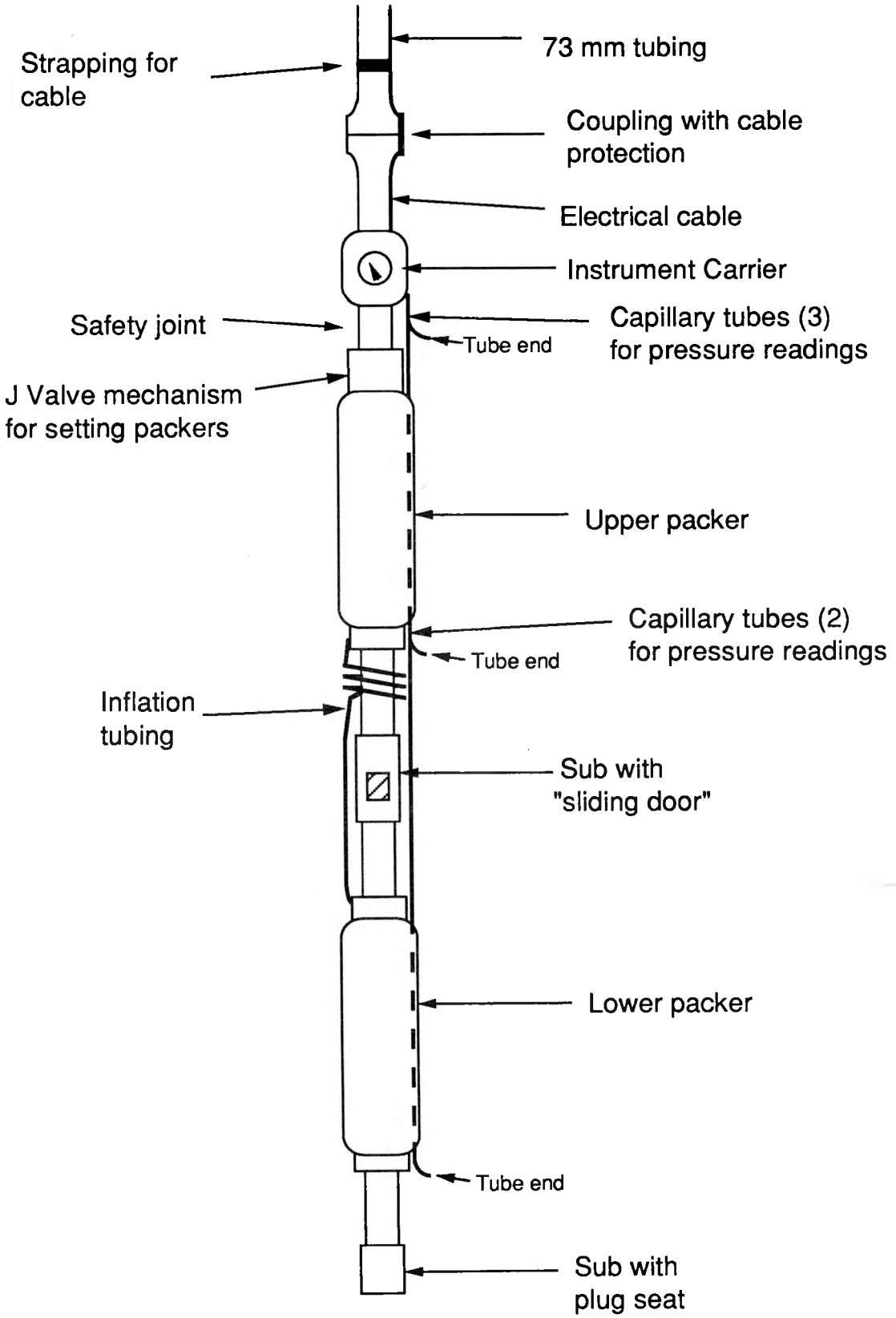


Fig. 5 Straddle packer testing assembly

that was strapped to the tubing. All gauges were powered by signal converters. Surface readout and recording was accomplished with portable computers.

The testing assembly was lowered down the hole with the J-valve open; thus, the packer inflation elements were open to the tubing. When the assembly reached the selected interval (depths for testing were determined based on the geology and hole conditions), the packers were inflated by pumping clean water into the tubing at 30 - 100 psia above the formation pressure and then shutting the J-valve and trapping the pressure within the packer elements. The tubing was then swabbed and the water level in the tubing was quickly tagged with a wireline. Depending on the interval to be tested, either the plug at the bottom of the assembly or the sliding door sleeve between the packers was opened. A pressure and temperature gauge was then lowered into the tubing on a logging cable and continuous recording of pressure and temperature commenced. The other two intervals, either below or between the packers and above the packers, were continuously monitored. The packers were unset by opening the packer J-valve and allowing the packer elements to deflate.

RESULTS

Depth intervals tested, the length of time for each test, and remarks on the performance of the gauges are summarized in Table 1. Fig. 6 shows the spatial relationship of Ue4t to U4t and U4t PS 1A, the stratigraphic setting, and the intervals tested. Test intervals are from the middle of the top packer to the middle of the bottom packer. Lengths of the test intervals were 61.2 m for the first three tests and 22.3 m for the last four tests. A limited amount of useful pressure data was collected from the pressure and temperature gauges mounted in the transducer carrier, due to problems with the equipment.

The pressure - time curves for Test 1 are shown in Fig. 7. During Test 1 the interval between 536.1 m and 597.4 m below LSD was isolated. After the packers were set, the pressure in the interval above the packers dropped dramatically for approximately 500 minutes, when the pressure rose slightly then resumed a less dramatic decline. Equipment problems thwarted efforts to obtain data from the interval between the packers. The pressure in the interval below the packers rose for the first 500 minutes, then declined sharply for the next 50 minutes; the pressure changed little during the remainder of the test. The upper zone also showed little change until the start of the third day of the test, when it began to rise abruptly.

During Test 1, the drop in pressure for the bottom zone at approximately 500 minutes was probably caused by hydrofracturing of the formation. The slight increase in pressure in the upper zone supports this contention. If leakage occurred merely around the packers equivalent pressure readings would be expected. The hydrofracture occurred in response to pressure buildup to approximately 428 psia. Hydrofracturing was also observed during drill stem testing in hole Ue4a, 235 m northeast of Ue4t (Thordardson and Winograd, written comm., 1988).

The increase in pressure in the upper interval beginning three days into the test was probably caused by leakage around the packers during injection of water into the isolated interval.

Table 1

Summary of Straddle Packer Testing

Test No.	Packer Interval Depth (m)	Start Time (PST)	End Time (PST)	Remarks
1	536.1 to 597.4	12:15 1/27/89	14:25 1/30/89	Leakage around the top packer at 13:17, 1/30/89. Monitoring of middle zone failed. Transducer hung on wireline to monitor bottom zone.
2	536.1 to 597.4	15:09 1/31/89	08:43 2/03/89	Monitoring of top zone failed. Leakage occurred around the packers after 12:08, 2/1/89.
3	568.1 to 629.4	9:52 2/03/89	10:06 2/06/89	Monitoring of top zone failed. Leakage occurred around the packers from the start.
4	495.0 to 517.2	19:59 2/06/89	13:00 2/07/89	Monitoring of middle and bottom zones failed.
5	542.2 to 564.5	13:30 2/07/89	13:37 2/09/89	Monitoring of middle and bottom zones failed. Transducer hung on wireline to monitor the middle zone from 11:30, 2/8/89 to 7:52, 2/9/89.
6	606.9 to 629.1	15:01 2/09/89	09:14 2/13/89	Monitoring of middle and bottom zones failed. Transducer hung on wireline to monitor the middle zone from 15:54, 2/9/89 to 14:35, 2/10/89; and the bottom zone from 14:58, 2/10/89 to 09:14, 2/13/84.
7	573.0 to 595.3	10:49 2/13/89	09:22 2/14/89	Monitoring of middle and bottom zones failed. Transducer hung on wireline to monitor the middle zone from 10:49, 2/13/89 to 11:58, 2/13/89.

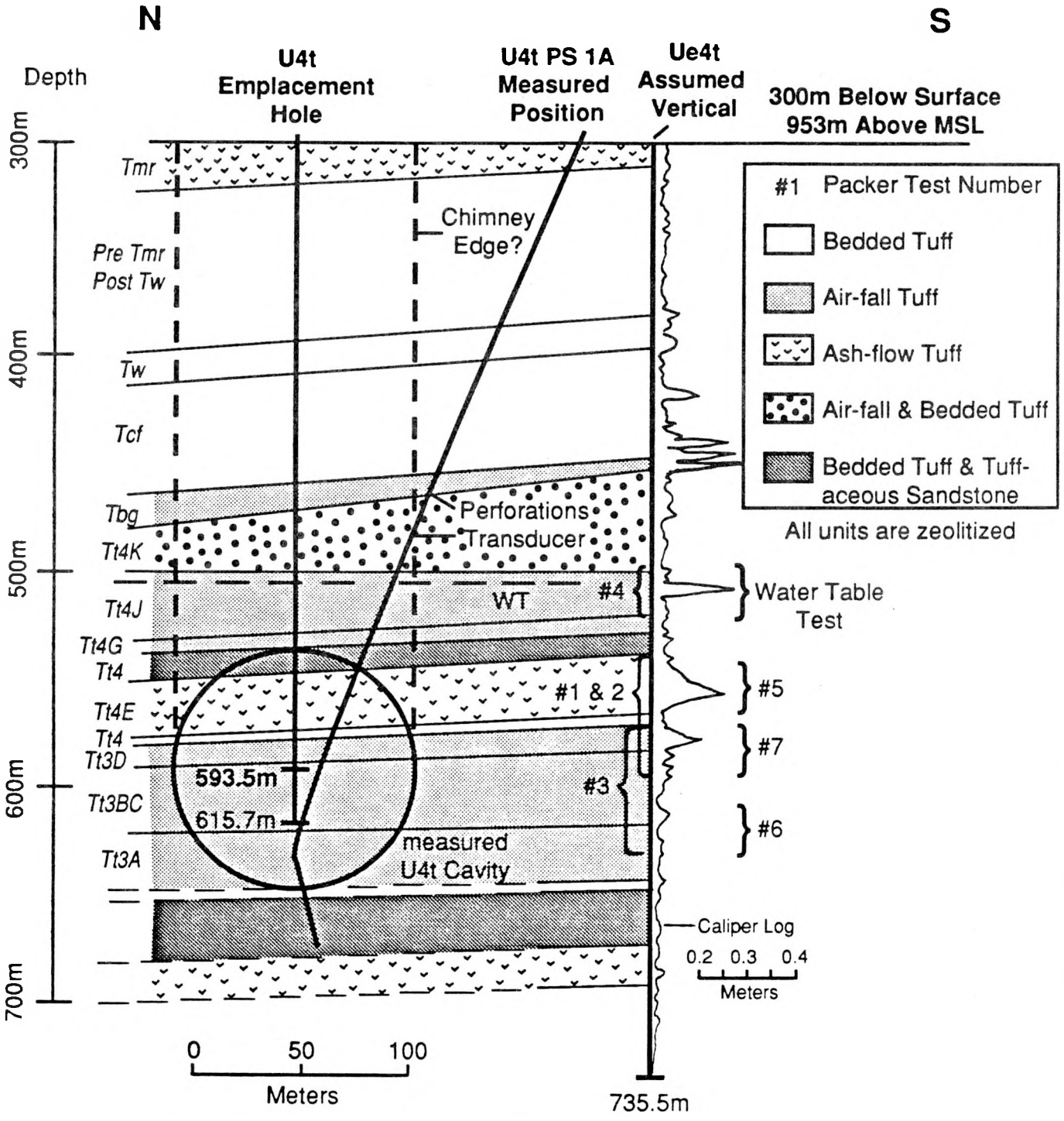


Fig. 6. Cross section through U4t, U4t PS 1A and Ue4t, showing stratigraphic intervals below 300 m depth, caliper log and intervals tested.

Unfortunately the transducer monitoring the zone below the packers had to be removed from the tubing prior to injection; therefore this hypothesis could not be confirmed. The stable pressure in the interval above 536.1 m is probably less than 357 psia.

Pressure - time curves for the transducers operating during Test 5 are shown in Fig. 8. The interval between 542.2 m and 564.5 m below LSD was isolated. Transducers monitoring the interval above and between the isolated interval were operational. Pressure in the zone above the packed interval was declining slightly during Test 5 while the pressure in the isolated interval appears to have risen rapidly, then slowed to a gradual rise. Due to time constraints, testing was terminated prior to complete stabilization of the pressures in both zones. Stable pressure for the isolated interval is higher than 208 psia, while the stable pressure in the interval above the packers is less than 320 psia.

For Test 6 the interval between 606.9 m and 629.1 m below LSD was isolated (Fig. 9). The pressure in the interval above the packers rose slightly after the packers were set, then began gradually falling to 441 psia by the end of the test. In the interval between the packers the pressure trend was downward and by the end of the test appeared to be approaching a stable level of just less than 161 psia. Below the packers the pressure rose rapidly, but also appeared to be approaching a stable level of slightly greater than 317 psia by the end of the test. There was a pressure difference across the bottom packer of almost 160 psia during Test 6, indicating a dramatic upward pressure gradient.

Pressure - time curves for Test 7 are shown in Fig. 10. The interval between 573.0 m and 595.3 m was isolated. The pressure trend in the zone above the packers was slightly downward during the entire test with the final pressure equal to 398 psia. The pressure trend in the isolated interval was initially upward, and was still increasing above 213 psia at the end of the test.

DISCUSSION

Table 2 is a summary of the results of the 7 straddle packer tests. The water level was computed using the depth of the transducer, a conversion factor to convert pressure to height of water above the transducer, and an assumed atmospheric pressure of 12.7 psi. The conversion factor included a temperature correction. The formation pressure was computed as the pressure at the top of the monitored interval except for the interval above the packers for which the measured pressure was used.

Results from the hydrologic testing indicate that there is a general upward hydraulic gradient in drill hole Ue4t, because the lowest formation pressure was measured in the top part of the hole while the highest formation pressure was measured in the lowest part of the hole. The lowest measured formation pressure, 287 psia, was measured in the interval between the surface and 495.0 m. The highest formation pressure of 755 psia was measured in the interval between 629.1 m and the bottom of the hole. The general upward pressure gradient is not as evident in the interval between

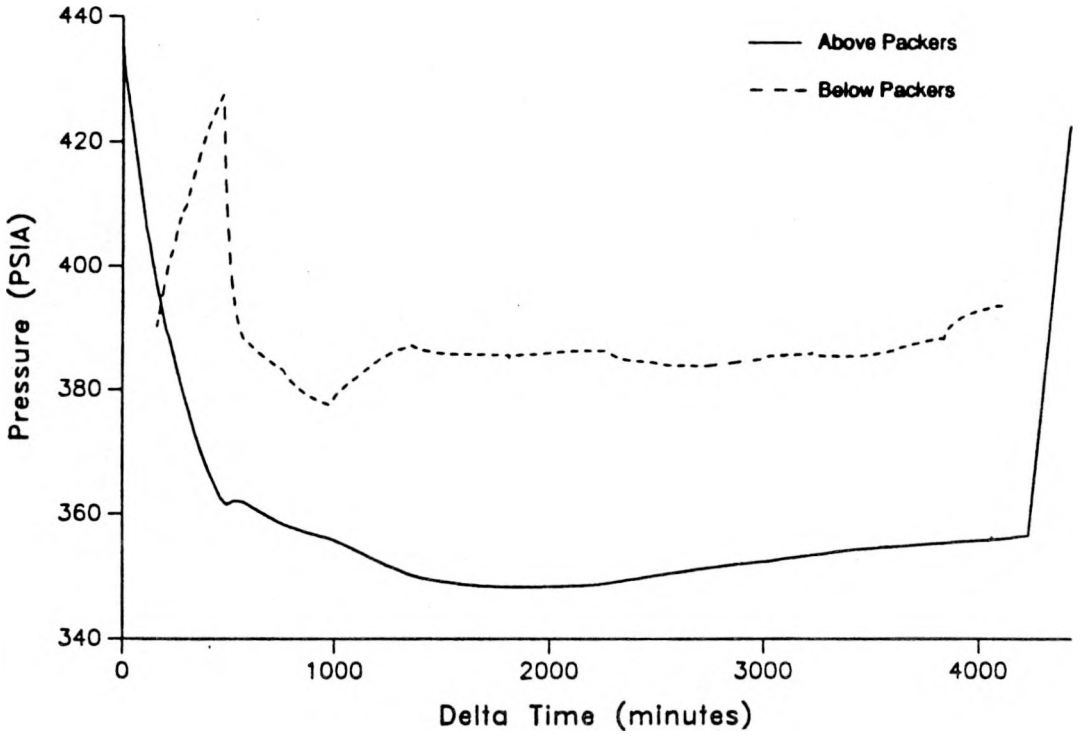


Fig. 7. Packer Test 1: packers set at 536.1 m and 597.4 m, hydrofracturing at 500 minutes.

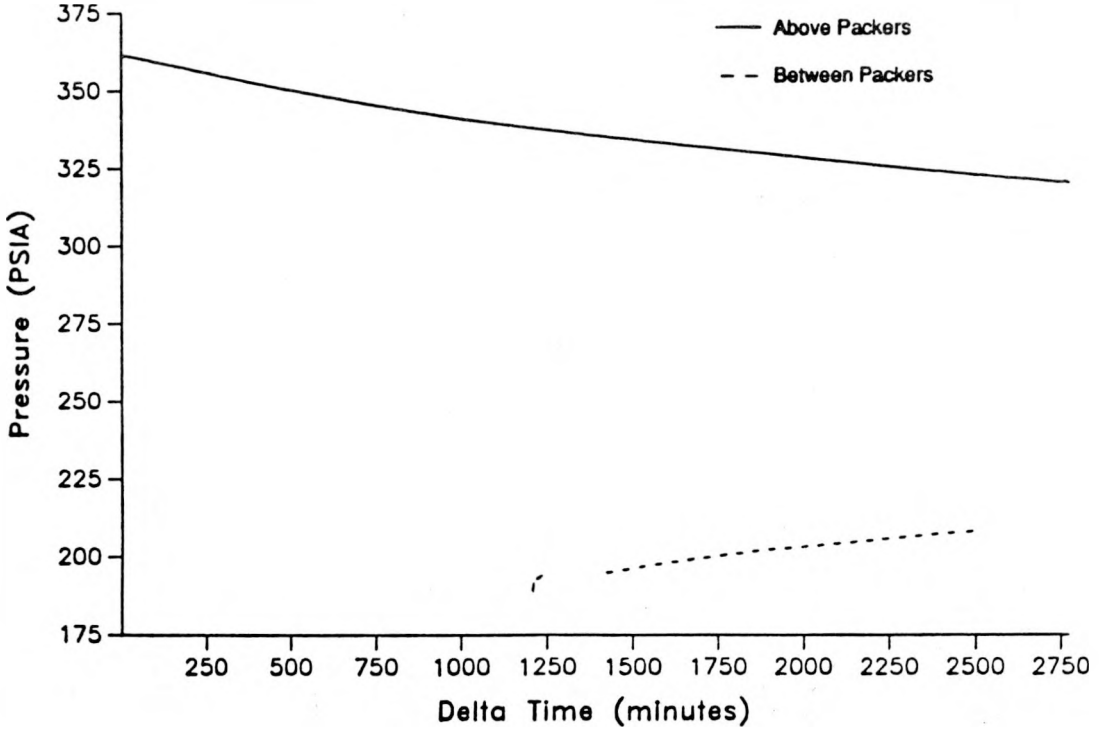


Fig. 8. Packer Test 5: packers set at 542.2 m and 564.5 m, apparent rapid pressure rise in zone between packers.

TABLE 2

Test No.	Transducer Depth (m below LSD)	Interval (m below LSD)	End Temp (°F)	End Pressure (psia)	End Time (PST)	Depth to Water (m below LSD)	Formation Pressure (psia)
1	533.7	0 to 536.1	85	357	10:50 1/30/89	240.5	357
1	524.0	597.4 to TD	82	428	20:10 1/27/89	230.7	532
2	533.7	536.1 to 597.4	83	360	12:08 2/01/89	288.6	363
2	533.7	597.4 to TD	83	421	12:07 2/01/89	245.7	468
4	492.9	0 to 495.0	92	287	13:00 3/07/89	299.3	287
5	540.1	0 to 542.2	84	320	13:36 2/09/89	323.1	320
5	363.9	542.2 to 564.5	73	208	09:15 2/09/89	197.8	501
6	604.7	0 to 606.9	87	441	09:10 2/13/89	302.4	441
6	320.0	606.9 to 629.1	73	161	14:13 2/10/89	215.5	567
6	320.0	629.1 to TD	73	317	07:43 2/13/89	105.5	755
7	570.9	0 to 573.0	85	398	09:21 2/14/89	299.0	398
7	320.0	573.0 to 595.3	73	213	08:36 2/14/89	178.9	571

542.2 - 629.1 m below LSD. In this interval, formation pressures are about the same, ranging from 501 - 571 psia.

Formation pressure differences across packers set at 542.2 - 629.1 m below LSD indicate that the 1.2 - m long packer element was set in a low permeability confining unit. There was a 181 psia pressure difference between the interval above 542.2 m and the interval 542.2 - 564.4 m. There was a 188 psia pressure difference between the interval 606.9 - 629.1 m and the hole below 629.1 m. The difference in pressure across the packers is probably greater than reported because the water levels had not fully stabilized.

During Test 1, the pressure below the bottom packer dropped abruptly after reaching a peak of 428 psia; hydrofracture apparently occurred at this time. During Test 6 pressure reached 441 psia between 606.9 m and 629.1 m, but no hydrofracture occurred. Therefore the formation between 597.4 m and 606.9 m is the interval in which hydrofracture must have occurred during Test 1.

The fluid level in hole U4t PS 1A, 145 m south-southeast of Ue4t, began rising approximately four days after the packer testing began and continued a gradual rise throughout the packer testing to a maximum of about 0.8 m above its pre-test level (Fig. 11). Shortly after the termination of the testing the fluid level rapidly dropped, but remained higher than the pre-test level by 0.3 m. Although the fluid level in the post-shot hole apparently was affected by the straddle packer testing in Ue4t, the depth to fluid, when both holes are open to the atmosphere, is about 244 m deeper in the post shot hole.

On May 5, 1989, in a cooperative effort between the DRI and the USGS, the straddle packer assembly was reset in Ue4t with the goal of determining the water table depth (Fig. 12). The packer assembly had the same configuration as used for the previous testing, with a separation of 33 m. Monitoring is being performed as a cooperative effort between the DRI and the USGS. The packers were set at 492 m and 525 m. In the first 113 hours of the test the pressure in the zone below the packers rose from an initial pressure of 323 psia to a maximum observed pressure of 409 psia. Pressure in the zone above the packers dropped rapidly during the same period. At 113 hours a rapid decrease of pressure in the bottom zone and an increase of pressure in the top zone suggest hydrofracture around the packers. Subsequent measurements indicate the formation pressure is dropping in all three zones. Once again the fluid level in U4T PS 1A responded to the packer test in Ue4t after a lag time of approximately 3 days.

Although the data gathered during the packer testing is considered usable, there are several difficulties regarding their interpretation. Because of a lack of concurrent data from all three zones of the packer assembly, leakage around the packers can only be positively ruled out for Tests 5 and 6. Inferences on water levels and pressures in the tested intervals have to be tempered by the fact that the hole was open for almost two years prior to the packer testing and, that, due to time constraints, stabilized pressures were not measured. Transducers used in Tests 5, 6 and 7 developed an offset of 12 psia between the time the transducers were calibrated and the end of packer testing. Comparison of the pressure data with water level measurements indicates the offset occurred during Test 5.

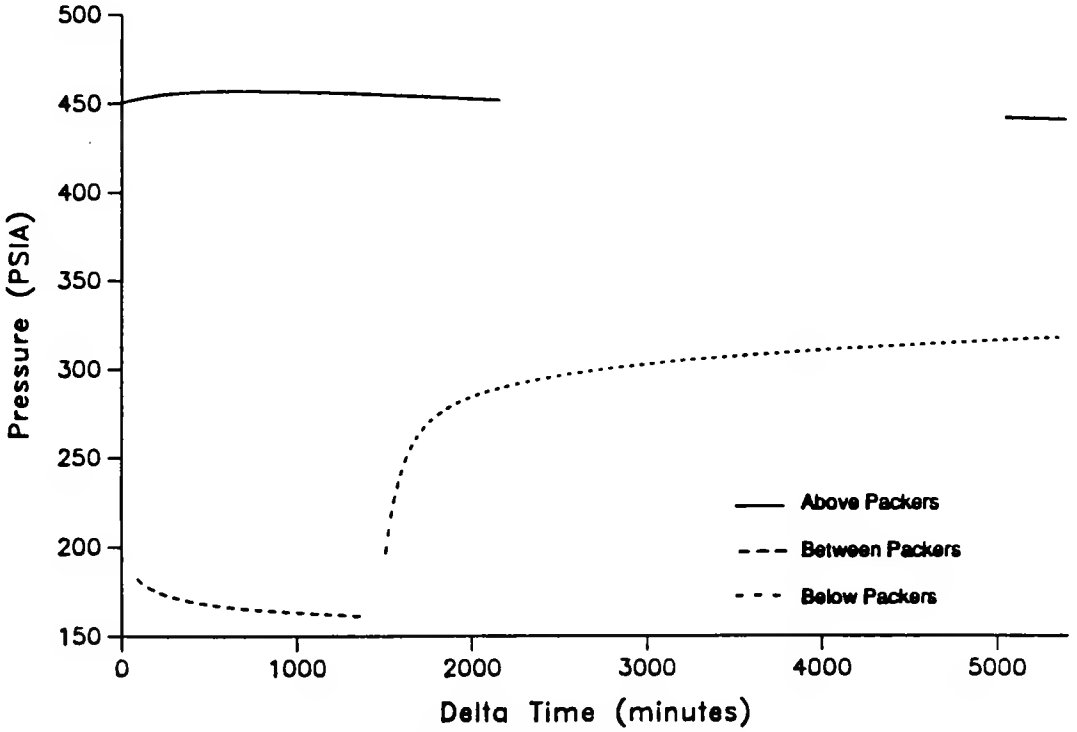


Fig. 9. Packer Test 6: packers set at 606.9 m and 629.1 m, pressure difference of almost 160 psia across lower packer.

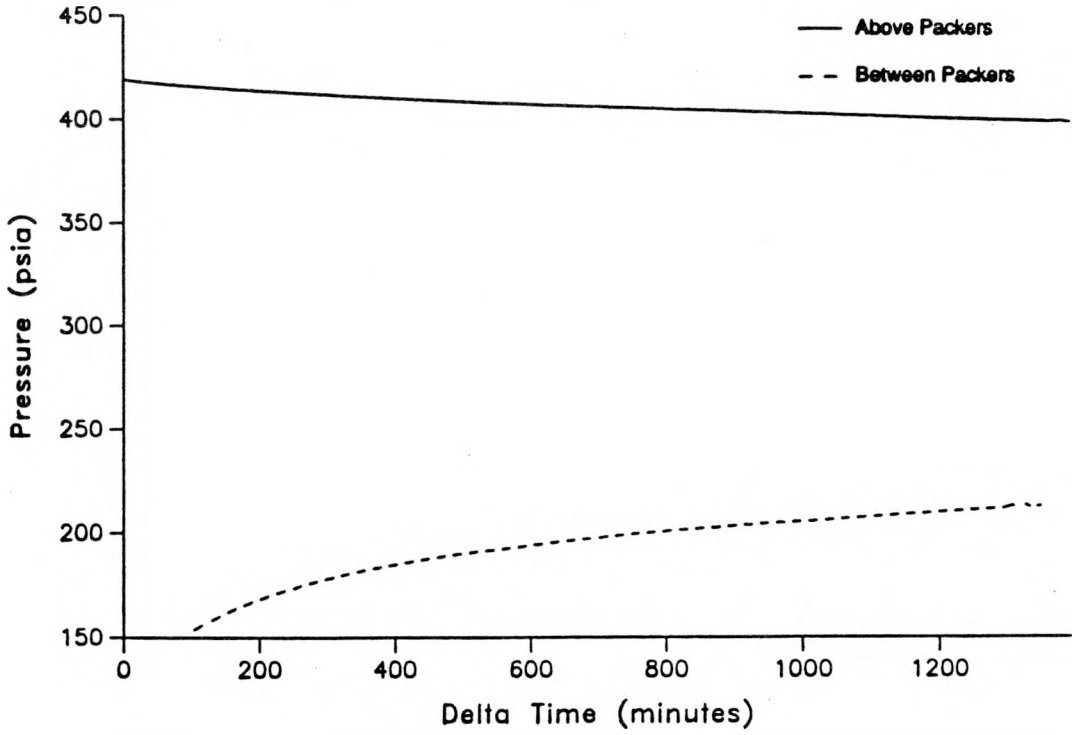


Fig. 10. Packer Test 7: packers set at 573.0 m and 595.3 m, gradual decline in pressure above packers, gradual increase in pressure between packers.

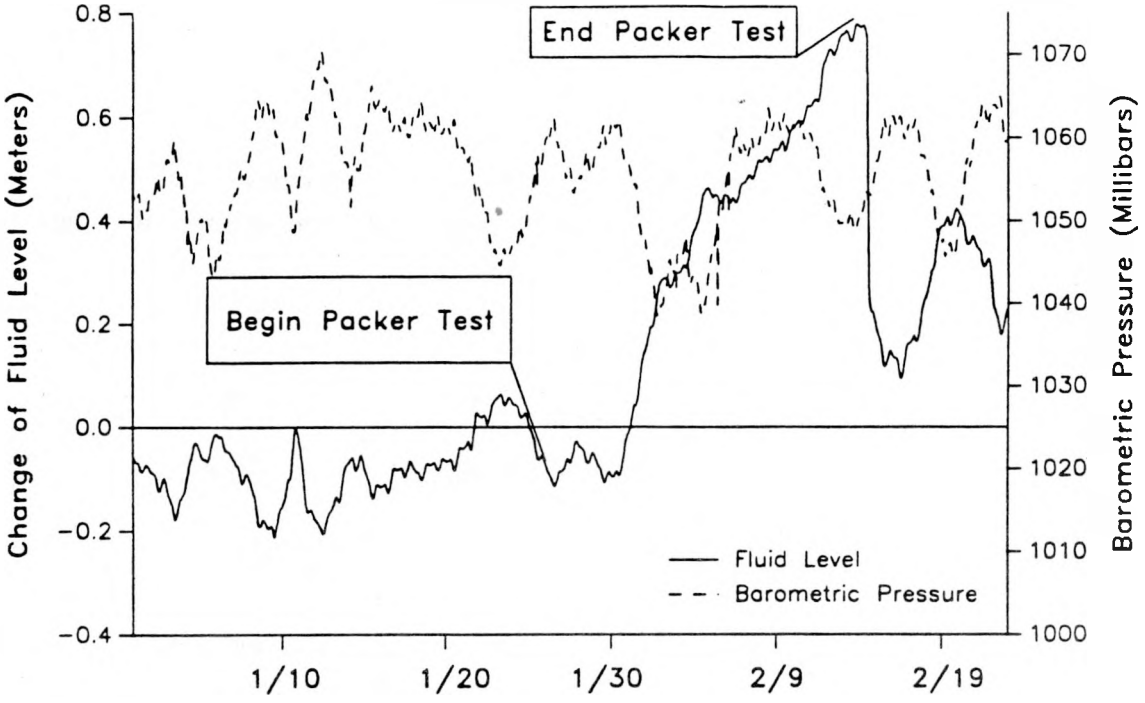


Fig. 11. Fluid level history in U4t PS 1A during packer testing in Ue4t.

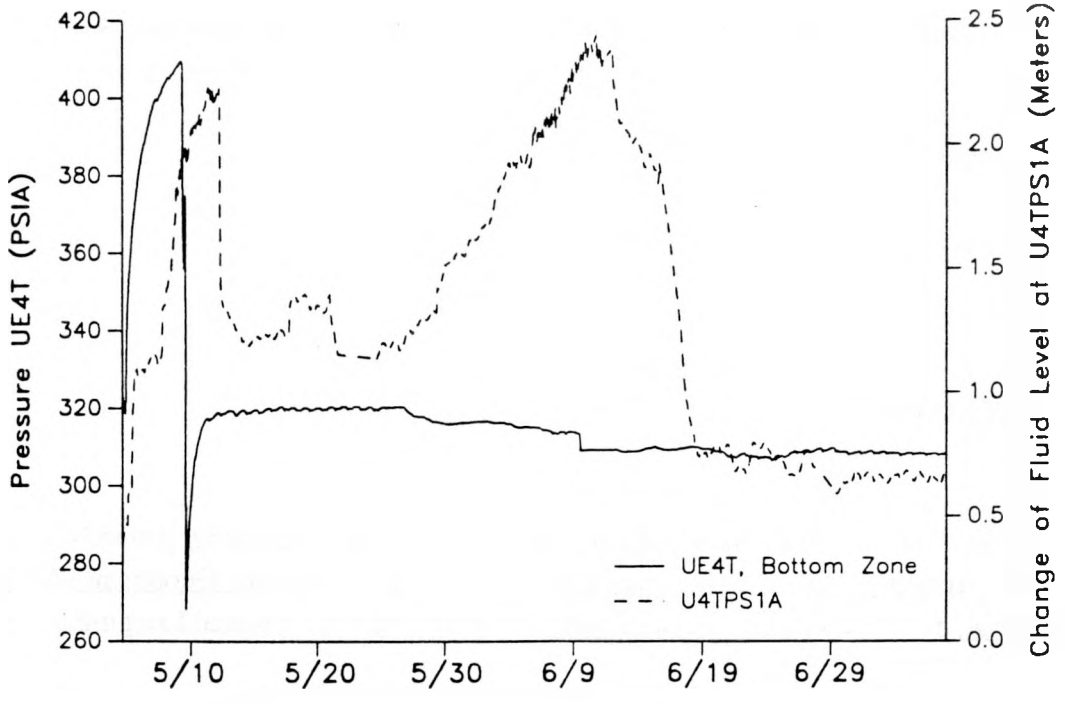


Fig. 12. Pressure history for Ue4t and U4t PS 1A during the water table test with packers set at 492 m and 525 m in Ue4t, hydrofracture around packers occurred at 113 hours.

CONCLUSIONS

Data from straddle packer testing in Ue4t indicate formation fluid pressures greater than 755 psia in the bedded tuff below 629 m. The zone (607 - 629 m) just above the deepest interval tested has a much lower pressure (567 psia), suggesting a confining layer within the interval, probably in the vicinity of the packer set at 629 m. Above 629 m pressures seemed to be fairly consistent. The testing of the interval below 597 m resulted in hydrofracture at a pressure of 428 psia. Packer testing to establish the water table was unsuccessful because of leakage around the packers.

Construction of emplacement holes in the general area of Ue4t and deeper than 620 m below LSD may experience construction problems due to high formation pressures. Holes drilled no deeper than 500 m below LSD should be above the water table and have a good chance of avoiding problems of anomalous water levels and high formation pressures.

More hydrologic testing is necessary to gain an understanding of the regional groundwater conditions and to determine the effect of underground testing on the groundwater system. Based on information from the hydrologic testing at Ue4t, this area, which has been avoided because of high formation fluid pressures collapsing casing, could provide suitable testing conditions if the emplacement hole is adequately designed.

ACKNOWLEDGMENTS

The authors wish to express their appreciation to the USGS, especially the Water Resources Division in Las Vegas, Nevada, the Desert Research Institute in Reno, Nevada, the Field Test Division at Los Alamos National Laboratory, TAM International and Fenix and Scisson of Nevada for their support of these hydrologic studies.

This work supported by the United States Department of Energy.

REFERENCES CITED

Conaway, John, 1987, Temperature logging as an aid to understanding groundwater flow in boreholes: Proceedings, Second International Symposium of Borehole Geophysics for Minerals, Geotechnical, and Groundwater Applications, Minerals and Geotechnical Logging Society, p 51.

Doty, G. C., and Thordardson, W., 1983, Water table in rocks of Cenozoic and Paleozoic age, 1980, Yucca Flat, Nevada Test Site, Nevada, [map] U.S. Geol. Survey, Water Resources Investigations Report 83-4067.

Drellack, S. L., Jr., 1988, Selected stratigraphic contacts for drill holes in LANL use areas of Yucca Flat, NTS: Fenix and Scisson, Inc., Geologic Report, DOE/NV/10322-33, 55 p.

Garber, M. S., 1963, Large rise and following decline of water level in Well 7, Area 3, Nevada Test Site--An effect from the Aardvark underground nuclear explosion: U.S. Geol. Survey Tech. Letter Yucca-48, 9 p.

Garber, M.S. and Koopman, F. C., 1968, Methods of measuring water levels in deep wells: U. S. Geol. Survey, Techniques of Water Resources Investigations Book 8, Chap. A1, 21 p.

Hale, W. E., Winograd, I. J., and Garber, M. S., 1963, Preliminary appraisal of close-in aquifer response to the Bilby event, Yucca Flat, Nevada: U.S. Geol.Survey Tech. Letter NTS-63, 32 p.

Hawkins, Ward L., Cavazos, A. P., and Thompson, P. H., 1987, Geologic and hydrologic investigations at the ALEMAN (U3kz) site, and other sites in Yucca Flat, the Nevada Test Site, Proceedings: Fourth Symposium on Containment of Underground Nuclear Explosions, Lawrence Livermore National Laboratory CONF-870961, v. 2, p. 18 - 26.

Winograd, I. J., and Thordardson, W., 1975, Hydrogeologic and hydrochemical framework, south-central Great Basin, Nevada-California, with special reference to the Nevada Test Site: U. S. Geol. Survey Prof. Paper 712-C, 126 p.

In-Situ Equivalent CO_2 Estimates Using a Neutron-Induced Gamma-Ray Spectroscopy Logging System

J. R Hearst
Lawrence Livermore National Laboratory

J. G. Conaway, and M. A. Mathews
Los Alamos National Laboratory

J. W. Barber
FSN Inc.

ABSTRACT

When a nuclear explosive is tested underground, rock in the immediate vicinity of the explosion is heated to very high temperatures. If any of that rock contains carbonates (dolomite or calcite), these are dissociated and the carbon may combine with oxygen to form carbon dioxide, increasing the hazard of a delayed leak. We are trying to adapt a commercial neutron-induced gamma-ray spectroscopy log to estimate carbonate content in emplacement (2- 4-m diameter) boreholes at the Nevada Test Site. Such a log would test a much larger (and therefore presumably more representative) sample than the few grams currently used in sample analysis and would be continuous rather than discrete.

We have performed large-scale laboratory experiments using test boxes filled with mixtures of silica sand and crushed limestone. The test boxes are 5 m long, and the material is screeded into a cylindrical arc of 1.2-m radius to simulate our borehole environment. These tests showed that the log is sensitive not only to carbonate content but also to water content of the formation as well as the gap between the logging sonde and the wall of the borehole. Consequently, we modified the sonde to measure the sonde-wall gap and developed procedures for correcting the measured carbonate content for water content and gap. When we used these procedures in the laboratory, with a moving sonde and a rough (3- 8-cm variations) surface on the test mixture, we obtained an accuracy of better than 0.02 equivalent dry weight fraction CO_2 (the amount of CO_2 that would be generated if all the carbonate were converted to CO_2). Tests in boreholes have shown good qualitative agreement with the trends in the sample data but generally indicated somewhat higher equivalent CO_2 content. It appears that the corrections developed in the laboratory may result in an overcorrection. Moreover, other minerals present in the field may decrease the accuracy of the measurement. We are dealing with these problems though further investigation, which is under way, involving the raw spectral data and through the use of Monte Carlo calculations.

*This work was performed under the auspices of the U.S. Department of Energy by Lawrence Livermore National Laboratory under contract No. W-7405-Eng-48.

INTRODUCTION

When a nuclear explosive is tested underground at the Nevada Test Site (NTS), rock in the immediate vicinity of the explosion is heated to very high temperatures. If any of that rock contains carbonates (dolomite or calcite), the carbonates are dissociated and the carbon combines with oxygen to form carbon dioxide. When the rock cools, the carbon dioxide remains a gas, resulting in elevated subsurface pressure. This pressure increases the hazard of a delayed leak. Consequently, the process of examining a potential site for an underground test to determine if it is suitable includes checking for substantial amounts of carbonates. Carbonate content of the rock is expressed as a dry weight fraction of equivalent carbon dioxide (CO_2), the amount of carbon dioxide that would be generated if all the carbon in the cavity region were combined with oxygen subsequent to detonation.

At present, we estimate the amount of carbonate as a function of depth by chemical analyses of drill cuttings from many depths in the borehole, or of sidewall samples obtained after the borehole has been completed. The accuracy of an individual estimate is stated by the contractor that performs these analyses to be 0.01 weight fraction carbon dioxide, corresponding to about 0.0225 weight fraction calcium carbonate. Evidence suggests this is an optimistic claim. In addition, we believe that both sampling methods (drill cuttings and sidewall sampling) are biased. Finally, sidewall sampling is a very costly procedure in our large diameter boreholes. For these reasons, we are making an effort to adapt a commercial neutron-induced gamma spectroscopy log to estimating carbonate content. Such a log would test a much larger (and therefore presumably more representative) sample than the few grams used in cuttings analysis and would be continuous rather than discrete.

Neutron-induced gamma-ray spectroscopy logging is used routinely in the petroleum industry where it is commonly called carbon-oxygen (C/O) logging. Logging contractors use variations on this method for specialized oilfield applications, especially distinguishing between oil and water behind casing (see, for example, Youmans, 1951; Caldwell et al, 1963; Hoyer and Rumble, 1965; Lock and Hoyer, 1974).

Conditions at NTS are very different from those in the petroleum industry. Boreholes are usually air-filled with diameters frequently between 2 m and 3.5 m. The borehole walls are often rough; 2-cm rugosity is common over much of the length of a typical borehole. Obviously, the standard petroleum industry calibrations and correction algorithms for small-diameter, liquid-filled, smooth-walled holes will not necessarily be appropriate for our conditions. We therefore conducted a series of experiments to determine whether a commercial log could be adapted and calibrated to give the required accuracy in large, air-filled boreholes with a varying

gap between the sonde and the borehole wall. Those experiments and the results obtained are described in this paper.

THEORY AND SYSTEM OPERATION

The logging sonde (tool) used in these experiments is a neutron-induced gamma-ray logging system run by the NTS logging contractor (Chace et al, 1985.) The instrument contains an accelerator neutron generator capable of producing 14 MeV neutrons on demand. The generator is pulsed 20,000 times per second, producing several thousand neutrons during each pulse. The neutrons interact with all matter in the vicinity, including the borehole fluid, the sonde housing and internal components, and the geologic materials of interest along the borehole. Some of these interactions produce gamma rays, and a few of the gamma rays produced from a given neutron burst (typically one to three gamma rays in the energy range of 0 to 8 MeV) may be detected by a sodium iodide scintillation detector located inside the sonde about 0.5 m above the neutron generator. The detector is coupled to a photomultiplier tube which produces an electrical pulse proportional to the apparent energy of each gamma ray detected. These pulses are amplified and fed into a multichannel analyzer in the sonde which sorts the apparent gamma-ray energies into 256 energy ranges or channels using a successive-approximation analog-to-digital converter. The energy range of the spectrum is approximately 0 to 8.5 MeV, with an electronic threshold eliminating gamma rays below about 0.5 MeV. The data are transmitted in digital form up the logging cable to the computer in the truck.

The signal from the gamma-ray detector is time-gated so that two distinct gamma-ray energy spectra are recorded, inelastic and capture. The total number of gamma counts is also recorded as a function of time, to create a third, "pulse arrival time" (PAT) spectrum, that is used to correct the inelastic spectrum for dead time and capture background. During the inelastic detection gate, for about 15 μsec after the beginning of each neutron burst, the detected gamma rays are added to the inelastic spectrum. During the rest of the time between neutron bursts the detected gamma rays are added to the capture spectrum. The inelastic spectrum results largely from inelastic scattering of energetic neutrons by nuclei while the accelerator tube is generating neutrons. The capture spectrum results largely from delayed emission of gamma rays from nuclei which have captured neutrons and, hence, have become unstable and subsequently decayed. Capture events can persist in the region near the source and detector for some time after a neutron burst; consequently capture gamma rays are counted during the inelastic gate. This unwanted background is subtracted from the inelastic spectrum during later processing to produce a spectrum consisting of principally inelastic events.

The three spectra are accumulated over sampling periods of typically 15 s, equivalent to about 7.5 cm of borehole travel at 0.5 cm/s (1 ft/min.)

The simplest way to analyze the gamma ray spectra for elemental composition is through the use of spectral energy windows, where the total number of gamma rays counted in a given energy region is attributed to a particular element having a strong contribution in that region. The logging contractor that performed these experiments uses ratios of window countrates for their analyses; no spectral stripping is performed. Figure 1 shows a typical pair of capture and inelastic spectra from this logging system, along with the standard energy windows used by the logging contractor. Another, more sophisticated method, least-squares spectral analysis, has been applied to a similar system (Hertzog, 1978; Hertzog and Plasek, 1979; Westaway et al, 1981; Grau and Schweitzer, 1982; Westaway et al, 1983; Schweitzer et al, 1984).

To date, we have been using the window method to analyze the experimental data. In particular, we are using the measured inelastic C/O parameter (the ratio of the gamma-ray countrate in the inelastic carbon window to the countrate in the inelastic oxygen window, referred to henceforth as simply the C/O parameter) to estimate carbonate content, since the oxygen content of common rocks at the NTS typically varies over a relatively narrow range.

The timing of the start and length of the voltage pulses to the neutron generator is well known, but the length and amplitude of the actual neutron burst depends on the condition of the generator. The PAT spectrum is used to determine the beginning and length of the actual neutron burst and those data are used to control the timing of the inelastic gate. The capture gate is then the time between voltage pulses except for the inelastic gate.

The deadtime corrections for the inelastic and the capture spectra are calculated from the count rate in the PAT spectrum and the known gamma-ray processing time in the system. Then the deadtime-corrected capture spectrum, multiplied by the ratio of the length of the inelastic gate to the length of the capture gate, is subtracted, channel by channel, from the raw, deadtime-corrected inelastic spectrum to obtain a capture-corrected inelastic spectrum.

At the beginning of the run a Pu-Be source, mounted in a polyethylene calibrator, is affixed to the sonde near the detector. This calibrator produces 2.23 MeV gamma rays from neutron capture in the polyethylene, and 4.43 MeV gamma rays from the $^{9}Be(\alpha,n)^{12}C$ reaction. These two gammas are used to calibrate the relation between energy and channel number;

$$E = m*N + B$$

where N is channel number and m and B are constants obtained from the calibration and are used as the initial energy calibration values.

During the logging run, the spectrum is displayed on a CRT screen in the logging truck to monitor drift due to temperature changes and other factors. At present the operator adjusts the gain to keep the oxygen peaks in the same channels, thus manually stabilizing the gain. Another option is the use of the automatic peak-tracking feature of the logging software in the truck. A third choice is to allow the gain to drift, and perform all drift corrections in later processing. We are still studying the relative advantages of these three choices.

Whether or not some form of real-time gain stabilization is used, the logging contractor uses a postprocessing program to ensure gain stability in the recorded spectral data. This program tracks one or more selected peaks in the inelastic or capture spectrum. Unlike the oilfield situation, where plenty of hydrogen in the form of water or hydrocarbons is available, and the hydrogen peak in the capture spectrum is frequently used for stabilization, the silicon peak in the inelastic spectrum is currently used in processing data from NTS boreholes.

After the spectral data have been corrected for drift, the counts in the energy ranges corresponding to each window are summed, and the required ratios (C/O parameter, Ca/Si, etc.) are taken. We receive the final corrected window ratios, along with the raw spectral data, on separate data tapes.

RESULTS OF THE EARLY EXPERIMENTS

A preliminary round of experiments using boxes approximately 2 m square by 1 m deep containing mixtures of silica sand and ground limestone showed that the C/O parameter depends not only on the limestone content but also on the water content of the mixture and on the gap between the sonde and the sand (Conaway, 1986). Fortunately, the dependence on both gap and water content was approximately linear, giving us hope that we could develop algorithms to correct the results for interference from these factors.

The early round of experiments suffered from a number of flaws. In particular, the test boxes were too small and did not adequately represent the geometry encountered in actual boreholes. Nonetheless, the results were sufficiently encouraging to allow us to proceed with more elaborate experiments.

THE NEW EXPERIMENTAL FACILITY

A new experimental facility was designed to simulate the wall of a 2.4 m diameter borehole. It consists of three reinforced concrete test boxes, each having inside dimensions of approximately 4.9 m long, 2.4 m wide, and a minimum of 1.2 m

deep. Figure 2 is a drawing of the facility, and Figure 3 is a photograph. One box is filled with silica sand and the other two boxes contain mixtures of silica sand and ground limestone. The ends of the boxes are circular arcs, so that the contents can be screeded with a long rod to simulate a section of a cylindrical borehole. The absence of an opposing borehole wall introduces some error. Computer modeling is needed to get a better estimate of this effect.

The three test boxes are aligned with a common longitudinal axis to allow the sonde to be pulled the length of the three boxes without operator intervention. At each end of each box is an adjustable sonde support to give a user-adjustable gap or standoff between the sonde and the cylindrical test surface. The commercial sonde was fitted with extensions at each end to allow it to remain well supported at all times while being pulled over the boxes. The boxes were designed to be water-tight so that after the experiments with dry material were completed, each box could be saturated with water. Since both the silica sand and ground limestone contain roughly the same range of particle sizes, the water contents of the saturated mixtures should be approximately the same.

A logging winch is used to pull the sonde slowly over the boxes, providing a continuous log. This continuous log represents an improvement over the static tests run in the early experiments since it more accurately represents normal logging conditions. In static tests, the capture spectrum builds up with time and may cause erroneous results.

The mixtures in the boxes were intended to contain weight fractions of 0, 0.12, and 0.24 limestone. In reality, the first logs showed that the carbonate content appeared to vary with "depth" (position along the axis of the boxes) within a given box. Detailed sampling of the mixes in the boxes showed that the carbonate content was indeed non-uniform and that, furthermore, the silica sand contained a small amount of carbonate material. The final mixes averaged 0.009, 0.118, and 0.238 weight fraction limestone, corresponding to 0.0041, 0.052, and 0.105 weight fraction CO_2. Water content for the saturated experiments was approximately 16% by weight for all boxes.

RESULTS OF THE REFINED EXPERIMENTS

Uniform Gap

The first set of experiments was performed with the test material dry and screeded into a smooth concave arc of radius 1.2 m (48"). Runs were made at 0.3 and 0.6 m/min at uniform standoff distances of 0, 2.5, 7.5, 12.5, and 20 cm with gamma-ray energy spectra being recorded approximately every 8 cm along the boxes. The sonde did not always move smoothly over the boxes, sometimes moving a centimeter or two at a time in a stick-slip motion. This is probably not a major problem since

the volume of investigation of the sonde is large in comparison with these irregularities and the resulting spectra should be little affected.

We averaged the C/O parameter over the central 3.5 m of each box for the constant-gap runs. Figure 4 shows average C/O parameter vs average dry weight fraction CO_2 as a function of gap for dry material.

Water

After completion of the dry experiments the boxes were saturated with water and the tests repeated; Figure 5 shows the data for water-saturated material. The fit to straight lines is good, and the lines are nearly parallel. By comparing Figures 4 and 5, it is also clear that the technique is quite sensitive to water content of the formation. Part of the difference, of course, is caused by the actual decrease in the ratio of carbon to oxygen in the box because of the added oxygen in the water, but the effect is much larger than the actual ratio change. Presumably it is caused by a difference in the neutron spectrum caused by the hydrogen in the water.

When the average C/O parameter was plotted against average carbonate content in the dry material using a different logging sonde we found that although the lines were similar, they were not the same, indicating that separate calibration is required for each sonde, as usual.

To obtain an algorithm for calculating carbonate content from the C/O parameter and gap we fitted a straight line to the intercepts of the four lines in Figures 4 and 5. The results (Figure 6) are good fits and permit us to assume that the intercept is a linear function of gap. We then fitted the form

$$COP = a + bg + cC + dW + eg^2 + fCg$$

where COP is the C/O parameter, g is the gap, C is the weight fraction CO_2, and W the volume fraction water, to all of the data. We found that e and f were negligibly small, which implies that the slopes of the lines in Figures 4 and 5 can be considered constant. Consequently, we dropped the last two terms from the fit, and used the algorithm

$$C = COP - a' - b'g - c'W$$

to obtain carbonate content.

Variable Gap

The above results led us to the conclusion that we can correct the C/O parameter for constant (known) gap. An important question was whether the same correction would be valid for varying gap. Consequently we ran experiments similar to those described earlier, but with the sand screeded into varying gap configurations using a notched template attached to the screed rod; we had four such templates manufactured for this

experiment. We used only the middle box having an average CO_2 content of 0.052 (dry) for these experiments. Figure 7 shows a surface screeded into a varying gap configuration, and Table I describes the four screeds used in the experiments. As in the earlier experiments, the sonde did not move smoothly over the boxes so we placed gamma-ray sources at known spacings in the adjacent box, and stacked a gamma-ray tool on the C/O tool so we could locate the C/O tool precisely with respect to the varying gaps.

We used four different templates to give four surface configurations, and for each of these we set the tool supports at each of four standoff distances. We found that the C/O parameter against position does not track the varying gap in a reproducible way. If, however, we average the gap and the C/O parameter over the 3.5 m central section of the box, agreement between calculated and true average carbonate content is good. Figure 8 shows the difference between the average CO_2 calculated from the algorithm and the true average value of 0.052 for the dry material, as a function of average gap for each of the four screeds. 75% of the differences are within $\pm$0.01, but the mean difference is -0.0065. Figure 9 shows the same result for saturated material. Again 75% of the differences are within $\pm$ 0.01, but the mean is now +0.0079. We do not understand these non-zero means, but suspect they are caused by differences in the angle of repose of the screeded sand causing the average gap calculated from the screed design to be incorrect for the actual sand surface.

USE OF THE CAPTURE SPECTRUM

The effects of carbonate content on the shapes of the capture and inelastic spectra (Fig. 10) are not obvious in a logarithmic plot, but the increase in inelastic countrate around 3-5 MeV (the carbon window) with increasing carbonate can be seen. The countrate in the oxygen window (around 5 - 6.5 MeV) remains relatively unaffected, since the fraction of oxygen changes minimally. The effects of gap (Fig. 11a) and formation water content (Fig. 12a) on the shape of the inelastic spectrum are small. Both gap and water cause a slight hardening of the spectrum, that is, an increase in the ratio of higher energy gamma rays to lower energy gamma rays. Small though these effects are, they are sufficient to introduce significant error into the C/O parameter (see Figures 4 and 5). The capture spectrum, on the other hand, is affected markedly by gap (Fig. 11b) and water (Fig. 12b) both in magnitude and in shape. The changes in the capture spectrum shown here are much greater than those caused by relatively large lithology variations (Figure 10b). These observations suggest that the capture spectrum may be useful in making the C/O system self-correcting for water in our application.

FIELD EXPERIMENTS

Two sets of logs have been run in 2.4-m-diameter boreholes about 10 km apart at the Nevada Test Site. The commercial sonde was mounted on a large steel skid to force the sonde against the borehole wall. To minimize bias in the gap correction, we installed a spacer to create a nominally constant gap of about 7.5 cm from a smooth borehole wall. We used an aluminum caliper arm to measure the true value of the gap midway between source and detector. The measurement, averaged over an appropriate depth range, was used to apply a gap correction. The presence of the skid increases the C/O parameter by an amount that varies depending on the distance between the skid and the sonde. We have no way of precisely measuring this distance at present, so we subtracted a constant value of approximately 0.01 from the raw C/O parameter. This value was determined from experiments on the test boxes and crude measurements of the distance, and should represent a reasonable average correction.

Figure 13a shows the dry weight fraction CO_2 equivalent from the skid-corrected log vs that obtained from measurements on samples from borehole U9cv. Agreement with samples appears excellent. The first epithermal neutron log in this part of the hole was run in 1985, and is of poor quality. A second neutron log, run in 1989, is worse; it is useless above 91 m and fragmentary between 91 and 200 m. It does, however, show that the wall of the hole has dried in the intervening four years, and so it was used between 91 m and 200 m. Because the logs were so poor, we estimated average values of water content from the logs rather than attempting to make the water correction point by point. We estimated the average volume fraction water to be 0.18 above 91 m and 0.20 below 91 m. Figure 13b shows the water-corrected log. Above 91 m agreement with samples is still reasonable; below 91 m there is substantial overcorrection. Eventually we hope to use the capture spectrum, rather than the neutron log, to obtain the water correction. This would eliminate problems such as drying of the borehole wall between logs and the strong possiblity that the two sondes will follow different paths up the borehole. Differences in the size of the hydrogen peak (around channel 60) at different depths in U9cv (Fig. 14) show that the capture spectrum may be useful for computing the water correction.

The results shown in Figure 13 are encouraging. There are several factors that we have not yet completely characterized which might explain the offset between the CO_2 estimates from the samples and the log-derived estimates. Chief among these is experimental geometry. We are not applying a correction for the difference in geometry between the borehole and our test models, which have no opposing wall. This problem is being addressed through computer modeling. Other factors contributing to this offset may be differences between the chemical composition of the rock metrix in the field and the composition of the models. Our test models contain relatively

pure mixtures of $CaCO_3$ and SiO_2, whereas the actual formations logged are likely to contain dolomite ($CaMg(CO_3)_2$) in place of all or some of the $CaCO_3$. It is improbable that the presence of dolomite caused the increased C/O parameter, since there is evidence (Smith and Schultz, 1974) that dolomite causes a decrease in the C/O parameter, but the situation should be checked for our geometry. Perhaps trace elements having high neutron cross-sections are responsible. We also plan to address this problem by computer modeling.

There is some evidence that the calibration of the logging system drifted somewhat (in a direction that would help explain the discrepancy) between the original test runs in August of 1987 and the field logs in January of 1989. We have built a field verifier to monitor drift in the future.

The results of the second log, in borehole U1d (Figure 15), are similar to those of the first, but since the neutron log shows less water, the overcorrection is significantly smaller, and the agreement between log and sample results is somewhat better.

CONCLUSIONS

Tests performed using a commercial neutron-induced gamma-ray spectroscopy logging system in a test facility simulating a 2.4 m diameter air-filled borehole indicate that the C/O parameter is affected not only by carbonate content of the material in the test boxes, but also by water content of the simulated formation and gap between the sonde and the borehole wall. An algorithm can be constructed, for a given water content, to calculate carbonate content from the C/O parameter and the gap; it seems that each sonde requires its own algorithm.

In our tests using the test box containing a CO_2 content of 0.052 (dry weight fraction), such an algorithm gave the CO_2 content averaged over depth correctly within 0.02 for both dry and saturated material, with the average gap between sonde and sample as large as 12.5 cm and the gap varying by as much as 7.5 cm along the box. Although our tests were not as comprehensive at other values of carbonate content, the results suggest that the corrections will be satisfactory. Preliminary field results appear to agree fairly well with data from chemical analyses.

It appears that we are close to having a useful geophysical technique for estimation of equivalent CO_2 concentration to replace or augment the sample analyses. At this point we have gone nearly as far as we can conveniently go with physical modeling, and must turn to computer simulations for further information. In particular, such simulations will be useful in

characterizing what happens in a cylindrical borehole, and in the presence of trace elements. Computer simulations may also be useful in helping to develop a water correction based on the capture spectrum. Senftle and Mikesell (1988) have shown that this effect is significantly nonlinear, but we are optimistic that a suitable correction can be developed.

REFERENCES

Caldwell, R. L., W.F. Baldwin, J.D. Bargainer, J.E. Berry, G.N. Salaita, and R.W. Sloan: Gamma-ray spectroscopy in well logging. Geophysics 28 (Aug. 1963), pg. 617.

Chace, D. M., M. G. Schmidt, M. P. Ducheck: The Multiparameter Spectroscopy Instrument Continuous Carbon/Oxygen Log - MSI C/O. Proc. Canadian Well Logging Society 10th Formation Evaluation Symposium Sept. 29 - Oct. 2, 1985.

Conaway, J.G.: Use of a pulsed neutron induced gamma ray spectroscopy logging system for accurate determination of equivalent CO_2 concentrations: a feasibility study. Los Alamos National Laboratory Report LA-UR 86-1230, 93p, 1986.

Grau, J.A., and J.S. Schweitzer: Elemental analysis of oil wells using NaI(Tl) and 14 MeV neutrons. Trans. Am. Nuc. Soc., 43, 260, 1982.

Hertzog, R.C.: Laboratory and field evaluation of an inelastic-neutron- scattering and capture gamma ray spectroscopy tool. Soc. Petrol. Eng. paper 7430, 53rd Annal Fall Technical Conf. and Exhib., Houston, Oct. 1-3, 1978.

Hertzog, R.C. and R.E. Plasek: Neutron-excited gamma-ray spectrometry for well- logging. IEEE Trans. Nuc. Sci., Vol. NS-26, 1558-1567, 1979.

Hoyer, W.A. and R.C. Rumble: Field experience in measuring oil content, lithology and porosity with a high-energy neutron induced spectral logging system. J. Pet. Tech., July 1965, Pg. 801-807.

Lock, G.A., and W.A. Hoyer: Carbon-oxygen (C/O) Log: Use and interpretation. J. Pet. Tech., Sept. 1974, 1044-1054.

Schweitzer, J.S., R.A. Manente, and R.C. Hertzog: Gamma ray spectroscopy tool: Environmental effects. J. Petr. Tech., 1527-1534, 1984.

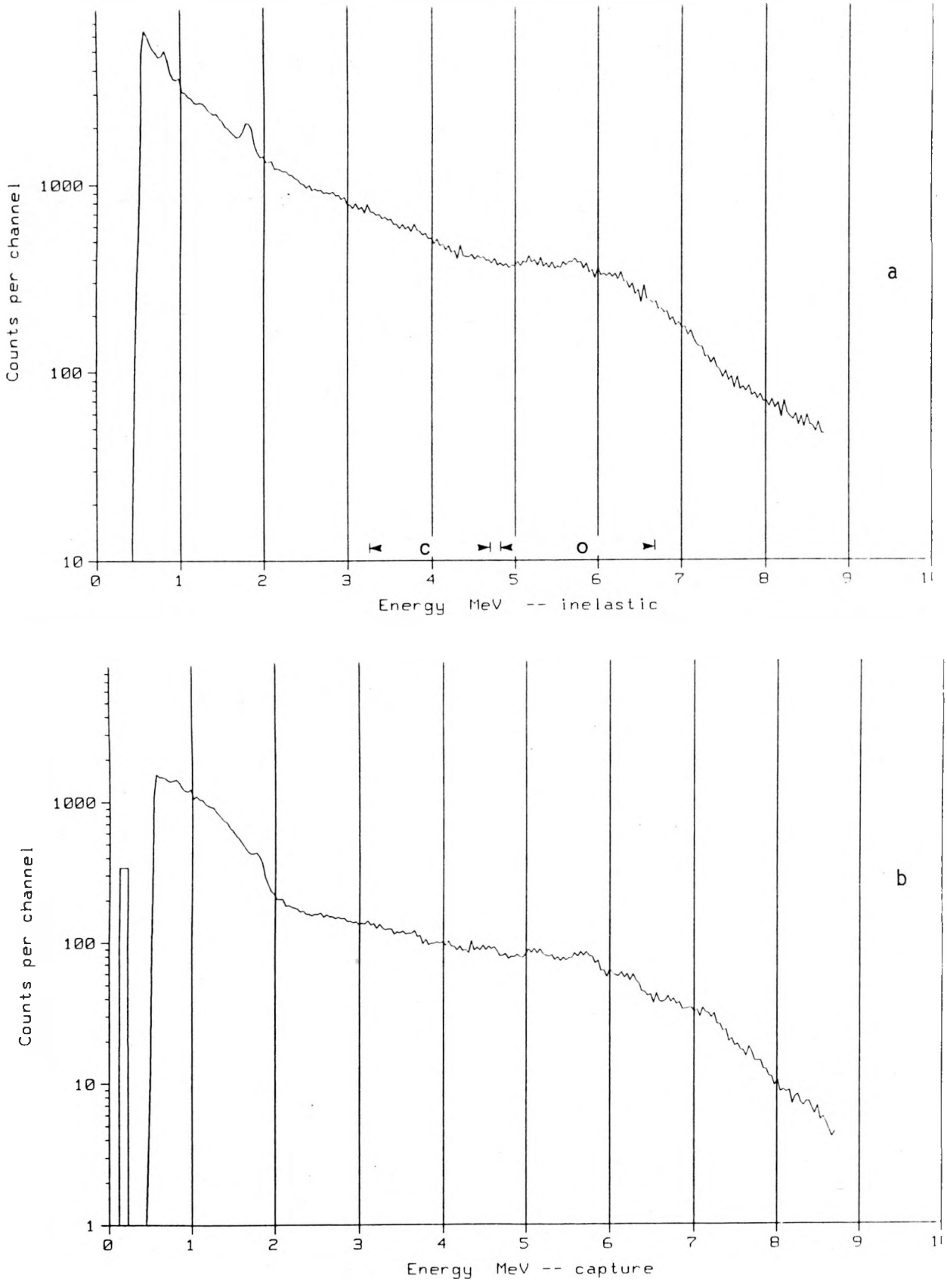
Senftle, F. E. and J. L. Mikesell: Borehole capture gamma-ray spectroscopy in very dry rock. Nuclear Geophysics vol 2, 151-162, 1988.

Smith, H.D., and W.E. Schultz: Field experience in determining oil saturations from continuous C/O and Ca/Si logs independent of salinity and shaliness. The Log Analyst, Nov.-Dec. 1974, 9-18.

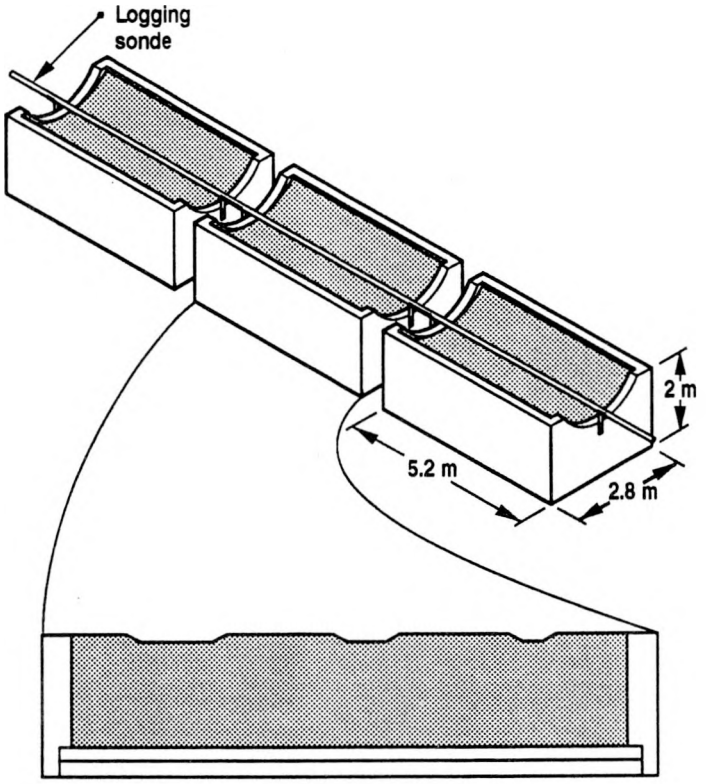
Westaway, P., R.C. Hertzog, and R.E. Plasek: Neutron-induced gamma-ray spectroscopy for reservoir analysis. Soc. Petr. Eng. J., 553-564, 1983.

Westaway, P., M. Whittman, and P. Rochette: Applications of nuclear techniques to reservoir monitoring. JPT, pg. 46-54, 1981.

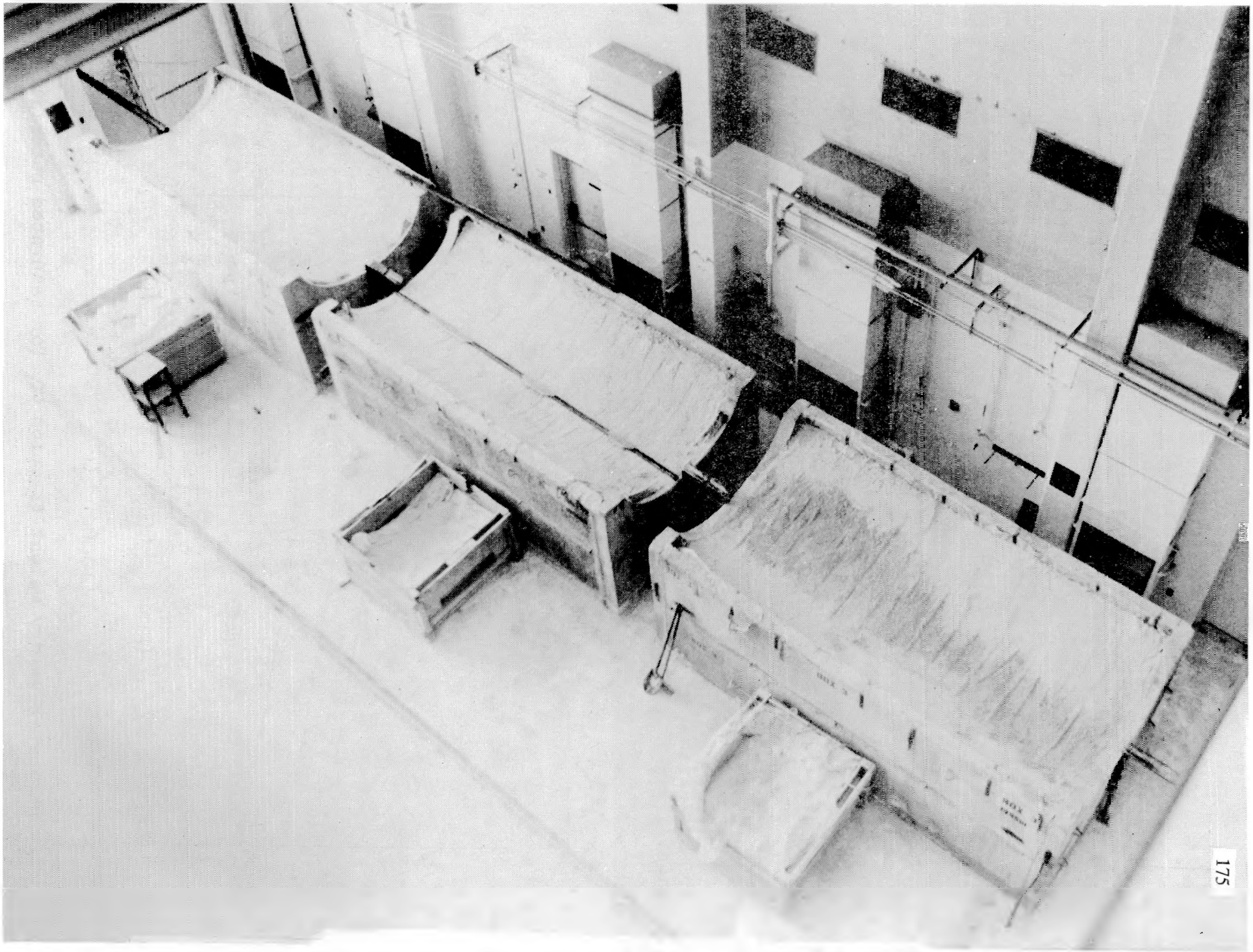
Youmans, A. H., U. S. Patent 3,294,972 file Aug. 23, 1951.



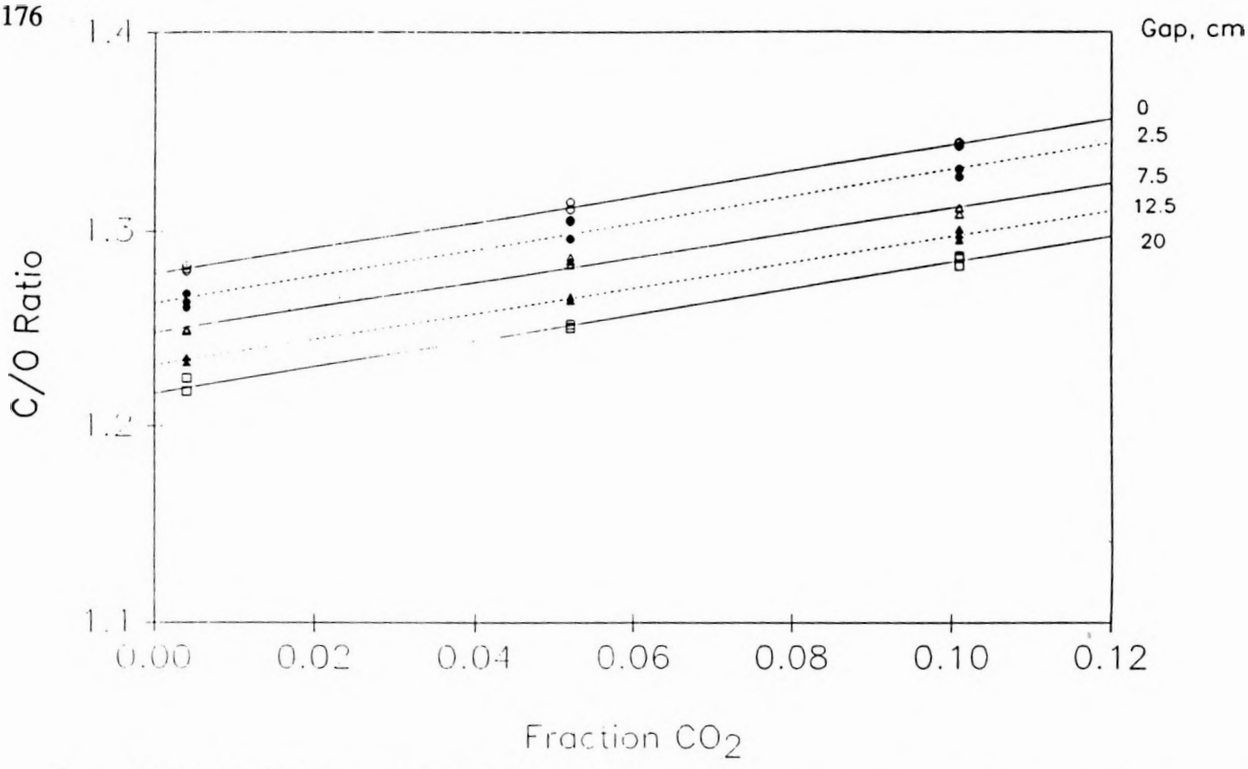
1. Inelastic (a) and capture (b) spectra from the logging sonde in silica containing 0.052 dry weight fraction CO_2, showing the carbon (C) and oxygen (O) windows.



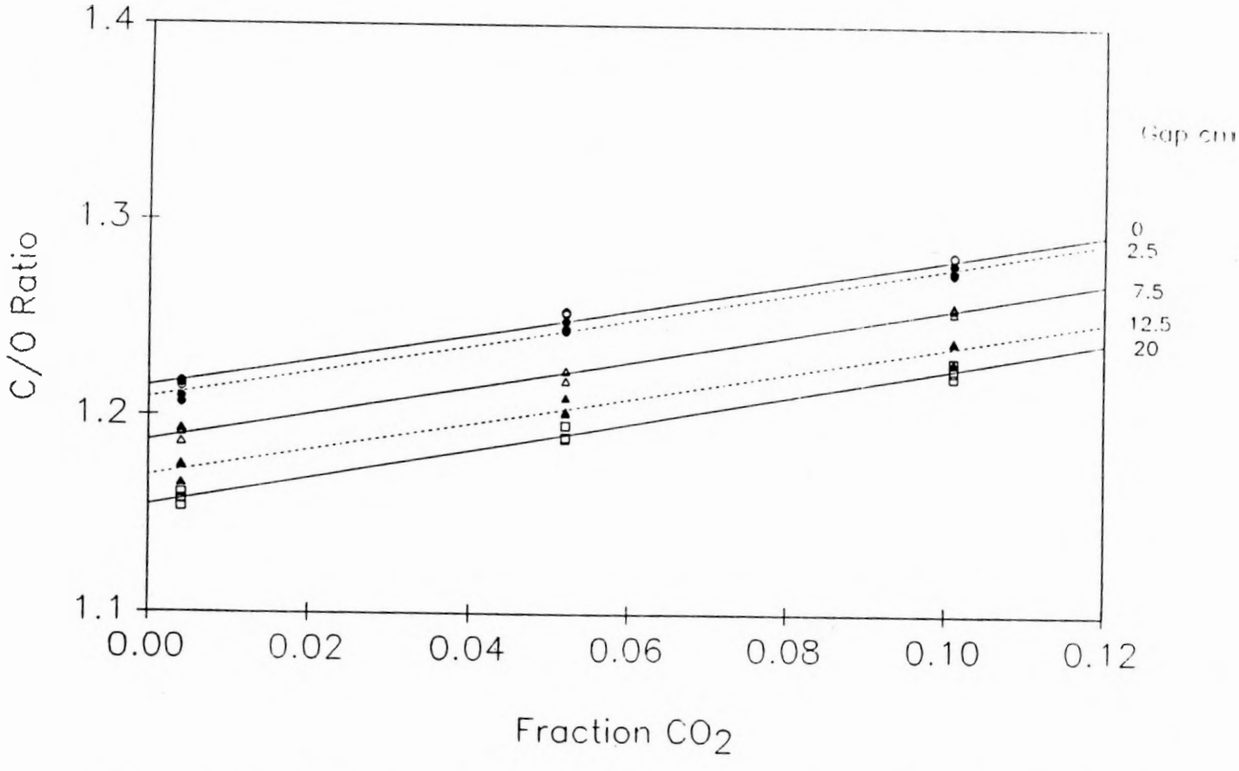
2. Drawing of the test facility.



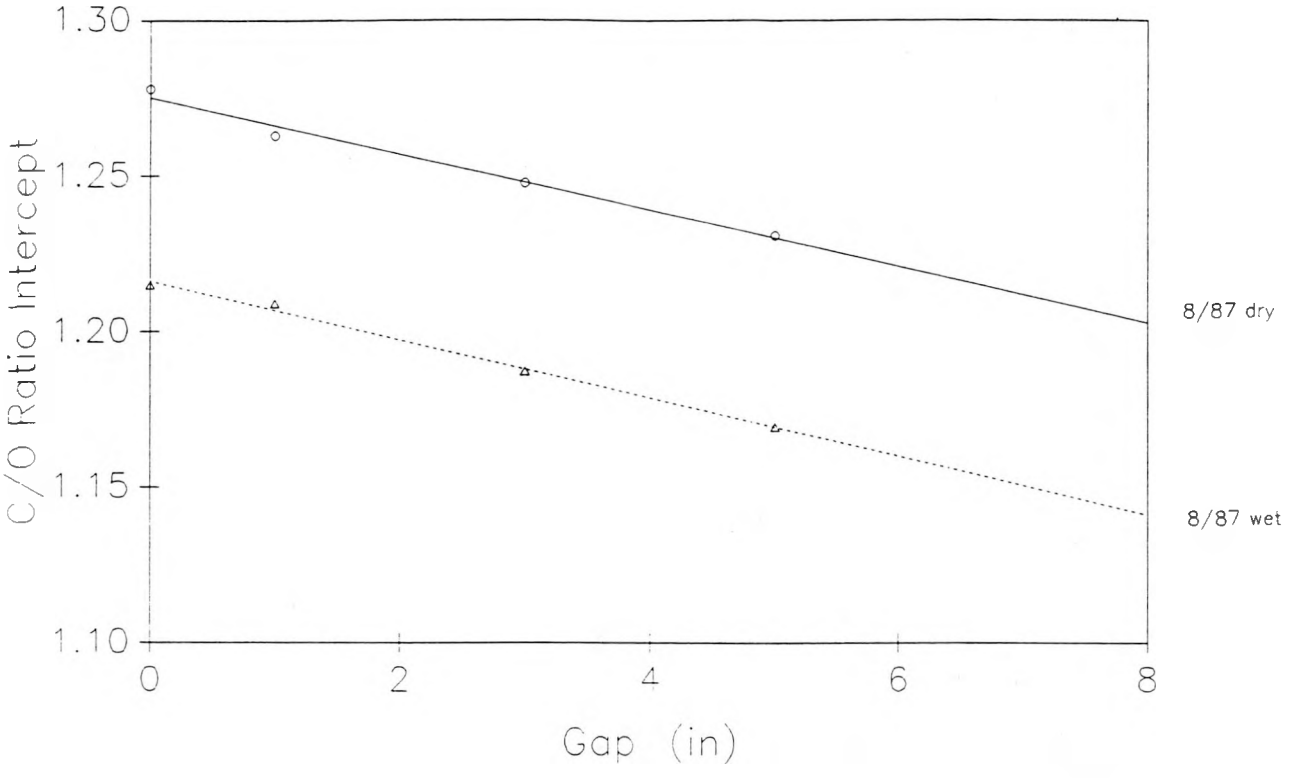
3. Photograph of the test facility



4. C/O parameter vs weight fraction CO_2 for dry material for four gaps.



5. C/O parameter vs dry weight fraction CO_2 for saturated material for four gaps.

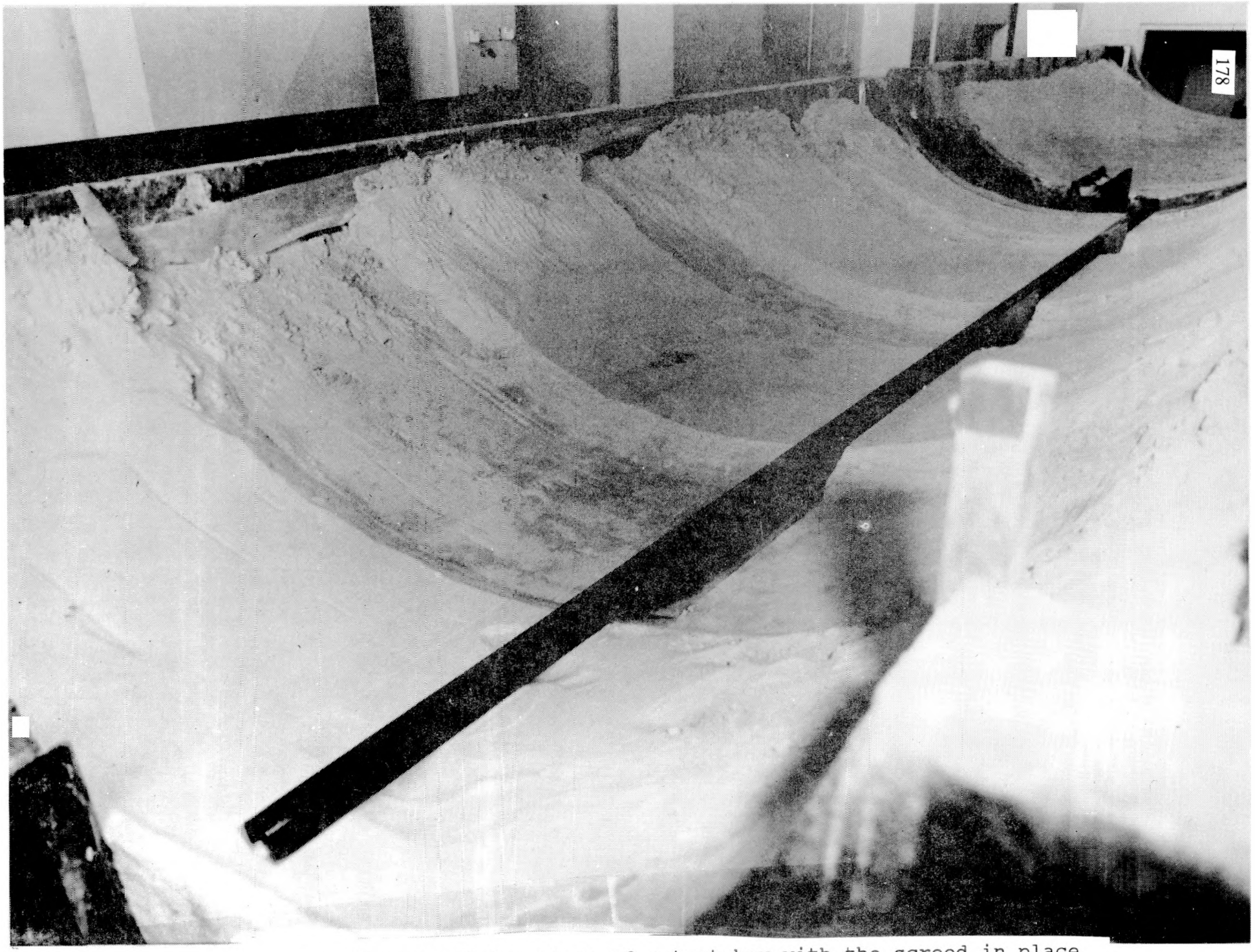


6. Intercept of the curve of C/O parameter vs dry weight fraction CO_2 vs gap for dry and saturated material.

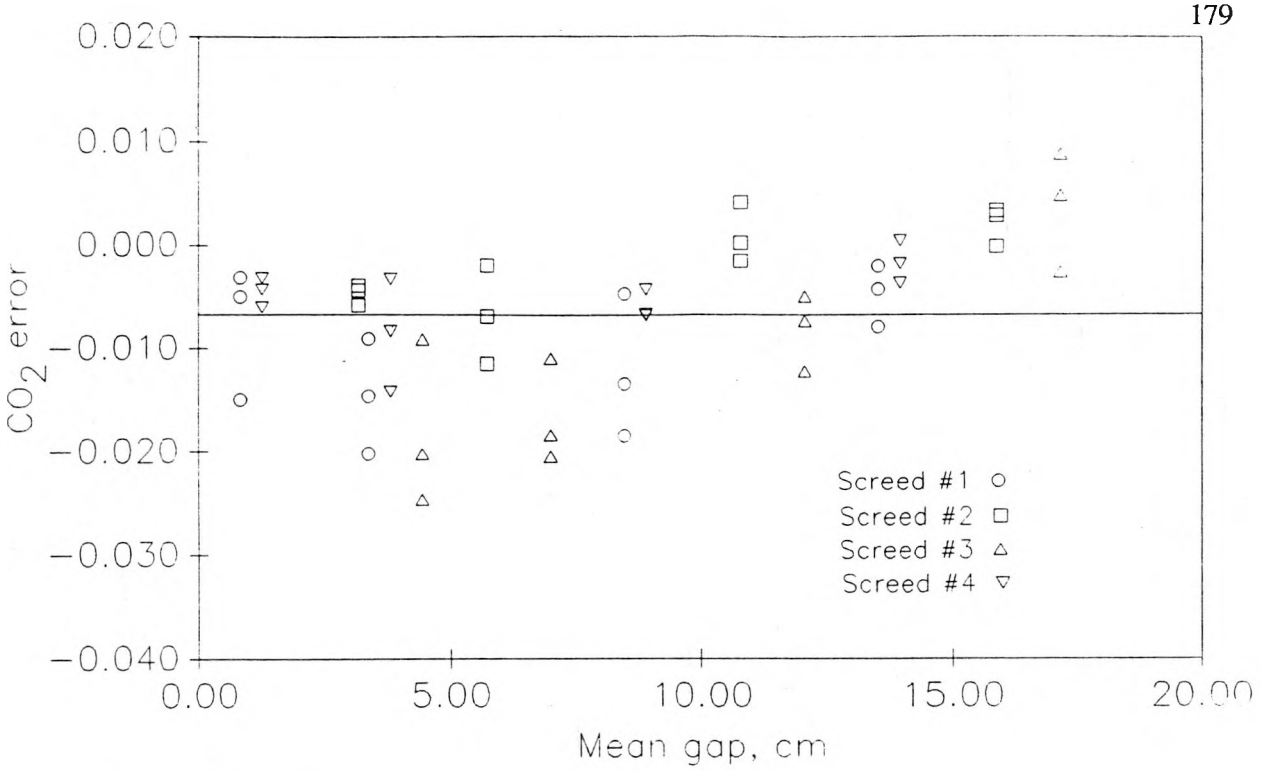
TABLE I

Design of the screed templates
The shapes and spacings of the washouts can be seen in Fig. 7.

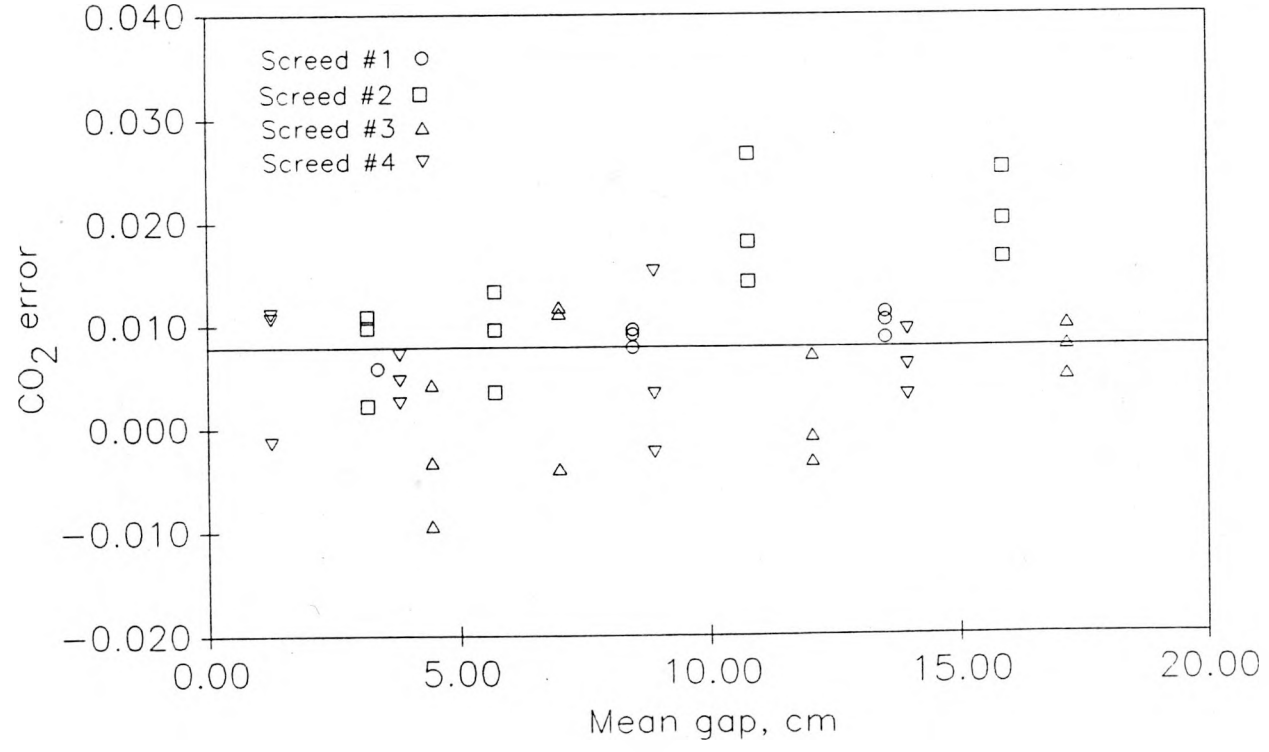
Screed Number	Washout depth, cm	Washout lengths at bottom, cm	Space between bottoms, cm	Mean depth, cm
1	2.5	61, 30.5, 15.25	101, 101	0.83
2	7.5	61, 30.5, 15.25	122, 122	3.17
3	7.5	48, 91, 91, 48	91, 61, 46	4.45
4	2.5	61, 30.5, 30.5, 15, 81	71, 41, 41, 25	1.25



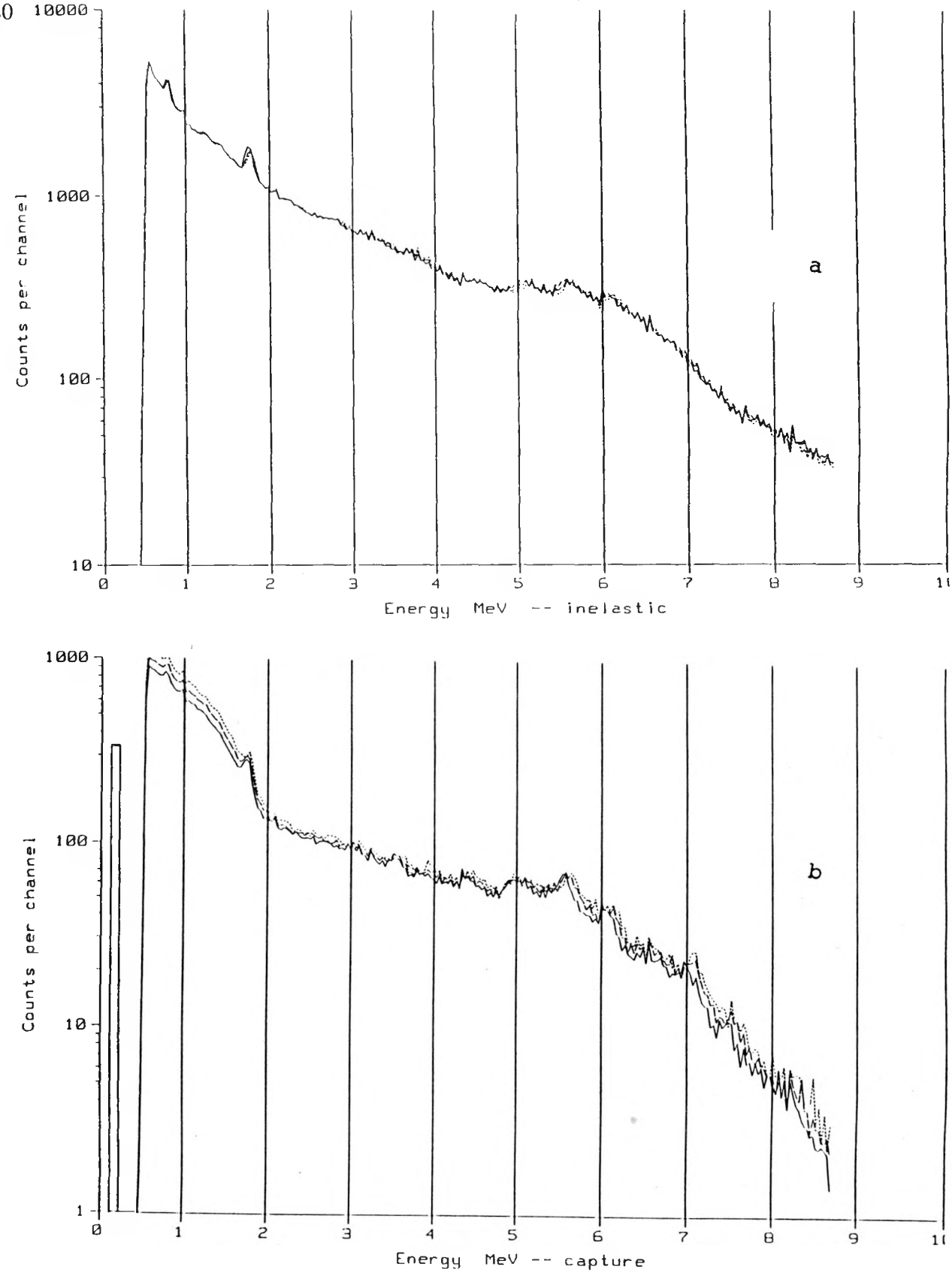
7. The screeded surface of a test box with the screed in place



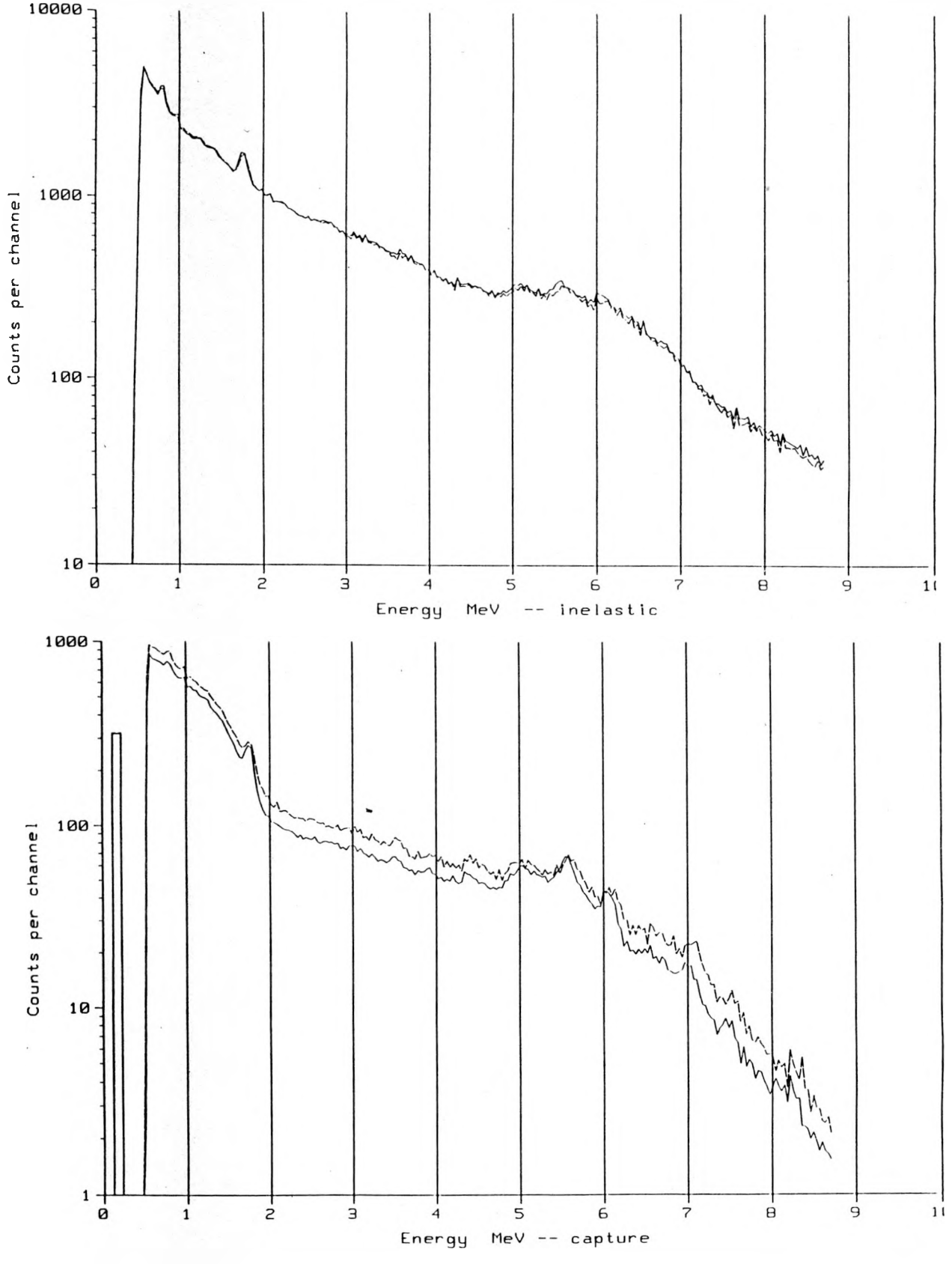
8. Difference between true weight fraction CO_2 (0.052) and dry weight fraction calculated from the logging system vs gap for four different sets of washouts in dry material. The horizontal line shows the mean difference.



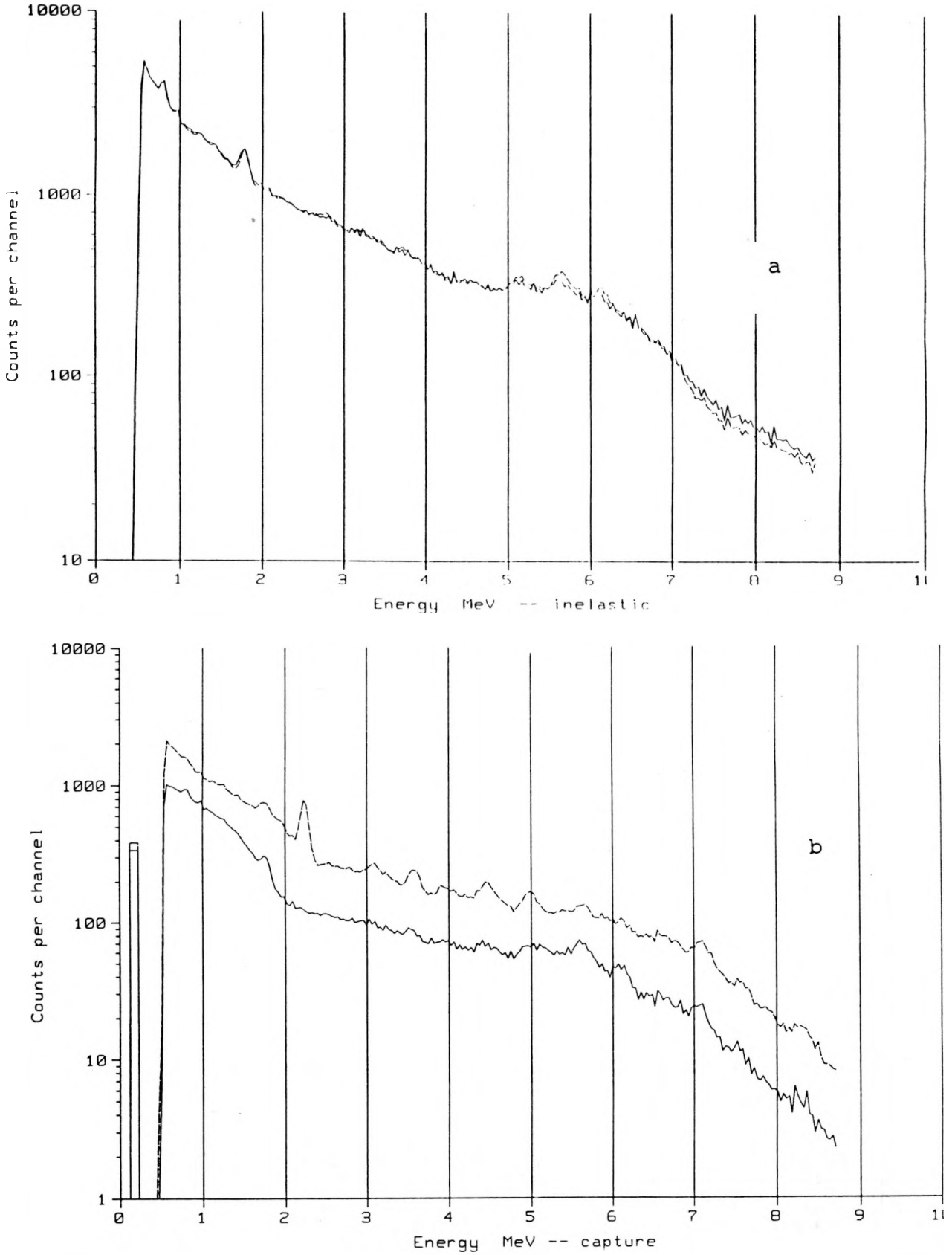
9. Difference between true dry weight fraction CO_2 (0.052) and dry weight fraction calculated from the logging system vs gap for four different sets of washouts in saturated material. The horizontal line shows the mean difference.



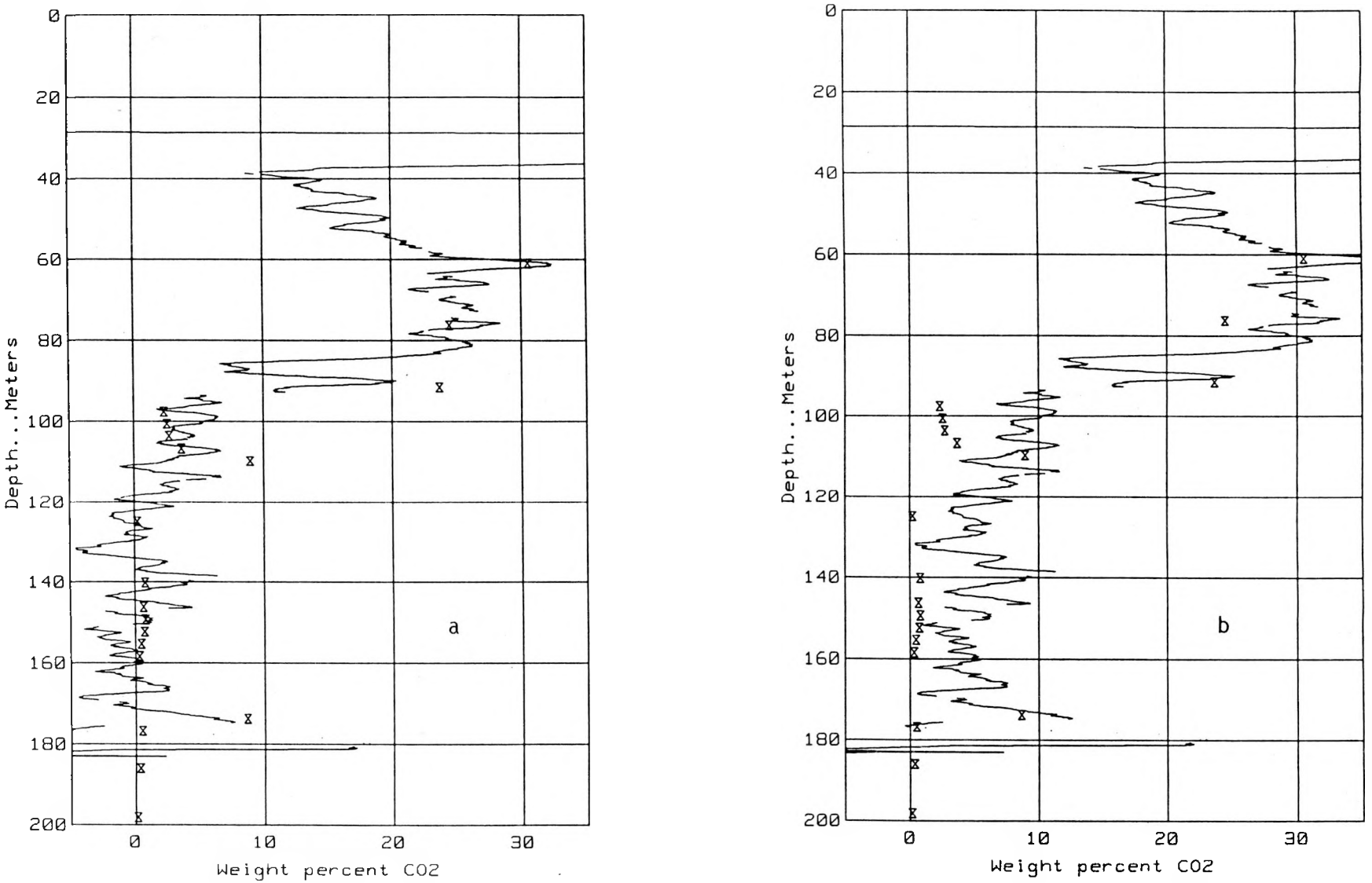
10. Inelastic (a) and capture (b) spectra for dry material for three values of dry weight fraction CO_2: 0.004 (solid), 0.052 (dashed) and 0.105 (dotted.)



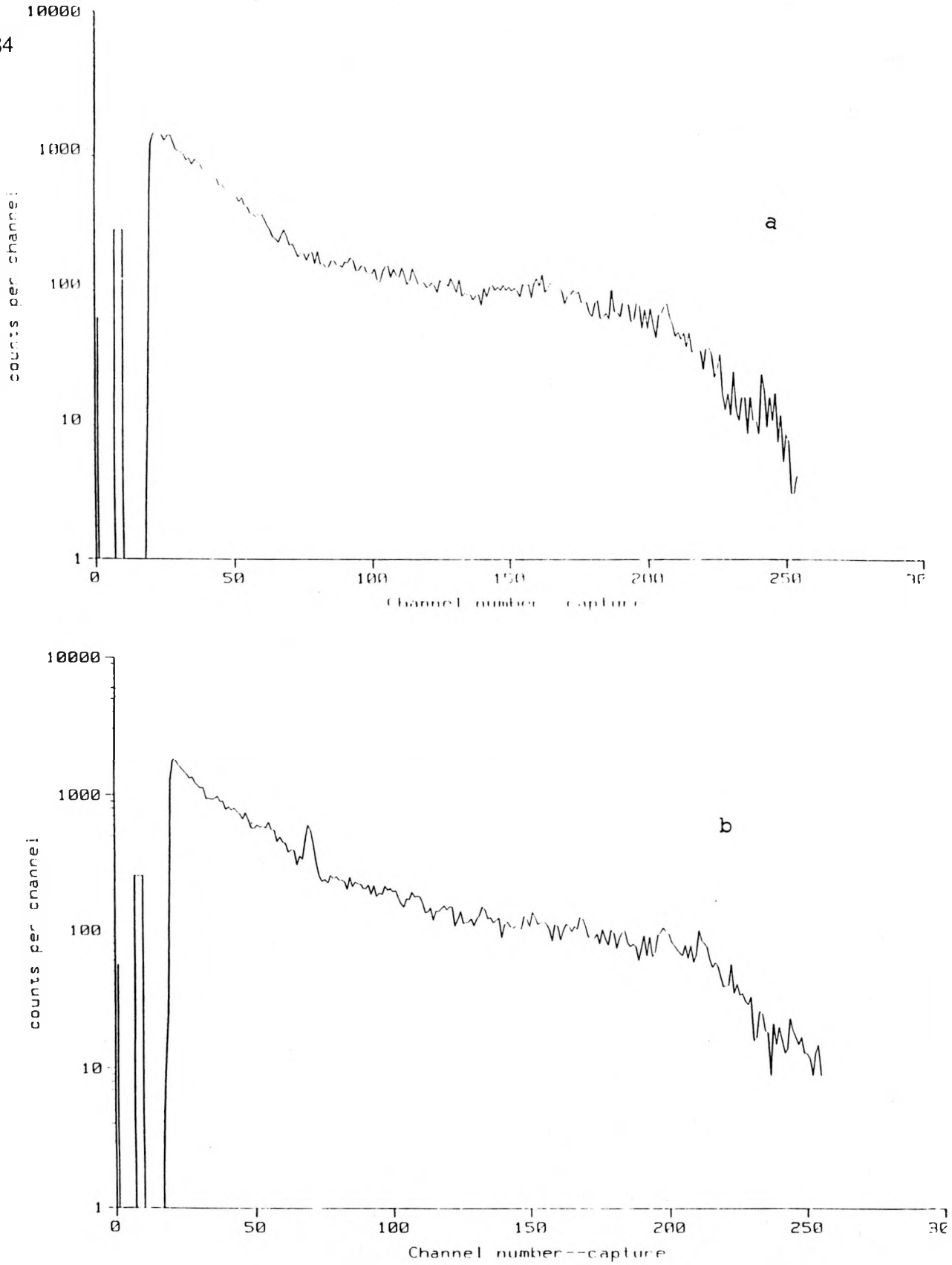
11. Inelastic (a) and capture (b) spectra for dry material with 2.5 cm (dashed) and 7.5 cm (solid) gap, with 0.052 weight fraction CO_2



12. Inelastic (a) and capture (b) spectra for dry (solid) and saturated (dashed) material with 2.5 cm gap and 0.052 dry weight fraction CO_2.



13. Gap- and skid-corrected (a) and gap-, skid- and water-corrected (b) log values of CO_2 content and values from samples in borehole U9cv at the Nevada Test Site. Water values are 0.18 by volume above 91 m and 0.20 below 91 m, corresponding to attempts at averaging a neutron log.



14. Spectra from the log in U9cv at 61 m (a) and 175 m (b).

OCCURRENCE, DISTRIBUTION AND MEASUREMENT OF CARBONATE IN THE ALLUVIUM OF SOUTHERN YUCCA FLAT, NEVADA TEST SITE

C. J. RAYBURN
S. L. DRELLACK, JR.
P. H. THOMPSON

FENIX AND SCISSON OF NEVADA, INC.
P. O. BOX 498
MERCURY, NV 89023

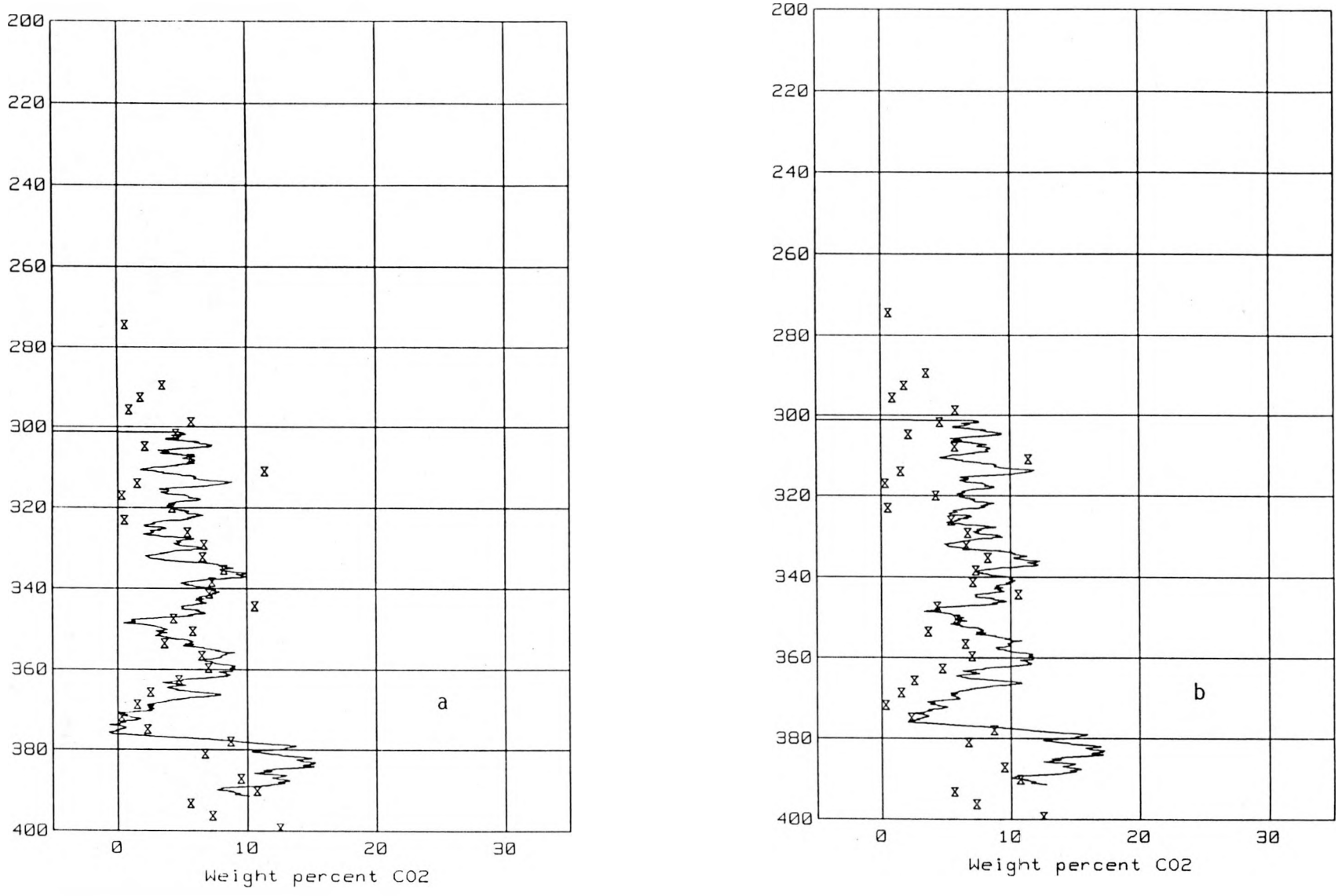
ABSTRACT

The alluvium of southern Yucca Flat, Nevada Test Site, has been utilized extensively as a medium for underground nuclear tests, and is expected to play an important role in the siting of future events. Nuclear detonation produces noncondensable carbon dioxide (CO_2) gas from naturally occurring carbonates in the alluvium. Generation of CO_2 in underground tests has been linked to a significant percentage of past containment failures. The carbonate content of the test medium is therefore an important parameter to the containment scientist, and is routinely measured as weight percent CO_2 of samples collected in emplacement holes.

Carbonate content in southern Yucca Flat alluvium varies with geographic location, reflecting differing depositional source areas and distance to these sources. Variation also occurs with stratigraphic position (depth) due to the changing lithology of detritus over time as erosion exposes new material, and also to the effects of depth on diagenetic processes.

The value of CO_2 data obtained through sample analysis is directly dependant upon how accurately the samples represent the test medium. A variety of techniques are used to obtain samples from emplacement holes, and each is subject to inherent limitations which must be understood if data are to be interpreted correctly. Because of these limitations, it is not realistic to treat laboratory CO_2 data independently as a precise measure of carbonate content for a particular depth or interval. Patterns of carbonate content in alluvium are recognizable and correlative, however, and can be used to successfully predict range, variability and mode of occurrence for carbonate content at a given location. Using this information, the containment scientist can select hole locations and working point positions to avoid potential high CO_2 sources, design an effective sampling program and increase the confidence in a successful test containment.

Work on this report was performed under the auspices of the United States Department of Energy.



15. Gap- and skid-corrected (a) and gap-, skid- and water-corrected (b) log values of CO_2 content and values from samples in borehole U1d at the Nevada Test Site. Water values were taken from a neutron log.

INTRODUCTION

Alluvium deposits in Yucca Flat, Nevada Test Site (NTS) were among the first media used for underground nuclear tests after the inception of subsurface testing. Almost thirty years later, the alluvium still is frequently utilized as a test medium, and is expected to play an important role in the siting of future events. Yucca Flat alluvium provides many characteristics advantageous to the containment of nuclear explosions. One of its less desirable containment attributes, however, is relatively high carbonate content in some intervals. Nuclear detonation produces noncondensable carbon dioxide (CO_2) gas from these naturally occurring carbonates. Generation of CO_2 gas in underground tests has been linked to a significant percentage of past containment failures, typically in the form of late-time gas seeps. The carbonate content of the test medium is therefore an important parameter to the containment scientist.

At the NTS, samples routinely collected from exploratory boreholes and emplacement holes are analyzed to determine their weight percentage of CO_2. The resulting value represents the maximum amount of CO_2 which can be produced from the carbonate contained in the sample. Measurements from samples throughout an interval are used to estimate an average CO_2 content, or more properly an average carbonate content, for the interval sampled.

Containment scientists have come to recognize several variables affecting CO_2 data from alluvium samples. Carbonate concentration, mode of occurrence and distribution are highly variable in southern Yucca Flat alluvium, and an understanding of these variations is imperative. Also important are such operational considerations as the technique used to obtain samples, any processing the sample undergoes before laboratory testing, and the accuracy or repeatability of the analysis. We believe the bulk of the CO_2 data obtained to date from Yucca Flat alluvium samples is credible and useful. Effective utilization of these data, however, requires an awareness of the variables influencing them.

This report focuses on Los Alamos National Laboratory (LANL) testing acreage in southern Yucca Flat, including portions of Areas 1, 3, 4, 6 and 7. While the conclusions drawn pertain specifically to this acreage, we believe that the basic principles underlying them are applicable throughout Yucca Flat.

GEOLOGIC SETTING

The structure and geomorphology of Yucca Flat are typical of arid intermontane basins occurring throughout the Basin and Range province of Nevada and adjoining states. Faulted and tilted blocks of Tertiary volcanic rocks and underlying Paleozoic sediments form low ranges to the east and west of Yucca Flat, bounding downdropped blocks of the same stratigraphy. Gradual erosion of the ranges over several millions of years has deposited a blanket of alluvium within the basin. The topography of the basin floor and ongoing structural activity during alluvium deposition combined to influence present alluvium thickness. Mid-basin alluvium thickness in southern Yucca Flat varies from less than 30 m to over 600 m.

Alluvial deposition is intermittent and localized, usually proceeding in short, intense episodes separated by comparatively long hiatuses. Alluvial fans debouch from the higher terrain bounding Yucca Flat and coalesce to form highly discontinuous, gradational and poorly sorted deposits. Drainage within the basin is from the margins inward and from north to south. Progressive fining and sorting of the alluvium towards the south and center of the basin reflect progressive mechanical abrasion and diminishing depositional energy. These trends result in the deposition of fine, relatively uniform sands in much of south central Yucca Flat (e.g. the Area 3 "Sand Pile"), and culminate with the silty, clay-rich playa deposits of Yucca Lake in the extreme southern end of the basin. Abrupt facies changes and complex interfingering, reflecting the localized nature of the deposits, make correlation of alluvium units difficult. This stratigraphic variability is somewhat less pronounced in south central Yucca Flat, where alluvium deposition is less energetic.

Alluvium composition reflects the specific source lithologies that were exposed to erosion at the time of deposition. New types of detritus become available to the alluvium as new lithologies are gradually exposed by erosion. Hence, older (deeper) lithologies are increasingly represented in the alluvium over time. In Yucca Flat, this trend is recognizable as tuffaceous alluvium overlain by more Paleozoic-rich detritus.

CARBONATE OCCURRENCE

One of the more important factors in the interpretation of CO_2 data is the nature of the CO_2 source being measured. There are two primary occurrences of carbonate in Yucca Flat alluvium: Limestone ($CaCO_3$) and dolomite ($Ca,Mg(CO_3)_2$) clasts weathered from Paleozoic sediments, and secondary $CaCO_3$ (caliche) deposited by groundwater (wind may also contribute to the initial transport and concentration of caliche in eolian dust). Caliche is best known for forming well-developed layers of dense, highly cemented material, but the term also applies to less-advanced stages of secondary carbonate deposition. Caliche deposition in alluvium is controlled by a number of factors, including the sedimentation rate of the alluvium, carbonate concentration in groundwater, groundwater movement, and the type of alluvium in which the caliche is deposited. Based upon the six-stage morphologic classification devised by Gile et al. (1966), caliche in southern Yucca Flat alluvium may be characterized as Stage I (finely disseminated), Stage II (coatings on individual clasts), and Stage III (firmly cemented aggregates of clasts). Because the distribution of these stages differs within the basin, they are considered individually in this report.

SAMPLING FOR CO_2 MEASUREMENT

The value of any data obtained through sample analysis is dependant upon how accurately the samples represent the medium. Sample representation of alluvium can be complicated by a wide range of grain sizes and by abrupt lateral and vertical changes. Samples submitted for the measurement of CO_2 content are collected using a variety of techniques, and no one technique is suitable for all types of alluvium. Choosing an appropriate sampling method must take into account the nature of the alluvium being sampled, in particular the relative coarseness of the alluvium and the CO_2 source, while considering such factors as cost and multiple sampling priorities.

Sidewall Samples

Successful sidewall sampling is dependent in large part upon borehole conditions. Sample recovery can sometimes vary in alluvium due to the friability of the deposit, particularly in older, dry boreholes, but usually is adequate for the desired laboratory measurements. Several methods are employed to collect sidewall samples. The Hunt technique relies on a hard "shoe", or barrel, which is forced into the borehole wall by the weight of a drill string. This method is described in detail by Drellack (1986). Hunt samples are 8 cm in diameter and range from 25 - 40 cm long depending upon the sample shoe used. A second sample type, percussion gun sidewalls, are obtained by shooting a small barrel into the borehole wall with an explosive charge. Samples are roughly 2 cm in diameter and up to 5 cm long. Recent development of a tool which obtains a rotary core 5 cm in diameter and up to 45 cm long from the borehole wall will provide another sidewall sampling option if the tool proves effective in alluvium.

The collection of sidewall samples is of course subject to practical constraints on time and cost. Much of the existing CO_2 data for southern Yucca Flat alluvium was measured from Hunt sidewalls routinely collected in LANL emplacement holes. Hunt sampling operations are time-consuming and expensive, however, and have been largely discontinued in favor of less costly methods. Percussion gun samples are comparatively inexpensive and can be collected in a relatively short time. Their utility is limited by their small size, particularly when samples are to be used for a number of analyses. Multiple percussion gun samples from the same interval may increase the quantity of material recovered but do not improve the ability to sample large clasts. The rotary sidewall coring tool may provide a less expensive means than the Hunt method of collecting large sidewall samples. Sample recovery is quite slow, however, limiting the number of samples which can be collected in a reasonable period of time. Use of this tool also is limited to boreholes larger than 2.2 m in diameter.

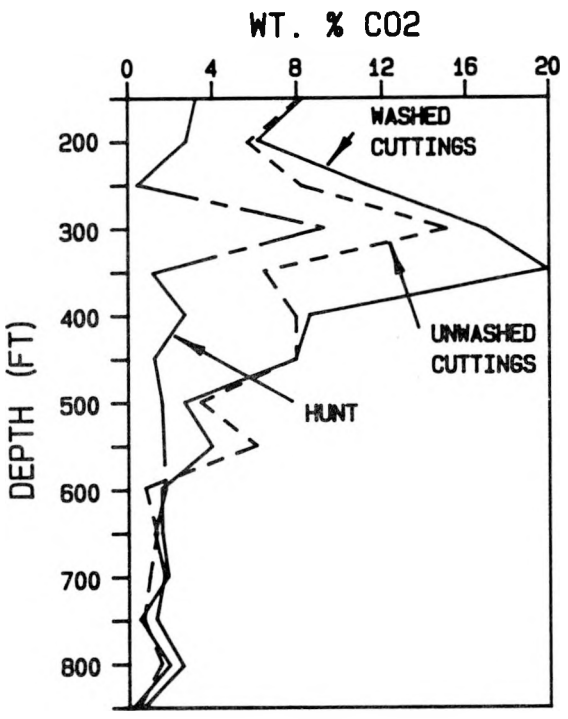
Drill Cuttings

Drill cuttings are collected routinely from all holes drilled on the NTS, and provide a readily available, inexpensive source of sample material. Cuttings differ from sidewall samples, however, in that the sample has undergone "processing" and is not obtained under exacting depth controls. These effects are greatly amplified in poorly indurated deposits such as alluvium and can bias the results of analyses performed on cuttings samples. The use of alluvium drill cuttings for CO_2 measurement is therefore subject to limitations not inherent to sidewalls.

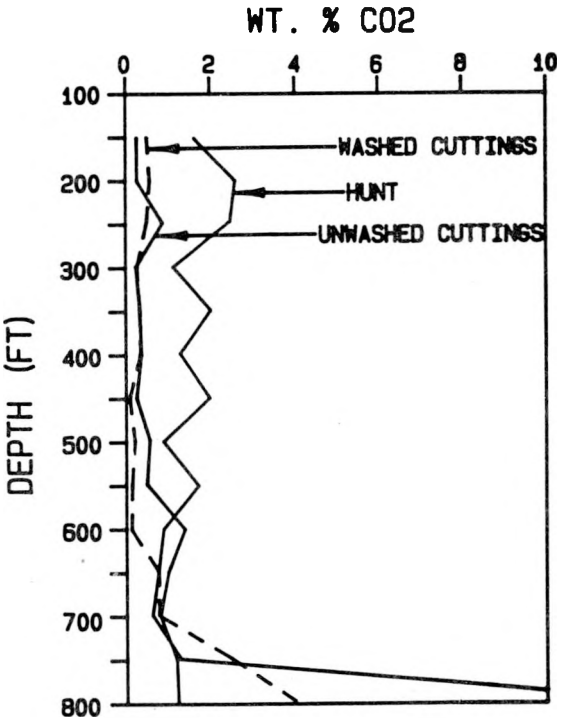
Drill cuttings samples are collected as drilling progresses by rig personnel at 3 m depth intervals. In principle, a sample of material representing the full interval is obtained; in practice, however, this ideal is not realized. A large volume of drilling fluid is circulated through the hole and a large quantity of cuttings are generated in drilling a typical large diameter emplacement hole. Diverting even a small stream of the circulating fluid quickly fills the sampling container used on LANL drill holes with cuttings. Each 3 m sample may contain material only from the first several minutes following the previous sample; thus, a cuttings sample marked "380 - 390 ft" may only hold material from 380 - 381 ft. Cuttings sometimes are caught early or late (i.e. shallower or deeper than the depth advertised on

the sample) owing to operational constraints. Problems are also encountered with "doghoused" samples, where cuttings collected from a single interval are labelled as coming from two or more separate intervals. Sample contamination can become a concern in alluvium intervals when relatively large amounts of material slough from uphole.

The most conspicuous limitation of alluvium cuttings is the processing they sustain. Unlike more lithified deposits, alluvium is disaggregated during drilling through the combined effects of bit action and fluid circulation. The grinding and washing tend to concentrate harder, coarse sand to pebble sized components of the deposit. Coarser material such as cobbles and boulders (rare in most southern Yucca Flat alluvium) are broken into smaller pieces, some of which may appear in cuttings samples. Most very fine sand and silt is held in suspension by the drilling fluid and is either washed past the sample container or lost as fluid overflows the container. This finer fraction comprises a significant portion of the alluvium in much of southern Yucca Flat. If the CO_2 source is relatively coarse (e.g. carbonate clasts or caliche rinds on pebbles), it will often be concentrated in samples and produce unrealistically high CO_2 values. Conversely, a very fine CO_2 source (e.g. disseminated caliche) will be washed away and the cuttings will yield low measurements. Sample type comparisons, such as those in Figure 1, illustrate these effects.



A) CO_2 content by sample type for drill hole U-7bs. Cuttings CO_2 > Hunt CO_2 above 500 ft indicates concentration of CO_2 source (in this case, carbonate clasts) in cuttings. Note lithology change from carbonate-bearing fan gravels to tuffaceous fan gravels at approximately 500 ft.



B) CO_2 content by sample type for drill hole U-3lh. Hunt CO_2 > cuttings CO_2 indicates that CO_2 source (disseminated caliche) is reduced in cuttings. High CO_2 at 800 ft is due to basal caliche; note that Hunt CO_2 remains higher than cuttings CO_2 in this carbonate environment.

Figure 1--Comparison of CO_2 content from different sample types

It is standard practice at the NTS to submit drill cuttings samples to the U.S. Geological Survey (USGS) Core Library and Data Center, where they are washed and screened to remove drilling mud before being archived. This washing removes any fine sand in the sample, and therefore further reduces cuttings representation of in situ alluvium.

Other Sample Methods

Portions of continuous rotary cores of alluvium may be submitted for CO_2 measurements when available. Continuous cores obviate the need for additional borehole samples, but cores of Yucca Flat alluvium are an exceedingly rare exception. Mined shafts and drifts in alluvium, also a rare exception, provide an opportunity to collect in situ alluvium samples in the subsurface (Drellack et al., 1989). Surface and outcrop samples can characterize the CO_2 content of contemporary deposits and provide an indication of CO_2 content in similar deposits in the subsurface.

CO_2 Sampling Programs

Designing an effective sampling program for alluvium CO_2 measurement involves choosing an appropriate sampling method (or methods) and sampling points or intervals.

In alluvium containing a carbonate form likely to be concentrated in cuttings (i.e. carbonate fragments and caliche rinds on larger clasts), cuttings samples, despite their limitations, can "flag" potentially high CO_2 content. If drill cuttings are to be used for CO_2 measurement, unwashed cuttings are preferable because they have not undergone the additional processing. Those intervals which present possible containment concerns can then be sidewall sampled to obtain CO_2 measurements more representative of in situ alluvium, or correlated with well-sampled intervals in nearby boreholes. It should be recognized that high CO_2 values from cuttings do not necessarily indicate high carbonate content in the alluvium.

The appropriate sidewall sampling method is again dependant upon grain size. It is intuitively evident that the sample size required to represent a coarse, heterogeneous interval of alluvium is greater than that necessary for fine, uniform intervals. A 2 x 5 cm percussion gun sample, for instance, cannot be expected to typify alluvium containing a significant percentage of clasts greater than 3-4 cm in size. Since discontinuation of routine Hunt sampling, NTS sampling programs have increasingly relied upon percussion gun sampling. If a significant portion of the carbonate in a deposit occurs in large carbonate clasts or caliche rinds on large clasts, percussion gun samples are likely to yield low estimates of overall CO_2 content. All other factors being equal, "true" CO_2 content probably falls somewhere between that measured from percussion gun samples and cuttings samples in such cases. The rotary sidewall coring tool should obtain sufficiently large samples to accurately represent most carbonate environments if coring in alluvium proves feasible.

As discussed previously, fine-grained alluvium is not accurately represented by cuttings samples. Experience in southern Yucca Flat has shown that the typically low CO_2 content of such deposits seldom presents a containment concern and can often be evaluated through correlation with nearby boreholes. Percussion gun samples can provide sufficient material when sample CO_2 data is required from fine-grained alluvium.

The stratigraphic variability of the deposit dictates appropriate sample spacing. Spacing between samples must decrease as vertical variation increases in order to maintain representation. Sample spacing can also be varied (rather than fixed at a rigid interval) to more fully cover intervals of suspected high CO_2 content or interbedded zones. When operational considerations permit, sampling methods can be combined to adjust for stratigraphic diversity. Both sidewall coring and percussion gun sampling might be utilized, for example, where coarse alluvial fans interfinger with finer-grained alluvium.

CARBONATE DISTRIBUTION

Data from the hundreds of holes drilled in Yucca Flat have produced a large geologic data base for the alluvial section. Although no single source of information can adequately define carbonate occurrence and distribution in all types of alluvium, combining information from different sources can provide corroborative evidence. Variations in carbonate often can be correlated between boreholes to help define alluvium stratigraphy. Where enough boreholes exist to delineate stratigraphic changes, correlations ultimately may be used to predict carbonate occurrence within the alluvial section in a particular area.

The first indication of carbonate content generally comes from detailed lithologic descriptions of samples. Most forms of carbonate in Yucca Flat alluvium are observable in samples, as are variations in clast size and lithology which reflect facies changes. These qualitative observations can be tied to quantitative data from sample analyses and geophysical logs.

Sample type comparisons such as those shown in Figure 1 can give strong evidence of the CO_2 source. Measurement of CO_2 content from size fractions of a sample separated by sieving can indicate the grain size of the carbonate, an important distinguishing characteristic. Carbonate grain size can also be established by correlating sample grain size data with CO_2 measurements in bivariate plots. Examples of these techniques are illustrated in Figures 3-6 accompanying the alluvium descriptions.

Geophysical log responses in southern Yucca Flat alluvium are, in general, less diagnostic than in more lithified deposits. Changes in signature may be lost in "noise" caused by the inhomogeneity of the deposit. Electric log signatures in Yucca Flat alluvium, although often correlatable, may reflect variation in water content, alteration of tuff fragments and/or degree of compaction in addition to lithologic changes (Grothaus & Howard, 1977). In some cases, however, logs can aid in defining carbonate content or mode of occurrence in alluvium by delineating facies changes. Examples of diagnostic geophysical log signatures for specific alluvium facies are included in Figures 3, 6 and 8. Where absence of wallcake permits observation, downhole video may also reveal facies changes or highlight certain carbonates (e.g. carbonate clasts, caliche stringers, and pumice stringers in playa deposits).

Previous alluvium studies, such as those performed by the USGS on the Yucca Flat "Sand Pile" (Fernald et al.) and work by Lawrence Livermore National Laboratory (LLNL) geologists (Wagoner, McKague, Pawloski et al.) with the alluvium in LLNL use areas of Yucca Flat, provide an excellent foundation for further interpretations. Drawing from these studies, the alluvium of southern Yucca Flat can be divided into five lithologic units, or "types". Each type has a primary carbonate occurrence which can be used to distinguish it from the other types (an exception to this is the similarity of Type III and Type V deposits,

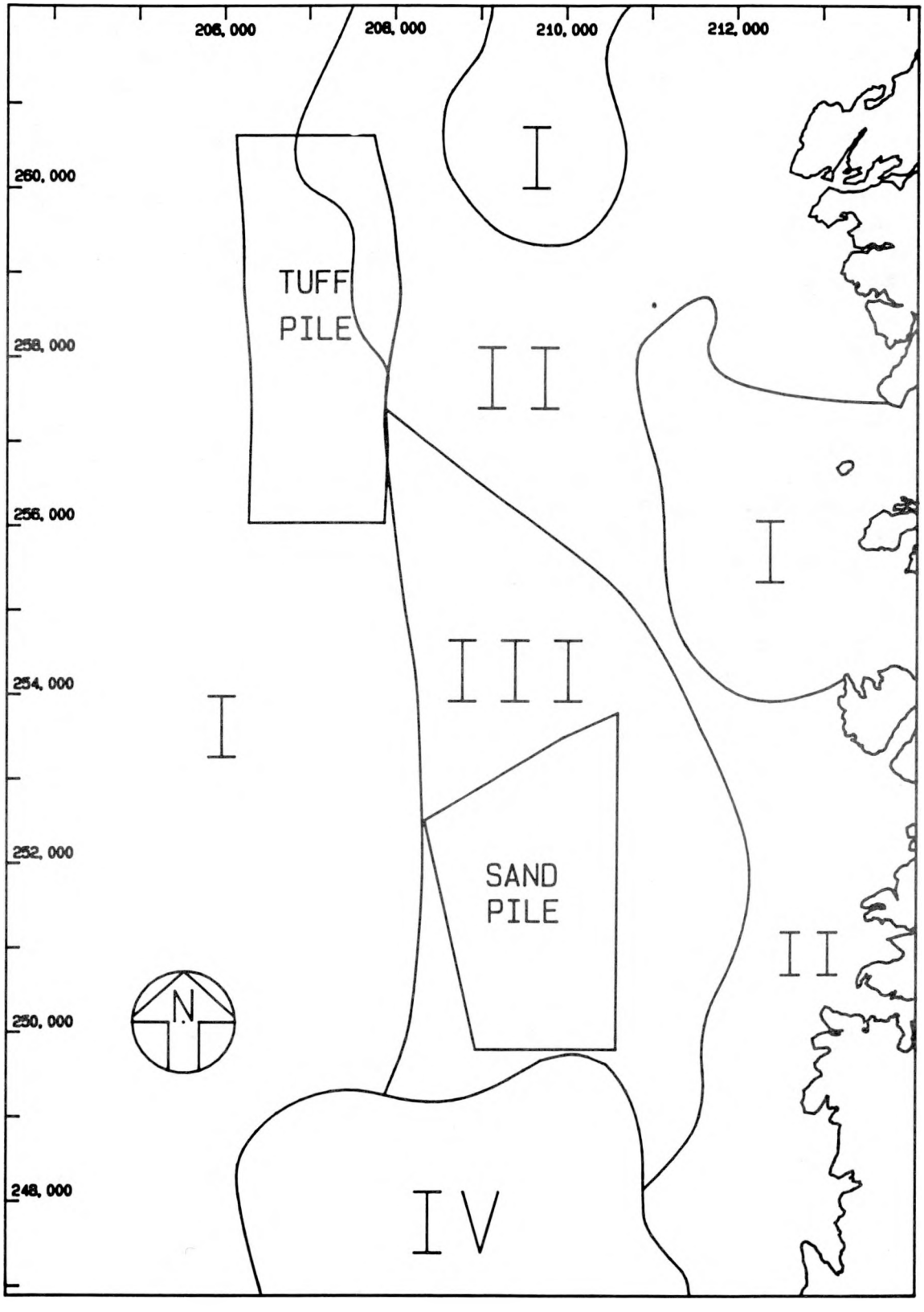


Figure 2--Areal distribution of alluvium Types I-IV in southern Yucca Flat

which, for purposes of this report, are distinguishable by stratigraphic position only). The areal distributions of Types I-IV are shown in Figure 2 (Type V is omitted because of its relatively ubiquitous occurrence at the base of the alluvium throughout southern Yucca Flat). These somewhat gross divisions provide guidelines which may aid in evaluating the carbonate environment at specific locations in southern Yucca Flat. Basal caliche-cemented zones occurring in some areas of southern Yucca Flat represent a distinct carbonate-bearing environment and are addressed separately. Table 1, following the descriptions, summarizes carbonate data for each type, and proposes the sampling method(s) we believe most appropriate for CO_2 measurements based upon each type's grain size and carbonate occurrence.

Type I

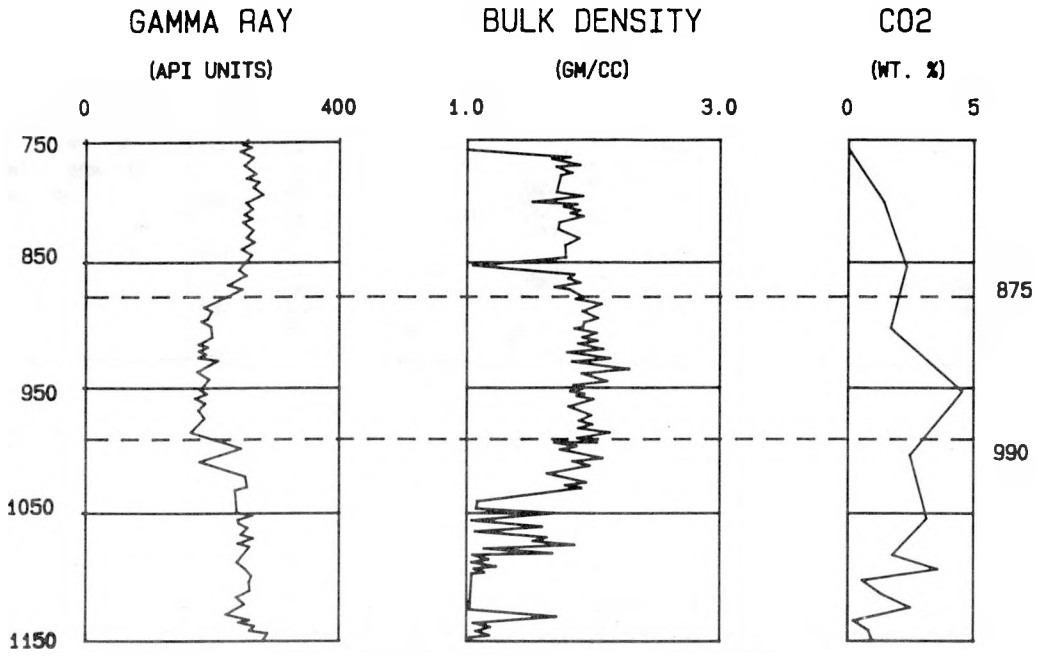
Type I alluvium consists of coarse alluvial fan deposits characterized by >5% Paleozoic carbonate clasts. This alluvium type is identified as "western Yucca gravel fans" and "central Yucca mixed alluvium" in the USGS "Sand Pile" report (Fernald et al., 1974). It can be considered gradational between the "Unit 2" and "Unit 3" alluvium types identified in LLNL use acreage of Yucca Flat (Wagoner, 1987). Type I deposits occur in three separate locations in southern Yucca Flat (Figure 2). These occurrences represent three different Paleozoic carbonate source areas in the higher terrain east and west of Yucca Flat. Near their contacts with other alluvium types, the Type I deposits tend to grade into and interfinger with the adjoining deposit, and the Paleozoic clast concentration often becomes "diluted" by tuffaceous material.

Paleozoic carbonate clasts, not unexpectedly, are the predominant CO_2 source in Type I alluvium. Secondary carbonate generally is present in varying amounts, but its contribution to CO_2 content is small compared to the carbonate clasts. The CO_2 content can be quite high in Type I deposits, averaging 10% or more across relatively thick intervals. Partly as a result of this, the alluvium west of the Yucca Fault is not frequently utilized as a testing medium although it is suitably thick for the purpose.

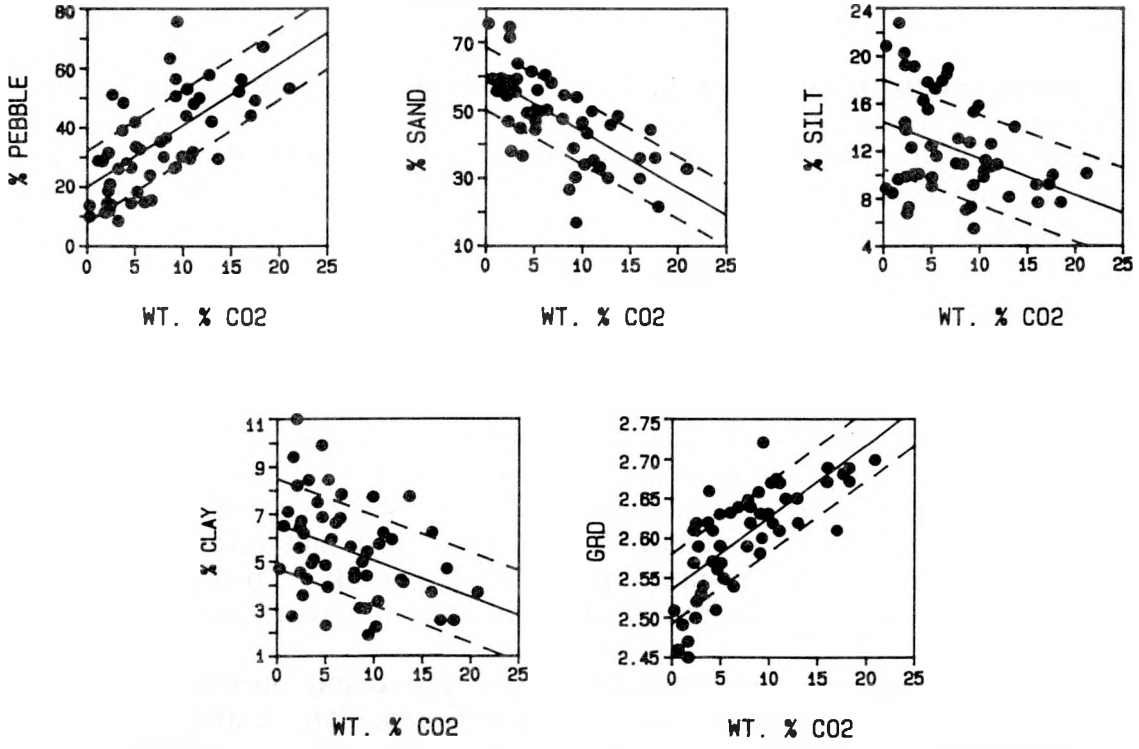
Type II

Type II alluvium consists of alluvial fan gravel rich in Tertiary volcanic detritus derived from the higher terrain east of Yucca Flat. Low Paleozoic carbonate content (<5%) distinguishes Type II from Type I alluvium; Type II fans are otherwise similar in character to Type I fans. Type II alluvium is comparable to the "Unit 3" alluvium described in LLNL Yucca Flat acreage (Wagoner, 1987) and to the "eastern Yucca gravel fans" identified in the USGS "Sand Pile" report (Fernald et al., 1974). Its primary occurrence in southern Yucca Flat is in southeastern Area 7 and along the eastern margin of the basin in Areas 3 and 6 (Figure 2).

Type I and Type II deposits sometimes coalesce and are gradational along their contacts. Near Type I/Type II contacts, carbonate clasts may constitute a significant portion of the total carbonate in the Type II deposit. In most Type II alluvium, however, carbonate clasts are conspicuously absent or very scarce. Secondary carbonate, most typically caliche rinds on larger clasts, is the primary carbonate occurrence. Measured CO_2 content in Type II alluvium generally is below 3%.



A) Correlation of geophysical logs and CO_2 data in drill hole U-4i. Decreased gamma ray count, increased bulk density and increased CO_2 content are evidence of increased Paleozoic detritus between 875 - 990'.



B) Bivariate plots comparing Hunt sidewall sample data for drill hole U-1e. Solid slope is "best-fit" linear regression; dashed slopes are $\pm$ 1 standard deviation. Plots indicate that the primary source of CO_2 is in pebble fraction. Positive correlation between CO_2 content and grain density suggests that CO_2 source is associated with higher-density detritus (i.e. Paleozoic carbonate clasts).

Figure 3--Identification of Type I alluvium (carbonate-bearing fan gravels)

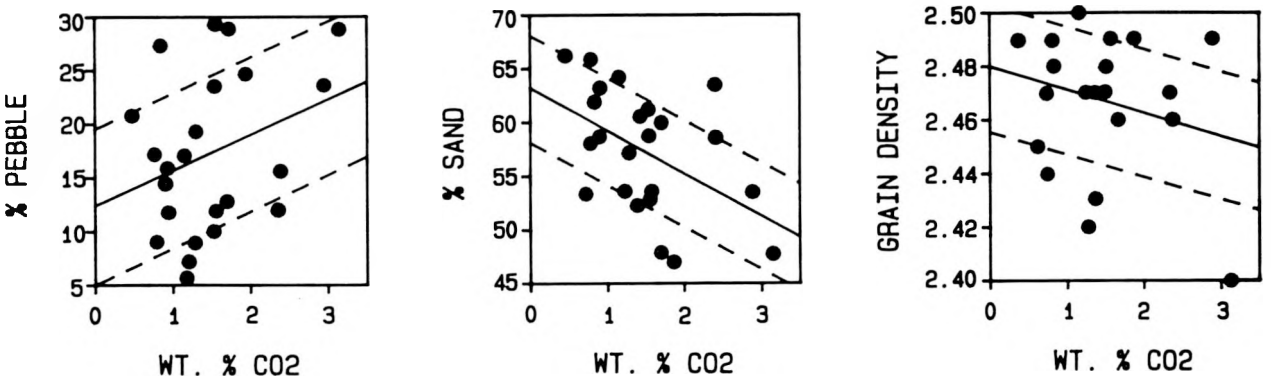


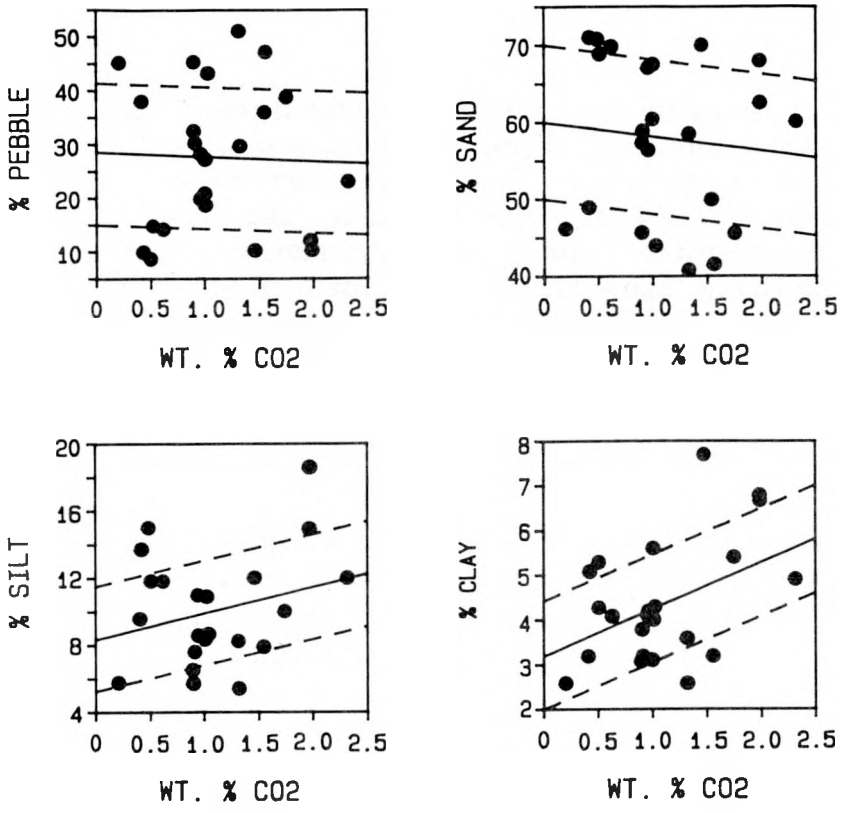
Figure 4--Identification of Type II alluvium (tuffaceous fan gravels) in drill hole U-3ke through bivariate plots comparing Hunt sidewall sample data. Solid slope is "best-fit" linear regression; dashed slopes are $\pm$ 1 standard deviation. Correlations indicate that primary CO_2 source is in pebble fraction. Negative correlation between CO_2 content and grain density suggests that CO_2 source is associated with lower-density detritus (i.e. caliche rinds on tuffaceous pebbles) rather than higher-density Paleozoic carbonate clasts.

In some areas of southern Yucca Flat, well-sorted and poorly indurated sand "lenses" occur within the alluvium (Drellack, 1982), often within Type II fans. These deposits, speculated to be eolian in origin, probably reflect winnowing and reworking of alluvium by wind. Although their impact on drilling operations can be significant, they are inconsequential in terms of carbonate content.

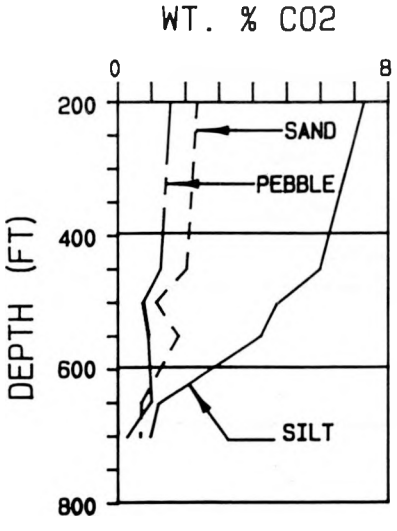
Type III

The highly uniform Area 3 "Sand Pile" typifies Type III alluvium deposits. Type III is the predominant alluvium type in south-central Yucca Flat (Figure 2), consisting of fine, well-sorted tuffaceous sand. It is identified as "sandy alluvium" in the USGS "Sand Pile" report (Fernald et al., 1974). Type III deposits reflect the decreasing energy of the dominant flow patterns within the basin. They gradually coarsen to the north and toward the eastern and western basin margins, and grade into Type I and II deposits. To the south, Type III deposits interfinger with and grade into the silts and clays of Yucca Lake playa (Type IV).

Type III deposits have been the most frequently tested and probably are the most thoroughly characterized alluvium type in southern Yucca Flat. Carbonate in Type III alluvium occurs primarily as disseminated caliche, sometimes concentrated in thin "stringers", or veinlets. Measured CO_2 content is low, averaging less than 2% by weight throughout the section, and diminishes somewhat with depth, particularly within the boundaries of the "Sand Pile". Successful prediction of CO2 content and other physical properties through correlation and extrapolation has eliminated the need for CO_2 samples from the highly uniform Type III alluvium in the "Sand Pile".



A) Bivariate plots comparing Hunt sidewall sample data from drill hole U-3mc. Solid slope is "best-fit" linear regression; dashed slopes are $\pm$ 1 standard deviation. Correlations indicate CO_2 source in silt and clay sized fractions of samples. U-3mc also contained several gravel fans rich in Paleozoic quartzite, resulting in high pebble content in some samples.



B) CO_2 analysis of sieved fractions (pebble, sand and silt) of Hunt sidewall samples from drill hole U-3lh, showing higher CO_2 content in silt-sized fraction. Downhole decrease in carbonate evident in graph is common in south central Yucca Flat. In larger-diameter boreholes near U-3lh, decreased induration in this downhole zone resulting from lower carbonate content has caused hole stability problems.

Figure 5--Identification of Type III alluvium (tuffaceous sand)

Type IV

Holes drilled north of Yucca Lake in northern Area 6 have encountered playa deposits, here designated Type IV alluvium, in the subsurface (Figure 2). These deposits grade into and interfinger with Type III alluvium to the north. They occur deeper in the alluvial section with increasing distance from the present surface of Yucca Lake, indicating a gradual southward migration of the playa surface. Type IV alluvium, analogous to the "fine alluvium" and "playa deposits" in the USGS "Sand Pile" report (Fernald et al., 1974), are a homogeneous, relatively impermeable mixture of silt and clay with minor sand. Pebbles and larger lithic fragments are very scarce. Carbonate content is quite low, occurring primarily as disseminated caliche.

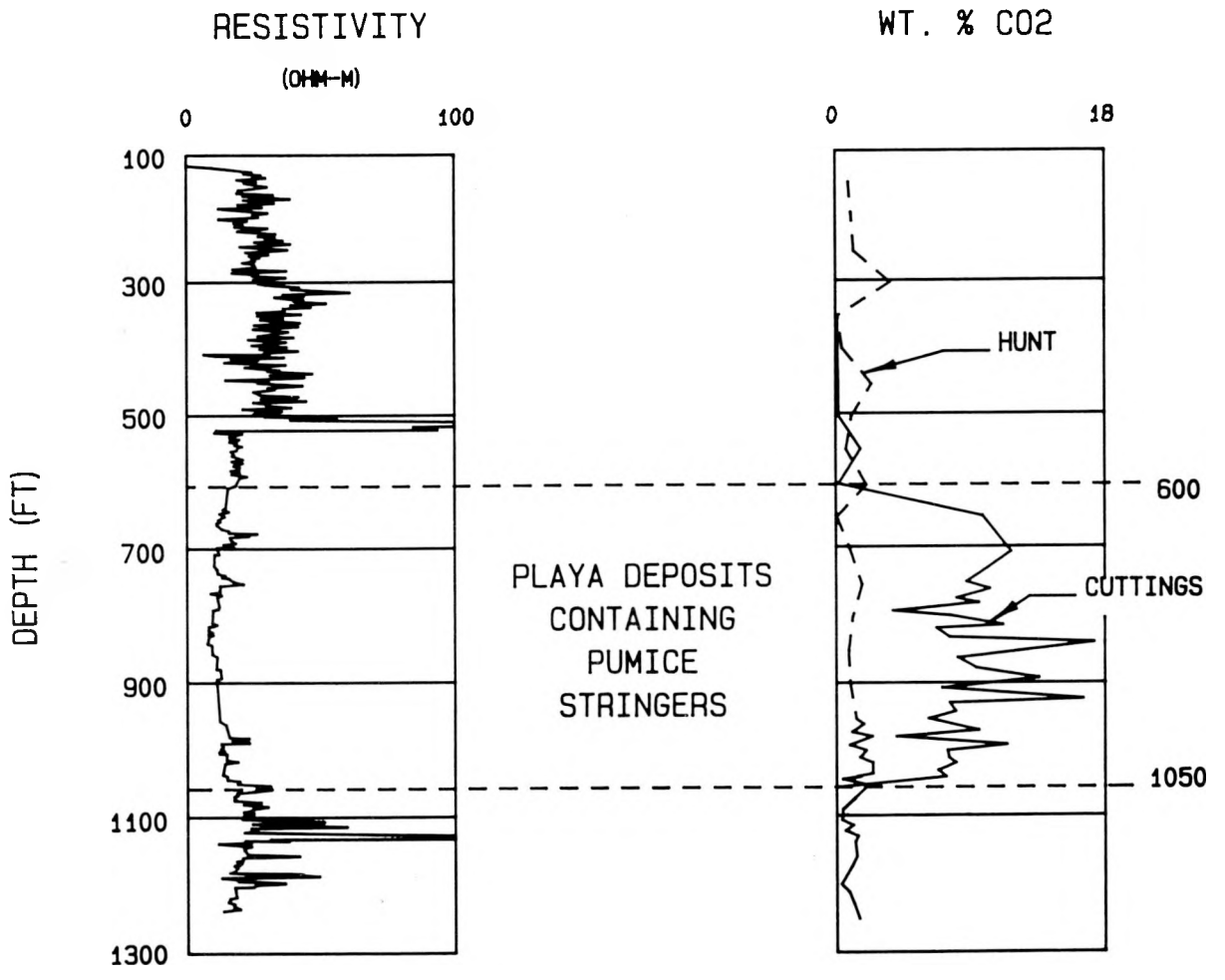


Figure 6--Identification of Type IV alluvium (playa deposits) in drill hole U-3lk through correlation of electric log and sample CO_2 data. Low resistivity due to increased clay content delineates "transition zone" of interbedded Type III and Type IV alluvium between 600 - 1050 ft. Cuttings CO_2 content rises sharply through this zone due to concentration of calcified pumice in cuttings while Hunt CO_2 content remains constant.

Occurring within the fine playa material are thin, discontinuous stringers of pumice weathered from tuffs. Field observations at Yucca Lake indicate that these features form when the low-density pumice is selectively washed onto the playa in thin layers by surface runoff. Borehole data suggests that the stringers rarely exceed several centimeters in thickness, and that they comprise only a small percentage of the playa deposit as a whole. Because of their high permeability relative to surrounding material, pumice stringers near the playa surface could be expected to saturate preferentially when water covers the playa, and thereby become enriched in water-borne carbonate. Pumice recovered from Type IV drill cuttings is indeed pervasively calcified, yielding up to 24% CO_2 by weight. A scarce amount of highly cemented playa deposit is also associated with the stringers. Because the bulk of the playa deposit is very fine and easily disaggregated, it is washed away in drilling fluid, and the pumice becomes highly concentrated in drill cuttings. Sidewall samples of Type IV deposits, in contrast, seldom contain pumice and usually measure less than 2% CO_2 by weight. Rare sidewall samples containing pumice yield higher CO_2 measurements. Although the calcified pumice stringers are a notable example of secondary calcium carbonate enrichment, their contribution to the overall CO_2 content of Type IV alluvium is small because of their very low volume.

Type V

Type V alluvium is the "basal tuffaceous alluvium" identified in Yucca Flat LLNL acreage (Wagoner, 1987). It is present in varying thickness throughout most of southern Yucca Flat, occurring immediately above the Tertiary volcanics at the base of the alluvial section. Type V reflects erosion of the youngest volcanic sediments in the Tertiary section during the first stages of alluvial deposition. Wide variation in Type V thickness, and its absence in some boreholes, suggest that deposition may have been controlled by existing topography, or that the deposits may have undergone erosion in some areas of southern Yucca Flat before being overlain by younger alluvium.

For all practical purposes, Type V is lithologically indistinguishable from Type III alluvium. Well-sorted tuffaceous sands typically comprise 98-100% of the deposit. Carbonate content generally is very low, occurring primarily as disseminated caliche.

Basal Caliche

The presence in some Yucca Flat drill holes of caliche-cemented zones at the base of the alluvial section has long been recognized. These zones can be classified as Stage III caliche development (Gile et al., 1966). Data from holes which penetrate the tuff/alluvium contact suggest that the occurrence of basal caliche is localized and somewhat restricted (Figure 7).

Sidewall samples of basal caliche often yield CO_2 values greater than 10%, in contrast with the typically low CO_2 content (1-3%) of the host alluvium (commonly Type V). Basal caliche in Yucca Flat is identifiable through correlation of this high CO_2 content with an increase in bulk density just above the tuff/alluvium contact (Figure 8). The log signature associated with the bulk density increase varies from subtle to quite distinct. Often the alluvium overlying the caliche zone will be washed out while the zone itself is in gauge, reflecting the competence imparted by the caliche cement. Increased resistivity and decreased natural gamma radiation sometimes highlight the intervals as well, but these

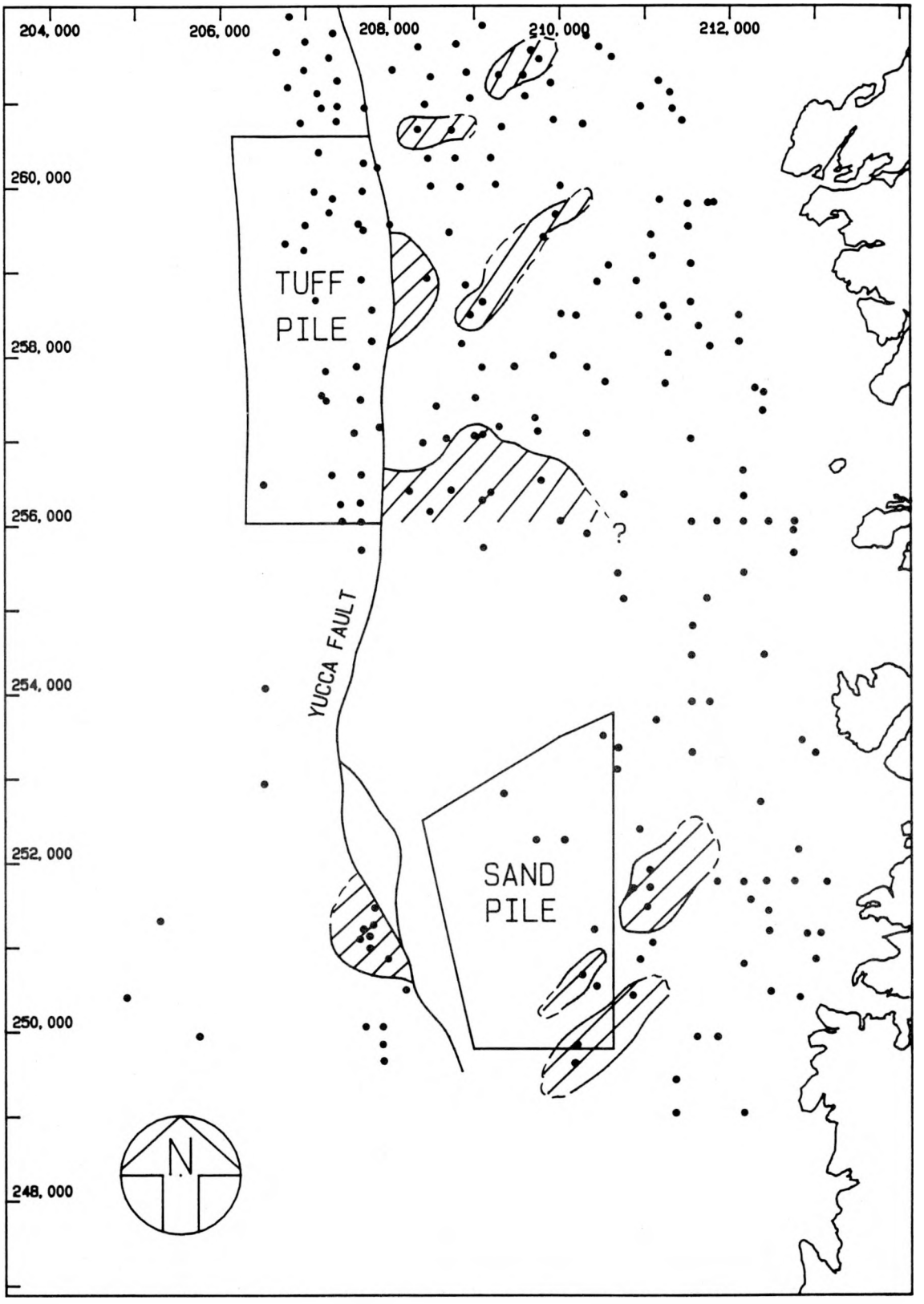


Figure 7--Basal caliche occurrence in southern Yucca Flat. Boundaries are dashed where more questionable. Dots represent boreholes which have penetrated the tuff-alluvium contact.

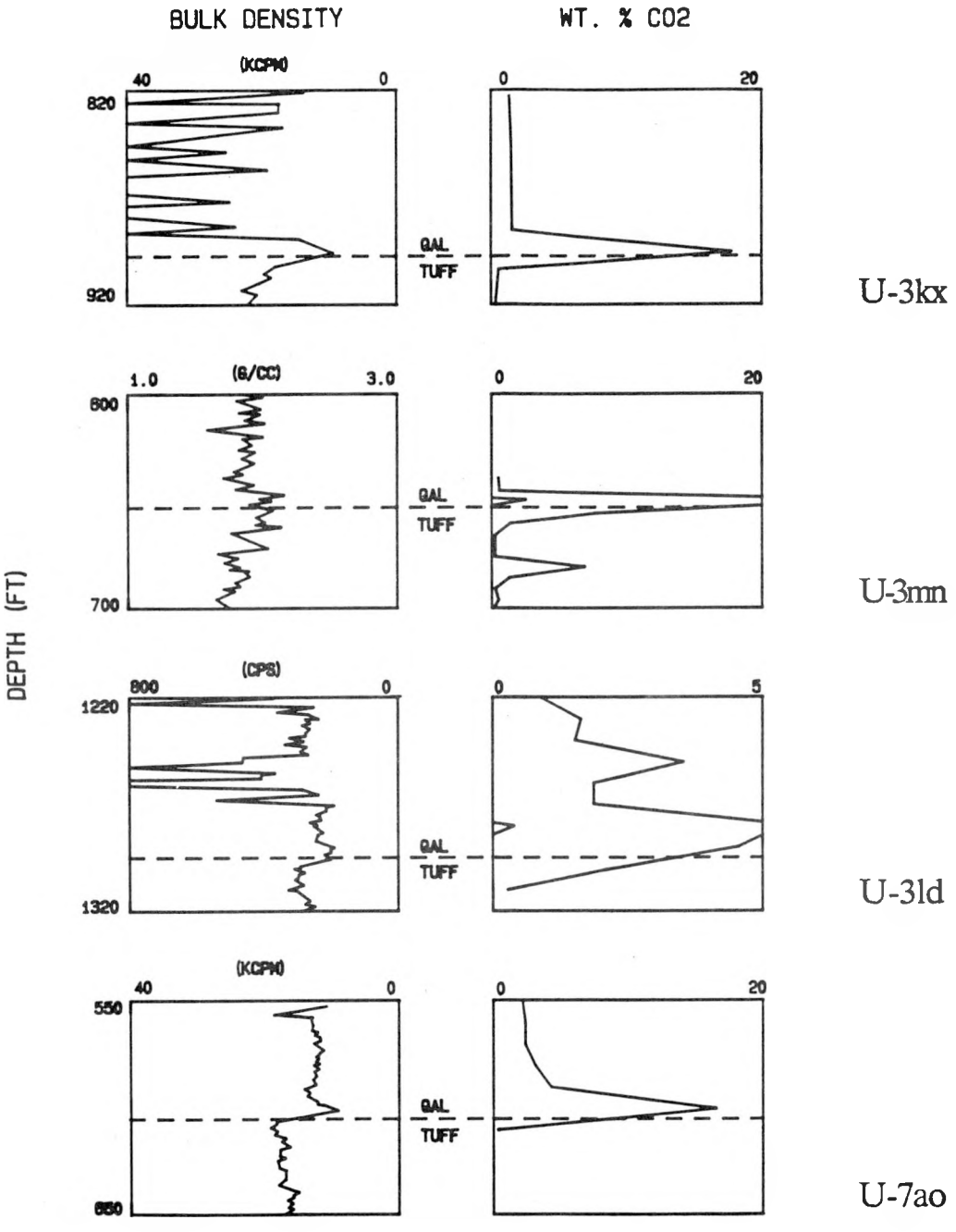


Figure 8--Identification of basal caliche in four southern Yucca Flat drill holes through correlation of increased bulk density and increased Hunt sidewall sample CO_2 content

signatures are not consistent. Sample descriptions sometimes corroborate CO_2 and geophysical data, identifying a zone of sharply increased caliche or calcareousness. Using these criteria, basal caliche ranging from 2-8 m thick can be identified in over 20 drill holes in southern Yucca Flat. In a few of these holes, the caliche zone is poorly developed, and is identified in samples as especially well-developed caliche rinds on individual clasts. The density log signature in such zones is correspondingly weaker than in well-developed zones.

Table 1--Characteristics of southern Yucca Flat alluvium types and carbonate occurrence

Alluvium Type	Lithologic Description	Primary Carbonate Occurrence	Weight % CO_2 Average	Weight % CO_2 Range	Recommended Sampling Method(s)	Diagnostic Tools
I	Fan gravels containing >5% carbonate clasts	Carbonate clasts (limestone and minor dolomite)	6	2.5 - 20	(1) Rotary sidewall[1] (2) Hunt sidewall[2] (3) Unwashed cuttings[3]	Sample descriptions Elevated CO_2 content Sample type comparison Bivariate plots Gamma and Density logs
II	Fan gravels containing <5% carbonate clasts	Caliche rinds on pebbles	2	0.5 - 3	(1) Rotary sidewall (2) Hunt sidewall (3) Unwashed cuttings	Sample descriptions Bivariate plots
III	Uniform tuffaceous sand	Disseminated caliche	1.4	0.1 - 2.5	Percussion gun sidewall	Uniform physical properties within and between boreholes Low CO_2 content Sample descriptions
IV	Playa deposits	Disseminated caliche with minor calcified pumice stringers	1.3	0.1 - 10[4]	Percussion gun sidewall	Electric log Sample type comparison
V	Tuffaceous sand at base of alluvial section	Disseminated caliche	1	0.1 - 2	Percussion gun sidewall	Stratigraphic position Sample descriptions Low CO_2 content
Basal Caliche	Zone of increased caliche at tuff/alluvium contact	Caliche-cemented aggregates, well-developed caliche rinds and stringers	9	4 - 21	(1) Rotary sidewall (2) Hunt sidewall (3) Percussion gun sidewall	Elevated CO_2 at base of alluvium Density log

1 Technique has not been tested extensively in alluvium
2 No longer routinely used at the NTS
3 See text for explanation of unwashed cuttings use for CO_2 measurements
4 Samples with CO_2 content >3% contain calcified pumice

Plotting the occurrence of basal caliche on an isopach map of Yucca Flat alluvium shows that the caliche tends to occur where the thickness contours become less steep and "flatten out", particularly beneath the central part of the basin. These areas may reflect paleotopographic lows and/or flat, less-active surfaces which were conducive to the formation of soils and caliche. Post-depositional tectonic activity certainly has influenced the steepness of the contours in some areas as well. The occurrence of the basal caliche can be highly localized; relatively thick intervals may pinch out or thin considerably between offsetting holes only several hundred meters apart.

Identification of depositional trends in basal caliche is complicated by lack of data, and particularly by the scarcity of holes penetrating the full alluvium section in central Area 3. A poorly defined north-south trend through the basin center is perhaps evident, and a number of the individual occurrences display northeast alignment. With the exception of the occurrence in extreme southwestern Area 3, identifiable basal caliche is limited to east of the Yucca Fault. Prospective zones may exist elsewhere in Yucca Flat which are not yet evident due to lack of drilling or incomplete data from existing holes.

CO_2 MEASUREMENT

Before being analyzed, CO_2 samples must undergo preparation to facilitate the analysis. Sample preparation introduces another step in which sample representation can be degraded if care is not exercised. A certain range of experimental error, intrinsic to the methods and the equipment used, is inevitable in the laboratory analysis itself. Measurement of CO_2 content from samples brings into consideration these operational variables.

Sample Preparation

The samples used for CO_2 measurements often are utilized for additional analyses. Multiple requirements necessitate splitting the sample into portions, with each split representing the sample as a whole. Once again, the uniformity and fineness of alluvium have a direct bearing on representation. Splitting fine, sandy material is clearly more straightforward than splitting a coarse, heterogeneous sample. This is particularly true of small splits, such as the 10-20 gm typically submitted for CO_2 measurement. A single small carbonate clast can have a disproportionately large effect in such cases.

Mechanical splitters have been tested on Yucca Flat alluvium samples, but these devices have been found to be of limited usefulness, unable to properly split samples containing large clasts. Probably the best way to ensure accurate splits is to pulverize a large portion of the sample, producing a homogeneous rock flour well suited for small splits. Because the procedure for measuring CO_2 requires a pulverized sample, this step serves the dual purpose of preparing the split for analysis. Many other routine analyses require pulverized samples as well, so that pulverizing most of the sample seldom presents a concern. It is advisable to thoroughly mix the pulverized sample before splitting it to be certain that it, too, is as homogeneous as reasonably achievable. If the sample cannot be pulverized before submitting it to the laboratory, it is important to make sure the laboratory has access to equipment suitable for grinding rock samples, and to emphasize that the entire submitted sample be pulverized rather than a portion of it.

Laboratory Analysis

Measurement of sample CO_2 content is performed at the NTS by the Health Physics Department of Reynolds Electrical and Engineering Company, Inc. (REECo). The analysis employed is simple and straightforward. A one gram portion of oven-dried, pulverized sample is treated with hydrochloric acid in a closed reaction vessel. The ensuing reaction produces CO_2 from carbonates within the sample. The vessel is heated to ensure that the reaction proceeds fully. The produced gas is passed through a tube filled with a desiccant to remove all water from it, and then into an absorption tube filled with a known quantity of Ascarite, a material which absorbs CO_2. When the carbonate in the sample has reacted fully with the acid, the absorption tube is weighed to determine the amount of CO_2 generated, and the results are reported as weight percent CO_2 of the sample. The maximum theoretical value obtainable in this procedure (i.e. the CO_2 content of a pure carbonate sample) is 44% CO_2 by weight.

The REECo laboratory routinely splits one sample in twenty into two portions, analyzes both to check repeatability, and reports both values. Quality control is also maintained through the analysis of two National Bureau of Standards reference samples for each twenty samples run. The results of these checks typically are well within the $\pm$ 10% experimental error which the laboratory assigns to CO_2 analysis results. Results from a suite of samples submitted by the Fenix & Scisson of Nevada Logging Department, consisting of known amounts of fine-grained carbonate combined with silica sand, suggest a significantly lower experimental error, on the order of $\pm$ 4%.

Attempts have been made in the past to assess laboratory consistency by submitting splits of previously analyzed samples and comparing the results with original CO_2 measurements. These studies have reported discrepancies between multiple splits of a single sample, particularly when the CO_2 content is relatively high. Such inconsistencies are almost certainly caused by a combination of the sampling and sample preparation factors discussed previously. It is not unusual in a suite of alluvium samples for one or more samples to yield high CO_2 measurements relative to the others. These "flyers" often are resubmitted for a second analysis. This necessitates resplitting the sample, and invariably draws special attention to the lithology of the sample and the representation of the split. Not surprisingly, the resubmitted splits often test much lower in CO_2 than the original split. In most cases, the anomalous measurement is found to result from a carbonate type which can easily be concentrated in a small sample split (e.g. carbonate clasts or thick caliche rinds on pebbles). It is apparent that the accuracy of laboratory CO_2 measurement is limited more by sampling technique and sample preparation (i.e. splitting) than by errors intrinsic to the laboratory procedure.

CONCLUSIONS

Experience in the containment of underground nuclear explosions has demonstrated an association between test media carbonate content and risk of containment failure. In the past, average carbonate content of approximately 11%, equating to 5% CO_2 by weight, was regarded by many to present an increased containment concern. To be sure, tests in environments containing in excess of 5% CO_2 have been successfully contained. Certainly each event is unique and must be considered on an individual basis. As testing acreage is exhausted and new testing areas are considered, the significance of the 5% CO_2 figure will likely come under increased consideration.

The containment scientist, in any case, has a need for accurate information about the carbonate content of the test media. Translation of alluvium CO_2 data into a meaningful estimate of carbonate content requires an appreciation of many factors influencing the data. Because of the variables involved, it is not realistic to treat individual sample CO_2 data as a precise measure of carbonate content for a particular depth or interval of alluvium. Patterns of carbonate content in alluvium are recognizable and correlative, however, and can be used to successfully predict range, variability and mode of occurrence for carbonate content at a given location. Using this information, the containment scientist can select hole locations and working point positions to avoid potential high CO_2 sources, design an effective sampling program and increase the confidence in a successful test containment.

REFERENCES

Bachman, G. O., and Machette, M. M., 1977, "Calcic Soils and Calcretes in the Southwestern United States": U. S. Geological Survey Open-File Report 77-794, 163 p.

Drellack, S. L., Jr., 1982, "Geologic Investigation into the U-7bp - U-7bc Hole Sloughing Problem": Fenix & Scisson, Inc. Report, 19 p.

-------, 1986, "Drill Hole Sample Report, Part 1: Grain Density Measurements": Fenix & Scisson, Inc. Report, 71 p.

Drellack, S. L., Jr., Thompson, P. H., and Rayburn, C. J., 1989, "Geology of the U-1a.01 Horizontal Drift Complex, Southwestern Yucca Flat, Nevada Test Site": U. S. Department of Energy Report DOE/NV/10322-37, 69 p.

Fernald, A. T., Corchary, G. S., and Williams, W. P., 1968, "Surficial Geologic Map of Yucca Flat, Nye and Lincoln Counties, Nevada": U. S. Geological Survey Map I-550.

Fernald, A. T., Brethauer, G. E., and Dixon, G. L., 1974, "Geology and Material Properties of the Area 3 Sand Pile, Southeastern Yucca Flat, Nevada Test Site": U. S. Geological Survey Special Projects Branch Report.

Gile, L. H., Peterson, F. F., and Grossman, R. B., 1966, "Morphological and Genetic Sequences of Carbonate Accumulation in Desert Soils": Soil Science, v. 99, no. 2, pp. 74-82.

Grothaus, B., and Howard, N., 1977, "Correlation of Alluvial Deposits at the Nevada Test Site": Lawrence Livermore National Laboratory Report UCRL-52335, 16 p.

Wagoner, J. L., 1983, "Influence of Geological Structure on Alluvial Sedimentation in Northwestern Yucca Flat, Nye County, Nevada": Proc. 2nd Symposium on Containment of Underground Nuclear Explosions, Kirtland AFB, Albuquerque, New Mexico, August 2-4, 1983, pp. 247-270. See also Lawrence Livermore National Laboratory Report UCRL-89415.

-------, 1987, "Making Sense of the Mixed Alluvium in the Yucca Flat Basin": Proc. 4th Symposium on Containment of Underground Nuclear Explosions, U. S. Air Force Academy, Colorado Springs, Colorado, September 21-24, 1987, vol. 2 Erratum, 27 p.

Wagoner, J. L., and McKague, H. L., 1984, "Variation of Physical Properties of Alluvium in an Arid Basin": Lawrence Livermore National Laboratory Report UCRL-90672, 25 p.

BOUND WATER CORRECTIONS TO EPITHERMAL-NEUTRON-DERIVED WATER CONTENTS

N. R. Burkhard and J. R Hearst
Lawrence Livermore National Laboratory
L-222, P.O. Box 808, Livermore, CA 94550

Abstract

Water contents from epithermal neutron logs are used with bulk density and grain density data to calculate the porosity, gas-filled porosity, and saturation of the geologic media surrounding emplacement holes. The epithermal neutron log measures the total hydrogen content of the formation; the water content is calculated from that . However, the derived water content includes both bound and free water. Four methods have been examined to separate the total water content into free and bound water. The methods are: 1.) determination of bound water from chemical formulae; 2.) corrections based upon epithermal neutron response to standard minerals; 3.) thermogravimetric analyses (heating) of samples; 4.) empirical corrections derived from the logging data. There are fundamental difficulties with each method. The problem centers around deciding what is free water and what is bound water and/or what is really present *in-situ*. But when a correction for bound water is made to the total water content, the calculated properties are changed. Gas porosity will always increase; porosity and saturation will always decrease. A case example illustrating all four techniques is presented.

Introduction

The porosity, gas-filled porosity, and saturation of the geologic media surrounding a nuclear test are calculated from measured bulk densities, measured grain densities, and measured water contents. The bulk densities are ordinarily determined from either density logs obtained with a gamma-gamma logging sonde or borehole gravimetry. The grain densities are obtained from pycnometer measurements on core or samples. The water contents are ordinarily determined from neutron logs obtained with an epithermal neutron sonde or occasionally from laboratory measurements on core or samples.

The neutron log measures the equivalent volume fraction water I_H, but at the Nevada Test Site water contents have traditionally been reported in terms of weight fraction, $F_W = I_H \rho_B$ where ρ_B is the bulk density. Then the "calculated properties" are obtained from:

porosity	$\phi = 1 - (\rho_B/\rho_G)(1 - F_w)$	(1)
gas - filled porosity	$\psi = \phi - F_w \rho_B$	(2)
saturation	$S = F_w \rho_B / \phi$	(3)

where ρ_G is the grain density. The value of F_W obtained from the neutron log includes not only the water in the pores, as assumed in Eq. (1-3), but also any water that may be bound in the matrix minerals. For the values in Eq. (1-3) to be correct, F_W must be the pore or "free" water. (The effect of the presence of the "bound" water is already included in ρ_G .)

If the water contents are not corrected to reflect only free water, the calculated saturation and porosity will always be too large and the calculated gas-filled porosity will be too small. In other words, if a correction for bound water is not made and the total water content from the epithermal neutron log is used to calculate these physical properties, we will always underestimate the amount of gas-filled porosity and overestimate the saturation and porosity of the formation. This is readily shown from the Eq. (1-3).

The separation of free and bound water has been extensively studied. At LLNL alone, three different sets of authors have studied the problem [1,2,3]. However, these studies all examined the question of separating the free water from the bound water when laboratory analyses using thermogravimetric techniques (heating) were utilized on core or samples. The epithermal neutron log is a totally different technique for determining water content. Hence, we decided to examine how corrections for bound water could be made to epithermal-neutron-derived water contents.

Water Content from Epithermal Neutron Logs

An epithermal neutron log measures the hydrogen content of the formation. High energy neutrons (~1-12 MeV) produced by logging sonde's neutron source are slowed down mostly by collisions with hydrogen atoms in the formation. The system counts the number of neutrons which are detected by the sonde in the epithermal neutron energy range (~0.1 eV to 1 keV). In essence, the sonde is measuring the number of hydrogen atoms which are present in the formation; the sonde is primarily sensitive to the hydrogen index I_H. The hydrogen index is

defined as the volume fraction of fresh water that would contain the same amount of hydrogen.

In other words, the epithermal neutron log does not directly measure the water content of the formation. The water content is inferred from the amount of hydrogen detected in the formation; all hydrogen is assumed to be associated with water. In a rock of porosity ϕ and saturation S_w, containing fresh water and no other hydrogen, $I_H = \phi S$. If the formation contains bound water or salt water, $I_H > \phi S$. Additional information on the theory of epithermal neutron logging for water content can be found in Hearst and Nelson [4].

Determination of Free Water

The problem of separating the bound from the free water is more difficult with the epithermal neutron log data than with laboratory heating of samples, since the epithermal-neutron water contents include water calculated from hydrogen atoms which would never be detected in the heating of laboratory samples. The weight fraction free water content F_{FW} can be calculated from the weight fraction total water content water F_{TW} and the weight fraction bound water F_{BW} using the following equations and definitions:

$$F_{FW} = (F_{TW} - F_{BW})/(1 - F_{BW}) \quad (4)$$

$$F_{FW} = M_{FW}/(M_{FW} + M_{BW} + M_{rock}) \quad (5)$$

$$F_{BW} = M_{BW}/(M_{rock} + M_{BW}) \quad (6)$$

$$F_{TW} = (M_{FW} + M_{BW})/(M_{FW} + M_{BW} + M_{rock}) \quad (7)$$

where M_{rock} = mass of rock per unit volume

M_{FW} = mass of free water per unit volume

M_{BW} = mass of bound water per unit volume

Four methods were tried to estimate the weight fraction bound water to insert into Eq. (4) to obtain estimates of F_{FW} from F_{TW}. The methods are: 1.) determination from chemical formulae; 2.) corrections based upon epithermal neutron response to standard minerals; 3.) thermogravimetric analyses (heating) of samples; 4.) empirical corrections derived from the logging data. There are fundamental difficulties with each method. The main problem centers around deciding what is free water and what is bound water and/or what is really present *in situ*.

Determination of Bound Water from Chemical Formulae

This technique requires that the mineralogy of the formation be known. LLNL obtains quantitative estimates of the mineralogy from X-ray diffraction (XRD) analyses. At the NTS, the geologic media are composed of a very limited number of minerals. Generally, this number does not exceed 13, with most samples being composed of only three or four main minerals. The minerals which contain the most hydrogen (to which the epithermal neutron log responds) are the clays and the zeolites. For example, these minerals are the typically found at NTS:

Clinoptilolite	$(Na,K,Ca)_6(Si,Al)_{36}O_{72} \cdot 20\ H_2O$
Kaolinite	$Al_2Si_2O_5(OH)_4$
Montmorillonite	$Al_4Si_8O_{20}(OH)_4 \cdot n\ H_2O$

Note that these minerals have hydrogen in both (OH) groups and bound water. The epithermal neutron log counts all hydrogen atoms. The equivalent weight fraction bound water that results from these hydrogen atoms can be determined from the quantitative estimates of the mineralogy in a sample and with chemical formulas obtained from standard references [5,6]. We used the following equation to obtain the weight fraction equivalent bound water:

$$F_{BW} = \sum_{i=1}^{\#\ of\ minerals} a_i \left\{ \frac{18\left(H_i/2\right)}{A_i} \right\} \qquad (8)$$

a_i = weight fraction of mineral i in sample

H_i = number of hydrogen atoms in mineral i

A_i = molecular weight of mineral i

If quantitative XRD data are available, the calculation is easily performed once a chemical formula is assigned to each mineral in the sample. In reality, unfortunately, the number of bound water molecules attached to a mineral *in situ* at NTS is not known. Moreover, the chemical formula of a mineral *in situ* is also not known, but, within reason, the exact form of the chemical formula for the mineral, excluding the number of bound water atoms, does not significantly affect this estimate of F_{BW}.

Bound Water from Epithermal Neutron Response to Standard Minerals

The response of an epithermal neutron logging tool to standard minerals was described by Edmundson and Raymer [7]. In this paper, the response of an epithermal neutron tool to pure laboratory-standard minerals (after heating to 105°C) was determined. From these responses, the apparent volume fraction water for each mineral was calculated by assuming that all hydrogen was locked into water molecules. Presumably, no free water was present, so the apparent water is a measure of the bound water for each mineral. The primary difficulty with this method is that the epithermal neutron tool used in the paper was not operating in the same large-hole environment as the NTS logging sonde; we use a decentered epithermal neutron sonde mounted on a large carriage. Another potential problem is that Edmundson and Raymer do not indicate whether they tested the samples "hot" at 105°C or whether they allowed the minerals to cool off first. If the samples had cooled before measuring the neutron response, the minerals would have reabsorbed water which would have been driven off at 105°C. A further problem is that some of the water driven off in the heating process before 105°C might actually be bound water. The total weight fraction bound water for a sample is calculated from the quantitative XRD analyses and the epithermal neutron responses as follows:

$$F_{BW} = \sum_{i=1}^{\#\ of\ minerals} a_i \left\{ \frac{\tau_i}{\rho_i} \right\} \qquad (9)$$

a_i = weight fraction of mineral i in sample

τ_i = apparent volume fraction of water in mineral i

ρ_i = bulk density of mineral i at 105°C in sample

This method still has the same problem as the chemical formula technique; we do not really know whether the laboratory standard minerals represents *in-situ* conditions at NTS. The number of bound water molecules in the standard minerals may be different than the number attached to the minerals *in situ*; the chemical composition for the minerals may also be slightly different.

Bound Water from Thermogravimetric Analyses

Thermogravimetric analyses measure the differences in the mass of a sample as it is heated to various temperatures. The procedure is the ordinary laboratory procedure to determine water content of a sample. The main difficulties involve knowing what type of water is being

liberated from the sample (free or bound water). A common technique is to declare that water liberated below 105°C is free water and that water liberated above 105°C is bound water. However, detailed analyses show that some bound water is liberated below 105°C as well and some free water is still present above 105°C. Therefore, it is difficult to determine exactly what is free and what is bound water from this technique. Another problem is that above certain temperatures other chemical reactions occur, which liberate gases other than water vapor from the minerals. (This issue can be dealt with by measuring the evolved water.) The method also requires a sample which is representative of *in-situ* conditions; however almost any sample-gathering process has the potential for changing the free and/or bound water content of the sample. The weight fraction bound water using the standard 105°C assumption is calculated:

$$F_{BW} = \frac{M_{500°C} - M_{105°C}}{M_{105°C}} \tag{10}$$

With F_{BW} from Equation (10), F_{FW} can be calculated using Equation (4).

Empirical Bound Water Corrections Derived from Logging Data

The empirical bound water correction is derived by directly examining the parameters calculated from the logs. The basic assumption is that the saturation can never exceed 100%. The correction is determined for a reasonably long region of the hole where the calculated saturation exceeds 100%; this procedure would not apply if just one depth horizon exceeded 100% saturation. If the bulk density log, the epithermal neutron log, and the grain densities are reliable in this region, then a lower limit on the bound water can be determined by calculating what the free water content needs to be in order to have only 100% saturation on the average across the zone. The weight fraction free water content can be calculated from the following equation:

$$F_{FW} = \left(\frac{1}{\rho_B} - \frac{1}{\rho_G}\right) \Big/ \left(1 - \frac{1}{\rho_G}\right) \tag{11}$$

F_{BW} can then be calculated from Equation (4). This value of F_{BW} is then used in the entire region for which the mineralogy is about the same as that in the region used for the calculation.

Case Example from U20az

In hole U20az Site Characteristic Report [8] , the lithology log indicates that the volcanic units were becoming zeolitic starting around 350 m depth and became highly zeolitic around 400 m. XRD analyses (Table 1) show that the samples from 427 m to 680 m have significant amounts of clinoptilolite (a member of the zeolite mineral family). The epithermal neutron log shows an increase in total water content from 12-13 wt % water content above about 350 m to about 20 wt % water content below about 400 m. If these water contents are used to calculate the porosity, saturation, and gas-filled porosity of the formation, the entire depth interval for the formation appears to be highly saturated between 400 m and 680 m even though the standing water level is around 661 m (Figure 1). Each of the methods listed above was tried to determine what the calculated properties would be if bound-water corrections were made to the total water content from epithermal neutron log. Of course, we still do not know the true *in-situ* conditions; thus we can only discuss the plausibility of the results and cannot determine which method is better.

The XRD analyses for U20az indicate that most of the hydrogen content of the minerals is in clinoptilolite and montmorillonite. From the XRD analyses alone, we are unable to determine the number of water molecules attached to each mineral, so to use the chemical formula technique, we assumed that the cliniptilolite and montmorillonite have twenty and five water molecules respectively bound to the mineral (n=20 and n= 5). The numbers seemed reasonable based upon standard formulas for the minerals given in the literature [5,6]. Tables 2 and 3 illustrate the sensitivity of the calculated properties to the assumptions regarding the number of water molecules attached to the minerals. Using reasonable values from the literature for the number of water molecules, the bound water weight fraction ranges from about 4 to 12 wt % for the U20az example.

The bound water weight fraction from the epithermal neutron response to standard minerals was calculated from the XRD analyses and the neutron log responses given in Edmundson and Raymer [7]. The bound water ranges from about 4 to 11 wt %. Table 4 illustrates the calculations for the U20az example.

Thermo-gravimetric analyses were done only for a sample at 427 m. This sample was almost pure climoptilolite (~86 wt %). For this sample, 4.1 wt % water was driven off from 105°C to 500°C. However, from 20°C to 105°C, about 7.5 wt % water was also driven off. This latter fraction contained both free and bound water, in unknown proportions. Hence a lower and

Table 1.

XRD Analyses of Samples from U20AZ
(Wt%)

Depth Ft	Depth M	*	Quar	Mont	Illi	Clin	Cris	Feld	Calc	Dolo	Glas	Horn	Kaol	Musc	Biot
1400.	427.	C	3.	0.	0.	89.	0.	8.	0.0	0.0	0.	0.	0.	0.	0.
1400.	427.	C	3.	6.	0.	83.	0.	8.	0.0	0.0	0.	0.	0.	0.	0.
1730.	527.	C	4.	0.	0.	88.	0.	8.	0.0	0.0	0.	0.	0.	0.	0.
1790.	546.	C	8.	0.	0.	81.	0.	10.	0.0	0.0	0.	0.	0.	0.	0.
1830.	558.	C	6.	7.	0.	65.	0.	21.	0.0	0.0	0.	0.	0.	0.	0.
1860.	567.	C	16.	0.	0.	72.	0.	12.	0.0	0.0	0.	0.	0.	0.	0.
1920.	585.	C	11.	7.	0.	68.	0.	13.	0.0	0.0	0.	0.	0.	0.	0.
1960.	597.	C	8.	5.	0.	72.	0.	15.	0.0	0.0	0.	0.	0.	0.	0.
2000.	610.	C	28.	0.	0.	56.	0.	15.	0.0	0.0	0.	0.	0.	0.	0.
2050.	625.	C	22.	12.	0.	50.	0.	15.	0.0	0.0	0.	0.	0.	0.	0.
2100.	640.	C	28.	13.	0.	41.	0.	18.	0.0	0.0	0.	0.	0.	0.	0.
2130.	649.	C	35.	0.	0.	40.	0.	25.	0.0	0.0	0.	0.	0.	0.	0.
2160.	658.	C	34.	0.	0.	42.	0.	24.	0.0	0.0	0.	0.	0.	0.	0.
2230.	680.	C	11.	14.	10.	50.	0.	15.	0.0	0.0	0.	0.	0.	0.	0.

Total number of samples: 14

Minerals

Quar = Quartz
Mont = Montmorillonite
Illi = Illite
Clin = Clinoptilolite
Cris = Cristobalite
Feld = Feldspars
Calc = Calcite
Dolo = Dolomite
Glas = Glass
Horn = Hornblende
Kaol = Kaolinite
Musc = Muscovite
Biot = Biotite

Analyst: Pawloski
XRD report date: 30-MAR-1989
Sample date: 02-DEC-1988

* Indicates sample type
C = Cuttings
G = Percussion gun
S = Hunt sidewall
M = Sidewall core

THE TWO ANALYSES AT 1400' ARE FROM TWO SPLITS OF THE SAME SAMPLE.

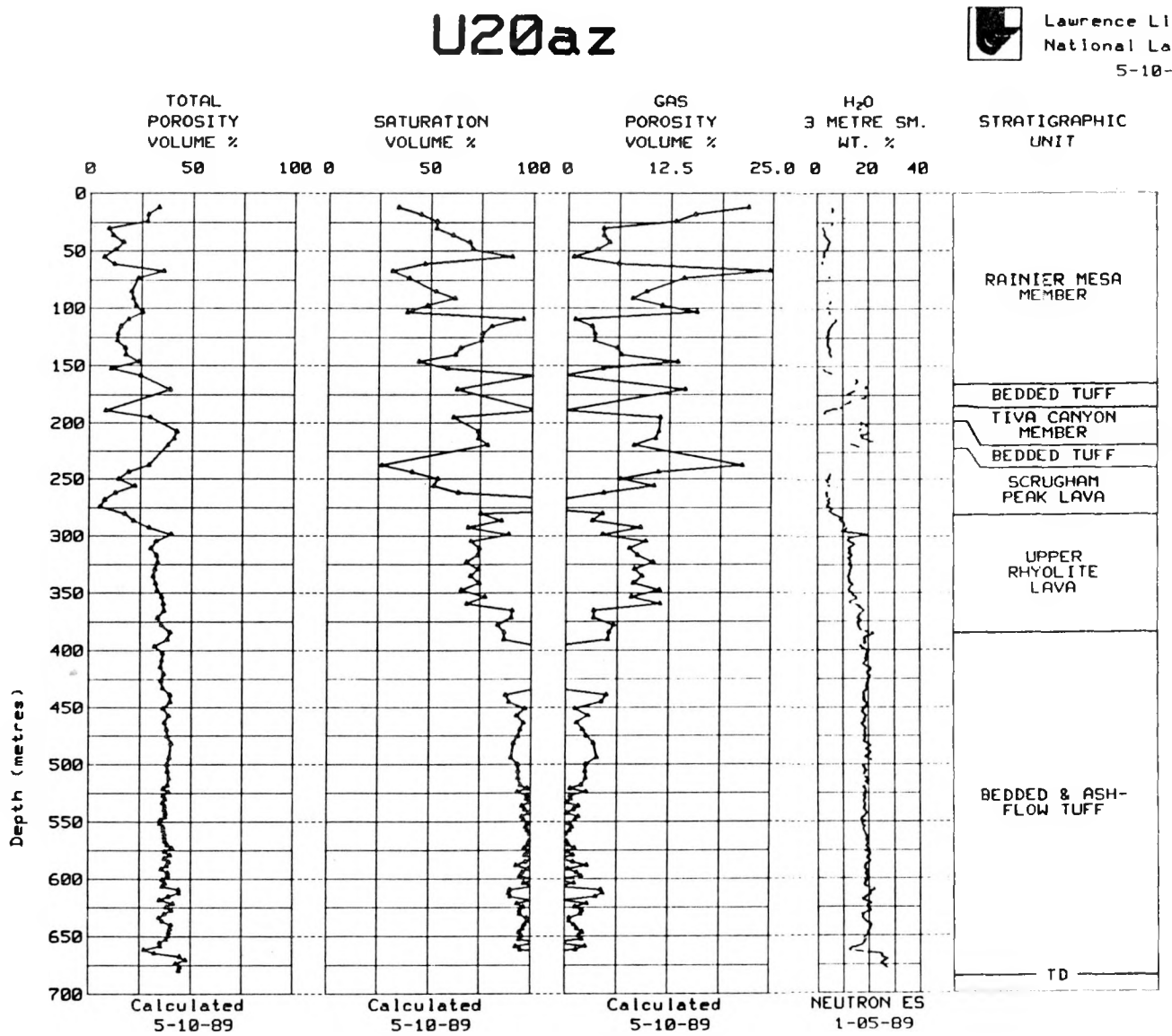


Figure 1. Water content log for U20az derived from epithermal neutron logging. The total porosity, saturation, and gas porosity calculated from the grain densities, bulk densities, and the water contents are also illustrated. Note that below 400 m depth, the formation is near 100% saturation and has little gas-filled porosity.

Table 2. Bound water corrections based upon XRD quantitative analyses and chemical formulae - the hydrogen associated with montmorillonite and clinoptilolite is contained in bound water molecules. In this example, 5 and 20 molecules were assumed to be associated with montmorillonite and clinoptilolite, respectively. The corrected values for gas porosity, saturation, and porosity are presented.

Depth	Mont	Clin	Clin corr	Mont corr	Bound Water	Free Water	Total Water	Grain	Bulk	Gas Por	Gas corr	Porosity	Por corr	Saturation	Sat corr
427	3	86	0.115	0.007	0.122	0.082	0.194	2.47	2	-0.041	0.093	0.347	0.256	1.117	0.636
527	0	88	0.118	0.000	0.118	0.070	0.18	2.59	2	0.007	0.142	0.367	0.282	0.981	0.498
546	0	81	0.109	0.000	0.109	0.082	0.182	2.58	1.97	0.017	0.137	0.375	0.299	0.955	0.542
558	7	65	0.087	0.017	0.104	0.085	0.18	2.58	2	0.004	0.121	0.364	0.291	0.988	0.585
567	0	72	0.097	0.000	0.097	0.103	0.19	2.55	1.96	0.005	0.108	0.377	0.311	0.987	0.652
585	7	68	0.091	0.017	0.108	0.105	0.201	2.54	1.92	0.010	0.122	0.396	0.323	0.974	0.621
597	5	72	0.097	0.012	0.108	0.093	0.191	2.56	1.93	0.021	0.137	0.390	0.316	0.945	0.566
610	0	56	0.075	0.000	0.075	0.157	0.22	2.53	1.81	0.044	0.113	0.442	0.397	0.901	0.715
625	12	50	0.067	0.028	0.095	0.107	0.192	2.53	1.93	0.013	0.113	0.384	0.319	0.966	0.647
640	13	41	0.055	0.031	0.086	0.133	0.207	2.55	1.91	0.011	0.097	0.406	0.350	0.974	0.723
649	0	40	0.054	0.000	0.054	0.149	0.195	2.56	1.93	0.017	0.070	0.393	0.359	0.957	0.804
658	0	42	0.056	0.000	0.056	0.116	0.166	2.54	1.97	0.026	0.086	0.353	0.315	0.926	0.728
680	14	50	0.067	0.033	0.100	0.174	0.257	2.53	1.89	-0.041	0.054	0.445	0.383	1.092	0.860
# H20	5	20		Mont=		Weigth fraction of sample that is montmorillonite									
attached to minerals				Clin =		Weight fraction of sample that is clinoptilolite									
				Clin corr =		Weight fraction bound water in clinoptilolite									
				Mont corr =		Weight fraction bound water in montmorillonite									
				Bound Water =		Weight fraction bound water in sample									
				Free Water =		Weight fraction free water in sample									
				Total Water =		Weight fraction total water from epithermal neutron log									
				Grain =		Grain density of sample									
				Bulk =		Bulk density of sample									
				Gas Por =		Gas porosity uncorrected for bound water									
				Gas corr =		Gas porosity corrected for bound water									
				Porosity =		Porosity uncorrected for bound water									
				Por corr =		Porosity corrected for bound water									
				Saturation =		Saturation uncorrected for bound water									
				Sat corr =		Saturation corrected for bound water									

Table 3. Bound water corrections based upon XRD quantitative analyses and chemical formulae - the hydrogen associated with montmorillonite and clinoptilolite is contained in bound water molecules. In this example, 3 and 6 molecules were assumed to be associated with montmorillonite and clinoptilolite, respectively. The corrected values for gas porosity, saturation, and porosity are presented.

Depth	Mont	Clin	Clin corr	Mont corr	Bound Water	Free Water	Total Water	Grain	Bulk	Gas Por	Gas corr	Porosity	Por corr	Saturation	Sat corr
427	3	86	0.038	0.005	0.043	0.158	0.194	2.47	2	-0.041	0.003	0.347	0.318	1.117	0.991
527	0	88	0.039	0.000	0.039	0.147	0.18	2.59	2	0.007	0.048	0.367	0.341	0.981	0.860
546	0	81	0.036	0.000	0.036	0.151	0.182	2.58	1.97	0.017	0.054	0.375	0.352	0.955	0.848
558	7	65	0.029	0.012	0.041	0.145	0.18	2.58	2	0.004	0.047	0.364	0.337	0.988	0.860
567	0	72	0.032	0.000	0.032	0.163	0.19	2.55	1.96	0.005	0.037	0.377	0.357	0.987	0.897
585	7	68	0.030	0.012	0.042	0.166	0.201	2.54	1.92	0.010	0.051	0.396	0.369	0.974	0.862
597	5	72	0.032	0.009	0.041	0.157	0.191	2.56	1.93	0.021	0.062	0.390	0.364	0.945	0.831
610	0	56	0.025	0.000	0.025	0.200	0.22	2.53	1.81	0.044	0.066	0.442	0.428	0.901	0.847
625	12	50	0.022	0.021	0.043	0.156	0.192	2.53	1.93	0.013	0.055	0.384	0.356	0.966	0.845
640	13	41	0.018	0.022	0.040	0.174	0.207	2.55	1.91	0.011	0.049	0.406	0.381	0.974	0.870
649	0	40	0.018	0.000	0.018	0.180	0.195	2.56	1.93	0.017	0.034	0.393	0.382	0.957	0.911
658	0	42	0.019	0.000	0.019	0.150	0.166	2.54	1.97	0.026	0.045	0.353	0.341	0.926	0.868
680	14	50	0.022	0.024	0.046	0.221	0.257	2.53	1.89	-0.041	0.000	0.445	0.418	1.092	0.999
# H20	3	6		Mont=		Weigth fraction of sample that is montmorillonite									
attached to minerals				Clin =		Weight fraction of sample that is clinoptilolite									
				Clin corr =		Weight fraction bound water in clinoptilolite									
				Mont corr =		Weight fraction bound water in montmorillonite									
				Bound Water =		Weight fraction bound water in sample									
				Free Water =		Weight fraction free water in sample									
				Total Water =		Weight fraction total water from epithermal neutron log									
				Grain =		Grain density of sample									
				Bulk =		Bulk density of sample									
				Gas Por =		Gas porosity uncorrected for bound water									
				Gas corr =		Gas porosity corrected for bound water									
				Porosity =		Porosity uncorrected for bound water									
				Por corr =		Porosity corrected for bound water									
				Saturation =		Saturation uncorrected for bound water									
				Sat corr =		Saturation corrected for bound water									

Table 4. Bound water corrections based upon XRD quantitative analyses and the response of the epithermal neutron sonde. The corrected values for gas porosity, saturation, and porosity are presented.

Depth	Quar	Mont	Illi	Clin	Cris	Feld	Calc	Dolo	Horn	Kaol	Musc	Biot	Bound Water	Free Water	Total Water	Grain	Bulk	Gas Por	Gas Corr	Porosity	Por Corr	Saturation	Sat Corr
427	4	2	0	86	0	8	0	0	0	0	0	0	0.111	0.094	0.194	2.47	2.00	-0.041	0.079	0.347	0.266	1.117	0.704
527	4	0	0	88	0	8	0	0	0	0	0	0	0.112	0.077	0.180	2.59	2.00	0.007	0.134	0.367	0.287	0.981	0.535
546	8	0	0	81	0	10	0	0	0	0	0	0	0.101	0.090	0.182	2.58	1.97	0.017	0.128	0.375	0.305	0.955	0.580
558	6	7	0	65	0	21	0	0	0	0	0	0	0.079	0.109	0.180	2.58	2.00	0.004	0.091	0.364	0.310	0.988	0.707
567	16	0	0	72	0	12	0	0	0	0	0	0	0.088	0.112	0.190	2.55	1.96	0.005	0.098	0.377	0.317	0.987	0.691
585	11	7	0	68	0	13	0	0	0	0	0	0	0.088	0.124	0.201	2.54	1.92	0.010	0.100	0.396	0.338	0.974	0.706
597	8	5	0	72	0	15	0	0	0	0	0	0	0.090	0.111	0.191	2.56	1.93	0.021	0.116	0.390	0.329	0.945	0.648
610	28	0	0	56	0	15	0	0	0	0	0	0	0.064	0.166	0.220	2.53	1.81	0.044	0.103	0.442	0.404	0.901	0.746
625	22	12	0	50	0	15	0	0	0	0	0	0	0.066	0.135	0.192	2.53	1.93	0.013	0.080	0.384	0.340	0.966	0.765
640	28	13	0	41	0	18	0	0	0	0	0	0	0.053	0.162	0.207	2.55	1.91	0.011	0.062	0.406	0.373	0.974	0.833
649	35	0	0	40	0	25	0	0	0	0	0	0	0.037	0.164	0.195	2.56	1.93	0.017	0.053	0.393	0.370	0.957	0.856
658	34	0	0	42	0	24	0	0	0	0	0	0	0.041	0.131	0.166	2.54	1.97	0.026	0.068	0.353	0.326	0.926	0.791
680	11	14	10	50	0	15	0	0	0	0	0	0	0.074	0.198	0.257	2.53	1.89	-0.041	0.027	0.445	0.401	1.092	0.933

Neutron Response			
Quartz=	0.00	Key for mineral names is given in Table 1.	
Mont=	0.08		
Illi=	0.06	Bound Water =	Weight fraction bound water in sample
Clin=	0.13	Free Water =	Weight fraction free water in sample
Cris=	-0.01	Total Water =	Weight fraction total water from epithermal neutron log
Feld=	-0.06	Grain =	Grain density of sample
Calc=	0.00	Bulk =	Bulk density of sample
Dolo=	0.01	Gas Por =	Gas porosity uncorrected for bound water
Horn=	0.01	Gas corr =	Gas porosity corrected for bound water
Kaol=	0.14	Porosity =	Porosity uncorrected for bound water
Musc=	0.04	Por corr =	Porosity corrected for bound water
Biot=	0.00	Saturation =	Saturation uncorrected for bound water
		Sat corr =	Saturation corrected for bound water

upper limit for bound water can be established for this sample; these limits are 4.1 and 11.6 wt % respectively.

An empirical correction to the logging data was determined at a depth of 427 m. Using measured epithermal neutron water contents the saturation was calculated as 112.6 %. Using Equations (4) and (11) and assuming 100% saturation, the lower limit for the bound water was calculated to be ~4.5 wt %. Obviously the weight fraction bound water could be much higher than this limit.

These estimates for the sample at 427 m can be summarized as follows:

Measurement Technique	Bound Water (wt %)
Chemical formulae	4.3-12.2
Neutron response	11.1
Thermo-gravimetric	>4.1 and <11.6
Empirical correction	>4.5

Figure 2 shows the calculated properties with these ranges applied over the entire interval from about 427 m to total depth. Note that the saturation now rises slightly and the gas-filled porosity falls as the SWL is approached. This is consistent with our expectations before performing any of these calculations. Note however, that we are unable to determine which bound water correction is appropriate for the *in-situ* conditions at U20az.

Conclusions

The epithermal neutron log measures the total hydrogen content of the formation, I_H. An apparent water content is calculated from I_H. However, the calculated total water content includes both bound and free water. Four methods have been examined to separate the total water content into free and bound water. The methods are: 1.) determination from chemical formulae; 2.) corrections based upon epithermal neutron response to standard minerals; 3.) thermogravimetric analyses (heating) of samples; 4.) empirical corrections derived from the logging data. There are fundamental difficulties with each method. The problem centers around deciding what is free water and what is bound water and/or what is really present *in-situ*. However, when a correction for bound water is made to the total water content, the calculated properties are changed. The gas-filled porosity will always increase; the porosity and saturation will always decrease.

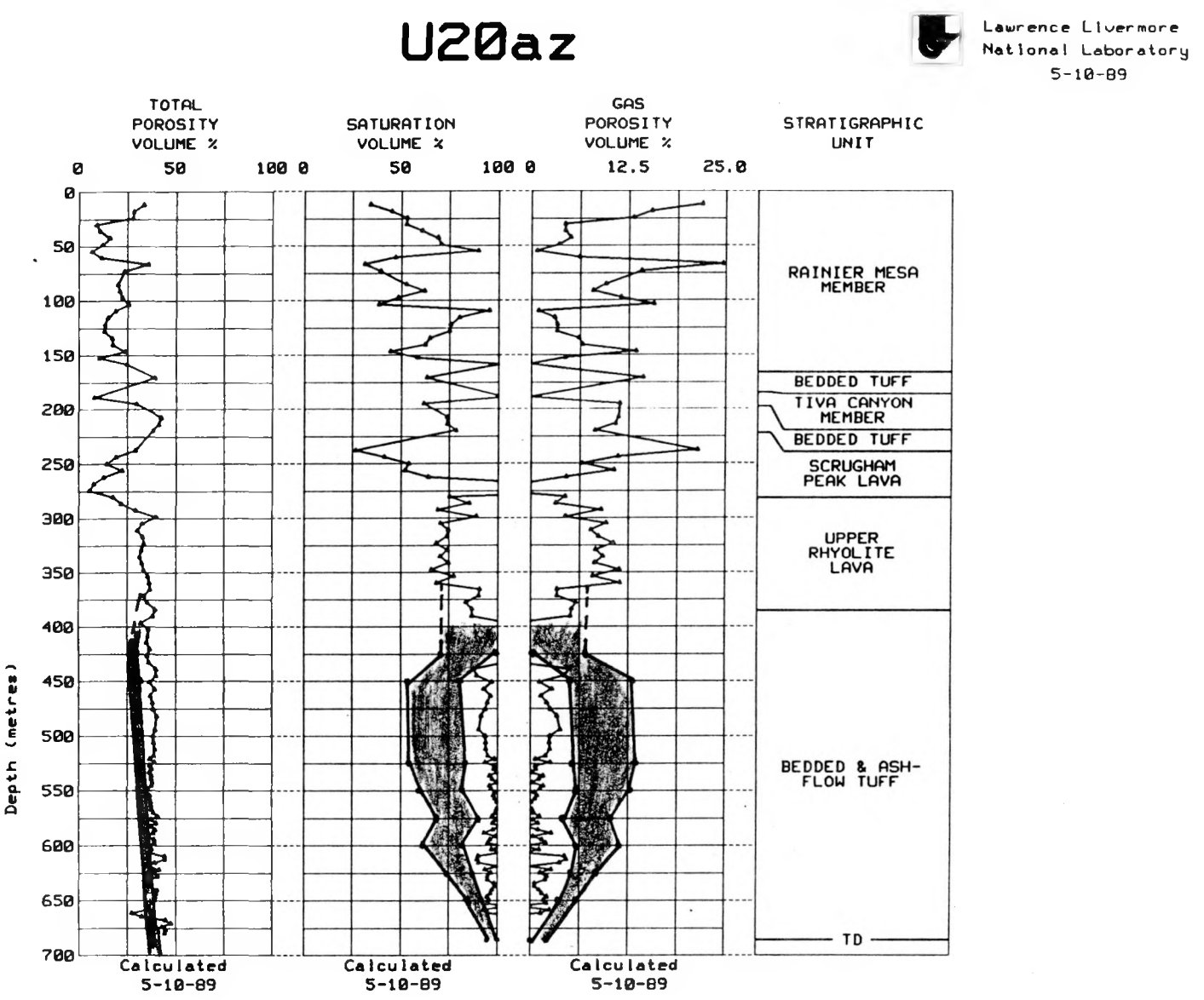


Figure 2. The total porosity, saturation, and gas porosity for U20az - the shaded region is the range for these properties after corrections for bound water using all four methods are made to the epithermal neutron log water contents.

Acknowledgements

The work was performed under the auspices of the U.S. Department of Energy by the Lawrence Livermore National Laboratory under Contract W-7405-ENG-48. This work was supported by the Nuclear Test Containment Program.

References

1. Knowlton, G. D. and H. L. McKague, "A Study of the Water Content in Zeolitic Tuffs from the Nevada Test Site", Lawrence Livermore National Laboratory, UCRL-78013 (1976).
2. Borg, I. Y. and Morris, C., "Some general information on water contained by clay minerals and some specific information on water released at > 105°C in caly-rich horizons in Area 8 (U8e, Ue8f, and Ue8i)", UCON 73-39, 1979 (Internal LLNL Memo).
3. Pawloski, Gayle A., "Water Contents of Samples from the Nevada Test Site: Total, Free (Natural State to 105°C), and More Tightly Bonded (105-700°C)", Lawrence Livermore National Laboratory, UCRL-53130 (1981).
4. Hearst, J. R and Nelson, P. H., "Well Logging for Physical Properties", McGraw Hill, New York, New York (1985).
5. Bayliss, P., Smith, D. K., Mrose, M. E., and Berry, L. G. (ed.), "Mineral Powder Diffraction File Data Book",International Centre for Diffraction Data, 1601 Park Lane, Swarthmore, Pennsylvania (1980).
6. Deer, W. A., Howie, R. A., Zussman, J., "An Introduction to the Rock-Forming Minerals", Longman Group Limited, London, England (1978).
7. Edmundson, H. and Raymer, L. L., "Radioactive Logging Parameters for Common Minerals", Proceedings of the SPWLA Twentieth Annual Logging Symposium, June 3-6, 1979.
8. Burkhard, N. R. and Wagoner, J. L., "U20az Site Characteristic Report", LLNL Internal Memorandum CP 89-67, April 30, 1989.

Geophysics and Material Properties



Physical Properties in LLNL Yucca Flat Areas: The ROCK PILE Concept

Norman R. Burkhard
Lawrence Livermore National Laboratory
L-222, P.O. Box 808, Livermore, CA 94550

Abstract

Physical properties measurements (grain density, bulk density, water content and seismic travel time) have been made for over two decades in Yucca Flat. These properties for LLNL portions of Yucca Flat have been studied to determine whether further measurements of these properties are needed. The basic data set consists of the zonal averages of the LLNL Yucca Flat stratigraphic units for bulk density, grain density, water content, porosity, gas-filled porosity, and saturation and of the average work point velocities and average overburden velocities. The errors associated with the zonal averages were calculated and used to determine whether future measurements are warranted. The velocity data were fitted with smooth functional forms to determine whether velocity is predictable from depth alone.

Analysis of the measurements indicates that an adequate sampling of the units in Yucca Flat has been obtained for the average physical properties of the stratigraphic units. Further measurement of grain densities at specific depth horizons is not needed because assuming that the grain density of a given stratigraphic unit is known would not increase the error in the calculated properties by a significant amount. Larger contributions to the calculated errors in porosity, gas-filled porosity, and saturation come from measurement errors in bulk density and water content. The error associated with assuming a bulk density and a water content for a stratigraphic unit is comparable to the measurement error for these properties. Therefore these properties and the properties calculated from them can usually be assumed with about the same accuracy as if measurements had been made. Consequently it appears that what is really needed is a measurement which would determine the presence of anomalous properties. The average overburden velocity and the average work point velocity are not as predictable as the physical properties of the stratigraphic units.

I propose that the following methodology be considered as an adequate characterization of the physical properties of a LLNL Yucca Flat site. The grain densities, bulk densities, water

contents, porosities, gas-filled porosities, and saturations of the stratigraphic units would be assumed from the overall zonal averages for each stratigraphic unit. The average overburden velocity and the average workpoint velocity would be taken from the curves fit to these properties as a function of depth. The average overburden density would be calculated from the stratigraphic thicknesses of the units and the densities associated with each unit. No other logs, samples, or measurements would be required to characterize the physical properties of a LLNL Yucca Flat site. The carbonate content of the alluvial portion of an interval about a proposed working point (based on 3300 metric tonnes/kiloton of yield) would be measured.

The stratigraphy would be determined from cuttings, downhole photography, a magnetic log, and a gamma log. A bulk density log would serve as the anomalous property indicator and would be used in two different ways. First, stratigraphic zonal averages from the bulk density log would be checked against the assumed data. If the zonal log average values fell outside two standard deviations of the assumed zonal average, the unit would be considered anomalous and a more complete analysis of the site would be required. Second, the bulk density log would be examined to determine whether any unusual variations in density which were outside of experience existed within a stratigraphic unit.

Introduction

During the past two decades, LLNL has measured repeatedly the grain density, bulk density, water content, and the seismic travel times of the geologic media encountered in its Yucca Flat drill holes. From these properties, the porosity, gas-filled porosity, saturation, overburden density, and seismic velocity of the media have been calculated. This paper examines these data to determine whether or not there is need to continue to make some or all of these measurements in the future. In particular, I examine the zonal averages of the stratigraphic units in Yucca Flat for their consistency and extrapolability to future LLNL Yucca Flat sites and the predictability of the seismic velocity data.

Basic Formula

The total porosity, gas-filled porosity, and the saturation of the media are calculated from bulk density, grain density, and water content measurements. These six parameters are defined as:

ρ_b	- bulk density	[total mass/total volume]
ρ_g	- grain density	[mass of solids/volume of solids]

ρ_w	- water density	[mass of water/volume of water]
Z	- water content	[mass of water/total mass of sample]
ϕ	- total porosity	[(total volume - volume of solids)/total volume]
ψ	- gas-filled filled porosity	[volume of gas-filled filled voids/total volume]
S	- saturation	[volume of water-filled voids/total volume of voids]

From these definitions, the following relationships are easily derived:

$$\phi = 1 - \frac{\rho_b}{\rho_g}(1 - Z) \tag{1}$$

$$\psi = \phi - \frac{Z\rho_b}{\rho_w} \tag{2}$$

$$S = \frac{Z\rho_b}{\phi\rho_w} = 1 - \frac{\psi}{\phi} \tag{3}$$

In our customary usage at the Nevada Test Site, I replace the water density (ρ_w) with the value of 1.0 Mg/m^3 and eliminate it from the equations.

When the medium is fully saturated, the water content of the medium is related to the bulk and grain densities:

$$Z_{100\%} = \frac{\rho_g - \rho_b}{\rho_g\rho_b - \rho_b} \tag{4}$$

The overburden burden density is typically calculated from bulk density data:

$$\bar{\rho} = \frac{\sum_i \rho_i \Delta z_i}{\sum_i \Delta z_i} \tag{5}$$

The average overburden velocity is calculated from the seismic travel times:

$$\bar{V}(z) = \frac{z}{t(z)} \tag{6}$$

where $t(z)$ is the seismic travel time to depth z. The average work point velocity is calculated in a similar fashion from the difference in seismic travel times from the surface, t_2 and t_1 between the

bottom, z_2 and top, z_1 of the work region:

$$\bar{V}_{WP} = \frac{z_2 - z_1}{t_2 - t_1} \tag{7}$$

Data Set

The data for this study were taken from the LLNL Site Characteristic Summary memoranda. I restricted this study to the LLNL Yucca Flat Areas 2, 4, 8, 9, and 10 for several reasons. First, I have more data from Yucca Flat as compared to Pahute Mesa or other areas at the NTS. Second, Yucca Flat is further away from the volcanic source region for most of the tuff units than is most of Pahute Mesa. I expect that the variability of a particular property for a volcanic unit will be less when the unit is further away from the volcanic source region.

I selected the calculated zonal averages for the stratigraphic units as my basic primary data source for grain density, bulk density, water content, porosity, gas-filled porosity, and saturation. The zonal averages were taken from the LLNL Site Characteristic Summary memoranda. The units were assumed to be as identified and reported in the Site Summaries. I selected these data as the primary data set for several reasons. The data are averages across the stratigraphic unit at the particular drill hole. Small variations due to measurement error or inhomogeneities in the unit are averaged out. In addition, the data for these zonal averages have in some cases been obtained with more than one type of measurement technique. For example, a reported zonal average water content may contain water contents from epithermal neutron logs and measured water contents from different sample types. The averages minimize the effect of obtaining the data with different techniques.

The basic assumption of this study is that the zonal averages presented truly represent the average property of the stratigraphic unit under consideration. Thus, I assume that no systematic bias exists in the data set even though the individual zonal averages for the holes may have been determined with different measuring techniques. However, I do acknowledge that an unknown amount of random error is present in each individual measurement that is averaged into the zonal averages. The entire set of zonal averages as listed in the Site Characteristic Summaries are listed in Appendix 1.

Next, I screened the data with the following criteria:

1. Eliminated all zonal averages that were obtained without measured grain densities.
2. Replaced all bulk density and water content averages with a * in Appendix 1 when the gas-filled porosity was not calculated for that unit.
3. Eliminated all zonal averages when the averaged gas-filled porosity was less than 7 Vol %.
4. Eliminated all zonal averages which include more than one stratigraphic unit.

These criteria were applied to obtain a data set that had measured grain densities, measured bulk densities, and measured water contents, were from the same unit, and were from units whose averages did not include data from below the water table. Zonal gas-filled porosity averages with less than 7 Vol % were examined in some detail. These zonal averages were found to include data from below the standing water level and/or were obtained from a small number of measurements (sometimes only one measurement), or were ambiguous about whether data was included from below the water table.

This data sets listed in Appendices 2 (alluvial units) and 3 (volcanic units) have been sorted by stratigraphic unit. The stratigraphic nomemclature utilized in this study was the nomemclature in existence at the time that the Site Characteristic Summary was originally written. The key for the geologic names is given in Table 1.

Table 1

Stratigraphic Nomemclature

QTAL	=	Alluvium
QTMA	=	Mixed alluvium
QTTA	=	Basal tuffaceous alluvium
TMA	=	Ammonia Tanks Member
TMB	=	Bedded Ammonia Tanks
TMR	=	Rainier Mesa Member
TP	=	Paintbrush Tuff
TBG	=	Grouse Canyon Member
TTB	=	Tunnel Beds
TTS	=	Tub Spring Member
TB	=	Bedded tuff
TF	=	Fraction Tuff
TRV	=	Red Rock Valley Tuff
TU	=	Undifferentiated tuff

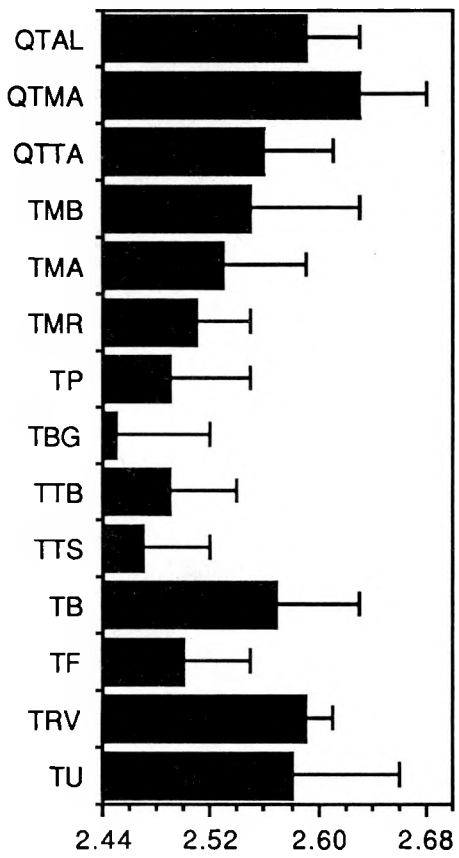
The average overburden velocity and the average work point velocity as a function of depth were taken from the Site Characteristics Summaries. These data already represent average values; no attempt was made in this study to determine the velocity of individual stratigraphic units. The average velocity value for an individual unit with a small thickness is highly uncertain because the average value is determined by differencing two travel time measurements to the surface. Hence, I avoided this problem by only considering the average velocity values which were already tabulated. These data are listed in Appendix 4.

Average Properties of the Stratigraphic Units

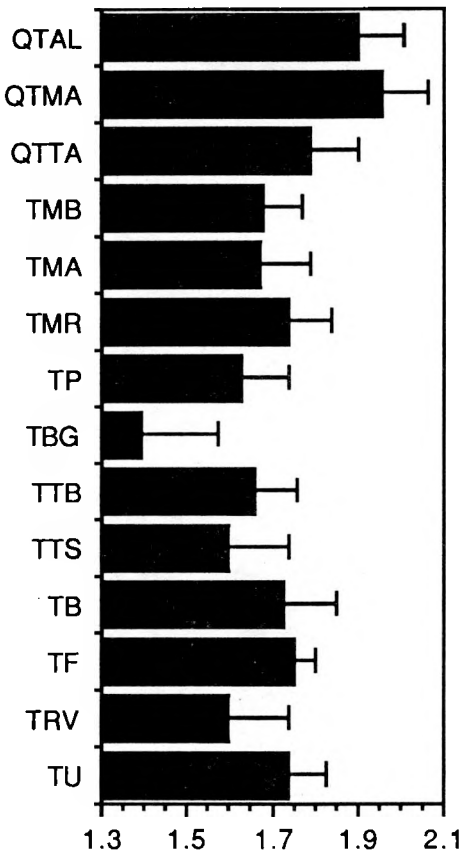
The means, maxima, minima, and standard deviations of the zonal values about the means for the grain density, bulk density, water content, porosity, saturation, and gas-filled porosity of the stratigraphic units are shown in Appendices 2 and 3. These means and standard deviations are summarized in Table 2. These properties are illustrated in Figures 1 and 2 in a form which resembles a normal log display. The mean value and the standard deviation of the values about the mean for each unit are displayed in proper stratigraphic sequence. Several characteristics of these properties are readily apparent in Figures 1 and 2. The porosity of the volcanic units is almost constant (~44 Vol %); the only exception is the TBG with a porosity of 54 Vol %. The saturation of the volcanic units is fairly constant (~60%); the exceptions are the TBG and the TRV with saturations of 51% and 42% respectively. A gradual increase in saturation with depth can be observed. The gas-filled porosity of the volcanic units is fairly constant (~17 Vol %); the exceptions are the TBG and the TRV with gas-filled porosities of about 27 Vol %. The water content of the volcanic units is fairly constant (~15 Wt %); the exceptions are the higher water contents in the TBG and TTS (~19 Wt %) and the lower water content in the TRV (~12 Wt %). The bulk density of the volcanic units is fairly constant (~1.68 Mg/m^3) and exhibits a small increase of bulk density with depth in the volcanic section; the only exception is the bulk density of the TBG (~1.39 Mg/m^3). The grain densities of the volcanic units vary considerably; however, the grain densities decrease with depth in the section through the TBG and then more or less increase with depth. The alluvial units (QTAL and QTMA), when compared with the volcanic units, have lower water contents, porosities, and gas-filled porosities, and have higher grain densities and bulk densities. The QTTA means fall between those for the volcanic units and the QTAL and QTMA. The saturations of the alluvial units (QTAL, QTMA, and QTTA) is comparable to the saturations of the volcanic units (~59 %).

The standard deviations of the properties about the mean are also tabulated in Table 2. These standard deviations compare favorably with the measurement accuracy for the property. The

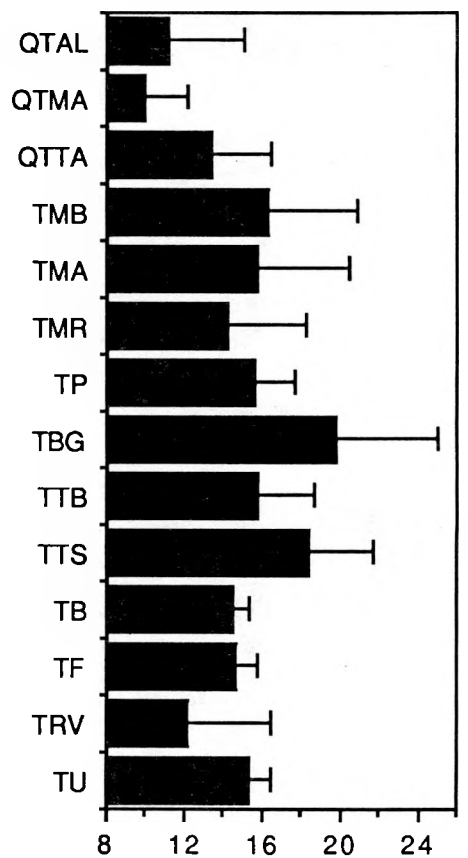
Figure 1. Measured properties - LLNL Yucca Flat Areas
The units are displayed in normal stratigraphic sequence.
Mean zonal averages with one standard deviation about the mean.



Grain density (g/cc)

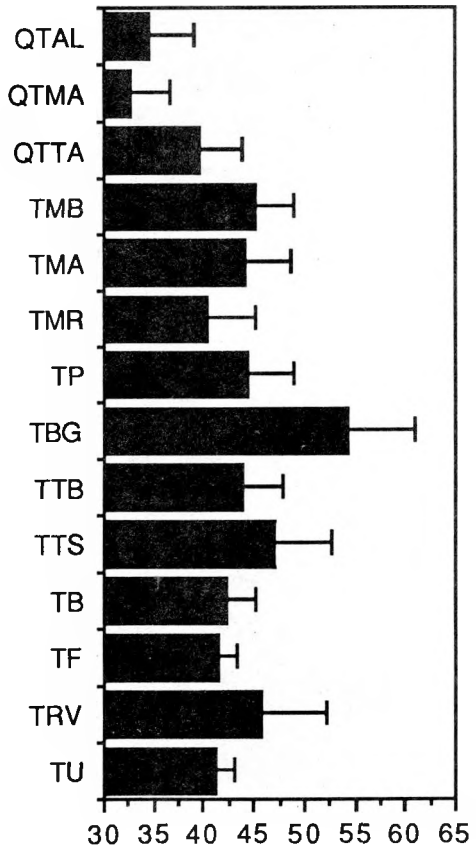


Bulk density (g/cc)

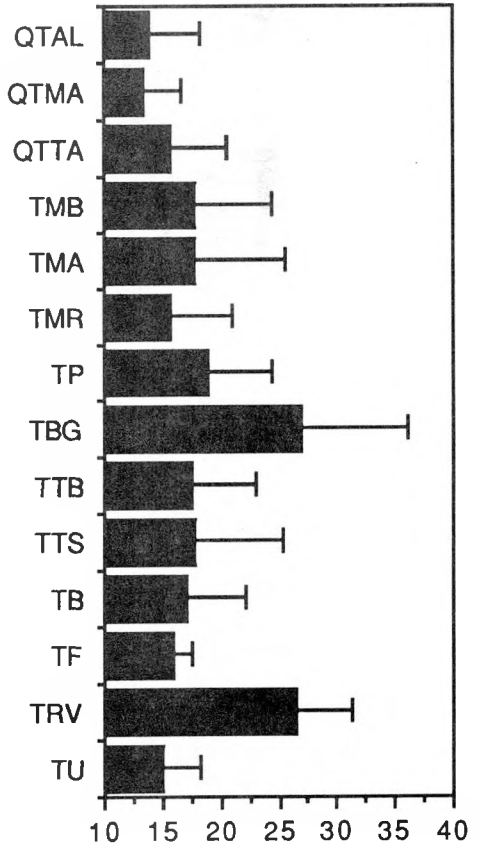


Water content (wt%)

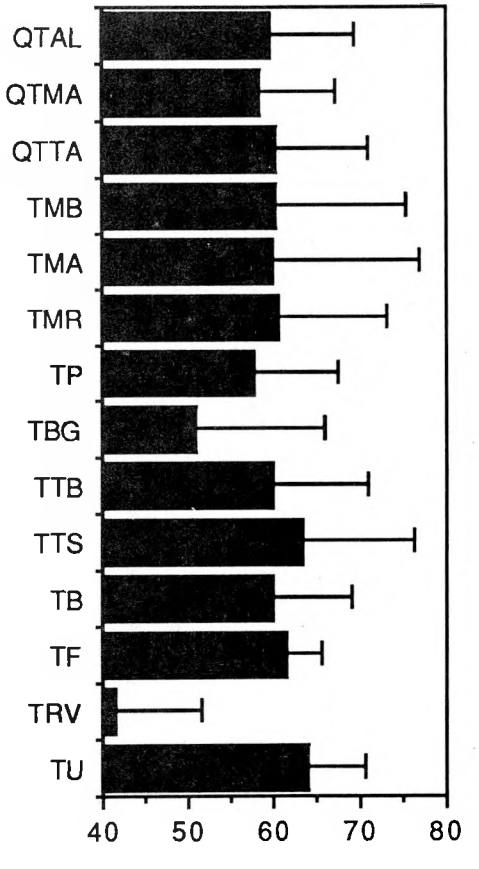
Figure 2. Calculated properties - LLNL Yucca Flat Areas
The units are displayed in normal stratigraphic sequence.
Mean zonal averages with one standard deviation about the mean.



Porosity (vol %)



Gas Porosity (vol %)



Saturation (%)

average of the standard deviations for the variations about the grain density means is ~0.05 Mg/m^3; about the same as the measurement accuracy for grain densities [1]. The average of the standard deviations for the variations about the bulk density means is ~0.11 Mg/m^3; about 1.3 times the measurement accuracy for the gamma-gamma density log measurements (~5% of the measured value). The average of the standard deviations for the variations about the water content means is ~3.1 Wt %; about 1.5 times the measurement accuracy for the epithermal neutron log measurements (greater of 2 Wt % or 8% of measurement).

Table 2

Mean Zonal Properties
and
Standard Deviations of the Zonal Properties about the Mean

Unit	Grain Density Mg/m^3	Bulk Density Mg/m^3	Water Content Wt %	Porosity Vol %	Saturation %	Gas Porosity Vol %
QTAL	2.59±0.04	1.90±0.12	11.2±3.9	34.6±4.4	59.7±9.7	14.0±4.2
QTMA	2.63±0.05	1.96±0.10	9.9±2.3	32.8±3.8	58.5±8.8	13.5±3.1
QTTA	2.56±0.05	1.79±0.11	13.4±3.1	39.5±4.5	60.2±10.6	15.7±4.8
TMA	2.53±0.06	1.67±0.12	15.8±4.6	44.2±4.5	59.9±17.0	17.7±7.8
TMB	2.55±0.08	1.68±0.10	16.3±4.6	45.2±3.9	60.3±15.0	17.8±6.6
TMR	2.51±0.04	1.74±0.10	14.2±4.0	40.3±5.0	60.7±12.3	15.8±5.3
TP	2.49±0.06	1.63±0.11	15.6±2.1	44.3±4.6	57.8±9.6	18.9±5.5
TBG	2.45±0.07	1.39±0.18	19.8±5.3	54.3±6.7	50.9±15.1	26.9±9.2
TTB	2.49±0.05	1.66±0.10	15.8±2.8	43.8±4.1	60.0±10.9	17.6±5.4
TTS	2.47±0.05	1.60±0.14	18.4±3.3	47.1±5.6	63.2±12.8	17.7±7.7
TB	2.57±0.06	1.73±0.12	14.5±0.9	42.2±2.9	59.9±9.3	17.1±5.1
TF	2.56±0.05	1.75±0.05	14.6±1.2	41.4±1.9	61.5±4.1	15.9±1.7
TRV	2.59±0.02	1.60±0.14	12.2±4.3	45.8±6.4	41.5±10.2	26.6±4.7
TU	2.54±0.08	1.74±0.09	15.4±1.0	41.9±2.0	64.0±6.5	15.1±3.1

I conclude from these comparsions that the units have been adequately sampled in the LLNL Yucca Flat areas and that further measurements of the grain density, bulk density, and water contents on average would not be significantly different from the averages listed in Table 2. It is absolutely certain that further measurements of grain density will not significantly affect the calculated properties. Figure 3 illustrates the effect of a grain density measurement error of 0.15 Mg/m^3 for a wide range of typical bulk densities and water contents. This error is about three times the standard deviation of values about the mean grain density (~99% of all measurements will fall within three standard deviations for measurements whose errors are normally distributed). The changes in the calculated properties that result from a grain density

Figure 3. The change in the calculated properties for an error of 0.15 g/cc in grain density. 5 different water contents for 3 pairs of bulk and grain densities are displayed. The changes in the calculated properties are not sufficiently large to matter in the containment evaluation.

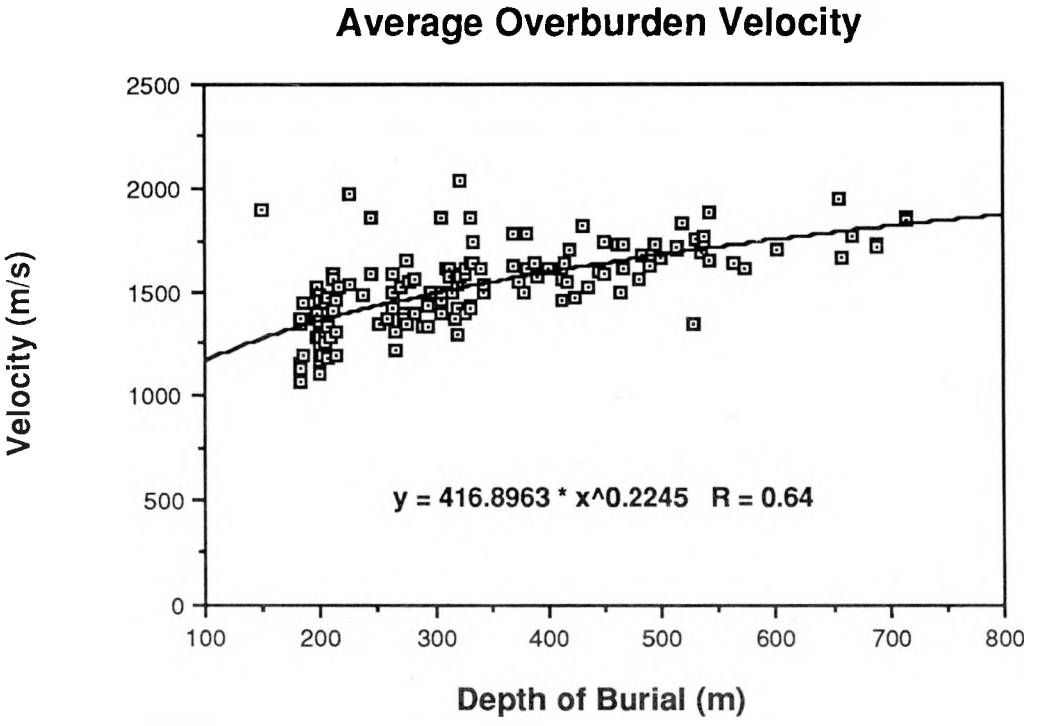
BULK DENSITY =	1.4	WATER	GAS POROSITY	POROSITY	SATURATION	Delta GAS POROSITY	Delta POROSITY	Delta SATURATION
GRAIN DENSITY =	2.5	0.00	0.44	0.44	0.00	0.03	0.03	0.00
		0.13	0.33	0.51	0.36	0.03	0.03	-0.02
Delta GRAIN =	0.15	0.26	0.22	0.59	0.63	0.02	0.02	-0.03
		0.39	0.11	0.66	0.83	0.02	0.02	-0.03
		0.52	0.00	0.73	1.00	0.02	0.02	-0.02
		Last water content in WATER column is calculated for 100% saturation.						

BULK DENSITY =	1.8	WATER	GAS POROSITY	POROSITY	SATURATION	Delta GAS POROSITY	Delta POROSITY	Delta SATURATION
GRAIN DENSITY =	2.5	0.00	0.28	0.28	0.00	0.04	0.04	0.00
		0.06	0.21	0.33	0.36	0.04	0.04	-0.04
Delta GRAIN =	0.15	0.13	0.14	0.37	0.63	0.04	0.04	-0.06
		0.19	0.07	0.42	0.83	0.03	0.03	-0.07
		0.26	0.00	0.47	1.00	0.03	0.03	-0.07
		Last water content in WATER column is calculated for 100% saturation.						

BULK DENSITY =	2.2	WATER	GAS POROSITY	POROSITY	SATURATION	Delta GAS POROSITY	Delta POROSITY	Delta SATURATION
GRAIN DENSITY =	2.5	0.00	0.12	0.12	0.00	0.05	0.05	0.00
		0.02	0.09	0.14	0.36	0.05	0.05	-0.13
Delta GRAIN =	0.15	0.05	0.06	0.16	0.63	0.05	0.05	-0.20
		0.07	0.03	0.18	0.83	0.05	0.05	-0.23
		0.09	0.00	0.20	1.00	0.05	0.05	-0.24
		Last water content in WATER column is calculated for 100% saturation.						

measurement that is in error by 0.15 Mg/m^3 are generally much smaller than the changes in the calculated properties that are obtained by propagation of the bulk density and water content measurement errors through Eqs. 1, 2, and 3. The only place where this difference might be important is when the unit is close to 100% saturation (0 Vol % gas-filled porosity). The response for a unit with 0 Vol % versus 4 Vol % gas-filled porosity during a nuclear explosion are considerably different. However, the measurement accuracies for the water content and bulk density place a lower limit to the accuracy of the calculated gas-filled porosity of about 5 Vol % in absolute value. Larger contributions to the calculated error in porosity, gas-filled porosity, and saturation come from the measurement error in bulk density and water content. Hence an error in grain density that is as large as 0.15 Mg/m^3 does not change the calculated properties sufficiently to be important in containment evaluation.

The average overburden velocity and the average work point velocity are plotted in Figure 4. The average overburden velocity and the average work point velocity are not as predictable as the physical properties of the stratigraphic units. Lines have been fit to the data and the equations for the fits and the correlation coefficients for the fits are given in the figure. I do not claim that these fits are unique. However, I do claim that these fits (or other fits) could be used for containment evaluation. The fits retain these two characteristics: first, the average overburden velocity increases with depth - rapidly at first and then more slowly with increasing depth; second, the work point velocity increases with depth. The main use for the average overburden velocity is the timing of the reflected stress wave from the earth's surface. It is thought that the residual stress field around a cavity on a nuclear explosion needs a sufficient time to "set up" before the reflected stress wave arrives from the surface. The time required is a primarily a function of the strength of the media. For media with compressive strengths of 50, 100, and 300 bars, the reflected wave's travel time should be greater than about 0.45, 0.30, and 0.20 seconds respectively [2]. These travel times for the reflected wave were calculated assuming that: 1.) the nuclear test had a scaled depth of burial (SDOB) of 122 $m/kt^{1/3}$; 2.) the overburden density was 2.0 Mg/m^3; 3.) the cavity radius can be determined by the CEP formula of 70.2 $Yield^{1/3}/ (\rho\ DOB)^{1/4}$; 4.) the path that the stress wave traverses is from the working point to the surface and back down to a depth that is two cavity radii above the depth of burial. Figure 5a depicts the travel time for the reflection from the surface for the average overburden velocity curve that was fit to the average overburden velocity data in Figure 4; also on Figure 5a are the times required for the residual stress to "set up" in the media. In Figure 5b, the times required for the residual stress to "set up" in the media have been converted to an equivalent average velocity for each depth. Figures 5a and 5b illustrate that for all depths in media with 300 bars of compressive strength, for depths greater than about 230 m in media with 100 bars of compressive strength, and for depth greater than about 400 m in media with 50 bars of



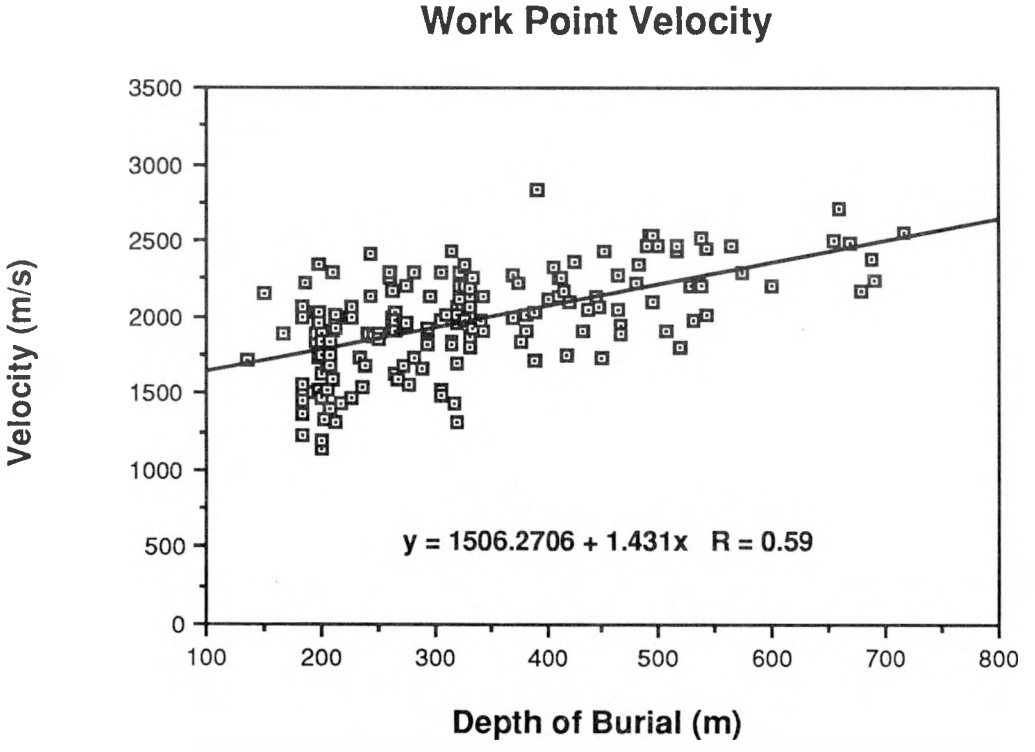
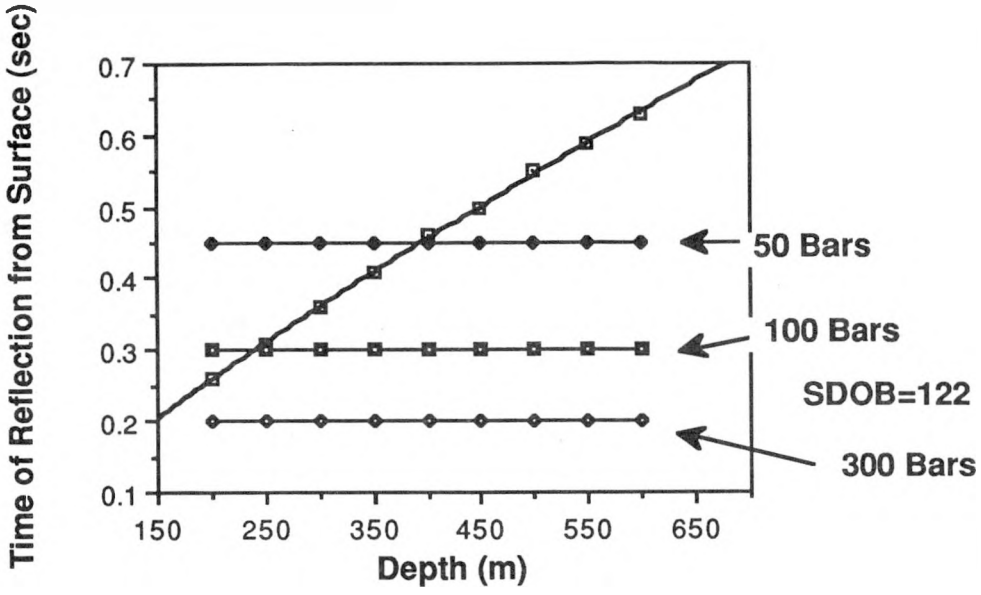


Figure 4. Plots of the average overburden velocity and the work point velocity for LLNL Yucca Flat sites. The equations are for the curves fit to the data. R is the correlation coefficient for the fit.

Figure 5a. Travel time required for a wave to traverse to the surface and return to a point two cavity radii above the working point. The horizontal lines are the times required for the residual stress to set up in media with different compressive strengths.



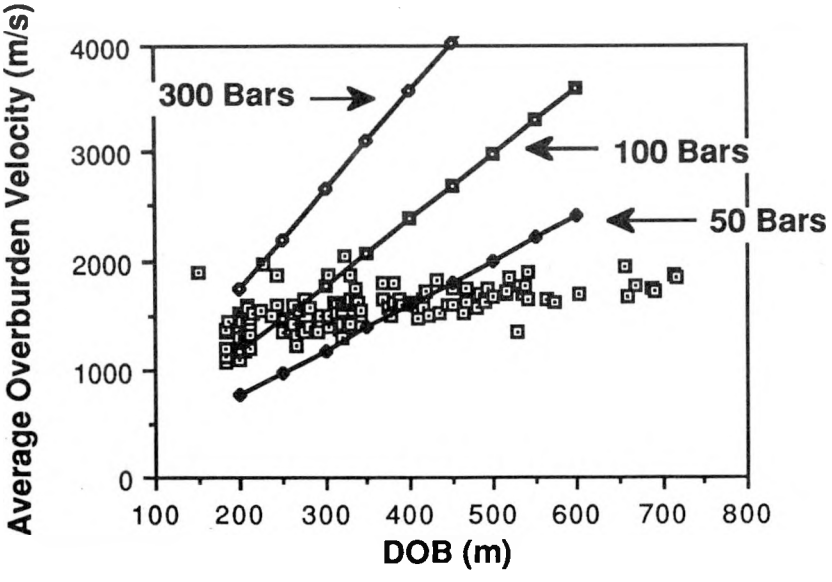


Figure 5b. Plotted lines are the average overburden velocity profiles for different compressive strength media that would result in the travel time to the surface and back to a point two cavity radii above the working point being equal to the residual stress set up time. The symbols are the measured average overburden velocity data.

compressive strength, the residual stress field has sufficient time to "set up". For depths shallower than these, the residual stress field will not have time to "set up". The average work point velocity generally increases with depth; this is typically observed in layered geologic media.

The ROCK PILE Concept

The physical property data have been gathered at the Nevada Test Site for over twenty years. The physical property data reported to the Containment Evaluation Panel (CEP) have followed formats developed by the 1974 ad hoc CEP committee on "Appraisal of Geological and Geophysical Measures Essential to Containment" and the 1983 CEP "Twenhofel" committee's "Final Data Needs Subcommittee Report to the Containment Evaluation Panel". Based upon the discussion presented above, I propose that a new method be used to determine and report physical property data to the CEP. The basic idea is that the existing data base is sufficient to predict the physical properties of the units for the containment evaluation of a proposed nuclear test. I have concluded that continuing to measure the physical properties of a site is not adding new information that is useful in the containment evaluation process.

I am proposing a method which I shall call the ROCK PILE Concept. An adequate characterization of the physical properties of a LLNL Yucca Flat site would consist of the following:

1. Physical properties are assumed from overall zonal averages by stratigraphic unit.
2. Velocity is assumed from curves fit to existing data.
3. Carbonate content of the alluvial portion of the working point region is measured.
4. No other logs, samples, or measurements are required to characterize the physical properties of a LLNL Yucca Flat site.

In implementing this idea, no other measurements in the field or laboratory would be made to determine the physical properties. However, some additional assumptions are required to implement the concept:

5. Regions below the standing water level are assumed to be 100% saturated and the water content calculated from the assumed grain density and bulk density.
6. Stratigraphy is determined from cuttings, downhole photography, magnetic log, gamma log, or nearby-hole stratigraphic data. The geologist should determine which data types from this list are sufficient to determine the stratigraphy at the site.
7. Bulk density or electric log is used to locate anomalous regions.

The anomalous-property-indicator log (density or electric log) would be used to determine if the properties were significantly different than the assumed properties at this site. A bulk density log used as the anomalous property indicator would be used in two different ways. First, stratigraphic zonal averages from the bulk density log would be checked against the assumed data. If the zonal log average values fell outside two standard deviations of the assumed zonal average, the unit would be considered anomalous and a more complete analysis of the site would be required. Second, the bulk density log would be examined to determine whether any unusual variations in density which were outside of experience existed within a stratigraphic unit. An electric log could be used to determine the presence of clay zones which might have unusually low strength (generally, clay zones are also seen in caliper logs as significant "wash-out" zones).

This concept by no means is original. The United States Geologic Survey (USGS) proposed a concept similar to the ROCK PILE Concept at an executive session of the Containment Evaluation Panel in 1978. Their plan developed by W. S. Twenhofel is presented in Appendix 5. The Los Alamos National Laboratory has partially implemented this concept when they use their Sand Pile and Tuff Pile areas. The ROCK PILE Concept is just an extension of the Sand Pile or Tuff Pile concept to a larger area; it is totally in harmony with the USGS 1978 proposal.

Reasons for the ROCK PILE Concept

I believe that LLNL, after twenty years of measuring the physical properties, knows the average properties of the stratigraphic units in Yucca Flat quite well. LLNL no longer needs to continue measuring properties that we can predict with an accuracy that compares favorably with actual measurement accuracy. I conclude that LLNL should concentrate its efforts now on the properties that we have learned over the past twenty years are important in the containment evaluation process but for which we do not yet either measure or measure accurately enough. For example, logs estimating the strength of the formation, the permeability of the formation, and the equivalent carbon dioxide content of the formation would add data to the containment evaluation process that we now know are important and have the potential to measure economically. We need to understand how to better use methods for assessing the hydrofracture potential at a proposed site. One might ask - "Why not measure it all?" The answer is that present day budgets simply will not permit the development of these new measurements and methods. Consciously deciding that we will no longer spend our resources gathering data for which we already know the answers sufficiently well to carry out containment evaluations is a way to free resources to develop new techniques and methods. Basically, I want to improve our understanding of the fundamental

physics of containment; to do so requires resources which are presently not available unless we terminate some other activity. Terminating the measurement of the physical properties of the media could free resources for this goal.

Case Example - U4at

I will use the PALISADE event in U4at as an example of how the physical properties for an event could be determined using the ROCK PILE Concept. The working point region at U4at was entirely within one stratigraphic unit, the Paintbrush Tuff (TP). Table 3 illustrates the physical properties for the U4at site as reported to the CEP from actual measurements and as would be reported under the ROCK PILE Concept.

Table 3

Physical Property	U4at (Measured)	U4at (ROCK PILE)	Units
Bulk Density	1.65	1.63	Mg/m^3
Grain Density	2.51	2.49	Mg/m^3
Water Content	18.6	15.6	Wt %
Porosity	46.5	44.3	Vol %
Saturation	65.7	57.8	%
Gas Porosity	15.9	18.9	Vol %
CO_2 Content	0.4	N/A	Wt %
Seismic Velocity	1836.	1986.	m/s
Overburden Density	1.81	1.76	Mg/m^3
Overburden Velocity	1606.	1538.	m/s
Overburden Gas Porosity	15.9	16.3	Vol %

The average overburden density and gas-filled porosity are easily calculated. Equation 5 was used to calculate the density; a similar technique was used to calculate the gas-filled porosity. Appendices 6 and 7 illustrate the calculation. The velocities were obtained from the curves fit to the data; the other physical properties except for the carbonate content were obtained from the average zonal averages for Paintbrush Tuff. The carbonate content of a work point entirely within tuff as at U4at would not be measured. However, if the working point had had alluvium within the working point region, measurements would have been made in the alluvial portion of the working point region. Figures 6 and 7 illustrate these assumed working point properties on the histogram plots traditionally presented to the CEP. The histrograms basically illustrate the point that the

Figure 6. Histograms comparing the ROCK PILE Concept derived properties with the measured properties and the overall average for the volcanic units.

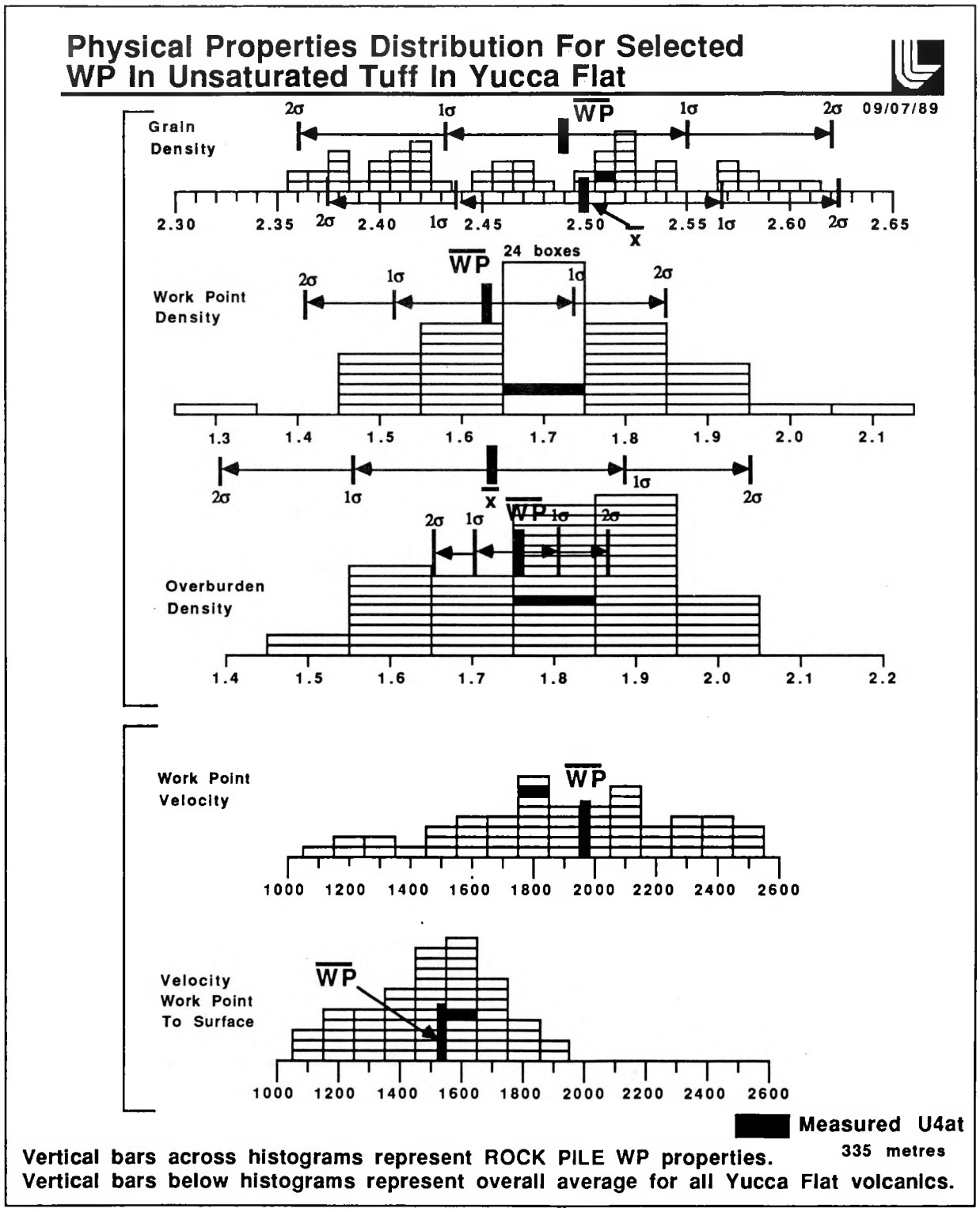
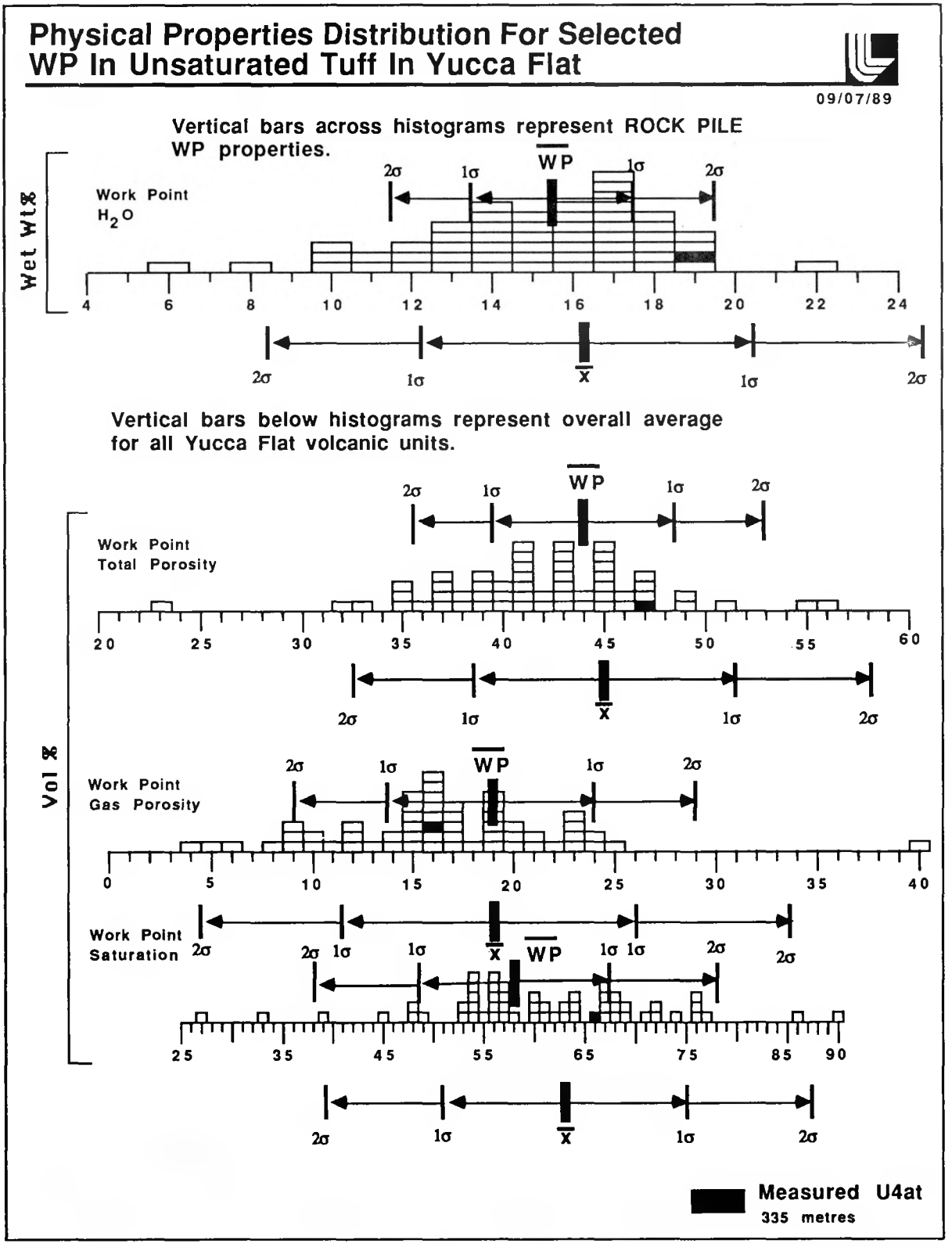


Figure 7. Histograms comparing the ROCK PILE Concept derived properties with the measured properties and the overall average for the volcanic units.



average properties of the working points around Yucca Flat have been sampled quite well; in fact, it is fair to say that the histograms represent the statistical distribution of the properties of the volcanic section as a whole. This is illustrated by the averages for the LLNL Yucca Flat data taken as a whole. The error bars represent approximately a 95% confidence interval (two standard deviations) for the working point properties for unsaturated tuff in the LLNL Yucca Flat areas. Also plotted are the working point properties that would be used for the PALISADE event at U4at under the ROCK PILE Concept. As seen in Table 3, these ROCK PILE properties match the measured properties quite well.

The anomalous property indicator log for this U4at example was a bulk density log. Figure 8 illustrates the bulk density log at U4at with the measured and assumed zonal averages overlain on the log. The zonal averages from the log are shown with the triangle symbol; the assumed averages from this study are displayed without any symbol. The agreement is in general quite good; the only zones where the two averages disagree are typically where the logging data are sparse and/or poor quality. In these cases the assumed zonal averages are probably a better representation of the formation. For example, in the zone from 406 to 420 m, the log has only two short zones which actually contain data; these zones are each 1/4 inch long! This hardly seems to be sufficient data to obtain a "true" zonal average. Repeat logging runs were unable to obtain more data as this zone had many washouts. Still even considering this, all measured zonal averages fall within two standard deviations of the assumed zonal averages. Therefore, under the ROCK PILE Concept, no further investigation would be needed to characterize this site.

Conclusions

The ROCK PILE Concept is a viable alternative to measurement of physical properties in LLNL Yucca Flat areas. The stratigraphic units have been adequately sampled such that the physical properties can be predicted accurately enough for containment evaluation purposes. There is no longer a need to continue measuring these properties. The ROCK PILE Concept also includes a check to determine if the site might, for some reason, be anomalous. The proposal uses the gamma-gamma bulk density log as the anomalous property indicator. The USGS in a proposal in 1978 suggested using an electric log to determine clay zones. The choice of density versus electric log depends upon the importance placed upon determining impedance boundaries or indicators of strength (density log) versus determining clay zones (electric log). I believe that large clay contents (large meaning clay contents large enough to affect containment) would already have been found via drilling problems, hole enlargements, or cuttings examination. Hence, I favor the density log.

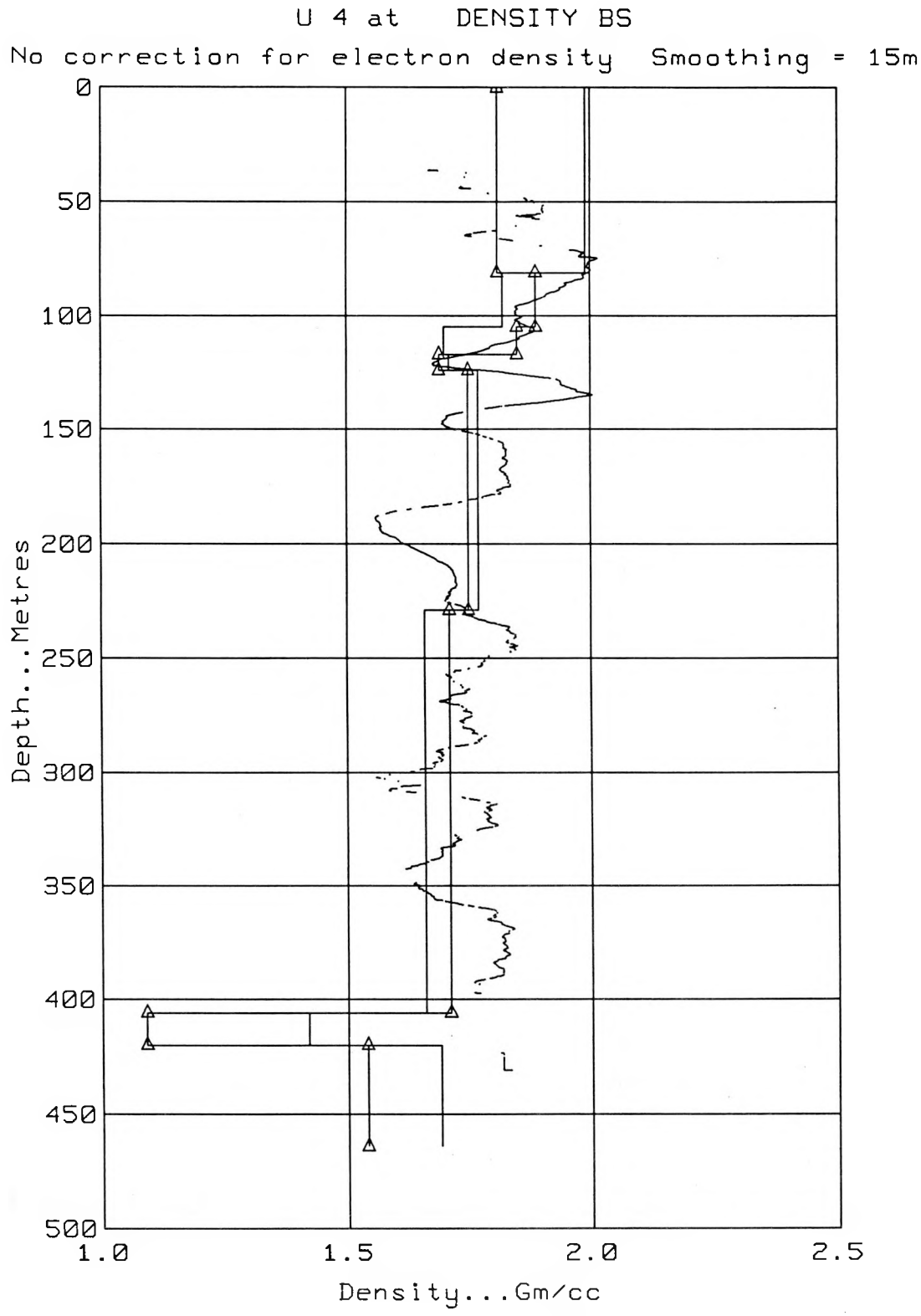


Figure 8. U4at density zonal averages from the ROCK PILE Concept and the zonal averages from the log are overplotted on the γ–γ density log. The zonal averages from the log are plotted with the triangle symbols.

The ultimate decision about the suitability ROCK PILE Concept probably resides in a value judgement. Is there value in continuing to measure these physical properties on the chance that conditions which are unsuitable for containment would be detected? My personal opinion is that there is not much value in continuing to measure them and that the ROCK PILE Concept will be adequate. The emphasis in containment evaluation is then on the phenomena that would result from the particular geologic setting proposed for the nuclear test.

Acknowledgements

The work was performed under the auspices of the U.S. Department of Energy by the Lawrence Livermore National Laboratory under Contract W-7405-ENG-48. This work was supported by the Nuclear Test Containment Program.

References

1. McKinnis, W., personal communication, Lawrence Livermore National Laboratory, Nevada Test Site Geology Group Leader, 1989.
2. App, F. N., "A Calculational Study of the Influence of Rock Compressive Strength upon Cavity and Residual Stress Formation about a Contained Underground Explosion", Los Alamos National Laboratory, 1977.

Appendix 1 - Zonal Averages for LLNL Yucca Flat Sites

This tablulates zonal averages for LLNL events in Yucca Flat							
HOLE	Grain den	Bulk den	Water Con	Porosity	Saturation	Gas Por	Unit
U10ay	2.64	1.97	8.94	31.9	55.2	14.3	QTAL
U10ay	2.61	2.04	9.59	29.2	67	9.7	QTAL
U10ay	2.56	1.95	44.6	32.5	69.5	9.9	QTAL
U10ay	2.53	1.59	15.6	47.2	52.6	22.4	QTAL
U10ay	2.43	*	21.2	*	*	*	TP
U10ba	2.66	1.97	7.8	31.6	48.7	16.2	QTAL
U10ba	2.65	2.06	8.4	28.7	60.2	11.4	QTAL
U10ba	2.68	2.11	6	25.9	48.7	13.3	QTAL
U10ba	2.61	2	9	30.4	59.2	12.4	QTAL
U10ba	2.54	1.81	13.7	38.4	64.7	13.6	QTAL
U10ba	2.5	1.73	14.1	38.9	64.6	13.8	TP
U10bc	2.61	1.83	12.9	38.7	61	15.1	QTAL
U10bc	2.45	1.36	18.1	54.5	45.1	29.9	TP
U10bc	2.41	1.32	20.8	56.5	48.7	29	TBG
U10bc	2.52	1.62	14	44.7	50.8	22	TTB
U10bc	2.42	1.71	13.8	39.2	60.2	15.6	TTB
U10bd	2.57	1.72	11.9	40.8	50.1	20.4	QTAL
U10bd	2.43	1.53	17.8	48.3	56.3	21.1	TP
U10bd	2.46	1.47	16.5	50	48.5	25.7	TBG
U10bd	2.45	1.62	13.4	42.9	50.7	21.1	TTB
U10bd	2.58	1.71	16.4	44.5	63	16.5	TU
U10be	2.7	2.1	5.2	26	41.7	15.2	QTMA
U10be	2.59	1.9	11.4	35	62.1	13.2	QTTA
U10be	2.48	1.64	12.8	42.3	49.8	21.2	TP
U10be	2.43	1.44	14.4	49.3	42	28.6	TBG
U10be	2.5	1.75	16.7	41.6	70	12.5	TTB
U10be	2.48	1.82	18.1	40	82.4	7	TTS
U10be	2.51	1.89	20.6	40	97.4	1	TU
U10bf	2.67	2.13	6.1	25.1	51.8	12.1	QTMA
U10bf	2.5	1.62	14.3	44.5	51.8	21.5	QTTA
U10bf	2.48	1.57	13	44.9	45.3	24.6	TP
U10bf	2.37	1.21	13.8	56.2	29.7	39.5	TBG
U10bf	2.49	1.85	15.8	37.6	77.9	8.3	TTB
U10bg	2.57	1.69	12.2	42.1	49.1	21.4	QTAL
U10bg	2.48	1.43	16.1	51.4	44.8	28.4	TP
U10bg	2.36	1.21	27	62.6	52.2	29.9	TBG
U10bg	2.39	1.53	14.6	45.4	49.3	23	TTB
U10bh	2.64	2.08	10.4	29.1	74.4	7.5	QTMA
U10bh	2.6	1.8	16.7	42.4	70.8	12.4	QTTA

U10bh	2.74						TP
U10ca	2.69	2.03	9	31.1	59	12.8	QTMA
U10ca	2.55	1.71	16.2	43.8	63.4	16	TTB
U10ca	2.53	1.71	18.2	44.7	69.3	13.7	TTS
U10ca	2.5	1.71	17.9	43.7	70.4	12.9	TTB
U10cb	2.76	2.11	8.6	30	60.3	11.9	QTMA
U10cb	2.55	1.74	16.8	43.4	67.5	14.1	TTB
U10cb	2.5	1.67	19.1	46	69.3	14.1	TTS
U10cc	2.68	2.08	6.6	27.4	49.9	13.7	QTMA
U10cc	2.48	1.69	16.9	43.3	66.2	14.6	TTB
U10cc	2.47	1.67	20.3	46.2	73.2	12.4	TTS
U9cn	2.57	1.87	10.3	34.6	55.7	15.3	QTAL
U9cn	2.44	1.45	15.1	49.5	44.3	27.6	TP
U9cn	2.38	1.22	17.3	57.8	36.4	36.7	TBG
U9cn	2.5	1.85	15.7	37.8	76.9	8.7	TTB
U9cp	2.63	1.91	7.5	32.9	43.5	18.6	QTAL
U9cp	2.45	1.78	15.6	38.7	72	10.8	TMR
U9cp	2.45	1.61	14.2	43.7	52.1	20.9	TP
U9cp	2.36	1.38	17.6	51.9	46.8	27.6	TBG
U9cp	2.48	1.61	16	45.4	56.8	19.6	TBR
U9cp	2.48	1.74	16.4	41.3	69.4	12.6	TBR
U9cq	2.57	1.82	11.6	37.3	56.6	16.2	QTAL
U9cq	2.5	1.66	14	42.9	54.1	19.7	TMR
U9cq	2.66	1.71	16.6	46.5	60.8	18.2	TP
U9cq	2.48	1.57	17.5	47.7	57.7	20.2	TP
U9cq	2.51	1.56	23.8	52.5	70.9	15.3	TBG
U9cq	2.52	1.72	18.6	44.5	71.6	12.6	TTB
U9cr	2.66	2.03	5.6	27.9	40.3	16.7	QTAL
U9cr	2.46	1.53	16.4	48	52.1	23	TMR
U9cr	2.45	1.52	16.5	48.2	52	23.1	TP
U9cr	2.37	1.27	23.5	58.9	50.8	29	TBG
U9cr	2.5	1.67	19.8	46.4	71.6	13.2	TTB
U9cs	2.59	1.77	10.2	38.8	46.6	20.7	QTAL
U9cs	2.55	1.63	12	43.6	45	24	TMR
U9cs	2.54	1.68	15.3	44	58.5	18.3	TP
U9cs	2.52	1.62	25.6	52	79.8	10.5	TBG
U9cs	2.55	1.81	18.5	42.2	79.1	8.8	TTB
U9cw	2.47	1.6	10.4	41.7	39.9	25.1	TMR
U9cw	2.51	1.54	11.6	45.7	39	27.9	TP
U9cw	2.37	1.33	14.9	52.1	38.1	32.3	TBG

Appendix 1 - Zonal Averages for LLNL Yucca Flat Sites

U9cw	2.56	1.44	15.4	52.4	42.3	30.2	TTB
U9cg	2.56	1.64	11.5	43.4	43.2	24.6	QTAL
U9cg	2.53	1.59	12.1	44.8	42.9	25.6	QTAL
U9cg	2.51	1.52	11.9	46.6	39	28.4	QTAL
U9cg	2.53	1.56	12.56	46	42.6	26.4	QTAL
U8c	2.68	2	8.1	31.5	51.7	15.2	QTMA
U8c	2.53	1.85	12.2	35.7	63.2	13.1	QTTA
U8c	2.47	1.59	13.3	44.1	48	23	TTB
U8c	2.5	1.29	15.9	56.7	36	36.3	TTS
U8c	2.47	1.51	14.1	47.6	45.8	25.8	TTB
U8c	2.57	1.55	13.6	48	43.9	26.9	TRV
U8c	2.5	1.58	13.6	45.4	47.4	23.8	TB
U8c	2.5	1.7	13.8	41.3	56.9	17.8	TF
U8c	2.59	1.83	15.9	40.4	71.9	11.3	TU
U8e	2.61	1.99	7.3	29.4	49.3	14.9	QTAL
U8e	2.45	1.77	12.3	36.7	59.2	15	TMR+TP
U8e	2.5	1.7	10.9	39.3	47.1	20.8	TBG
U8e	2.45	1.55	13.8	45.5	46.8	24.2	TTB
U8e	2.43	1.53	12.6	44.9	42.8	25.7	TTB
U8e	2.58	1.71	14.8	43.6	58	18.3	TB
U8e	2.56	1.94	18	37.7	92.7	2.8	TB
U8j	2.67	2.14	6.9	25.2	58.4	10.5	QTMA
U8j	2.6	1.78	8.3	36.9	39.9	22.2	QTTA
U8j	2.49	1.33	20	57.1	46.7	30.4	TBG
U8j	2.51	1.68	15.2	43.1	59.4	17.5	TTB
U8j	2.48	1.57	16.1	47	53.5	21.9	TTS
U8j	2.52	1.65	16.1	45.2	58.5	18.8	TTB
U8j	2.62	1.79	6.6	36.3	32.7	24.4	TRV
U8j	2.62	1.87	13.9	38.7	67.4	12.6	TB
U8j	2.58	1.9	17.1	39.1	83	6.6	TF
U8j	2.62	1.95	19.6	40.1	95.3	1.9	TU
U8k	2.64	2.07	9.4	29	66.7	9.7	QTAL
U8k	2.41	1.7	17.2	41.7	70.2	12.4	TTB
U8k	2.38	1.49	22.4	51.6	64.7	18.2	TTS
U8k	2.48	1.67	14.9	42.8	58.1	18	TTB
U8k	2.57	1.59	16.8	48.7	54.8	22	TRV
U8k	2.57	1.8	14.5	40.1	64.8	14.1	TU
U8k	2.54	1.79	14	39.5	63.2	14.5	TF
U8l	2.65	1.96	9.1	32.7	54.4	14.9	QTAL
U8l	2.47	1.63	16.3	44.7	59.5	18.1	TTB
U8l	2.42	1.46	27.1	56.1	70.5	16.6	TTS
U8l	2.44	1.57	16.1	46.1	54.6	20.9	TTB

U8m	2.68	1.96	5.3	30.7	33.6	20.4	QTMA
U8m	2.5	1.72	9.6	37.7	43.6	21.2	TMR
U8m	2.46	1.66	13.3	41.4	53.4	19.3	TP
U8m	2.5	1.49	19.5	52	56	22.9	TBG
U8m	2.52	1.69	14.6	42.6	58.3	17.8	TTB
U8m	2.53	1.47	16.3	51.4	46.6	27.5	TTS
U8m	2.55	1.63	12.5	44.1	46.1	23.8	TTB
U8m	2.6	1.46	11.9	50.3	34.5	33	TRV
U8m	2.64	1.66	*	*	*	*	TB
U8m	2.59	1.75	16	43.3	64.5	15.4	TF
U8n	2.67	2.14	9.9	27.8	76.3	6.6	QTMA
U8n	2.52	1.9	9.6	31.7	57.3	13.5	TMR
U8n	*	1.49	15.3	*	*	*	TP
U8n	2.4	1.38	22.2	55.1	55.7	24.4	TBG
U8n	2.47	1.66	16.9	44	63.8	15.9	TTB
U8n	2.48	1.62	18.5	47	63.7	17.1	TTS
U8n	2.49	1.74	15.8	40.9	67.1	13.5	TTB
U8n	2.58	1.75	*	*	*	*	TRV
U8n	*	1.92	*	*	*	*	TB
U8n	2.61	1.88	*	*	*	*	TF
U4j	2.53	1.87	10.7	34	58.8	14	QTMA
U4j	2.52	1.82	12.4	36.9	61.2	14.3	QTTA
U4j	2.48	1.49	10.5	46.1	33.9	30.5	TMA
U4j	2.51	1.77	11.6	37.6	54.6	17.1	TMR
U4j	2.48	1.75	16.1	40.6	69.3	12.5	TP
U4j	2.42	1.7	24.9	47.4	89.2	5.1	TBG
U4j	2.49	1.84	20.6	41.3	91.8	3.4	TTB
U4ar	2.57	1.85	11.4	36.3	58	15.3	QTMA
U4ar	2.69	2	10.2	33.2	61.2	12.9	QTMA
U4ar	2.6	1.88	11.1	35.7	58.4	14.8	QTMA
U4ar	2.66	2	13.2	34.8	76.2	8.3	QTMA
U4ar	2.6	1.9	15.3	38.2	76.1	9.1	QTMA
U4ar	2.55	1.83	16.3	39.9	74.8	10	TMB
U4ar	2.57	*	*	*	*	*	TMA
U4ac	2.64	1.88	11.6	37.2	58.4	15.5	QTMA
U4ac	2.55	1.81	12.3	37.8	58.8	15.6	QTMA
U4af	2.63	1.84	10.4	37.4	51.1	18.3	QTAL
U4af	2.58	1.85	13.1	37.7	64.2	13.5	QTAL
U4af	2.46	1.63	20.8	47.5	71.4	13.6	TP+TBG
U4af	2.49	1.73	19.34	43.8	76.6	10.2	TTB
U4ah	2.62	1.91	10.7	34.9	58.7	14.4	QTAL
U4ah	2.56	1.89	11	34.4	60.6	13.6	QTAL
U4ah	2.44	1.62	13.5	42.6	51.5	20.6	TP

Appendix 1 - Zonal Averages for LLNL Yucca Flat Sites

U4ah	2.39	1.41	14.8	49.7	42	28.8	TBG
U4ah	2.42	1.63	14.6	42.4	56.1	18.6	TU
U4ai	2.6	1.9	12	35.9	63.4	13.1	QTAL
U4ai	2.56	1.91	15.2	36.8	78.9	7.8	QTAL
U4ai	2.52	1.84	19.9	41.7	87.4	5.3	TMA
U4ai	2.55	1.81	24.8	46.6	96.3	1.7	TMA
U4ai	2.53	1.96	24.8	41.9	115.9	-6.7	TMR
U4ai	2.55	1.9	23.5	43	103.7	-1.6	TP
U4ai	2.57	1.75	23.2	47.7	84.9	7.2	TBG
U4ai	2.57	1.91	24.4	44	105.9	-2.6	TTB
U4aj	2.53	1.87	10.7	34	58.8	14	QTMA
U4aj	2.52	1.82	12.4	36.9	61.2	14.3	QTTA
U4aj	2.48	1.49	10.5	46.1	33.9	30.5	TMA
U4aj	2.51	1.77	11.6	37.6	54.6	17.1	TMR
U4aj	2.48	1.75	16.1	40.6	69.3	12.5	TP
U4aj	2.42	1.7	24.9	47.4	89.2	5.1	TBG
U4aj	2.49	1.84	20.6	41.3	91.8	3.4	TTB
U4al	2.64	1.84	13.1	39.3	61.3	15.2	QTAL
U4al	2.59	1.83	12.8	38.6	60.8	15.1	QTAL
U4al	2.57	1.8	12.1	38.3	56.9	16.5	QTAL
U4al	2.57	1.87	13.3	37	66.9	12.2	QTAL
U4al	2.58	1.87	14.4	37.8	71.3	10.9	QTAL
U4am	2.63	1.85	11.6	37.3	56.9	16.2	QTMA
U4am	2.67	1.99	10.7	33.5	63.9	12.2	QTMA
U4am	2.58	1.84	11.7	37	58.1	15.5	QTMA
U4am	2.52	1.48	12.4	48.8	37.6	30.4	QTTA
U4am	2.51	1.56	17.2	48.6	55	21.8	TP
U4am	2.56	*	*	*	*	*	TP
U4am	2.51	*	*	*	*	*	TBG
U4ak	2.63	1.85	9.3	36.3	47.5	19	QTMA
U4ak	2.54	1.84	11.9	36.3	60.1	14.5	QTMA
U4ak	2.55	1.93	15.2	35.8	82.1	6.4	QTMA
U4ak	2.47	1.65	15	43.3	57.2	18.5	QTTA
U4ak	2.61	1.82	19.8	44	82.1	7.9	TMA
U4ak	2.53	1.82	22.1	44	91.4	3.8	TMR
U4ak	2.51	1.88	21.7	41.4	98.3	0.7	TP
U4ak	2.55	1.79	20.3	44.1	82.3	7.8	TBG
U4ak	2.55	1.85	22	43.5	93.6	2.8	TTB
U4at	2.61	1.79	9.8	38.2	46	20.7	QTMA
U4at	2.56	1.87	12.1	35.9	62.9	13.3	QTTA
U4at	2.62	1.83	9.9	37	49.1	18.8	TMA
U4at	2.5	1.66	14.3	43.2	55	19.5	TMB
U4at	2.48	1.73	12.5	38.9	55.4	17.4	TMR

U4at	2.52	1.68	17.5	45	65.1	15.7	TP
U4at	2.54	1.06	21.8	67.5	34	44.5	TBG
U4at	2.55	1.52	11.8	47.5	37.7	29.6	TTB
U4as	2.64	1.96	9.4	32.5	56.5	14.1	QTMA
U4as	2.61	1.88	11.4	36.2	59.4	14.7	QTTA
U4as	2.53	1.67	12.9	42.7	50.4	21.2	TMA
U4as	2.58	1.58	16.8	49	54.3	22.4	TMB
U4as	2.5	1.66	13.9	42.8	53.8	19.8	TMR
U4as	2.51	1.64	17	45.7	61.3	17.7	TP
U4as	2.56	1.27	26.4	63.6	52.5	30.2	TBG
U4as	2.56	1.53	24.6	55.1	68.2	17.5	TTB
U4au	2.58	1.87	13.4	37.1	67.6	12	QTMA
U4au	2.41	1.75	18.1	40.3	78.6	8.6	TMA
U4au	2.54	1.75	17.4	43.1	70.4	12.8	TMA
U4au	2.52	1.92	16.6	36.6	87	4.8	TMR
U4au	2.52	1.83	24.5	45	100	0	TP
U2ao	2.63	1.82	12.8	39.6	58.7	16.3	QTAL
U2ao	2.61	1.92	9.4	33.4	53.8	15.4	QTAL
U2ao	2.49	1.74	14.7	40.5	63	15	QTAL
U2ao	2.54	1.92	12.8	34.2	71.8	9.6	QTAL
U2ar	2.62	1.97	8.25	31.1	52.3	14.8	QTAL
U2ar	2.62	1.93	8.42	32.3	50.4	16	QTAL
U2ar	2.56	1.89	10	33.7	56.1	14.8	QTAL
U2ar	2.6	1.84	11.4	37.4	56.1	16.4	QTAL
U2ar	2.55	1.8	13.2	38.7	61.5	14.9	QTAL
U2ar	2.58	1.82	17	41.3	74.7	10.5	QTAL
U2bx	2.62	1.75	10.4	40	45	22	QTAL
U2bx	2.57	1.81	10.7	37	53	18	QTAL
U2bx	2.54	1.93	10.4	32	63	12	QTAL
U2bx	2.47	1.8	11.1	35	57	15	QTAL
U2bw	2.59	1.89	10.5	34.7	57.3	14.8	QTAL
U2bw	2.57	1.87	12.7	36.5	65	12.8	QTAL
U2bw	2.54	1.93	10.5	32	63.6	11.6	QTAL
U2bw	2.55	2.07	9.3	26.3	73.4	7	QTAL
U2bw	2.48	1.88	12.3	33.4	69.3	10.3	QTAL
U2bw	2.48	1.87	13	34.6	70	10.4	QTAL
U2do	2.52	1.68	11.7	41	47	22	QTAL
U2do	2.61	1.88	11.1	36	58	15	QTAL
U2do	2.62	2.06	8.6	28	63	11	QTAL
U2do	2.63	1.94	11	34	62	13	QTAL
U2do	2.59	2.03	10.2	30	70	9	QTAL

U2cu	2.65	2.07	7.6	27.8	56.6	12.1	QTMA
U2cu	2.56	1.92	13.4	35.1	73.3	9.4	QTTA
U2cu	2.51	1.62	19.1	47.8	64.5	16.9	TP
U2cu	2.39	1.27	27.3	61.5	56.1	27	TBG
U2cu	2.49	1.65	19.1	46.4	67.9	14.9	TTB
U2cu	2.43	1.78	16.8	39	76.9	9	TTS
U2cu	2.48	1.75	18.8	42.6	77.3	9.7	TTB
U2co	2.62	2.06	8.3	28.2	60.6	11.1	QTMA
U2co	2.55	1.82	12.3	37.5	59.5	15.2	QTTA
U2co	2.5	1.59	10.7	43.1	39.8	25.9	TMB
U2co	2.48	1.65	10	40.4	41	23.8	TMR
U2co	2.43	1.72	11.1	37	51.5	17.9	TP
U2co	2.39	1.34	9.3	49.3	25.1	36.9	TBG
U2co	2.42	1.74	10.9	36	52.3	17.2	TTB
U2co	2.45	1.61	15.4	44.4	55.7	19.7	TTS
U2co	2.43	1.71	13.2	38.7	58.6	16	TTB
U2cp	2.63	2.02	9.5	30.3	63.7	11	QTMA
U2cp	2.55	1.66	14.3	44.2	53.7	20.5	QTTA
U2cp	2.45	1.62	15.3	44	56.5	19.2	TMB
U2cp	2.49	1.67	14.8	43	57.2	18.4	TMR
U2cp	2.45	1.72	16.1	41	67.8	13.2	TP
U2cr	2.7	2.03	8.6	31.1	56.3	13.6	QTMA
U2cr	2.52	1.5	17.8	50.9	52.5	24.2	TP
U2cr	2.45	1.13	30.1	67.9	49.9	34	TBG
U2cr	2.52	1.55	18.6	49.9	57.6	21.2	TTB
U2cr	2.4	1.64	15.4	41.9	60.4	16.6	TTS
U2cr	2.53	1.63	15.7	45.5	56.5	19.8	TTB
U2cs	2.66	1.91	6.6	32.8	38.6	20.1	QTMA
U2cs	2.67	1.86	12.1	38.9	57.9	16.4	QTTA
U2cs	2.48	1.71	13.6	40.3	57.8	17	TMR
U2cs	2.5	1.61	17	46.5	59	19.1	TP
U2cs	2.55	1.29	13.6	56.1	31.4	38.5	TBG
U2cs	2.5	1.6	15.9	46.2	54.8	20.9	TTB
U2cs	*	1.79	13.9	*	*	*	TTS
U2cs	2.43	1.63	12.8	41.6	49.9	20.8	TTB
U2cq	2.65	2.09	11.6	29.9	82.9	5.2	QTMA
U2cq	2.62	1.89	14.1	38.1	88.8	4.3	QTTA
U2cq	2.68	1.77	15.1	46	56.2	20.2	TMB
U2cq	2.47	1.76	16.2	39.3	71.2	11.7	TMR
U2cq	2.47	1.77	16.5	39.6	73.4	10.8	TP
U2cq	2.44	*	*	*	*	*	TBG
U2cq	2.59	*	*	*	*	*	TTB
U2dq	2.56	1.73	11.1	40	47.8	20.9	QTAL

U2dq	2.59	1.84	12.1	37.4	59.6	15.1	QTAL
U2dq	2.63	2.04	9.9	30.3	67	10	QTAL
U2dq	2.65	2.18	9.5	25.6	80.2	5.1	QTAL
U2dq	2.46	1.68	18.2	44.2	69.2	13.6	TMA
U2dq	2.51	1.96	11.6	30.8	73.7	8.1	TMR
U2dq	2.47	1.83	16.3	38	78.5	8.2	TP
U2dq	2.42	1.47	20.8	51.8	59.1	21.2	TBG
U2dq	2.49	1.76	18.4	42.1	77	9.7	TTB
U2dz	2.63	1.94	8.7	32.7	51.7	15.8	QTAL
U2dz	2.63	2.1	9.2	27.5	70.6	8.1	QTAL
U2dz	2.63	2.17	9.4	25.3	80.5	4.9	QTAL
U2dz	2.56	1.98	13.5	33.1	80.9	6.3	QTAL
U2dz	2.6	2.07	12.1	29.9	84.2	4.7	QTAL
U2dz	2.61	2.03	13.4	32.6	83.7	5.3	QTAL
U2dz	2.54	1.8	17.4	41.4	75.5	10.1	QTAL
U2ef	2.65	1.99	9.1	31.6	57.2	13.5	QTAL
U2ef	2.65	2.03	8.4	29.9	56.8	12.9	QTAL
U2ef	2.58	2	10.3	30.3	68	9.7	QTAL
U2ef	2.55	1.87	11.5	35.1	61.2	13.6	QTAL
U2ek	2.59	1.92	9.8	33	57	14	QTAL
U2ek	2.53	1.85	13	36	66	12	QTAL
U2ek	2.51	1.67	14.7	43	57	19	TMR
U2ek	2.53	1.97	13.9	33	83	6	TMR
U2ek	2.44	1.68	20.8	45	77	10	TMR+TP
U2ek	2.5	1.84	23.8	44	100	0	TP
U2ek	2.51	1.78	26.7	48	99	1	TP+TBG
U2ek	2.51	1.86	22.5	43	99	1	TIBR
U2eh	2.67	2.05	8	29.5	55.4	13.2	QTAL
U2eh	2.66	2.04	8.1	29.5	56.4	12.9	QTAL
U2eh	2.63	2.02	8.8	30.1	58.8		QTAL
U2eh	2.63	1.95	10.3	33.4	59.9		QTAL
U2eh	2.6	1.78	20.3	45.4	79.8		QTAL
U2eh	2.63	1.98	11.7	33.5	69.1		QTAL
U2eh	2.58	1.88	15.7	38.7	76		QTAL
U2ec	2.62	1.78	7.82	37.5	37.1	23.6	QTAL
U2ec	2.59	1.79	8.36	36.7	40.7	21.8	QTAL
U2ec	2.59	1.87	9.95	35.1	53.1	16.5	QTAL
U2ec	2.57	1.9	10.64	34	59.5	13.8	QTAL
U2ec	2.57	1.94	10.18	32.2	61.4	12.4	QTAL
U2ec	2.6	1.93	8.49	32.2	50.8	15.9	QTAL
U2ec	2.54	1.82	11.48	36.6	57.2	15.7	QTAL
U2ei	2.61	1.9	8.44	33.4	48	17.3	QTAL
U2ei	2.54	1.86	11.14	34.8	59.5	14.1	QTAL

U2ei	2.49	1.85	14.28	36.3	72.7	9.9	TMR
U2ei	2.44	1.74	14.52	39.1	64.7	13.8	TP
U2ei	2.42	1.54	17.19	47.6	55.5	21.2	TBG
U2ei	2.56	1.84	23.16	44.8	95.1	2.2	TTB
U2el	2.63	1.97	10.48	33.1	62.2	12.5	QTAL
U2el	2.58	1.96	11.7	33	69.6	10	QTAL
U2el	2.55	1.86	14.83	37.8	73	10.2	QTAL
U2el	2.5	1.68	24.48	49.1	83.7	8	TMR
U2el	2.56	2.06	20.12	35.7	116.1	-5.7	TMR
U2el	2.51	1.79	26.41	47.6	99.2	0.4	TMR
U2el	2.59	1.95	22.87	42	106.1	-2.6	TP
U2en	2.58	1.9	12.4	35.3	66.8	11.7	QTAL
U2en	2.55	1.86	20	41.7	89.4	4.4	QTTA
U2en	2.57	1.82	22.1	45	89.3	4.8	QTTA+TMB
U2en	2.54	1.73	23.1	47.6	84.3	7.5	TMA
U2en	2.57	2.07	22.8	37.7	125.4	-9.6	TMR
U2en	2.57	2.3	2.5	12.7	45.1	7	TMR
U2en	2.51	1.97	27.8	43.3	126.2	-11.3	TMR
U2en	2.53	1.91	27.9	45.6	116.9	-7.7	TP
U2eo	2.6	2	4.6	26.6	34.6	17.4	QTAL
U2eo	2.56	1.96	9.4	30.9	59.3	12.6	QTAL
U2eo	2.47	1.72	10.5	37.6	48	19.5	TMA
U2eo	2.5	1.8	17.2	40.4	76.8	9.4	TMR
U2eo	2.44	1.77	11.8	36.1	57.8	15.3	TP
U2eo	2.38	1.8	28.1	45.6	110.7	-4.9	TBG
U2eo	*	*	*	*	*	*	TTB
U2ep	2.62	1.96	8.8	31.8	54	14.6	QTAL
U2ep	2.55	1.8	14.1	39.2	64.9	13.7	QTAL
U2ep	2.62	2.01	12.2	32.7	74.7	8.3	QTAL
U2ep	2.58	1.85	16	39.9	74.2	10.3	QTAL
U2eq	2.6	1.92	11.3	34.3	63.7	12.5	QTAL
U2eq	2.57	1.91	11.6	34.3	65	12	QTAL
U2eq	2.55	1.93	13.6	34.7	75.7	8.4	QTAL
U2eq	2.54	1.98	14.5	33.3	86.1	4.6	QTAL
U2eq	2.61	2.01	15.2	34.6	88.5	4	QTAL
U2er	2.61	1.96	10.2	32.8	61	12.8	QTMA
U2er	2.5	1.69	13.2	41.4	53.9	19.1	QTTA
U2er	2.4	1.35	21.8	56	52.3	26.7	TBG
U2er	2.43	1.48	19	50.6	55.8	22.3	TTB
U2eu	2.63	1.82	8.5	36.7	42	21.3	QTMA
U2eu	2.66	2.04	8	29.6	54.9	13.4	QTMA
U2eu	2.7	2.07	7.4	28.9	53.3	13.5	QTMA

U2eu	2.64	2.11	7.1	25.6	58.4	10.6	QTMA
U2eu	2.61	1.96	10.1	32.4	61.3	12.5	QTMA
U2eu	2.62	2.05	*	*	*	*	QTMA
U2eu	2.56	*	*	*	*	*	QTTA
U2es	2.61	1.96	10	32.5	60.3	12.9	QTMA
U2es	2.55	1.83	12.5	37.3	61.5	14.3	QTTA
U2es	2.55	1.82	15	39.3	69.3	12	TMR
U2es	2.46	1.71	17.3	42.4	69.8	12.8	TP
U2et	2.63	1.9	10.4	35.2	56.3	15.4	QTMA
U2et	2.62	1.92	11.8	35.3	64.2	12.6	QTTA
U2et	*	1.52	21	*	*	*	TBG
U2et	2.42	1.79	9	32.8	48.9	16.8	TTB
U2et	2.48	1.73	12.5	38.9	55.7	17.2	TTB
U2ev	2.67	1.99	9.3	32.4	57.4	13.8	QTMA
U2ev	2.6	1.89	12.3	36.3	64.2	13	QTMA
U2ex	2.59	1.89	11.4	35.3	61.2	13.7	QTMA
U2ex	2.6	1.72	14.2	43.4	56.2	19	QTTA
U2ex	2.56	1.72	15.5	43.4	61.3	16.8	TMA
U2ex	2.56	1.94	11.4	32.8	67.5	10.7	TMR
U2ey	2.66	2.01	10.6	32.6	65.2	11.3	QTMA
U2ey	2.53	1.7	19.2	45.6	71.4	13	QTTA
U2ey	2.59	1.61	18	48.9	59.3	19.9	TTB
U2ew	2.56	1.91	13.3	37.1	70.1	11.2	QTMA
U2ew	2.5	1.84	12.9	35.8	65.4	12.4	QTTA
U2ew	2.53	1.77	13	38.2	56.8	16.9	TMR
U2fa	2.66	2.04	8.2	29.9	56	13.1	QTAL
U2fa	2.66	2.02	8.6	30.6	56.5	13.3	QTAL
U2fa	2.63	1.94	10.8	34.2	61.3	13.2	QTAL
U2fa	2.61	1.88	11.6	36.3	60.4	14.4	QTAL
U2fa	2.61	1.88	12.3	37	62.5	13.9	QTAL
U2fa	2.61	1.94	14.4	36.5	76.6	8.5	QTAL
U2fa	2.59	1.88	19.2	41.4	87.2	5.3	QTAL
U2fa	2.58	1.94	25.8	44.1	113.2	-5.8	QTAL
U2fa	2.53	1.89	23.6	43	103.5	-1.5	QTAL
U2fa	2.49	1.78	26.8	47.6	100.4	-0.2	TMR
U2fa	2.44	1.82	22.5	42.2	96.9	1.3	TP
U2fa	2.57	1.84	25.5	46.8	100	0	TBG
U2fb	2.64	2.03	10.2	31	67.1	10.2	QTMA
U2fb	2.6	1.97	11.9	33.3	70.3	9.9	QTTA
U2fb	2.5	1.74	19.3	43.7	76.7	10.2	TMR
U2fb	2.51	1.76	24.9	47.3	92.7	3.5	TMR

Appendix 1 - Zonal Averages for LLNL Yucca Flat Sites

U2fb	2.45	1.81	24.6	44.2	100.8	-0.4	TP
U2fb	2.39	1.69	28.6	49.6	97.2	1.4	TBG
U2fb	2.48	1.78	26.8	47.5	100.6	-0.3	TBR
U2fc	2.67	2.02	7.4	29.9	49.8	15	QTAL
U2fc	2.65	2.05	7.6	28.5	55	12.8	QTAL
U2fc	2.58	1.96	12.2	33.3	71.6	9.4	QTAL
U2fc	2.57	1.92	14	35.7	75.1	8.9	QTAL
U2fc	2.54	1.88	15.7	37.7	78.4	8.1	QTAL
U2fd	2.64	1.92	9.6	34.2	53.7	15.8	QTAL
U2fd	2.64	2.06	8	28.1	58.9	11.5	QTAL
U2fd	2.63	2.12	8.7	26.4	70.1	7.9	QTAL
U2fd	2.64	2.05	9.8	29.9	67	9.9	QTAL
U2fd	2.61	1.94	12.3	34.7	68.8	10.8	QTAL
U2fd	2.61	1.92	11.9	35.1	65	12.3	QTAL
U2fd	2.63	1.99	12.3	33.7	72.3	9.3	QTAL
U2fe	2.66	2.1	9.1	28.1	68	9	QTMA
U2fe	2.62	2.06	13	31.4	85.5	4.5	QTMA
U2fe	2.6	2.04	14.8	33.2	90.8	3	QTMA
U2ff	2.62	1.99	7.4	29.5	49.9	14.8	QTMA
U2ff	2.48	1.73	7.1	35.1	35.1	22.8	QTTA
U2gas	2.61	1.9	14.9	38	74.2	9.8	QTMA
U2gas	2.53	1.7	22.7	48.3	79.7	9.8	QTTA
U2gas	2.53	1.57	22	51.7	66.6	17.3	TMA
U2gas	2.62	*	*	*	*	*	TMR
U2gb	2.58	1.87	10.2	35	54.6	15.9	QTMA
U2gb	2.56	1.51	17.2	51.2	50.7	25.3	TMA
U2gb	2.58	1.83	11.4	37.4	55.6	16.6	TMR
U2gb	2.54	1.56	*	*	*	*	TP
U2ge	2.62	2.02	9.9	30.6	65.7	10.5	QTMA
U2ge	2.58	1.85	14.4	38.5	69.3	11.8	QTTA
U2ge	2.58	1.97	19.6	38.5	100	0	QTTA
U2ge	2.6	1.91	22.8	43.4	100	0	TMA
U2gf	2.58	1.97	12.4	32.6	73.5	8.7	QTAL
U2gf	2.61	1.71	25.7	51.4	85.3	7.6	TMB
U2gf	2.52	1.74	25.4	48.7	90.7	4.5	TMR
U2gf	2.57	1.63	25.7	53	78.8	11.2	TMR
U2gg	2.61	1.89	11.6	35.9	60.8	14.1	QTMA
U2gg	2.6	1.76	16.5	43.5	67	14.3	QTTA
U2gg	2.54	2	12.2	30.9	79.2	6.4	TMR
U2gg	2.53	1.77	15.5	41	66.6	13.7	TB

HOLE	Grain Density (g/cc)	Bulk Density (g/cc)	Water Content (wt %)	Porosity (vol %)	Saturation (vol %)	Gas Porosity (vol %)	Unit
U10ay	2.64	1.97	8.9	31.9	55.2	14.3	QTAL
U10ay	2.61	2.04	9.6	29.2	67.0	9.7	QTAL
U10ay	2.56	1.95	44.6	32.5	69.5	9.9	QTAL
U10ay	2.53	1.59	15.6	47.2	52.6	22.4	QTAL
U10ba	2.66	1.97	7.8	31.6	48.7	16.2	QTAL
U10ba	2.65	2.06	8.4	28.7	60.2	11.4	QTAL
U10ba	2.68	2.11	6.0	25.9	48.7	13.3	QTAL
U10ba	2.61	2.00	9.0	30.4	59.2	12.4	QTAL
U10ba	2.54	1.81	13.7	38.4	64.7	13.6	QTAL
U10bc	2.61	1.83	12.9	38.7	61.0	15.1	QTAL
U10bd	2.57	1.72	11.9	40.8	50.1	20.4	QTAL
U10bg	2.57	1.69	12.2	42.1	49.1	21.4	QTAL
U9cn	2.57	1.87	10.3	34.6	55.7	15.3	QTAL
U9cp	2.63	1.91	7.5	32.9	43.5	18.6	QTAL
U9cq	2.57	1.82	11.6	37.3	56.6	16.2	QTAL
U9cr	2.66	2.03	5.6	27.9	40.3	16.7	QTAL
U9cs	2.59	1.77	10.2	38.8	46.6	20.7	QTAL
U9cg	2.56	1.64	11.5	43.4	43.2	24.6	QTAL
U9cg	2.53	1.59	12.1	44.8	42.9	25.6	QTAL
U9cg	2.51	1.52	11.9	46.6	39.0	28.4	QTAL
U9cg	2.53	1.56	12.6	46.0	42.6	26.4	QTAL
U8e	2.61	1.99	7.3	29.4	49.3	14.9	QTAL
U8k	2.64	2.07	9.4	29.0	66.7	9.7	QTAL
U8l	2.65	1.96	9.1	32.7	54.4	14.9	QTAL
U4af	2.63	1.84	10.4	37.4	51.1	18.3	QTAL
U4af	2.58	1.85	13.1	37.7	64.2	13.5	QTAL
U4ah	2.62	1.91	10.7	34.9	58.7	14.4	QTAL
U4ah	2.56	1.89	11.0	34.4	60.6	13.6	QTAL
U4ai	2.60	1.90	12.0	35.9	63.4	13.1	QTAL
U4ai	2.56	1.91	15.2	36.8	78.9	7.8	QTAL
U4al	2.64	1.84	13.1	39.3	61.3	15.2	QTAL
U4al	2.59	1.83	12.8	38.6	60.8	15.1	QTAL
U4al	2.57	1.80	12.1	38.3	56.9	16.5	QTAL
U4al	2.57	1.87	13.3	37.0	66.9	12.2	QTAL
U4al	2.58	1.87	14.4	37.8	71.3	10.9	QTAL
U2ao	2.63	1.82	12.8	39.6	58.7	16.3	QTAL
U2ao	2.61	1.92	9.4	33.4	53.8	15.4	QTAL
U2ao	2.49	1.74	14.7	40.5	63.0	15.0	QTAL
U2ao	2.54	1.92	12.8	34.2	71.8	9.6	QTAL
U2ar	2.62	1.97	8.3	31.1	52.3	14.8	QTAL
U2ar	2.62	1.93	8.4	32.3	50.4	16.0	QTAL
U2ar	2.56	1.89	10.0	33.7	56.1	14.8	QTAL
U2ar	2.60	1.84	11.4	37.4	56.1	16.4	QTAL
U2ar	2.55	1.80	13.2	38.7	61.5	14.9	QTAL
U2ar	2.58	1.82	17.0	41.3	74.7	10.5	QTAL
U2bx	2.62	1.75	10.4	40.0	45.0	22.0	QTAL
U2bx	2.57	1.81	10.7	37.0	53.0	18.0	QTAL
U2bx	2.54	1.93	10.4	32.0	63.0	12.0	QTAL
U2bx	2.47	1.80	11.1	35.0	57.0	15.0	QTAL
U2bw	2.59	1.89	10.5	34.7	57.3	14.8	QTAL

U2bw	2.57	1.87	12.7	36.5	65.0	12.8	QTAL
U2bw	2.54	1.93	10.5	32.0	63.6	11.6	QTAL
U2bw	2.55	2.07	9.3	26.3	73.4	7.0	QTAL
U2bw	2.48	1.88	12.3	33.4	69.3	10.3	QTAL
U2bw	2.48	1.87	13.0	34.6	70.0	10.4	QTAL
U2do	2.52	1.68	11.7	41.0	47.0	22.0	QTAL
U2do	2.61	1.88	11.1	36.0	58.0	15.0	QTAL
U2do	2.62	2.06	8.6	28.0	63.0	11.0	QTAL
U2do	2.63	1.94	11.0	34.0	62.0	13.0	QTAL
U2do	2.59	2.03	10.2	30.0	70.0	9.0	QTAL
U2dq	2.56	1.73	11.1	40.0	47.8	20.9	QTAL
U2dq	2.59	1.84	12.1	37.4	59.6	15.1	QTAL
U2dq	2.63	2.04	9.9	30.3	67.0	10.0	QTAL
U2dz	2.63	1.94	8.7	32.7	51.7	15.8	QTAL
U2dz	2.63	2.10	9.2	27.5	70.6	8.1	QTAL
U2dz	2.54	1.80	17.4	41.4	75.5	10.1	QTAL
U2ef	2.65	1.99	9.1	31.6	57.2	13.5	QTAL
U2ef	2.65	2.03	8.4	29.9	56.8	12.9	QTAL
U2ef	2.58	2.00	10.3	30.3	68.0	9.7	QTAL
U2ef	2.55	1.87	11.5	35.1	61.2	13.6	QTAL
U2ek	2.59	1.92	9.8	33.0	57.0	14.0	QTAL
U2ek	2.53	1.85	13.0	36.0	66.0	12.0	QTAL
U2eh	2.67	2.05	8.0	29.5	55.4	13.2	QTAL
U2eh	2.66	2.04	8.1	29.5	56.4	12.9	QTAL
U2eh	2.63	2.02	8.8	30.1	58.8		QTAL
U2eh	2.63	*	*	*	*	*	QTAL
U2eh	2.60	*	*	*	*	*	QTAL
U2eh	2.63	*	*	*	*	*	QTAL
U2eh	2.58	*	*	*	*	*	QTAL
U2ec	2.62	1.78	7.8	37.5	37.1	23.6	QTAL
U2ec	2.59	1.79	8.4	36.7	40.7	21.8	QTAL
U2ec	2.59	1.87	10.0	35.1	53.1	16.5	QTAL
U2ec	2.57	1.90	10.6	34.0	59.5	13.8	QTAL
U2ec	2.57	1.94	10.2	32.2	61.4	12.4	QTAL
U2ec	2.60	1.93	8.5	32.2	50.8	15.9	QTAL
U2ec	2.54	1.82	11.5	36.6	57.2	15.7	QTAL
U2ei	2.61	1.90	8.4	33.4	48.0	17.3	QTAL
U2ei	2.54	1.86	11.1	34.8	59.5	14.1	QTAL
U2el	2.63	1.97	10.5	33.1	62.2	12.5	QTAL
U2el	2.58	1.96	11.7	33.0	69.6	10.0	QTAL
U2el	2.55	1.86	14.8	37.8	73.0	10.2	QTAL
U2en	2.58	1.90	12.4	35.3	66.8	11.7	QTAL
U2eo	2.60	2.00	4.6	26.6	34.6	17.4	QTAL
U2eo	2.56	1.96	9.4	30.9	59.3	12.6	QTAL
U2ep	2.62	1.96	8.8	31.8	54.0	14.6	QTAL
U2ep	2.55	1.80	14.1	39.2	64.9	13.7	QTAL
U2ep	2.62	2.01	12.2	32.7	74.7	8.3	QTAL
U2ep	2.58	1.85	16.0	39.9	74.2	10.3	QTAL
U2eq	2.60	1.92	11.3	34.3	63.7	12.5	QTAL
U2eq	2.57	1.91	11.6	34.3	65.0	12.0	QTAL
U2eq	2.55	1.93	13.6	34.7	75.7	8.4	QTAL
U2fa	2.66	2.04	8.2	29.9	56.0	13.1	QTAL
U2fa	2.66	2.02	8.6	30.6	56.5	13.3	QTAL

U2fa	2.63	1.94	10.8	34.2	61.3	13.2	QTAL
U2fa	2.61	1.88	11.6	36.3	60.4	14.4	QTAL
U2fa	2.61	1.88	12.3	37.0	62.5	13.9	QTAL
U2fa	2.61	1.94	14.4	36.5	76.6	8.5	QTAL
U2fc	2.67	2.02	7.4	29.9	49.8	15.0	QTAL
U2fc	2.65	2.05	7.6	28.5	55.0	12.8	QTAL
U2fc	2.58	1.96	12.2	33.3	71.6	9.4	QTAL
U2fc	2.57	1.92	14.0	35.7	75.1	8.9	QTAL
U2fc	2.54	1.88	15.7	37.7	78.4	8.1	QTAL
U2fd	2.64	1.92	9.6	34.2	53.7	15.8	QTAL
U2fd	2.64	2.06	8.0	28.1	58.9	11.5	QTAL
U2fd	2.63	2.12	8.7	26.4	70.1	7.9	QTAL
U2fd	2.64	2.05	9.8	29.9	67.0	9.9	QTAL
U2fd	2.61	1.94	12.3	34.7	68.8	10.8	QTAL
U2fd	2.61	1.92	11.9	35.1	65.0	12.3	QTAL
U2fd	2.63	1.99	12.3	33.7	72.3	9.3	QTAL
U2gf	2.58	1.97	12.4	32.6	73.5	8.7	QTAL
AVERAGE=	2.59	1.90	11.2	34.6	59.7	14.0	
MAX=	2.68	2.12	44.6	47.2	78.9	28.4	
MIN=	2.47	1.52	4.6	25.9	34.6	7.0	
VARIANCE=	0.002	0.013	15.35	19.6	93.7	17.8	
S.D.=	0.044	0.116	3.92	4.4	9.7	4.2	
U10be	2.70	2.10	5.2	26.0	41.7	15.2	QTMA
U10bf	2.67	2.13	6.1	25.1	51.8	12.1	QTMA
U10bh	2.64	2.08	10.4	29.1	74.4	7.5	QTMA
U10ca	2.69	2.03	9.0	31.1	59.0	12.8	QTMA
U10cb	2.76	2.11	8.6	30.0	60.3	11.9	QTMA
U10cc	2.68	2.08	6.6	27.4	49.9	13.7	QTMA
U8c	2.68	2.00	8.1	31.5	51.7	15.2	QTMA
U8j	2.67	2.14	6.9	25.2	58.4	10.5	QTMA
U8m	2.68	1.96	5.3	30.7	33.6	20.4	QTMA
U4j	2.53	1.87	10.7	34.0	58.8	14.0	QTMA
U4ar	2.57	1.85	11.4	36.3	58.0	15.3	QTMA
U4ar	2.69	2.00	10.2	33.2	61.2	12.9	QTMA
U4ar	2.60	1.88	11.1	35.7	58.4	14.8	QTMA
U4ar	2.66	2.00	13.2	34.8	76.2	8.3	QTMA
U4ar	2.60	1.90	15.3	38.2	76.1	9.1	QTMA
U4ac	2.64	1.88	11.6	37.2	58.4	15.5	QTMA
U4ac	2.55	1.81	12.3	37.8	58.8	15.6	QTMA
U4aj	2.53	1.87	10.7	34.0	58.8	14.0	QTMA
U4am	2.63	1.85	11.6	37.3	56.9	16.2	QTMA
U4am	2.67	1.99	10.7	33.5	63.9	12.2	QTMA
U4am	2.58	1.84	11.7	37.0	58.1	15.5	QTMA
U4ak	2.63	1.85	9.3	36.3	47.5	19.0	QTMA
U4ak	2.54	1.84	11.9	36.3	60.1	14.5	QTMA
U4at	2.61	1.79	9.8	38.2	46.0	20.7	QTMA
U4as	2.64	1.96	9.4	32.5	56.5	14.1	QTMA
U4au	2.58	1.87	13.4	37.1	67.6	12.0	QTMA
U2cu	2.65	2.07	7.6	27.8	56.6	12.1	QTMA
U2co	2.62	2.06	8.3	28.2	60.6	11.1	QTMA

U2cp	2.63	2.02	9.5	30.3	63.7	11.0	QTMA
U2cr	2.70	2.03	8.6	31.1	56.3	13.6	QTMA
U2cs	2.66	1.91	6.6	32.8	38.6	20.1	QTMA
U2er	2.61	1.96	10.2	32.8	61.0	12.8	QTMA
U2eu	2.63	1.82	8.5	36.7	42.0	21.3	QTMA
U2eu	2.66	2.04	8.0	29.6	54.9	13.4	QTMA
U2eu	2.70	2.07	7.4	28.9	53.3	13.5	QTMA
U2eu	2.64	2.11	7.1	25.6	58.4	10.6	QTMA
U2eu	2.61	1.96	10.1	32.4	61.3	12.5	QTMA
U2eu	2.62	*	*	*	*	*	QTMA
U2es	2.61	1.96	10.0	32.5	60.3	12.9	QTMA
U2et	2.63	1.90	10.4	35.2	56.3	15.4	QTMA
U2ev	2.67	1.99	9.3	32.4	57.4	13.8	QTMA
U2ev	2.60	1.89	12.3	36.3	64.2	13.0	QTMA
U2ex	2.59	1.89	11.4	35.3	61.2	13.7	QTMA
U2ey	2.66	2.01	10.6	32.6	65.2	11.3	QTMA
U2ew	2.56	1.91	13.3	37.1	70.1	11.2	QTMA
U2fb	2.64	2.03	10.2	31.0	67.1	10.2	QTMA
U2fe	2.66	2.10	9.1	28.1	68.0	9.0	QTMA
U2ff	2.62	1.99	7.4	29.5	49.9	14.8	QTMA
U2gas	2.61	1.90	14.9	38.0	74.2	9.8	QTMA
U2gb	2.58	1.87	10.2	35.0	54.6	15.9	QTMA
U2ge	2.62	2.02	9.9	30.6	65.7	10.5	QTMA
U2gg	2.61	1.89	11.6	35.9	60.8	14.1	QTMA
AVERAGE=	2.63	1.96	9.9	32.8	58.5	13.5	
MAX=	2.76	2.14	15.3	38.2	76.2	21.3	
MIN=	2.53	1.79	5.2	25.1	33.6	7.5	
VARIANCE=	0.002	0.009	5.14	14.2	78.0	9.3	
S.D.=	0.048	0.096	2.27	3.8	8.8	3.1	
U10be	2.59	1.90	11.4	35.0	62.1	13.2	QTTA
U10bf	2.50	1.62	14.3	44.5	51.8	21.5	QTTA
U10bh	2.60	1.80	16.7	42.4	70.8	12.4	QTTA
U8c	2.53	1.85	12.2	35.7	63.2	13.1	QTTA
U8j	2.60	1.78	8.3	36.9	39.9	22.2	QTTA
U4j	2.52	1.82	12.4	36.9	61.2	14.3	QTTA
U4aj	2.52	1.82	12.4	36.9	61.2	14.3	QTTA
U4am	2.52	1.48	12.4	48.8	37.6	30.4	QTTA
U4ak	2.47	1.65	15.0	43.3	57.2	18.5	QTTA
U4at	2.56	1.87	12.1	35.9	62.9	13.3	QTTA
U4as	2.61	1.88	11.4	36.2	59.4	14.7	QTTA
U2cu	2.56	1.92	13.4	35.1	73.3	9.4	QTTA
U2co	2.55	1.82	12.3	37.5	59.5	15.2	QTTA
U2cp	2.55	1.66	14.3	44.2	53.7	20.5	QTTA
U2cs	2.67	1.86	12.1	38.9	57.9	16.4	QTTA
U2er	2.50	1.69	13.2	41.4	53.9	19.1	QTTA
U2eu	2.56	*	*	*	*	*	QTTA
U2es	2.55	1.83	12.5	37.3	61.5	14.3	QTTA
U2et	2.62	1.92	11.8	35.3	64.2	12.6	QTTA
U2ex	2.60	1.72	14.2	43.4	56.2	19.0	QTTA
U2ey	2.53	1.70	19.2	45.6	71.4	13.0	QTTA
U2ew	2.50	1.84	12.9	35.9	65.4	12.4	QTTA

U2fb	2.60	1.97	11.9	33.3	70.3	9.9	QTTA
U2ff	2.48	1.73	7.1	35.1	35.1	22.8	QTTA
U2gas	2.53	1.70	22.7	48.3	79.7	9.8	QTTA
U2ge	2.58	1.85	14.4	38.5	69.3	11.8	QTTA
U2gg	2.60	1.76	16.5	43.5	67.0	14.3	QTTA
AVERAGE=	2.56	1.79	13.4	39.5	60.2	15.7	
MAX=	2.67	1.97	22.7	48.8	79.7	30.4	
MIN=	2.47	1.48	7.1	33.3	35.1	9.4	
VARIANCE=	0.002	0.012	9.40	20.1	113.0	23.4	
S.D.=	0.048	0.111	3.07	4.5	10.6	4.8	

HOLE	Grain Density (g/cc)	Bulk Density (g/cc)	Water Content (wt %)	Porosity (vol %)	Saturation (vol %)	Gas Porosity (vol %)	Unit
U8c	2.50	1.58	13.6	45.4	47.4	23.8	TB
U8e	2.58	1.71	14.8	43.6	58.0	18.3	TB
U8j	2.62	1.87	13.9	38.7	67.4	12.6	TB
U8m	2.64	*	*	*	*	*	TB
U2gg	2.53	1.77	15.5	41.0	66.6	13.7	TB
AVERAGE=	2.57	1.73	14.5	42.2	59.9	17.1	
MAX=	2.64	1.87	15.5	45.4	67.4	23.8	
MIN=	2.50	1.58	13.6	38.7	47.4	12.6	
VARIANCE=	0.003	0.015	0.75	8.6	87.0	26.0	
S.D.=	0.059	0.121	0.87	2.9	9.3	5.1	
U10bc	2.41	1.32	20.8	56.5	48.7	29.0	TBG
U10bd	2.46	1.47	16.5	50.0	48.5	25.7	TBG
U10be	2.43	1.44	14.4	49.3	42.0	28.6	TBG
U10bf	2.37	1.21	13.8	56.2	29.7	39.5	TBG
U10bg	2.36	1.21	27.0	62.6	52.2	29.9	TBG
U9cn	2.38	1.22	17.3	57.8	36.4	36.7	TBG
U9cp	2.36	1.38	17.6	51.9	46.8	27.6	TBG
U9cq	2.51	1.56	23.8	52.5	70.9	15.3	TBG
U9cr	2.37	1.27	23.5	58.9	50.8	29.0	TBG
U9cs	2.52	1.62	25.6	52.0	79.8	10.5	TBG
U9cw	2.37	1.33	14.9	52.1	38.1	32.3	TBG
U8e	2.50	1.70	10.9	39.3	47.1	20.8	TBG
U8j	2.49	1.33	20.0	57.1	46.7	30.4	TBG
U8m	2.50	1.49	19.5	52.0	56.0	22.9	TBG
U8n	2.40	1.38	22.2	55.1	55.7	24.4	TBG
U4ah	2.39	1.41	14.8	49.7	42.0	28.8	TBG
U4ai	2.57	1.75	23.2	47.7	84.9	7.2	TBG
U4am	2.51	*	*	*	*	*	TBG
U4ak	2.55	1.79	20.3	44.1	82.3	7.8	TBG
U4at	2.54	1.06	21.8	67.5	34.0	44.5	TBG
U4as	2.56	1.27	26.4	63.6	52.5	30.2	TBG
U2cu	2.39	1.27	27.3	61.5	56.1	27.0	TBG
U2co	2.39	1.34	9.3	49.3	25.1	36.9	TBG
U2cr	2.45	1.13	30.1	67.9	49.9	34.0	TBG
U2cs	2.55	1.29	13.6	56.1	31.4	38.5	TBG
U2cq	2.44	*	*	*	*	*	TBG
U2dq	2.42	1.47	20.8	51.8	59.1	21.2	TBG
U2ei	2.42	1.54	17.2	47.6	55.5	21.2	TBG
U2er	2.40	1.35	21.8	56.0	52.3	26.7	TBG
AVERAGE=	2.45	1.39	19.8	54.3	50.9	26.9	
MAX=	2.57	1.79	30.1	67.9	84.9	44.5	
MIN=	2.36	1.06	9.3	39.3	25.1	7.2	
VARIANCE=	0.005	0.033	27.68	44.6	227.8	85.0	
S.D.=	0.069	0.181	5.26	6.7	15.1	9.2	
U9cp	2.48	1.61	16.0	45.4	56.8	19.6	TBR
U9cp	2.48	1.74	16.4	41.3	69.4	12.6	TBR

U8c	2.50	1.70	13.8	41.3	56.9	17.8	TF
U8k	2.54	1.79	14.0	39.5	63.2	14.5	TF
U8m	2.59	1.75	16.0	43.3	64.5	15.4	TF
U8n	2.61	*	*	*	*	*	TF
AVERAGE=	2.56	1.75	14.6	41.4	61.5	15.9	
MAX=	2.61	1.79	16.0	43.3	64.5	17.8	
MIN=	2.50	1.70	13.8	39.5	56.9	14.5	
VARIANCE=	0.002	0.002	1.48	3.6	16.5	2.9	
S.D.=	0.050	0.045	1.22	1.9	4.1	1.7	
U4j	2.48	1.49	10.5	46.1	33.9	30.5	TMA
U4ar	2.57	*	*	*	*	*	TMA
U4aj	2.48	1.49	10.5	46.1	33.9	30.5	TMA
U4ak	2.61	1.82	19.8	44.0	82.1	7.9	TMA
U4at	2.62	1.83	9.9	37.0	49.1	18.8	TMA
U4as	2.53	1.67	12.9	42.7	50.4	21.2	TMA
U4au	2.41	1.75	18.1	40.3	78.6	8.6	TMA
U4au	2.54	1.75	17.4	43.1	70.4	12.8	TMA
U2dq	2.46	1.68	18.2	44.2	69.2	13.6	TMA
U2en	2.54	1.73	23.1	47.6	84.3	7.5	TMA
U2eo	2.47	1.72	10.5	37.6	48.0	19.5	TMA
U2ex	2.56	1.72	15.5	43.4	61.3	16.8	TMA
U2gas	2.53	1.57	22.0	51.7	66.6	17.3	TMA
U2gb	2.56	1.51	17.2	51.2	50.7	25.3	TMA
AVERAGE=	2.53	1.67	15.8	44.2	59.9	17.7	
MAX=	2.62	1.83	23.1	51.7	84.3	30.5	
MIN=	2.41	1.49	9.9	37.0	33.9	7.5	
VARIANCE=	0.004	0.014	20.91	19.9	288.9	60.6	
S.D.=	0.059	0.119	4.57	4.5	17.0	7.8	
U4ar	2.55	1.83	16.3	39.9	74.8	10.0	TMB
U4at	2.50	1.66	14.3	43.2	55.0	19.5	TMB
U4as	2.58	1.58	16.8	49.0	54.3	22.4	TMB
U2co	2.50	1.59	10.7	43.1	39.8	25.9	TMB
U2cp	2.45	1.62	15.3	44.0	56.5	19.2	TMB
U2cq	2.68	1.77	15.1	46.0	56.2	20.2	TMB
U2gf	2.61	1.71	25.7	51.4	85.3	7.6	TMB
AVERAGE=	2.55	1.68	16.3	45.2	60.3	17.8	
MAX=	2.68	1.83	25.7	51.4	85.3	25.9	
MIN=	2.45	1.58	10.7	39.9	39.8	7.6	
VARIANCE=	0.006	0.009	21.07	15.2	225.1	43.7	
S.D.=	0.078	0.095	4.59	3.9	15.0	6.6	
U9cp	2.45	1.78	15.6	38.7	72.0	10.8	TMR
U9cq	2.50	1.66	14.0	42.9	54.1	19.7	TMR

U9cr	2.46	1.53	16.4	48.0	52.1	23.0	TMR
U9cs	2.55	1.63	12.0	43.6	45.0	24.0	TMR
U9cw	2.47	1.60	10.4	41.7	39.9	25.1	TMR
U8m	2.50	1.72	9.6	37.7	43.6	21.2	TMR
U8n	2.52	1.90	9.6	31.7	57.3	13.5	TMR
U4j	2.51	1.77	11.6	37.6	54.6	17.1	TMR
U4aj	2.51	1.77	11.6	37.6	54.6	17.1	TMR
U4at	2.48	1.73	12.5	38.9	55.4	17.4	TMR
U4as	2.50	1.66	13.9	42.8	53.8	19.8	TMR
U2co	2.48	1.65	10.0	40.4	41.0	23.8	TMR
U2cp	2.49	1.67	14.8	43.0	57.2	18.4	TMR
U2cs	2.48	1.71	13.6	40.3	57.8	17.0	TMR
U2cq	2.47	1.76	16.2	39.3	71.2	11.7	TMR
U2dq	2.51	1.96	11.6	30.8	73.7	8.1	TMR
U2ek	2.51	1.67	14.7	43.0	57.0	19.0	TMR
U2ei	2.49	1.85	14.3	36.3	72.7	9.9	TMR
U2el	2.50	1.68	24.5	49.1	83.7	8.0	TMR
U2eo	2.50	1.80	17.2	40.4	76.8	9.4	TMR
U2es	2.55	1.82	15.0	39.3	69.3	12.0	TMR
U2ex	2.56	1.94	11.4	32.8	67.5	10.7	TMR
U2ew	2.53	1.77	13.0	38.2	56.8	16.9	TMR
U2fb	2.50	1.74	19.3	43.7	76.7	10.2	TMR
U2gas	2.62	*	*	*	*	*	TMR
U2gb	2.58	1.83	11.4	37.4	55.6	16.6	TMR
U2gf	2.57	1.63	25.7	53.0	78.8	11.2	TMR
AVERAGE=	2.51	1.74	14.2	40.3	60.7	15.8	
MAX=	2.62	1.96	25.7	53.0	83.7	25.1	
MIN=	2.45	1.53	9.6	30.8	39.9	8.0	
VARIANCE=	0.002	0.011	16.20	25.1	150.3	27.7	
S.D.=	0.039	0.104	4.02	5.0	12.3	5.3	
U8e	2.45	1.77	12.3	36.7	59.2	15.0	TMR+TP
U2ek	2.44	1.68	20.8	45.0	77.0	10.0	TMR+TP
U10ay	2.43	*	*	*	*	*	TP
U10ba	2.50	1.73	14.1	38.9	64.6	13.8	TP
U10bc	2.45	1.36	18.1	54.5	45.1	29.9	TP
U10bd	2.43	1.53	17.8	48.3	56.3	21.1	TP
U10be	2.48	1.64	12.8	42.3	49.8	21.2	TP
U10bf	2.48	1.57	13.0	44.9	45.3	24.6	TP
U10bg	2.48	1.43	16.1	51.4	44.8	28.4	TP
U10bh	2.74	*	*	*	*	*	TP
U9cn	2.44	1.45	15.1	49.5	44.3	27.6	TP
U9cp	2.45	1.61	14.2	43.7	52.1	20.9	TP
U9cq	2.66	1.71	16.6	46.5	60.8	18.2	TP
U9cq	2.48	1.57	17.5	47.7	57.7	20.2	TP
U9cr	2.45	1.52	16.5	48.2	52.0	23.1	TP
U9cs	2.54	1.68	15.3	44.0	58.5	18.3	TP
U9cw	2.51	1.54	11.6	45.7	39.0	27.9	TP
U8m	2.46	1.66	13.3	41.4	53.4	19.3	TP
U4j	2.48	1.75	16.1	40.6	69.3	12.5	TP

U4ah	2.44	1.62	13.5	42.6	51.5	20.6	TP
U4aj	2.48	1.75	16.1	40.6	69.3	12.5	TP
U4am	2.51	1.56	17.2	48.6	55.0	21.8	TP
U4am	2.56	*	*	*	*	*	TP
U4at	2.52	1.68	17.5	45.0	65.1	15.7	TP
U4as	2.51	1.64	17.0	45.7	61.3	17.7	TP
U2cu	2.51	1.62	19.1	47.8	64.5	16.9	TP
U2co	2.43	1.72	11.1	37.0	51.5	17.9	TP
U2cp	2.45	1.72	16.1	41.0	67.8	13.2	TP
U2cr	2.52	1.50	17.8	50.9	52.5	24.2	TP
U2cs	2.50	1.61	17.0	46.5	59.0	19.1	TP
U2cq	2.47	1.77	16.5	39.6	73.4	10.8	TP
U2dq	2.47	1.83	16.3	38.0	78.5	8.2	TP
U2ei	2.44	1.74	14.5	39.1	64.7	13.8	TP
U2eo	2.44	1.77	11.8	36.1	57.8	15.3	TP
U2es	2.46	1.71	17.3	42.4	69.8	12.8	TP
U2gb	2.54	*	*	*	*	*	TP
AVERAGE=	2.49	1.63	15.6	44.3	57.8	18.9	
MAX=	2.74	1.83	19.1	54.5	78.5	29.9	
MIN=	2.43	1.36	11.1	36.1	39.0	8.2	
VARIANCE=	0.004	0.013	4.47	21.0	92.6	30.6	
S.D.=	0.064	0.113	2.11	4.6	9.6	5.5	
U4af	2.46	1.63	20.8	47.5	71.4	13.6	TP+TBG
U8c	2.57	1.55	13.6	48.0	43.9	26.9	TRV
U8j	2.62	1.79	6.6	36.3	32.7	24.4	TRV
U8k	2.57	1.59	16.8	48.7	54.8	22.0	TRV
U8m	2.60	1.46	11.9	50.3	34.5	33.0	TRV
U8n	2.58	*	*	*	*	*	TRV
AVERAGE=	2.59	1.60	12.2	45.8	41.5	26.6	
MAX=	2.62	1.79	16.8	50.3	54.8	33.0	
MIN=	2.57	1.46	6.6	36.3	32.7	22.0	
VARIANCE=	0.000	0.019	18.19	41.2	103.0	22.3	
S.D.=	0.022	0.139	4.26	6.4	10.2	4.7	
U10bc	2.52	1.62	14.0	44.7	50.8	22.0	TTB
U10bc	2.42	1.71	13.8	39.2	60.2	15.6	TTB
U10bd	2.45	1.62	13.4	42.9	50.7	21.1	TTB
U10be	2.50	1.75	16.7	41.6	70.0	12.5	TTB
U10bf	2.49	1.85	15.8	37.6	77.9	8.3	TTB
U10bg	2.39	1.53	14.6	45.4	49.3	23.0	TTB
U10ca	2.55	1.71	16.2	43.8	63.4	16.0	TTB
U10ca	2.50	1.71	17.9	43.7	70.4	12.9	TTB
U10cb	2.55	1.74	16.8	43.4	67.5	14.1	TTB
U10cc	2.48	1.69	16.9	43.3	66.2	14.6	TTB
U9cn	2.50	1.85	15.7	37.8	76.9	8.7	TTB
U9cq	2.52	1.72	18.6	44.5	71.6	12.6	TTB
U9cr	2.50	1.67	19.8	46.4	71.6	13.2	TTB

U9cs	2.55	1.81	18.5	42.2	79.1	8.8	TTB
U9cw	2.56	1.44	15.4	52.4	42.3	30.2	TTB
U8c	2.47	1.59	13.3	44.1	48.0	23.0	TTB
U8c	2.47	1.51	14.1	47.6	45.8	25.8	TTB
U8e	2.45	1.55	13.8	45.5	46.8	24.2	TTB
U8e	2.43	1.53	12.6	44.9	42.8	25.7	TTB
U8j	2.51	1.68	15.2	43.1	59.4	17.5	TTB
U8j	2.52	1.65	16.1	45.2	58.5	18.8	TTB
U8k	2.41	1.70	17.2	41.7	70.2	12.4	TTB
U8k	2.48	1.67	14.9	42.8	58.1	18.0	TTB
U8l	2.47	1.63	16.3	44.7	59.5	18.1	TTB
U8l	2.44	1.57	16.1	46.1	54.6	20.9	TTB
U8m	2.52	1.69	14.6	42.6	58.3	17.8	TTB
U8m	2.55	1.63	12.5	44.1	46.1	23.8	TTB
U8n	2.47	1.66	16.9	44.0	63.8	15.9	TTB
U8n	2.49	1.74	15.8	40.9	67.1	13.5	TTB
U4af	2.49	1.73	19.3	43.8	76.6	10.2	TTB
U4at	2.55	1.52	11.8	47.5	37.7	29.6	TTB
U4as	2.56	1.53	24.6	55.1	68.2	17.5	TTB
U2cu	2.49	1.65	19.1	46.4	67.9	14.9	TTB
U2cu	2.48	1.75	18.8	42.6	77.3	9.7	TTB
U2co	2.42	1.74	10.9	36.0	52.3	17.2	TTB
U2co	2.43	1.71	13.2	38.7	58.6	16.0	TTB
U2cr	2.52	1.55	18.6	49.9	57.6	21.2	TTB
U2cr	2.53	1.63	15.7	45.5	56.5	19.8	TTB
U2cs	2.50	1.60	15.9	46.2	54.8	20.9	TTB
U2cs	2.43	1.63	12.8	41.6	49.9	20.8	TTB
U2cq	2.59	*	*	*	*	*	TTB
U2dq	2.49	1.76	18.4	42.1	77.0	9.7	TTB
U2er	2.43	1.48	19.0	50.6	55.8	22.3	TTB
U2et	2.42	1.79	9.0	32.8	48.9	16.8	TTB
U2et	2.48	1.73	12.5	38.9	55.7	17.2	TTB
U2ey	2.59	1.61	18.0	48.9	59.3	19.9	TTB
AVERAGE=	2.49	1.66	15.8	43.8	60.0	17.6	
MAX=	2.59	1.85	24.6	55.1	79.1	30.2	
MIN=	2.39	1.44	9.0	32.8	37.7	8.3	
VARIANCE=	0.002	0.009	7.87	16.8	118.8	29.3	
S.D.=	0.049	0.096	2.81	4.1	10.9	5.4	
U10be	2.48	1.82	18.1	40.0	82.4	7.0	TTS
U10ca	2.53	1.71	18.2	44.7	69.3	13.7	TTS
U10cb	2.50	1.67	19.1	46.0	69.3	14.1	TTS
U10cc	2.47	1.67	20.3	46.2	73.2	12.4	TTS
U8c	2.50	1.29	15.9	56.7	36.0	36.3	TTS
U8j	2.48	1.57	16.1	47.0	53.5	21.9	TTS
U8k	2.38	1.49	22.4	51.6	64.7	18.2	TTS
U8l	2.42	1.46	27.1	56.1	70.5	16.6	TTS
U8m	2.53	1.47	16.3	51.4	46.6	27.5	TTS
U8n	2.48	1.62	18.5	47.0	63.7	17.1	TTS
U2cu	2.43	1.78	16.8	39.0	76.9	9.0	TTS
U2co	2.45	1.61	15.4	44.4	55.7	19.7	TTS

U2cr	2.40	1.64	15.4	41.9	60.4	16.6	TTS
AVERAGE =	2.47	1.60	18.4	47.1	63.2	17.7	
MAX=	2.53	1.82	27.1	56.7	82.4	36.3	
MIN=	2.38	1.29	15.4	39.0	36.0	7.0	
VARIANCE=	0.002	0.021	11.04	30.8	163.3	59.5	
S.D.=	0.047	0.144	3.32	5.6	12.8	7.7	
U10bd	2.58	1.71	16.4	44.5	63.0	16.5	TU
U8c	2.59	1.83	15.9	40.4	71.9	11.3	TU
U8k	2.57	1.80	14.5	40.1	64.8	14.1	TU
U4ah	2.42	1.63	14.6	42.4	56.1	18.6	TU
AVERAGE =	2.54	1.74	15.4	41.9	64.0	15.1	
MAX=	2.59	1.83	16.4	44.5	71.9	18.6	
MIN=	2.42	1.63	14.5	40.1	56.1	11.3	
VARIANCE=	0.006	0.008	0.90	4.2	42.2	9.9	
S.D.=	0.080	0.091	0.95	2.0	6.5	3.1	

Appendix 4 - Overburden and WP Velocity at LLNL Yucca Flat Sites

Hole	DOB (m)	WP Velocity (m/s)	Overburden Velocity (m/s)	WP Media
U2A	135	1999		QTA
U2AD	150	1731		QTA
U2AH	166	1712		QTMA
U2AO	167	1962	1342	QTTA
U2AR	167	1800	1440	QTTA
U2AW	183	2286	1615	TMR
U2AX	183	2499	1950	TP
U2B	183	1887		QTA
U2BC	183	2134	1859	TTU
U2BD	183	2210	2035	QTA
U2BR	183	1798	1829	TP
U2BS	184	2469	1646	TP
U2BU	186	2200	1340	TP
U2BV	192	1951	1737	QTTA
U2BW	195	1895	1360	QTMA
U2BX	195	1829	1372	QTMA
U2BY	196	1920	1463	QTMA
U2BZ	198	2012	1615	QTTA
U2C	198	1887		QTA
U2CO	198	2250	1745	TP
U2CP	198	1920	1640	TP
U2CQ	199	1713	1641	TP
U2CR	200	1822	1580	TTU
U2CS	200	2008	1785	TTU
U2CU	200	1905	1826	TTU
U2CU	200	1999	1778	TTU
U2DH	200	1737	1280	QTMA
U2DH	200	2256	1372	QTMA
U2DI	200	2073	1646	QTA
U2DJ	200	2377	1737	TMR
U2DJ	200	2042	1524	QTA
U2DK	201	2286	1585	QTMA
U2DL	203	2195	1646	QTA
U2DM	204	1981	1615	QTA
U2DN	205	1524	1280	QTA
U2DO	207	2347	1585	QTA
U2DP	207	2134	1494	QTA
U2DQ	207	2436	1504	TMR
U2DR	208	2200	1700	QTTA
U2DS	208	1829	1615	TMR
U2DU	210	2070	1340	QTMA
U2DV	210	1890	1615	QTMA
U2DW	210	2225	1554	QTMA
U2DW	213	1951	1402	QTMA
U2DY	213	2260	1560	TBG
U2DZ	213	2204	1747	QTMA
U2E	216	2072	1974	QTA

U2EA	225	1966	1402	QTMA
U2EB	226	1911	1411	QTMA
U2EC	226	1780	1250	QTMA
U2EF	226	1725	1230	QTMA
U2EG	226	1825	1300	QTMA
U2EH	227	1757	1557	QTMA
U2EI	233	1981	1752	TBG
U2EK	236	2560	1840	TTU
U2EL	238	2235	1716	TP
U2EM	241	1672	1260	QTMA
U2EN	244	2708	1673	TP
U2EO	244	2518	1774	TP
U2EP	247	2040	1505	QTMA
U2EQ	247	2358	1480	QTTA
U2ER	250	1820	1440	TTU
U2ES	250	2100	1730	TP
U2ET	250	1900	1535	TTU
U2EU	259	1963	1578	QTMA
U2EV	259	2071	1540	QTMA
U2EW	262	1843	1337	QTTA
U2EX	263	2435	1699	TMA
U2EY	263	1673	1486	QTTA
U2EY	263	1747	1475	QTTA
U2F	265	2154	1892	QTA
U2FA	265	2486	1770	QTTA
U2FB	265	2455	1649	TMR
U2FC	266	2221	1688	QTTA
U2FD	267	2270	1630	QTMA
U2FE	271	2030	1580	QTMA
U2FF	272	2334	1615	QTMA
U2G	273	1999		QTA
U2GA	274	1903	1620	QTMA
U2GB	275	2219	1565	TMR
U2GE	278	2004	1881	QTTA
U2GF	282	2269	1728	QTMA
U2GG	282	2459	1664	TMR
U2J	289	1887		QTA
U2L	293	1999		QTA
U2M	293	1887		QTA
U2N	294	1999		QTA
U2P	296	2322		QTA
U2U	305	1873		QTA
U2X	305		1854	TP
U2Y	305	1873		QTA
U4AA	305	2175	1500	QTTA
U4AB	311	1975	1425	QTTA
U4AC	314	1675	1338	QTMA
U4AF	314	1752	1288	QTMA
U4AH	315	1880	1423	TTU

U4AI	317	1725	1589	QTTA
U4AJ	320	2120	1610	TP
U4AK	320	2140	1600	QTTA
U4AL	320	2250	1610	QTMA
U4AM	320	1918	1460	TP
U4AR	320	2347	1679	TMB
U4AS	323	2175	1647	TTU
U4AU	323	2474	1622	TMR
U8C	323	1962	1532	TB
U8D	326	1554	1554	TMA
U8E	326	2096	1710	TTU
U8E	326	1587	1588	QTMA
U8J	326	2460	1721	TF
U8K	331	2120	1580	TB
U8L	331	1831	1484	TTU
U9M	331	2430	1740	TF
U9BB	331	1463		TTU
U9CG	331	1310	1292	QTMA
U9CG	335	1407	1179	QTMA
U9CH	335	1829	1494	TP
U9CI	341	1859	1341	TP
U9CJ	343	1524	1067	QTMA
U9CK	343	1524	1524	QTMA
U9CL	369	2300	1400	TTU
U9CM	370	2210	1400	TTU
U9CN	374	1670	1337	TTU
U9CP	378	1694	1540	TTU
U9CQ	381	2010	1420	TTU
U9CR	381	1970	1620	TTU
U9CS	388	1625	1313	TP
U9CW	390	1551	1126	TP
U9IS	391	2134	1463	TTU
U9IV	400	1909		TTU
U9IV	406	1888		TTU
U9IW	411	1372	1189	TP
U9IW	412	1189	1189	TTU
U9IX	413	2031		TTU
U9IX	415	1895		TTU
U9IX	417	1888		TTU
U9IXY31	420	1676	1372	TTU
U9IY	424	1544		TTU
U9IYZ26	431	1311	1189	TTU
U9IYZ26	436	1219	1158	TTU
U9IZ	445	1512		TTU
U9IZ	447	2408	1859	TTU
U10A	450	2286		QTA
U10AQ	451	1524	1463	TTU
U10AR	463	1494	1859	QTTA
U10AS	464	2134	1494	TTU

U10AS	466	1737	1402	QTTA
U10AS	466	2012	1311	QTMA
U10AT	480	1981	1494	QTMA
U10AV	483	1981	1219	QTMA
U10AW	489	2134	1585	QTMA
U10AX	493	1585	1311	TTU
U10AY	493	1433	1370	QTTA
U10BA	494	2284	1567	QTMA
U10BA	500	2002	1378	QTMA
U10BB	506	2200	1650	QTMA
U10BB	515	2350	1500	QTMA
U10BC	515	1454	1129	TTU
U10BD	519	1627	1100	TP
U10BE	529	2300	1570	QTMA
U10BF	530	1442	1527	QTTA
U10BG	536	1143	1162	TTU
U10BH	536	1911	1592	QTTA
U10BH	536	2006	1538	QTMA
U10BH	542	2231	1449	QTMA
U10C	543	1909		TMR
U10CA	564	1754	1462	TBT
U10CB	573	1474	1283	TBT
U10CC	601	1327	1449	TTU
U10D	655	2060		TTU
U10E	658	2531		TTU
U10I	668	2835		TTU
U10K	679	2164		TTU
U10M	688	1829		QTA
U10S	690	2027		QTA
U10T	715	2531		TF
U10W	716	2027		QTA

Appendix 5
USGS Proposal for a Concept Similar to the ROCK PILE Concept

United States Department of the Interior
GEOLOGICAL SURVEY
Box 25046
Denver Federal Center
Denver, Colorado 80225

IN REPLY REFER TO: Mail Stop 954

December 12, 1978

Dr. J. E. Carothers, L-7
Lawrence Livermore Laboratory
P.O. Box 808
Livermore, California 94550

Dear Jim:

At the executive session of the Containment Evaluation Panel held at LaJolla on November 29-30, 1978, I presented a plan initiated by the U.S. Geological Survey to eliminate much of the geologic and material properties data collection that presently is required for containment purposes.

The purpose of this letter is to summarize the USGS plan.

The plan has as its thesis the following principal points:

1. The extensive and thorough geologic investigations in the last 8 years (post-Baneberry) have provided an excellent geologic data base for Pahute Mesa and Yucca Flat.

2. The information in the geologic data base provides sufficient knowledge to adequately characterize the general geologic setting and some of the material properties required for containment evaluation.

3. Surface effects mapping, geologic examination of drill cuttings, and minimal geophysical logging can provide the additional information needed that is not available from the geologic data base.

The geologic data base contains two principal types of information for Pahute Mesa and Yucca Flat:

1. Data on the geologic environment, including location of major faults, thickness and distribution of tuff units and alluvium, and depth to Paleozoic surface.

AMERICAN REVOLUTION BICENTENNIAL 1776

2. Material-properties data versus rock type and stratigraphic unit.

The USGS maintains that the existing geologic data base is sufficient to enable an accurate prediction to be made to characterize the geologic setting and material properties of most future event sites, except for clay content, CO_2 content, faults or anomalous structure, and depth to Paleozoics. For these exceptions we recommend the following procedures:

1. Clay--Resistivity and caliper logs.

2. CO_2--Analysis of total cuttings (alluvium only).

3. Faults and anomalous structure--Magnetic and resistivity logs, litho-stratigraphic identification from drill cuttings, surface effects maps.

4. Depth to Paleozoic--Surface gravity, interpretation, stratigraphic method.

Should prediction from the geologic data base and the minimal procedures outlined above disclose the need for additional information there are available the following backup procedures:

1. Down-hole photography

2. Sidewall samples

3. Exploratory holes and cores

4. Additional geophysical logs

This plan eliminates the need for the following procedures that currently are routinely used:

1. Sidewall samples and the measurement of water content and grain density.

2. Vibroseis and velocity log.

3. Density log and gravimeter log.

4. Calculations of porosity, saturation, and gas-filled porosity.

Sincerely yours,

W. S. Twenhofel

W. S. Twenhofel, Chief
Special Projects Branch

Appendix 6 - Overburden Density Calculation - U4at

Unit	Average Density	Thickness of units down to the WP		
	(g/c)	(m)		
	INPUT THIS COLUMN			
QTAL	1.90			
QTMA	1.96	81		
QTTA	1.79	24		
TMB	1.68	7		
TMA	1.67	12		
TMR	1.74	105		
TP	1.63	106		
TBG	1.39			
TTB	1.66			
TTS	1.60			
TB	1.73			
TF	1.70			
TRV	1.60			
TU	1.74			
Depth of Burial =		335	m	
Hole Name =	U4at			
Overburden Density =		1.76	Mg/m3	
1 SD estimated error =		0.05	Mg/m3	
2 SD estimated error =		0.11	Mg/m3	

Unit	Gas Porosity	Thickness of units down to the WP		
	Vol %	(m)		
		INPUT THIS COLUMN		
QTAL	14.00			
QTMA	13.50	81		
QTTA	15.70	24		
TMB	17.80	7		
TMA	17.70	12		
TMR	15.80	105		
TP	18.90	106		
TBG	26.90			
TTB	17.60			
TTS	17.70			
TB	17.10			
TF	15.90			
TRV	26.60			
TU	15.10			
Depth of Burial =		335	m	
Hole Name =	U4at			
Overburden Gas Porosity =		16.33	Vol%	

CARBONATE ROCK EMPLACEMENT SITES AT THE NEVADA TEST SITE

Allen H. Cogbill
Michael T. Gerety
Fred N. App
Ward L. Hawkins

Los Alamos National Laboratory

ABSTRACT

In the Spring of 1988 Los Alamos National Laboratory began a search to locate an unusual NTS emplacement site. Constraints established for the site were rather severe. The site must be in carbonate rock, preferably a massive carbonate, beneath the water table; the carbonate unit must be at least 100 m thick. For containment, the carbonate should be overlain by at least 300 m of porous, unsaturated materials such as tuff or alluvium. Finally, the rocks serving as the working point medium must be suitably separated from the main carbonate aquifer that exists throughout much of southeastern Nevada. The last requirement was established to insure that radioactive products of the nuclear detonation would not migrate rapidly into the regional aquifer. The Tippipah Limestone, a limestone exposed in the Syncline Ridge area on the western margin of Yucca Flat, seemed to be the best candidate rock, because where exposed it is usually underlain by the Eleana Formation, a highly impermeable, rather thick, clastic formation.

Our studies have concentrated on the western margin of Area 4. After examination of the available geological and geophysical information, we acquired new gravity and magnetic data along three roughly west-east traverses, each about 3 km in length. Resistivity data comprising two approximately perpendicular, crossed Schlumberger profiles were acquired, as well. If a significant thickness of the more resistive limestone were present at depths less than 1000 m, the electrical survey should detect it.

No resistive units of significant thickness were detected. The implication is that the exposed Tippipah Limestone probably represents an allochthonous geologic unit, and is unlikely to be present in significant thickness beneath the sediments and volcanic units of Yucca Flat. The probability of finding a carbonate rock emplacement site at NTS that meets the criteria above is considered rather small.

INTRODUCTION

In the Spring of 1988 the Containment Program Office at Los Alamos requested that geologic and geophysical studies be made in order to locate an emplacement site with unusual requirements. Siting criteria proposed for the emplacement site were rather severe, and there was then and still is doubt that a site meeting all the criteria exists on the Nevada Test Site (NTS). Briefly, the constraints that were established were as follows.

1. The site must be located in carbonate rock, preferably a rather massive carbonate; the carbonate rocks were required to have a minimum thickness of 100 m.

2. The site must be located at least 100 m beneath the static water level (SWL).

3. For containment purposes, the carbonate rock should be overlain preferably by at least 300 m of porous, unsaturated materials such as tuff or alluvium.

4. The carbonate rocks serving as the working point medium must be suitably separated from the main carbonate aquifer that is widespread in southeastern Nevada.

Requirement (4) turned out to be the most severe constraint affecting the search for the emplacement site. Initially, no such requirement was specified, and several locations were believed to be suitable. The requirement that the emplacement medium be separated from the principal aquifer was imposed in order to insure that radioactive products of the nuclear detonation would not migrate rapidly into the main aquifer. Because most of the carbonate rocks known at the NTS are in direct communication with the main aquifer, the imposition of requirement (4) drastically reduced the number of potential sites.

U. S. Geological Survey (USGS) personnel suggested that a possible medium might be the Tippipah Limestone. At most locations where exposed, the Tippipah Limestone is underlain by the Eleana Formation, a highly impermeable, rather thick, clastic formation. The Eleana Fm. is known to act as an aquitard, and USGS personnel believed that if rocks of the Tippipah Limestone could be located that met requirements 1-3, the probability that requirement 4 would also be met was very high.

Following this advice, our task was to find a sufficient thickness of Tippipah Limestone in the subsurface below the SWL. Because the SWL is always at least 300 m below the surface in the nuclear testing areas, we were hopeful that any Tippipah Limestone found below the SWL would be overlain by a sufficient thickness of tuff or alluvium to make containment of the event probable.

At NTS, the Tippipah Limestone is exposed at Syncline Ridge (Figure 1); small exposures also occur on the north side of Mine Mountain and just west of the Eleana Range (Orkild, 1963). Given the constraints outlined above, we believed that the only feasible emplacement sites would be immediately southwest or north of Syncline Ridge itself. However, a number of operational and containment-related difficulties were anticipated for a site southwest of Syncline Ridge, making a site north of Syncline Ridge much more desirable. Thus, we have focused our attention on the area immediately north of Syncline Ridge.

GEOLOGIC SETTING

Geological studies of the Syncline Ridge area were conducted by the USGS in the late 1970's as part of an effort to evaluate the Eleana Fm. as a suitable medium for a nuclear waste repository; an open-file report by Hoover and Morrison (1980) summarizes the investigations. These studies characterized the surface and subsurface geology near Syncline Ridge rather well. We present a brief synopsis of these studies below.

Major Stratigraphic Units

For our purposes only 4 major stratigraphic units are of interest. These are the Eleana Fm. (Mississippian and Devonian), the Tippipah Limestone (Permian(?) and Pennsylvanian), undifferentiated Tertiary tuffs, and Quaternary alluvium. Brief lithologic descriptions of these units are provided below; these descriptions are taken from Hoover and Morrison (1980), which describes the units in greater detail.

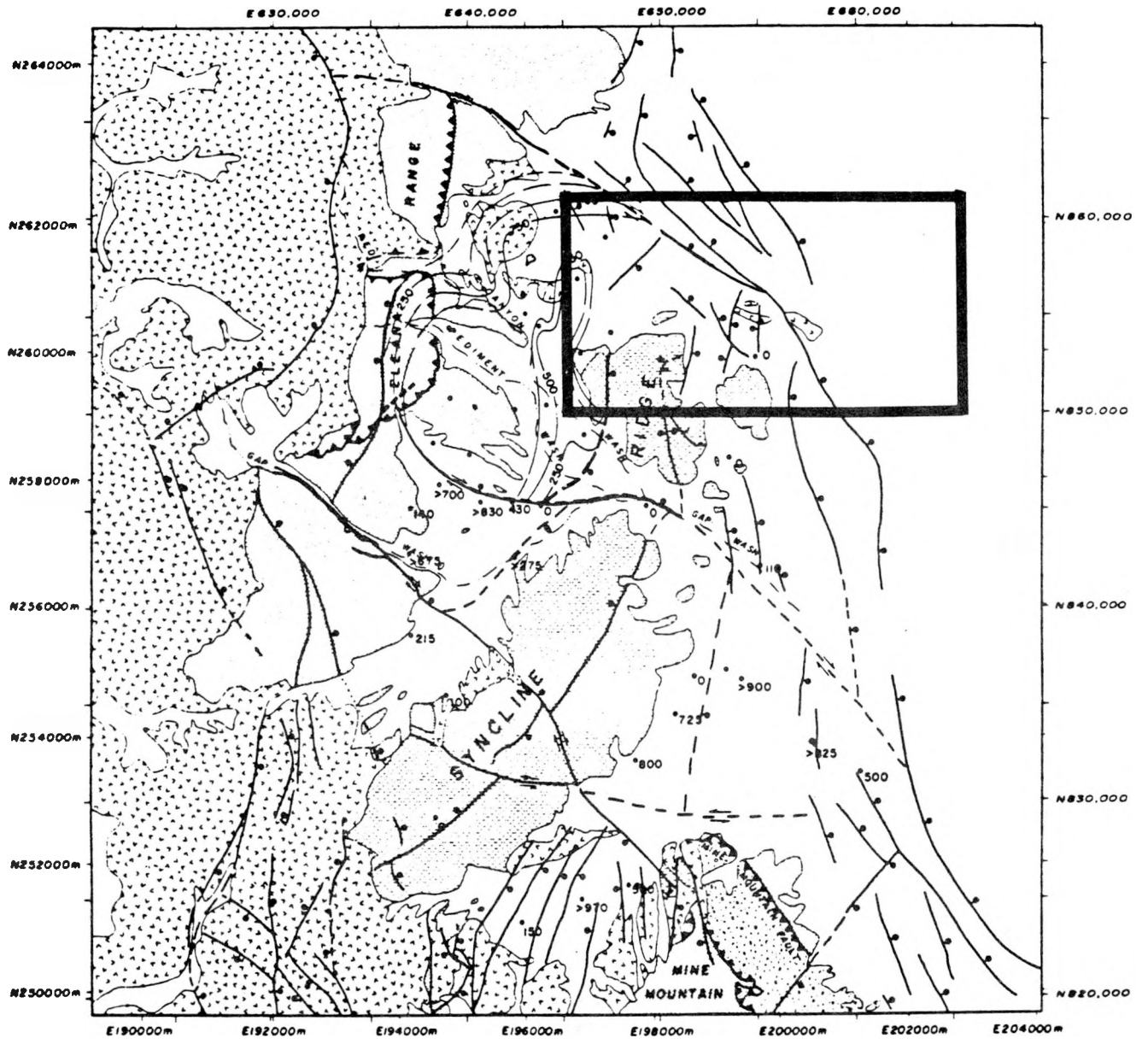


FIG. 1. Geologic map of the Syncline Ridge area, western Yucca Flat (from Hoover and Morrison, 1980). The area of this study is indicated by the rectangular box.

Eleana Formation. The Eleana Fm. has a straigraphic thickness of at least 2350 m and perhaps as much as 3000-4000 m. Although the unit is divided into 10 major sub-units designated A-J, unit J being stratigraphically highest, only units G-J are present in the Syncline Ridge area. The rock types of units G-J include both siliceous and argillaceous sediments; unit I includes a significant amount of limestone, as well. Most of the outcrops of Eleana Fm. in the vicinity of Syncline Ridge are of unit J, and thus it is the only unit that we describe in greater detail. The stratigraphic thickness of unit J is significant, approximately 1100 m. Unit J is divided into 3 subunits, which are (from bottom to top) a lower subunit, an argillite subunit, and a quartzite subunit. The stratigraphic thicknesses of these subunits are 300, 700, and 100 m, respectively.

The argillite subunit is important for two reasons. First, its hydraulic transmissivity is extremely low (Dinwiddie and Weir, 1979), and thus the argillite subunit is thought to be largely responsible for the fact that the Eleana Fm. is a hydrologic aquitard. Second, the more argillaceous portions of the argillite subunit have low electrical resistivities (less than 30 ohm-m); this relatively low resistivity has been used to map the Eleana Fm. using electrical soundings (Hoover and others, 1982).

Tippipah Limestone. The Tippipah Limestone actually forms Syncline Ridge. It is divided into a lower unit and an upper unit; the respective stratigraphic thicknesses are 100-200 m and 850-900 m. The lower unit is nowhere exposed in the vicinity of Syncline Ridge, leading Hoover and Morrison (1980) to conclude that, at Syncline Ridge, the contact between the Tippipah Limestone and the underlying Eleana Fm. is probably a thrust contact, rather than a depositional contact.

The upper unit of the Tippipah Limestone is relatively pure, light- to medium-gray limestone; individual beds range from 1 to 10 m in thickness. According to Hoover and others (1982), well logs from drill holes in the immediate vicinity of Syncline Ridge indicate that the electrical resistivity of the unit is "...generally over 1000 ohm-m..." Although measured resistivities greater than 1000 ohm-m are often suspect, it seems clear that the Tippipah Limestone is a much more resistive unit than the argillaceous subunit of unit J of the Eleana Fm. This fact was used in planning the geophysical surveys that we conducted.

Undifferentiated Tertiary tuffs. Tertiary silicic tuffs are present nearly everywhere in the subsurface of Yucca Flat, where they lie unconformably upon Paleozoic rocks. The lithologic variation in the tuffs is very large. Zeolitized bedded tuffs, non-welded ash-flow tuffs, vitric bedded tuffs, and welded tuffs are all present. In the immediate vicinity of Syncline Ridge, outcrops of such units are sparse, but are assumed to be present in the subsurface.

Quaternary alluvium. The surface deposits in the area northeast of Syncline Ridge are almost exclusively Quaternary alluvial deposits, although small outcrops of tuff are occasionally present. According to Hoover and Morrison (1980), some of these deposits mapped as Quaternary may in fact be Tertiary; however, for our purposes what is important is that the deposits are younger than the tuffs. Just northeast of Syncline Ridge, the known thickness of the alluvial deposits varies from 0-155 m (McArthur, 1976); greater thicknesses of alluvium may be present. Alluvium immediately overlies Tippipah Limestone at the extreme northern and northeastern end of Syncline Ridge.

Geologic Structures

Syncline Ridge is bounded on the east by high-angle faults that form the western boundary of Yucca Flat. Hoover and Morrison (1980) indicate that the faults immediately north of Syncline Ridge have NNW strikes; the amount of offset on such faults is uncertain, but the

collective offset probably is less than 400 m, because the estimated amount of overburden (tuff and alluvium) is less than 400 m (Orkild, 1963). Strike-slip faults of relatively minor displacement cut Syncline Ridge in three locations.

According to Hoover and Morrison, the Tippipah Limestone forming Syncline Ridge is probably completely allochthonous, having been thrust over unit J of the Eleana Fm.; however, these thrusts are described as local thrusts. Thus, the Tippipah Limestone at Syncline Ridge is, in their view, an outlier that is unlikely to be found in the subsurface of Yucca Flat.

The Tippipah Limestone occurs as a syncline overlying the Eleana Fm. An axial fault that is mapped for nearly the entire length of the syncline; offset on this fault is rather uncertain. Hoover and Morrison indicate that the offset is 100-200 m, but Hoover and others (1982), on the basis of electrical studies, believe the offset to be much greater.

Hydrologic Data

The water table map of Doty and Thordarson (1983) indicates that the elevation of the SWL just north of Syncline Ridge should be 1065 ± 60 m, or about 365 m below ground surface. The elevation of the SWL decreases rapidly to the east, however, because only 3.5 km east, the elevation of the SWL is shown to be 760 m. Our area of interest is on the margin of the data used to make the water table map; therefore the stated uncertainty of the SWL elevation may be too small.

PREVIOUS GEOPHYSICAL STUDIES

Hoover and others (1982) summarized much of the geophysical work performed in the Syncline Ridge area prior to 1980. They also conducted a series of electrical and seismic experiments designed to elucidate the structure of Syncline Ridge itself; however, their experiments did not extend to the area north of Syncline Ridge. Some of the results of their compilation of previous data and their own experiments are summarized below.

- The faults along the axis of Syncline Ridge and the faults bounding the east and west margins of the ridge have large vertical offsets.
- Evidence was found to support the existence of at least one of the strike-slip faults of Hoover and Morrison (1980).
- The Eleana Fm. appeared electrically heterogeneous, which was attributed to structural complexity.
- No significant density contrast exists between the Eleana Fm. and the Tippipah Limestone.
- Seismic reflection surveys run within and on the margins of Syncline Ridge displayed very poor record quality and were thus not very useful for delineating structure. The poor record quality was attributed to large velocity variations within the upper few hundred meters.

In 1982 a seismic reflection survey was run for the Lawrence Livermore National Laboratory (LLNL). The western end of line 2 of this survey lies immediately north of Syncline Ridge (Figure 2). This line crosses an exploratory borehole, Ue4ac, that was drilled into the Paleozoic carbonates 479 m beneath the overlying tuff and alluvium of Yucca Flat. Ue4ac

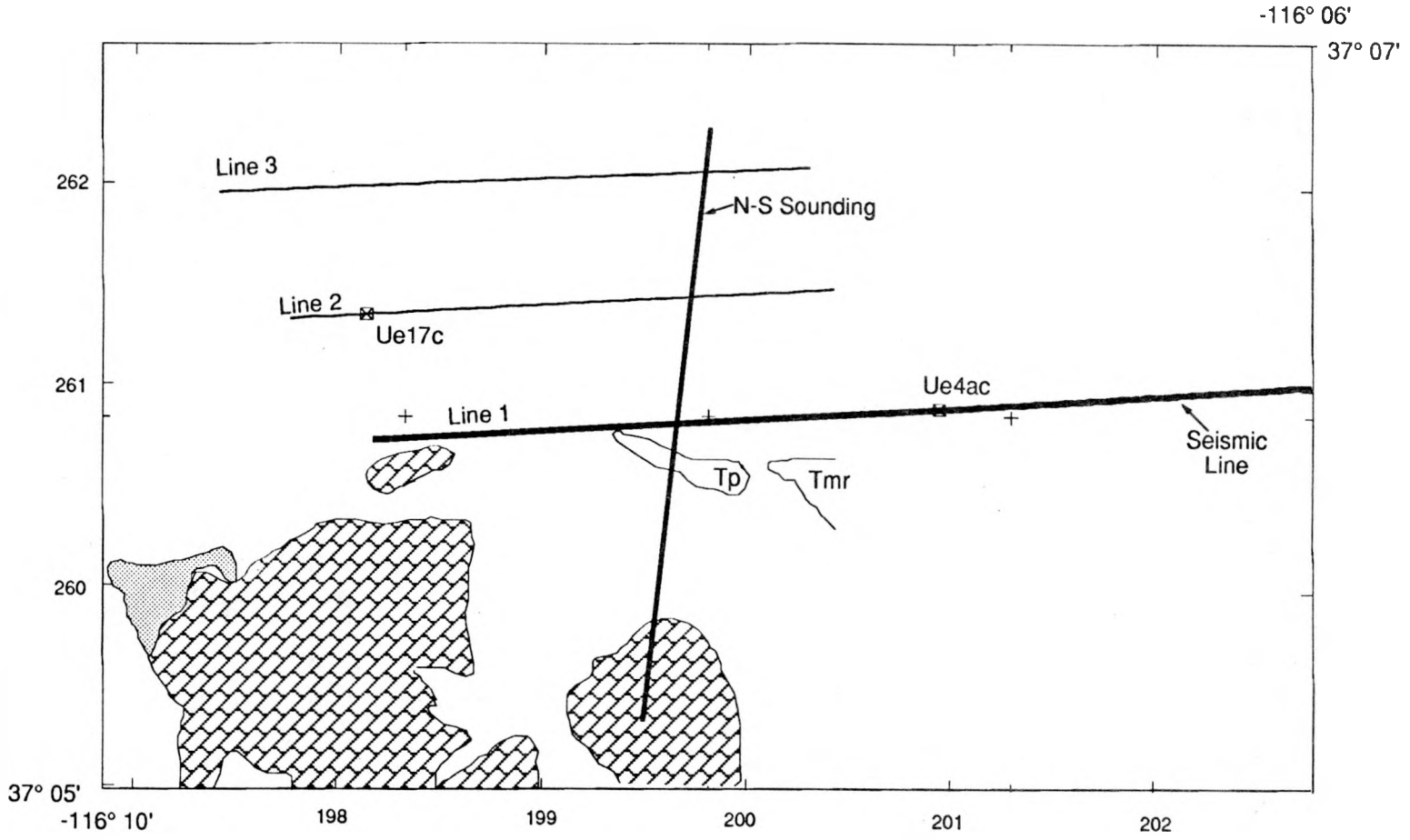


FIG. 2. Map of the area studied, showing the locations of gravity-magnetic lines 1-3, the seismic reflection line, and the two Schlumberger sounding lines (the E-W sounding is coincident with line 1 and the seismic line). Outcrops of Paintbrush Tuff (Tp) and Rainier Mesa Tuff (Tmr) are indicated. Tippipah Limestone outcrops are indicated by the diagonal brick pattern; unit J of the Eleana Fm. is shown by stippling. Rectangular coordinates used are Nevada State Plane, central zone, in km.

provides the only deep stratigraphic and geophysical data immediately north of Syncline Ridge; such data are summarized by McArthur (1976). A checkshot (geophone) survey is available to a depth of 507 m in Ue4ac; these data permit the times observed on the reflection line to be converted to depths.

A portion of the migrated reflection line is shown as Figure 3; the position of Ue4ac is indicated on the figure. The spatial location of Ue4ac is indicated on Figure 3. A fault of significant offset (down to the east) is apparent near shot point 35 on the line. At Ue4ac, the prominent reflectors occurring at and below 910 ms two-way travel time are actually within the Paleozoic section. The tuff-Paleozoic contact should occur at 810 ms; however, no prominent reflections are present at that time.

RECENT GEOPHYSICAL INVESTIGATIONS

Gravity and Magnetic Surveys

Gravity survey. From the previous geophysical studies it seemed evident that, if the Tippipah Limestone occurred in the subsurface north of Syncline Ridge, it could probably best be detected using an electrical technique, as its resistivity was thought to be quite high compared to units nearby. To aid in locating the electrical survey, we chose to make gravity and magnetic measurements along three parallel lines north of Syncline Ridge; our hope was that such measurements might be able to more precisely locate the horizontal positions of the sub-alluvial fault or faults that form the western boundary of Yucca Flat in the region north of Syncline Ridge. The existing gravity data were also used to some extent; however, their uncertain accuracy and coarser spacing largely limited their utility to identifying trend directions.

Gravity measurements were made every 45.7 m along the three lines, denoted lines 1, 2, and 3, from south to north (Figure 2). Note that part of line 1 was coincident with the western end of seismic line 2 (1982) of LLNL. The data were corrected for earth tides and terrain effects; the near-station terrain corrections were made using a USGS digital elevation model of grid size 30 m, and are believed to be precise to 20 μGal. The gravity anomaly data from all three lines are shown in Figure 4. Figures 5-7 show the horizontal gradients observed along each of these gravity survey lines. Locations identified as those of possible faults are shown on the displays of the horizontal gravity gradients. Note that the fault inferred between 2600-3000 m along all the lines is coincident with the surface projection of the fault noted on the seismic reflection line; thus, this fault appears to strike nearly north-south. Figure 8 is a contour map of the gravity field made from the previously existing gravity measurements. A strong gradient is present near the northeasternmost exposures of the Tippipah Limestone. Projected along strike, this gradient is coincident with the fault seen on the LLNL seismic line 2 (1982).

Magnetic survey. A ground magnetic survey was conducted along the same lines as the gravity survey. Digitally recording, proton-precession magnetometers were used. Measurements were made every 3 m along the lines. Our hope was that a sufficient thickness of Rainier Mesa Member of the Timber Mountain Tuff (Tmr) would be present beneath the alluvial cover to provide a strong signal where the tuff might be cut by faults. The Tmr is strongly (reversely) magnetized, and has been used previously as a useful unit for mapping faults with magnetic surveys (Bath, 1976).

Figures 9-11 show the magnetic data acquired on lines 1-3. A distinct anomaly having a peak-to-peak amplitude of 300 nT occurs near the eastern end of line 1 (between 1800-2150 m

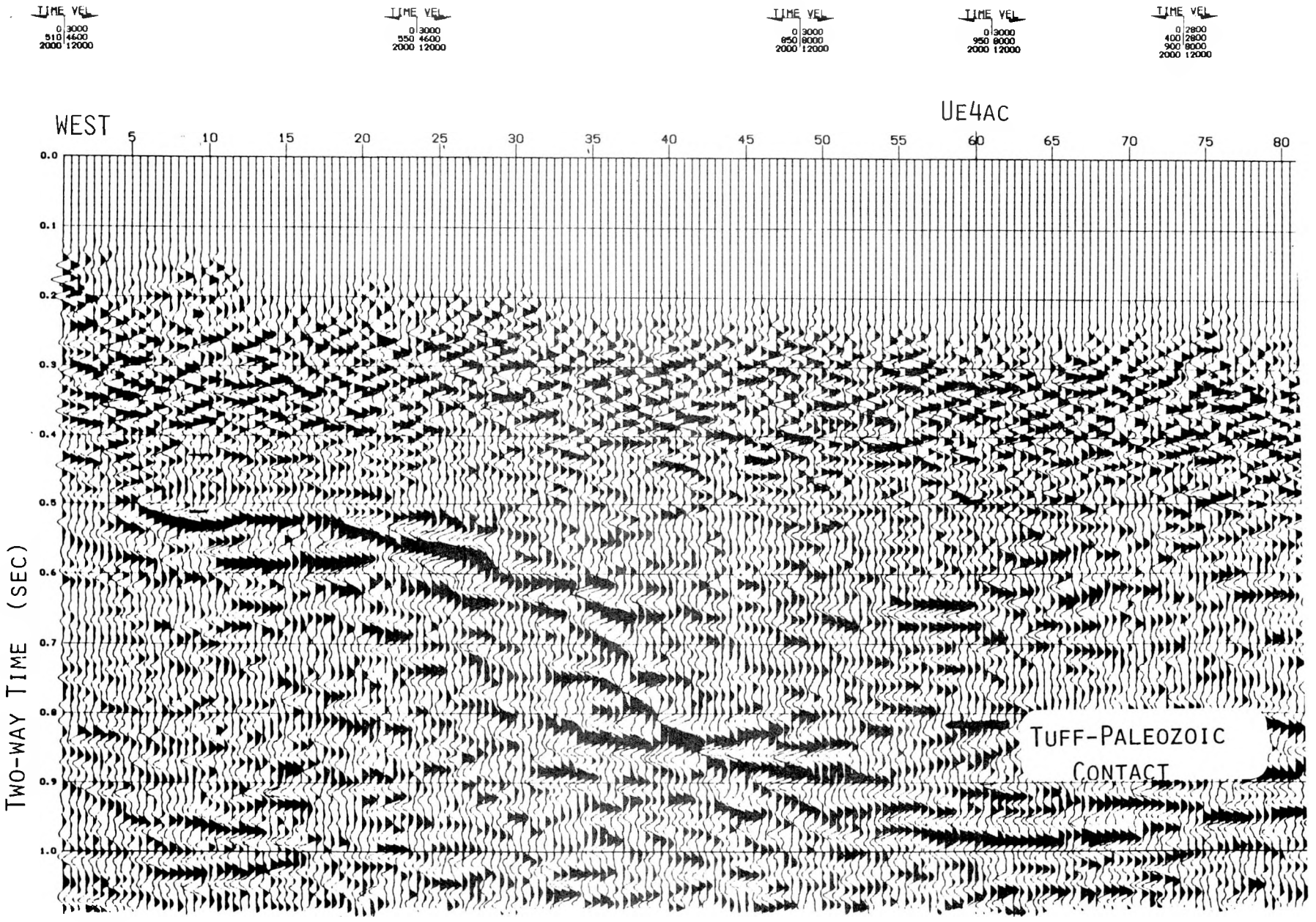


FIG 3. Western portion of LLNL seismic reflection line 2 (1982). The position of exploratory hole Ue4ac is indicated. The distance between shot points is 25 m. At the location of Ue4ac, the tuff-Paleozoic contact should occur at 810 ms.

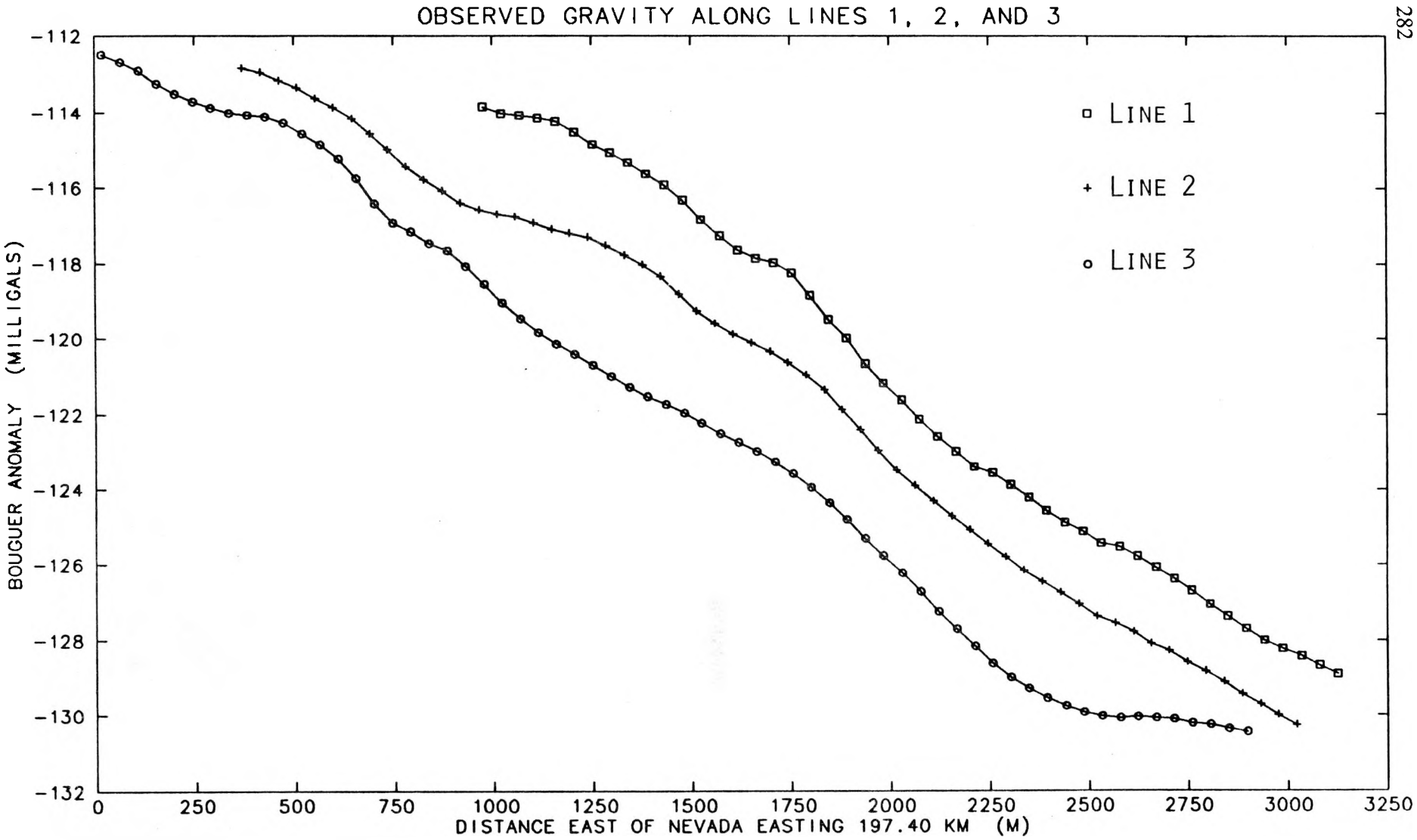


FIG 4. Gravity data (Bouguer anomaly) observed along lines 1-3. Reduction density was 1600 kg/m^3. Coordinates are distances measured along the lines from each line's extrapolated intersection with Nevada easting 197.4 km.

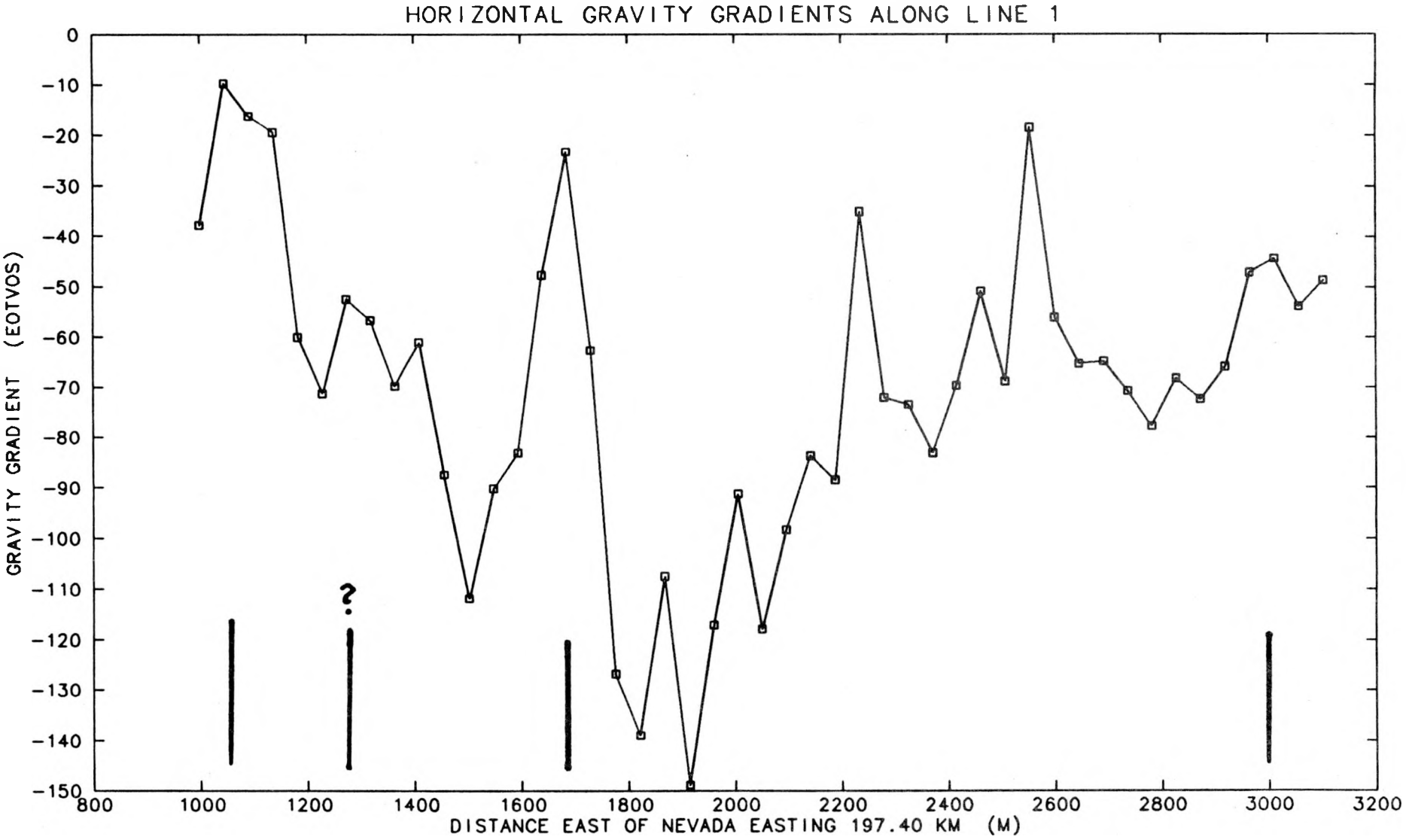


FIG. 5. Horizontal gravity gradients along line 1, in Eotvos units (an Eotvos unit = $10^{-9}/s^2$). Distances are measured as in Figure 4. Locations of possible faults are indicated by vertical lines.

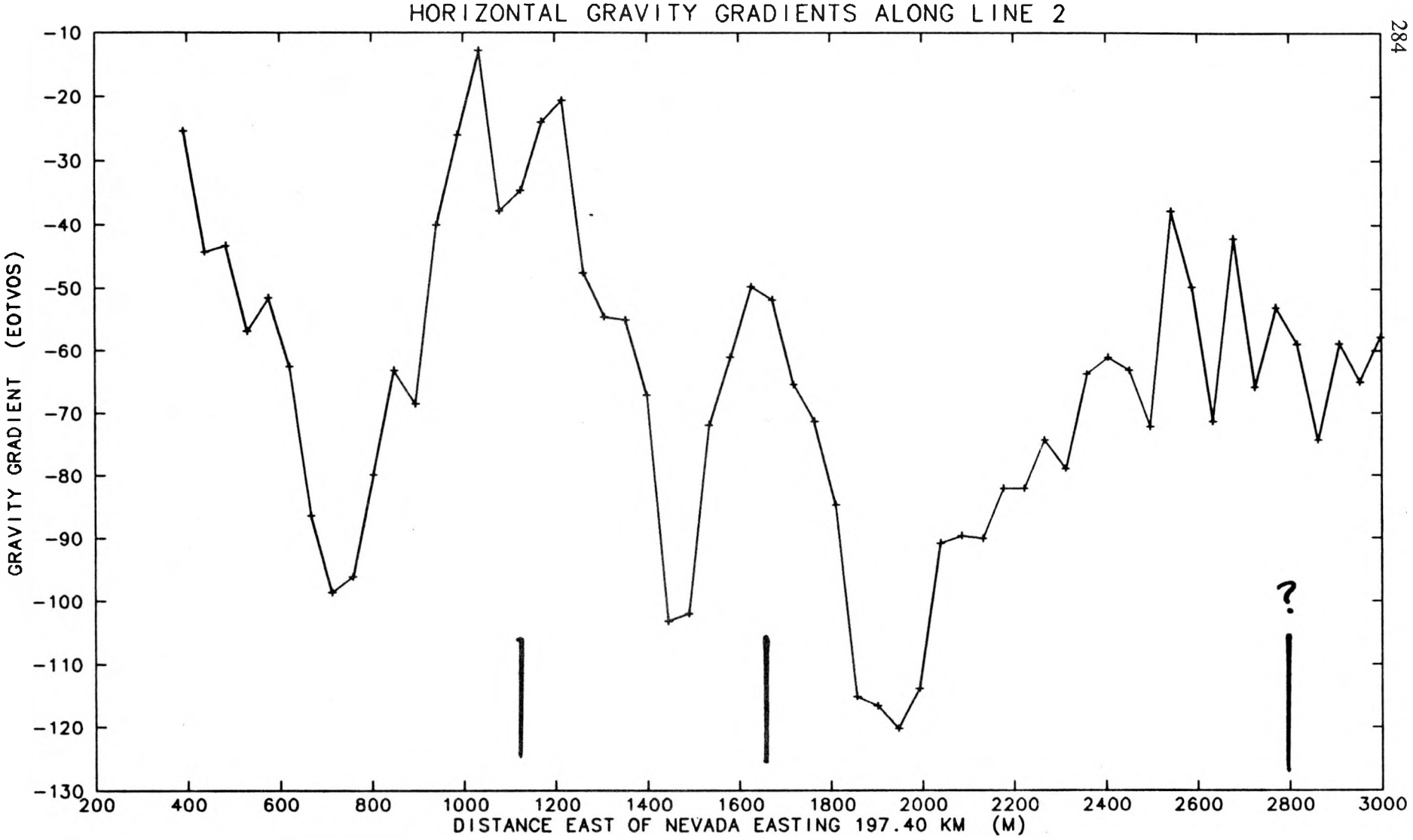


FIG. 6. Horizontal gravity gradients along line 2, in Eotvos units (an Eotvos unit = $10^{-9}/s^2$). Distances are measured as in Figure 4. Locations of possible faults are indicated by vertical lines.

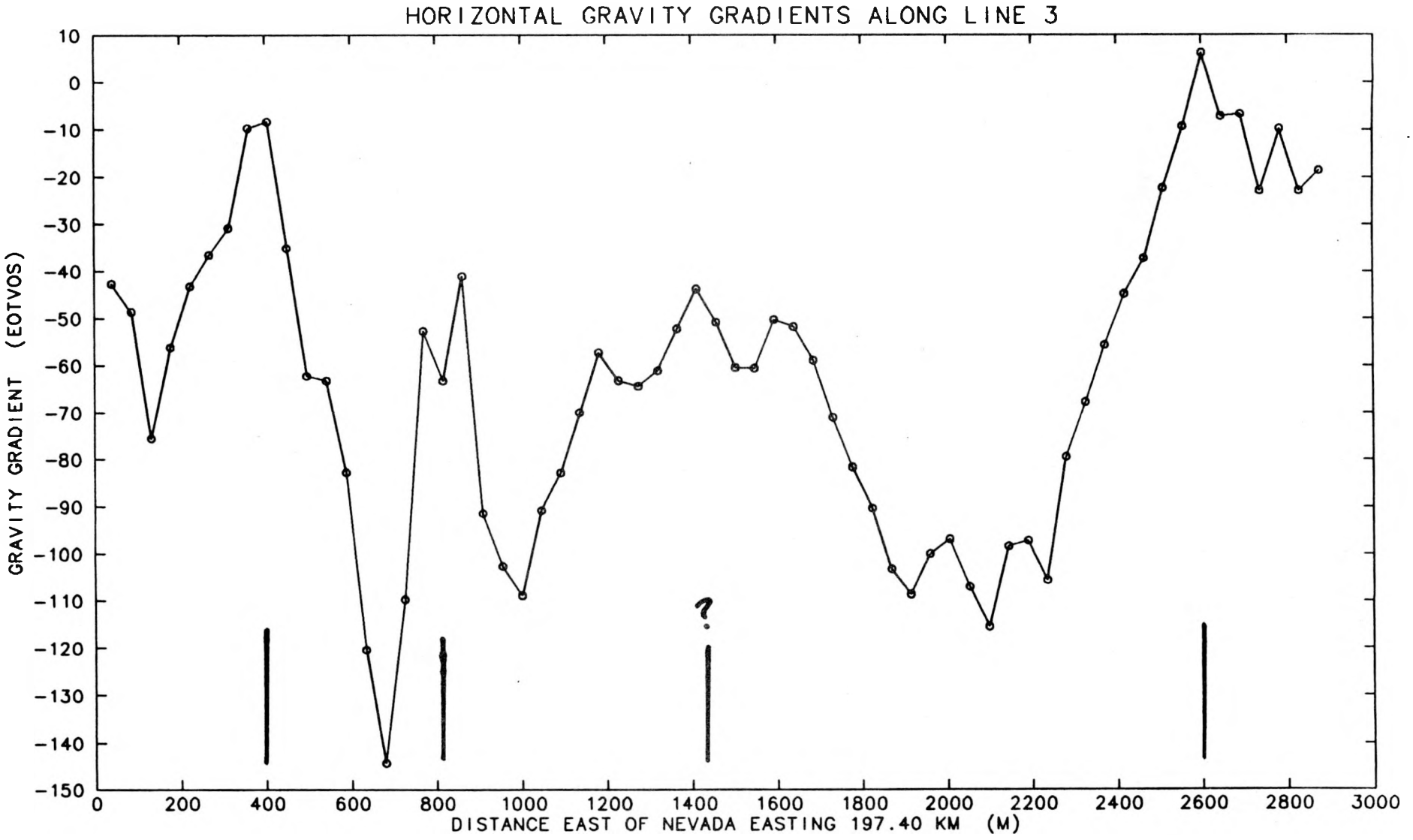


FIG. 7. Horizontal gravity gradients along line 3, in Eotvos units (an Eotvos unit = $10^{-9}/s^2$). Distances are measured as in Figure 4. Locations of possible faults are indicated by vertical lines.

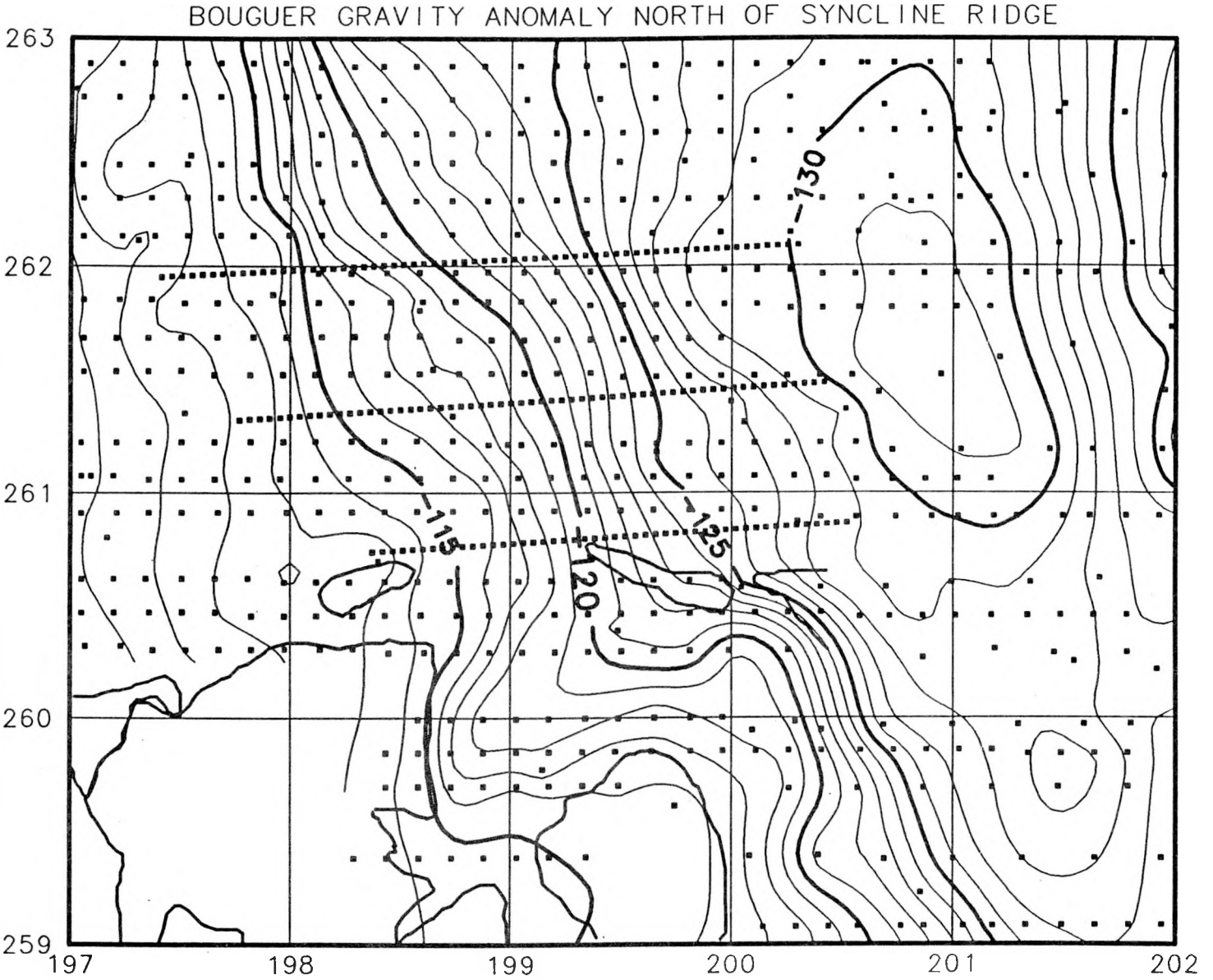


FIG 8. Contour map of the Bouguer anomaly in the study area. This map was generated using only those gravity data that were available prior to acquisition of the data along lines 1-3. Locations of gravity measurements are indicated by small squares. Outcrop patterns shown are those of Figure 2. Coordinates are Nevada State Plane, central zone, in km.

on the line). An attenuated version of the anomaly occurs near the eastern end of lines 2 and 3, as well. This anomaly is almost certainly due to a fault dropping the Tmr down to the east. Such a fault correlates well with the one observed on the seismic reflection line and inferred from the gravity data on line 1. Note that Tmr outcrops just south of line 1, but outcrops of Tmr do not occur west of the magnetic anomaly. Instead, a small outcrop of Paintbrush Tuff, which is stratigraphically lower than Tmr, is present.

The western portions of the magnetic anomaly lines show little character, other than high-wavenumber noise due to near-surface features. An exception is an area of relatively low magnetic field between 300-1000 m along line 2. An adequate explanation for this feature is lacking, but it possibly represents a region of thin alluvium overlying limestone. If so, the limestone would not be buried sufficiently to be of interest to us.

The lack of character on the western portions of the magnetic lines indicates that the Tmr is probably absent or at least very thin. Thus, except for the fault near the eastern end of the lines, the magnetic profiles cannot be used to help verify the faults inferred from the gravity data.

Results. The gravity and magnetic data acquired on lines 1-3 have been used to infer three fault locations (Figure 12). The easternmost of these faults is inferred on the basis of gravity, magnetic, and seismic data, and seems well-established. The two western faults are inferred using only the gravity data. All faults strike slightly west of north. Tmr is probably absent or nearly so west of the easternmost fault. The block between the easternmost fault and the fault immediately west seems relatively free of structure.

Electrical Survey

Expected resistivity structure. In order to get a better grasp of the actual range of resistivities that might be observed in an electrical survey, we made a number of resistivity measurements at several outcrops near Syncline Ridge; these measurements were made using a hand-held induction instrument and only sample the upper 1-2 m of outcrop. Our results are shown in Table 1.

It is apparent from Table 1 that a large resistivity contrast exists between the Tippipah Limestone and the argillite subunit of the Eleana Fm. However, there is little difference in resistivity between the Tippipah Limestone and the more siliceous portions of the Eleana Fm. For this reason, it may not be possible to distinguish between the Tippipah Limestone and the upper quartzite subunit of unit J of the Eleana Fm. using resistivity measurements. In addition, the electric log from Ue4ac indicates the lower portion of the Tunnel Beds tuff to be quite conductive (resistivity about 10 ohm-m); this conductive portion of the tuff is described as "...partially argillized-zeolitized..." (McArthur, 1976). Such conductive zones of tuff are probably indistinguishable from the argillite subunit of the Eleana Fm.; however, we presume that such zones would be too thin to be mistaken as Eleana Fm.

Objectives of the survey. Our objective for the electrical survey was simply to try to detect Tippipah Limestone in the subsurface, rather than to infer a complete picture of the resistivity structure of the area. To accomplish this, we needed to detect a fairly thick, resistive unit beneath the tuff and alluvium. Failing to detect such a unit would imply that the limestone was not present, at least not in sufficient thickness to be useful to us. Detecting a resistive unit overlying a very thick, conductive layer would not necessarily imply the presence of the limestone, though, because we might have located the quartzite subunit that is at the top of unit J of the Eleana Fm.

Table 1. Resistivity measurements at selected outcrops.

Lithologic Unit	Resistivity of Outcrop
Alluvium	65-120, average 80
Quartzite/siliceous argillite (Eleana Formation)	240-650, average 340
Argillite subunit, Eleana Fm.	20-35, average 25
Tunnel Beds Tuff (zeolitized)	40-80, average 60
Devitrified and welded tuff	70-310, average 110
Tippipah Limestone	200-650, average 300

Table 2. Models for E-W sounding; responses appear in Figure 13.

	Model A		
	(ohm-m)	(m)	(m)
Layer	Resistivity	Thickness	Depth to Top
1	50	4.0	0.0
2	12	4.5	4.0
3	350	6.0	8.5
4	28	∞	14.5

	Model B		
	(ohm-m)	(m)	(m)
Layer	Resistivity	Thickness	Depth to Top
1	50	4.0	0.0
2	12	4.5	4.0
3	50	6.0	8.5
4	28	500.0	14.5
5	700	100.0	515.0
6	28	∞	615.0

Table 3. Model for N-S sounding; response appears in Figure 14.

	(ohm-m)	(m)	(m)
Layer	Resistivity	Thickness	Depth to Top
1	30	10	0
2	80	70	10
3	28	400	80
4	1000	∞	480

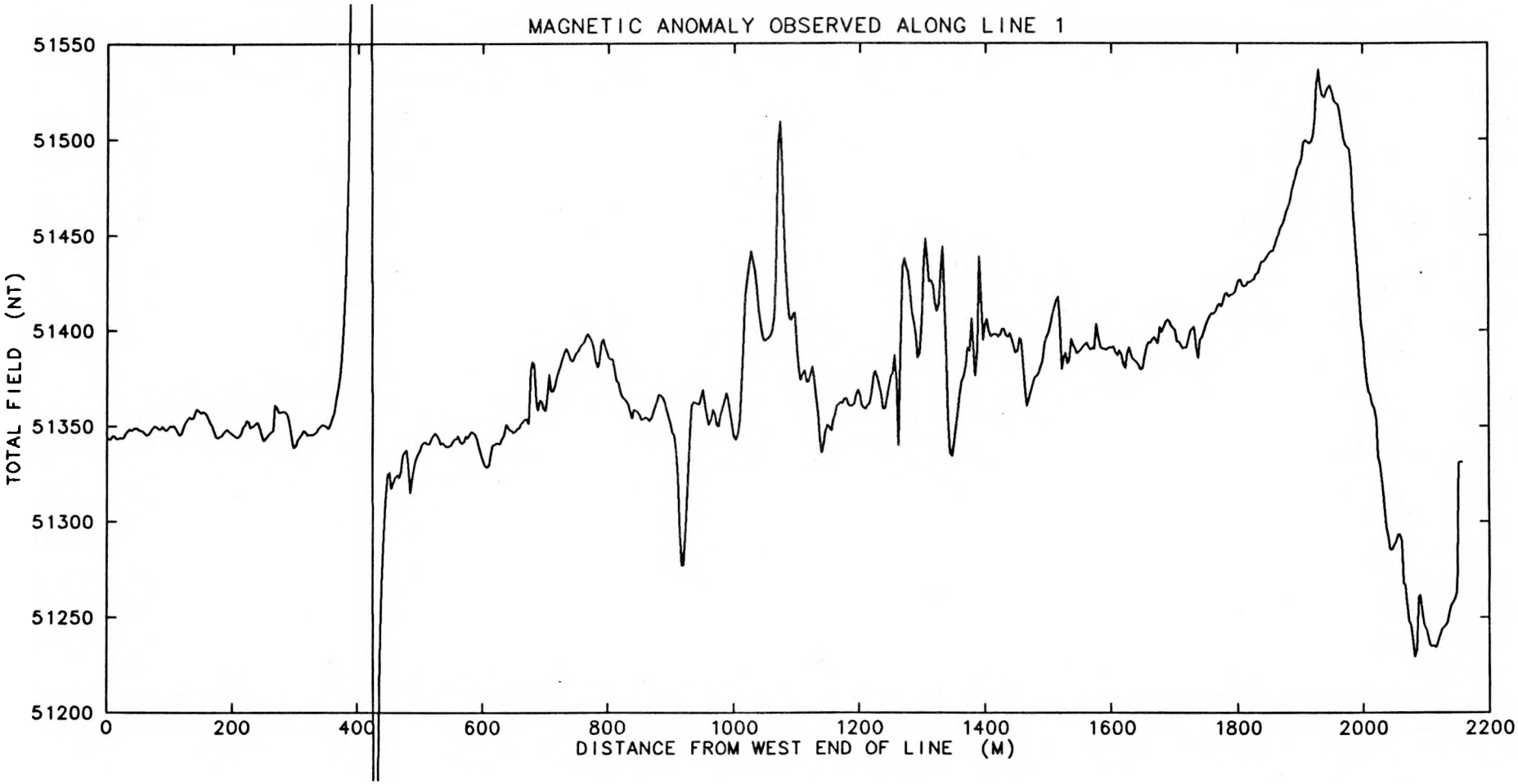


FIG 9. Unsmoothed total field magnetic anomaly observed along line 1. Distances are measured from the west end of the line. The high-amplitude anomaly near 400 m is due to a steel culvert beneath the Tippipah Highway.

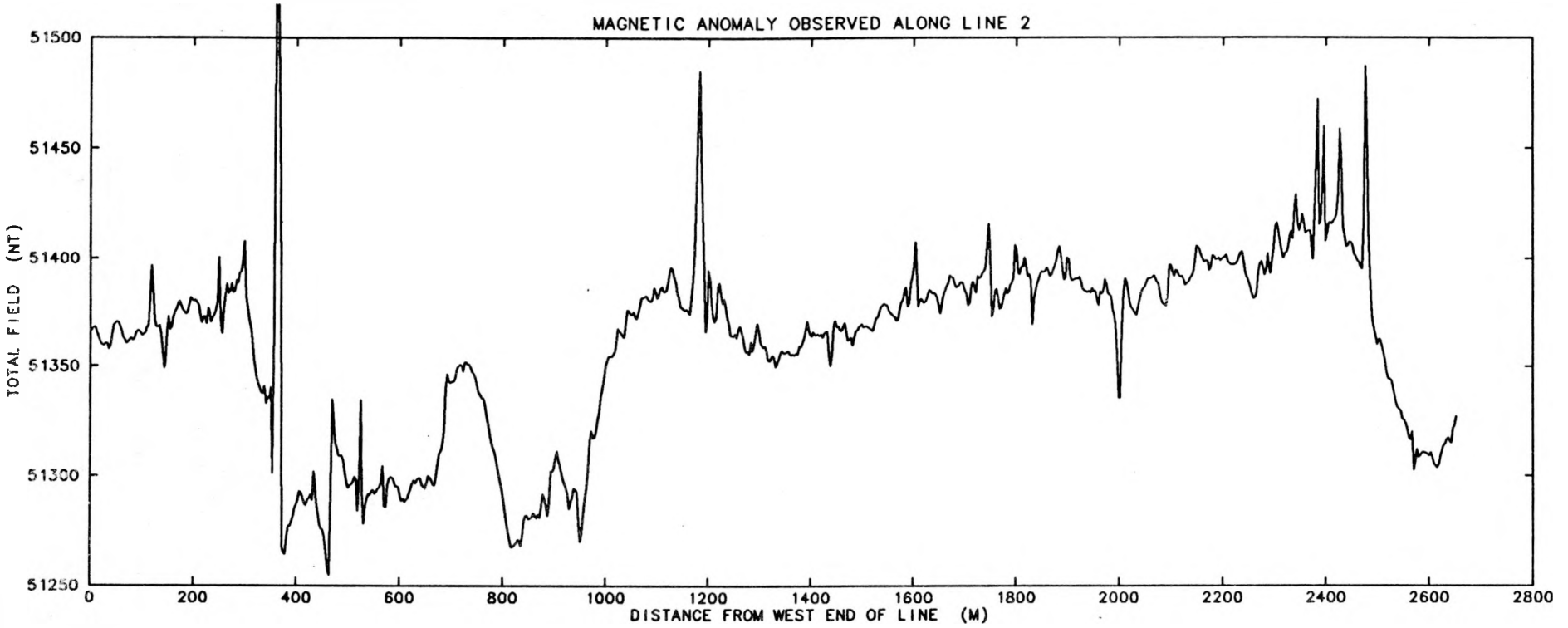


FIG 10. Unsmoothed total field magnetic anomaly observed along line 2. Distances are measured from the west end of the line. The high-amplitude anomaly near 350 m is due to the surface casing for exploratory borehole Ue17c.

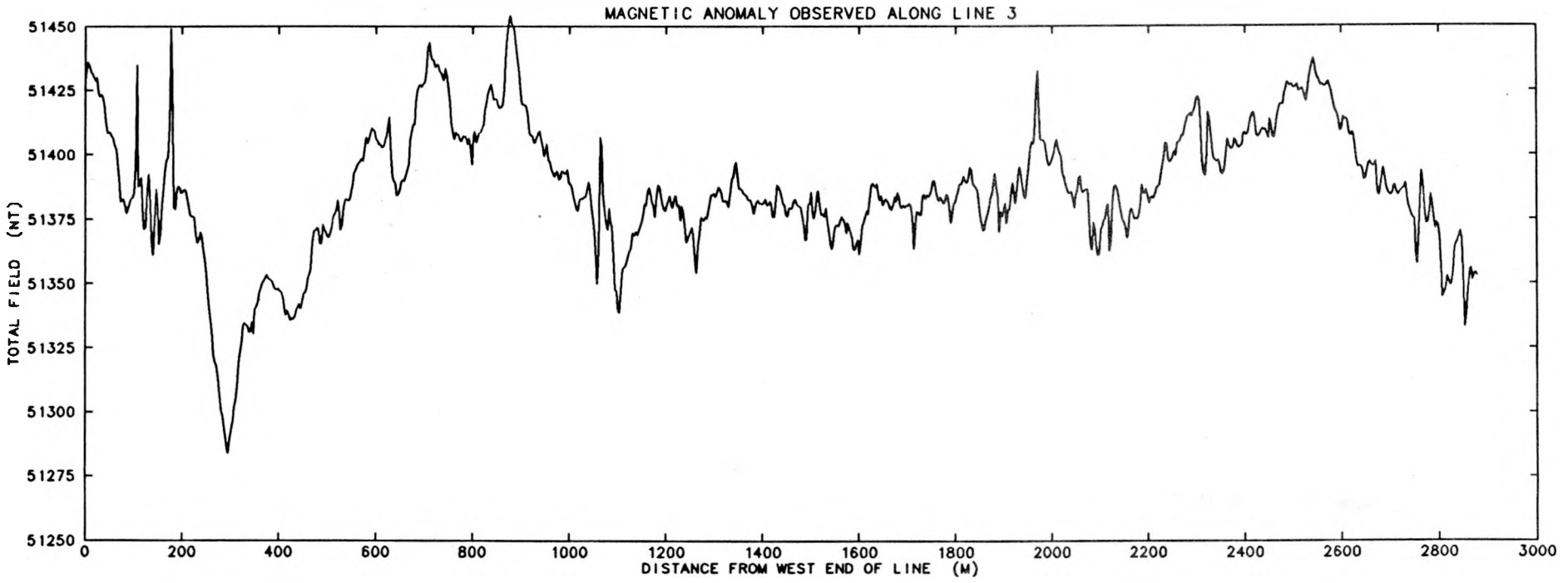


FIG 11. Unsmoothed total field magnetic anomaly observed along line 3. Distances are measured from the west end of the line.

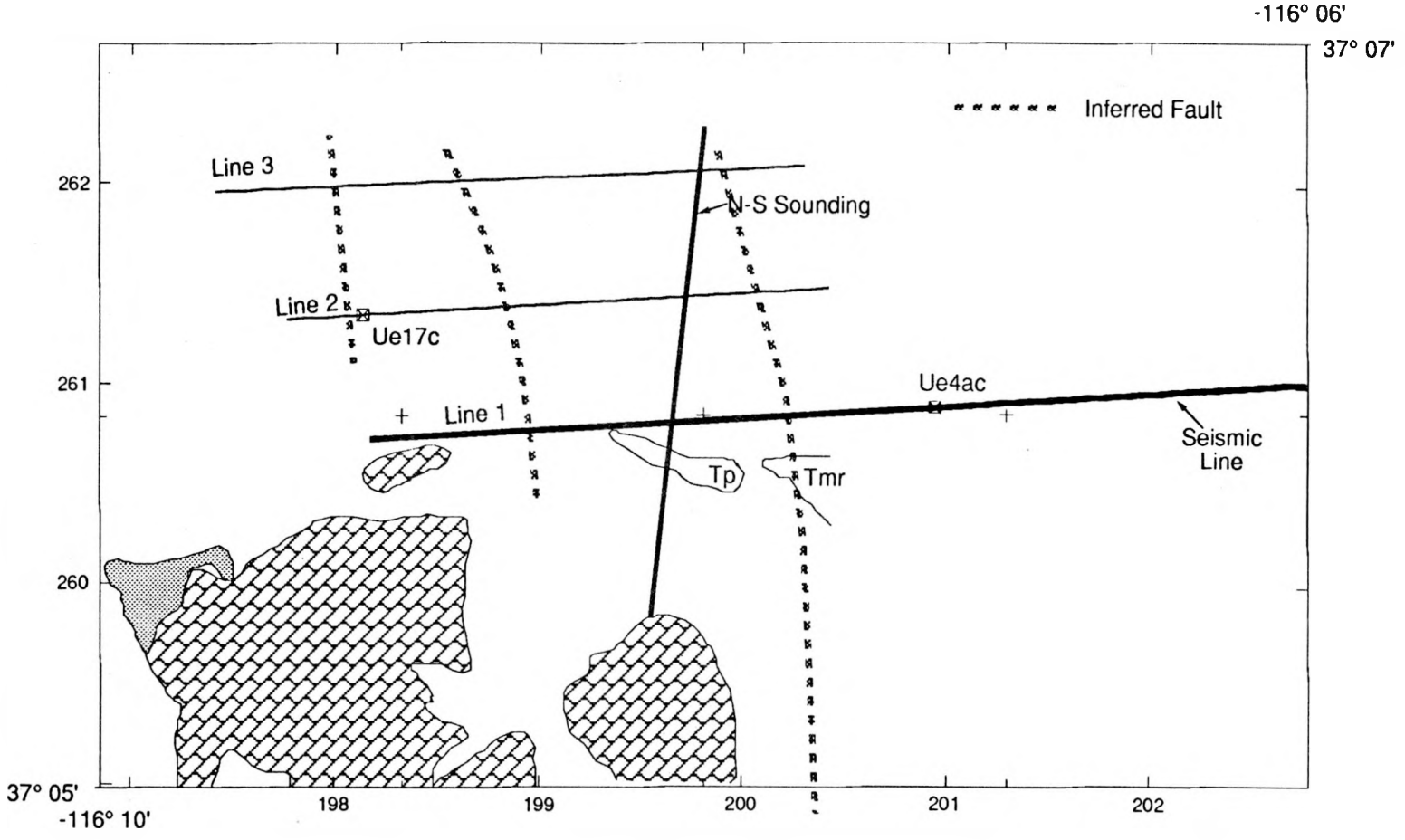


FIG. 12. Fault locations inferred from gravity, magnetic, and seismic data. The easternmost fault is well-established, but the two faults west of it are less well known. Only those faults inferred along more than one gravity-magnetic line are indicated. Other symbols as in Figure 2.

Data acquisition and interpretation. We conducted two crossed Schlumberger soundings on September 26-28, 1988. The center of the sounding pair was located at Nevada state coordinates N.260,813 km, E.199.653 km (geodetic coordinates 37°05′59″N; 116°08′06″). One sounding was taken along gravity-magnetic line 1; this line will be called the E-W line. The other sounding was taken approximately normal (81° difference in strike) to the first; its strike was N6°E. Both soundings attained AB/2 spacings (half-widths) of 1470 m.

Figure 13 is a graph of the data from the E-W sounding and the response of a layered model (model A of Table 2) that fits these data reasonably well. There appears to be a lateral discontinuity present between AB/2=68 m and AB/2=100 m, which means that a layered interpretation is incorrect. There are two important points to be made concerning these data. The resistivity high located between AB/2=(20-200) m was modeled with a 350 ohm-m layer 6 m thick at 15 m depth. This feature is the only resistive element in the sounding. Other resistivity-thickness combinations could fit the data as well, but the interpretation shown uses the expected value for the resistive limestone that we are seeking.

Figure 13 also shows the response of model B of Table 2; B is the same as A, except that a 100-m thick, 700 ohm-m unit has been added at a depth of 515 m to establish if such a layer would have been detected by the sounding. The result of this exercise is that a resistive layer would have been detected at 515 m. Our conclusion is that, if the Tippipah Limestone underlies the site, it is either not resistive or it is less than 100 m in thickness.

When using a resistivity value of 1000 ohm-m for the basement, the effective depth of penetration of the survey is approximately 1000 m. That is, if there were resistive rocks underlying the entire area at a depth any shallower than 1000 m, the effect of such rocks would have been apparent in the data.

Figure 14 is a graph of the data from the N-S sounding and the response of a layered model that fits these data reasonably well. Table 3 provides the details of the model used. These data were taken on two different days (September 27-28). The first day's data showed low noise levels until AB/2=100 m was reached, at which point the quality deteriorated. On the following day, we repeated the noisy data points with good results. The noise in the data was probably due to inadequate current control and high contact resistance at the electrodes.

An apparent lateral discontinuity becomes evident in the data between 464 and 681 m. The discontinuity is such that one or both of the electrodes has crossed into a more resistive environment. Geologically, the most likely location for the discontinuity is to the south of the center point, rather than to the north.

These data show two resistive units: 70 m of 80 ohm-m material at 10 m depth and what we have modeled as electrical basement at 480 m. The lateral discontinuity crossed by one or both of the electrodes between AB/2=464 and 681 m invalidate a basement interpretation. In fact, the resistivity begins to fall again at the last point measured. These data indicate that there is no thick (>100 m), resistive section of rock underlying the soundings.

Conclusions. There is no laterally extensive section of resistive rock in the immediate vicinity of the soundings. It is unlikely that the models presented in Tables 2-3 represent the geology at this location, either. The maximum detection depth for a laterally extensive unit is approximately 1000 m. Both soundings, but especially the N-S one, show indications of lateral inhomogeneity. Such inhomogeneity invalidates the assumptions used to model the data. However, the data from both lines are sufficiently similar that a reasonable interpretation can be made.

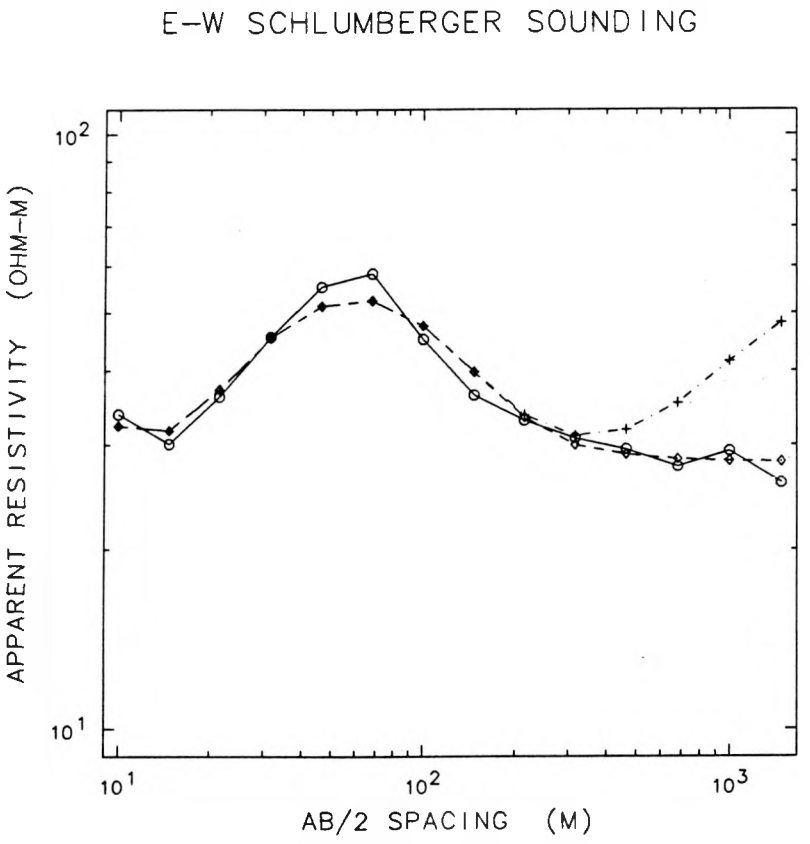


FIG. 13. Observed apparent resistivity on the E-W Schlumberger sounding (circles); responses of Models A and B of Table 2 are shown as diamonds and plus symbols, respectively.

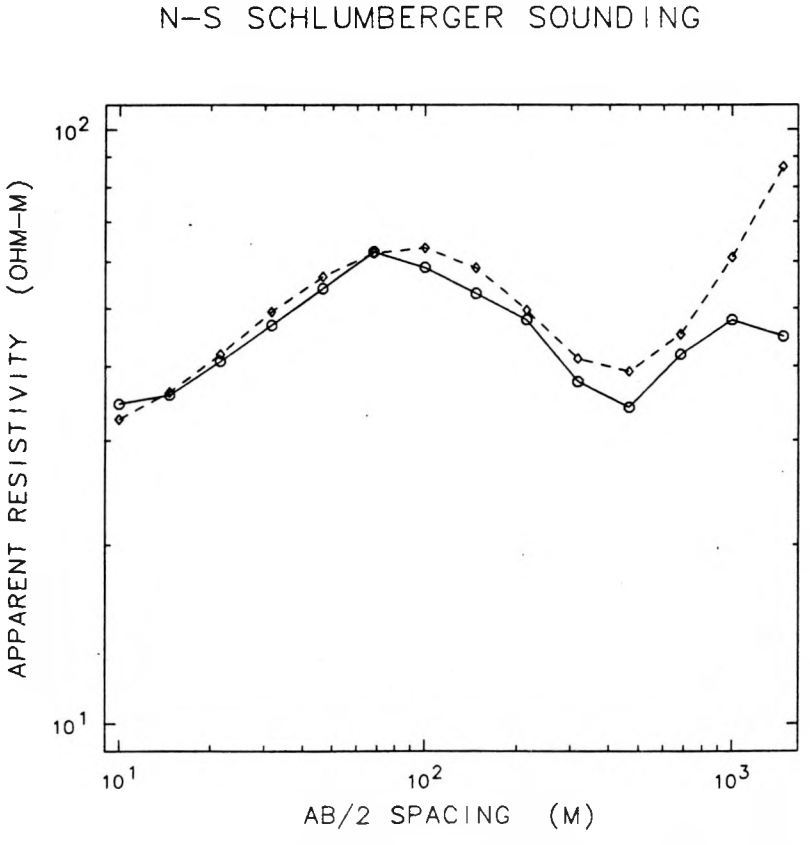


FIG. 14. Observed apparent resistivity on the N-S Schlumberger sounding (circles); the response of the model of Table 3 is shown using diamond symbols.

Both apparent resistivity curves show a near surface resistive unit. On the N-S sounding, the curve was modeled with 70 m of 80 ohm-m material. On the E-W sounding the same unit was modeled with 6 m of 350 ohm-m material. In reality, this resistive unit is not laterally extensive, or it has been broken by faulting and is probably closer to 80 ohm-m than 350 ohm-m.

CONCLUSIONS

In searching for a testing site in saturated carbonate rock, we have attempted to locate the Tippipah Limestone in the subsurface north of its northernmost exposures at Syncline Ridge. A dc resistivity survey conducted immediately north of Syncline Ridge has detected no significant (> 100 m) thickness of resistive material. Our conclusion is that the Tippipah Limestone is very unlikely to be present at this location. It appears that Tippipah Limestone may be present at NTS only where it outcrops.

Other potential carbonate-rock emplacement sites may exist in the small basin northeast of the area we have studied. For example, Ue4ac penetrated carbonates beneath 479 m of overburden. If Eleana Fm. underlies these rocks, and if the carbonates are sufficiently thick, a site meeting the search criteria may be available near Ue4ac. However, the SWL at Ue4ac was below the total depth of the borehole; thus, the carbonate unit would need to be thicker than the specified 100 m thickness. Tippipah Limestone was one of the few limestone units that we expected to be fairly thick. We do not expect the thickness of other limestone units to be especially great, making it unlikely, in our view, that such rocks will be thick enough to meet the criteria. Therefore, the basin north of Ue4ac is presently the only area in which we have much hope of finding a suitable carbonate rock site.

ACKNOWLEDGMENTS

This work was performed under the auspices of the U. S. Department of Energy. We would like to thank Sigmund Drellack and Peter Thompson of Fenix & Scisson, Inc., who made the the magnetic measurements along the ground magnetic traverses. Thanks are also due to Ron Wahl of the USGS, who provided the digital terrain data used to correct the gravity measurements.

REFERENCES CITED

Bath, G. D., 1976, Interpretation of magnetic surveys in intermontane valleys of Nevada and southern New Mexico, *U. S. Geol. Surv. open-file report 76-440*, iii+37 pages.

Doty, G. C. and William Thordarson, 1983, Water Table in Rocks of Cenozoic and Paleozoic Age, 1980, Yucca Flat, Nevada Test Site, Nevada [map], *U. S. Geol. Surv. Water-Resources Report 83-4067*.

Hoover, D. B., W. F. Hanna, L. A. Anderson, V. J. Flanigan, and L. W. Pankratz, 1982, Geophysical studies of the Syncline Ridge area, Nevada Test Site, Nye County, Nevada, *U. S. Geol. Surv. open-file Report 82-145*, 55 pages.

Hoover, D. L. and J. N. Morrison, 1980, Geology of the Syncline Ridge Area Related to Nuclear Waste Disposal, Nevada Test Site, Nye County, Nevada, *U. S. Geol. Surv. open-file Report 80-942*, 70 pages.

McArthur, R. D., 1976, The subsurface geology of the Lawrence Livermore Laboratory portion of Area 4 and the Nevada Test Site, *Lawrence Livermore Laboratory report UCRL-52061*, 31 pages.

Orkild, Paul P., 1963, Geologic map of the Tippipah Spring Quadrangle, Nye County, Nevada, *U. S. Geol. Surv. Map GQ-213.*

Winograd, I. J. and William Thordarson, 1975, Hydrogeologic and hydrochemical framework, south-central Great Basin, Nevada-California, with special reference to the Nevada Test Site, *U. S. Geol. Surv. Prof. Paper 712-C*, 126 pages.

AN EXPERT SYSTEM FOR ASSISTING IN GEOLOGIC SITE CHARACTERIZATION

Nancy L. Marusak
Kathryn P. Berkbigler
and
George J. Papcun
Los Alamos National Laboratory

ABSTRACT

The Geologist's Assistant is an expert system under development at Los Alamos designed to aid containment scientists with the analysis of geologic and geophysical data obtained from drilled holes at the Nevada Test Site. As more information becomes available, it is imperative that the geoscientist consider all data relevant to a specific site characterization. This expert system is intended to be an interactive tool to help with an initial analysis of a site location using all the available data. Geological and geophysical information from each drilled hole is stored in GEODES, a database management system developed at Los Alamos to retain all the accumulated data. The expert system has on-line access to the GEODES database as required in order to analyze a site. A distinctive feature of the Geologist's Assistant expert system is that it combines symbolic computing in the form of rules with numerical computing in the form of pattern matching techniques. Geologists employ a variety of heuristics when characterizing the subsurface stratigraphy surrounding a hole. These heuristics are implemented as rules in the expert system. Inferencing using the rules guides the direction of the analysis by producing tentative conclusions which are further invesitgated by applying numerical pattern matching techniques to the appropriate geophysical logs from GEODES. The specific numerical technique used is called dynamic pattern warping. The system is developed using carefully evaluated expert system tools. The implementation is distributed between a VAX where the expert system, pattern matching algorithm, and GEODES database management system reside, and an IBM PC/AT which provides the user interface.

I. INTRODUCTION

Los Alamos stores information from the drilled holes at the NTS (Nevada Test Site) in GEODES (GEOscience Data Evaluation System - see Winterkamp et al. 1985), a vector database management system designed and written at Los Alamos National Laboratory to handle the data. Information from these holes includes discrete data such as coordinates, drilled depth, elevation,

hole diameter, and key stratigraphic contacts as well as downhole information. The downhole data could consist of only general stratigraphy, but more commonly includes caliper, resistivity, and gamma-gamma density logs as well as grain density and water measurements. Additional logs in more recent holes include gamma, epithermal neutron, magnetic susceptibility, and gravity. The GEODES database where this information is stored has, in addition to its user-friendly interactive interface, a programmatic interface that allows access to the data by other computer programs.

Clearly there is a plethora of information available to the expert when evaluating a geologic site. Consequently, there is a need to help the expert be assured that all pertinent information is considered in the geological analyses.

II. SYSTEM DESCRIPTION

The driving force for the development of the Geologist's Assistant expert system was the process involved in generating a site characterization for underground nuclear testing. However, an attempt has been made to generalize the geologic characterization so that this system could be applied to similar analyses for mining or hydrocarbon exploration. Publications describing similar projects related to geologic data interpretation include Prospector by Duda et al. (1978), Dipmeter Advisor by Davis et al, (1981), ELAS by Weiss et al. (1982), and LITHO by Bonnet et al. (1983); other proprietary work may exist.

The region of the test site being incorporated into the Geologist's Assistant (i.e., the Los Alamos use area) was divided into sixteen geologic areas. Some controlling parameters of this division include geographic area, structural complexity, unique or limiting physical properties, thickness of the volcanic sequence, and amount and quality of available data in the area. Each area includes the same parameters.

When the geoscientist wishes to evaluate possible geologic interpretations for a particular geologic site, the Geologist's Assistant can help with several tasks. A menu of these tasks is shown in Figure 1.

Retrieving The Data

The first three menu items in Figure 1 deal with setting up the knowledge base that the Geologist's Assistant needs in order to operate. This involves specifying the hole of interest and retrieving its information from GEODES. Data from holes near the site of interest are also retrieved, and the system is told which pairs of holes are to be compared. For each hole, the information that is obtained from GEODES includes the pertinent discrete data and the names of

the geological and geophysical logs recorded for the hole. The hole's geologic area is derived by comparing its coordinates with the coordinates of the defined geologic areas. When all of this data has been retrieved for the population of holes that are to be compared, pairwise analysis of the population can proceed.

The menu items pertaining to the various types of analysis will be described in the following sections. The last menu item simply clears the knowledge base in preparation for analysis of a different hole.

Stratigraphic Log Analysis

The stratigraphic logs for each pair of holes being compared are analyzed by the heuristic classification method - see Clancey (1985), which systematically relates the data in the logs to a pre-enumerated set of structural features that we are interested in identifying if they are present, e.g., a fault through one of the holes. First, the actual thickness and position measurements of each of the layers in the logs is qualitatively abstracted into whether they are the "same" or "different". The qualitative determinations are specific to each geologic area, with allowable variations being a function of distance between the holes and taking into account regional structural trends. Heuristic relationships have been established among patterns of variation seen in the stratigraphic layers and the characteristics of geologic sturctures that might be present. These heuristics have been formed into rules that allow the expert system to perform a rule-based analysis of the stratigraphic logs. A data-directed search is applied; that is, the program works forwards from the data, forming tentative conclusions about the subsurface structure and stratigraphy, until all possible inferences have been made. When the rules looking for specific patterns do not apply, the Geologist's Assistant concludes that the structure is too complex to be determined by simple rules of thumb and further analysis by the geologist is required.

Figure 2 shows plots of the stratigraphic logs from two holes that are relatively close together. Note that the corresponding layers in each hole have approximately the same thickness and position except the TMR and TP layers, which have different thicknesses and relative positions. This is an example of how the stratigraphic logs can appear when there is a fault that cuts through both holes. In the upper plot, a portion of the TMR layer has been shortened, while in the lower plot it is a portion of the TP layer that is missing.

The heuristic that represents this situation can be stated in English as follows:

If one or more corresponding layers have different thicknesses and different positions AND the layer below them has a different thickness but the same position THEN suspect a fault through both holes in ? layers.

The *?* represents the names of the shortened or missing layers and is filled in as the rule is executed.

Similar heuristics are used to identify a fault through one hole, a fault between two holes, a thinned layer, etc.

Material Properties Analysis

In addition to geophysical logs, other downhole information is obtained in different ways for a variety of analyses. Samples from the hole are taken with a sidewall sampler, a percussion gun sampler, or from drill cuttings. These samples are used for grain density, clay and CO_2 determinations, as well as lithologic and petrologic identifications. The Geologist's Assistant examines the CO_2, clay and grain density logs and identifies regions where log values exceed assigned limits.

Geophysical Pattern Matching

Another important aspect of geological evaluation of test site data is the analysis of geophysical data logs such as electrical resistivity and bulk density. This analysis is normally performed by skilled geoscientists who visually examine plots of this data and discern regions of match or discontinuity. An example is shown in Figure 3, where the electrical resistivity logs of two holes are used to infer a missing geologic section in log A. The interpretation of these results is shown in Figure 4 by Marusak et al. (1981).

The problem of interpreting geophysical logs bears interesting similarities to a problem in another field of artificial intelligence, viz., speech recognition. Just as geological layers may differ in *thickness* from one region to another and within a region from one location to another, so speech sounds may vary in *duration* depending on context, speech rate, and nuances of emphasis. Moreover, in both geology and speech recognition, the relationship between the two samples to be compared may be nonlinear. In the case of speech, the nonlinearity results from the fact that when syllables are lengthened, certain sounds (e.g., vowels) tend to stretch out more than others (e.g., "p" and "t", but not all consonants). In the case of geology, the nonlinearity may result from varying depositional rates, as well as many other causes.

Standard methods of analyzing signals are neither adequate nor appropriate to deal with these problems, because their underlying assumptions are violated. Spectral analysis presupposes that the data were formed as a result of a reasonance structure, which is not the case with a sequence of speech sounds or with geophysical data.

To deal with these problems in speech recognition, an efficient method of comparing time-warped words against template examples has been developed. This method, called "dynamic time warping," by Bellman et al. (1962) works as follows: An outer difference matrix is calculated between the two curves of interest. If the curves match perfectly, a "valley" of low values is formed along the diagonal. If one of the curves is stretched with respect to the other, the "valley" wanders above or below the diagonal in the direction of the curve that is stretched. We can see these effects in Figure 5, which depicts the path that follows the bottom of the valley through the outer difference matrix for the holes shown in Figure 3.

An additional similarity between speech recognition and the comparison of geophysical logs is that both may entail local discontinuities in the comparisons. In speech, this problem may arise when there is a sound in one utterance of a word that is omitted in a repetition of the word. For example, on one occasion a speaker might say "pumpkin", and on another occasion the speaker might say "pumkin", omitting the second "p" sound. In geophyhsical logs, discontinuities might be caused by minor inclusions or by locally eroded surfaces. In both speech recognition and geophysical log comparison, it is necessary for the system to ignore such minor differences and recognize the overall similarities.

As shown in Figure 5, parallel paths may develop at points of local discontinuities. To obtain an algorithm that reproduces the expert's interpretations, it is necessary to tune the algorithm to pursue an appropriate number of parallel paths and to calculate a "cost" for each path. Path cost can be pictured metaphorically by imagining pouring water that is needed to obtain a stream that flows a given distance. In the application of the algorithm, it is assumed that minor discontinuities can be ignored and major similarities can be detected by proper adjustment of the cost metric as well as setting appropriate thresholds. In practical application, it is necessary to add constraints such as preventing the path from backtracking.

Use of individual data points in the difference matrix encounters problems when abrupt changes in the data occur in both logs. Setting a threshold that reliably distinguishes matching from non-matching logs proved to be impossible. For such cases, an approach that relies more on the shapes of the curves rather than absolute differences appears to perform better. In order to properly take account of similarities in shape, it is necessary to analyze successive portions of the logs within windows long enough to reveal those similarities, yet not so long as to conflate differing structures. Windows with a length of thirty meters seem to work best for the cases considered so far.

A number of different techniques were tried for evaluating the similarities of the logs within windows. Correlation works well for identifying similar shapes, but has the undesirable property of ignoring differences in the magnitude of the variation in the data. This application

requires a measure that makes use of both shapes and magnitudes in assessing the degree of similarity. Current experiments are focused on using correlation to find similar shapes, but penalizing the correlation according to the degree to which the curves being compared differ in variance. Other measures may perform better than this one, and we continue to search for a measure that can be tuned to adequately discriminate between allowable variations and inadmissible variations which disclose geologic structure.

A remaining weakness of the dynamic space/time-warping method in geology (as well as in speech recognition) is that it does not take into account the *reasons* for the warping. It does not know, for example, that geological layers are eroded from the top rather than from the bottom. It does not know that a particular stratigraphic sequence in the center of a basin might tend to be thicker than the same sequence near the edge of the basin.

III. IMPLEMENTATION

The primary source of data for the Geologist's Assistant is the GEODES database management system, which resides on a large multi-user VAX/VMS mainframe. The database is voluminous and is updated frequently, so down-loading it to another computer would be inefficient and subject to error. Therefore, it is desirable for the expert system to reside on the same machine as the database. Also a multi-user system is preferable so that more than one person may simultaneously use the expert system. Several candidate expert system tools were considered. The Knowledge Engineering Environment (KEE) software - Geverter et al. (1987) and Mettry et al. (1987) from Intellicorp was selected for its powerful functionality and user interface, as well as for its availability on the VAX for descriptions of a variety of expert system development tools.)

KEE Expert System Environment

KEE is a hybrid expert system development environment allowing the mixed use of several expert system paradigms by KEE User's Guide (1988). In the Geologist's Assistant, we use the frame system, the rule system, and make extensive use of the object-oriented programming facilities. Demons, functions that are automatically executed when values change, are used to display the plots of the logs. The initial knowledge base that is loaded is quite small, with most units dynamically created as driven by the analysis. User interface development facilitities for graphics include KEE Pictures and the Common Windows extension to Common Lisp.

Development of the Geologist's Assistant is taking place on a Digital Equipment Corporation (DEC) AI-VAXstation equiped with 16 Mbytes of memory and the KEE software development system. KEE is implemented on top of VAX Lisp, DEC's implementation of Common Lisp. An abbreviated version of the GEODES database management system has been installed on the

VAXstation for the purpose of debugging the interface between the expert system and the database management system. GEODES is accessed via its Fortran interface, which in turn is accessible from VAX Lisp.

In order to deliver the Geologist's Assistant on the VAX mainframe, we are using the companion Runtime KEE/PC-Host product from Intellicorp. This delivery system is implemented in a distributed manner with the knowledge representation and inference engine residing on our host VAX 8650 and the user interface on the IBM PC/AT. A portion of the common Windows subsystem of KEE has been implemented on top of Microsoft Windows on the PC/AT. The two computers communicate with each other over a dynamic asynchronous DECnet link using the DECnet-DOS software package from DEC. The PC/AT has been enhanced with a 19-inch high-resolution monitor and 8 Mbytes of extended memory, which is being used as a RAM disk. The GEODES database management system also resides on the VAX 8650, where it is accessed from the expert system via the Lisp-Fortran interface as described for the development system. Figure 6 is a block diagram of the components of this distributed delivery system.

User Interface

The user interface to an expert system is a crucial element for its acceptance by the user community. Research in man-machine interface techniques has begun to produce guidelines for when to use specific interaction styles - see Sheniderman et al. (1987) and Hendler et al. (1988). Presenting information in a form that is familiar to the user is an important goal in the Geologist's Assistant. Its users already understand the terminology and graphical presentations used in GEODES and might be reluctant to learn different representations.

The user interface for the Geologist's Assistant is primarily menu-based using a mouse to select the menu items. The Geologist's Assistant tasks appear in a menu that is always present on the screen so that the user may select tasks in a preferred order and see which task is currently being performed. Placing control in the hands of the user is in keeping with the view of the Geologist's Assistant as an assistant rather than the master of the interaction. Some direct manipulation is used for overlaying plots of logs. Minimal use is made of the keyboard to input selections for which menus are not effective.

Interaction takes place on a high-resolution bit-mapped screen that contains multiple windows for different types of output. One window contains a map showing the hole of interest and its surrounding holes so that the user may see how they are spatially oriented. An example is illustrated in Figure 7. Another window is used to plot each log as it is being analyzed. These logs can be overlaid by the user at his discretion in order to facilitate understanding of the information. Window management is generally controlled by the expert system so as not to burden the user, but it may be overridden if desired.

IV. SUMMARY

A prototype of the Geologist's Assistant expert system, utilizing the distributed architecture of the Runtime/KEE PC-Host system, is operational. It communicates online with the GEODES database management system to obtain downhole data for analysis. Rule-based analysis of stratigraphic logs and some material properties analysis is available.

Future enhancements might include refining the knowledge in the expert system to make it a more robust tool, and incorporating additional analysis. Also, efforts to improve the pattern-matching technique are currently underway. Analyses related more specifically to site characterization at the NTS are desirable. These enhancements will incrementally improve the performance of the system. To truly model the knowledge the geoscientist brings to bear on the analyses requires the inclusion of deeper, less heuristic models of the underlying physical processes. Adding such understanding of the physical world is a major challenge to the development of artificial intelligence.

V. ACKNOWLEDGEMENTS

This work is supported by the United States Department of Energy.

VI. REFERENCES

Bellman, R. E., Applied Dynamic Programming, Princeton University Press, Princeton, NJ (1962).

Bonnet, A. and C. Dahan, "Oil-well Data Interpretation Using Expert System and Pattern Recognition Technique," Proc. Eighth Intl. Joint Conf. on Artificial Intelligence, Karlsruhe, West Germany, August 8-12, 1983, Vol. I, p. 185, International Joint Conferences on Artificial Intelligence, Inc. (1983).

Davis, R., H. Austin, I. Carlbom, B. Brawley, P. Pruchnik, R. Sneiderman, and J. A. Gilreath, "The Dipmeter Advisor: Interpretation of Geologic Signals," Proc. Seventh Intl. Joint Conf. on Artificial Intelligence , Vancouver, B. C., Canada, August 24-28, 1981, Vol. II, p. 846, International Joint Conferences on Artificial Intelligence, Inc. (1981).

Duda, R. O., P. E. Hart, P. Barrett, J. G. Gaschnig, K. Konolige, R. Reboh, and J. Slocum, "Development of the Prospector Consultation System for Mineral Exploration," SIR International (1978).

Clancey, W. J., "Heuristic Classification," Artificial Intelligence, 27,289 (1985).

Gevarter, W. B., "The Nature and Evaluation of Commercial Expert System Building Tools," IEEE Computer, 20, 5, 24 (May 1987).

Hendler, J. A., Expert Systems: The User Interface, Ablex Publishing Corporation, Norwood, NJ (1988).

"KEE User's Guide," K3.1-UG-1, Intellicorp, Inc. (1988).

Sheniderman, B., Designing the User Interface, Addison-Wesley Publishing Company, Inc., Reading, MA (1987).

Marusak, N. L., "Stratigraphic Interpretation Using Electric Logs," Proc. Monterey Containment Symposium, Monterey, California, August 26-28, 1981, Vol.I, p. 147, LA-9211-C, Los Alamos National Laboratory (1981).

Mettrey, W., "An Assessment of Tools for Building Large Knowledge-Based Systems," AI Magazine, 8,4,81 (Winter 1987).

Weiss, S., C. Kulikowski, C. Apte, M. Uschold, J. Patchett R. Brigham, and B. Spitzer, "Building Expert Systems for Controlling Complex Programs," Proc. Natl. Conf. on Artificial Intelligence, Pittsburgh, Pennsylvania, August 18-20, 1982, p. 322, American Association for Artificial Intelligence (1982).

Winterkamp, J. L., J. R. Neergaard, C. F. Mills, and C. A. Watson, "GEOscience Data Evaluation System," LA-CP-85273, Los Alamos National Laboratory (1985).

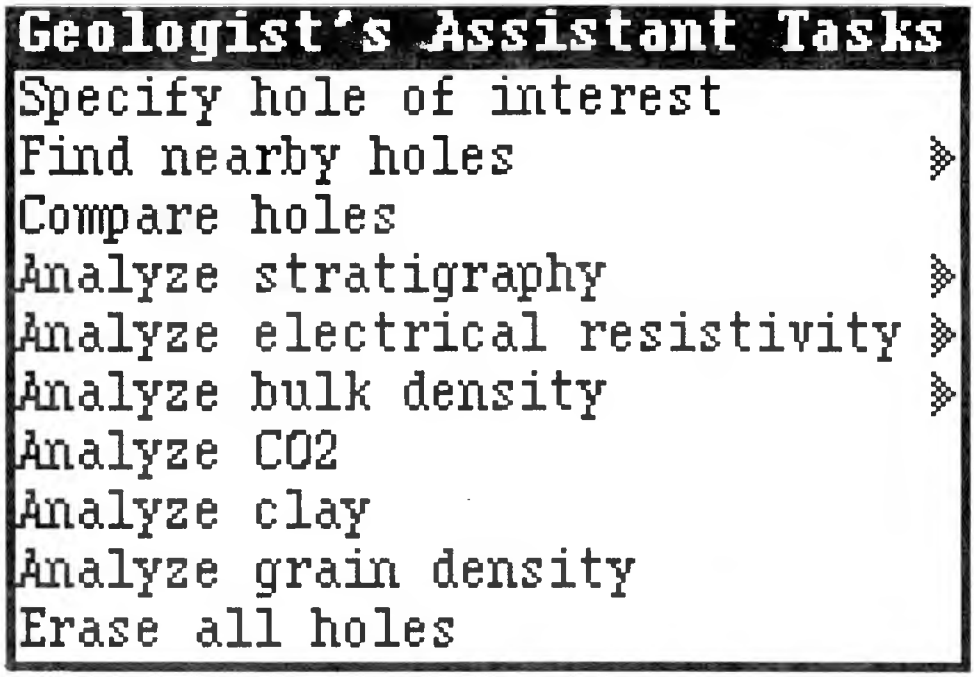


Figure 1 - The initial selection menu for the Geologist's Assistant expert system.

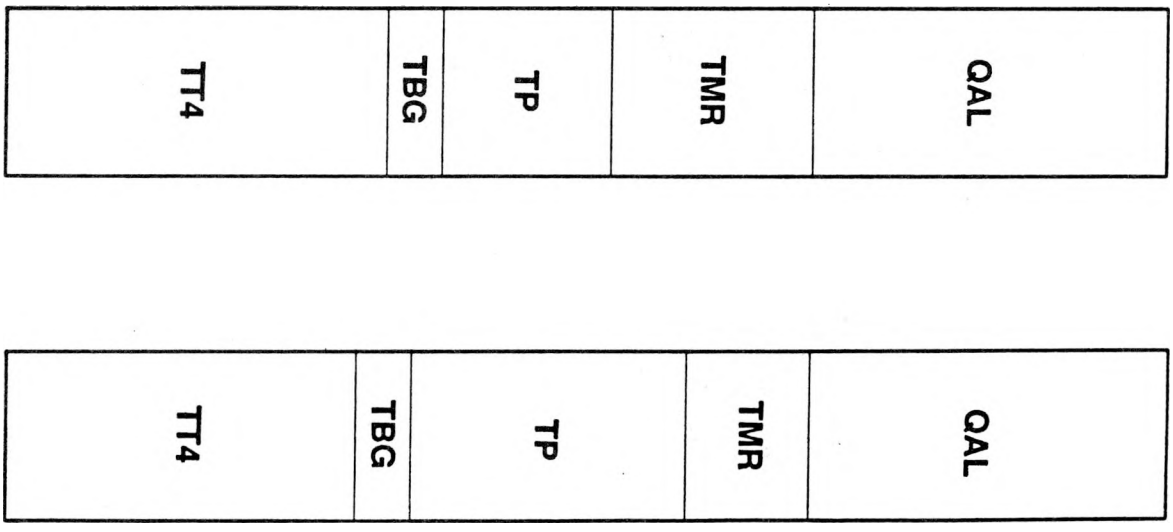


Figure 2 - Two holes with a fault cutting through both.

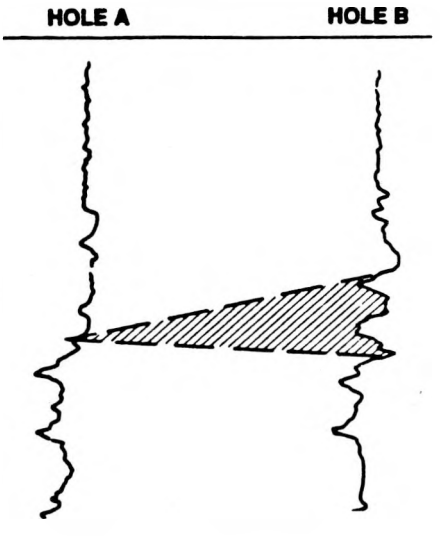


Figure 3 - A comparison of electrical resistivity logs.

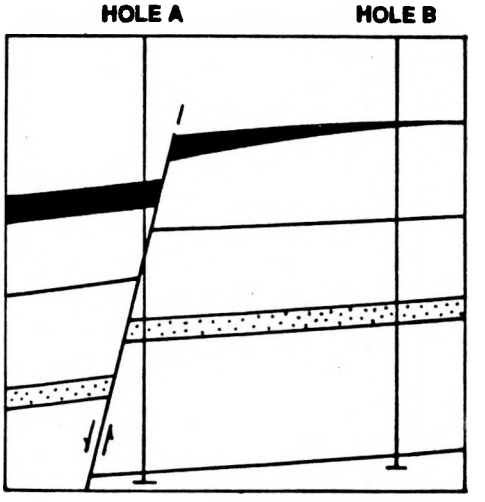


Figure 4 - An interpretation based in part on a comparison of electrical resistivity logs.

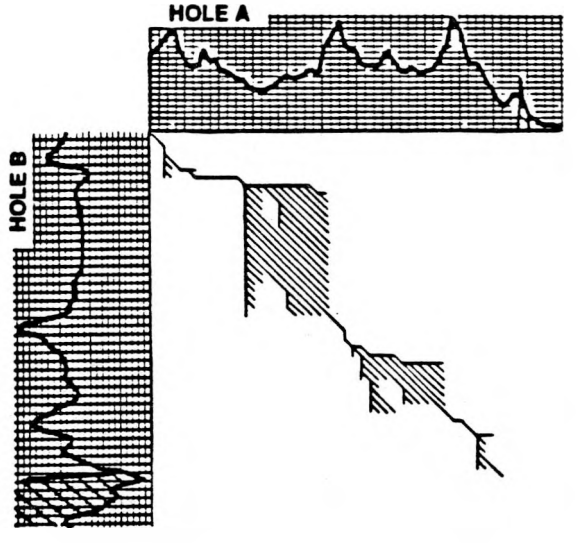


Figure 5 - The path that follows the bottom of the "valley" formed by the outer difference matrix of the electrical resistivity logs shown in Figure 3.

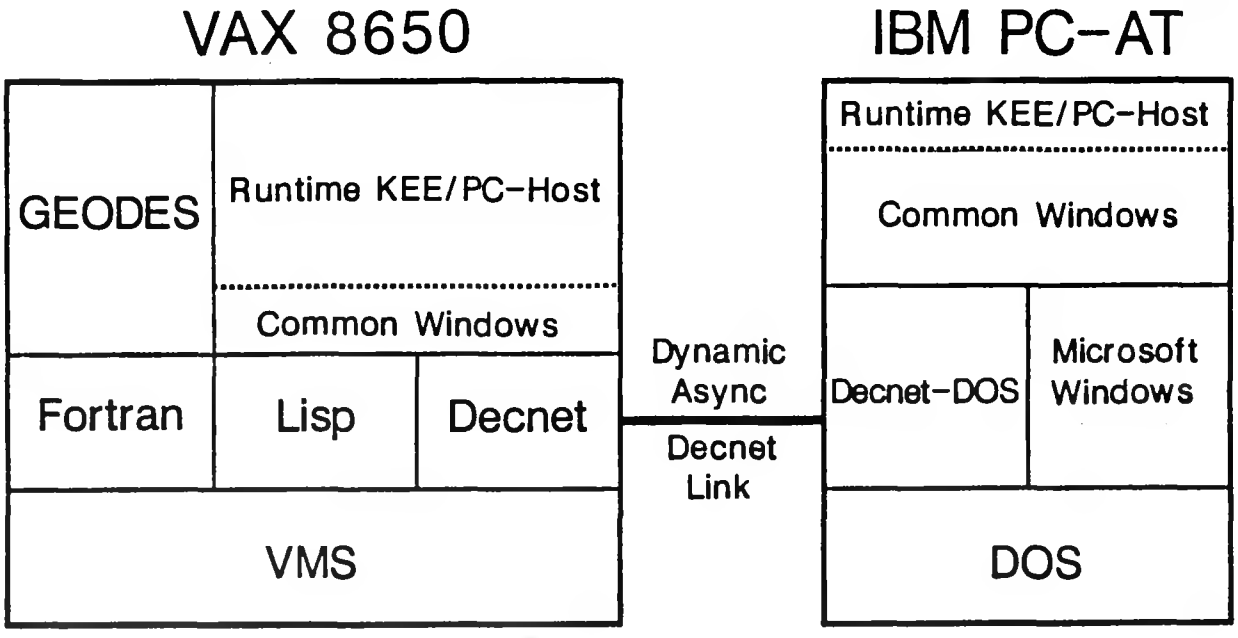


Figure 6 - Components of the Geologist's Assistant delivery system.

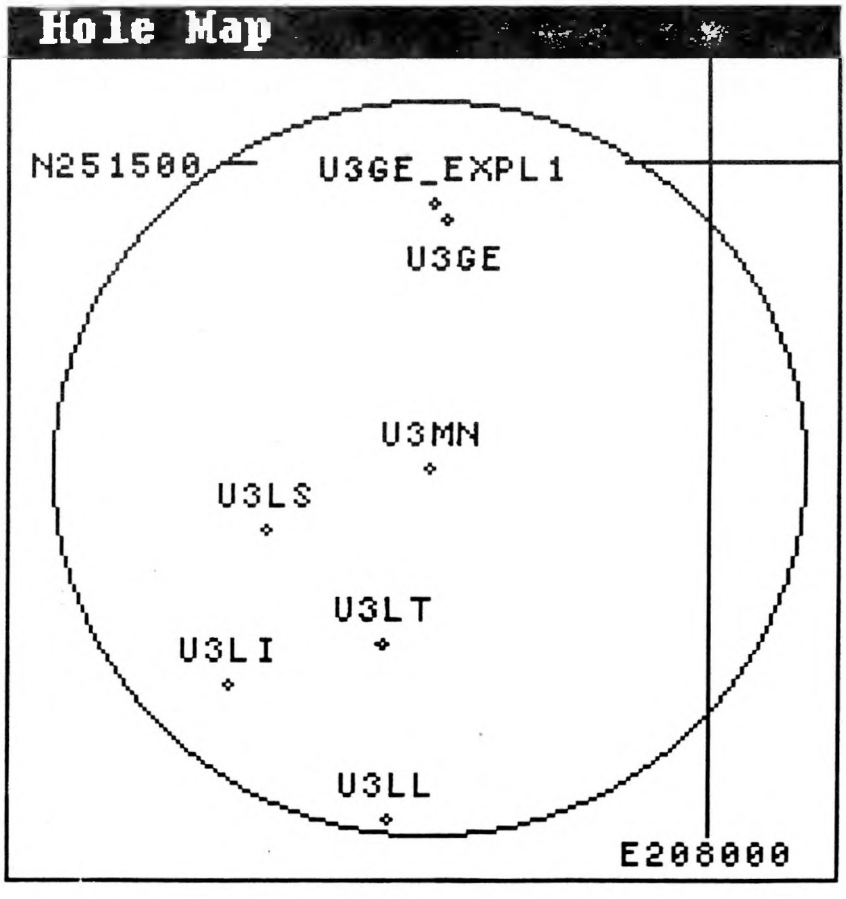


Figure 7 - A map showing a hole of interest and its nearby holes.

A STUDY OF THE DIFFERENCE BETWEEN GRAVIMETRIC AND GAMMA-GAMMA DENSITY NEAR THE SURFACE IN NORTHERN YUCCA FLAT

ABSTRACT

J. R Hearst and N. R. Burkhard

Although the mean and median of the difference between average density from 50 to 200 m below the surface in 43 holes in northern Yucca Flat computed from a density log and that computed from borehole gravity using the measured free air gradient is very close to zero, the range of values is very large. Many individual values of the difference are significantly different from zero. When the gravimetric density is computed using a free air gradient calculated from the surface gravity on an irregular but approximately 300 m grid, the mean and median of the difference between gravimetric and gamma-gamma density is slightly closer to zero than when the measured free air gradient is used. The range of values is not significantly decreased. Proposed explanations for this large range fall into two categories: anomalies in the gravity field or its horizontal derivative at the sites with a large difference range, causing changes in the free air gradient or the near-surface gravimetric density, and mechanisms that affect the bulk density near the borehole, causing changes in the gamma-gamma density. We have investigated many proposed explanations and have found no single mechanism that is consistent with the data. These results indicate that the choice of method of determining free air gradient causes no significant change in the difference between near-surface gamma density and gravimetric density, and that there is no obvious method of eliminating the range. Because calculation from surface gravity is much less expensive than tower measurement, and there is no evidence that it is less accurate, we consider it the logical method for routinely obtaining free air gradient until some evidence is found to suggest the contrary. We are attempting to optimize the calculational procedure. The tradeoff is between the accuracy of the calculated free air gradient and the amount of surface gravity data required.

* Work performed under the auspices of the U.S. Department of Energy by the Lawrence Livermore National Laboratory under Contract W-7405-Eng-48.

Introduction

For many years we have used the difference between bulk density obtained from a gamma-gamma density log and the bulk density calculated from borehole gravity to infer subsurface structure at the Nevada Test Site (NTS) (Hearst and McKague, 1976; Hearst et al, 1986). The formula for calculating density from gravity measurements in a borehole is

$$\rho = C(F - \Delta g/\Delta z) \qquad (1)$$

where ρ is the bulk density, C is a constant, g is the measured gravity, and z is the depth at which the gravity measurement is made. F, called the "free air gradient" (the FAG) is the value of $\Delta g/\Delta z$ in the absence of rock, usually taken as the value above the surface. There are many ways of obtaining a value for the FAG. Some investigators calculate the FAG using a standard formula (Heiskanen and Vening Meinesz, 1958) that depends only on latitude and elevation. Others, who are fortunate enough to work in areas where the density of some formations is very well known, compute the FAG from Eq. (1), using gravity measurements in the well-known formations. We have been unable to obtain plausible values of the FAG routinely with either of these methods, and have either measured the FAG directly on a 15-m tower, or calculated it from surface gravity data (Beyer, 1971; Heiskanen and Moritz, 1967).

We usually infer subsurface structure from differences between gamma-gamma and gravimetric density in the deepest part of the hole. We frequently choose between the measured and calculated FAG (if they disagree) by trying to make the two densities agree at intermediate depths. Recently, gravity measurements on the 450-m- tall BREN tower (Thomas et al, 1989) have shown that the measured FAG near the surface disagrees with that measured at higher elevations, tending to inhibit our use of the FAG measured on a short tower and to encourage the use of the calculated FAG. Quite often, whatever plausible value of the FAG is used, the two densities disagree substantially above 150 or 200 m.

Although these near-surface disagreements between gamma-gamma and gravimetric densities have troubled many geophysicists studying the properties of NTS sites, no one has been able to explain or eliminate them. This study was undertaken as an attempt to characterize the disagreements, to use the understanding obtained from characterization to explain them, and to use the explanation to change our procedures to eliminate them. We have succeeded only in eliminating many possible explanations.

These proposed explanations can be divided into two categories: those that depend on some type of error in obtaining the FAG, causing anomalous near-surface gravimetric density, and those depending on some peculiarity of the rock near the borehole, causing anomalous near-surface gamma-gamma density. We shall first discuss the characteristics of the disagreement, and then examine the two types of proposed explanations in turn.

Characteristics of the Disagreement

We studied gravimetric and gamma-gamma density logs from 43 holes in Northern Yucca Flat. We chose all emplacement (2 to 4 m diameter) holes in Areas 2, 4, 8, 9 and 10 at NTS for which good-quality logs of both types were available, and in which the density log used one of the two big-hole density sondes, the FDS or the DBS. We obtained values of the density vs depth from the LLNL Containment Data Base. We then averaged gravimetric and gamma-gamma density over the depth ranges 50-100 m, 100-150 m, and 150-200 m, choosing only those depth ranges where both logs appeared to be valid. We overplotted the logs in each hole (Figure 1 is a typical example) to determine validity over the depth regions.

The gravimetric density logs in the data base were calculated using values of the FAG chosen by the geophysicist studying the hole in question; there was no uniform procedure for this choice. We therefore converted the gravimetric density values to those that would have been obtained using three different values of the FAG: the measured value, the value calculated by the method described by Beyer (Beyer, 1971), and the value calculated for us by A. Cogbill (Cogbill, 1985), extrapolated from the 300 m elevation to the surface by adding .0009 mgal/m to Cogbill's results. This constant was obtained by extrapolating the variation of FAG with elevation from Cogbill's (1985) Table 2. Finally we subtracted the average gravimetric density for each depth range from the gamma- gamma density for that range to obtain a density difference $\delta\rho$.
The input data are shown in Table I.

Figure 2 shows histograms of the value of the difference. Note that there are fewer values in the 50-100 m range than in the 100-150 m range, and fewer in the latter range than in the 150-200 m range. Some values were left out of the first two ranges because of the poor quality of the gamma-gamma density log. Table II shows the mean, median, and standard deviation of the differences.

It has been suggested that perhaps the difference occurs only in alluvium, or is different in alluvium and tuff. Figure 3 shows the same data as Figure 2, but restricted to those depth ranges that are entirely in alluvium, and Table III gives the mean, median, and standard deviation of those data. The results are, if anything, closer to zero, indicating that it is unlikely that the difference can be attributed to alluvium alone. There are not enough pure tuff data to provide similar plots.

From these results we can conclude that the mean and median differences are quite small. Many of the observed means, in fact, are consistent with a true mean equal to zero. This implies that it is quite unlikely that we either can or need to explain the mean. The range of values is the quantity that requires explanation.

Explanations Based on the Free Air Gradient

It has been suggested (Kasameyer, private communication) that using standard complete Bouguer-corrected surface gravity data introduces truncation error into the calculated FAG, and that the free-air corrected surface gravity, rather than the Bouguer- corrected surface gravity should be used to calculate the FAG. Figure 4 and Table IV show results of using the free-air corrected surface gravity and Beyer's method of calculating the FAG. These results are not significantly different from those using the Bouguer-corrected gravity.

Perhaps at the holes where $\delta\rho$ is large the FAG is anomalous. If this is the case, then the FAG at such a hole should be markedly different from the FAG at nearby holes. Figure 5 shows $\delta\rho$ vs the FAG at each hole minus the mean value of the FAG at all holes within 1 km of the hole. Only those holes where there are at least three other FAG values within 1 km are shown. Figure 6 shows the same plot but with the mean FAG for all holes within 2 km of the hole. There is no obvious correlation, indicating that it is unlikely that $\delta\rho$ can be attributed to anomalies in the FAG.

Another indication of an anomalous FAG might be the value of the difference between measured FAG and calculated FAG. Figure 7 is a plot of $\delta\rho$ vs the difference between the measured FAG and calculated FAG. No significant correlation is observed.

The gravity data for the measured FAG and the borehole gravity are corrected for terrain. Ordinarily, although in principle it should, the terrain correction does not account for craters near the hole. Figure 8 is a plot of $\delta\rho$ vs the fraction of the inner Hammer zones (outer radius 370 m) used for terrain correction that were occupied by craters when the gravity log was run. If the

craters affected the gravity data, one would expect large values (either positive or negative) of $\delta\rho$ to be associated with large values of the fraction. No significant correlation can be seen.

Over the past two decades parts of Area 2 in Yucca Flat have subsided as much as 10 m. The terrain corrections are calculated using terrain elevations from maps showing the original terrain elevations, whereas the datum elevation (at the top of the hole) uses the true current elevation. Consequently the terrain correction could include the effect of the top of the borehole being in a bowl as much as 10 m deep. Figure 9 shows gravimetric density vs depth at U2gh, where the datum elevation is about 5 m below the nearby terrain elevation used in the terrain correction. The gravimetric density was calculated with the normal terrain correction and with the datum raised 5 m to be level with the terrain. The gravimetric density increases by almost 0.07 g/cc at the surface, but at a depth of 50 m, the shallowest of interest to us, the difference almost vanishes. There is no greater value of elevation difference at any Area 2 hole where $\delta\rho$ is large, so it is unlikely that this difference accounts for large $\delta\rho$.

Another possible explanation involving the terrain correction considers errors in the estimate of the elevations of the terrain surrounding the hole. Raising or lowering the Hammer D, E and F zones (outer radius 895 m) by as much as 7 m causes an effect similar to that in Figure 9. It can be as large as 0.1 g/cc but only extends down about 50 m.

Values of measured and calculated FAG, and $\delta\rho$, were overplotted on contour maps of the Bouguer-corrected gravity in northern Yucca Flat, to see if there was any correspondence between unusual values of FAG, or large values of $\delta\rho$, with unusual features of the gravity map. Figure 10 shows the gravity map with the hole names superposed, and Figures 11 thru 16 show the overplots. There are no obvious correlations between large positive or negative values of $\delta\rho$ and steep or flat gravity contours, nor are there any simple spatial correlations.

Finally, on Figure 17 we plotted the value of the FAG that would be needed to make $\delta\rho$ zero vs the value of $\delta\rho$. If $\delta\rho$ were caused by a bad FAG, we would expect plausible values of FAG for large absolute values of $\delta\rho$. In fact, for most large absolute values of $\delta\rho$ the FAG required to eliminate $\delta\rho$ is implausible.

Evidently none of the proposed explanations relating $\delta\rho$ to anomalous values of gravity or its (first) derivatives is satisfactory.

Explanations Based on Peculiarities of the Rock

The most obvious explanation of either a positive or negative value of $\delta\rho$ is that the density of the medium surrounding the borehole is in fact larger or smaller than the average density of the medium seen by the gravimeter. In fact, a two-dimensional BIFUR (Hearst and McKague, 1976) calculation shows that if the borehole were in the center of an old river valley 100 m wide and 200 m deep that was filled with a material 0.2 g/cc denser than the surrounding medium, the value of $\delta\rho$ using a FAG calculated with surface data on a grid large enough that the FAG would not be affected by the valley would be about 0.12 down to 200 m, and using a measured FAG would be between 0.07 and 0.04, depending on depth. The difference is caused by the effect of the density contrast on the measured FAG.

If this explanation were correct, then positive values of $\delta\rho$ would in general be observed in situations where the density near the hole was greater than the average density observed at the same depth interval in northern Yucca Flat, and negative values of $\delta\rho$ would be observed where the density near the hole was less than the average density. If $\delta\rho$ depended on the near-hole density, one would expect to see a correlation between $\delta\rho$ and the difference between near-hole density and

overall average density. Figure 18 is a plot of $\delta\rho$ vs the log density at each hole minus the average log density for all the holes studied; no trend is obvious.

Another proposed explanation is invasion of the near-hole formation by drilling fluid, causing higher density near the hole. Drying could cause a decrease in density. Figure 19 is a plot of $\delta\rho$ vs the average water content from neutron logs in each hole. There is a weak correlation between $\delta\rho$ and water content when the measured FAG is used, but it is not strong enough to consider invasion a major contributor to $\delta\rho$.

Discussion

We have found no single mechanism that can be shown to be responsible for the large range of values of $\delta\rho$. It is, of course, quite possible that all of the individual large values of $\delta\rho$ were caused by one or another of the proposed mechanisms, but that no mechanism dominated. In that case, there is really no way to correct either log or gravimetric density to eliminate $\delta\rho$. Therefore, until some correct explanation is found, we must continue to live with the large range of $\delta\rho$.

One thing that this study shows, however, is that none of the three methods of obtaining the FAG: measurement, calculation by Beyer's method, or calculation by Cogbill's method, is any better than another at reducing $\delta\rho$. Therefore, the most sensible method of obtaining the FAG is the cheapest and most convenient. Measuring the FAG takes many man-hours and requires the measurers to be in the forward area very early in the morning to avoid strong winds. It is obviously the most expensive and least convenient method. Consequently the method of choice, for ordinary situations, is calculation.

J. Thomas (1989) has shown that when surface gravity measurements are used to calculate the FAG over a given elevation range (specifically the FAG that would be measured on a tower under ideal conditions), measurements within a radius equal to 0.3 times the elevation range contribute half of the information for the calculation. If this is correct, and if we assume that for borehole gravity measurements on the order of 500 m deep the FAG should be calculated for an effective height of 500 m (and then extrapolated to the surface), half of the effect of the surface gravity measurements will be caused by measurements within 150 m of the hole. Since the data used in our present calculations of the FAG are on an approximately 300 m grid, for most of the holes in this study there are no surface measurements within that range. (If a lower effective height is desired, the radius of interest will of course be smaller.)

On the other hand, we have seen (Figure 17) that improving the calculation of the FAG within a plausible range of values is unlikely to remove many of the large values of $\delta\rho$. But it is quite possible that plausible changes in FAG could markedly reduce large values of $\delta\rho$, or eliminate smaller values, thereby increasing our comfort level. Consequently we are considering the feasibility of making some surface gravity measurements near several of the holes in Table I, to see what effect a FAG obtained using the new measurements would have on the observed $\delta\rho$.

Acknowledgments

We would like to thank Alan Cogbill of Los Alamos National Laboratory for making his calculations of the FAG at the 43 sites we requested.

References:

Beyer, L. A.; "The Vertical Gradient of Gravity in Vertical and Near-vertical Boreholes", Dissertation, University Microfilms, Ann Arbor, 1971

Cogbill, A. H., Calculation of Free-air Gradients at Yucca Flat, Nevada; Proc. Third Sym. on Containment of Underground Nuclear Explosions, Sept. 9-13, 1985

Hearst, J. R and H. L McKague; Structure Elucidation with Borehole Gravimetry; Geophysics v. 41, p. 491, 1976

Hearst, J. R, R. E. Carlson and S. R. Clark; Calculation of Gravimetric Density Caused by Three-dimensional Structure; Proc. Soc. Prof. Well Log Analysts 27th Logging Symposium, June 9-13 1986

Heiskanen, W. A. and F. A. Vening Meinesz; "The Earth and its Gravity Field", McGraw-Hill, New York, 1958, p. 148.

Heiskanen, W. A. and H. Moritz; "Physical Geodesy", W. H. Freeman, San Francisco, 1967

Thomas, J., P. Kasameyer, O. Fackler, D. Felske, B. Harris, J. Kammeraad, M. Millett and M. Mugge; Testing the Inverse Square Law of Gravity on the BREN Tower; Physical Review Letters, to be published, 1989.

Thomas, J., Testing the Inverse Square Law of Gravity: Error and Design with the Upward Continuation Integral; Physical Review D., to be published, 1989.

Table I

Data used in this study. The three values of the free air gradient (FAG) are the measured value and the values calculated using Beyer's method and the values calculated by Cogbill, corrected to the surface. The log density and the gravimetric density calculated using the three values of the FAG are averaged over depth intervals of 50 - 100 m, 100 - 150 m, and 150 - 200 m.

Hole	FAG			Log Density			Gravimetric Density								
		Calculated					Measured FAG			Beyer			Cogbill		
	Meas-ured	Beyer	Cog-bill	50-100m	100-150m	150-200m	50-100m	100-150m	150-200m	50-100m	100-150m	150-200m	50-100m	100-150m	150-200m
U2co	0.0919	0.0926	0.0918	2	2.09	1.81	2.02	2.10	1.87	2.05	2.13	1.90	2.03	2.11	1.88
u2cq	0.0906	0.0917	0.0914	2.09	2.15	1.83	1.98	1.98	1.73	2.02	2.02	1.77	2.06	2.06	1.81
u2cr	0.089	0.0910	0.0918	2.05	1.54	1.38	2.02	1.52	1.49	2.09	1.59	1.56	1.91	1.41	1.38
U2cu	0.0910	0.0930	0.0922			2.06	2.15	2.16	2.05	2.23	2.24	2.13	2.10	2.11	2.00
U2ei	0.0934	0.0911	0.0922	1.81	1.98	1.99	2.05	1.97	1.91	1.96	1.88	1.82	2.09	2.01	1.95
U2el	0.0914	0.0921	0.0916	1.89	1.9	1.92	1.97	1.9	1.91	1.99	1.92	1.93	1.96	1.89	1.90
u2ep	0.0948	0.0926	0.0918	2.03	1.98	1.98	2.07	2.03	2.04	1.98	1.94	1.95	2.02	1.98	1.99
U2eq	0.093	0.0916	0.0919	1.94	1.96	1.93	1.95	1.9	1.94	1.89	1.84	1.88	1.99	1.94	1.98
U2eu	0.0922	0.0953	0.0923		1.97	2.03	2.05	2.13	2.11	2.17	2.25	2.23	2.03	2.11	2.09
U2ev	0.0904	0.0913	0.0916	1.94	2.04	2	2.03	2.08	2.06	2.07	2.12	2.10	1.99	2.04	2.02
u2ew	0.0910	0.0925	0.0916	1.9	1.97	1.96	1.82	1.82	1.79	1.88	1.88	1.85	1.91	1.91	1.88
U2ex	0.0918	0.0923	0.0917	1.94	2.02	2.03	2.03	2.02	2.01	2.05	2.04	2.03	2.04	2.03	2.02
U2ey	0.0947	0.0934	0.0937		2.03	2.06	2.02	1.98	1.89	1.97	1.93	1.84	1.93	1.89	1.80
u2fa	0.0911	0.0907	0.0915	1.92	2.03	2.1	2.02	2.05	2.03	2.00	2.03	2.01	2.00	2.03	2.01
U2fe	0.092	0.0910	0.0918	1.98	2.08	2.12	2.09	2.16	2.15	2.05	2.12	2.11	2.09	2.16	2.15
U2ff	0.094	0.0914	0.0928	1.9	1.95	2.03	1.9	1.96	2.23	1.79	1.85	2.12	1.94	2.00	2.27
u2fg	0.0924	0.0916	0.0920			2.02	2.09	2.13	2.12	2.06	2.10	2.09	2.00	2.04	2.03
u2fh	0.0932	0.0911	0.0928	1.9	1.99	2.19	1.86	1.95	2.22	1.78	1.87	2.14	1.86	1.95	2.22
U2gb	0.0946	0.0946	0.0916		2.04	2.06	1.94	1.91	1.93	1.94	1.91	1.93	2.01	1.98	2.00
u2gd	0.0972	0.0952	0.0934	1.94	2.1	1.93	2.07	2.15	1.98	1.99	2.07	1.90	2.20	2.28	2.11
U2gf	0.0912	0.0925	0.0917		2.05	2.05	1.99	1.96	1.94	2.04	2.01	1.99	2.10	2.07	2.05
U4ac	0.0902	0.093	0.0930	1.93	1.88	1.86	1.84	1.80	1.78	1.95	1.91	1.89	1.72	1.68	1.66
u4ad	0.093	0.0939	0.0934	1.92	1.9	1.84	1.87	1.80	1.75	1.90	1.83	1.78	1.93	1.86	1.81
U4ak	0.0906	0.0932	0.0922	1.97	1.98	1.94	1.79	1.87	1.81	1.89	1.97	1.91	1.76	1.84	1.78
U4al	0.0925	0.0926	0.0924	1.88	1.95	1.76	1.85	1.95	1.88	1.85	1.95	1.88	1.85	1.95	1.88
U4am	0.0930	0.0923	0.0925	1.96	1.94	1.9	1.93	1.93	1.91	1.90	1.90	1.88	1.94	1.94	1.92
u4ap	0.0925	0.0933	0.0931		2	2.12	1.79	1.85	1.98	1.82	1.88	2.01	1.80	1.86	1.99
U4as	0.0905	0.0908	0.0912	2.01	1.83	1.71	2.02	1.82	1.67	2.03	1.83	1.68	1.95	1.75	1.60
U4at	0.0895	0.0907	0.0911		1.83	1.74	1.82	1.69	1.67	1.86	1.73	1.71	1.75	1.62	1.60
u8j	0.09	0.0913	0.0911		1.58	1.61	2.14	1.59	1.58	2.19	1.64	1.63	2.09	1.54	1.53
u8k	0.0906	0.0923	0.0915	2.14	1.85	1.72	2.06	1.69	1.55	2.13	1.76	1.62	2.03	1.66	1.52
u8l	0.0915	0.0937	0.0915	1.87	1.67	1.57	1.87	1.59	1.48	1.95	1.67	1.56	1.86	1.58	1.47
u9cp	0.0940	0.0944	0.0925	1.92	1.7	1.64	1.76	1.96	1.65	1.77	1.97	1.66	1.81	2.01	1.70
u9cq	0.0927	0.0933	0.0923	1.86	1.77	1.62	1.72	1.63	1.51	1.74	1.65	1.53	1.73	1.64	1.52
u9cr	0.0935	0.0926	0.0924	2.06	1.64	1.57	2.06	1.67	1.58	2.02	1.63	1.54	2.14	1.75	1.66
u9cs	0.0914	0.0940	0.0921	1.71	1.76	1.6	1.64	1.67	1.52	1.75	1.78	1.63	1.74	1.77	1.62
u9ct	0.0917	0.0918	0.0916	1.84	1.87	1.88	1.82	1.72	1.74	1.82	1.72	1.74	1.84	1.74	1.76
u9cv	0.0925	0.0949	0.0923	1.7	1.63	1.4	1.85	1.58	1.52	1.94	1.67	1.61	1.89	1.62	1.56
u9cw	0.0922	0.0951	0.0925	1.53	1.58	1.45	1.47	1.44	1.41	1.58	1.55	1.52	1.67	1.64	1.61
u10bc	0.094	0.0940	0.0923	1.73	1.55	1.7	1.60	1.39	1.39	1.60	1.39	1.39	1.66	1.45	1.45
u10bg	0.093	0.0932	0.0922	1.68	1.4	1.56	1.75	1.4	1.6	1.75	1.40	1.60	1.77	1.42	1.62
u10bh	0.089	0.0929	0.0921	2.05	2.13	2.14	1.99	2.05	2.09	2.14	2.20	2.24	1.86	1.92	1.96
u10ca	0.0895	0.0903	0.0926	2.04	1.97	1.72	1.89	1.80	1.51	1.92	1.83	1.54	2.04	1.95	1.66

Table II

Median, mean, and standard deviation of the log density minus the gravimetric density, with the gravimetric density calculated from the measured free air gradient (FAG), the FAG calculated using Beyer's method and the FAG calculated by Cogbill, corrected to the surface. Log and gravimetric densities are averaged over depth intervals of 50 - 100 m, 100 - 150 m, and 150 - 200 m.

	50 - 100 m	100 - 150 m	150 - 200 m
Measured FAG			
Median	0.018	0.03	0.03
Mean	0.007	0.041	0.032
Std. Dev.	0.095	0.091	0.101
Calc. FAG Beyer method			
Median	-0.002	0.004	0.02
Mean	-0.011	0.019	0.011
Std. Dev.	0.09	0.096	0.107
Calc. FAG by Cogbill corrected to surface			
Median	-.004	.008	.018
Mean	-.0118	.025	.021
Std. Dev.	.116	.107	.113

Table III

Data as in Table II but restricted to depth regions entirely in alluvium.

	50 - 100 m	100 - 150 m	150 - 200 m
Measured FAG			
Median	0.0	0.009	0.025
Mean	0.013	0.029	0.026
Std. Dev.	0.098	0.081	0.098
Calc. FAG Beyer Method			
Median	0.0	0.001	0.015
Mean	-0.002	0.016	0.015
Std. Dev.	0.081	0.095	0.106
Calc. FAG by Cogbill corrected to surface			
Median	-.004	-.004	.001
Mean	.004	.028	.029
Std. Dev.	.107	.087	.114

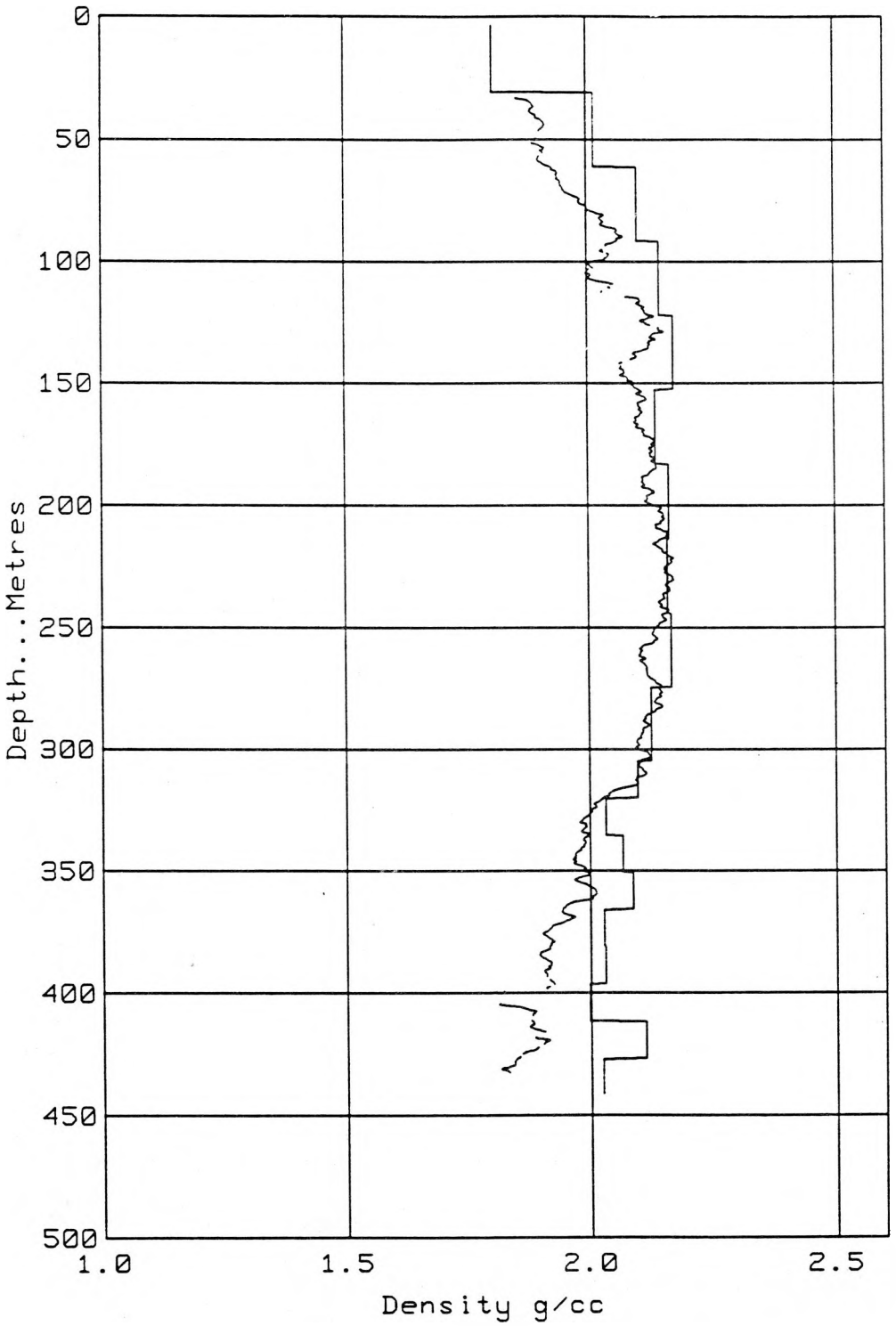


Figure 1 Overplot of gamma-gamma and gravimetric densities at a typical hole.

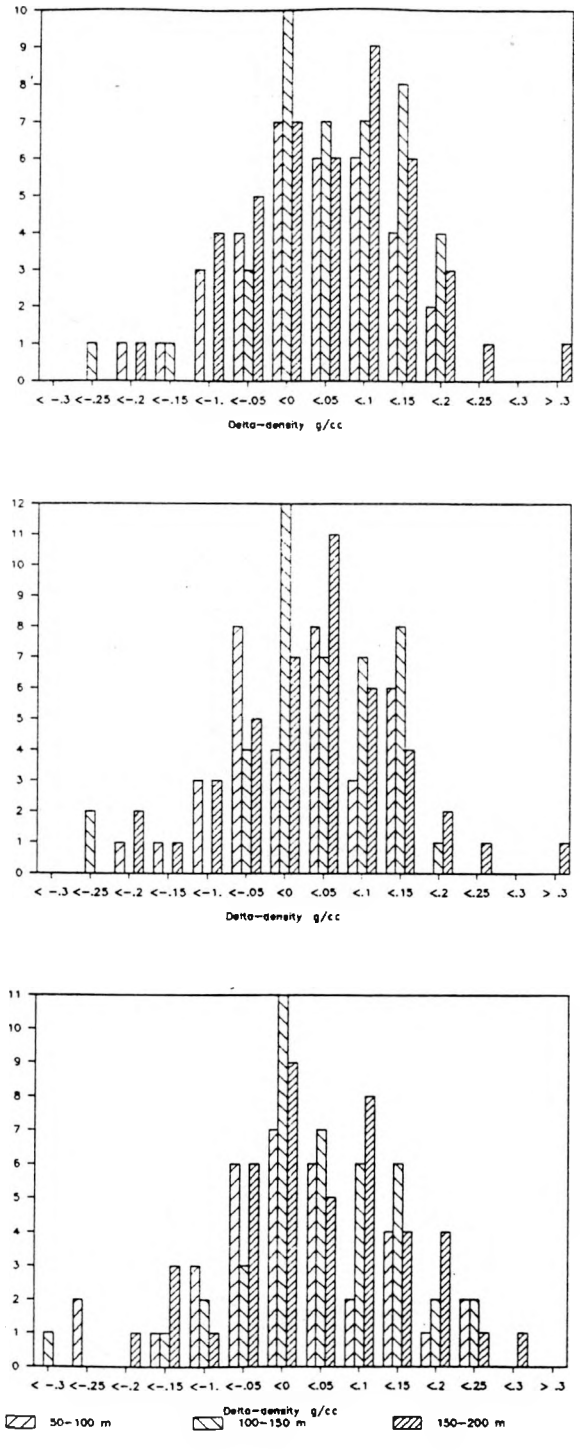


Figure 2 Histogram of the log density minus the gravimetric density calculated using a) the measured free air gradient b) the free air gradient calculated using Beyer's method c) the free air gradient calculated by Cogbill, corrected to the surface. Note that each bar represents the range of values between the value printed under the bar and the value below it.

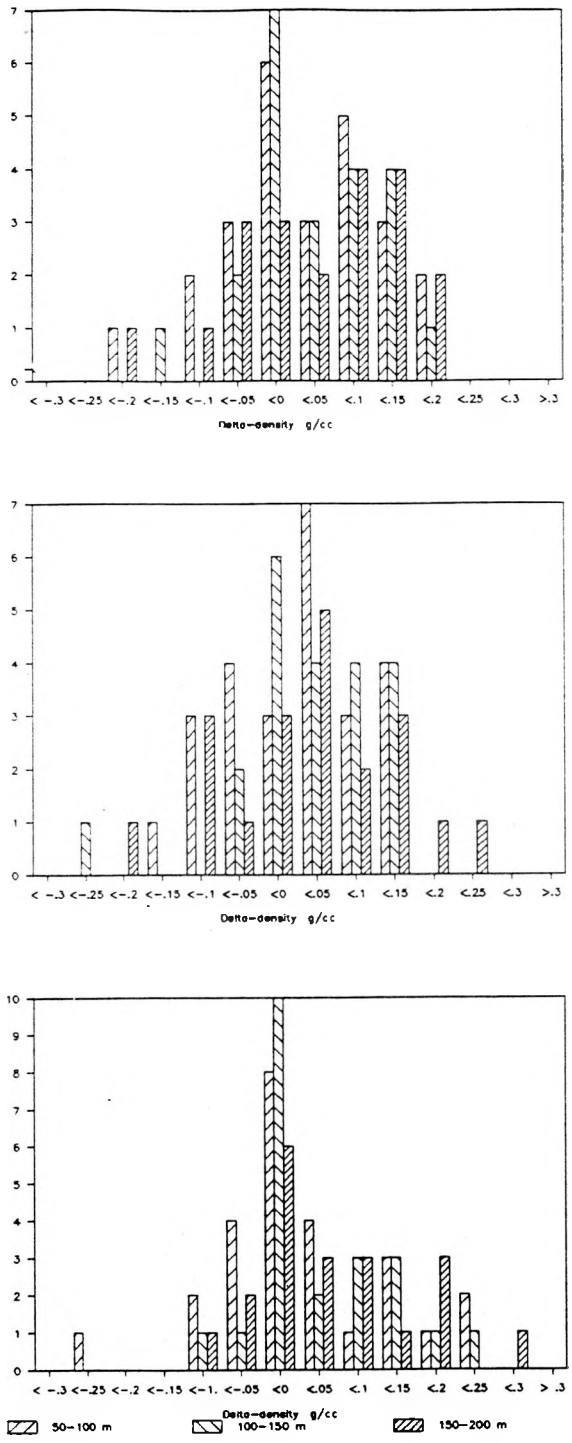


Figure 3 Histogram of the log density minus the gravimetric density in sections of hole entirely in alluvium calculated using a) the measured free air gradient b) the free air gradient calculated using Beyer's method c) the free air gradient calculated by Cogbill, corrected to the surface. Note that each bar represents the range of values between the value printed under the bar and the value below it.

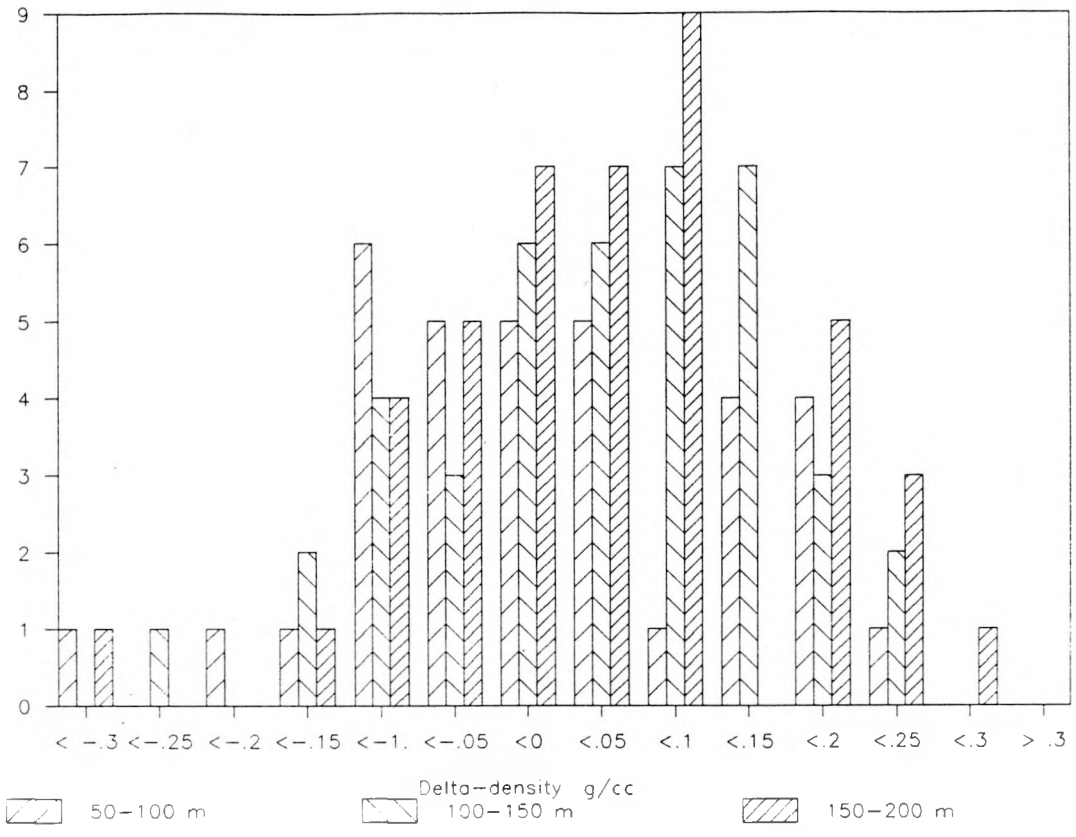


Figure 4 Histogram of the log density minus the gravimetric density calculated using the free air gradient calculated using Beyer's method and surface gravity data corrected only for free air. Note that each bar represents the range of values between the value printed under the bar and the value below it.

Table IV

Median, mean, and standard deviation of the log density minus the gravimetric density, with the gravimetric density calculated using Beyer's method and surface gravity corrected only for free air. Log and gravimetric densities are averaged over depth intervals of 50 - 100 m, 100 - 150 m, and 150 - 200 m.

	50 - 100 m	100 - 150 m	150 - 200 m
Median	-.005	.012	.012
Mean	-.013	.028	.023
Std. Dev.	.130	.113	.123

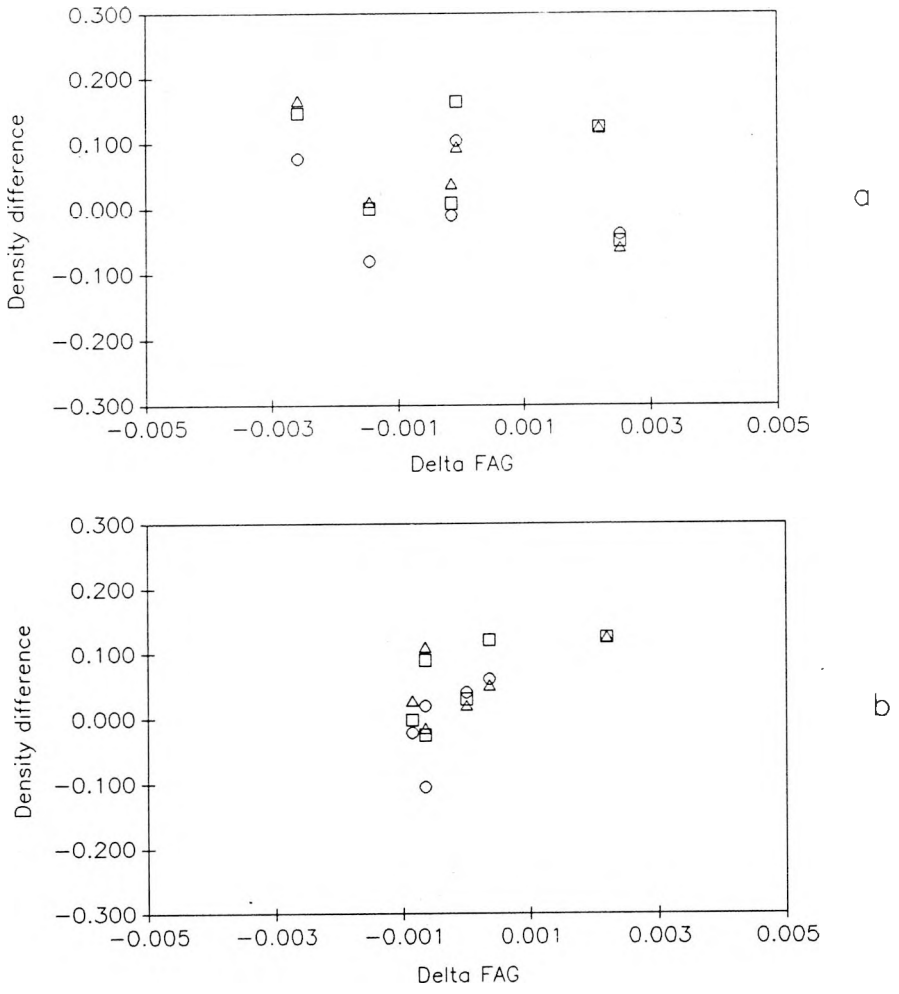


Figure 5 Log density minus gravimetric density calculated using a) the measured free air gradient, b) the free air gradient calculated using Beyer's method vs that free air gradient at each hole minus the mean of that free air gradient at all holes within 1 km of each hole. Circles represent depth range of 50 - 100 m, squares represent depth range of 100 - 150 m, and triangles represent depth range of 150 - 200 m.

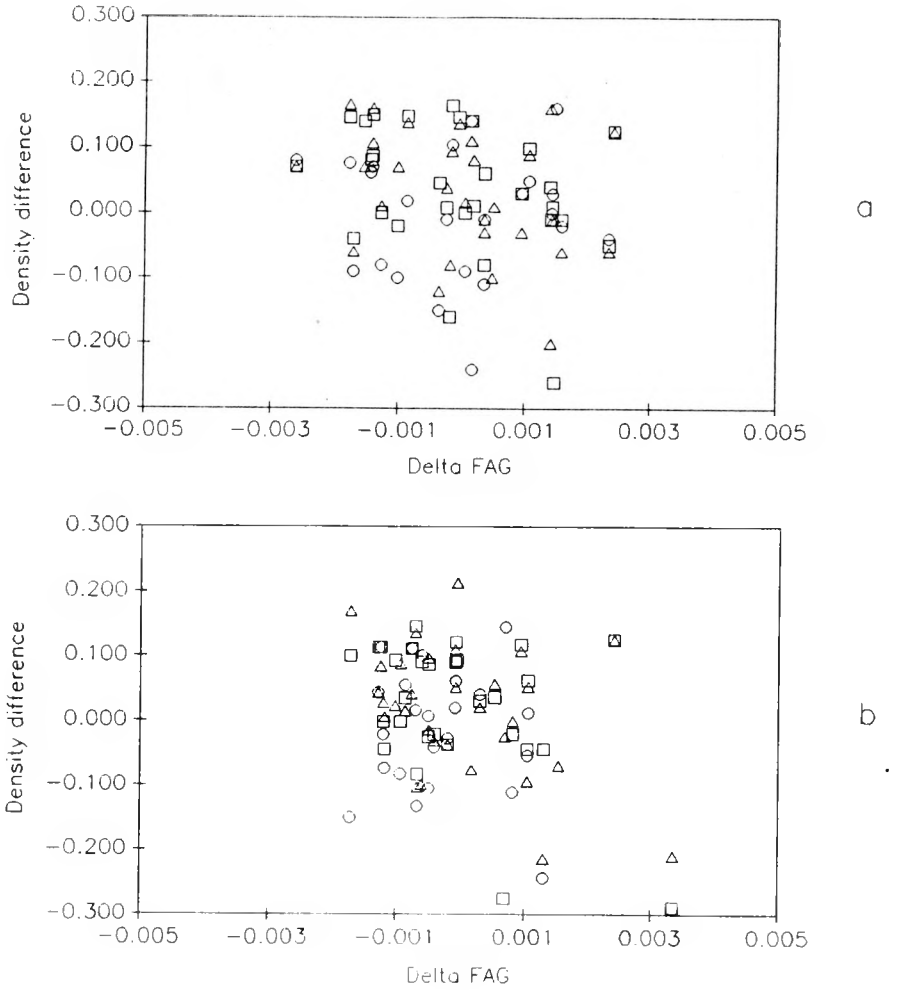


Figure 6 Log density minus gravimetric density calculated using a) the measured free air gradient, b) the free air gradient calculated using Beyer's method vs that free air gradient at each hole minus the mean of that free air gradient at all holes within 2 km of each hole. Circles represent depth range of 50 - 100 m, squares represent depth range of 100 - 150 m, and triangles represent depth range of 150 - 200 m.

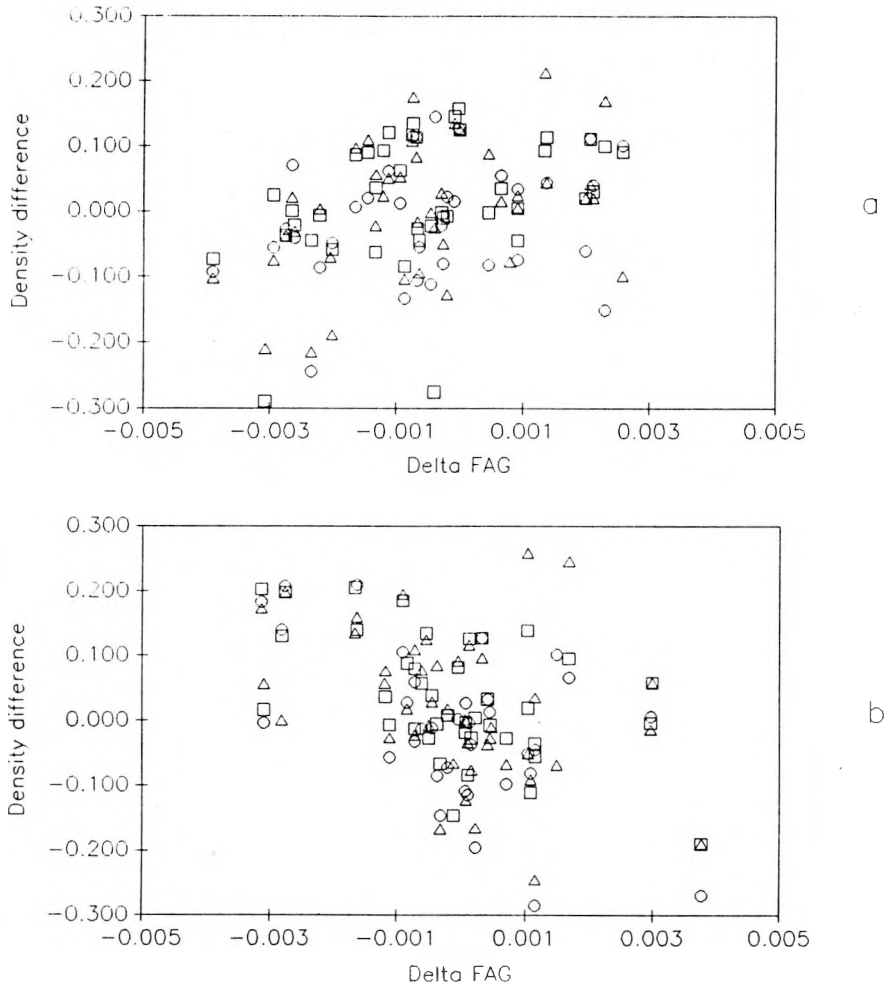


Figure 7 Log density minus gravimetric density calculated using the free air gradient calculated by a) Beyer's method and b) Cogbill corrected to the surface vs the difference between the measured free air gradient and the free air gradient calculated by that method, expressed in mgal/ft. Circles represent depth range of 50 - 100 m, squares represent depth range of 100 - 150 m, and triangles represent depth range of 150 - 200 m.

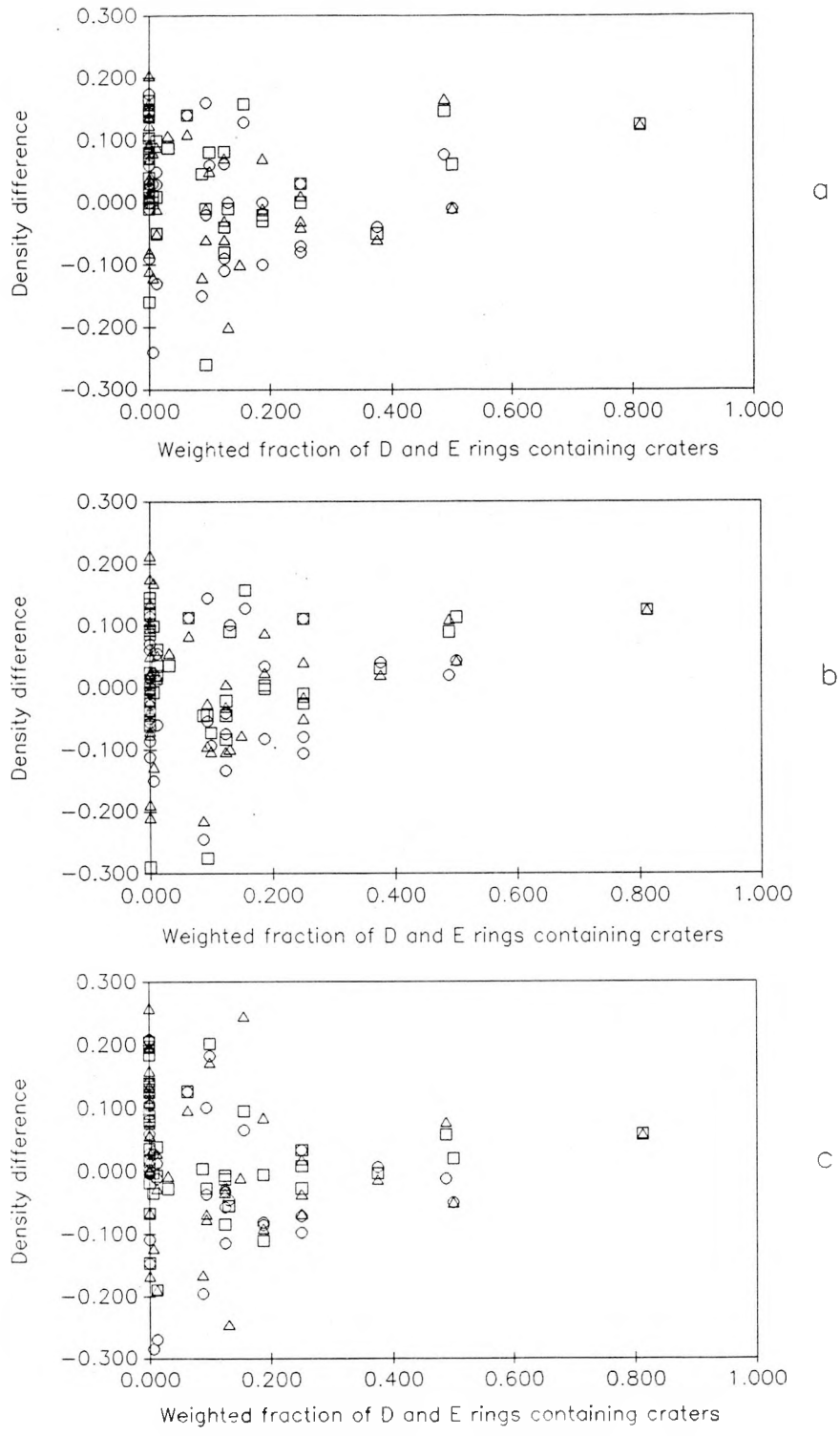


Figure 8 Log density minus gravimetric density calculated using a) the measured free air gradient, b) the free air gradient calculated using Beyer's method and c) the free air gradient calculated by Cogbill corrected to the surface vs the fraction of the area within a radius of 390 m occupied by craters. Circles represent depth range of 50 - 100 m, squares represent depth range of 100 - 150 m, and triangles represent depth range of 150 - 200 m.

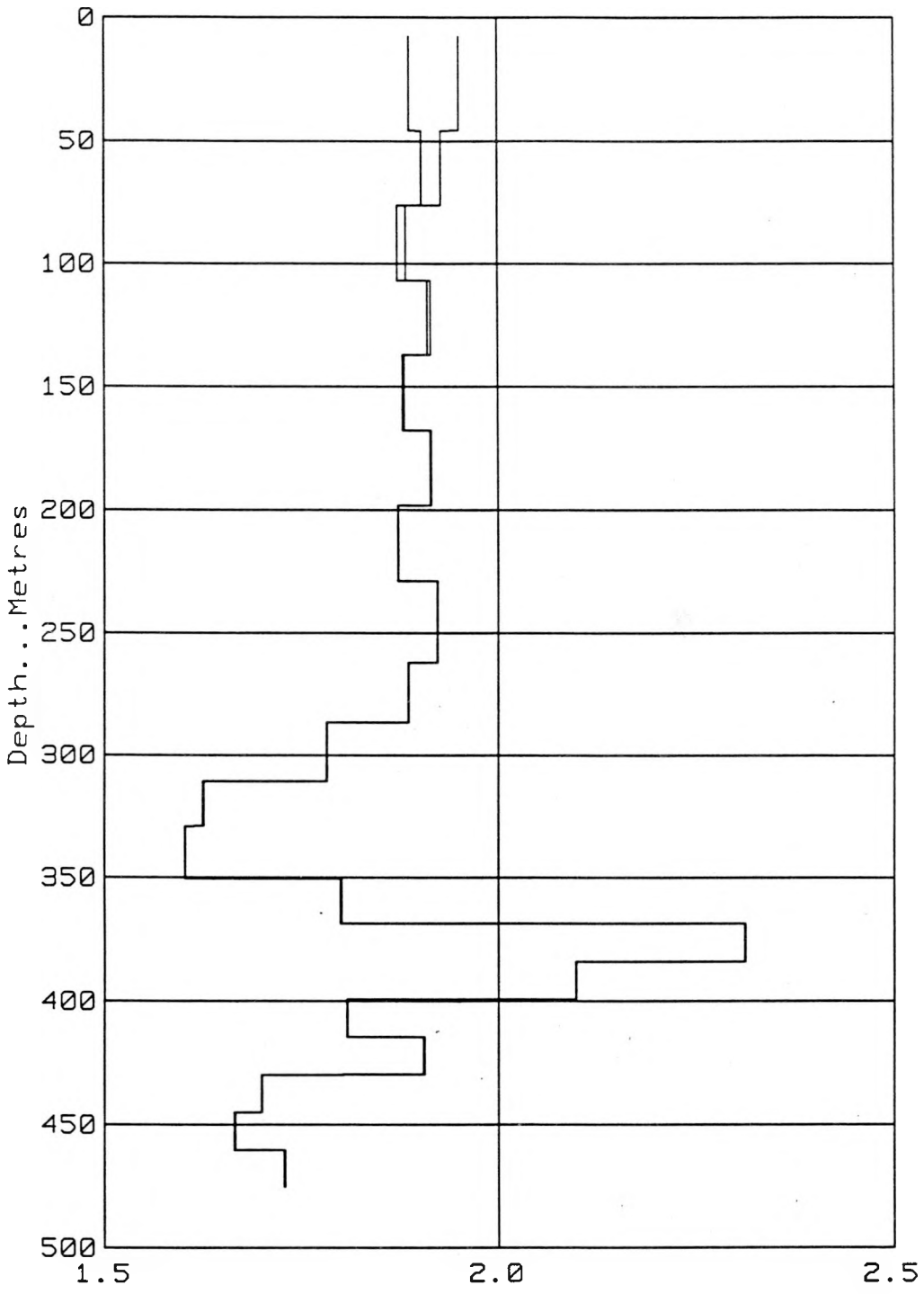


Figure 9 Gravimetric density vs depth at hole U2gh. The curve with lower density was calculated using the standard method of terrain correction, the curve with higher density was calculated using a terrain correction with the datum elevation set equal to the average elevation of the nearby terrain.

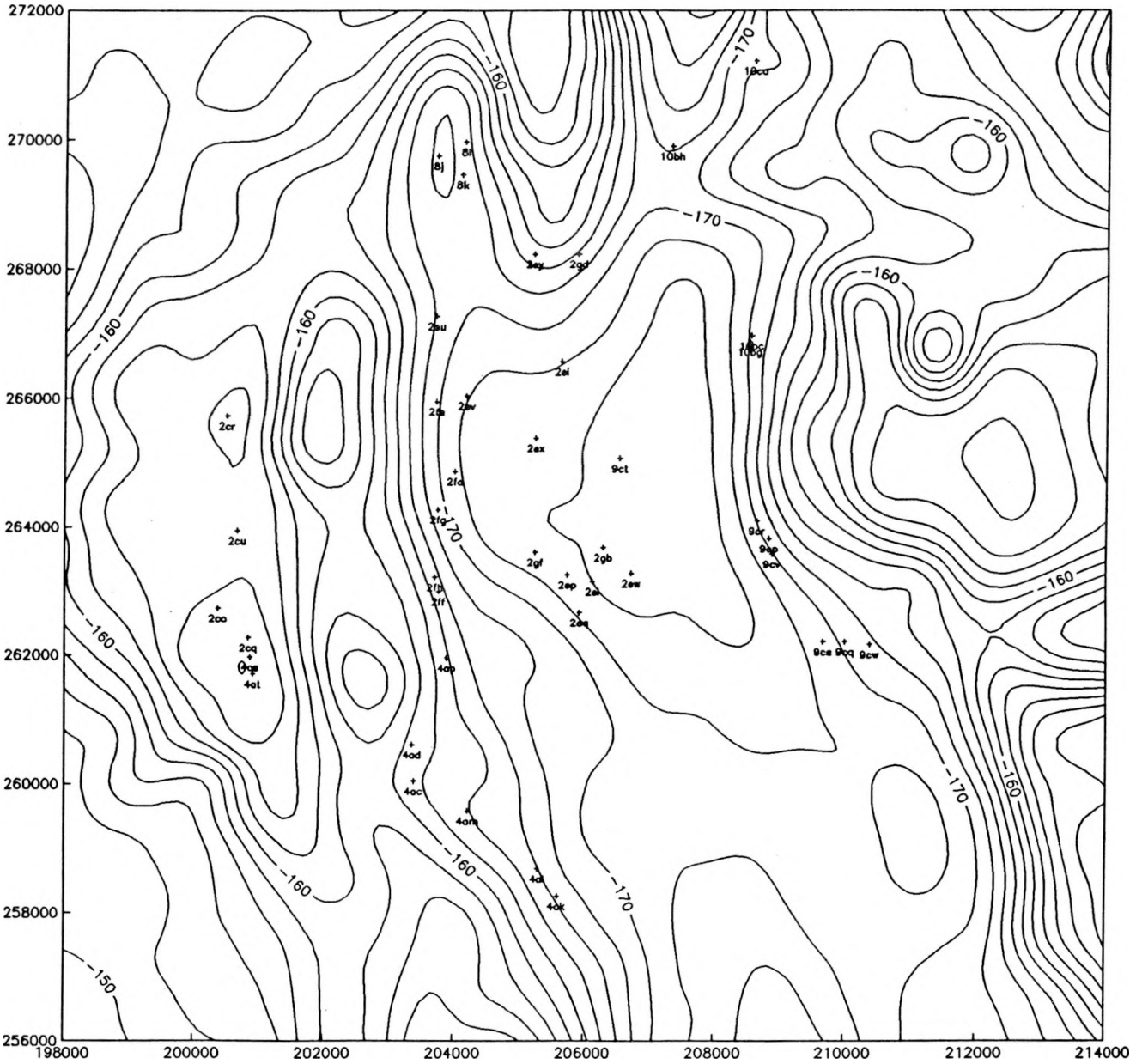


Figure 10 Map of Bouguer-corrected surface gravity in northern Yucca Flat, with the names of the holes used in this study superposed.

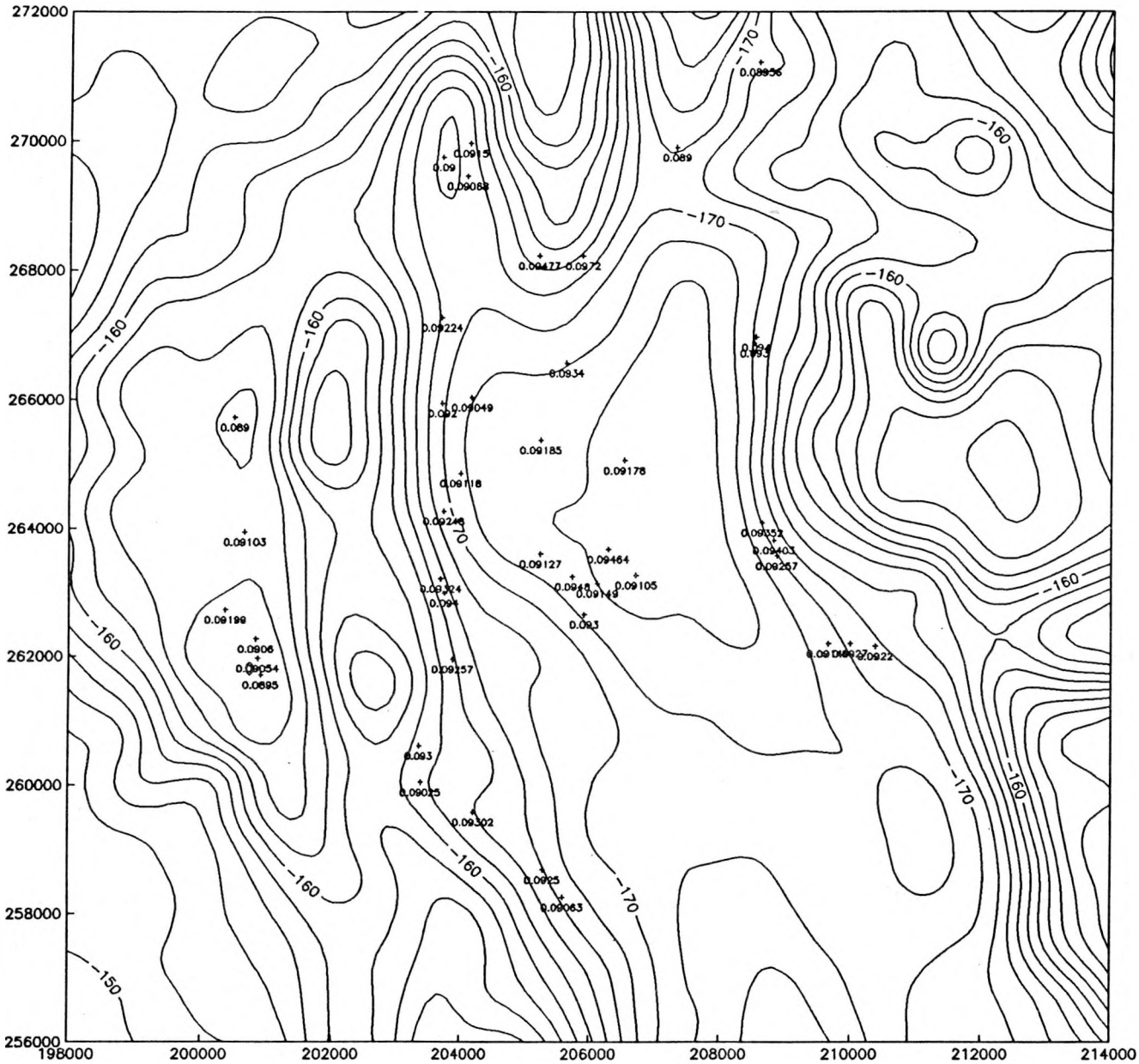


Figure 11 Map of Bouguer-corrected surface gravity in northern Yucca Flat, with the measured free air gradient superposed.

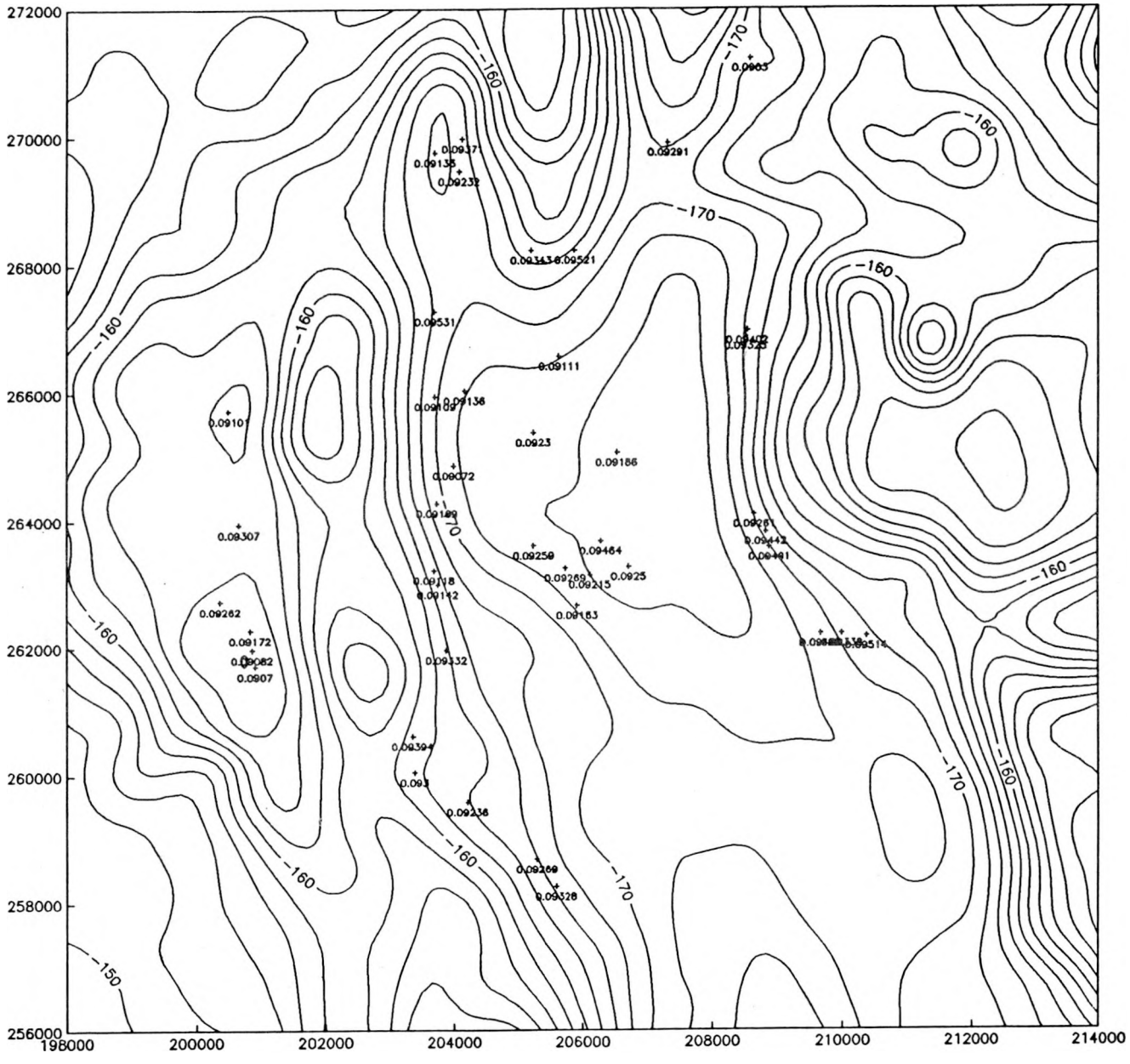


Figure 12 Map of Bouguer-corrected surface gravity in northern Yucca Flat, with the free air gradient calculated using Beyer's method superposed.

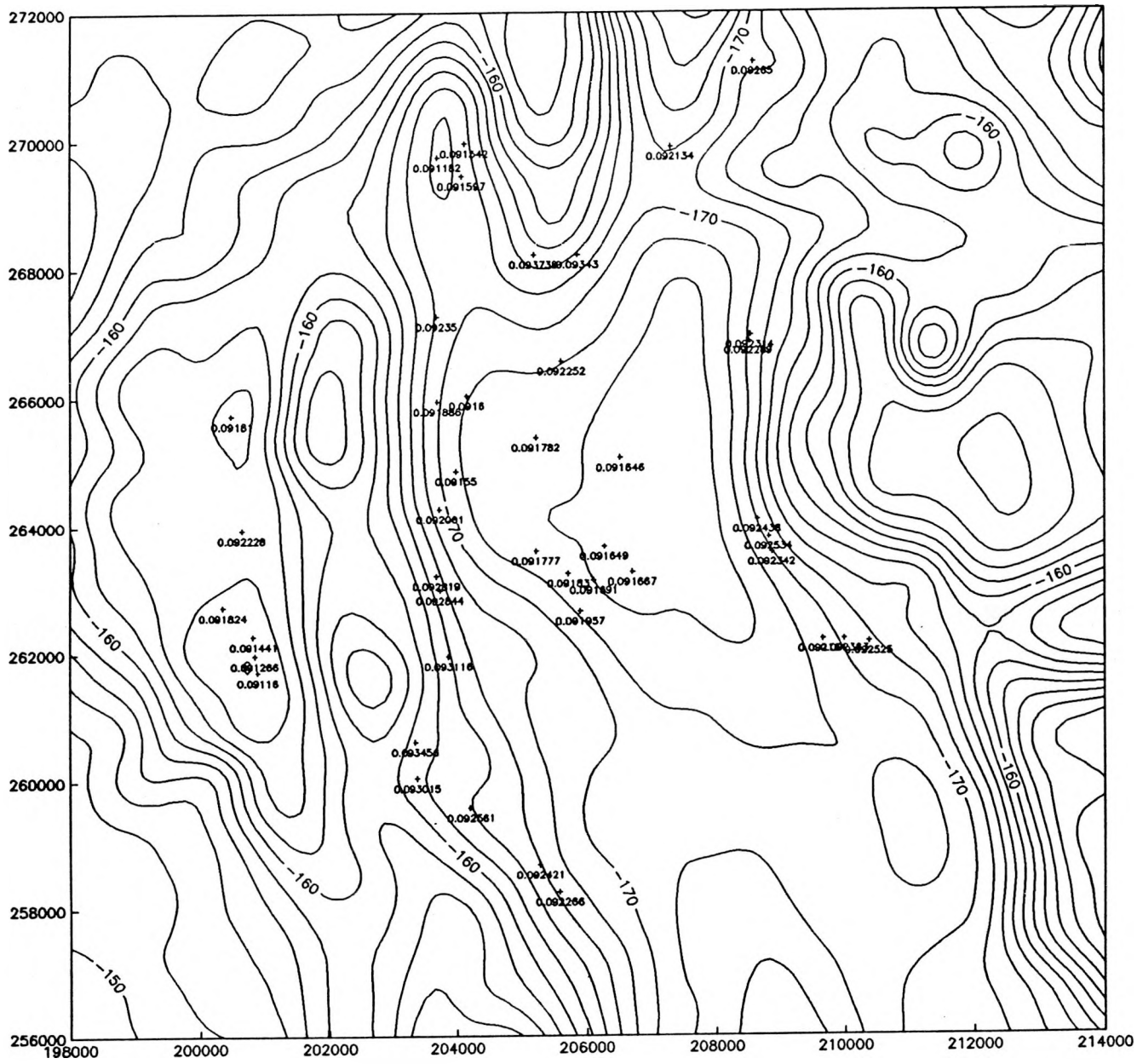


Figure 13 Map of Bouguer-corrected surface gravity in northern Yucca Flat, with the free air gradient calculated by Cogbill, corrected to the surface superposed.

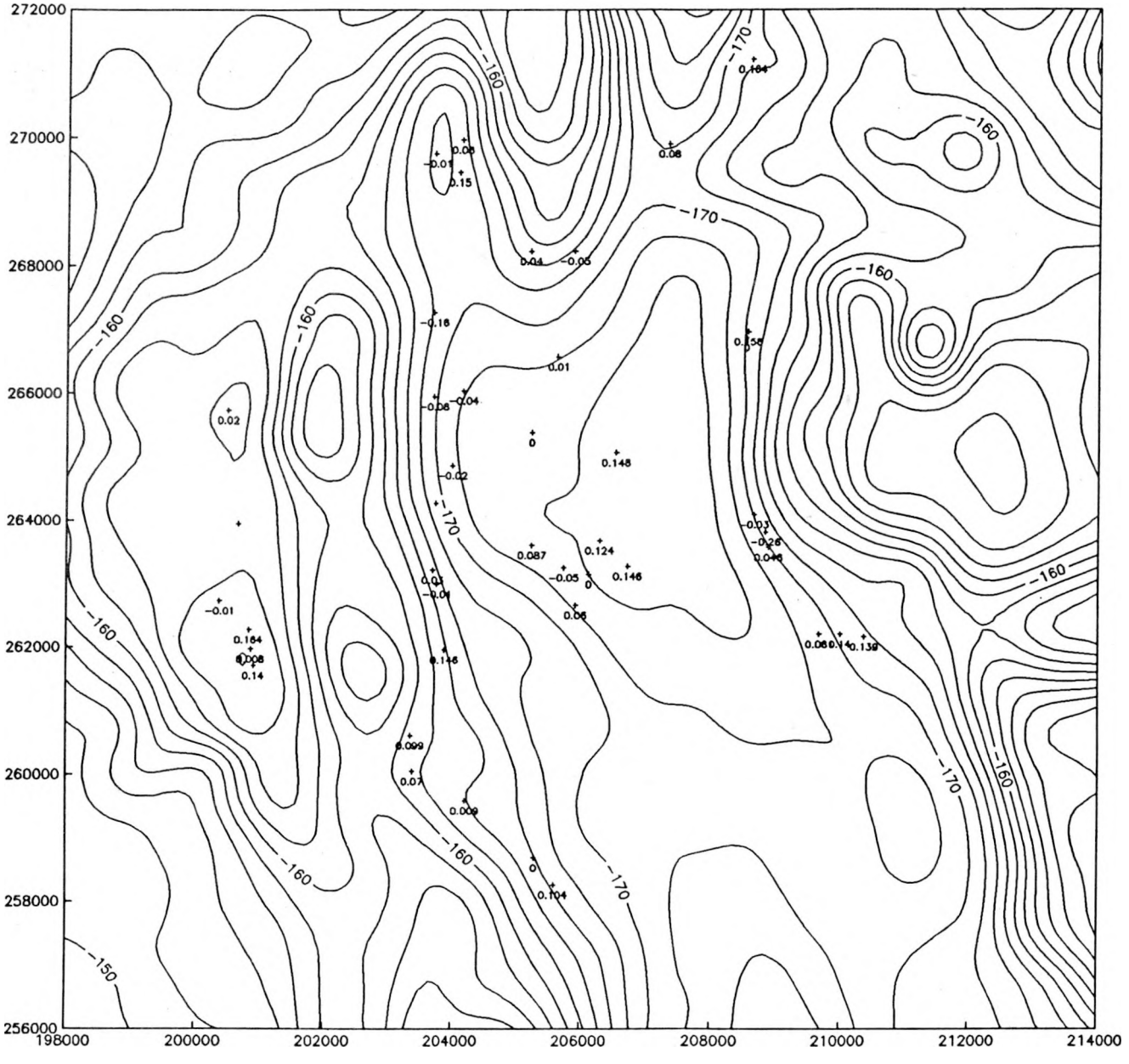


Figure 14 Map of Bouguer-corrected surface gravity in northern Yucca Flat, with the difference between log density and gravimetric density calculated using the measured free air gradient in the depth range of 100 - 150 m superposed.

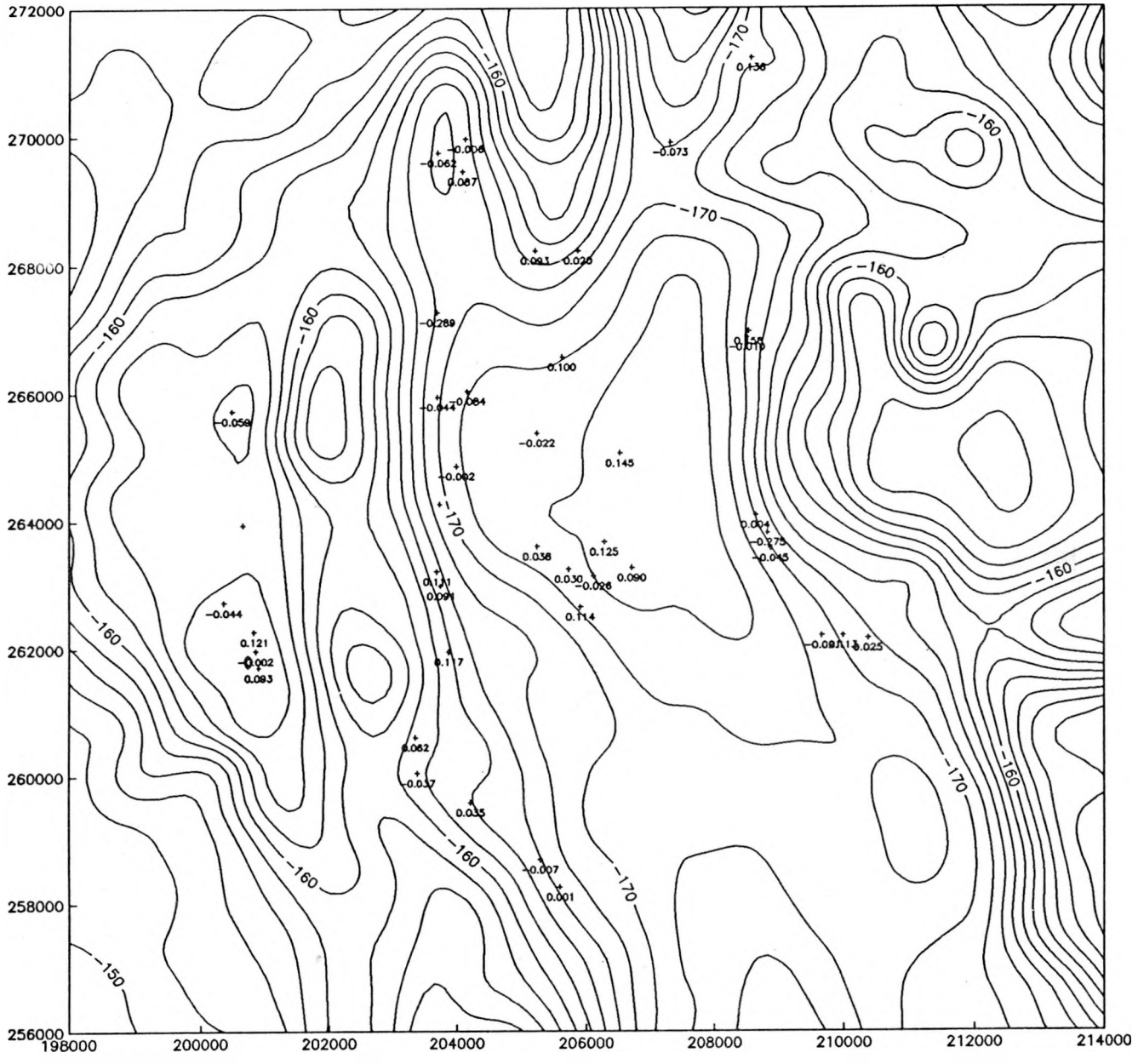


Figure 15 Map of Bouguer-corrected surface gravity in northern Yucca Flat, with the difference between log density and gravimetric density calculated using the free air gradient calculated using Beyer's method superposed.

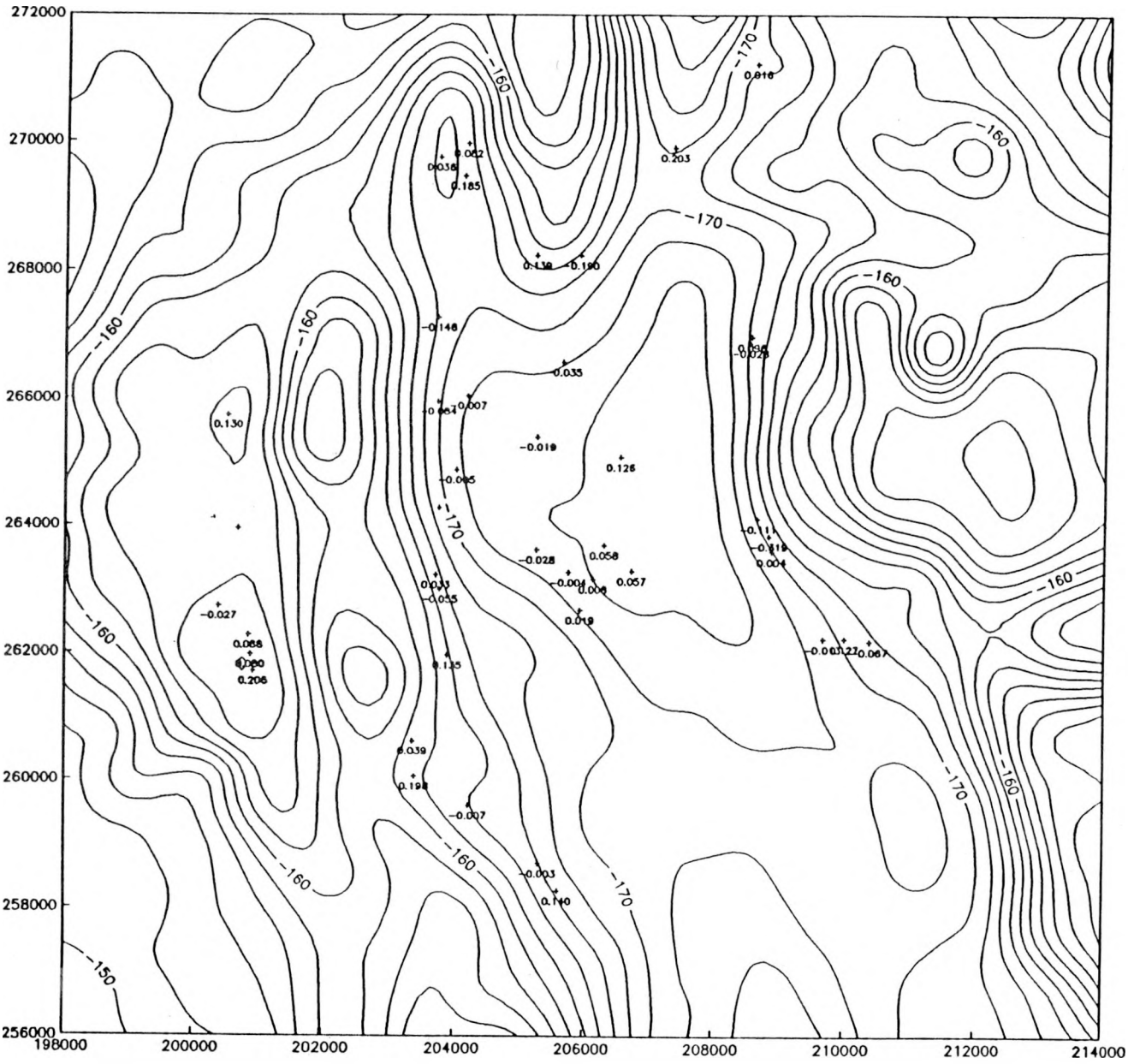


Figure 16 Map of Bouguer-corrected surface gravity in northern Yucca Flat, with the difference between log density and gravimetric density calculated using the free air gradient calculated by Cogbill, corrected to the surface, superposed.

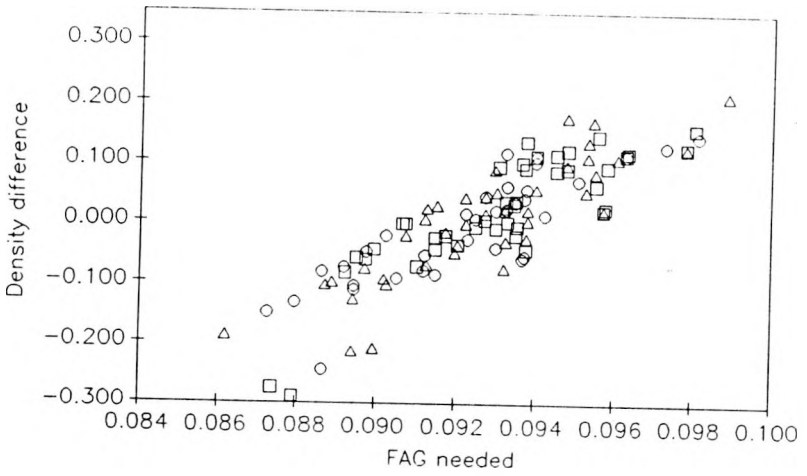


Figure 17 Log density minus gravimetric density calculated using free air gradient calculated by Beyer's method vs the value of the free air gradient needed to reduce the density difference to zero. Circles represent depth range of 50 - 100 m, squares represent depth range of 100 - 150 m, and triangles represent depth range of 150 - 200 m.

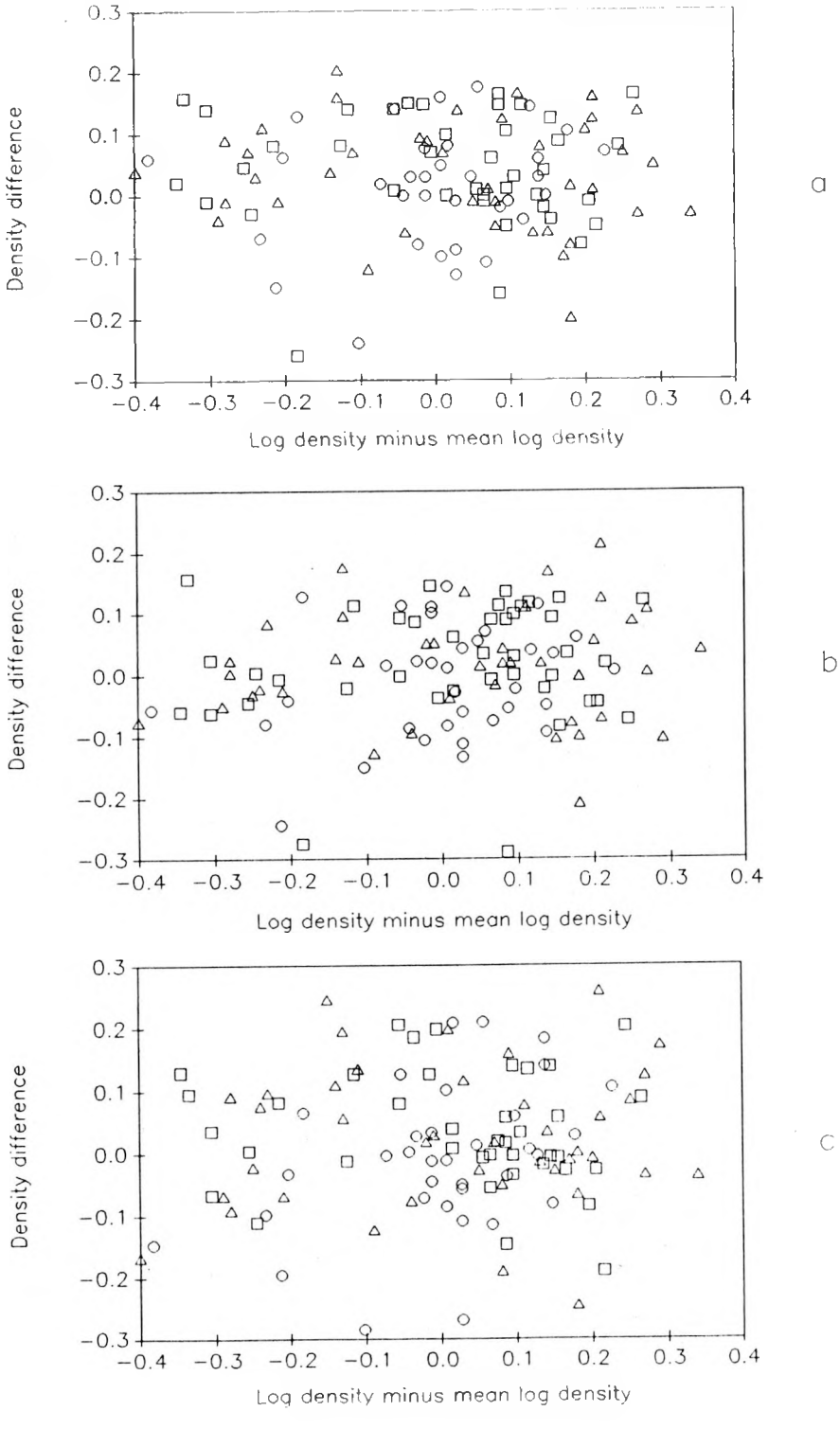


Figure 18 Log density minus gravimetric density calculated using a) the measured free air gradient, b) the free air gradient calculated using Beyer's method and c) the free air gradient calculated by Cogbill corrected to the surface vs the difference between the log density and the mean log density. Circles represent depth range of 50 - 100 m, squares represent depth range of 100 - 150 m, and triangles represent depth range of 150 - 200 m.

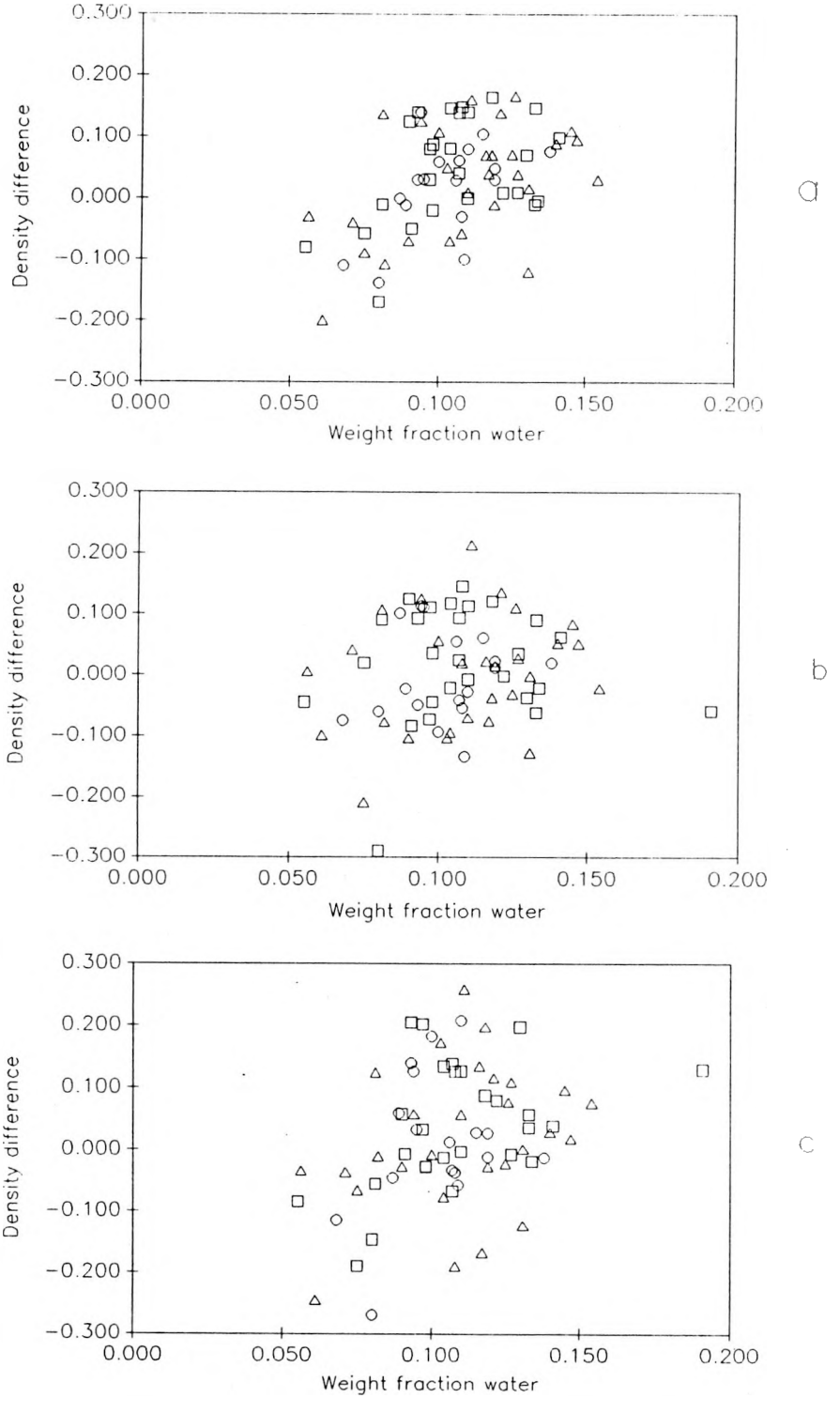


Figure 19 Log density minus gravimetric density calculated using a) the measured free air gradient, b) the free air gradient calculated using Beyer's method and c) the free air gradient calculated by Cogbill corrected to the surface vs the mean water content measured at each hole. Circles represent depth range of 50 - 100 m, squares represent depth range of 100 - 150 m, and triangles represent depth range of 150 - 200 m.

DISTORTION OF GEOPHYSICAL LOGS NEAR BED BOUNDARIES AND IN COMPLEX LITHOLOGIES

John G. Conaway
Los Alamos National Laboratory

ABSTRACT

A properly calibrated geophysical logging sonde or tool can give accurate formation physical property estimates in borehole regions where those properties are uniform or slowly varying. However, in general, the logs will be distorted in the vicinity of bed boundaries or in complex lithologies. Thin zones in particular give rise to logs which in some cases can be very inaccurate, even to the extent of indicating a decrease in some physical property when an increase was actually the case. This paper presents a discussion of the theoretical responses of several NTS logging tools under such conditions.

I. INTRODUCTION

When raw data from a geophysical logging sonde or tool are processed to obtain formation physical property estimates, the assumption is often made, at least implicitly, that the tool is moving through a uniform homogeneous formation. Given a properly calibrated logging tool, accurate physical property estimates can often be made in uniform formations by applying correction factors for non-standard borehole conditions such as mudcake, fluid invasion into the borehole wall, or a borehole diameter different from the diameter for which the tool is calibrated. The presence of bed boundaries or complex lithology where formation properties vary over small depth ranges, however, makes it vastly more difficult to obtain an accurate physical property estimate at any precise depth. Fortunately, accuracy on a depth scale smaller than a few meters is rarely needed in containment work, and some of these errors will average out (more or less) over such distances. Nonetheless, in some applications detailed information may be desired from the logs, and the character of the logs, even though completely repeatable, may well be inaccurate, perhaps even extremely misleading. Those who use the logs or data derived from them can benefit from an understanding of the distorting processes and how they might affect the logs under a variety of conditions

II. SOME THEORETICAL TOOL RESPONSES

Gamma Ray and Spectral Gamma Ray

Rock is a translucent substance as far as gamma rays are concerned. Gamma rays from naturally occurring radioelements will typically travel a few centimeters to as much as a meter or so through rock before being absorbed. Thus, the gamma ray tool will begin to detect a radioactive layer some distance away. Also, gamma rays travel a greater distance along an air or water filled borehole than through rock, so in a large diameter air-filled borehole a radioactive zone will be detected a meter or more before the tool reaches it and after it has passed it.

Typically, gamma-ray and spectral gamma-ray tools have a single detector. The response of an ideal gamma ray tool with a point detector (i.e., occupies no volume) moving through the rock (no borehole effects) past an infinitesimally thin bed of radioactive material would look something like the solid curve in Figure 1. A typical gamma-ray tool with a 15 cm long detector running in a liquid filled borehole of 25 cm (10 in) diameter

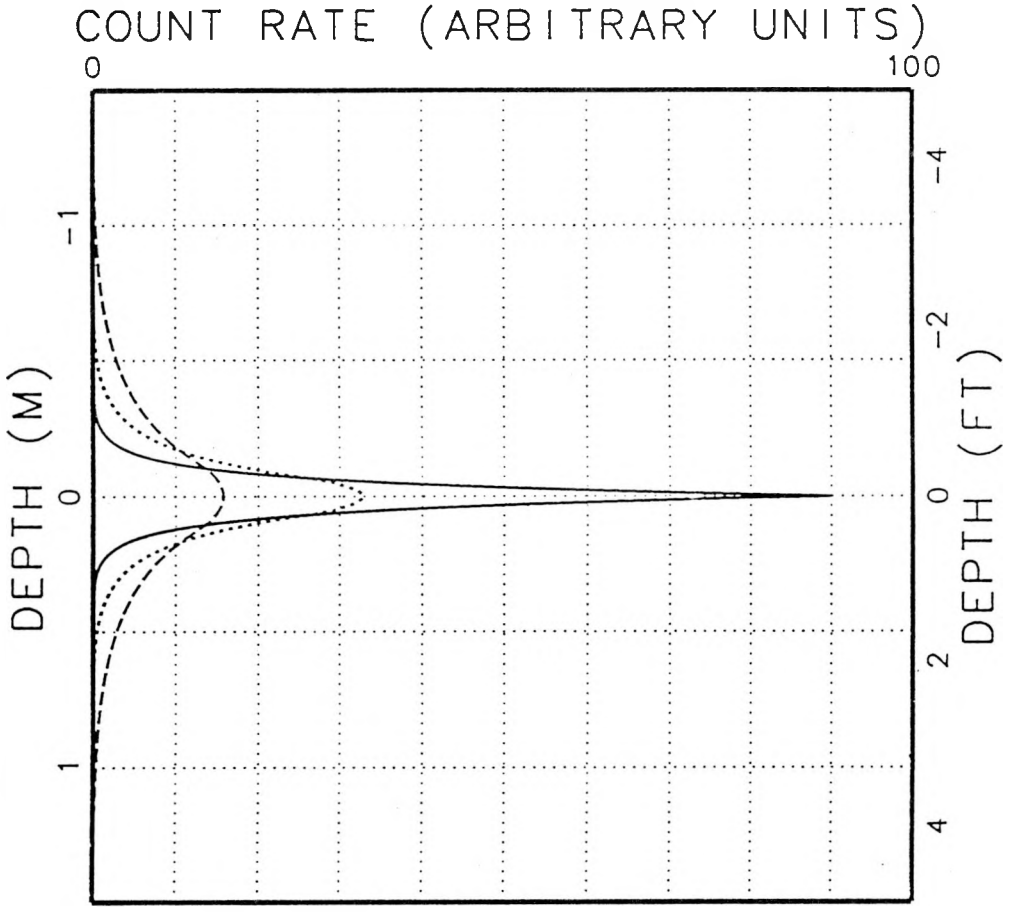


Figure 1 - Several thin-bed response functions for gamma-ray and spectral gamma-ray tools. The solid line represents the gamma radiation field in the rock from a thin planar zone of radioactive material. This is the log we would record if we could measure the radiation with a detector of infinitesimal volume along a borehole of zero diameter. The dotted line represents the sort of response function one would expect in a liquid filled borehole with a 25 cm diameter. The dashed line represents the sort of response function which would be observed in a 2.4 m diameter air-filled borehole.

would yield a curve like the dotted one. A typical spectral gamma-ray tool with a 25 cm long detector running in a 2.4 m (8 ft) air-filled emplacement borehole would produce a response such as the dashed curve. Increasing borehole diameter or detector length tends to broaden the response curve and reduce its amplitude. Experiments aimed at improving the thin-bed resolution of the gamma-ray log in air-filled emplacement holes were performed several years ago (Conaway et al, 1987). Neither collimation nor digital response-enhancement filtering led to any significant improvement in the log.

Even in the case of a gamma ray tool which has been properly calibrated, the height of a typical anomaly on the log is not proportional to the concentration of radioactive material in the rock (grade G, according to uranium industry convention). As shown in Figure 2, it is the area A under the anomaly which is linearly related to the grade by the relationship:

$$G = K A / T,$$

where T is the thickness of the uniform gamma-emitting rock layer and K is the calibration constant for the logging tool. This relationship has certain implicit assumptions discussed elsewhere (Scott et al, 1961; Czubek, 1971; Conaway et al, 1980; Conaway, 1980).

The gamma ray tool response to varying radioactivity in the formation is typically fairly linear. For a linear system, the response of the tool to a thick zone is equal to the sum of the responses that the tool would exhibit to the thinner zones which comprise the thick zone (Figure 3). Only in the case of a thick uniform radioactive zone (generally around a meter or so) does the height of the anomaly become proportional to grade (compare Figures 2 and 3).

Figure 4a shows another, more complicated radioactive zone and the individual anomalies which would result from the constituent thin zones. Figure 4b shows the total anomaly as it would be seen on an ideal gamma ray log, obtained by adding the thin zone response curves at each depth point. Figure 4c compares the observed gamma-ray anomaly with the log as we would prefer to see it, proportional to radioelement content. Figure 4d shows another complicated zone and the resulting anomaly. These examples illustrate that the shape of the anomaly can be misleading in terms of the true distribution of radioactive material. Similarly, sometimes the full-width half-maximum of the anomaly is cited as being equal to the thickness of the anomalous zone. It is seen in Figures 2-4 that this rule of thumb is only true in the case of a thick uniform radioactive zone. As with all such rules of thumb, this one should be used with care and an understanding of its limitations.

Gamma-Gamma Density

Like most borehole-compensated density tools, the DBS (Density Borehole Special) gamma-gamma density tool used at the NTS contains a high-intensity gamma ray source and two gamma ray detectors (Figure 5). Gamma rays from the source scatter through the formation, and a very small percentage of these reach the detectors and are counted. The recorded far-detector count rate is related to the electron density of the formation, but is also influenced by other factors including mudcake, fluid invasion, and gap between the tool and the borehole wall. The near-detector countrate is more highly influenced by these perturbing factors, and hence may be used for correcting the density estimates based on data from the long-spaced detector. Although this is standard procedure in petroleum logging, we currently do not do this on a routine basis, although such a procedure is under consideration (Fenster, 1987). The response function of the gamma-gamma tool will be illustrated here based on information in the literature (Flaum et al, 1989; Mathis and Gearhart, 1989).

Figure 6 shows the normalized responses of the near and far detectors of a commercial gamma-gamma density tool to a 15 cm (6 in) bed of material having higher density than the surrounding medium (adapted from Mathis and Gearhart, 1989). The two detectors, reasonably enough, have different depth resolution properties. This can cause problems when the short-spaced detector count rate is used to compute a borehole correction for the long-spaced detector count rate. This is illustrated in Figure 7, where the two curves were corrected with two different depth alignments of the long- and short-spaced detector data. Neither of these curves is a

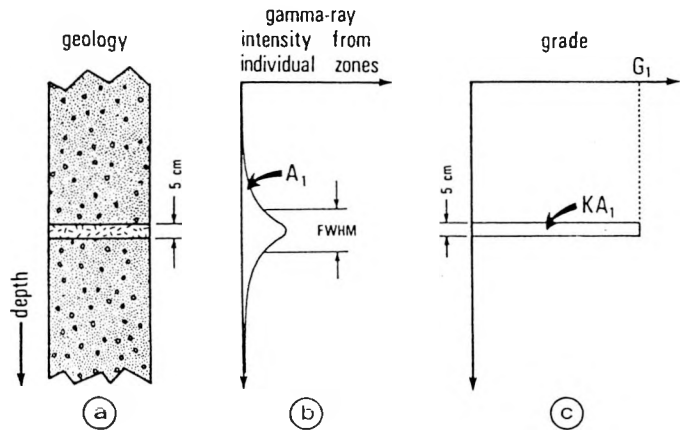


Figure 2 - (a) Geologic column showing a 5-cm thick zone of gamma-emitting rock embedded in barren rock. (b) Simulated noise-free gamma-ray log past the zone shown in (a). Note that the full-width half-maximum (denoted FWHM) of this anomaly is *not* equal to the thickness of the radioactive zone, nor is the height of the anomaly proportional to radioelement concentration. (c) Plot of the actual concentration of radioactive material (grade) vs. depth (i.e., distribution of radioactive material along the borehole).

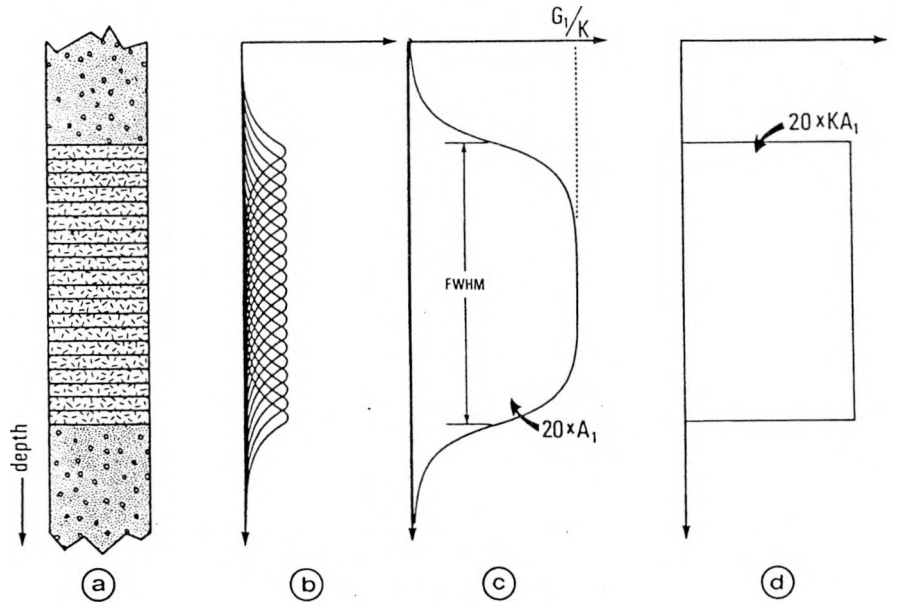


Figure 3 - (a) Geologic column showing twenty 5-cm thick zones of gamma-emitting rock (each identical to the zone in Figure 2a) embedded in barren rock. Each zone individually would cause one of the twenty gamma-ray log anomalies shown in (b). These twenty anomalies are summed to give the total gamma-ray log past the entire 1-m radioactive zone (c). Note that the full-width half-maximum of this anomaly *is* equal to the thickness of the radioactive zone, and the height of the anomaly in the center is proportional to the radioelement concentration. (c) Plot of actual concentration of radioactive material (grade) vs. depth.

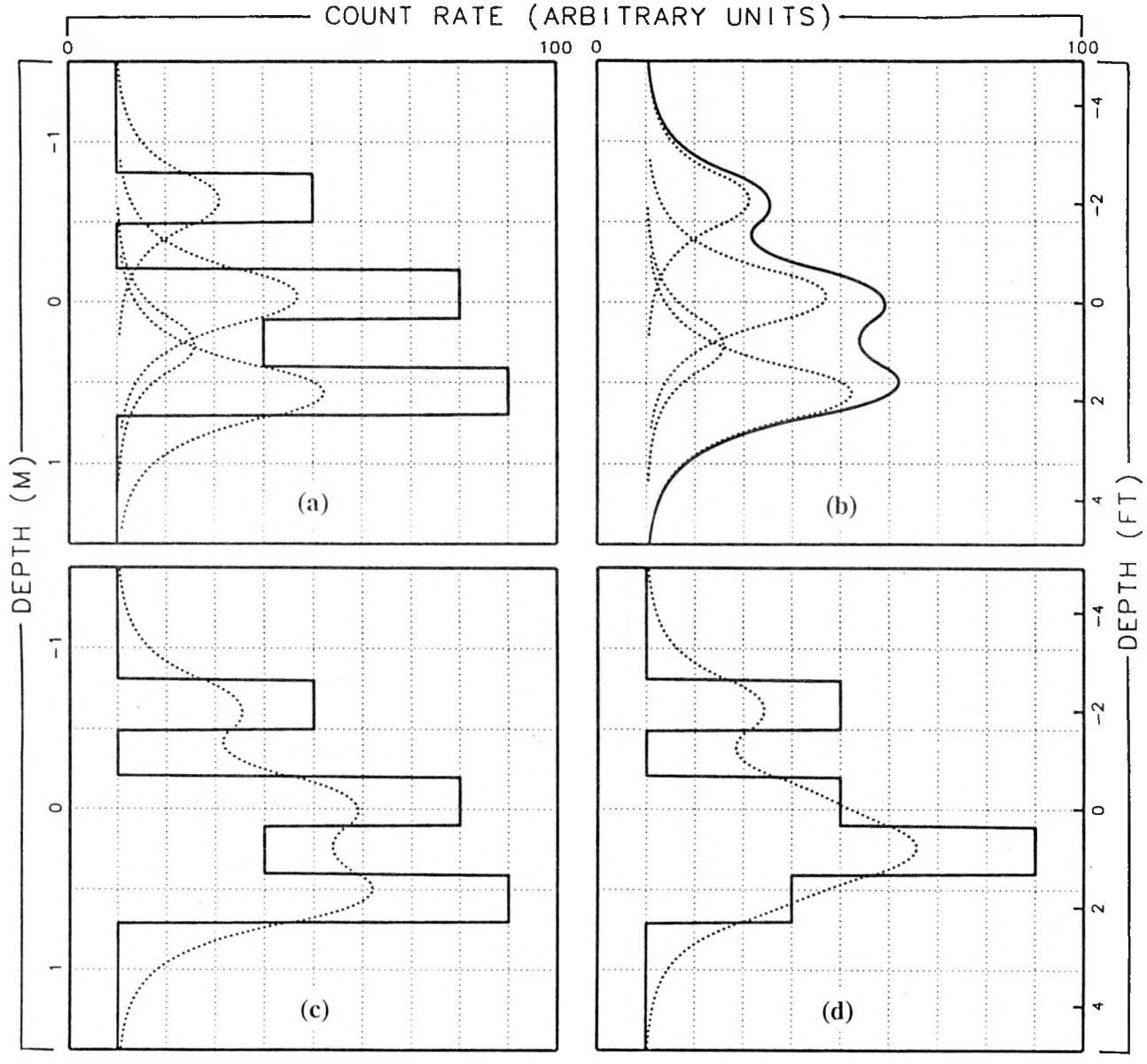


Figure 4 - (a) Complex radioactive zone made up of several 30-cm (1 ft) thick uniform beds. The solid line shows what we would like the tool response to look like, with the countrate at any given depth proportional to the concentration of radioactive material in the formation. The dashed curves show the response of a gamma ray tool to each zone individually. The precise shape of the thin zone response curve depends on many factors, including rock density, borehole diameter and fluid, detector length, and so forth. The actual anomaly which would be recorded is the sum of the individual curves, and is shown by the solid line in (b). This anomaly only bears a vague resemblance to the actual distribution of radioactive material (c). Another complex radioactive zone is shown in (d) for comparison.

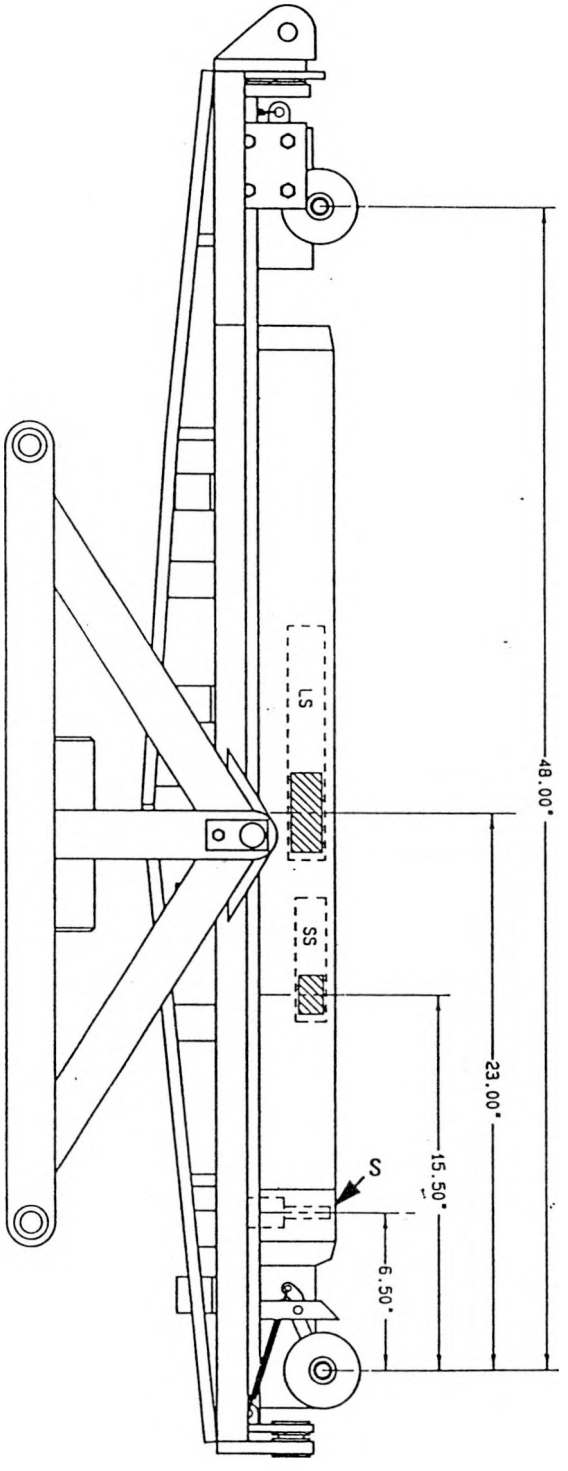


Figure 5 - Sensing head of the DBS density tool which is pressed against the borehole wall when logging. It contains a gamma-ray source (marked S), short- and long-spaced detectors (SS and LS, respectively), and two gap measuring wheels at either end (Courtesy, Fenix & Scisson of Nevada).

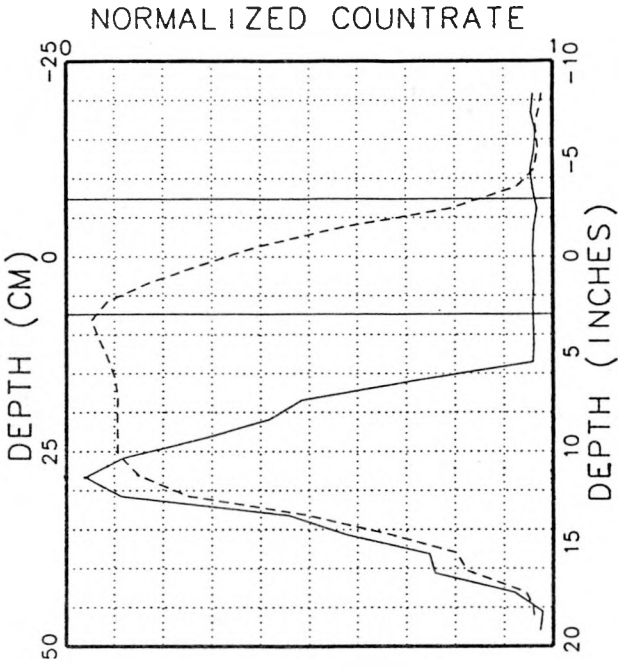


Figure 6 - Normalized responses of the two gamma-ray detectors in a commercial compensated density tool to a 15 cm (6 in) bed having density higher than the surrounding medium. The bed is delineated by the pair of solid horizontal lines centered at +/- 7.5 cm depth. The normalized countrate of the long-spaced detector is shown by the dashed line and that of the short-spaced detector is shown by the solid line (adapted from Mathis and Gearhart, 1989).

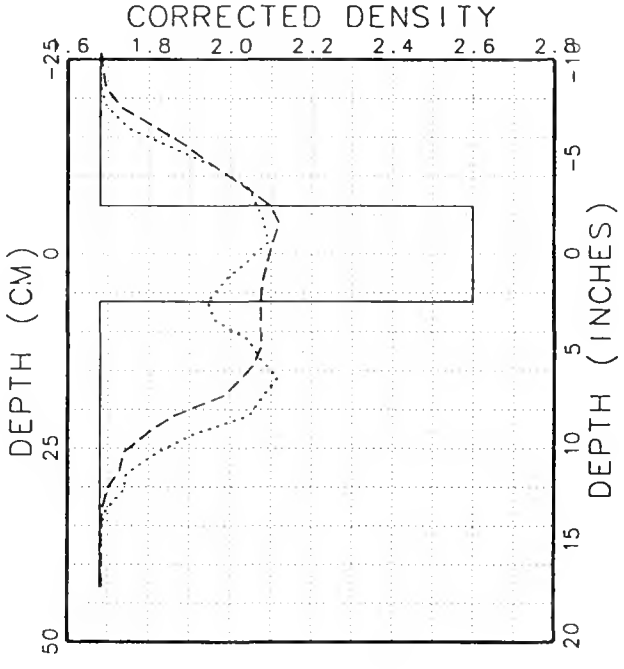


Figure 7 - Computed density (Mg/m^3) based on the long-spaced detector countrate curve shown in Figure 6, corrected for borehole conditions using the short-spaced detector curve from that same figure. The two different dashed curves shown in this figure are for two different depth alignments of the long- and short-spaced detector data, while the solid curve shows the true density profile (adapted from Mathis and Gearhart, 1989).

good approximation of the ideal density log, which should indicate a zone 15 cm thick with a density of about 2.6 Mg/m^3. Techniques have been presented recently which, when applied to the raw gamma-gamma data, can improve the thin bed accuracy of the tool (Flaum et al, 1989; Mathis and Gearhart, 1989). We are currently studying whether similar techniques might usefully be applied to the density data from the NTS.

Resistivity - Normal Array

The normal resistivity electrode array configuration is shown in Figure 8, with a current electrode (A) and a potential-measuring electrode (M) downhole and a second current electrode and a second potential-measuring electrode (B and N, respectively) located a relatively large distance away from each other and from the downhole pair. Generally, these remote electrodes are located either on the surface, as shown in this sketch, or higher up the cable. The spacing between the A and M electrodes defines the array, the two most common being *16-inch normal* (0.4 m) and *64-inch normal* (1.6 m).

The response of the ideal normal array to a resistive layer of rock R_2 embedded in rock of lower resistivity R_1 is shown in Figure 9 (the figures in this section are based on Hilchie, 1979, who adapted them from Chombart, 1949). Note that the depth axes are marked off in A-M units; for instance, for the 16-inch (0.4 m) normal the space between two adjacent tick marks is 16 inches. The three depth axes in this figure have different scales. In Figure 9a, the resistive zone is six A-M units thick, i.e., 96" (2.4 m) for the 16-inch (0.4 m) normal. The actual resistivity profile is shown by the curve composed of long dashes. The ideal tool response in the absence of any borehole effect is shown by the curve composed of short dashes. The solid curve shows the tool response in a borehole of diameter and fluid conductivity typical for the petroleum industry. As the borehole diameter or fluid conductivity increases, this curve will become smoother and more attenuated. In Figure 9b, the resistive zone is two A-M units thick, i.e., 32" (0.8 m) for the 16-inch (0.4 m) normal. The curve designations are the same as in Figure 9a. In this thinner zone, the recorded anomaly never reaches the true formation resistivity even in the absence of any borehole effect. In Figure 9c, the resistive zone is considerably smaller than the electrode spacing, about 5" (13 cm) for the 16-inch (0.4 m) normal. The tool response in this thin zone bears no resemblance to the true resistivity profile whatsoever, appearing to indicate a conductive bed flanked by two thin resistive beds. Such strange behavior makes it perilous for the inexperienced to read very much significance into the fine structure of a geophysical log.

In the case of a layer of low-resistivity rock embedded in rock of higher resistivity, the response of the ideal normal array is shown in Figure 10. Once again, the depth axes are marked off in A-M units In Figure 10a, the conductive zone is four A-M units thick, i.e., 64" (1.6 m) for the 16-inch (0.4 m) normal. The actual resistivity profile is shown by the thick dashed curve. The ideal tool response in the absence of any borehole effect is shown by the solid curve. The thin dashed curve shows the tool response in a borehole of diameter and fluid conductivity typical for the petroleum industry. As the borehole diameter or fluid conductivity increases, this curve will become smoother and more attenuated. In Figure 10b, the resistive zone is considerably smaller than the electrode spacing, about 5" (13 cm) for the 16-inch (0.4 m) normal. This example is not as bizarre as the case of a thin resistive zone shown earlier (Figure 9c).

Resistivity - Dry Hole Wenner

The Wenner resistivity electrode array consists of four equally-spaced electrodes; the space between two adjacent electrodes is denoted *a*. In the case of the big-hole dry-hole resistivity tool, the electrodes are actually porous wheels kept wet with a salt solution, and *a* is 1.02 m (40 in). The configuration is shown in Figure 11; a fifth electrode wheel used to make a normal measurement is not shown. The tool electronics are also not ideal, and that could cause some differences between the actual and theoretical response of the tool.

Van Nostrand and Cook (1966) produced a large volume of response curves for several resistivity arrays, for surface exploration. Some of the Wenner array response curves presented there are equally useful for our purposes here. These are theoretical curves; in theory we would expect the dry-hole Wenner tool

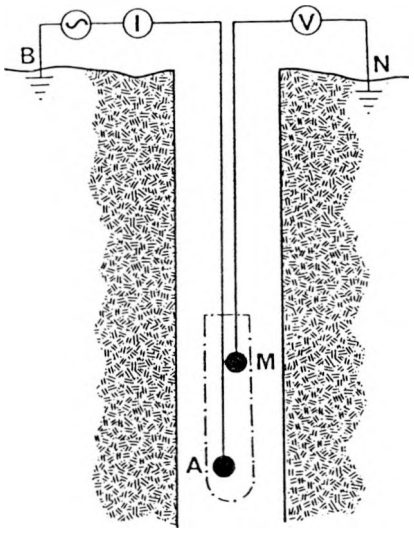


Figure 8 - This sketch illustrates one configuration of the normal electrode array, which consists of two current electrodes, A and B, and two potential-measuring electrodes, M and N. A and M generally consist of metal bands on a non-conducting tool housing (the tool housing is phantomed in on this schematic), while B and N are located on the surface as shown or along the logging cable well above the tool.

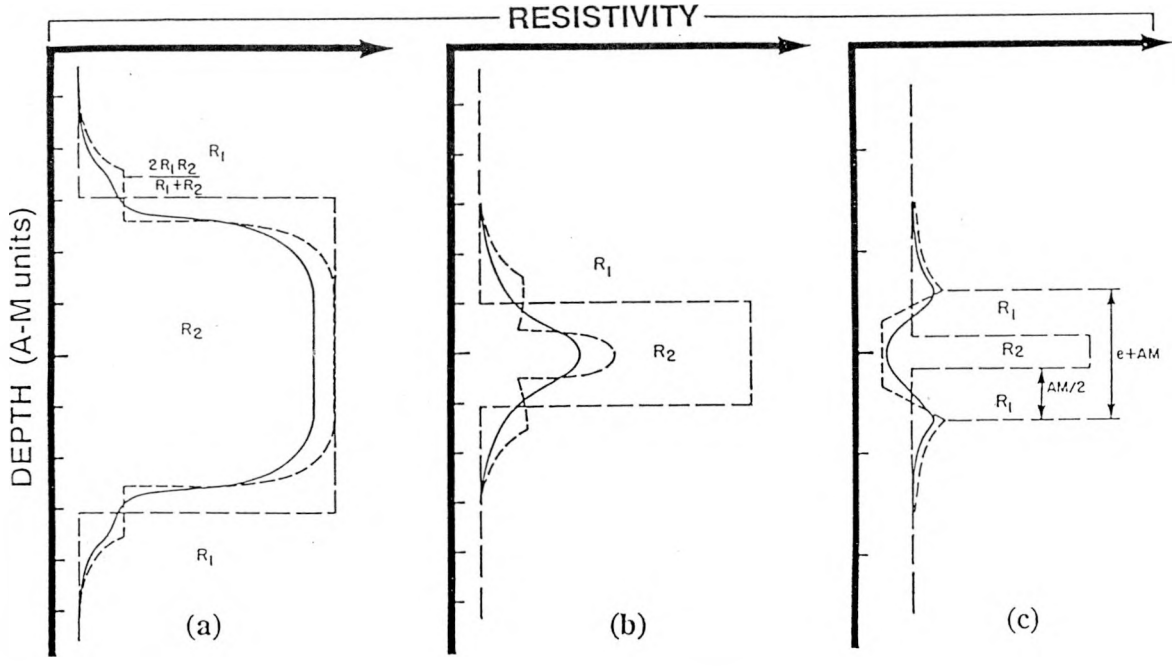


Figure 9 - Three examples of the response of the normal electrode array to resistive beds of various thicknesses (denoted by the letter *e*). The depth axes are marked off in units equal to the A-M electrode spacing. In (a), the resistive zone is six A-M units thick. The actual resistivity profile is shown by the curve composed of long dashes. The ideal tool response in the absence of any borehole effect is shown by the curve composed of short dashes. The solid curve shows the tool response in a borehole of diameter and fluid conductivity typical for the petroleum industry. In (b), the resistive zone is two A-M units thick, while in (c), the resistive zone is considerably smaller than the electrode spacing, about 5" (13 cm) for the 16-inch (0.4 m) normal. (Adapted from Hilchie, 1979; Chombart, 1949).

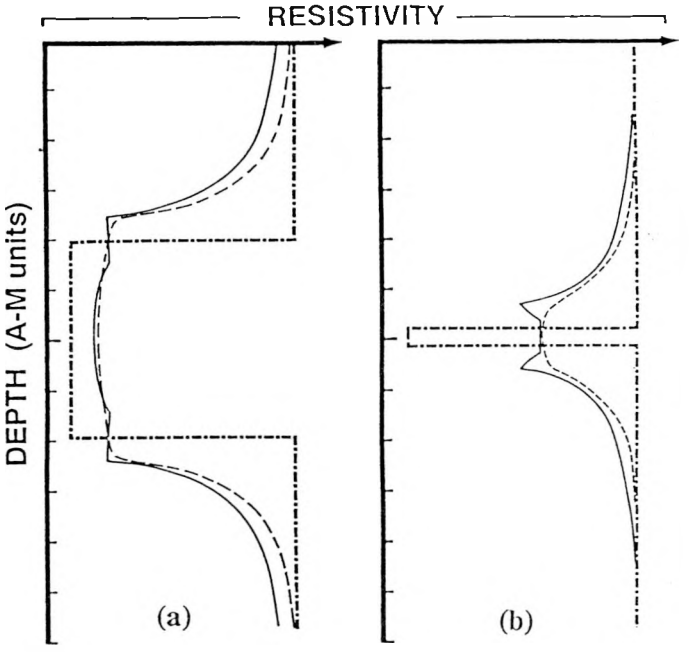


Figure 10 - Two examples of the response of the normal electrode array to conductive beds of various thicknesses. The depth axes are marked off in units equal to the A-M electrode spacing. In (a), the conductive zone is four A-M units thick. The actual resistivity profile is shown by the curve composed of the dash-dot pattern. The ideal tool response in the absence of any borehole effect is shown by the curve composed of short dashes. The solid curve shows the tool response in a borehole of diameter and fluid conductivity typical for the petroleum industry. In (b), the conductive zone is considerably smaller than the electrode spacing, about 5" (13 cm) for the 16-inch (0.4 m) normal. (Adapted from Hilchie, 1979; Chombart, 1949).

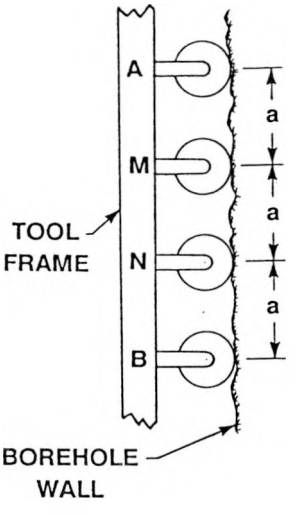


Figure 11 - The Wenner electrode array consists of two current electrodes, A and B, and two potential-measuring electrodes, M and N. The current electrodes can be the outer pair, as shown, or the inner pair. The electrodes in the dry-hole resistivity tool consist of porous wheels which are kept wetted with a salt solution to provide electrical contact with the dry borehole walls.

response to be somewhat smoother (ignoring noise) because the electrodes cover a finite area and are not theoretical points.

Figure 12 shows the step response as the tool moves from a 5 ohm-m layer to a 20 ohm-m layer. The tool does not respond sharply as we would hope, nor does it move smoothly from one resistivity to the other in the manner, say, of the gamma-ray curve. Rather, the readings swing back and forth as each successive electrode wheel crosses the interface between the two beds. This gives the appearance of representing fine-structure in the formation bedding, when what we are actually seeing is an artifact of the tool design.

Figure 13 shows the response of the dry-hole Wenner tool to a thin zone of highly contrasting resistivity. In the case of curve (a), a thin zone of zero resistivity is embedded in 20 ohm-m material, while in curve (b), a thin zone of infinite resistivity is embedded in the same 20 ohm-m material. Again, the actual log is quite misleading because of the swings the log takes as each successive electrode wheel crosses each of the two bed interfaces.

Figure 14 shows the tool response in the vicinity of thicker zones of 80 ohm-m resistivity, again embedded in 20 ohm-m material. Figure 15 shows the tool response in the vicinity of thicker zones of 5 ohm-m resistivity flanked above and below by 20 ohm-m material. It is clear from these figures that determining the true resistivity of any layer less than 5 or 6 meters thick from the dry-hole Wenner resistivity log would be difficult or impossible.

Big Hole Caliper

The big-hole caliper tool run for us by the logging contractor at the NTS has six arms, each 72 cm (28.5 inches) in length. Each arm is attached by a pivot connection to an adjustable rail, the position of which is pre-set before running the log to a few cm less than the borehole bit radius. The geometry is shown in Figure 16.

If we visualize a washout that has horizontal top and bottom (Figure 17b), geometrical considerations dictate that the washout must be on the order of 0.7 m (27 inches) high and 0.6 m (23 inches) deep for the caliper arm to just reach its full extent. Given a washout of those proportions, the recorded log is shown in Figure 17a (solid line) along with the ideal log (dashed line). The path that the arm tip would follow is shown in Figure 17b. This shape occurs because, as the tip moves up the borehole wall and clears the bottom of the washout, the arm snaps out either to its maximum extent or until it touches the washout wall. The upper part of the arm then strikes the top of the washout and holds the tip of the arm away from the borehole wall as the tool moves past the washout (Figure 18).

Figure 19a shows the ideal (dashed) and theoretical actual (solid) log traces for a higher, more shallow washout with horizontal top and bottom (Figure 19b). There is little resemblance between the ideal logs and the simulated recorded logs shown in Figures 17a and 19a. These are perhaps extreme examples, however. Video examination of the walls of emplacement holes shows most washouts to be irregular rather than abrupt, and typical caliper logs recorded in rough holes do not show a great deal of evidence of the effect seen in Figures 17a and 19a, although apparent examples of this behavior can be seen.

III. RESPONSE ENHANCEMENT

The attempt to improve the depth resolution of logging tools is an ongoing effort in the logging community. In earlier years this was confined to the physical design of the tool (collimation of the gamma-gamma density source and detectors, for instance), and analog electronics (computed focusing circuitry for the induction tool).

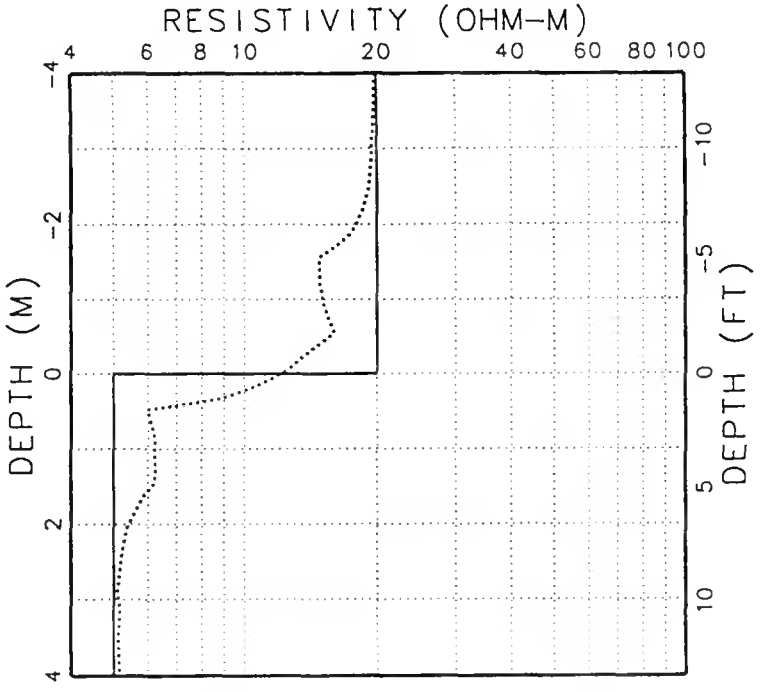


Figure 12 - Theoretical response of the Wenner resistivity array to a step change in resistivity, from 5 ohm-m to 20 ohm-m. The solid line represents the true formation resistivity, while the dotted line shows the ideal output of the Wenner resistivity array with 1 m electrode spacing. (After Van Nostrand and Cook, 1966).

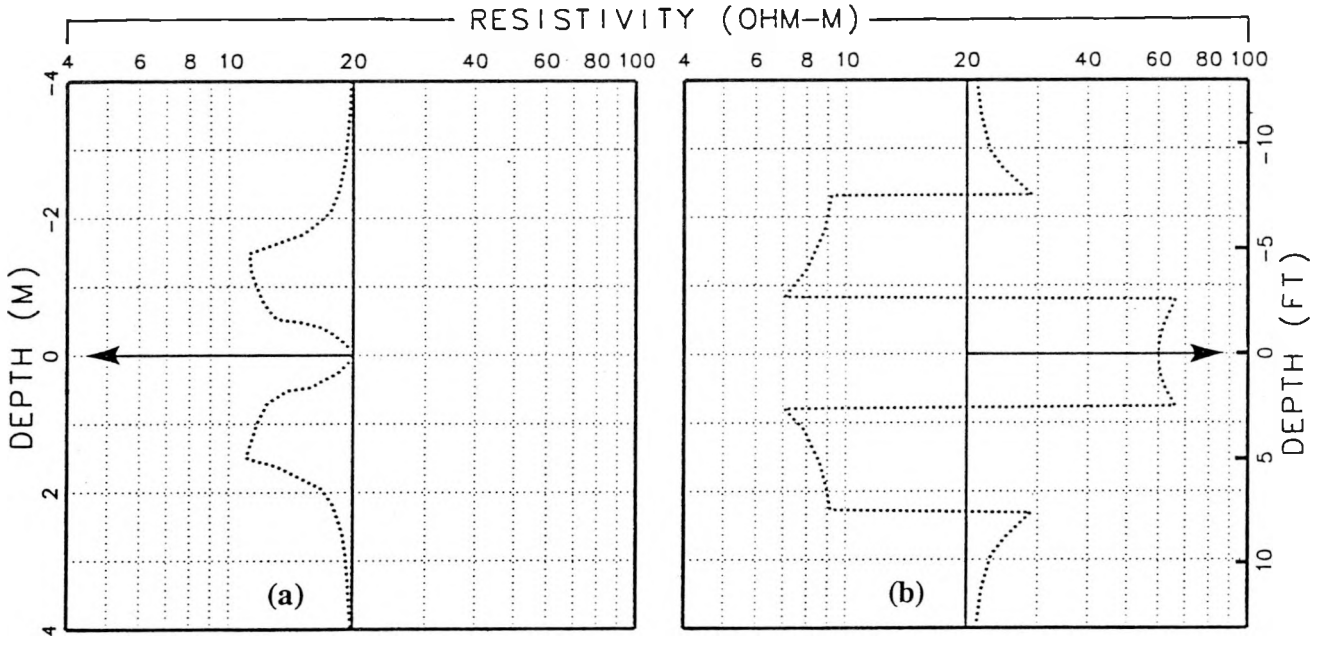


Figure 13 - Theoretical response of the Wenner resistivity array to a thin zone having (a) zero resistivity and (b) infinite resistivity. The solid line represents the true formation resistivity, while the dotted line shows the ideal output of the Wenner resistivity array with 1 m electrode spacing. (After Van Nostrand and Cook, 1966).

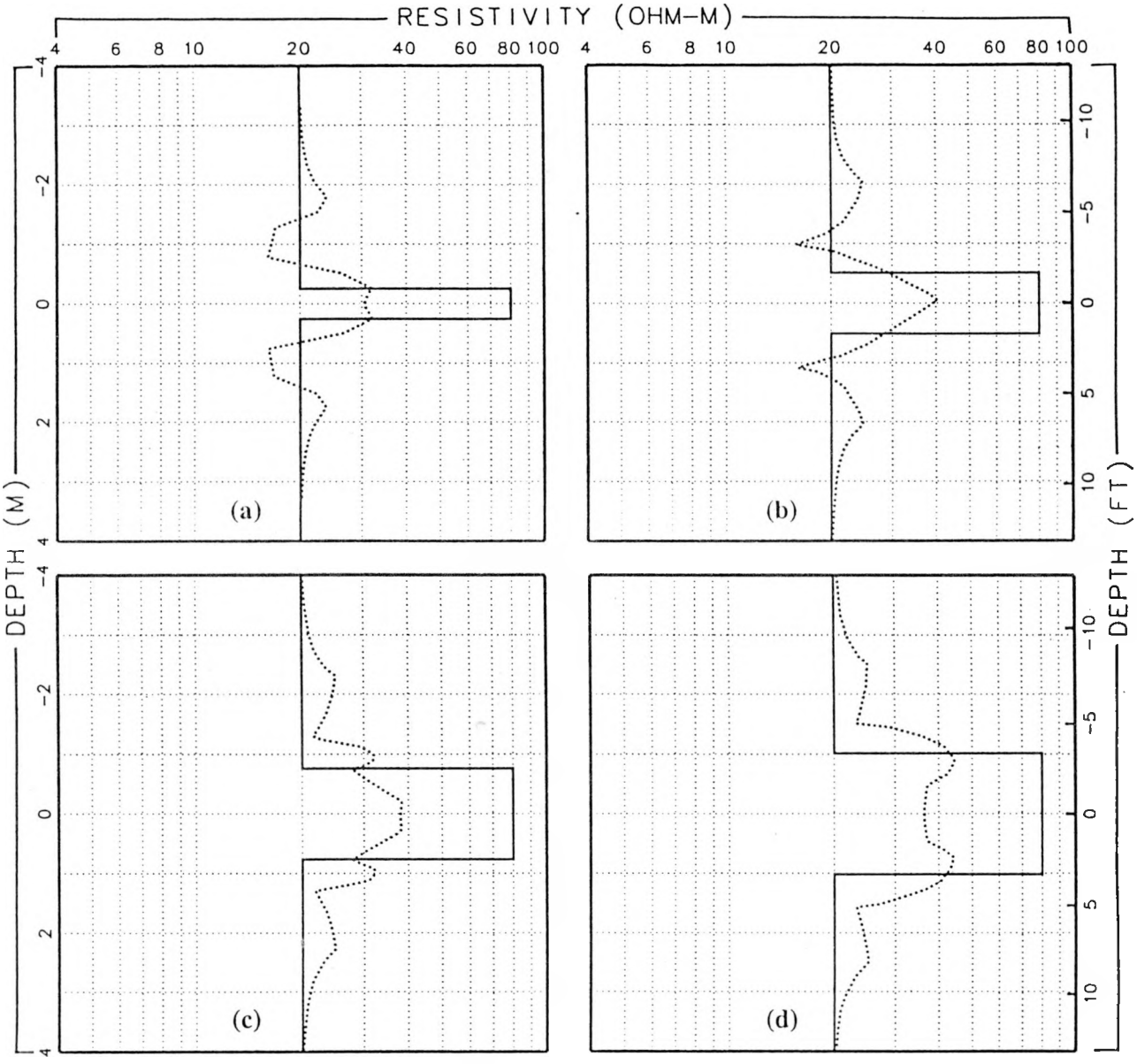


Figure 14 - Theoretical response of the Wenner resistivity array to an 80 ohm-m zone embedded in a 20 ohm-m zone. The resistive zones are of four different thicknesses, which are: (a) 50 cm (20 in); (b) 100 cm (40 in); (c) 150 cm (60 in); (d) 200 cm (80 in). The solid line represents the true formation resistivity, while the dotted line shows the ideal output of the Wenner resistivity array with 1 m electrode spacing. (After Van Nostrand and Cook, 1966).

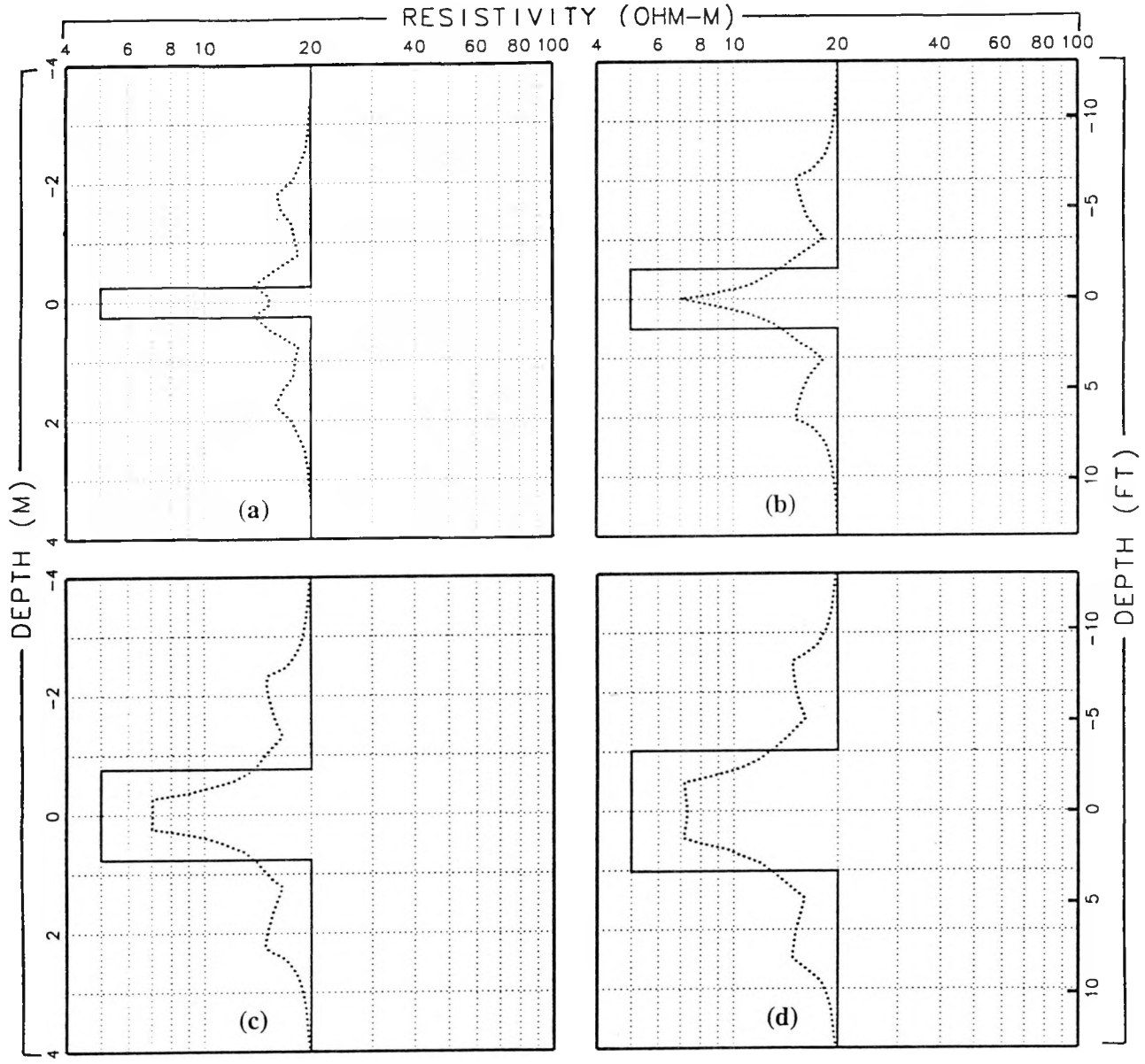


Figure 15 - Theoretical response of the Wenner resistivity array to a 5 ohm-m zone embedded in a 20 ohm-m zone. The conductive zones are of four different thicknesses, which are: (a) 50 cm (20 in); (b) 100 cm (40 in); (c) 150 cm (60 in); (d) 200 cm (80 in). The solid line represents the true formation resistivity, while the dotted line shows the ideal output of the Wenner resistivity array with 1 m electrode spacing. (After Van Nostrand and Cook, 1966).

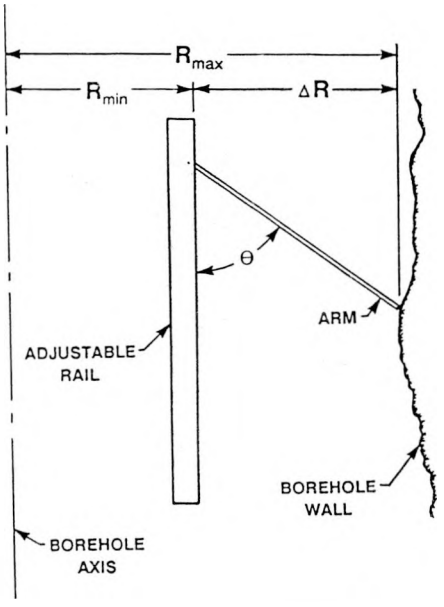


Figure 16 - Sketch of the geometry of one arm of the big-hole caliper at maximum extension. The adjustable rails are preset to a radius R_{min} before the log is run. This the smallest radius which can be measured by a given arm if the tool is centered in the borehole. The largest radius is R_{max}, the full extension of the arm.

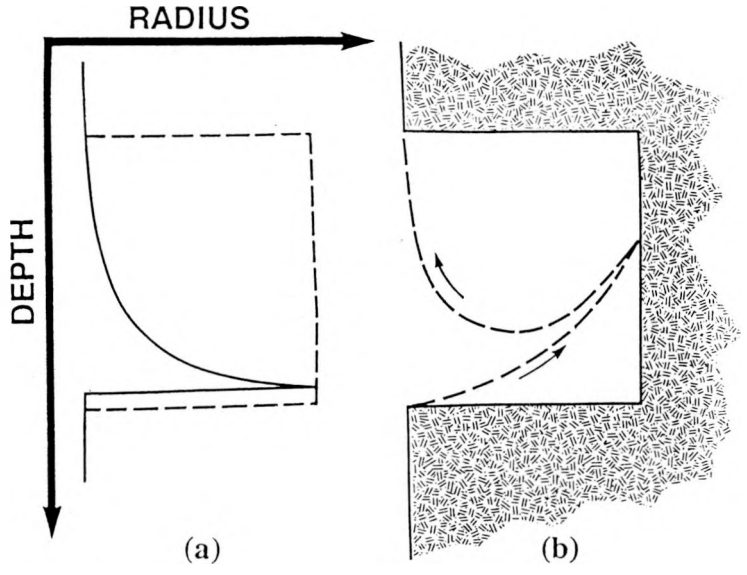


Figure 17 - (a) The solid line represents the actual log which would be recorded with the big-hole caliper tool in a washout with dimensions as described in the text. The dashed line represents the ideal log as we would like to see it, showing the washout as it actually is. A diagram of the washout is shown in (b), along with the path the arm tip would follow as the tool moves up the hole (dashed line).

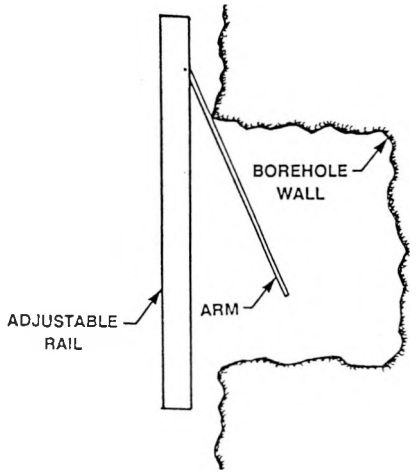


Figure 18 - This sketch shows the caliper arm striking the top of the washout and failing to reach the borehole wall at the tip.

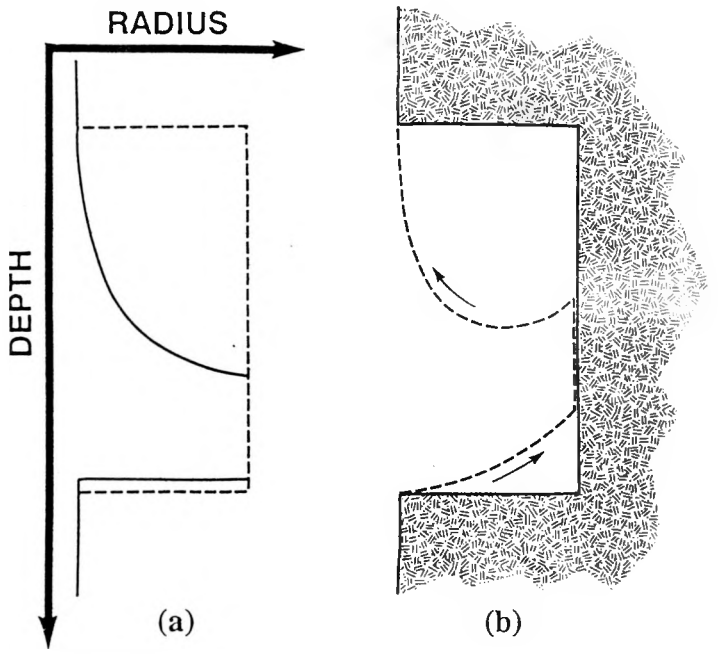


Figure 19 - This figure is similar to Figure 17, with the washout higher and more shallow. (a) The solid line represents the actual log which would be recorded, while the dashed line represents the ideal log as we would like to see it, showing the washout as it actually is. A diagram of the washout is shown in (b), along with the path the arm tip would follow as the tool moves up the hole (dashed line).

A growing effort has involved design of digital filters for response enhancement. The state of this particular art is not well evolved, largely due to non-linearities and substantial signal-to-noise deficiencies, but progress is accelerating. A review was given by Conaway (1983).

In recent years, the major petroleum logging service companies have been developing logging tools and digital processing techniques designed to complement each other; in other words, the output of the analog instrumentation is not intended to be an end product but rather is designed to have characteristics which make it specifically amenable to digital processing. The NTS containment programs do not, in general, benefit from such state-of-the-art logging services.

IV. DISCUSSION AND CONCLUSIONS

Analysis of geophysical borehole logs is a science which sometimes looks more like an art from outside. This is because the investment in time and money required to fully characterize and understand the tool behavior under all conditions can be formidable. When time or budget does not permit a complete study of a given tool and the associated interpretation theory, the log analyst may be reduced to educated guesswork.

This paper has dealt with one complicating factor involved in geophysical log interpretation - the thin bed response of the tool. Even a tool which is properly calibrated for uniform, homogeneous conditions will likely give incorrect data when considered on a point-by-point basis past a thin zone or through a complex section. As stated earlier, rules of thumb can be misleading and should be used with caution; for that reason they have not been emphasized here. The fine detail of the logs can be used freely for hole-to-hole correlation, but should not be considered accurate, as shown by the examples presented in this paper.

V. ACKNOWLEDGEMENTS

This work is supported by the United States Department of Energy. The author is grateful to Evan Jenkins of the U. S. Geological Survey, and to Rick Warren and Don Krier of Los Alamos National Laboratory, for suggesting and encouraging this line of investigation. Jim Barber of Fenix & Scisson of Nevada supplied the DBS tool schematic and other information. Lorraine Medina performed the digitizing of the dry-hole Wenner data and Mark Mathews supplied critical feedback on the manuscript.

VI. REFERENCES

Chombart, L. G., "Factors involved in practical electric log analysis," A Symposium on Subsurface Logging Techniques, Univ. Okla. (1949).

Conaway, J. G., "Uranium concentrations and the system response function in gamma ray logging," *in Current Research*, Geol. Surv. Can., Paper 80-A, 77-87 (1980).

Conaway, J. G., "Digital filtering of geophysical logs," *in Developments in Geophysical Exploration Methods - 5*, A. A. Fitch, ed., 65-105, Applied Science Publishers, London (1983).

Conaway, J. G., Hearst, J. R, Mathews, M. A., "Optimization of gamma-ray logging procedures in very large diameter boreholes," Los Alamos National Laboratory report LA-UR 87-1107 (1987).

Conaway, J. G., Bristow, Q., and Killeen, P. G., "Optimization of gamma-ray logging techniques for uranium," *Geophysics* **45** (2), 292-311 (1980).

Czubek, J. A., "Differential interpretation of gamma-ray logs: I. case of the static gamma-ray curve," Report No. 760/1, Nuclear Energy Information Center, Polish Government Commissioner for Use of Nuclear Energy, Warsaw (1971).

Fenster, R. A., "Idealized proximity response of the DBS," *in* Proceedings of the Fourth Symposium on Containment of Underground Nuclear Explosions, **2**, 3-17 (1988).

Flaum, C., Galford, J. E., and Hastings, A., "Enhanced vertical resolution processing of dual detector gamma-gamma density logs," *The Log Analyst*, **30** (1), 139-149 (1989).

Hilchie, D. W., "Old Electrical Log Interpretation," Douglas W. Hilchie, Inc., Golden CO (1979).

Mathis, G. L., and Gearhart, G., "The vertical resolution of Pe and density logs," *The Log Analyst*, **30** (1), 150-161 (1989).

Scott, J. H., Dodd, P. H., Droullard, R. F., and Mudra, P.J., "Quantitative interpretation of gamma-ray logs," *Geophysics* **26**, 182-91 (1961).

Van Nostrand, R. G., and K. L. Cook, "Interpretation of Resistivity Data," 310 pp., U. S. Geological Survey Professional Paper 499 (1966)

Fifth Symposium on the Containment of
Underground Nuclear Detonations

Computerized Tomography as a Geoscience Tool

by

G. Torres, V. J. Tester, J. Sharer, Terra Tek;
and J. W. LaComb, DNA

ABSTRACT

The purpose of utilizing computerized tomography was to evaluate the potential for change in saturation of NTS tuff during coring operations. This was addressed by characterizing the migration of fluids (primarily water) into and out of tuff specimens from the Nevada Test Site. Several drying tests and fluid intrusion tests were conducted at ambient conditions over a 48 hour period. Each test was monitored with the CT-scanner and density profiles created to show fluid movement.

NOTE: Color plates are referenced throughout the paper to previously issued Terra Tek reports. Copies are available by contacting Terra Tek Research.

Terra Tek Research
420 Wakara Way
Salt Lake City, Utah 84108

INTRODUCTION

Data from laboratory characterization of Nevada Test Site tuff has been used as input into models for underground containment of nuclear explosions. The question as to whether the material has been significantly changed due to migration of water into or out of a test specimen due to handling techniques has never been answered. Changing the water content of a test specimen can significantly alter the material properties (i.e. air voids) most critical to containment. With this in mind, a technique to study the movement of water into and out of a specimen was developed utilizing computerized tomography (known as a "CT-Scan or CAT SCAN").

Using CT technology a density profile can be created as a function of time so that it is possible to follow water migration into or out of the sample. Manipulation allows creation of three dimensional density profiles of the sample.

TECHNICAL DISCUSSION

Computerized tomography is a radiological imaging technique which generates one-dimensional projections of a specimen that are processed to create a cross-sectional image. The one-dimensional images are formed by revolving an X-ray source around the specimen as shown by the schematic in Figure 1.

CT measures the linear attenuation coefficient of the X-rays as they are passed through a specimen. When a test specimen is inserted in the scanner, an X-ray source and detector are passed in a plane past the sample and are rotated. This is repeated through a 180 degree rotation which requires approximately 120 seconds. With this data, a cross-sectional image of the test specimen can be generated by dividing the sample into small discrete

elements (pixels). Each pixel is characterized by a linear attenuation coefficient.

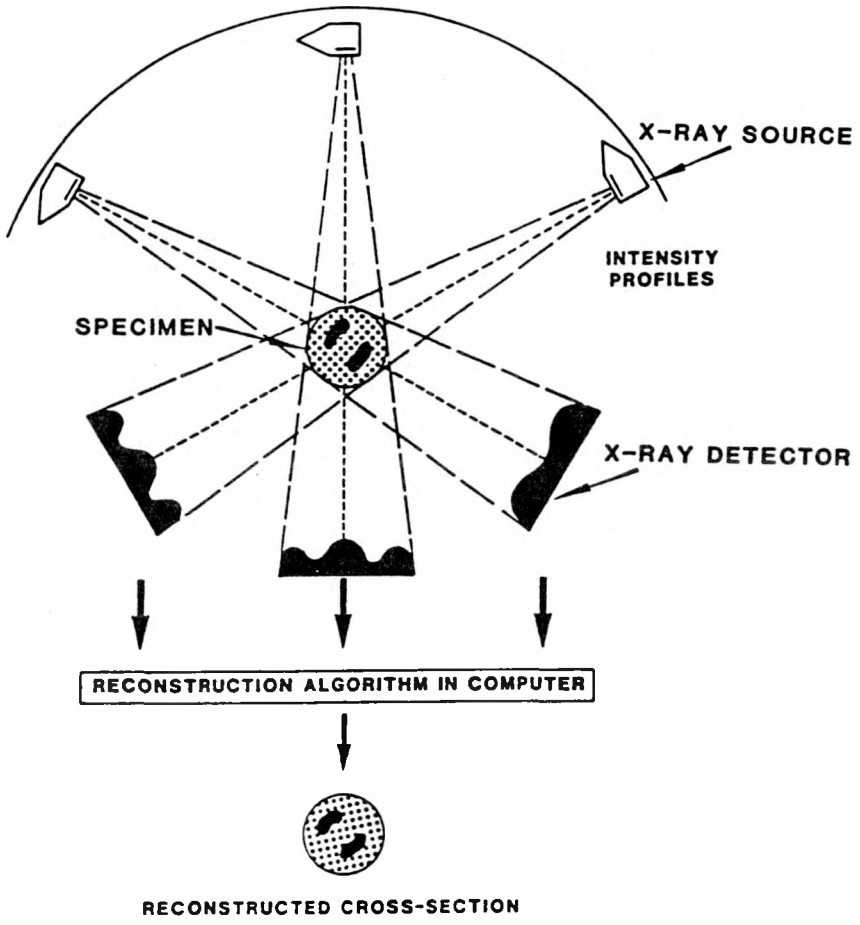


Figure 1. Schematic of the Computerized Tomography Technique which generates one-dimensional projections of a specimen that are processed to create a cross-sectional image.

A cross-sectional image of a test specimen is divided into an array of elements or pixels. A typical array of pixels is 256 x 256 in size. The thickness of the collimated X-ray beam determines the volume of material called a voxel. The resolution of the X-ray beam utilized scans a one millimeter slice of core. Figure 2 presents a schematic of these definitions.

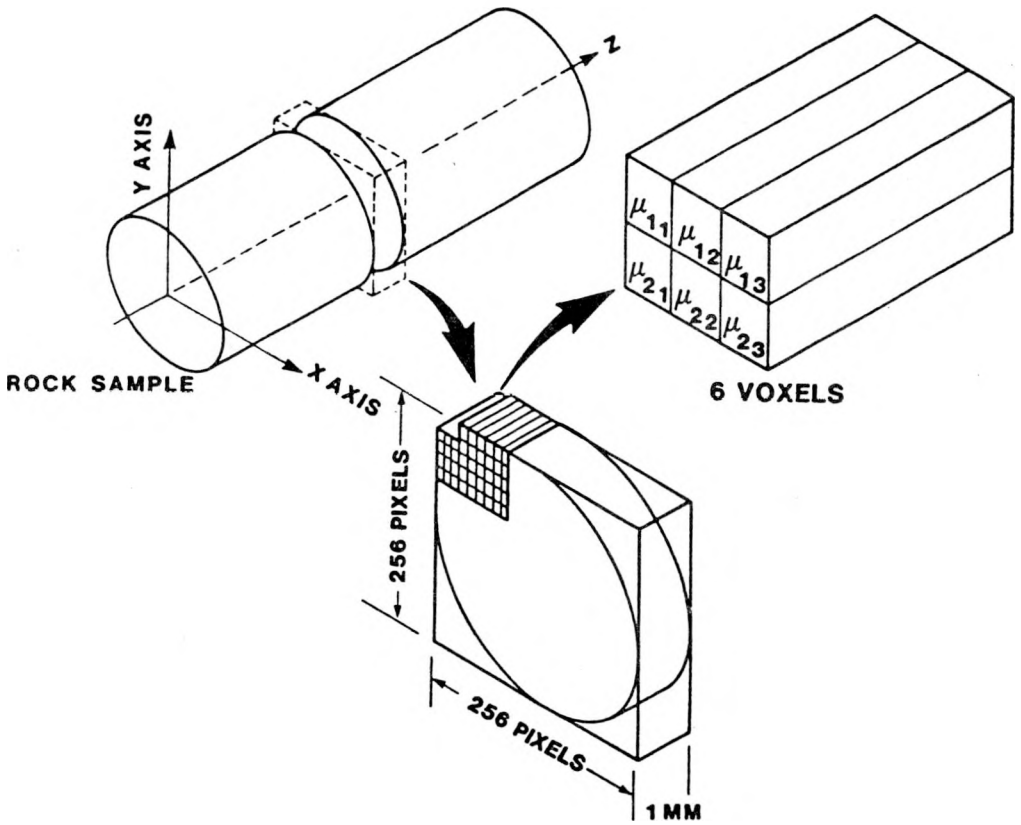


Figure 2. Schematic of the CT-Scanner Terminology. The CT-scanner X-rays a 1 millimeter slice of core with a diameter of 2 inches.

The attenuation of X-rays is affected by photoelectric absorption and by Compton scattering. Photoelectric absorption is dependent on the electron density (bulk density) and the effective atomic number of the material, and is predominant in terms of X-ray energies below 100 kilovolt (Kv). Compton scattering is dependent on the density of the material and becomes a more predominant term at energy levels above 100 Kv. Therefore, the linear attenuation coefficient of a material is a function of the density, effective atomic number of the material, and the energy level of the X-ray. This relationship[1,2] is described as follows:

EQUATION 1: $\mu = p (a + bZ^{3.8} / E^{3.2})$

where:

μ = linear attenuation coefficient of the material
p = density of the material
Z = effective atomic number
E = X-ray energy level
a = Klein-Nishina coefficient
b = constant

Since NTS tuff has an as-received density of approximately 2.00 gram per cubic centimeter (gm/cc), a calibration of densities that ranged from 1.77 to 2.11 gm/cc allowed Equation 1 to be approximated as a linear relationship. The density range corresponded to CT-numbers between 0 and -200 with a resolution of one. By simplifications, measurement techniques, and calibrations, Equation 2 which relates the measured CT number and the bulk density of the material can be derived. This linear approximation should not be extrapolated past the designated boundaries.

EQUATION 2: p = density = 0.0017 (CT no.) + 2.110 gm/cc

EXPERIMENTAL PROCEDURES

Three CT-scanner experiments were completed on tuff. Each experiment refined the procedure and added insight on the mechanism of water migration into and out of a tuff specimen.

Tuff specimens, 2 inches in diameter and one inch thick, were placed in a clear, semi-circular holding tray which was set on the positioning table of the CT-Scanner. Three X-ray sources and three detectors are mounted on a rotating frame above the positioning table which scan a 1 millimeter (mm) slice of the specimen. Each scan was 1 mm apart. A detailed schematic of the CT-Scanner hardware utilized is presented in Terra Tek report 89-45 entitled "Computerized Tomography--A Geoscience Application Characterization of

Tuff from the Nevada Test Site Material from UE12p.#4, U12p.02 IH-1, and U12n.23 UG-1" as Figure 1.

Phase I. P- and N-tunnel tuff with known physical properties (measured using water pycnometry methods) were used in Phase I. One sample of P-tunnel tuff was exposed to ambient conditions for 23 hours and scanned intermittently as it dried out. The drying was not accelerated by external heaters. Four preserved core samples from N-tunnel were utilized in the fluid intrusion study. Each sample was submerged in a different fluid for 48 hours and then scanned many times (nine of which are presented) in order to characterize the penetration of the fluid into the sample. The fluids were water and three brine solutions: 5% KCl, 5% KBr, and 5% KI. The purpose of the brines was to develop a drilling fluid tracer for use in the field.

Phase II. The objective of the Phase II tests was to provide data for comparing the results between the P- and N-tunnel samples from Phase I. In the Phase II tests, one sample of N-tunnel tuff was used in the drying study and one sample of P-tunnel tuff was used in the fluid intrusion study. The fluid intrusion study only used one brine solution, KI.

Phase III. The tests conducted under Phase III consisted of drying and resaturating the same samples. Initially five samples were allowed to dry simultaneously in the same holder to save time and increase data. The samples were weighed prior to the beginning of the test and at the end of the drying stage before immersion in water. It was very difficult to align the samples in the holder at the start of the water immersion. This therefore became the limiting factor in the data acquisition. The samples were submerged in a water bath to monitor the fluid intrusion.

In a final test only one sample was monitored. This eliminated moving the positioning table and therefore exact alignment was possible allowing for

extensive data reduction and manipulation. This test was considered to have provided the most reliable results due to the more refined and higher quality testing procedures.

RESULTS OF TESTING

Phase I. The P-tunnel material had previously been characterized[7] as having the following properties:

Table 1. Physical Properties of P-Tunnel Tuff for Phase I.

UE12p.#4 Depth (ft)	Density			Water by Wet Weight (%)	Por-osity (%)	Satur-ation (%)	Calc. Air Voids (%)
	As-Rec'd (gm/cc)	Dry (gm/cc)	Grain (gm/cc)				
846.3	1.92	1.56	2.49	19.0	37.4	97.8	0.80

The purpose of the first test of Phase I was to understand how NTS tuff dries under ambient conditions. From the CT-scans taken during the test, subtractive images were formed. Subtractive images are developed by subtracting the time zero scan from the remaining images, thus showing the relative differences as the specimen dries out. The color plates for the CT-scans and the subtractive images are presented in Terra Tek report TR 88-62 entitled "Utilization of Computerized Tomography to Characterize Volcanic Tuff" as Figures 5 and 6. It should be noted that these color plates can not be meaningfully reproduced for these proceedings; therefore, they are not included within this paper (see note on title page).

It was observed in the color plates representing the net effect of drying that fluid was preferentially lost from select materials and not annularly. Two distinct, lower density spots, determined to be pumice inclusions, were noted as losing water rapidly by preferential paths.

The loss of water from select areas may not be dependent only on the permeability of the material, but on the distribution of the water in the specimen. These drying regions were thought to be controlled by capillary effects started by sporadic boundary drying, and sample inhomogeneity. The density steadily decreased from 1.98 gm/cc to 1.88 gm/cc, as can be seen in Figure 3 as density versus time. Determination of the density had not been refined; therefore, the density values in Figure 3 may be slightly high.

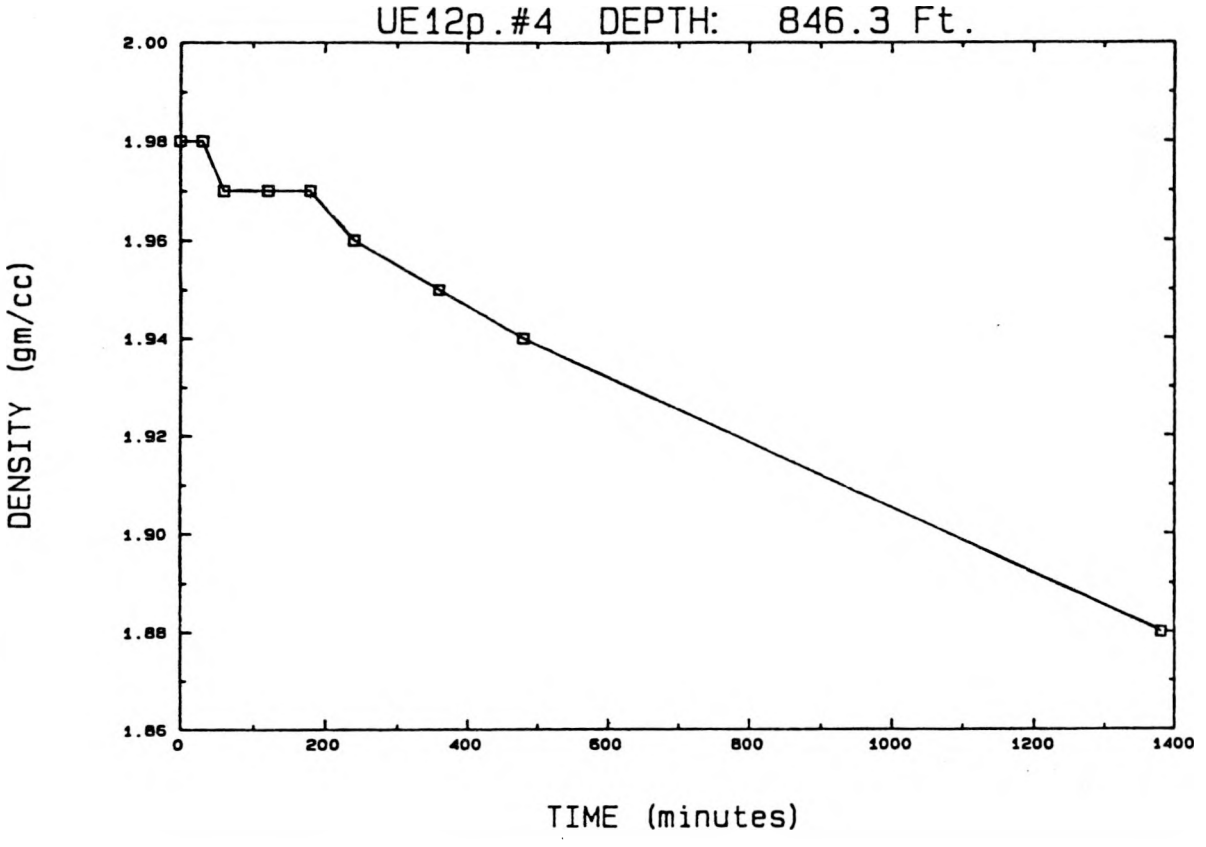


Figure 3. Phase I Drying Test. Note the steady decrease in density.

The N-tunnel material had previously been characterized[8] as having the following properties:

Table 2. Physical Properties of N-Tunnel Tuff for Phase I.

U12n.23 UG1 Depth (ft)	Density			Water by Wet Weight (%)	Por-osity (%)	Satur-ation (%)	Calc. Air Voids (%)
	As-Rec'd (gm/cc)	Dry (gm/cc)	Grain (gm/cc)				
1199.0	1.94	1.59	2.47	17.9	35.4	97.9	0.70

The purpose of the remaining Phase I tests was to study fluid intrusion. The matrix permeability was assumed to be low and therefore was ignored in most tests. Direct detection of small fractures is beyond the resolution of the current system; however, obvious flow patterns would be an indicator of fractures if there were many present.

It was evident that there was dispersion of brine ions into the specimens due to extreme changes in the CT-scans. It should be noted that the scans were taken after the specimen soaked in the fluid for 48 hours; therefore, the fluid intrusion mechanism cannot be assessed. The color plates for the specimens are shown in Terra Tek report 88-62 as Figures 10 through 12. Figure 8 in TR 88-62 presents the as-received specimen images for comparison. Generally the CT-scans are yellow-blue with small regions of red. The specimens infiltrated with ions yielded mostly yellow to red scans which indicated an increase in CT number throughout the entire specimen. With no pressure driving the migration of the fluid into the specimens, it was likely that the migration was atomic diffusion and not wholesale replacement of water within the sample. Since the tuff is usually thought of as having a low permeability, this would add credence to the theory that the ions were preferentially penetrating the specimen. Note that the specimens were

approximately 98.0% saturated; therefore not expected to gain more fluid.

It is important to note that the atomic number of the brine affects the CT number which effects the density determination. Therefore, the simplifications discussed earlier cannot be applied to determine the density. It is not clear how much of the change in density was due to atomic absorption, rather than capillary pressure, fracture permeability, or matrix permeability. The specimen infiltrated with KI was especially suspect, since it is known that iodine's atomic number does affect the attenuation of X-rays.

The specimen immersed in water experienced very little fluid infiltration. It is difficult to determine any increase in the density from the CT-scans (TR 88-62, Figure 9). The high saturation of the specimens may have prevented any further water gain.

Phase II. The purpose of the Phase II tests was to provide a comparison with the Phase I tests. The physical properties for the N- and P-tunnel tuff were remeasured and are presented in Table 3.

Table 3. Physical Properties of N- and P-Tunnel Tuff for Phase II.

Tunnel Depth (ft)	Density			Water by Wet Weight (%)	Por-osity (%)	Satur-ation (%)	Calc. Air Voids (%)
	As-Rec'd (gm/cc)	Dry (gm/cc)	Grain (gm/cc)				
U12n.23 UG1 1204.1	1.91	1.55	2.45	19.0	36.8	98.9	0.40
UE12p.#4 847.6	1.94	1.59	2.48	18.1	35.8	97.7	0.80

The drying test was conducted on N-tunnel tuff, and the results are presented in Figure 4 as Density versus Time. As can be seen, the density fell from 1.94 gm/cc to 1.66 gm/cc in 47 hours, and was noted to still be losing water after 24 hours. In comparison with the P-tunnel drying

experiment, N-tunnel tuff lowered its density by 0.10 gm/cc more than P-tunnel for the same time frame.

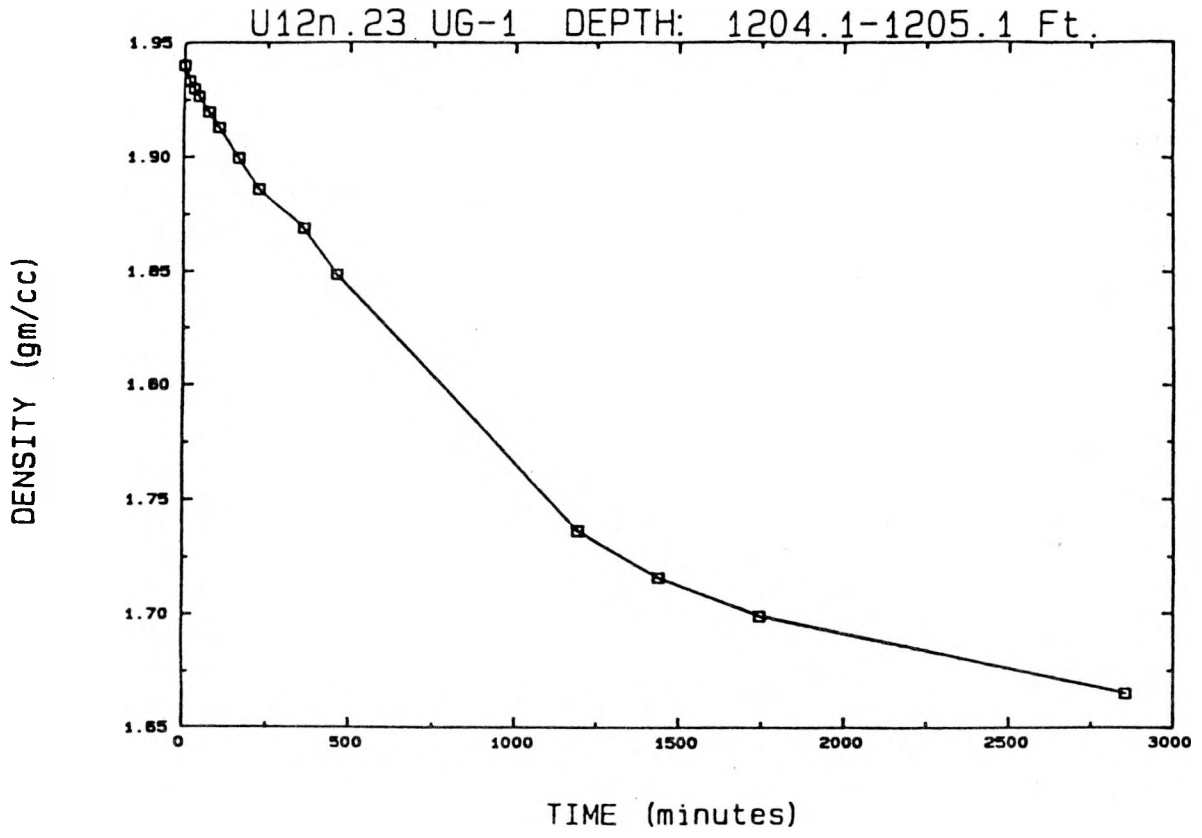


Figure 4. Phase II Drying Test. The density continues to decrease after 24 hours.

However, the drying is thought to be dependent on the evaporation rate and not capillary effects. The rate of the density change does not rapidly decrease with time; therefore, the controlling factor was assumed to be the evaporation rate since it was essentially held constant at ambient conditions.

Subtractive CT-images for the drying test of Phase II again indicated water loss in preferential pathways. It was noted that there were regions which started at a higher density and lost less water than the other material and where identified as lithic inclusions. The subtractive images are presented in Terra Tek report 89-45 entitled "Computerized Tomography--A

Geoscience Application Characterization of Tuff from the Nevada Test Site Material from UE12p.#4, U12p.02 IH-1, and U12n.23 UG-1" as Figure 5.

The fluid intrusion test was conducted on P-tunnel tuff with a 5% KI brine solution. Figure 5 shows CT-number versus time.

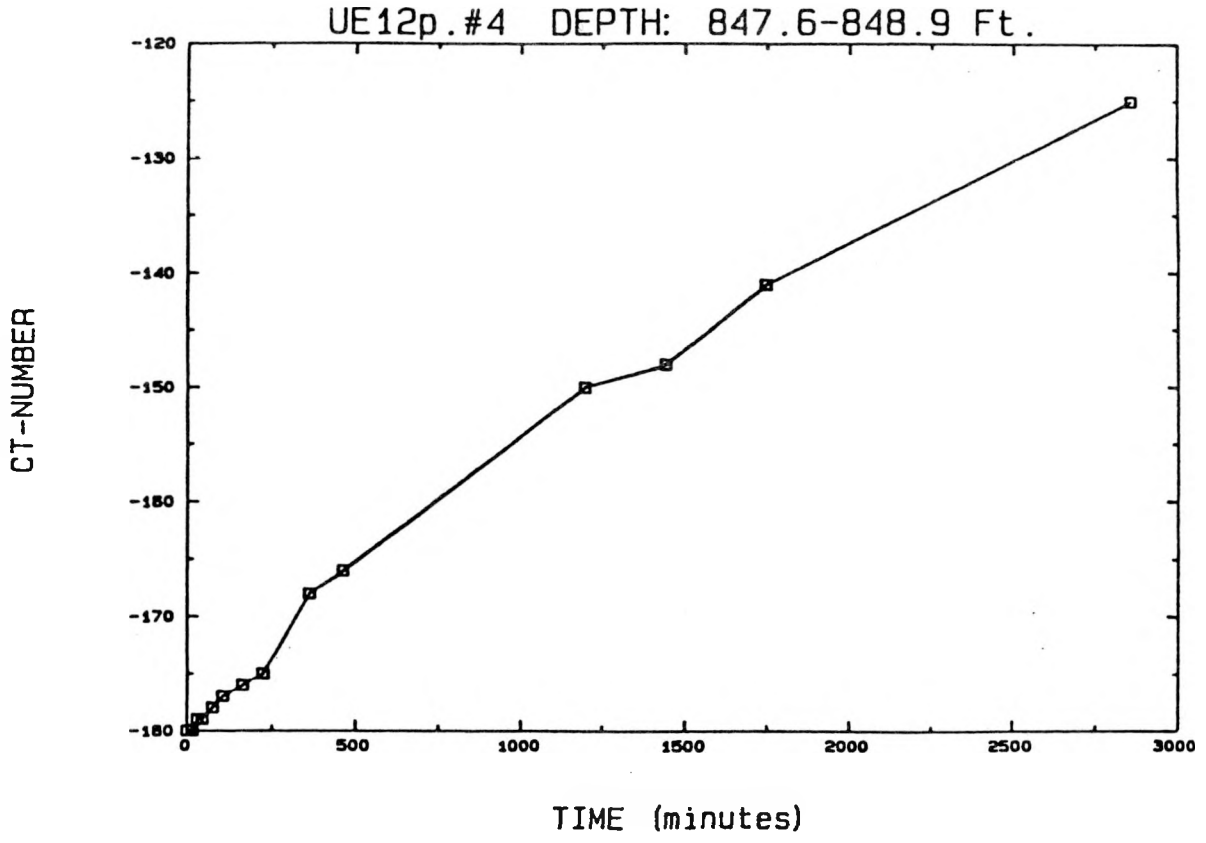


Figure 5. Phase II Fluid Intrusion Test. Note the CT-number decreases as ions are dispersed into the specimen.

In this case, CT-numbers cannot be converted into density due to the effect of the atomic number on the diffusing KI. However, the subtractive CT-scans, seen as Figure 8 in TR 89-45, revealed that the ions were annularly penetrating the specimen. The high density spots observed in the drying test were found not to be greatly affected by the brine.

Phase III. The physical properties for the P- and N-tunnel tuff[10] utilized in Phase III are presented in Table 4 and Table 5, respectively.

Table 4. Physical Properties of P-Tunnel Tuff for Phase III.

U12p.02 IH1 Depth (ft)	Density			Water by Wet Weight (%)	Por-osity (%)	Satur-ation (%)	Calc. Air Voids (%)
	As-Rec'd (gm/cc)	Dry (gm/cc)	Grain (gm/cc)				
24.5	1.754	1.286	2.578	26.7	50.1	93.4	3.3
226.0	1.843	1.470	2.440	20.2	39.8	93.8	2.5
259.3	1.794	1.391	2.391	22.2	41.6	95.6	1.8

Table 5. Physical Properties of N-Tunnel Tuff for Phase III.

U12n.23 UG1 Depth (ft)	Density			Water by Wet Weight (%)	Por-osity (%)	Satur-ation (%)	Calc. Air Voids (%)
	As-Rec'd (gm/cc)	Dry (gm/cc)	Grain (gm/cc)				
787.9	1.995	1.691	2.514	15.2	32.7	92.9	2.3
1580.3	2.052	1.749	2.594	14.8	32.6	93.0	2.3

The first test, which included five specimens, saw a decrease in bulk density during the first 24 hours. It is assumed that the rate of the water loss was again controlled by the evaporation rate. The next 24-hour period represented the specimens re-gaining most of the lost water. Figure 6 shows Bulk Density versus Time. Note that the initial slope of the resaturation was very steep. This indicates the sample may have a higher permeability and therefore absorbs water very rapidly. It appears that the specimens do not resaturate to their initial saturation.

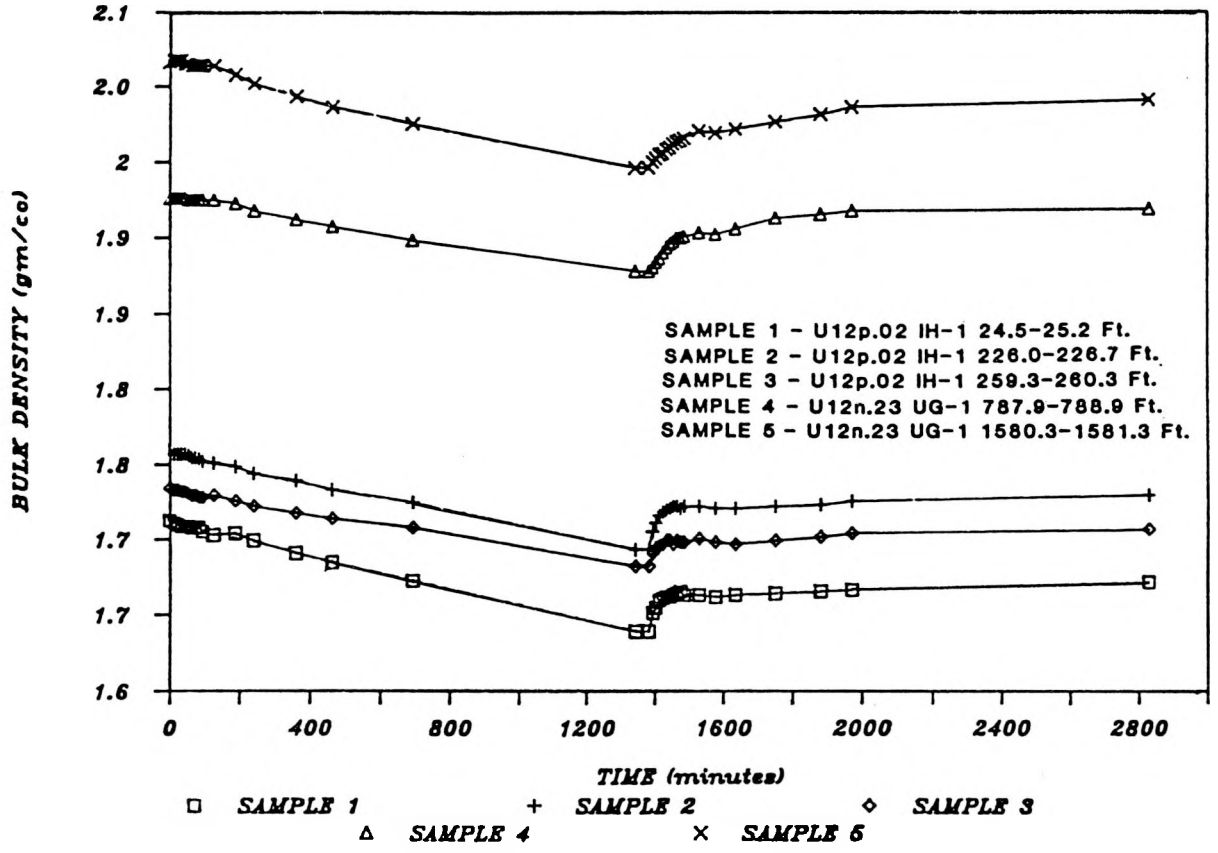


Figure 6. Phase III Drying then Resaturation of Five Tuff Specimens. Note that the specimens do not resaturate to their original density.

Figure 7 presents the results from the final test in a graphical format. These data are consistent with the data presented in Figure 6. There is a decrease in density during the first 24 hour period and a rapid increase in density upon first immersion in water. The rapid increase in density is followed by essentially no additional water gain. The density level plateaued at approximately 18% less than the initial density for the final specimen.

The subtractive images which show the net effect of the drying and resaturation tests are presented in Terra Tek report TR 89-45 as Figures 13 and 15. From the subtractive CT-images of the specimen as it dried, two high density regions, thought to be lithic inclusions, and a low density region,

thought to be a pumice inclusion, were observed. Preferential water migration pathways were formed extending from the pumice inclusion and surrounding the lithic inclusions as the specimen dried out. A change in density was present throughout the entire specimen.

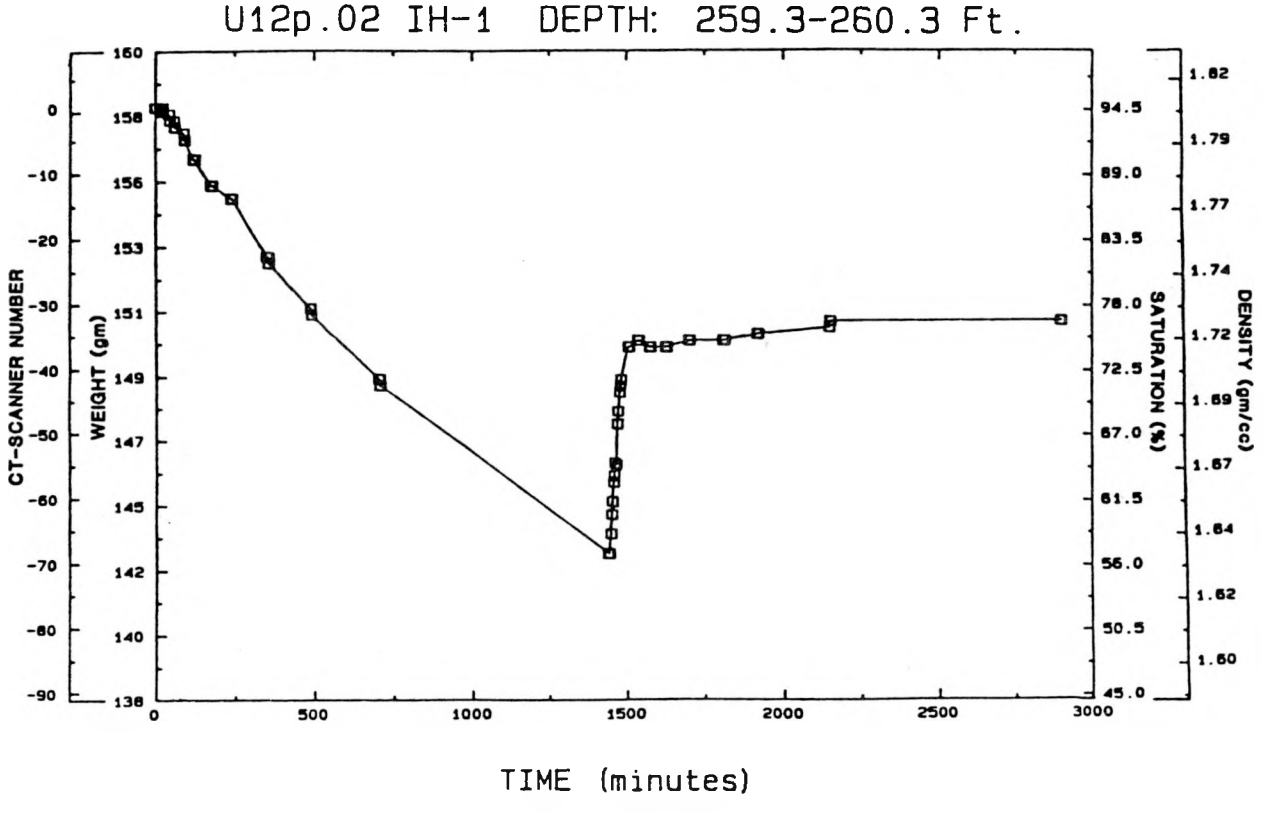


Figure 7. Phase III Drying and Resaturation of Tuff. The specimen's final density is approximately 18% less than the original density.

The subtractive CT-images of the specimen as it was resaturated show the specimen initially gaining water annularly, then found preferred paths back into the specimen's central region. The lithic regions were noted not to change in density.

CONCLUSIONS

In summary, the following were observed as the specimens were dried and then resaturated:

- Fluid was preferentially lost during the drying test, not annularly.
- The rate of water lost was thought to be controlled by the evaporation rate since there was no driving force present.
- Capillary effects caused rapid redistribution of water in the samples.
- Water migration was along clearly delineated paths, possibly small fractures.
- The matrix permeability of the tuff was generally low.
- The intrusion of water was seen to first be annularly and then along preferential pathways.
- After a specimen was allowed to dry out, the initial saturation could not be achieved by immersion only.

List of References

1. Houndsfield, G.N.: "A Method of and Apparatus for Examination of a Body by Radiation Such as X- or Gamma-Radiation," British Patent No. 1,283,915. London (1972).

2. Brooks, R.A. and DiChiro, G.: "Principles of Computer-Assisted Tomography in Radiographic and Radioisotopic Imaging," Phys. Med. Biol. (1976) 21, 689-732.

3. Reconstruction Tomography in Diagnostic Radiology and Nuclear Medicine, M. Ter-Pogossian, M.M. Phelps, and G.L. Brownell, (eds.), University Park Press, Baltimore (1977).

4. Barrett, H.H. and Swindell, W.: Radiological Imaging, Academic Press, New York City (1981).

5. Evans: The Atomic Nucleus, McGraw-Hill Book Co., New York City (1955).

6. Wellington, S.L. and Vinegar, H.J., "X-Ray Computerized Tomography," Journal of Petroleum Technology, August 1987, Vol. 39, No. 8, pp 885-898.

7. Lupo, J.F., etc., Physical and Mechanical Characteristics of Tuff from UE12p.#4, TR 87-94.

8. Lupo, J.F., Physical and Mechanical Characterization of Cored Tuff from U12n.23 UG-1, TR 88-24.

9. Torres, G., Utilization of Computerized Tomography to Characterize Volcanic Tuff, TR 88-62.

10. Torres, G., Computerized Tomography--A Geoscience Application Characterization of Tuff from the Nevada Test Site Material from UE12np.#4, U12p.02 IH-1, and U12n.23 UG-1, TR 89-45.

A STATISTICAL ANALYSIS OF GRAIN DENSITY MEASUREMENTS FROM CUTTINGS AND PERCUSSION GUN SAMPLES

Gayle A. Pawloski
Lawrence Livermore National Laboratory
L-221, P.O. Box 808, Livermore, CA 94550

ABSTRACT

Statistical tests on 113 pairs of grain density measurements show that the grain densities from cuttings samples are different from those measured on gun samples. The difference of the means of the two samples types is 0.02 Mg/m^3, which is small. When stratigraphic subsets were tested, grain densities from cuttings samples could not be distinguished from those of gun samples for the Rainier Mesa Member and the Tunnel Beds. The measurements on the two sample types could be distinguished for the Paintbrush Tuff and the "induced zone" (Wahmonie Formation). The differences of the means of the two sample types are again small. Testing of lithologic subsets also indicates that grain density measurements from cuttings can be distinguished from those of gun samples. Again, the differences of the means are small.

For containment applications, grain density measurements from cuttings and gun samples are virtually identical when measurement accuracy is taken into consideration. Thus, grain densities from cuttings samples are adequate for calculating physical properties.

INTRODUCTION

Grain densities are commonly viewed as a simple indicator of a sample's mineral components. Grain density measurements from Nevada Test Site (NTS) samples are used with bulk density and water content measurements to calculate physical properties (porosity, gas porosity, and saturation). These calculated physical properties are used, along with other data, to help predict the phenomenology of a given event. LLNL routinely collects unwashed cuttings samples as holes are drilled. These are utilized for lithologic description and identification and laboratory measurements (typically grain density measurements and x-ray diffraction analyses). Percussion gun samples are collected to provide supplemental data. Obtaining them requires additional cost. Grain density measurements have been made on both cuttings and gun samples. There have been recent discussions concerning the validity of measurements on these two samples types. The issue frequently ends with the question being asked "which gives the most representative grain density measurement?" Unfortunately, we have no real understanding of what a representative sample of the rock is. We rarely get large volumes of intact sample, and homogeneity of the in situ rock (or lack of it) can depend on the volume under investigation.

The size of a sample and the collection methods are often topics when people discuss sample merits for use in characterizing a drill hole. Each sample type presents intrinsic problems. Unwashed cuttings are derived from bit advancement in the rock material as drilling progresses. They represent a volume of rock. The chips of material then pass up the drilling column with the drilling fluid. There is widespread agreement among NTS geologists that stronger, more consolidated material (welded ash-flow tuff and lava, for example) breaks

up as coherent chips of rock and passes up the drilling column with little to no disintegration. On the other hand, weaker or less consolidated material (vitric bedded or nonwelded tuff, for example) may disintegrate upon drilling and/or turbulent flow up the drilling column. Light and heavy components may fractionate, completely changing the appearance of the samples from the in situ habit. We know that this occurs, because we have seen samples that appear to be crystal slurries (heavier components) when we expect glass to also be present. The glass shards are smaller and lighter, and therefore become separated from their accompanying crystal component. (One could ask where the glass shards go. Conservation of mass says they have to come out somewhere. Maybe the heavier and lighter fractions show slightly different flow rates, but over time shouldn't everything even out?) Percussion gun samples are roughly 1" by 2" samples obtained by explosively shooting a barrel into the rock material. The sample obtained is an intact sample. But it is a small, discrete sample of the volume.

Cuttings, though representing a large volume of rock material, may be fractionated; i.e. the original composition may be changed by drilling and/or turbulent flow. Gun samples are intact samples of the in situ rock material, but they are small. These would be fine if everything was homogeneous, but that is an open question. Which sample type gives a more accurate grain density? Unfortunately, we don't know the absolute answer. I looked for statistical studies that examined the problem, and since I found no published data, I undertook this investigation. A key factor in this study was that paired data was used, so an unwashed cuttings sample taken at a specific depth should theoretically compare well with a gun sample taken at the same depth. Changes in lithology, alteration, structure, or whatever, should occur similarly to both samples. Since the grain density measurement follows the same laboratory procedure no matter what type of sample is used, we should be able to determine if the samples are different. There were two purposes to the study: (1) to determine the variability of the grain density measurements from the two sample types, and (2) to determine if one sample type may be better to use for containment evaluation.

STUDY DESCRIPTION

The data set consisted of 113 pairs of grain density data measurements made at the same depths from four holes in northwestern Yucca Flat (Table 1). All four holes are in the same structural basin. All of these hole were recently drilled (between May 1986 and April 1987). We feel fairly confident that our cuttings collection procedures were operating correctly (McKinnis, 1989a). This means that the collection of each cuttings sample occurred over a small amount of time, and represents a volume of rock at a specific depth. We have no reason to suspect that the samples were unusual in any way. No indications of "doghousing" were evident. The cuttings samples were used "as received". They were not washed, which removes smaller components. They were mechanically split to reduce the sample size prior to the actual grain density measurements. No pieces were handpicked for inclusion or exclusion; i.e. no bias was introduced via purposeful human intervention. The entire gun sample was used for the grain density measurement, due to their small volume. These were also used "as received". All samples were inspected for lithologic description and identification.

Current LLNL procedure requires the geologist to visually inspect each sample, evaluate its integrity, and judge how representative each is (Wagoner, 1988). The geologist can choose intact fragments of a sample to use for grain density measurements and x-ray diffraction analysis. Ideally, only representative samples are used for measurements. Samples biased by a high percentage of crystals, lithics, or cobbles would not be used. This study utilized the entire volume of the samples, with the exception of mechanically splitting the cuttings samples to reduce sample size. Visual inspection indicated no reason to exclude a

HOLE	NUMBER OF SAMPLES
U2ct	25
U2cu	37
U2cv	25
U4at	26

Table I Data set from four holes in Yucca Flat.

sample because it appeared "unrepresentative". There was no opportunity to select intact fragments since most of the samples were nonwelded, bedded, and air-fall tuffs and were completely disaggregated. At worst, the grain densities measured on the cuttings might be higher than inspected, since crystals might concentrate and glass wash away. This study tests either a typical case if we assume all samples are representative, or a worst case if we acknowledge that we did not introduce judgment to select what might be "representative".

Standard statistics (mean, standard deviation, maximum, and minimum) and t-tests were applied to the entire data set, stratigraphic subsets, and lithologic subsets. Accompanying plots show distributions of the data sets.

RESULTS

ENTIRE DATA SET

The first analysis was done utilizing the entire data set. The histograms (Fig. 1) show the distributions of the cuttings and guns samples. Both sample types are normally distributed, with similar upper ranges. Modes (the mode is the highest bin of each histogram) are similar in count, and are one bin different in grain density, with gun samples having the lower mode. The measurements from the cuttings samples are distributed almost symmetrically around the mode, while the measurements from the gun samples show an abrupt drop off in population below 2.40 Mg/m^3. The gun population also displays a lower minimum than the cuttings. Statistically, the means of the two sample types are slightly different (cuttings = 2.52 Mg/m^3 and guns = 2.49 Mg/m^3). The standard deviations are the same for both sample types (0.08 Mg/m^3).

To correctly handle pairs of data we look at differences between the measurements of the data pair (the measurements from the cuttings and gun samples taken at the same depths). The histogram in Figure 2 shows the distribution of the differences of the cuttings measurement minus the gun measurement. The population is normally distributed, and slightly skewed to higher values, with a mode slightly greater than zero. The mean of the differences is 0.02 Mg/m^3, with a standard deviation of 0.08 Mg/m^3. If grain density measurements from cuttings and guns were equal, the mean of the differences would be zero; this is not the case. It is important to note that the mean difference of 0.02 Mg/m^3 is not very large.

A paired t-test was done to test if grain density measurements from cuttings samples were equal to those from gun samples. It tested the null hypothesis that the mean of the cuttings population was equal to the mean of the gun population. A t-test takes into

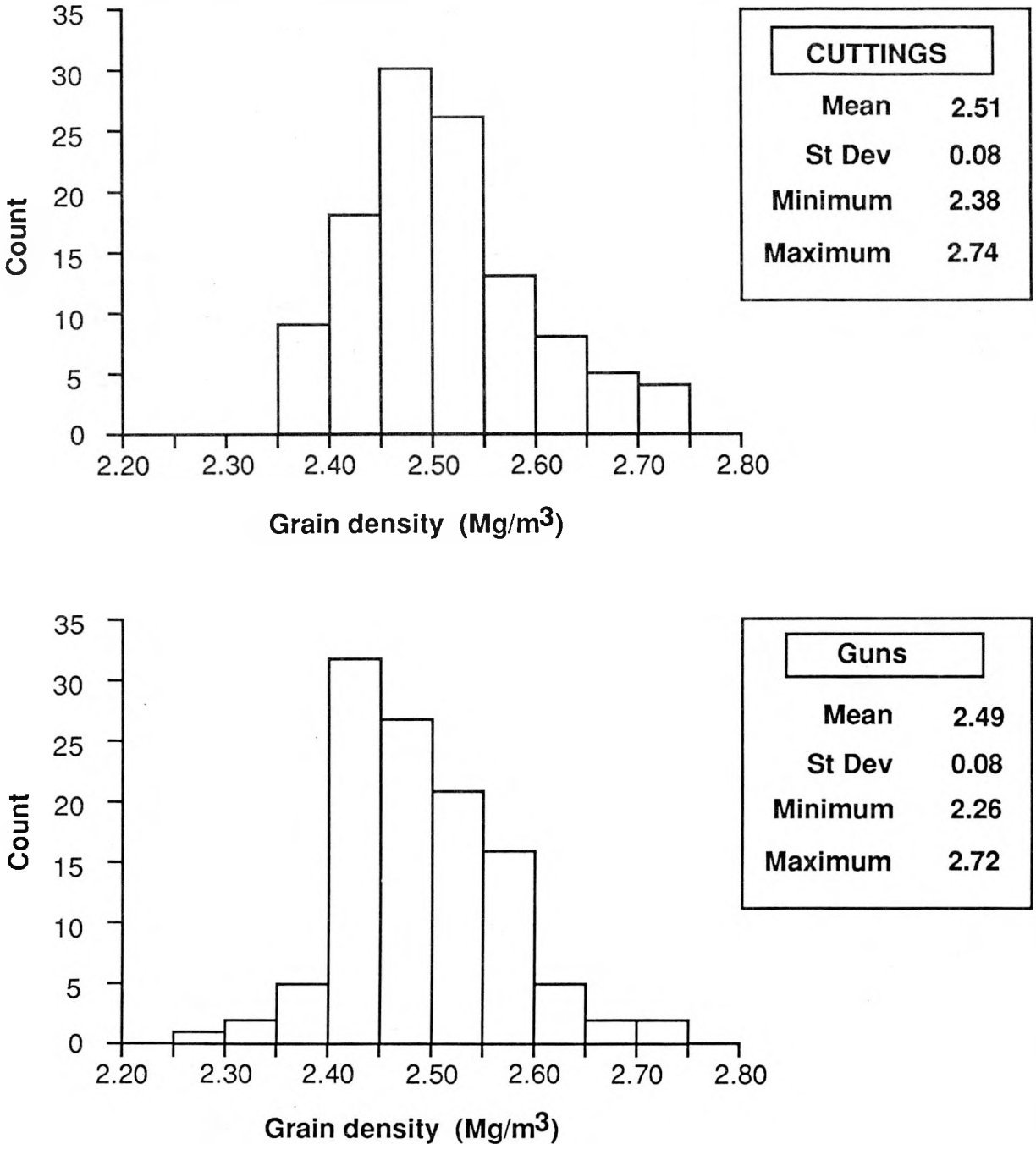


Figure 1 Distribution of cuttings and gun samples.

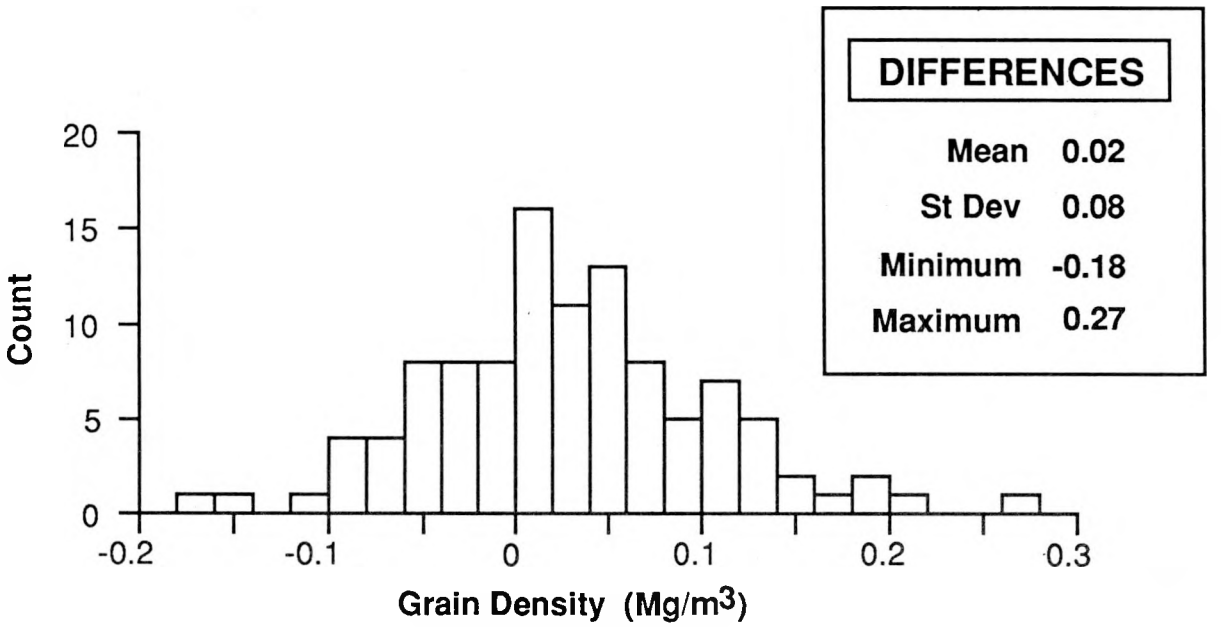


Figure 2 Distribution of differences of means for the cuttings and gun sample pairs.

consideration not only the numerical means of the populations, but also the distributions of the populations. "Paired" means it tests the differences of the pairs of data. This test requires that the data be random, normally distributed, and the variances be equal. The data are assumed to be random. Analysis of the depth selections, data collection and laboratory procedures indicate no reason to suspect that this is not true. The histograms in Figure 1 show that the distributions are normal. Also, statistically speaking, as a population approaches 20-30 in size, it can be assumed to be normally distributed. The variances were tested, and there is no reason to suspect that they are not equal. Results of the paired t-test indicate that the mean of the grain density measurements from the cuttings is from a different population than the mean of the measurements from the gun samples, at a 5% significance level. Simply speaking, grain density measurements from the cuttings samples are not equal to those from gun samples. How different are they? As seen in the paragraph above, the difference of the means is 0.02 Mg/m^3.

STRATIGRAPHIC SUBSETS

The data set was divided into stratigraphic groups and these subsets were tested. We commonly work with stratigraphic groups (lithologic logs and cross sections are two examples), so this seemed to be a logical way to divide and test the data. Again, since the data are paired, we should be able to ignore variations within the stratigraphic unit. Table 2 shows the stratigraphic groups and their population size. Statistical tests were performed on only four of the groups (Rainier Mesa Member, Paintbrush Tuff, "induced zone" or Wahmonie Formation, and Tunnel Beds), because the other groups had too few data pairs to obtain what could be believed as representative results.

Figure 3 shows the relationship of the measurements from the data pairs when divided into stratigraphic groups. The solid diagonal line represents perfect correlation, what one would expect if the measurements from the two sample types at the same horizon were equal. The dashed lines show one standard deviation of all the data in the specific stratigraphic group plotted parallel to 1:1 correlation between the two sample types. Two things are obvious from these plots. One, most of the measurements fall within one standard deviation of the mean. Two, the grain density measurements from cuttings samples tend to be higher than those from gun samples. This second fact is not surprising, since it was also witnessed in Figures 1 and 2. The asterisk symbol shown on the Rainier Mesa Member, Paintbrush Tuff, and Tunnel Beds plots shows the average zonal grain density calculated for Yucca Flat (Burkhard, 1989). It is interesting to note that the Yucca Flat zonal averages fall comfortably within these data sets.

STRATIGRAPHIC UNIT	NUMBER OF SAMPLES
Mixed alluvium	1
Basal tuffaceous alluvium	1
Ammonia Tanks Member	4
Rainier Mesa Member	16
Paintbrush Tuff	50
"Induced zone" or Wahmonie Formation	11
Grouse Canyon Member	6
Tunnel Beds	31
Tub Spring Member	4

Table 2 Stratigraphic subsets and size.

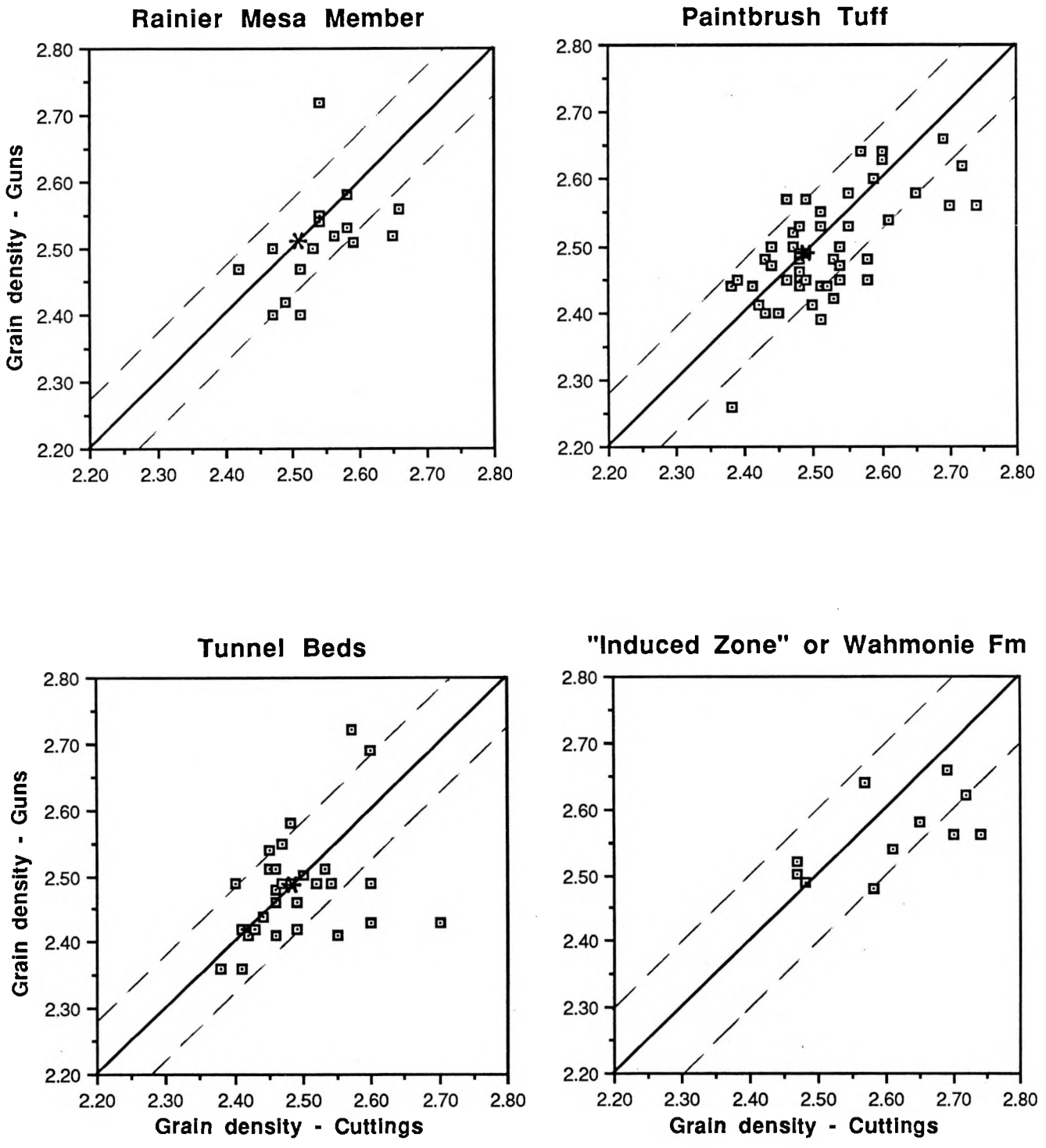


Figure 3 **Comparison of grain density measurements for cuttings and gun samples for stratigraphic subsets.**

Stratigraphic unit	Mean	St Dev	Mean of differences	Paired t-test
Tmr	Cuttings 2.54 Guns 2.51	0.06 0.08	0.03	accept
Tp	2.52 2.49	0.09 0.08	0.02	reject
"Induced zone" or Tw	2.61 2.56	0.06 0.10	0.05	reject
Ttu	2.49 2.48	0.07 0.08	0.009	accept

significance level $\alpha = 5\%$

Table 3 Summary of statistical tests for stratigraphic subsets.

Table 3 summarizes data from statistical tests for the stratigraphic groups. The mean of the cuttings samples is higher than the mean of the gun samples for all stratigraphic groups. This matches what was seen in the plots in Figure 3. Standard deviations are comparable for the two different sample types within each stratigraphic group. In fact, the standard deviations are very similar for all stratigraphic units shown in Table 3. Also, the means of the differences are small. Results of paired t-tests (at a 5% significance level) using data from each stratigraphic group are also shown in Table 3. The null hypothesis is accepted for the Rainier Mesa Member and the Tunnel Beds. Statistically, there is no reason to suspect that the means of the two populations are different. To put this into terms that are applicable to our usage, one can not tell the difference between the means of the grain density measurements from the cuttings samples and the means of those from the gun samples for the Rainier Mesa Member and the Tunnel Beds. One can tell the difference between the means of the measurements from the two sample types for the Paintbrush Tuff and the "induced zone".

LITHOLOGIC SUBSETS

The data set was divided into lithologic groups and these subsets were tested. This division was intended to address the idea that cuttings and gun samples from stronger, more consolidated units (welded tuffs and lavas) ought to compare well since the cuttings travel up the drilling column as intact pieces, while weaker, less consolidated units (bedded, air-fall and nonwelded tuffs) might not show as good as a comparison since all components of the cuttings sample may not travel coherently up the drilling column. Again, since we are using paired data, variation in lithology should not affect comparison of grain density measurements on two different sample types, but this would be a good way to actually test it. Unfortunately, there were very few samples of stronger, more consolidated rock in the data set. There were, however, many examples of weaker, possibly less consolidated rock. By testing the weaker rocks, we actually were testing the worst possible case - where one might actually expect to

see the worst comparison. Therefore, if the grain density measurements from the cuttings samples compared well with those from the gun samples, then one could say that measurements from the two sample types could be used interchangeably.

Table 4 shows the lithologic divisions and their population sizes. Because the alluvium group was very small and the results would not be statistically representative, it was not tested. Table 5 summarizes data from statistical tests on the lithologic subsets. The mean of the cuttings samples is higher than the gun samples for both lithologic units; the standard deviations are very similar. Results from the paired t-tests show that, at a 5% significance level, the means of the two sample types are distinguishable for nonwelded tuffs and bedded and air-fall tuffs. Grain density measurements from cuttings samples can be distinguished from those from gun samples. But again, the means of the differences are small. Plots of the grain density measurements of the samples from the nonwelded tuffs and the bedded and air-fall tuffs are shown in Figure 4. The diagonal line shows perfect correlation between the measurements from the cuttings and gun samples. As in Figure 3, it is possible to see that the cuttings samples tend to have higher grain densities than the gun samples.

LITHOLOGIC UNIT	NUMBER OF SAMPLES
Alluvium	2
Nonwelded tuff	18
Bedded and air-fall tuff	93

Table 4 Lithologic subsets and size.

Lithologic unit	Mean		St Dev	Mean of differences	Paired t-test
Nonwelded tuff	Cuttings	2.55	0.06	0.04	reject
	Guns	2.51	0.08		
Bedded and air-fall tuff		2.50	0.08	0.02	reject
		2.48	0.08		

significance level
$\alpha = 5\%$

Table 5 Summary of statistical tests for lithologic subsets.

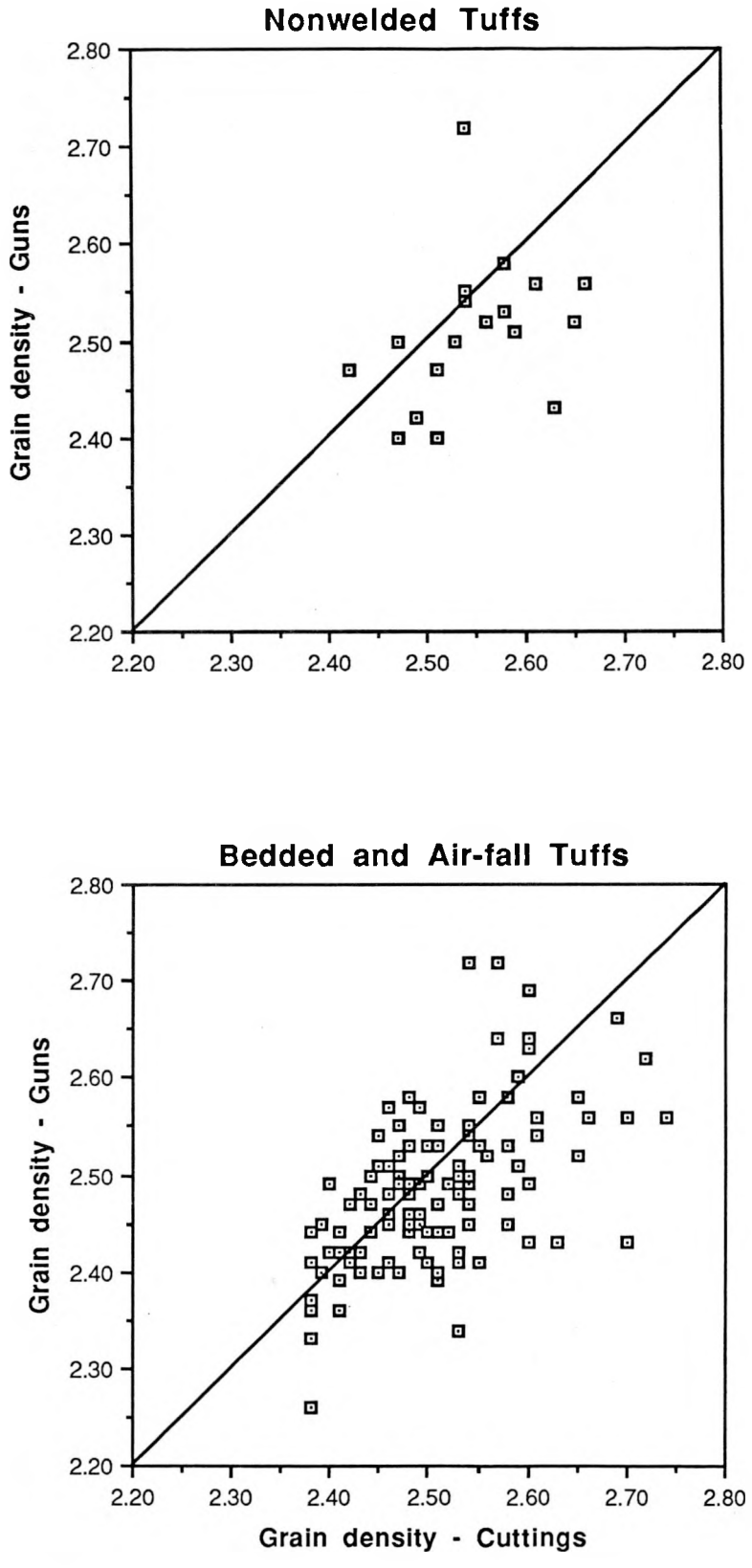


Figure 4 **Comparison of grain density measurements for cuttings and gun samples for lithologic subsets.**

SUMMARY

Plots of measured data and results from statistical analysis compared grain density measurements from cuttings and gun samples. Based on results shown in this paper, the following conclusions can be made. The measurements from cuttings samples tend to be higher than those from gun samples. The standard deviations for the two sample types are very similar. Stratigraphically, grain density measurements from the two sample types can not be distinguished for the Rainier Mesa Member and the Tunnel Beds. Measurements from the two sample types can be distinguished for the Paintbrush Tuff and the "induced zone". Lithologically, for nonwelded, bedded, and air-fall tuffs, measurements from cuttings and gun samples are distinguishable. But, in each case where the data can be statistically distinguished, the mean paired difference is small for the two sample types (ranging from 0.009 to 0.05 Mg/m^3).

The testing of the lithologic subsets probably shows the worst case for comparing grain density measurements for the two sample types. The subsets consisted of rock types that can show the highest degree of fractionation of components for the cuttings samples, while the gun sample is intact. The mean paired differences are small, ranging from 0.02 to 0.04 Mg/m^3. So, even when we compare the two sample types when we think they ought to be at their worst, the differences between the grain density measurements are small.

The procedure for measuring grain density is the same for both cuttings and gun samples at NTS. The accuracy in the measurements is about 0.03-0.05 Mg/m^3 (McKinnis, 1989b). When the accuracy in the measurement procedure is taken into account, the differences in the means of the tested data become insignificant. For this reason, and coupled with the additional cost of acquiring gun samples, grain density measurements from cuttings samples are adequate for calculating physical properties for containment application.

DISCUSSION

Several questions come to mind. (1) Is there any evidence that cuttings samples change as a result of drilling and/or turbulent flow so they are not representative of the in situ material (and should not be compared with gun samples)? The best way to examine this is to compare the grain density measurements where the cuttings samples might fractionate the most. The results of the t-test comparing the lithologic subsets (nonwelded and bedded and air-fall tuffs) show that the two samples types are indeed different populations. The value of difference, though, is small (0.04 Mg/m^3 for nonwelded tuff and 0.02 Mg/m^3 for bedded and air-fall tuff). These results also address the question concerning handpicking intact fragments of rock to obtain a "representative" sample. This is probably the worst case to test, and even though the sample types are statistically distinguishable, the differences are small and comparable to the measurement accuracy. The conclusion, then, for containment application is that cuttings samples do not fractionate to a degree to render them useless for grain density measurements. Comparison of grain density measurements from cuttings and gun samples is valid. (2) Does the quality of the collection and handling of the samples affect this study? Since the technique for collecting gun samples has changed little over time, this does not seem suspect. On the other hand, the procedure and the *quality* of the collection of cuttings samples has changed over time. The changes in the procedure probably do not affect the quality of the samples. Rather, the diligence of the sample collector is the most important control of the quality of the samples. We rely on a drill hand to collect a cuttings sample at the appropriate time, transfer it to the container for saving, and label it correctly. We know that cuttings samples collected in the past have been of varied quality, from completely doghoused to very good. We feel confident that the cuttings samples used in this study were collected

according to procedures, and quality was not compromised. Unfortunately, samples collected prior to when we had this high confidence may not be as good, and measurements on them are probably questionable. It is possible that for older holes, when our handling procedures may not have been operating optimally, the differences between cuttings and gun grain densities would be larger. However, cuttings samples obtained in the time frame of the samples used in this study and subsequently ought to be of high quality, and adequate for grain density measurements. (3) Are cuttings and gun samples from the same depth comparable? Or, asked another way, does the geology vary over a small distance in and across the hole, making the comparison of these sample types invalid? The farthest apart that the samples could logically be is 10', which is the normal separation of cuttings samples. As a geologist I do not believe that NTS geology, in general, varies by this small amount. One case that might cause a problem would be if the hole sloughed, contaminating the currently drilling sample with material from above. But, generally speaking, this does not happen frequently. Sloughing is usually recognized when the samples are examined, would be noted, and questionable samples would not be used as measurement locations anyway. Thus, comparison of cuttings and gun samples should not suffer because of sample collection location in a drill hole. (4) Can the conclusions from this study, i.e. there is no difference in grain densities measured on either cuttings and gun samples, be applied to a larger area, or should they be restricted to this small, structurally similar area until more data confirms the results? Because this study tests differences of *pairs* of data obtained at the same depth, and if (3) above is true, variation of other features can be ignored. This is the joy of using paired data! Variations in lithology and alteration should have occurred to both samples. The possibility that there are structural differences between the cuttings and gun sample acquired at the same depth (i.e. the occurrence of a fault) is low, and should be recognized by the geologist. Thus, the conclusions from this study can be extended to other areas.

ACKNOWLEDGEMENTS

The work was performed under the auspices of the U.S. Department of Energy by the Lawrence Livermore National Laboratory under Contract W-7405-ENG-48. This work was supported by the Nuclear Test Containment Program.

REFERENCES

Burkhard, N. R., 1989, Physical Properties in the LLNL Yucca Flat Areas: the Rock Pile Concept: in the proceedings from the Fifth Symposium on the Containment of Underground Explosions.

McKinnis, W. B., 1989a, personal communication, Lawrence Livermore National Laboratory, Nevada Test Site Geology Group Leader.

McKinnis, W. B., 1989b, personal communication, Lawrence Livermore National Laboratory, Nevada Test Site Geology Group Leader.

Wagoner, J. L., 1988, Procedures for handling drillhole samples: Lawrence Livermore National Laboratory internal memo CP88-104.

Geologic Structure and Related Topics



ABSTRACT

REVISED VOLCANIC STRATIGRAPHY OF THE SOUTHWESTERN NEVADA VOLCANIC FIELD

R.G. Warren,
Los Alamos National Laboratory,
P.O. Box 1663, Los Alamos, NM 87545

D.A. Sawyer, U.S. Geological Survey,
P.O. Box 25046,
Denver, CO 80225

and

H.R. Covington, U.S. Geological Survey,
P.O. Box 327,
Mercury, NV 89023

All principal and proposed areas for testing of nuclear weapons at the Nevada Test Site (NTS) are underlain by 6 to 16 Ma old volcanic units of the southwestern Nevada volcanic field (SWNVF). The most recent comprehensive stratigraphic treatment of volcanic units within the SWNVF was published in 1976. Since that time, detailed petrologic studies at Pahute Mesa, Yucca Flat, and Yucca Mountain have clarified several stratigraphic problems. Also, petrographic and chemical characterization of nonwelded tuffs regionally has established a comprehensive correlation of units between the principal testing areas. To incorporate these advances in stratigraphy, and to facilitate database management of geologic information, we propose a revised volcanic stratigraphy for the SWNVF.

We arrange all 6 to 16 Ma old volcanic units of the SWNVF into 10 major assemblages, each symbolized with a unique second letter. Examples are volcanics of Fortymile Canyon (Tf) and Wahmonie Formation (Tw). Each assemblage consists of units with petrologic characteristics readily distinguishable from units of assemblages above and below. Each unit represents eruption of a batch of magma significantly evolved from or unrelated to the next older unit and thus provides a very restricted but not necessarily geologically instantaneous stratigraphic datum. Unit symbols are designated by a unique third letter, e.g., Tpd for the rhyolite of Delirium Canyon. Variations in eruption mechanics may result in lithologic variations within each batch of magma which may be locally mappable as lithologic subunits. Additionally, zoned magmas may be erupted, or magmas from different crustal or mantle levels may be co-erupted, resulting in petrologic subunits. Symbols for each subunit are designated by a unique fourth letter, e.g., Ttsc for comendite lavas of Pillar Spring and Ttsy for trachyte lavas of Pillar Spring, both petrologic subunits, or Twlb for tuff of Wahmonie Flat, a lithologic subunit of the lower member of the Wahmonie Formation.

The proposed revised stratigraphy of the SWNVF offers several advantages for containment evaluation: (1) direct relation of stratigraphic experience among all test areas and user agencies; (2) a systematic and formal symbology for easier computer management of containment experience relative to stratigraphy; (3) less burdensome nomenclature consistent with current NTS usage, e.g., "rhyolite of Delirium Canyon" rather than "hornblende-bearing rhyolite flows of Scrugham Peak quadrangle"; (4) the hierarchy of units and symbols serves as guide for further research into causes for temporal and spatial petrologic variations within the SWNVF.

GEOLOGY OF THE U-1a.01 HORIZONTAL DRIFT COMPLEX, SOUTHWESTERN YUCCA FLAT, NEVADA TEST SITE

S. L. DRELLACK, JR.
P. H. THOMPSON
C. J. RAYBURN

FENIX AND SCISSON OF NEVADA, INC.
P.O. BOX 498
MERCURY, NV 89023

ABSTRACT

The U-1a.01 complex, site of the Los Alamos National Laboratory-sponsored Ledoux experiment, is located in southwestern Yucca Flat on the Nevada Test Site. The complex is comprised of the U-1a shaft, two large-diameter cable access holes, and approximately 229m of horizontal drift mined within unsaturated Quaternary alluvium 292.6m below the surface. Geologic mapping and related work afforded a unique opportunity to observe and evaluate the characteristics of alluvium in the subsurface of Yucca Flat, and to compare the results with surface and drill hole alluvium data. The Los Alamos Support Group of the Fenix and Scisson of Nevada, Inc. Geology/Hydrology Division carried out a program of mapping, sampling and photography while mining was in progress, with the dual purpose of characterizing the geology of the site and documenting the mining operation.

The geology observed at the U-1a.01 complex is consistent with present understanding of the geologic character and alluvial deposition of southwestern Yucca Flat. The complex is situated in an alluvium-filled, north-south trending structural basin bounded on the west by a fault scarp and on the east by west-dipping Tertiary volcanic rocks. The alluvium at the drift level is comprised of poorly sorted detritus from Paleozoic sediments and Tertiary volcanic rocks, deposited as coalescing fans debouching from higher terrain to the west. Deposition was intermittent and localized , forming highly discontinuous, poorly stratified deposits. Bedding and diagenetic features are typical of those observed in contemporary alluvial fan deposits. Gentle southwesterly dips in the alluvium bedding are believed to reflect post-depositional westward rotation of the basin block. Two small faults mapped in the drift probably are related to this structural adjustment. Tests performed on in-situ alluvium and drift samples provided information about the physical properties of the alluvium and aided in the site characterization.

Work at U-1a.01 was supported by the United States Department of Energy.

INTRODUCTION

U-1a.01 Drift Complex

The U-1a.01 drift complex is located in the southeast corner of Area 1, Nevada Test Site (NTS), at the U-1a vertical shaft (Figure 1). The complex is centered

about a 140.2m Main Access drift heading due south from the shaft, 292.6m below the surface.

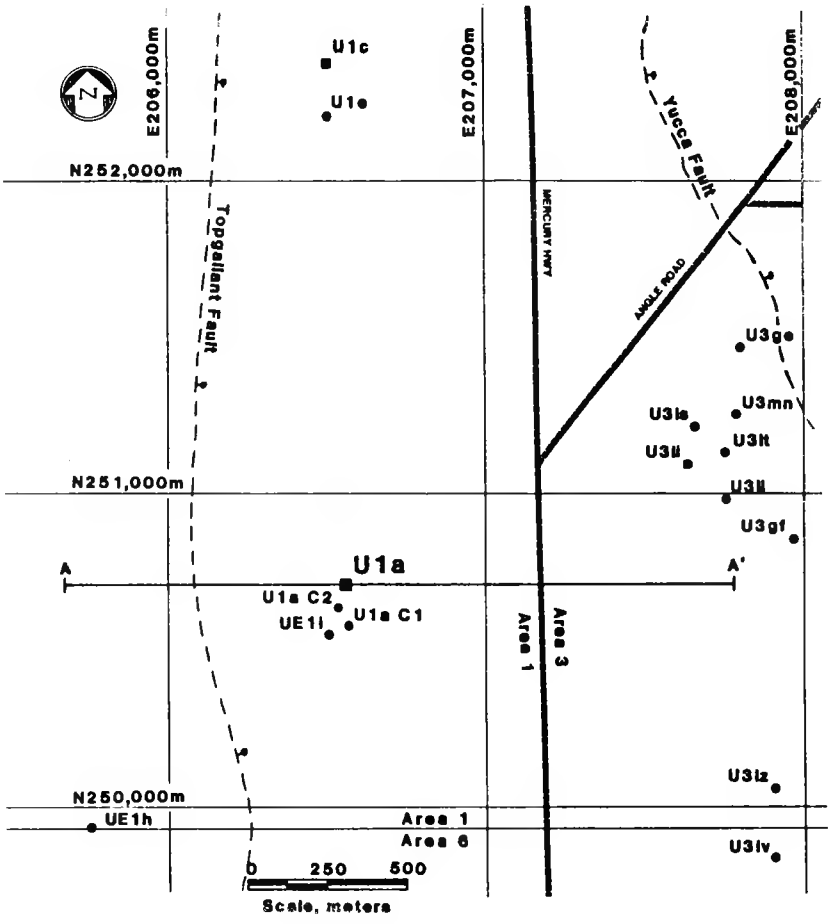


Figure 1--Area Map of the U-1a Site

The 3.1 x 4.9m U-1a shaft was mined in late 1968 and early 1969 to a total depth of 304.8m. The shaft is in excellent condition, and only minor renovation was required to ready it for use. Work on the U-1a.01 drift complex commenced with the opening of a mine station near the base of the shaft. The drifts and alcoves within the complex were mined between September 8, 1988 and December 9, 1988. Conventional mining methods were used, and a typical cycle of drilling, blasting and mucking advanced the drift face about 1.8m.

Operational Information

Our standard activities included mapping and photographing new exposures as they became available, sampling the alluvium for laboratory analysis and detailed description, and documenting the progress of the mining operation. These aspects are addressed in detail along with a complete presentation of the data in the report: "Geology of the U1a.01 Horizontal Drift Complex, Southwestern Yucca Flat, Nevada Test Site", DOE/NV/10322-37, March 1989. Analysis results, photographs, field maps and geologic notebooks are on file at the FSN Geology/Hydrology office in Mercury, NV.

Geologic Setting

The U-1a.01 complex is mined entirely within unsaturated Quaternary alluvium. The alluvium at U-1a.01 is estimated to be 550m thick. It is underlain by approximately 350m of Tertiary volcanic tuffs. The uppermost tuff unit is presumed to be the Rainier Mesa Member of the Timber Mountain Tuff, based upon projection from drill holes UE-1r and UE-1k, which lie along the axis of the structural basin in which U-1a.01 is located. These Tertiary tuffs are underlain by Paleozoic carbonates and minor clastic rocks. Surface gravity data from the U.S. Geological Survey indicate the disconformable Tertiary/Paleozoic contact at an approximate depth of 900m. Static water level is estimated at 490m below the surface (Doty and Thordarson, 1983). A generalized west-east cross-section of the site is shown in Figure 2.

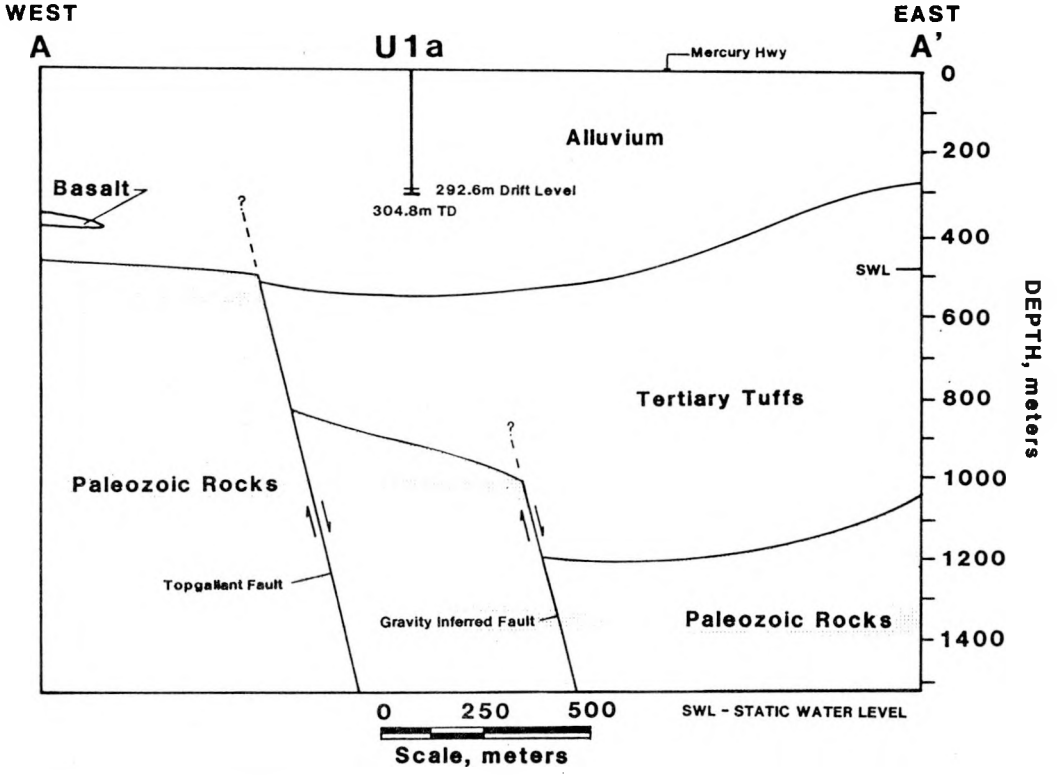


Figure 2--Generalized West-East Cross-Section Through U-1a

The nearest significant fault to U-1a.01 is the north-south trending, east-dipping Topgallant Fault, approximately 480m to the west. The surface trace of the east-dipping Yucca Fault is approximately 1580m to the east.

Stratigraphic control for the alluvium overlying the drift complex is based upon two cable holes drilled for the experiment, U-1a C-1 and U-1a C-2, and exploratory hole UE-1i, 160m south-southwest of the U-1a shaft. The two cable holes were intercepted by the drift complex. This allowed comparison of borehole data with data obtained directly from subsurface alluvium. A discussion of this comparison is included in this report.

U-1a.01 GEOLOGY

On a gross scale, the composition and character of the U-1a.01 alluvium does not vary throughout the drift complex. Sediment source and distance to this source, as well as mode of transport, remained uniform during deposition. The alluvium is termed "mixed alluvium" due to its significant percentage of Paleozoic detritus, following the informal NTS/Yucca Flat convention where mixed alluvium contains greater than 5% Paleozoic rock fragments (Wagoner and McKague, 1984).

The geologic cross-sections of the U-1a.01 drifts (Figures 4,5&6) are derived from the following descriptions and interpretations of U-1a.01 geology.

Deposition and Bedding

The alluvium in the U-1a.01 area is composed of slightly to moderately indurated channel, slope wash and debris flow deposits. These deposits are a heterogeneous mixture of detritus from Tertiary volcanic rocks, primarily ash-flow tuffs, and Paleozoic carbonates with lesser Paleozoic clastic sediments. Deposition of the alluvium was intermittent and localized, forming highly discontinuous, interfingered, poorly stratified deposits. The large lenticular units recognizable on the north-south geologic cross-sections (Figures 4,5&6) imply that many of the beds could be channel deposits or semi-confined slope wash deposits.

Grain sizes range from silt and clay to cobbles and small boulders. Percent ranges for clast sizes in individual map units are given in Table 1.

Table 1--Percentage Ranges for Clast Sizes in Individual Map Units[1]

Map Unit (bed type)	Cobbles %	Pebbles %	Sand %	Silt %	Clay[2] %
Type 1 (sand bed)	0-1	6-19	64-85	4-16	1-4
Type 2 (sandy pebble bed)	0-5	10-50	46-72	3-9	0-3
Type 3 (pebbly cobbly sand bed)	5-20	10-30	42-65	2-11	1-6
Type 4 (cobbly sandy pebble bed)	0-10	25-54	36-62	3-5	1-2
Type 5 (cobble bed)	25-40	10-30	40-60	8-9	2-3

[1] Pebble through clay size analysis by Holmes & Narver Material Testing Laboratory; percent cobbles estimated by the authors.
[2] Includes all colloidal-sized material

The alluvium generally is poorly sorted; a few beds, particularly minor sand beds and some channel fill deposits, approach moderate sorting. Individual clasts are subrounded to subangular. The average bed dip is 3-5° southwest and ranges from 0-10°, with locally steeper contacts reflecting depositional boundaries. Proximity to sediment source is suggested by poor sorting, a relative abundance of coarse material, and degree of rounding. The lack of well-developed soil horizons reflect a dynamic depositional environment.

Mappable beds in the drifts generally range from 15cm to 1m thick. The more massive, coarser beds typically are thickest, while finer grained intervals (e.g. relatively well-sorted sand beds) usually are thinner, more well-bedded and more laterally extensive than coarser beds. Intervals are often so finely intercalated that separation of individual units is impractical. It was necessary in such instances to interpret the gross lithology of the interval as a whole.

Cut and fill channels are a common feature in the U-1a.01 alluvium. Present-day analogies of these channels are conspicuous on active alluvial fans in the region. Channels recognized during mapping typically were 1.0-1.3m wide by 30-60cm thick, and displayed a lenticular cross-section which often appeared asymmetrical in drift exposures. Randomly skewed symmetry, especially when evident on adjacent ribs, implies channel meandering. Larger lenticular features, not recognizable during mapping of individual faces, became evident as units were correlated between faces on the north-south cross-sections and are also interpreted as channel deposits. Lower channel contacts are sharp and distinct, while upper contacts often are gradational. Channels occur in all bed types, but are most frequently scoured into a sandy bed. Typical fill material is moderately sorted pebbly gravel.

An evaluation of depositional flow direction based upon more than intuitive evidence is difficult to make. Probable rapid, chaotic deposition of much of the coarser material, as well as the blocky character of many of the clasts, were not conducive to the development of an imbricated fabric. Flow direction is also difficult to glean from channel orientation due to lack of channel continuation between exposures and to the probability of channel meandering. In the few instances where channel orientation could be estimated, the channel axes range from southwest-northeast to northwest-southeast and average roughly west-east, or subparallel to present bed dip. Poorly-developed imbrication implying a general west-to-east flow was also noted in a few isolated pebble beds with longitudinal exposure.

Vertical gradation within beds and between beds is common in the U-1a.01 alluvium. It is more characteristic of thin, finer-grained beds (e.g. sands and small pebbles). The gradation is normal (i.e. finer upward) and is on a comparatively small scale, typically occurring across less than a meter. It appears to reflect relatively slower and more steady fluvial deposition than that implied by the more chaotic fabric of the coarser units. Lateral gradation, less common than vertical gradation, occurs most often in thicker, coarser units. A notable occurrence is within the largest channel deposits, which in addition to commonly displaying vertical gradation, often grade laterally from coarse in the thickest part of the deposit to finer near the edges. Lateral gradation occurs on a larger scale than vertical gradation, typically across several meters. When interpreting the geologic cross-sections (Figures 4,5&6), it should be noted that the combination of bed assignment and the visual effect of drawn

contacts gives the mistaken impression that vertical gradation between beds is absent or infrequent.

Lithology

For mapping purposes, the U-1a.01 alluvium is divided into five units based upon relative abundance of sand, pebble and cobble size clasts as defined by Wentworth. The units incorporate the less discernable silt and clay with sand. Similarly, granules are included with pebbles for convenience, and boulders are included with cobbles because of their relative scarcity. These "map units" (Figure 3) developed as the most flexible and practical divisions to apply to the drift alluvium. Although constraints on time and access did not allow a detailed description of each individual bed exposed in the drifts, the five map units were applied consistently throughout the mapping.

There is a tendency in field mapping to "weight" coarser material over finer material (for example, the idealized pebbly sand bed would usually be identified in the field as a sandy pebble bed). By incorporating laboratory size analysis data from samples (Table 1) into the unit descriptions, this strong visual bias is reduced to an academic issue. The lithology of the map units is described in detail in Table 2; bed characteristics and occurrences for each type are also included.

Note--see Table 2 for detailed lithologic descriptions and characteristics of individual map units.

Ranges for map units based upon size analysis by H&N.

a includes silt and clay
b includes granules
c includes boulders

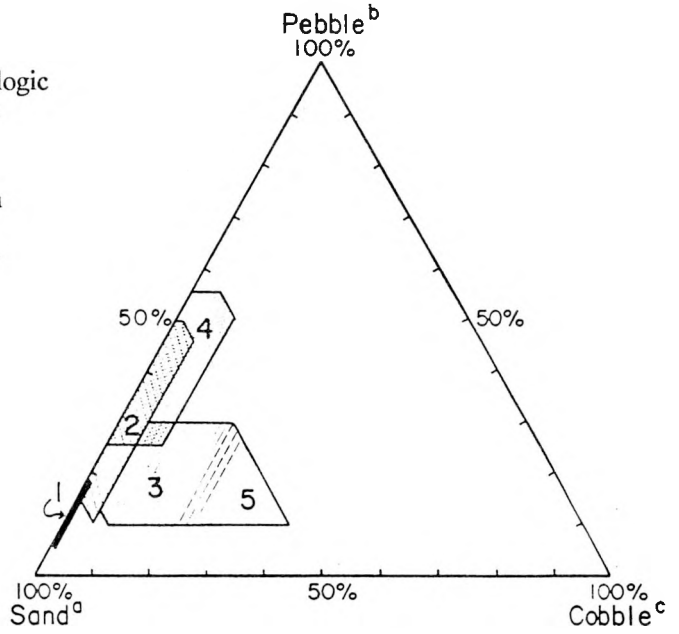


Figure 3--Ternary Diagram Showing Grain Size Distribution for Map Units

the most prevalent lithology is type 4, accounting for over 40% of the drift alluvium. This unit can be visualized as the "matrix" in which other, more conspicuous bed types occur. Type 4 commonly occurs as highly intercalated intervals in which beds are too thin, discontinuous and gradational to be mapped individually. Also included in this unit are poorly sorted, massive mixtures of sand and pebbles with minor cobbles, interpreted as debris flow deposits. The most continuous and discrete lithology, on the other hand, is the type 1 sand

Table 2--Detailed Lithologic Descriptions, Bed Characteristics and Occurrences for U-1a.01 Map Units

Lithologic Description[1]	Bed Characteristics and Occurrences
Type 1--"Sand Bed"	
Moderate-yellowish-brown (wet color); fair to moderate induration is supported by caliche (sample disaggregates to small chips in water; these gradually disaggregate completely in HCl); slightly to moderately calcareous; relatively well sorted; rounded to subangular; coarser sand is richer in Paleozoic lithologies than finer sand; overall sand fraction averages 60-70% tuffaceous material (loose felsic and mafic phenocrysts, pumice, intact tuff fragments), 30-40% Paleozoic lithologies (siltstone, limestone, dolomite, quartzite); pebble fraction is roughly half tuff and half Paleozoic lithologies, with trace dark-reddish-brown rhyolitic lava; trace white, highly calcareous, "case-hardened" pumice occurs sporadically throughout drift in association with finest, siltiest sands, perhaps indicating pedogenic development; pebbles have poorly-developed (thin and patchy) caliche rind; trace MnO_2 dendrites on larger siltstone clasts.	Massive to bedded; matrix-supported; contains 5-20% pebbles and variable amounts of sand, silt and clay; some beds approach unimodal grain size distribution; beds commonly 15-60cm thick, rarely thicker than 60cm; fluvial deposition (more unimodal beds possibly eolian?); greater lateral continuity than other bed types; caliche present as a disseminated cement and rarely as thin horizontal or vertical stringers; more likely than other bed types to have pedogenic development (rarely displays "vesicular A horizon" soil development); comprises approximately 15% of U-1a.01 alluvium.
Type 2--"Sandy Pebble Bed"	
Overall dark-yellowish-brown, sandier samples are moderate-yellowish-brown; slightly indurated, caliche rinds around pebbles commonly form highly indurated aggregates; slightly to moderately calcareous; fair to moderate sorting; subrounded to subangular; pebble fraction ranges from 50-90% Paleozoic lithologies (typically 50% carbonates, 50% other lithologies) and 10-50% tuff; sand fraction ranges from 30-60% Paleozoic lithologies (Paleozoic content increases where sample pebble content increases); perhaps half of pebbles have well-developed caliche rind, remainder have thin, patchy rind; rare pebbles in isolated, highly porous pockets coated with drusy calcite crystals; MnO_2 dendrites common on siltstone clasts.	Typically bedded, rarely massive; typically clast-supported, can be matrix-supported in sandier, massive intervals (debris flow?); contains less than 65% sand and silt, and less than 5% cobbles; individual mappable units are 15cm to 1.2m thick; often occurs as well-sorted channel deposits or in discontinuous lenses; channels display asymmetric profile, implying meandering character; often displays normal (finer-upward) grading; minor imbrication noted in isolated channel deposits; comprises 35-40% of U-1a.01 alluvium.
Type 3--"Pebbly Cobbly Sand Bed"	
Moderate-yellowish-brown to dark-yellowish-brown; poorly indurated; highly calcareous due to high carbonate content and caliche rinds; poorly sorted; larger clasts are subangular, remainder is subrounded to subangular; cobbles average 65% limestone, 35% quartzite and other Paleozoic lithologies; pebble fraction averages 65% Paleozoic lithologies, 35% tuff, trace lava; sand fraction averages 60% tuffaceous material, 40% Paleozoic lithologies; most larger grains have well-developed caliche rinds.	Typically massive; cobbles and pebbles supported within a sandy matrix; typically contains 5-20% cobbles, 20% pebbles and 70% sand and silt; bimodal; beds tend to be relatively thick, 0.6-1.2m; possible debris flow deposition; lateral gradation often evident; vertical gradation not uncommon with overlying units, much less frequent with underlying beds; comprises approximately 5% of U-1a.01 alluvium.

Type 4--"Cobbly Sandy Pebble Bed"

Moderate-yellowish-brown; poorly to slightly indurated (finer material is more indurated); moderately to highly calcareous; poorly sorted; larger clasts subangular, remainder subrounded to subangular; well graded from cobble to silt; grain size content varies widely, averaging 60% sand/silt and 40% pebble/cobble; pebble/cobble fraction is predominantly limestone and dolomite, with minor quartzite and tuff (smaller pebbles are richer in tuff than larger pebbles); sand averages 50% Paleozoic lithologies and 50% tuffaceous material; larger clasts have well-developed caliche rinds in part, remainder have thin, patchy rind.

Typically thinly bedded and clast-supported (fluvial); rarely massive and matrix-supported (debris flow); typically contains 40% pebbles, 55% sand and silt and 5% cobbles; bimodal; mappable units 15 cm-1.2 m thick; massive (debris flow) intervals usually thicker than thinly bedded (fluvial) intervals; poorly sorted overall, although individual beds sometimes display moderate sorting; can exhibit both lateral and vertical gradation. Intercalated beds too thin to map individually were included in this description. This is the most common bed type, comprising 40-45% of U-1a.01 alluvium, and can be visualized as the "matrix" in which other, more discrete bed types occur.

Type 5--"Cobble Bed"

Moderate-yellowish-brown to dark-yellowish-brown; poorly indurated; highly calcareous due to carbonate content and caliche rinds; poorly sorted; subrounded to subangular, largest clasts tend to be blocky rather than elongate; cobbles typically 75% limestone, 25% quartzite and other Paleozoic lithologies; pebble fraction predominantly Paleozoic lithologies; sand fraction averages 60% Paleozoic lithologies, 40% tuffaceous material; most larger grains have well-developed caliche rinds.

Massive; clast-supported, cobble interstices filled with smaller clasts and sand; typically contains 30% cobbles, 50% sand/silt and 20% pebbles; bimodal; beds generally 15-30cm thick and laterally discontinuous, pinching out within 4.6m; sometimes present as coarsest material in channel fill deposits. This is the rarest of bed types in U-1a.01, comprising 1-2% of the alluvium.

Fault Gouge (sample 120588D, 4+54, Main Access Drift)

Silty Sand: Moderate-brown; moderately to highly indurated; chips soften but do not disaggregate in HCl, suggesting presence of clay; slightly to moderately calcareous; moderately well sorted; subrounded to subangular; grains show no evidence of grinding or breakage due to fault movement; 10% silt/clay, 71% sand, 19% pebble; grain size percentages and lithology are typical of sandier "type 2" bed; pebbles have well-developed caliche rinds in part, with common highly indurated aggregates formed by caliche rinds around pebbles; several pieces of sample display small slickensides.

This lithology occurs as gouge in a minor fault mapped at the south end of the Main Access drift between 4+42 and 4+60. The gouge was 1-2cm thick and intermittent.

---

1 The terms explained below are applied in these descriptions specifically to U-1a.01 alluvium, and are meant only to highlight the relative differences between the mapping units. They should not be confused with their wider usage as descriptive terms for tuffs and other NTS rocks.

Induration: The alluvium, on a whole, probably would be considered "poorly indurated" or "slightly indurated" when compared with other rocks at the NTS.

Calcareousness: Most of the alluvium would be considered "highly calcareous" when its reaction with dilute HCl is compared to that of other rocks at the NTS.

Sorting: Most of the U-1a.01 alluvium would be considered a "poorly sorted" sedimentary deposit, reflecting the wide mixture of grain sizes inherent in a proximal alluvial fan.

bed. These thin, uniformly brown beds sometimes could be correlated from face to face for over ten meters. Cobble beds, designated type 5, are the rarest map unit, comprising only 1-2% of the alluvium. Table 2 includes estimates of the relative abundance of each of the five map units. These estimates are based upon the measured thicknesses of individual beds in face exposures, and take into account lateral discontinuity (the tendency of certain units to pinch out or grade into another bed type over short distances). It should be noted that lower portions of freshly mucked faces sometimes were obscured by sandy muck residue; in other cases, mud generated by the drilling of shot holes for blasting covered features beneath the holes. It is possible that non-type 4 beds may have been inadvertently mapped as type 4 in such instances.

The largest clasts in the U-1a.01 alluvium, the coarser pebbles and cobbles, are predominantly Paleozoic limestone and dolomite, with minor quartzite and rare Tertiary tuff fragments. High Paleozoic content is also reflected in relatively high bulk densities on the gamma-gamma density logs from the two U-1a.01 cable holes (averaging 2.0 gm/cc below 150m depth), and in relatively high grain densities for U-1a.01 samples (averaging 2.61 gm/cc). The lithology of smaller pebbles, granules and coarse sand varies according to occurrence; the matrix associated with coarser Paleozoic clasts tends to be higher in Paleozoic clasts than the more well-sorted fine grained beds. Siltstone often comprises a significant portion of smaller pebbles and sand in these Paleozoic-rich matrixes. The more well-sorted, finer-grained beds are composed primarily of tuffaceous lithologies. Small pebbles and granules in these beds are variable proportions of intact tuff fragments and Paleozoic lithologies, while the sand is rich in pumice and mineral components weathered from tuffs (i.e. quartz, feldspar and mafic minerals). Based on sample lithologic descriptions and field observations, the alluvium as a whole is estimated to contain 20-30% Paleozoic carbonate clasts.

Structure

The U-1a.01 complex is located within a north-south trending structural basin along the western side of Yucca Flat. This basin is bounded on the east by west-dipping Tertiary volcanic beds and on the west by a north-south scarp on the Paleozoic rock surface, a southern projection of the Topgallant Fault, a normal fault downdropped on the east and located about 480m west of U-1a.01. The present surface surrounding U-1a is a distal alluvial fan which dips gently southeastward. Bedding attitude remains quite consistent throughout the complex, averaging 3-5° to the southwest. Apparent dips measured in drift exposures did not vary significantly from true dip. A northwest strike, consistent with southwest dips, is substantiated by detailed correlation of dry hole resistivity logs from the two U-1a.01 cable holes. These logs indicate virtually no apparent dip in bedding between the two holes, suggesting strike subparallel to the N35W line delineated by the holes. Although alluvial fan deposition can account for gentle bedding dip, westerly dip is contrary to that which could be expected from the inferred west-to-east depositional flow direction. The observed dip is believed to reflect post-depositional westward rotation of the basin block due to dip-slip movement along the Topgallant and/or Yucca Fault(s).

As might be expected, no fractures or joints were noted in the alluvium. Two very minor faults, similar in character and probably related to the structural adjustment suggested by bedding attitude, were mapped near the south end of the

Main Access drift. One fault, first noted at 4+42 (134.7m) (see Explanation in Figure 6 regarding the 4+42 nomenclature) and followed through to the drift end at 4+60 (140.2m), strikes N10E to N15E and is nearly vertical, dipping 80+° to the southeast. Displacement is down on the east (normal) and measures between 30-45cm. A thin (1-2cm), intermittent gouge, more indurated and finer grained than the surrounding alluvium and displaying rare, small slickensides, was sampled in two locations for detailed analysis. The clay content of these samples, measured by X-ray diffraction, is only slightly higher than average compared to other samples, and CO_2 content also is comparable to that of other samples. The mineralogy of the fault gouge does not appear to differ significantly from typical drift alluvium. A lithologic description of the gouge is included in Table 2. A second fault, mapped between 3+52 (107.3m) and 3+72 (113.4m), was much less conspicuous due to absence of gouge, and could be identified only discontinuously where exposed. Strike is estimated at N15E and dip, where measurable, varies between 63° and 80° southeast. Displacement is again approximately 30cm down on the east. Strike-slip movement along these faults is indeterminate, but is probably not significant based on the known tectonic character of Yucca Flat.

Induration

Induration of the alluvium in the U-1a.01 complex is controlled by several factors, including disseminated calcium carbonate (caliche) cement, grain interlocking and overburden pressure. Caliche cement is most evident in sand beds and in the sandy matrix of poorly sorted coarse beds, both of which tend to disaggregate more readily in dilute HCl than in water. Minor silt and clay also impart cohesiveness to the finest and most competent of the beds. In general, the alluvium is slightly friable, capable of being excavated with a rock pick but quite competent in vertical exposures, and is therefore termed moderately indurated. Nonindurated eolian sand lenses, which have caused sloughing problems in a few Yucca Flat drill holes, were not encountered. Slabbing and caving were only a minor problem during the mining operation, and appeared related to well-sorted, friable pebble beds frequently encountered in the drift back. Parting along bedding also may have contributed to caving.

Caliche

Rinds on coarser clasts are the most conspicuous occurrence of secondary calcium carbonate (caliche) in the U-1a.01 alluvium. Caliche is pervasive also as finely disseminated cement in finer material, and is present rarely as poorly-developed horizontal and vertical stringers in sand beds. Well-developed caliche beds or highly-cemented strata were not observed. Caliche rinds, formed on clasts at or near the surface, are ubiquitous in the alluvium, coating most grains larger than 0.5cm in size. The rinds typically are discontinuous, perhaps due to abrasion, but can be fairly well-developed, averaging 1mm thick and ranging up to several millimeters thick on the larger pebbles and cobbles. They tend to be thicker and more developed on carbonate clasts and in association with higher-carbonate intervals, but occur on all lithologies. The rinds often are thickest on the undersides of clasts. Caliche deposition in U-1a.01 would be characterized as Stage I and II based upon the morphologic classification of Gile, Peterson and Grossman (1966).

Euhedral calcite coatings up to 3mm thick occur on pebbles in rare, isolated "pockets" about 30 - 60cm in diameter. These coatings are deposited over pre-existing caliche rinds. Larger clasts in the alluvium sometimes display post-depositional fracturing due to adjustment to overburden pressure; in several instances, euhedral calcite coatings covered or infilled such fractures. This indicates that the euhedral coatings were deposited at depth, presumably by $CaCO_3$-saturated groundwater in open pores within relatively permeable, well-sorted gravels.

Comparison With Cable Hole Wellbore Geologic Data

Work at the U-1a.01 complex provided a unique opportunity to directly compare and correlate geologic data from the drift level of the two cable holes with in-situ alluvium. U-1a C-1 was percussion gun sidewall sampled and logged with the LANL Borehole Inspection System (BIS) prior to being intersected by the drift complex, and a full suite of geophysical logs is available from both holes. Cuttings samples from both holes were logged at the USGS Core Library in Mercury. Comparison of borehole physical properties data with those derived from drift samples is included in the "Sample Analysis and Physical Properties Tests" section.

Samples of muck from the immediate vicinity of U-1a C-2 provided insight into the effects that drilling, sample catching and processing have on alluvium cuttings samples. Before washing, the muck samples consisted primarily of intact, slightly friable alluvium fragments. They were subjected to the same washing and screening cycle that washed cuttings routinely undergo during sample preparation at the USGS Core Library, and were still found to contain predominantly intact alluvium. Dry sieving was necessary to disaggregate the muck samples into their individual components. Intact alluvium fragments are virtually nonexistent in borehole cuttings samples from the drift level. This indicates that drilling can disaggregate even the moderately indurated alluvium found in the drift, and that degree of induration in alluvium is impossible to gauge from cuttings samples.

Comparison of the sample components suggests that the coarse sand to small pebble fraction of alluvium is better represented in washed cuttings than the finer and coarser materials. Washed cuttings sand is enriched in Paleozoic material, which is typically coarser than tuffaceous sand. The pebble fraction of the cuttings is enriched in unbroken tuff clasts, which tend to be smaller and more rounded than Paleozoic clasts and are perhaps less likely to be broken by drilling. Freshly broken pieces of larger Paleozoic clasts are indeed present in the cuttings, however the quantity is considerably less than the quantity of coarse material observed in the borehole alluvium at drift level. These discrepancies may result due to processes inherent to the drilling process, sample catching techniques, sample processing procedures, or a combination of these factors.

The abundance of coarse material throughout the U-1a.01 drift complex, as well as the alluvium's thinly bedded, highly discontinuous character, suggest that percussion gun samples from this level could prove misleading. Individual percussion gun samples from the drift level of U-1a C-1 reflect the lithology of a single bed, or at best a contact between two beds, and give only a clue of the lithology of the alluvium as a whole. Multiple samples from an interval might represent the alluvium more accurately, as would reconciling percussion

gun data with evidence of bedding or coarse material visible on BIS videotapes. The BIS Camera run at U-1a C-1 revealed little pertinent geological information at the drift level due to wallcake. Where the borehole is exposed in the drift, wallcake is visible as a thin, persistent mud coating which adheres tightly to the porous alluvium and completely obscures the bedding visible in the adjacent drift.

SAMPLE ANALYSIS AND PHYSICAL PROPERTY TESTS

Porosity and Permeability

Short of in-situ testing, the porosity of the U-1a.01 alluvium can only be estimated or inferred from cable hole geophysical data. It is assumed that porosity depends upon both degree of sorting and silt/clay content. Grain interstices in the alluvium are typically infilled with finer material; open voids or large pores are evident only in rare, isolated pockets within relatively well-sorted pebbles. Euhedral calcite coatings were commonly noted in these pockets, and size analysis confirmed low silt and clay content in association with calcite-coated pebbles. Silt and colloid contents determined by Holmes & Narver suggest that while porosity could be expected to vary on a small scale between the different bed types, overall porosity does not vary significantly throughout the drift complex.

Using grain density measurements from nearby hole UE-1i and bulk density and water content values from the two U-1a.01 cable holes, calculated porosity at drift level falls between 25-30%. This range is somewhat below average compared to previously calculated porosities for southern Yucca Flat alluvium, and probably reflects poorer sorting. Using data from the cable holes, saturation is calculated at 52%, roughly average for southern Yucca Flat alluvium.

Permeability probably varies directly with porosity in U-1a.01 alluvium, due to the poorly sorted, relatively coarse nature of the material. Soil development, although weak in U-1a.01 sediments, would effectively reduce permeability where present. It therefore seems reasonable that horizontal permeability should be slightly higher than vertical permeability over distances greater than several bed thicknesses (i.e. >1-2m). In-situ permeability tests were performed in the Main Access drift and in the U-1a shaft by Science & Engineering Associates, Inc. Measured permeability in the Main Access drift fell between 0.02-3.0 darcies, with an average value of 0.6 darcies for thirteen tests. While these data indicate significant permeability variation between several different test locations along the Main Access drift, the range compares well with published permeability values for sediments similar to U-1a.01 alluvium (Fetter, 1980). It should also be noted that the permeability measurements were made over relatively short distances and sub-parallel to bedding planes.

Tests in the U-1a shaft indicate a general decrease in permeability with depth, as would be expected with decreasing porosity due to increasing compaction. The results also suggest that permeability is lower than that measured in alluvium at the U-1c vertical shaft, approximately 1.7km north of U-1a (Keller et al., 1973).

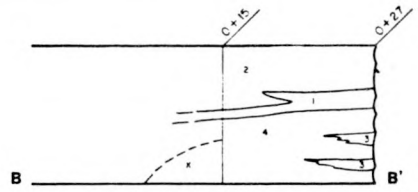
Carbonate Content

Representative splits of selected U-1a.01 samples were analyzed for carbonate content by the Environmental Sciences Division of REECo. CO_2 content averages 11% in the 40 samples analyzed. This figure equates to an average alluvium carbonate content of 25%, which is consistent with the 20-30% average carbonate clast content estimated from field observations and sample descriptions. A plot of CO_2 content versus pebble content indicates a high carbonate content in the pebble fraction in U-1a.01 alluvium. A similar correlation exists in nearby drill holes U-1e, U-1d and UE-1i. Although individual sample results vary widely, the data also indicate that average carbonate content is lower in finer beds (types 1 and 4) and higher in coarser beds (types 2 and 5). The data suggest that the relative contribution of caliche to alluvium carbonate content is insignificant compared to that of limestone and dolomite clasts. This conclusion is also supported by the lack of well-developed caliche beds in the complex, and by the observation that caliche rind development varies directly with carbonate clast content.

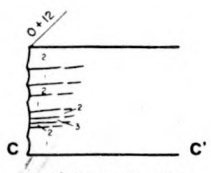
H_2O Content

The measured water content of several samples collected from freshly exposed faces ranges from 4.4% to 10.4% and averages 7.2% by weight. As might be expected, higher water contents generally occur in finer-grained beds. The samples analyzed were considered "typical" drift alluvium and were similar in character to samples collected throughout the drifts, suggesting that water content does not vary significantly. Samples and exposed faces displayed gradual color and apparent textural changes over several days, reflecting progressive water loss.

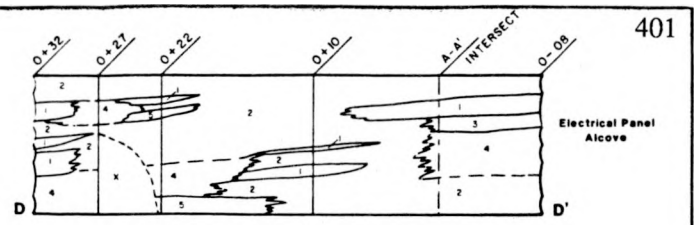
Water content derived from Epithermal Neutron log data from the 291.1 $\pm$ 10m interval (drift level) of the U-1a.01 cable holes averages 8.2% for U-1a C-1 and 9.0% for U-1a C-2, slightly higher than the measured drift sample values. While invasion of drilling fluid into the borehole wall may account for the difference, measured and calculated values seem in reasonable agreement. Calculated water contents for the cable holes agree closely with those from unsaturated alluvium in the nearest emplacement holes.



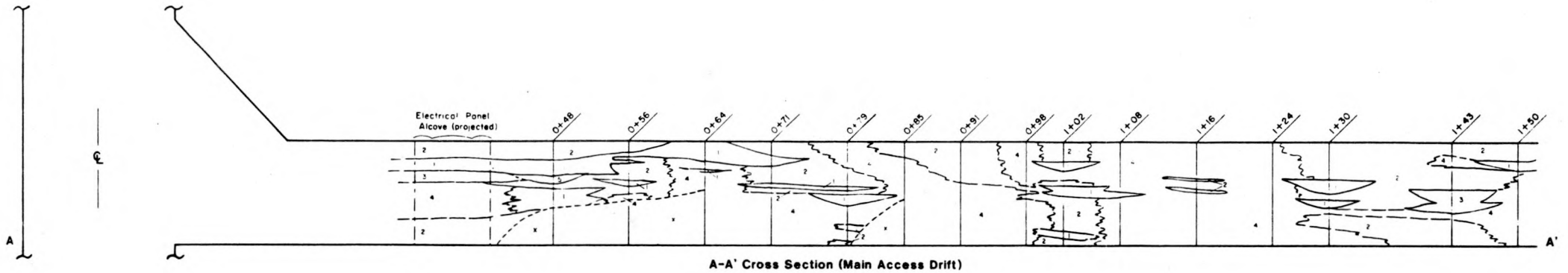
B-B' Cross Section (North Refuge Chamber)



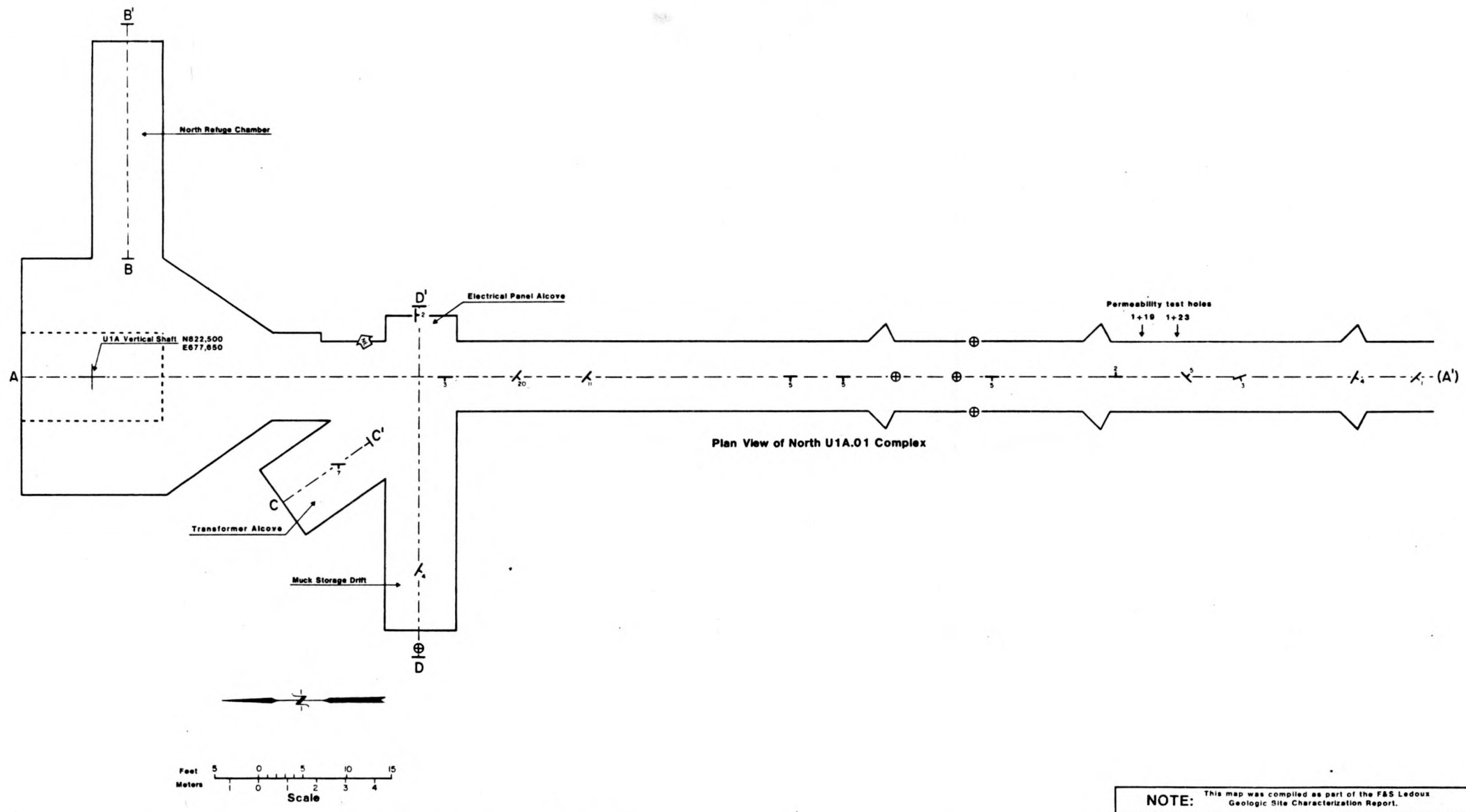
C-C' Cross Section (Transformer Alcove)



D-D' Cross Section (Muck Storage Drift)



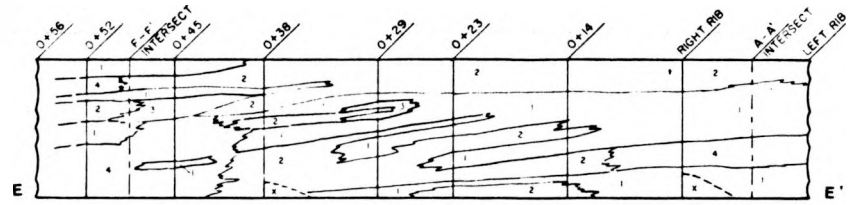
A-A' Cross Section (Main Access Drift)



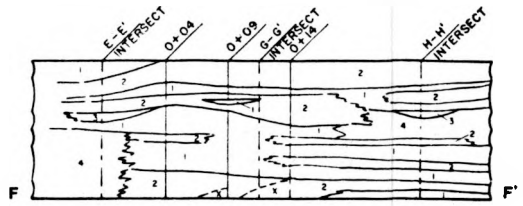
Plan View of North U1A.01 Complex

Figure 4--Geology of the North Section of the U-1a.01 Drift Complex

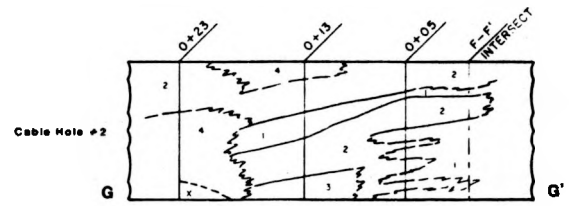
NOTE: This map was compiled as part of the F&S Ledoux Geologic Site Characterization Report.		
NOTE: For explanation of symbols, see southern portion of this map.	Date 1-18-89	Sheet 1 of 3
	Geology by: Dreiack, Thompson, Rayburn	Drawn by: PHT



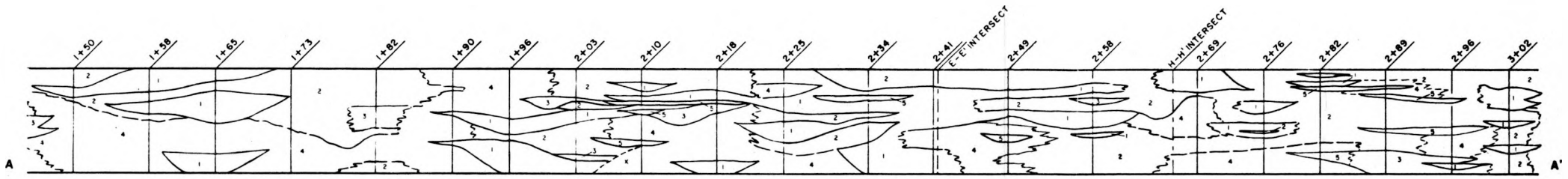
E-E' Cross Section (CH2N Drift)



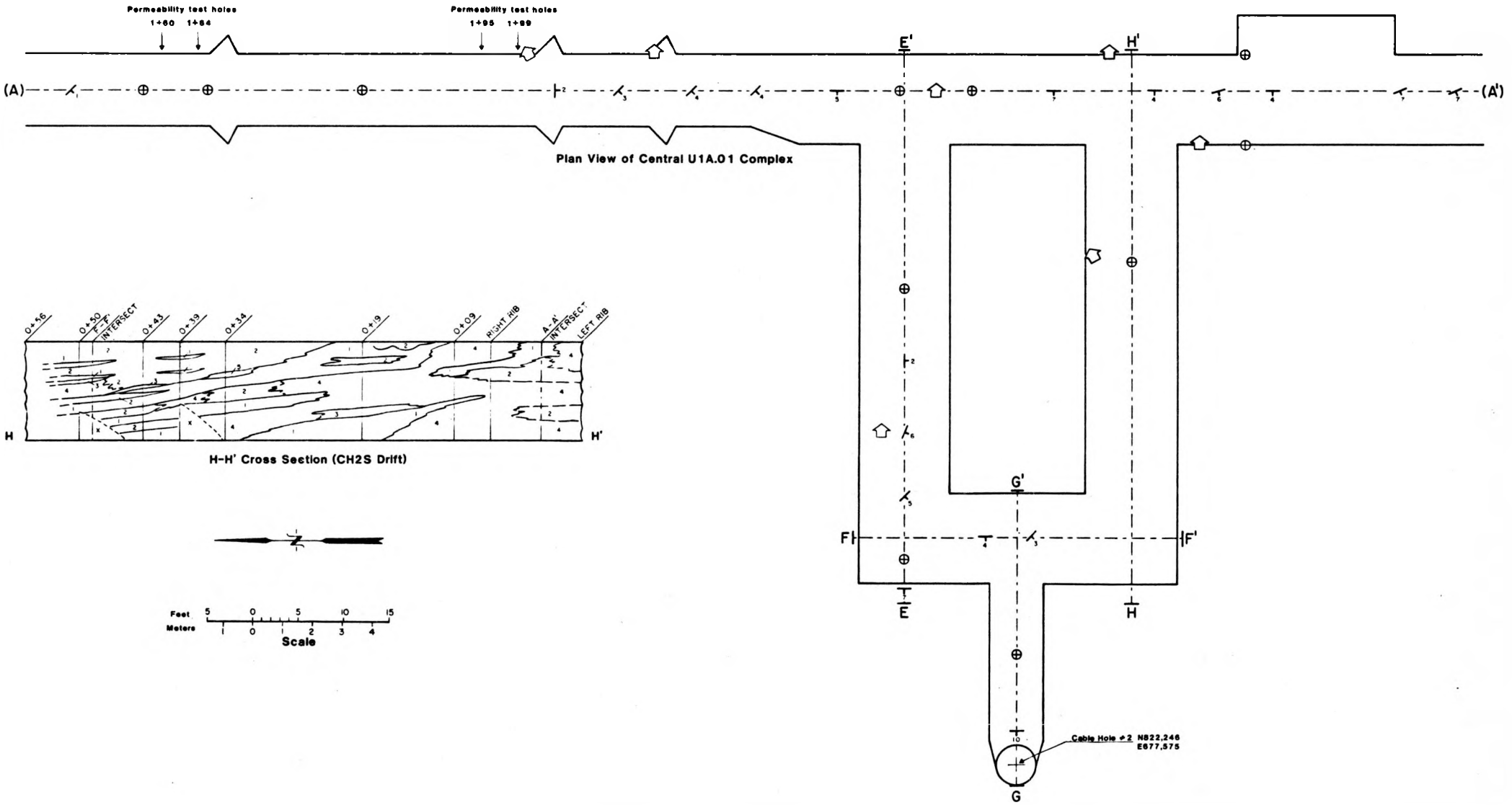
F-F' Cross Section (CH2NS Drift)



G-G' Cross Section (CH2 Intercept Drift)



A-A' Cross Section (Main Access Drift)

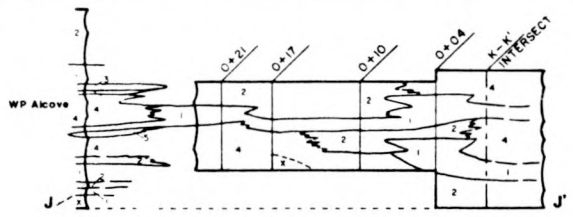


Plan View of Central U1A.01 Complex

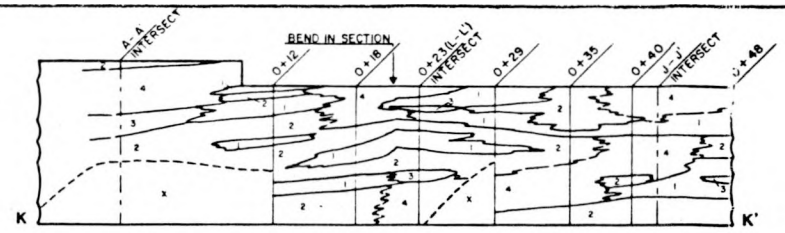
H-H' Cross Section (CH2S Drift)

Figure 5--Geology of the Central Section of the U-1a.01 Drift Complex

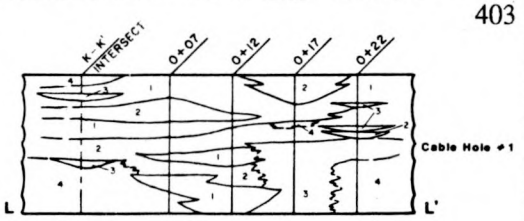
NOTE: This map was compiled as part of the F&S Ledoux Geologic Site Characterization Report.		
NOTE: For explanation of symbols, see southern portion of this map.	Geology by: Dretsack, Thompson, Reyburn	Drawn by: PHT
	Date: 1-18-89	Sheet 2 of 3



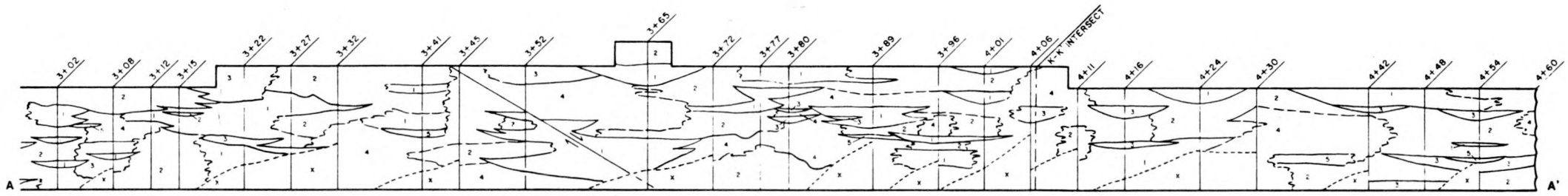
J-J' Cross Section (Experiment Room)



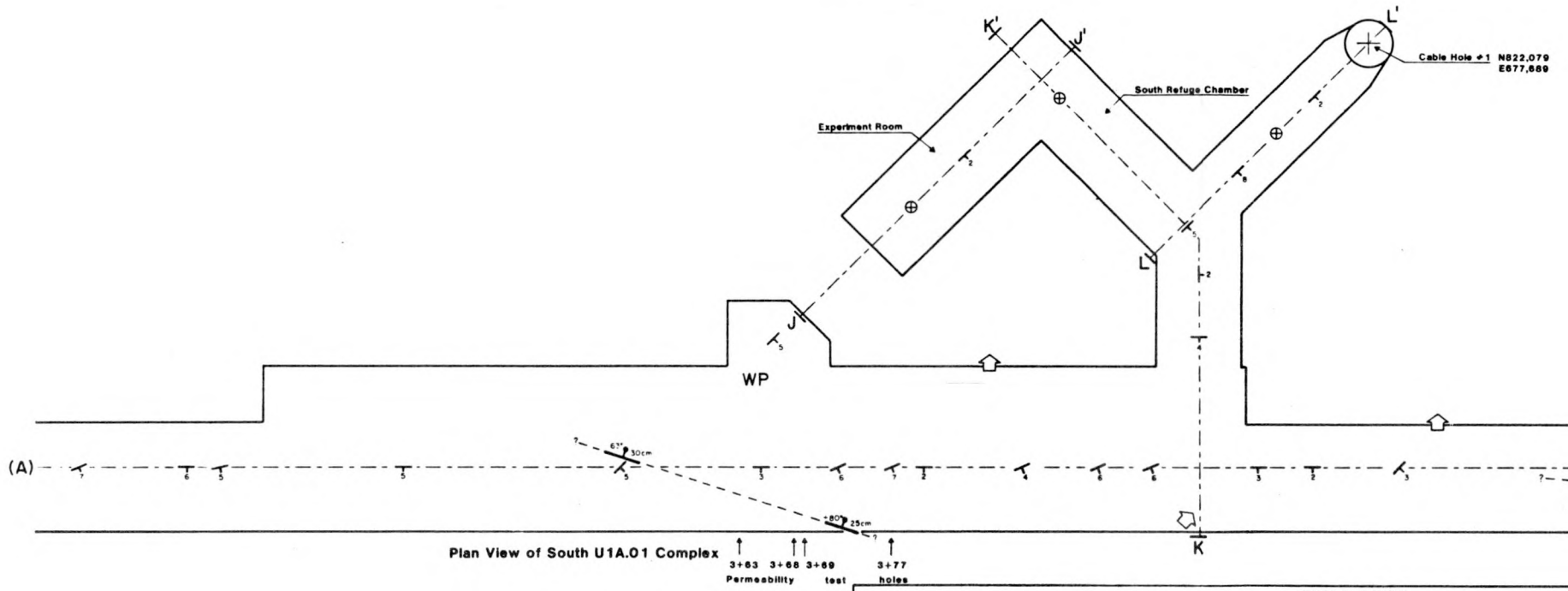
K-K' Cross Section (South Refuge Chamber and CH1 Access Drift)



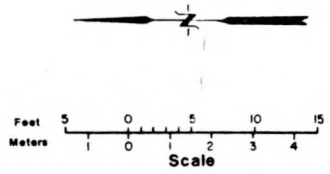
L-L' Cross Section (CH1 Intercept Drift)



A-A' Cross Section (Main Access Drift)



Plan View of South U1A.01 Complex



EXPLANATION

- 2+45 — Location of face (in feet) from shaft or parent drift centerline
- A' — Cross-Section Line
- Top of muck pile
- 80° 50cm — Fault: Bar and ball on downthrown side, vertical displacement in cm
- Drift outline
- Geologic contact
- Gradational or inferred contact
- Lateral gradational contact
- Horizontal beds
- Strike and dip of bedding. See text regarding true vs. apparent dips.
- Channel (cut & fill); Arrow points in direction of paleoflow, plunge direction (when known) given within arrow.

MAP UNITS

- 1 Sand bed
- 2 Sandy pebble bed
- 3 Pebbly cobbly sand bed
- 4 Cobbly sandy pebble bed
- 5 Cobble bed
- X Face covered by muck

Note: See Table 16 for detailed descriptions of map units

Figure 6--Geology of the South Section of the U-1a.01 Drift Complex

NOTE: This map was compiled as part of the F&S Ledoux Geologic Site Characterization.	Geology by: Drellack, Thompson, Rayburn	Drawn by: PHT
	Date: 1-18-89	Sheet 3 of 3

REFERENCES

Ander, H. D., 1984, "Rotation of Late Cenozoic Extensional Stresses, Yucca Flat Region, Nevada Test Site, Nevada", Ph.D. Thesis, Rice University, Houston, Texas, 77 p.

Bachman, G. O., and Machette, M. M., 1977, "Calcic Soils and Calcretes in the Southwestern United States": U. S. Geological Survey Open-File Report 77-794, 163 p.

Denny, C. S., 1967, "Fans and Pediments": American Journal of Science, vol. 265, pp 81-105.

Drellack, S. L., Jr., Thompson, P. H., Rayburn, C. J., 1989, "Occurrence, Distribution and Measurement of Carbonate in the Alluvium of Southern Yucca Flat, Nevada Test Site": Proc. Fifth Symposium on Containment of Underground Nuclear Explosions, Santa Barbara, California, Sept. 19-21, 1989.

Fetter, C. W., Jr., 1980, "Hydraulic Conductivity of Earth Materials", Chapter 4, in Applied Hydrogeology, 1st edition: Charles E. Merrill, Publishers, pp. 60-103.

Fernald, A. T., Corchary, G. S., and Williams, W. P., 1968, "Surficial Geologic Map of Yucca Flat, Nye and Lincoln Counties, Nevada": U. S. Geological Survey Map I-550.

Gile, L. H., Peterson, F. F., and Grossman, R. B., 1966, "Morphological and Genetic Sequences of Carbonate Accumulation in Desert Soils": SoilScience, v. 99, no. 2, pp. 74-82.

Grothaus, B., and Howard, N., 1977, "Correlation of Alluvial Deposits at the Nevada Test Site": Lawrence Livermore National Laboratory Report UCRL-52335, 16 p.

Keller, C., Engstrom, D., West, F., 1973, "In Situ Permeability Measurements for the Event in U-1c": Los Alamos Scientific Laboratory Report LA-5425-MS, 16 p.

Pettijohn, F. J., 1975, "Gravels, Conglomerates and Breccias", Chapter 6, in Sedimentary Rocks, 3rd edition: Harper and Row, Publishers, pp. 154-194.

Shroba, R. R., Muhs, D. R., and Rosholt, J. N., 1988, "Physical Properties and Radiometric Age Estimates of Surficial and Fracture-Fill Deposits Along a Portion of the Carpetbag Fault System, Nevada Test Site, Nye County, Nevada": U. S. Geological Survey, DOE/NV/10853-1, 31 p.

Wagoner, J. L., and McKague, H. L., 1984, "Variation of Physical Properties of Alluvium in an Arid Basin": Lawrence Livermore National Laboratory Report UCRL-90672, 25 p.

Wagoner, J. L., 1983, "Influence of Geological Structure on Alluvial Sedimentation in Northwestern Yucca Flat, Nye County, Nevada": Proc. 2nd Symposium on Containment of Underground Nuclear Explosions, Kirtland AFB, Albuquerque, New Mexico, August 2-4, 1983, pp. 247-270. See also UCRL-89415.

THE DELAMAR FRACTURE ZONE: RECOGNITION OF UNMAPPED ZONES OF WEAKNESS ON PAHUTE MESA, NEVADA TEST SITE

by

H. R. Covington

U.S. Geological Survey
Mercury, Nevada

ABSTRACT

The Delamar underground nuclear test, conducted at Pahute Mesa, Nevada Test Site, formed extensive fracture zones. The orientation, extent (more than 500 m north and south of surface ground zero), and linear distribution of the fractures suggest the presence of two preexisting zones of weakness. Because these zones had not been identified prior to the test, studies were initiated to determine the nature of these zones and to define methods to identify similar zones in the future.

The methods selected to characterize the fracture zones were (1) mapping surface effects on low-altitude aerial photographs, (2) trenching, (3) exploratory drilling, and (4) surface magnetic surveys. Preliminary results of these investigations show that the two fracture zones occurred along preexisting zones of weakness.

The studies also determined that previously unrecognized zones of weakness may be identified using surface mapping techniques. The primary surface features that can be used in the recognition of such zones are (1) a linear feature or an albedo change across a linear feature, on aerial photographs, (2) a linear break between areas of very little and abundant caliche clasts in the surface soil, (3) a linear disruption of rock varnish, and (4) a linear distribution of chalcedony clasts in the surface soil.

The recognition of these zones of weakness during pre-drill field investigation at future sites will allow an early assessment of the possible impact of these structures on containment, and provide data for possible relocation of the site.

INTRODUCTION

An underground nuclear test, Delamar, was conducted on April 18, 1987, at Pahute Mesa, Nevada Test Site, at Nevada State coordinates N. 909,250 m, E. 545,850 m (fig. 1). The principal surface effects of the explosion are fractures and pressure ridges that occur as much as 600 m from surface ground zero (SGZ), and a collapse sink 180 m in diameter (fig. 2). The most conspicuous surface effects are two parallel zones of fracturing, approximately 150 m to 200 m apart, that extend more than 500 m north and south of SGZ. No known geologic structures occur in this area, however, the orientation and extent of these fractures suggest the presence of faults near the surface. Because these zones had not been identified prior to the Delamar test, studies were initiated to: (1) determine the nature of the structures and (2) develop methods to identify similar zones in the future.

GEOLOGY

Pahute Mesa, within the Nevada Test Site testing areas, is a relatively flat plateau capped by two ash-flow tuff units, the Thirsty Canyon Tuff and the Timber Mountain Tuff of Miocene age. Both units are cut by north-trending normal faults (fig. 3). The Silent Canyon caldera underlies most of the Pahute Mesa testing areas and is filled by an accumulation of volcanic tuffs and lavas that exceed 4000 m in thickness (Orkild and others, 1969). The north-trending normal faults resulted from Basin and Range extensional tectonics, and have been extensively reactivated by underground nuclear explosions. These faults closely control the orientation of many explosion-induced fractures on Pahute Mesa (Covington, 1987).

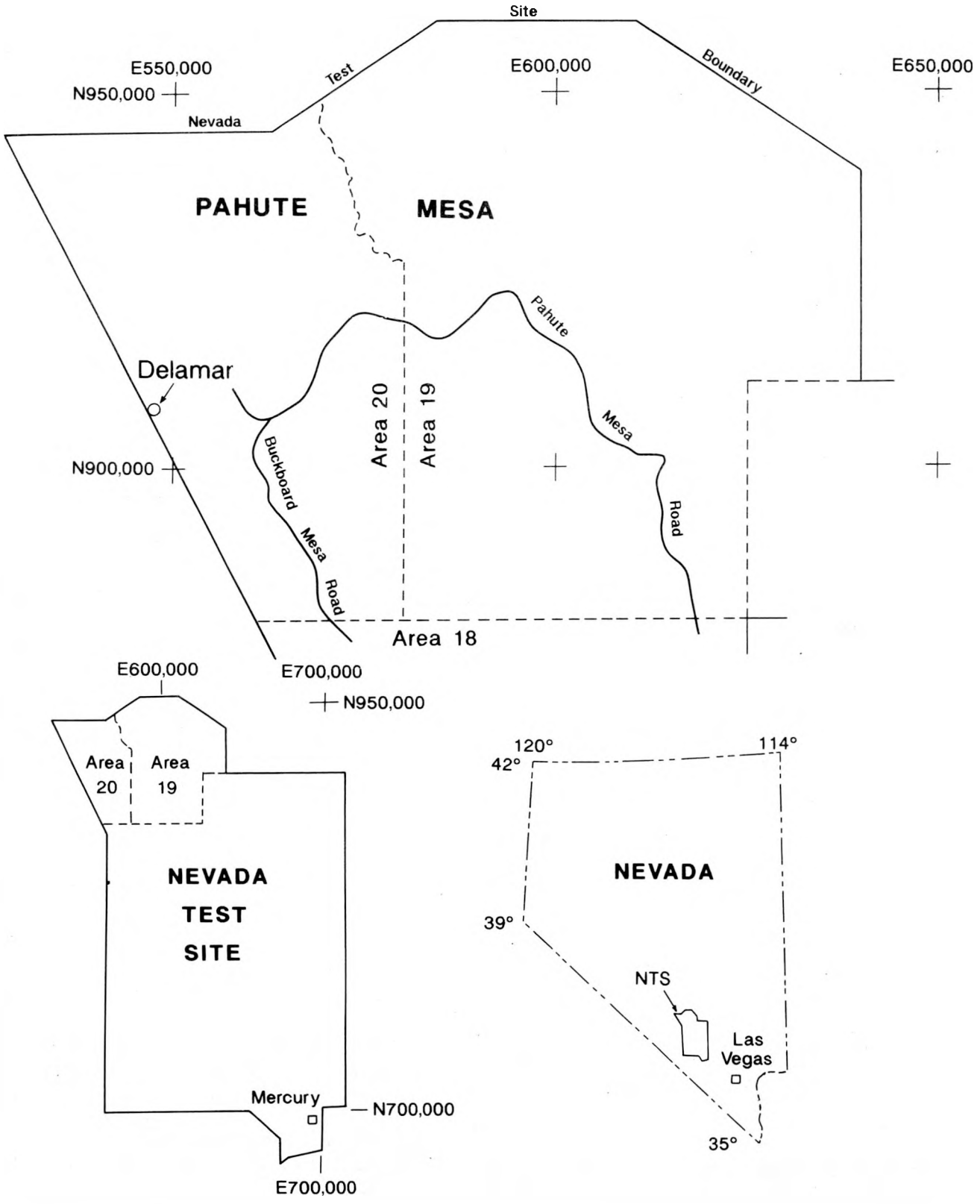


Figure 1.--Location map showing Nevada Test Site, Pahute Mesa testing areas (19 and 20), and the Delamar site.

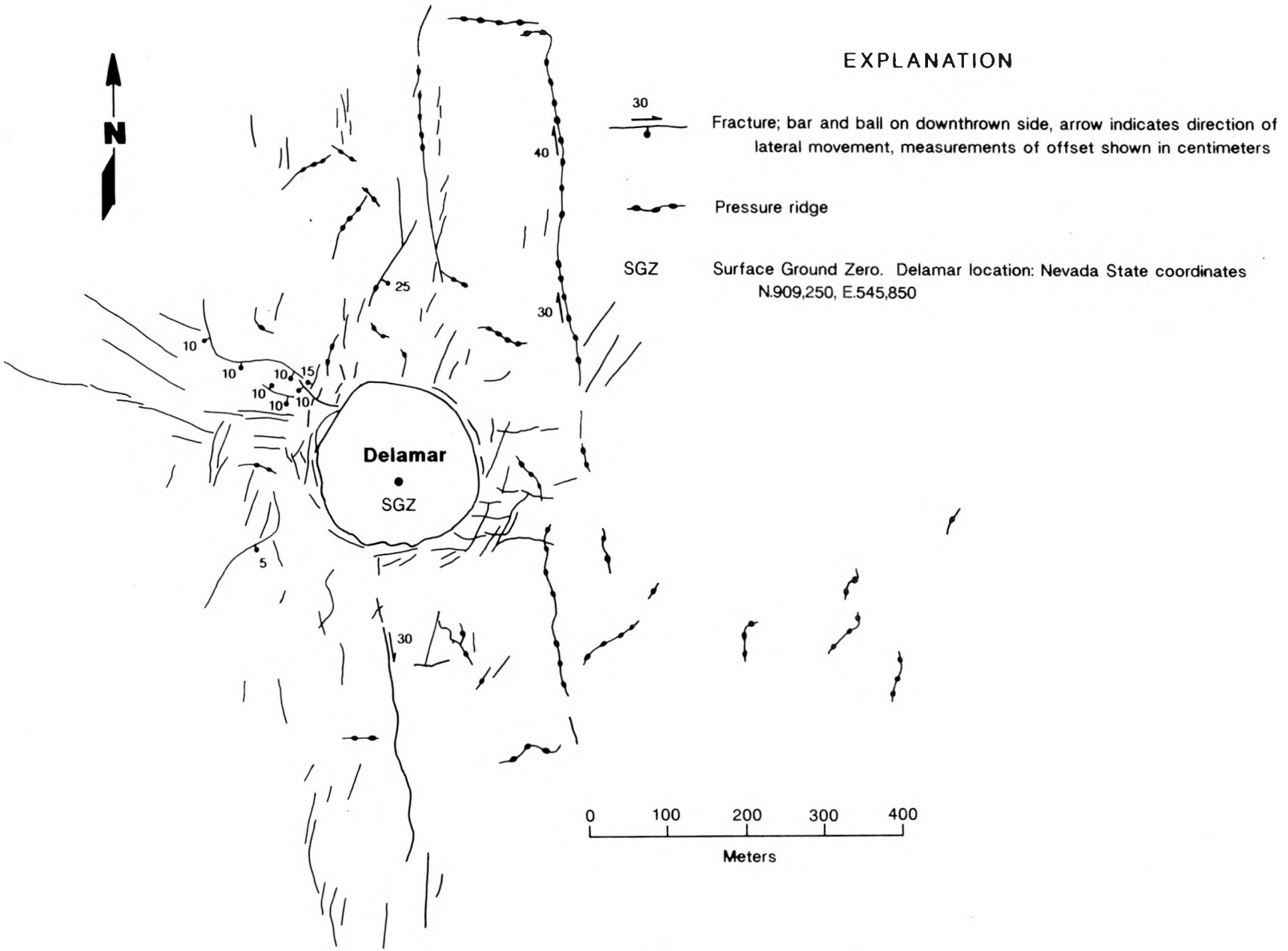


Figure 2.--Surface effects produced by the Delamar underground nuclear test. Modified from the Delamar post-test fracture map. Field mapping by W.B. McKinnis and C.S. Schmidt (Lawrence Livermore National Laboratory) and photogrammetric mapping by F.W. Simonds (U.S. Geological Survey).

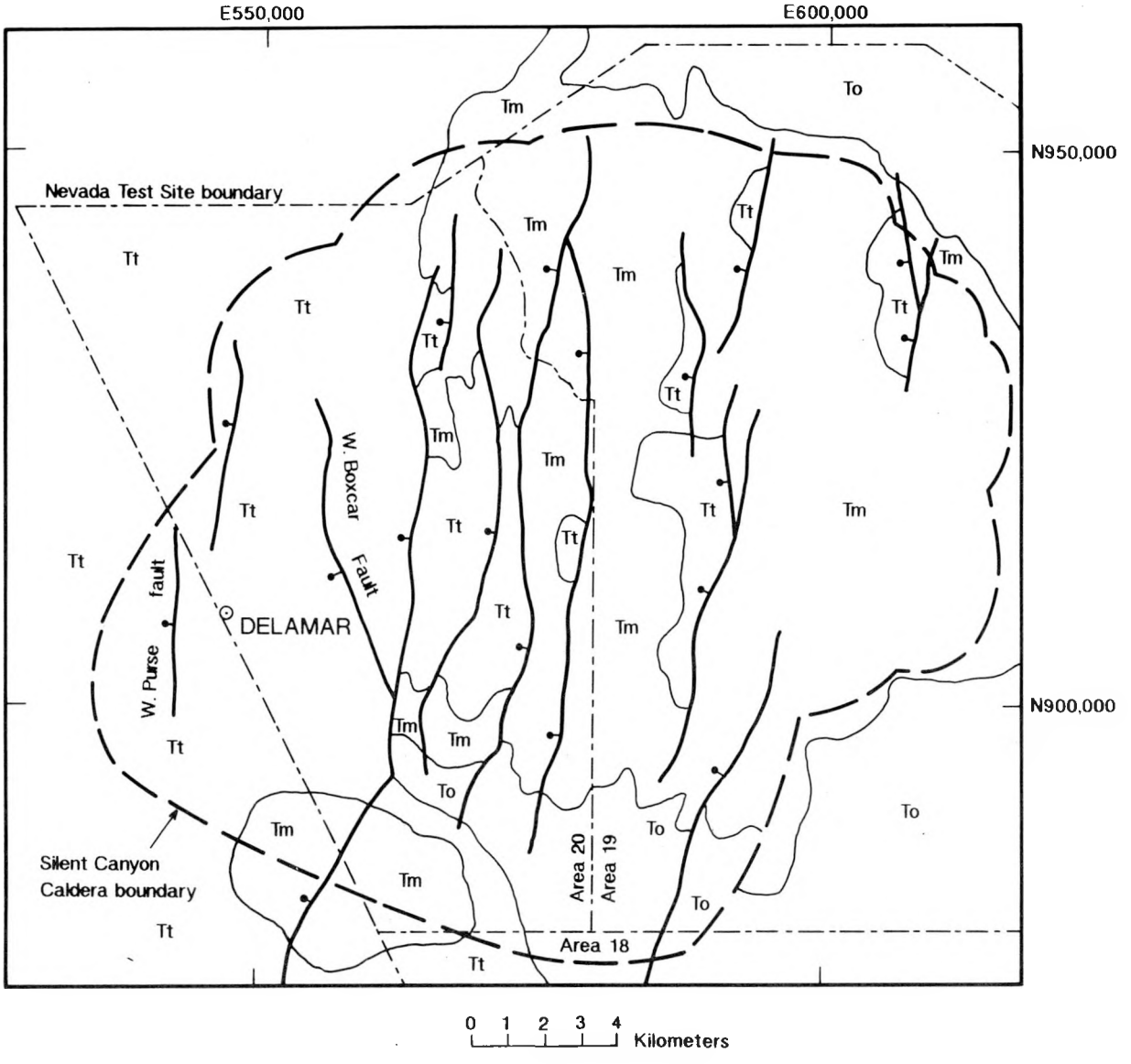


Figure 3.--Generalized geologic map of the Pahute Mesa testing areas.

The surface geology surrounding the Delamar site consists of the nearly flat-lying Trail Ridge Member of the Thirsty Canyon Tuff (fig. 3). Faults are distant: the West Purse fault more than 1100 m west and the West Boxcar fault more than 3200 m east of the Delamar site. The Trail Ridge Member is a moderately welded, vitric, ash-flow tuff, more than 35 m thick in the area of the Delamar site. The ash-flow tuff contains nearly vertical cooling joints that are filled by silica or calcareous deposits. A thin caliche layer, 0-60 cm thick, has formed on the surface of the ash-flow tuff, and in most places a thin, 0-10 cm thick, colluvial soil has developed above the caliche. The caliche horizon and the thin soil have provided much of the evidence for a preexisting zone of weakness near the Delamar site.

FRACTURE ZONE CHARACTERIZATION

To determine if the fracture zones reflect a buried fault, four lines of investigation were followed: (1) mapping of surface effects, (2) trenching, (3) exploratory drilling, and (4) surface magnetic surveys (fig. 4).

Surface effects were mapped as part of the routine post-test investigations. Pressure ridges as much as 1 m high, open fractures as much as 60 cm wide, and fractures produced by differential block motion along cooling joints were found in abundance. No vertical displacement of the surface could be documented along the extensive north-trending fracture zones.

Five trenches were excavated across the north-trending fracture zones. A sixth trench was then excavated in an undisturbed area as a reference trench. In each case where a trench crossed a fracture, a nearly vertical zone of unconsolidated material was found. Close examination revealed that the unconsolidated material within the fracture is surface soil that moved downward during periods when the fracture stood open. No vertical displacement across the fracture zones could be documented at any of the trench locations.

Exploratory holes were drilled on opposite sides of the fracture zone northeast of the Delamar site. These holes were drilled through the Thirsty Canyon Tuff and into the Timber Mountain Tuff in an attempt to document vertical displacement across the fracture zone at depth. No vertical displacement at the Timber Mountain Tuff contact could be documented by the drilling or borehole geophysical logging.

A magnetic survey was conducted across the fracture zones both north and south of the Delamar site. If vertical displacement has occurred at the depth of the reversed polarity Rainier Mesa Member of the Timber Mountain Tuff, a magnetic anomaly should be indicated by the survey. No vertical displacement could be documented by this method within the area of the fracture zones.

The preliminary results of these investigations show that the two fracture zones occurred along preexisting zones of weakness that have had pretesting movement. However, no vertical displacement has been documented across the zones.

RECOGNITION OF UNMAPPED ZONES OF WEAKNESS

No known faults occur or project within 500 m of the Delamar site, and no test-induced surface effects were found during pre-drill field investigations. One linear feature seen on aerial photographs was identified as a stratigraphic feature enhanced by erosion.

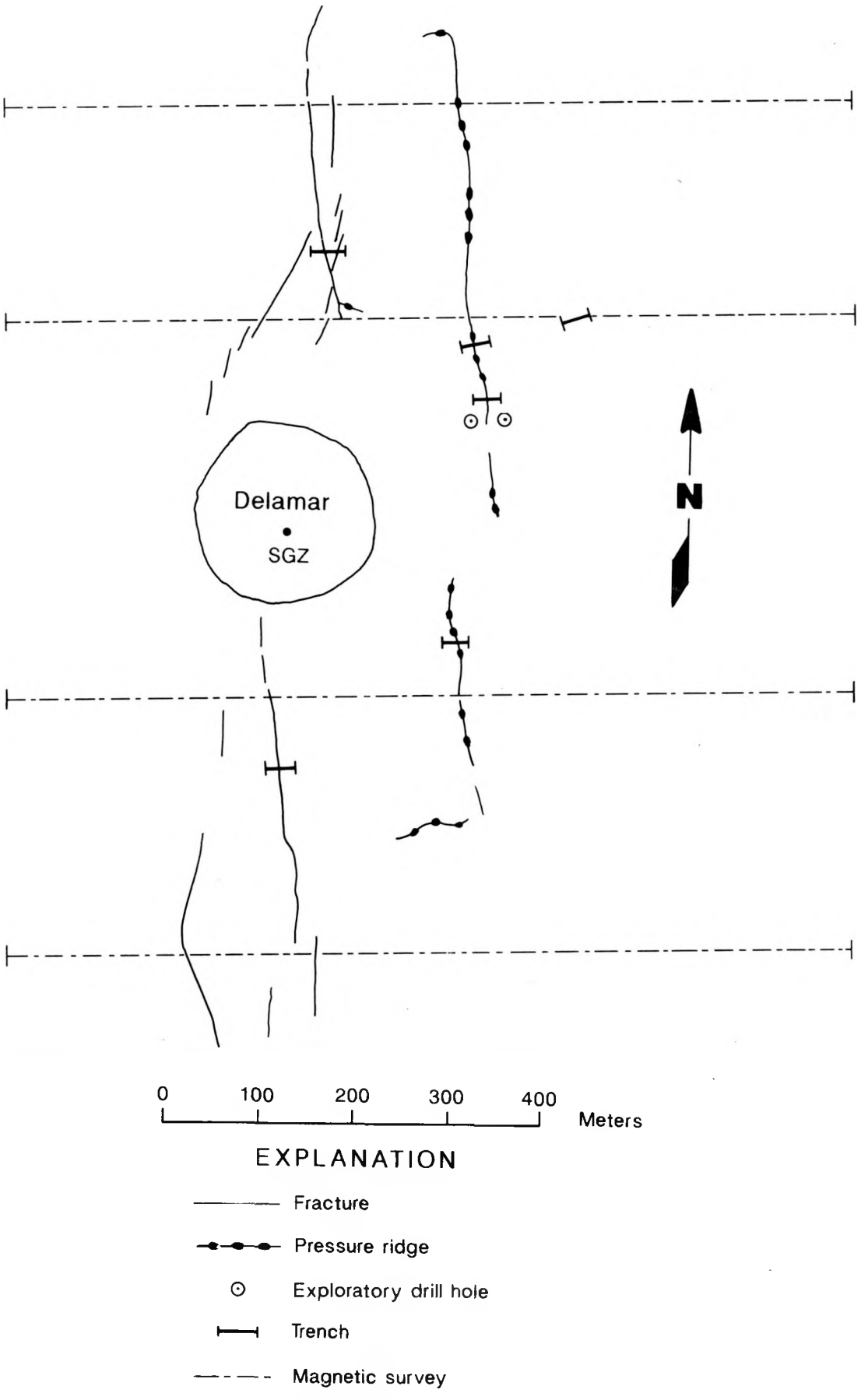


Figure 4.--Delamar site map showing location of north-trending fracture zones, trenches, exploratory drill holes, and surface magnetic surveys. Modified from the Delamar post-test fracture map. Field mapping by W.B. McKinnis and C.S. Schmidt (Lawrence Livermore National Laboratory) and photogrammetric mapping by F.W. Simonds (U.S. Geological Survey).

Following detonation of the Delamar event and subsequent identification of the resulting fracture zones as preexisting zones of weakness, a detailed examination of the site was conducted. This examination was designed to establish a set of criteria by which unmapped structures may be identified. The following items developed from this examination may be used, either in conjunction or separately, to directly or indirectly identify zones of structural weakness: (1) a linear feature or an albedo change across a linear feature on aerial photographs, (2) a linear change between areas of very little and abundant caliche clasts at the surface, (3) a linear disruption of rock varnish, and (4) a linear distribution of chalcedony clasts at the surface.

Linear features and albedo changes are readily observed on aerial photographs. All such lines and changes should be inspected in the field, because they may indicate the location of a fault (fig. 5A) or the location of indirect surface evidence (fig. 5B). The linear feature seen on figure 5A was identified during the Egmont field investigations as a previously unmapped fault having surface displacement down to the west. This fault moved as a result of the Egmont test.

The contact between areas of differing albedo seen on figure 5B was identified during the U19bf field investigations as the location of a change in caliche clast abundance in the soil. Surface fracturing has occurred along this contact as the result of nearby tests, and this location is now identified as an inferred fault.

Throughout most of the Pahute Mesa testing areas a thin caliche horizon has developed within the soil. If this horizon is displaced by fault motion, the caliche on the upthrown block may be stripped off during degradation of the fault scarp and deposited as clasts within the soil on the downthrown block. This contrast in caliche clast content of the soil may or may not produce a linear feature on aerial photographs, depending on the type of soil or rock present. In the field, however, the contact is easily identified and mapped based on the caliche clast content.

Rock varnish occurs at many locations within the Pahute Mesa testing areas, and where present may aid in the location of inferred fault zones. Rock varnish is a thin coating of ferro-mangenese oxides that occurs in semiarid and arid regions on exposures of bedrock and on gravel clasts on stable geomorphic surfaces (Harrington and Whitney, 1987). When a stable geomorphic surface is broken by fault movement, an unstable condition exists during the time when the fault scarp is being regraded. This unstable condition of the surface inhibits the development of rock varnish and in turn helps identify inferred fault zones (C.D. Harrington, Los Alamos National Laboratory, written commun.). This change in surface conditions or in rock varnish development can easily be mapped in the field (fig. 6), but it may or may not be expressed as an albedo change on aerial photographs. Field examination of surface effects following the Delamar event showed that rock varnish occurs on clasts east of the fracture zone, northeast of SGZ, while there is no rock varnish west of the fracture zone. Locations where rock varnish does not occur were mapped for the area affected by the Delamar event. The map shows that the area of no rock varnish parallels the north-trending fracture zones (fig. 7).

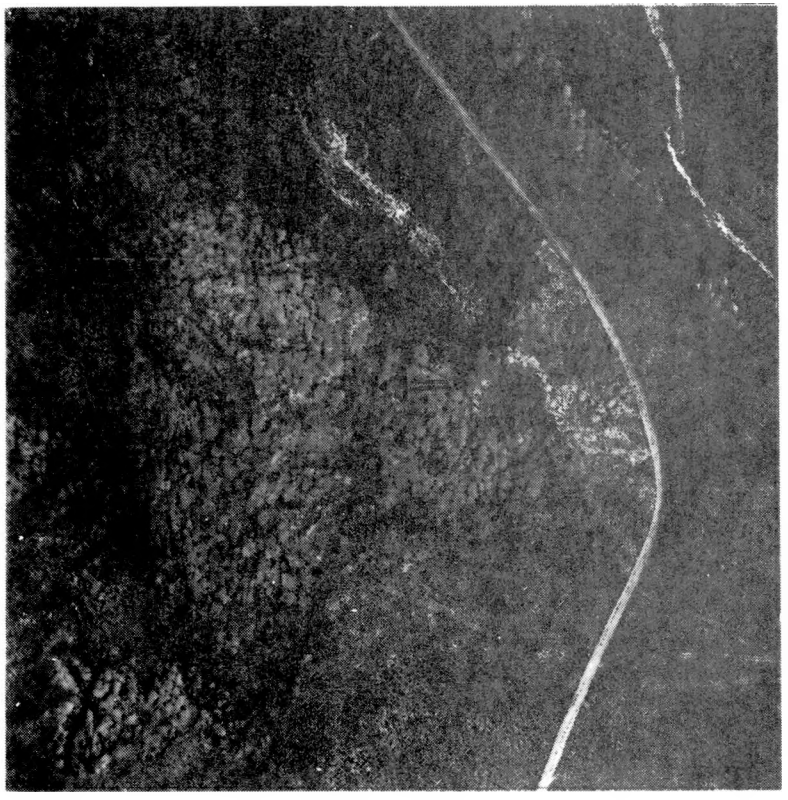
Field studies on Pahute Mesa have shown an increase in chalcedony clasts in the soil near mapped faults. Trench studies of the Delamar fracture zones show extensive chalcedony deposits near these zones. Linear distributions of chalcedony may prove useful in the identification of unmapped faults, however, to date this technique has not been proven.

DISCUSSION

A major concern in the design of an underground nuclear test is the containment of the explosion products. Considerable care is taken to characterize the geologic medium near the working point. A potential threat to the ability of the working point medium to contain the explosion products is the presence of a fault. Because there is no consensus within the containment community on when a fault becomes a threat to containment, the identification of unmapped zones of weakness or inferred faults becomes very important to the site selection process. In an attempt to improve our understanding of what surface features tell us about the location of buried structures, the criteria for identification presented above were developed. The recognition of these zones of weakness, by the field geologist during site selection, will allow an early assessment of the impact of these structures on containment and provide data for possible relocation of a site.

ACKNOWLEDGMENTS

I thank the Lawrence Livermore National Laboratory, Nuclear Test Containment Group, for their continuing support of surface effects studies at Pahute Mesa. I also thank J.D. Donithan and W.B. McKinnis of Lawrence Livermore National Laboratory-Nevada for their operational support during field studies.



5A

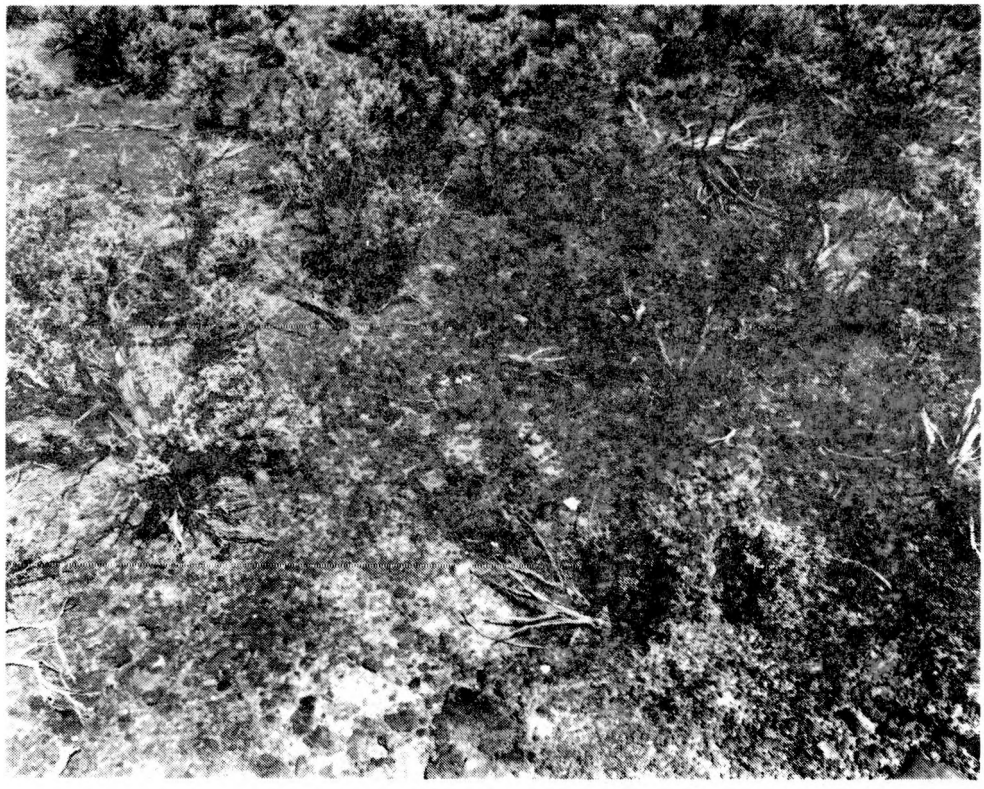


5B

Figure 5.--Linear features and albedo changes. (A) Linear feature; arrow points to linear feature on aerial photograph field identified as a fault. Photograph by American Aerial Surveys, Inc. (B) Adjacent areas of differing albedo; arrow points to albedo change on aerial photograph field identified as contrasting areas of caliche clast content in the soil. Photograph by American Aerial Surveys, Inc.



6A



6B

Figure 6.--Rock varnish development. (A) Well developed rock varnish on stable surface. (B) No rock varnish on unstable surface. Photographs by Lawrence Livermore National Laboratory-Nevada, Photographic Applications Group.

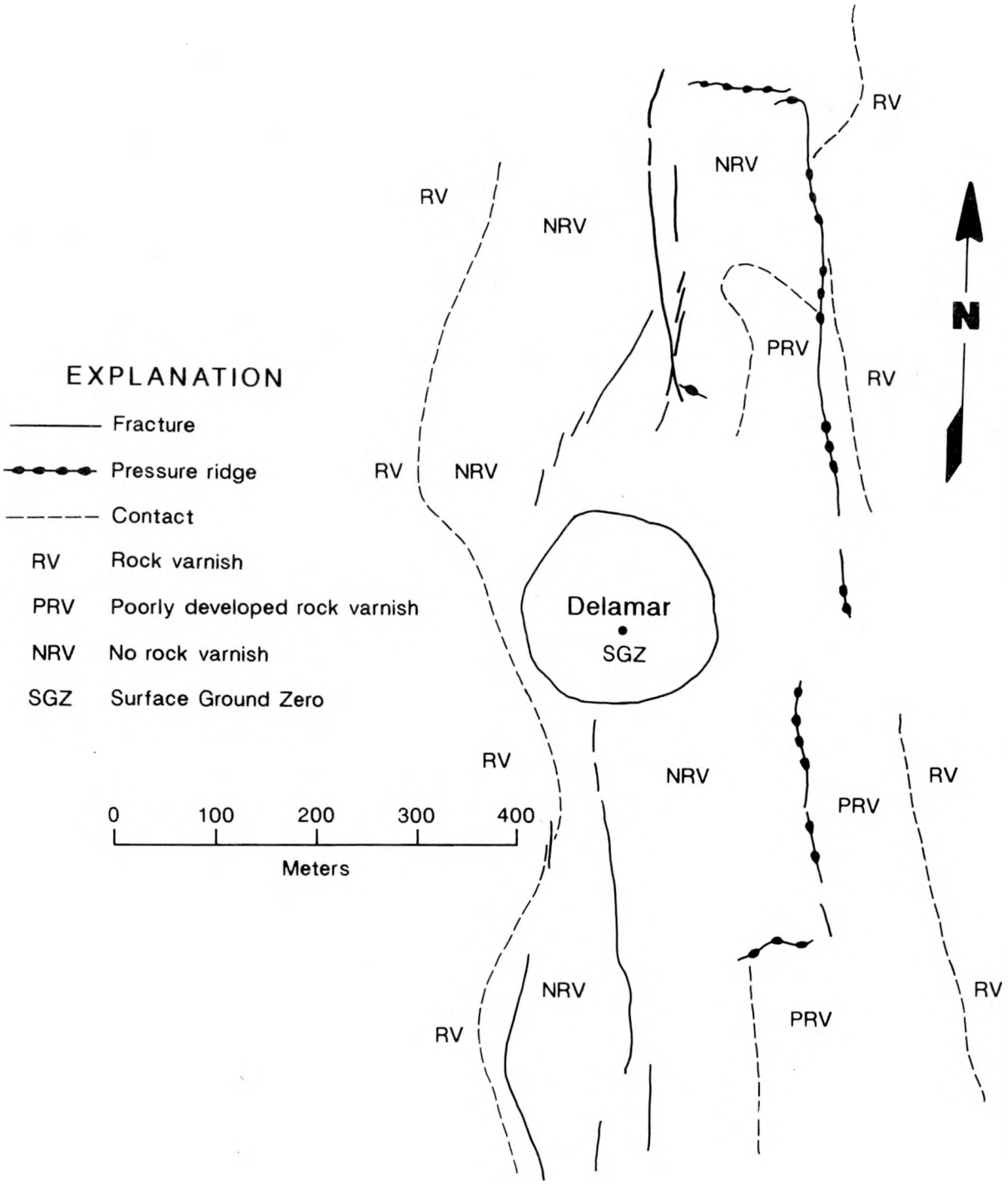


Figure 7.--Major north-trending fracture zones resulting from the Delamar event, and contacts between areas of clasts having rock varnish and those without rock varnish. Modified from the Delamar post-test fracture map. Field mapping by W.B. McKinnis and C.S. Schmidt (Lawrence Livermore National Laboratory) and photogrammetric mapping by F.W. Simonds (U.S. Geological Survey).

REFERENCES

Covington, H.R., 1987, Map showing surface features induced by underground nuclear explosions at Pahute Mesa, Nevada Test Site, Nye County, Nevada, April 1976 through December 1983: U.S. Geological Survey Miscellaneous Investigations Series Map I-1872, scale 1:48,000.

Harrington, C.D., and Whitney, J.W., 1987, Scanning electron microscope method for rock-varnish dating: Geology, v. 15, no. 10, p. 967-970.

Orkild, P.P., Sargent, K.A., and Snyder, R.P., 1969, Geologic map of Pahute Mesa, Nevada Test Site and vicinity, Nye County, Nevada: U.S. Geological Survey Miscellaneous Investigations Series Map I-567, scale 1:48,000.

PALEOMAGNETIC EVALUATION OF THE YUCCA-FRENCHMAN FLEXURE, SOUTHERN NEVADA

Mark R. Hudson
U.S. Geological Survey
Box 25046, Mail Stop 913
Denver, Colorado 80225

ABSTRACT

The eastern margin of the Yucca Flat basin, southern Nevada, is bounded by north-northwest-striking tilted fault blocks of the Halfpint Range that curve as much as 90° clockwise into east-northeast strikes in the French Peak-Massachusetts Mountain (FPMM) area. This pattern of arcuate structures was termed the Yucca-Frenchman flexure by previous workers who attributed the arcuate pattern to clockwise drag along a proposed northwest-trending, right-lateral shear zone. The flexure model implies that rocks within the FPMM area have been rotated strongly clockwise about a vertical axis. Paleomagnetic data indicate no systematic vertical-axis rotation in the FPMM area and disprove the flexure model. Directions of remanent magnetization of the Ammonia Tanks and Rainier Mesa Members (about 11.5 Ma) of the Timber Mountain Tuff and of the Topopah Spring Member (about 13.5 Ma) of the Paintbrush Tuff were determined to assess vertical-axis rotation. After tilt correction, declinations of 30 site means obtained from the three ash-flow sheets in the FPMM area are more dispersed, but not systematically different than declinations of 12 site means from the Halfpint Range or declinations of 10 site means from little deformed reference areas to the west (Rainier and Pahute Mesas, Shoshone and northern Yucca Mountains).

Paleomagnetic data indicate that structures in the FPMM area initiated with arcuate trends; not as originally straight elements that were rotated by right-lateral drag. The structures must have formed under the influence of locally different orientations and (or) ratios of principal stresses. The French Peak-Massachusetts Mountain area lies in an accommodation zone between domains of predominantly west- and east-tilted Miocene and Pliocene extensional fault blocks to the north and south, respectively. I suggest that local interaction between stress fields associated with fault zones that simultaneously propagated from north and south into the accommodation zone may have been responsible for the arcuate structures in the FPMM area.

INTRODUCTION

On the southeast margin of the Yucca Flat basin (figs. 1, 2), Miocene volcanic rocks and the faults that offset the rocks change strike from north-northwest in the Halfpint Range to east-northeast south of the French Peak area of Massachusetts Mountain, and to northeast in the southern part of Massachusetts Mountain. As well, the French Peak-Massachusetts Mountain (FPMM) area lies between domains in which rocks of extensional fault blocks have opposing dips. Rocks in fault blocks to the north (e.g., Halfpint Range, Yucca Flat) dip west, whereas rocks in fault blocks to the south (e.g., southern Massachusetts Mountain, Frenchman Flat) dip east. Areas separating domains of oppositely-tilted extensional fault blocks are termed "accommodation zones" in recent literature (e.g., Bosworth and others, 1986; Faulds and others, 1988).

In his review of structural features of the Nevada Test Site area, W.J. Carr (1984) attributed the pattern of arcuate structures in the FPMM area to clockwise flexure of originally north-northwest-trending structures above a northwest-trending right-lateral

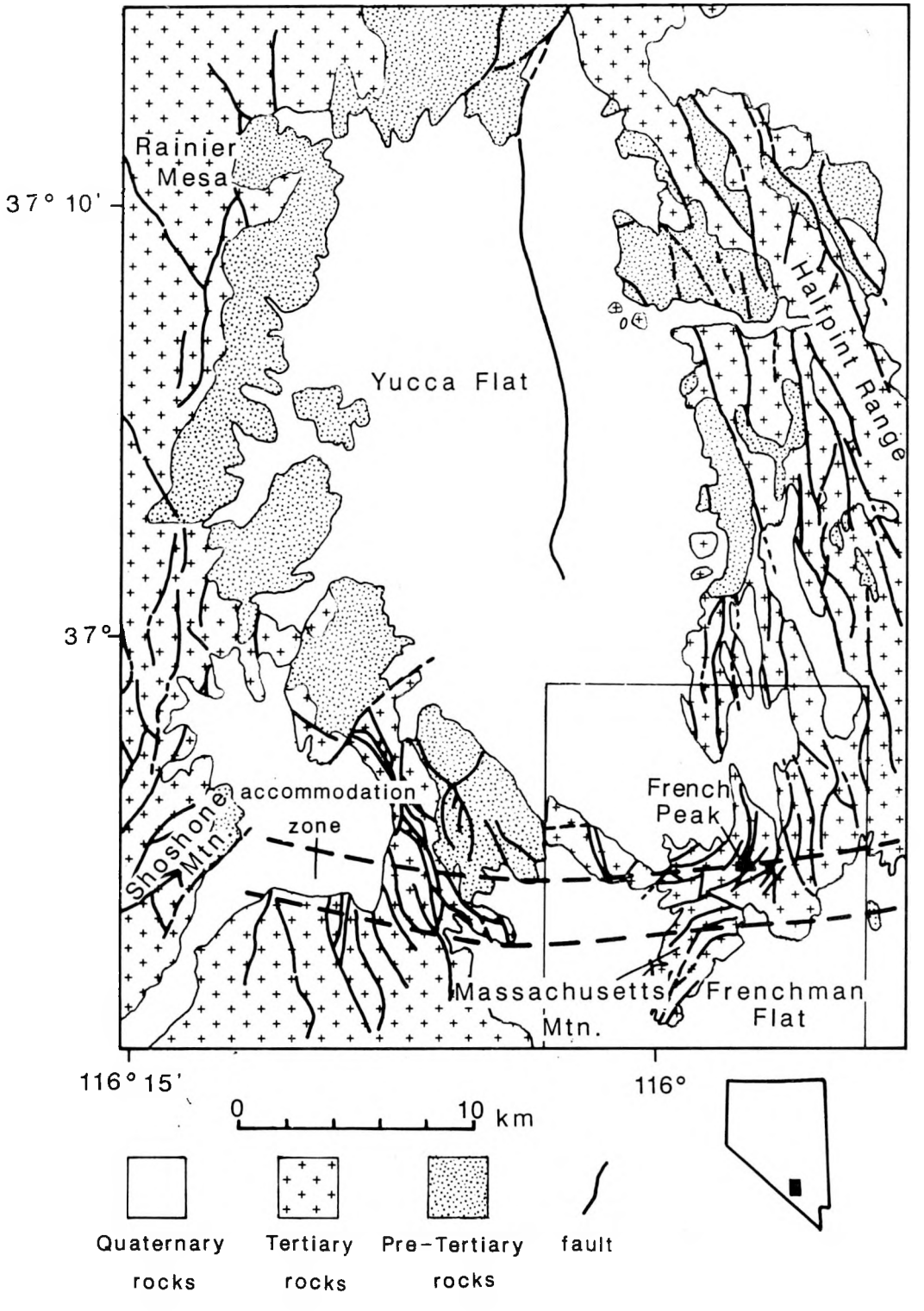


Figure 1. Generalized geologic map of the Yucca Flat area showing the location of the French Peak-Massachusetts Mountain area and an accommodation zone that separates fault blocks with west-dipping strata to the north from fault blocks with east-dipping strata to the south. Inset box shows area of figures 2 and 5.

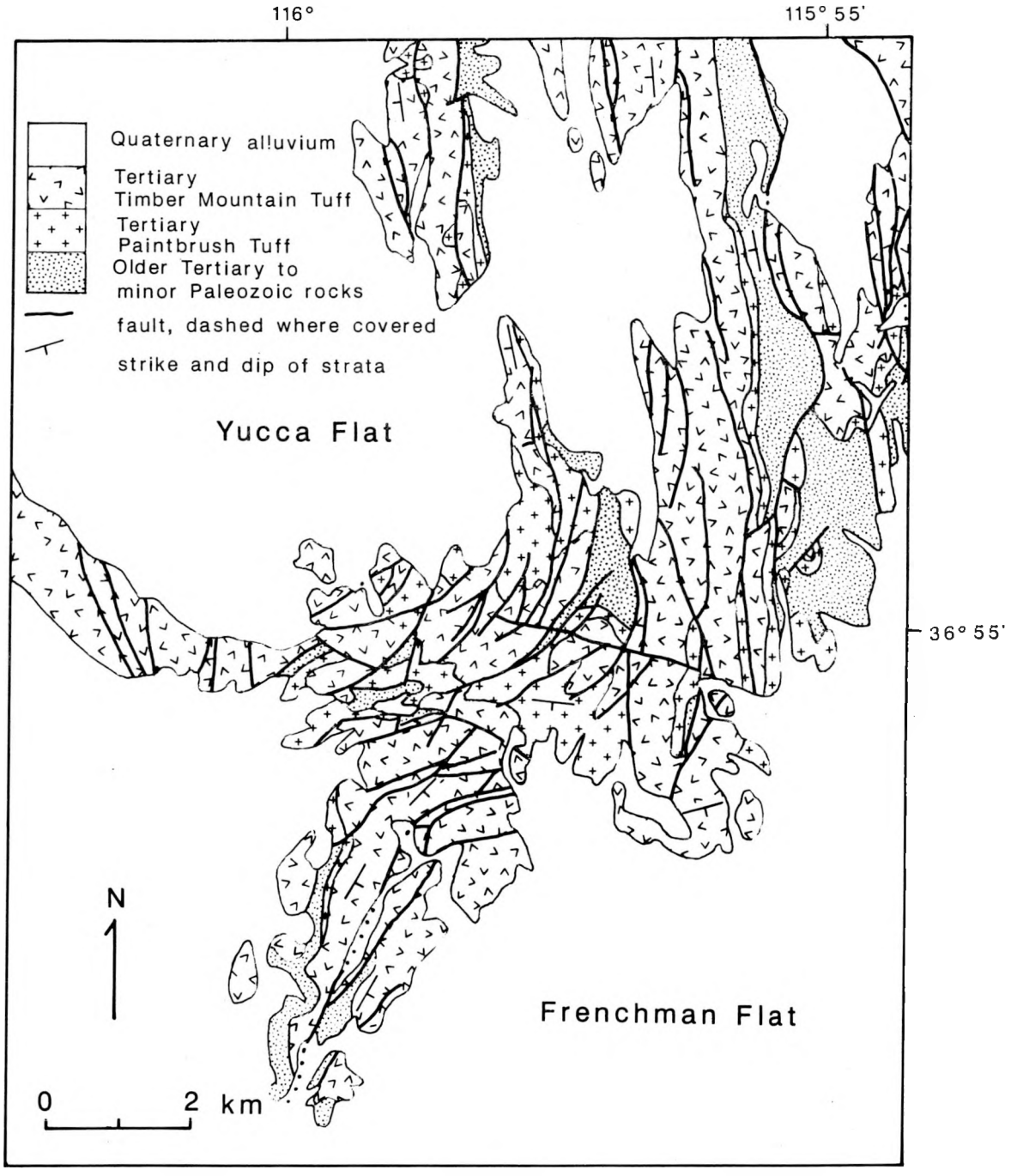


Figure 2. Geologic map of the Massachusetts Mountain-French Peak area (generalized from Hinrichs and McKay, 1965; Poole, 1965; Poole and others, 1965; McKeown and others, 1976).

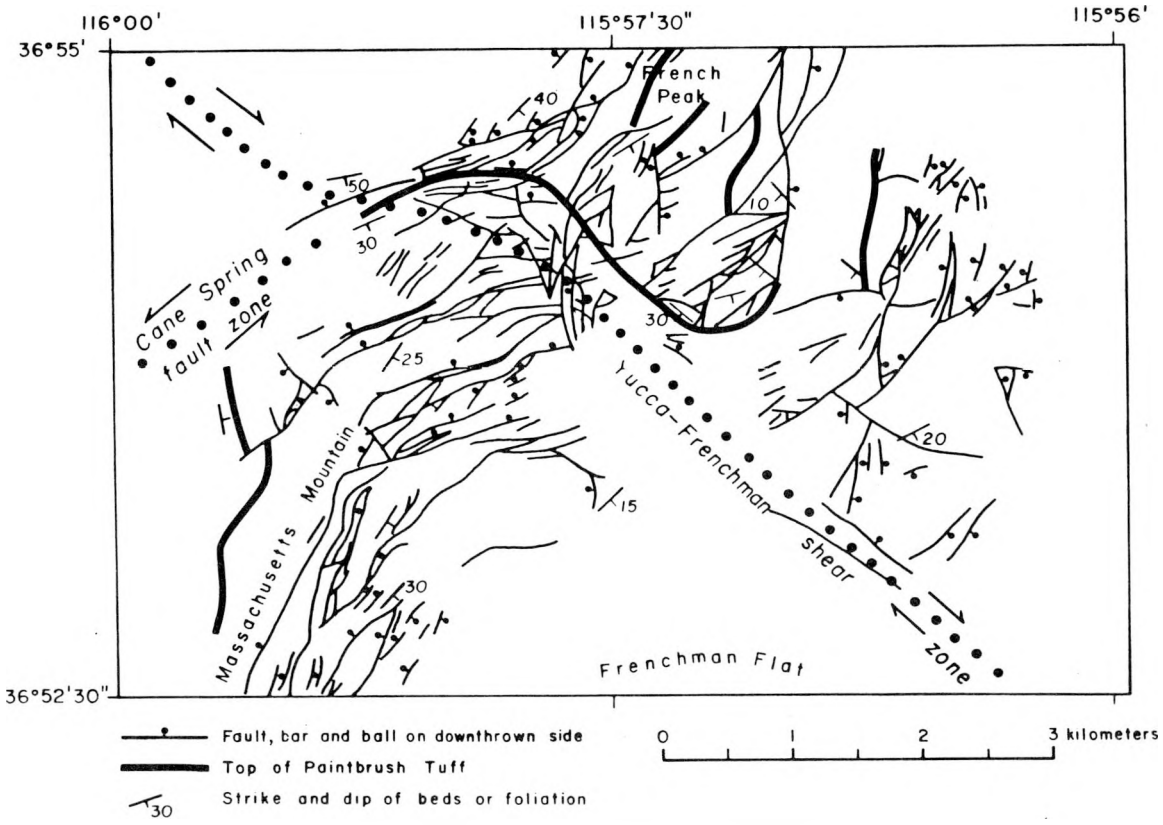


Figure 3. Yucca-Frenchman flexure and shear zone model from Carr (1984).

shear zone (fig. 3). The right-lateral shear zone was postulated to extend about 40 km from the Spotted Range northwestward across northern Frenchman Flat and into southern Yucca Flat. This feature was termed the Yucca-Frenchman shear and flexure zone. The proposed clockwise flexure of rocks and structures above the shear zone required about 4 km of right-lateral offset on the shear zone. If such a major shear zone lies beneath Yucca Flat and Frenchman Flat, it might strongly influence structural properties of Tertiary rocks used in nuclear testing, and it would be expected to extend downward into Paleozoic rocks, thereby providing a potential pathway for radionuclides into regional ground-water systems.

The flexure model for the Yucca-Frenchman shear and flexure zone requires that rocks and their included structures in the FPMM area have been rotated clockwise by as much as 90° about a vertical axis. Alternatively, arcuate structures in the FPMM area may have nucleated under the influence of a spatially variable stress field without clockwise rotation of rocks. A test to discriminate between these models is to determine whether rocks in the FPMM area have been strongly rotated about a vertical axis. In this study, paleomagnetism of Miocene ash-flow tuffs involved in deformation in the FPMM area was investigated. Comparison of directions of remanent magnetization of tuffs at sites on and away from the FPMM area reveals no evidence for systematic clockwise vertical-axis rotation.

GEOLOGY OF THE FRENCH PEAK-MASSACHUSETTS MOUNTAIN AREA

The FPMM area (fig. 2) primarily is comprised of Miocene volcanic rocks (Hinrichs and McKay, 1965; Poole, 1965; Poole and others, 1965; McKeown and others, 1976). The Rainier Mesa and Ammonia Tanks Members (about 11.5 Ma) of the Timber Mountain Tuff make up most surface exposures. The Topopah Spring Member (about 13.5 Ma) of the Paintbrush Tuff also has significant areal exposures. Other Miocene rocks are principally bedded tuffs.

All Miocene rocks exposed in the FPMM area are clearly involved in the deformation. The Timber Mountain units, the youngest of the area, are offset hundreds of meters by normal faults and typically dip from 15° to 35°.

PALEOMAGNETIC TEST FOR VERTICAL-AXIS ROTATION

Test Procedures, Assumptions, Uncertainties

Directions of remanent magnetization carried by the Ammonia Tanks, Rainier Mesa, and Topopah Spring Members were determined from samples collected at numerous sites in the FPMM area and in the Halfpint Range. To test for vertical-axis rotation, declinations of these directions were compared to declinations of reference directions determined for these units at sites from less extended regions to the west (e.g., Rainier Mesa).

Several factors influence the accuracy to which tectonic rotations can be detected using paleomagnetism of a single ash-flow tuff. To be used as a structural marker, remanent magnetization should have a consistent direction throughout the tuff. For tuffs that acquire their magnetization during post-emplacement cooling, a single direction of magnetization typically will be recorded in thin, simple cooling units that cool rapidly with respect to changes (secular variation) of the Earth's geomagnetic field. For thick, compound cooling units, however, care must be taken to determine whether rocks recorded different directions due to protracted cooling relative to secular variation. Care also must be taken to assess whether later processes may have altered the primary magnetization or added secondary magnetization in the unit. For example, Rosenbaum (1986) has documented a decrease in inclination of remanent magnetization related to welding that occurred after acquisition of remanent magnetization in basal parts of thick sections of the Topopah Spring Member at Yucca Mountain about 45 km west of the FPMM area.

Paleomagnetic data used to test for vertical-axis rotation must include corrections for tectonic tilt of sites. Correction for tilt is accomplished by rotation of the direction of magnetization about the horizontal strike axis for the site by the amount of dip estimated for the site. Tilt correction may introduce error in a site mean if the stratal attitude estimated for the site is incorrect or if the dip of a site was not the result of simple rotation about the strike axis.

Paleomagnetic Data - Methods and Results

All samples for the study were collected with a portable rock drill and oriented with an inclinometer and both a magnetic and solar compass. Typically 7 to 9 cores were collected at a site from several blocks of rock spread over several tens of square meters. At some sites, samples (from 8 to 36) were collected in traverses through stratigraphic intervals of the Rainier Mesa or Ammonia Tanks Members to test for stratigraphically controlled variation of remanent magnetization. Samples from the Topopah Spring

Member typically were collected from the upper few meters of the ash-flow to minimize potential effects of sub-blocking-temperature welding as described by Rosenbaum (1986). Stratal attitudes of sites for tilt corrections were estimated by measurement of compaction foliations, stratigraphic contacts, and boundaries between welding zones.

To establish reference directions for the individual units, samples were collected from sites in areas to the west of the Halfpint Range and the FPMM area that are relatively little deformed. Reference directions for the Rainier Mesa Member were determined from samples collected on Rainier Mesa (5 sites). Reference directions for the Ammonia Tanks Member were determined from samples collected on Rainier Mesa (2 sites) and Pahute Mesa (1 site), located northwest of Rainier Mesa. Reference directions for the Topopah Spring Member were determined from samples collected near Shoshone Mountain (1 site) and at northern Yucca Mountain (1 site), located southwest of Shoshone Mountain. For all reference sites, dips of the rocks are small (0° - 12°). This minimizes errors arising from tilt corrections.

In the laboratory, samples were subjected to alternating field and thermal demagnetization. Most samples were processed by alternating field demagnetization (typically 9 steps per sample). Representative samples were thermally demagnetized for comparison with results from alternating field demagnetization, and to assess unblocking temperature ranges. Demagnetization results were plotted on vector diagrams and directions of components were determined by principal-component analysis (Kirschvink, 1980) for visually determined linear segments. Site means and dispersion parameters were calculated using Fisher statistics (Fisher, 1953).

Each unit carries a principal component of magnetization that is interpreted to have been acquired during initial cooling. After removal at low demagnetization levels of small components that were probably acquired in recent fields, most samples retained a single magnetization component through all higher demagnetization levels. For samples collected over restricted stratigraphic intervals, the direction of this component is tightly grouped. Values of the precision parameter, k (Fisher, 1953), typically exceed 100 (table 1; more tightly grouped directions have greater k values). At some sites the primary component of magnetization has been overprinted to a variable extent by lightning-induced magnetization. Data were omitted for samples for which demagnetization did not completely remove lightning-induced components. Tilt-corrected site means for the Topopah Spring Member have steep inclinations (58°-76°) and high k values, suggesting that they have not been strongly affected by post-blocking welding and shallowing of inclination as described by Rosenbaum (1986). After tilt correction, site means from each unit become much more tightly grouped. This demonstrates that the units acquired their magnetization before tilting.

Characteristics cited above indicate that magnetizations in the three geologic units predate deformation, were probably formed during initial cooling of each sheet, and were little altered afterward. Systematic changes of remanent directions, however, have been observed in basal portions of the Rainier Mesa Member in several stratigraphic traverses. Compared to little-dispersed remanent directions from middle and upper portions of the Rainier Mesa, declinations in lowermost portions shift as much as 10-15° counterclockwise and inclinations may be shallow by as much as 15°. Tentatively, this change of remanent directions is ascribed to cooling of the basal flow of the Rainier Mesa compound cooling unit in an geomagnetic field of different orientation than that recorded by overlying flows.

Table 1. -- Paleomagnetic data

{# - number of site on fig. 5. Lat., Long. - latitude (° N) and longitude (° W) of site. N/No - number of samples accepted/number of samples demagnetized. D_o, I_o - in situ site-mean declination (° clockwise from north) and inclination (° from horizontal, negative values are up). α_{95} - cone of 95 percent statistical confidence about site mean. k - precision parameter (Fisher, 1953). D_1, I_1 - tilt-corrected declination and inclination of site mean.}

#	Site	Lat.	Long.	N/No	D_o	I_o	α_{95}	k	D_1	I_1
				Reference areas						
Ammonia Tanks Member										
	7YF-3	37.174	116.208	9/9	2.6	62.6	3.2	256	354.9	62.5
	8YF-29	37.223	116.167	5/9	342.2	55.9	5.0	239	349.6	57.0
	JR89-2	37.197	116.479	7/7	355.7	64.5	1.8	1118	352.9	63.1
Rainier Mesa Member										
	7YF-2	37.182	116.221	6/8	181.5	-49.0	3.0	487	170.1	-48.3
	7YF-4	37.197	116.210	7/7	173.6	-53.4	2.4	650	168.4	-52.8
	7YF-5	37.203	116.203	7/7	169.9	-51.3	1.2	2475	170.5	-51.5
	7YF-16	37.128	116.171	20/25	161.7	-49.0	2.4	194	175.9	-52.4
	8YF-54	37.171	116.219	29/29	178.1	-47.6	2.7	101	168.9	-52.3
Topopah Spring Member										
	8YF-43	36.959	116.216	7/7	310.1	70.2	2.7	518	310.1	70.2
	JR89-22	36.902	116.488	8/8	299.5	55.1	2.9	355	299.3	67.1
				Halfpint Range						
Ammonia Tanks Member										
6	8YF-10	36.959	115.932	8/8	36.4	60.5	3.9	202	326.5	65.1
Rainier Mesa Member										
5	7YF-6	36.950	115.963	8/8	190.7	-53.2	1.9	827	155.4	-54.6
4	7YF-7	36.965	115.982	7/8	209.7	-48.1	4.2	209	172.4	-57.8
3	7YF-8	36.965	115.983	8/8	208.4	-54.6	1.9	868	175.5	-62.8
1	7YF-9	36.984	115.981	8/9	179.0	-53.9	3.4	269	154.6	-52.6
2	7YF-10	36.984	115.981	10/10	193.1	-50.9	2.0	573	169.6	-54.4
	7YF-12	37.119	116.007	5/7	172.9	-43.2	2.1	1288	151.4	-42.0
	7YF-13	37.039	115.982	7/7	183.2	-57.8	2.1	804	175.2	-58.5
7	8YF-9	36.959	115.931	7/7	208.2	-47.8	2.4	625	165.4	-55.2
Topopah Spring Member										
8	8YF-8	36.959	115.928	8/8	47.2	76.3	2.0	784	279.5	67.4
9	8YF-11	36.932	115.908	7/7	54.9	85.9	3.7	261	261.7	70.7
10	FP	36.919	115.924	39/39	3.0	79.5	1.7	189	295.0	68.9
				French Peak-Massachusetts Mountain area						
Ammonia Tanks Member										
40	7YF-15	36.926	116.032	7/7	2.8	47.1	3.1	393	351.7	55.2
24	7YF-18	36.861	115.992	4/7	345.4	43.7	4.4	432	353.1	53.7
31	JR87-16	36.895	115.988	4/8	298.4	40.8	4.8	375	321.1	53.3
22	8YF-22	36.878	115.980	6/6	326.8	40.2	4.5	225	339.8	64.5
33	8YF-24	36.896	115.980	7/7	332.8	24.4	2.8	479	345.0	54.4
20	8YF-25	36.895	115.972	8/8	358.6	42.2	6.0	87	9.1	55.2
34	8YF-34	36.903	115.981	8/8	356.5	34.8	3.0	337	357.6	61.8
26	8YF-35	36.886	115.989	9/9	329.0	31.5	8.6	37	347.2	55.6
Rainier Mesa Member										
39	7YF-14	36.926	116.031	12/12	181.2	-42.9	1.5	850	171.6	-50.6
25	7YF-17	36.861	115:993	10/10	169.5	-42.7	2.1	558	177.7	-52.1
23	7YF-19	36.870	115.988	8/8	164.8	-28.0	2.9	380	178.5	-43.1
36	JR87-17	36.895	115.990	4/8	123.6	-36.3	3.9	544	145.3	-47.9
18	8YF-12	36.894	115.937	10/10	167.0	-29.6	6.6	54	167.6	-39.6
16	8YF-14	36.903	115.941	5/7	161.5	-30.7	2.1	1340	157.0	-41.0
15	8YF-16	36.913	115.948	5/7	147.1	-19.3	3.3	547	143.9	-40.6
11	8YF-17	36.916	115.952	7/7	150.4	-40.8	4.7	164	154.8	-49.8
12	8YF-18	36.914	115.956	8/8	170.9	-37.3	2.1	684	181.8	-54.5
21	8YF-21	36.877	115.979	8/8	167.3	-35.9	2.7	409	183.4	-52.3
32	8YF-23	36.894	115.982	7/8	138.7	-33.6	1.9	986	140.2	-48.5
19	8YF-26	36.894	115.966	8/8	179.1	-25.1	1.4	1471	190.0	-46.7
37	8YF-31	36.912	115.992	7/8	190.8	-10.3	4.9	180	189.1	-45.2
33	8YF-33	36.903	115.981	8/8	175.9	-26.2	7.4	58	176.3	-51.2
27	8YF-36	36.886	115.990	6/8	140.2	-33.6	4.1	265	159.6	-56.8
Topopah Spring Member										
29	JR87-18	36.895	115.991	7/8	264.4	43.0	3.4	321	274.7	73.5
17	8YF-13	36.902	115.940	5/7	314.6	61.4	2.9	719	291.6	66.3
13	8YF-19	36.911	115.955	8/8	320.8	51.3	3.1	321	303.7	63.2
14	8YF-20	36.908	115.951	8/8	321.7	52.3	2.7	421	298.3	58.3
30	8YF-30	36.912	115.994	8/8	0.0	44.4	3.3	280	326.6	75.7
36	8YF-32	36.904	115.981	6/8	336.3	36.0	4.0	280	310.0	61.6
28	8YF-37	36.887	115.992	8/8	287.8	33.3	2.6	465	277.8	62.5

Estimates of Vertical-Axis Rotation

If the pattern of arcuate structures in the FPMM area arises from the proposed clockwise flexure of Carr (1984), site means of tuffs from this area should have declinations that are as much as 90° clockwise from declinations of site means from the reference areas and the Halfpint Range. Figure 4, which portrays tilt-corrected site means for the three units, shows that although site means from the FPMM area are more dispersed than those from the reference areas or from the Halfpint Range, their declinations are not systematically different than declinations of site means from the reference areas or the Halfpint Range. This demonstrates that tuffs in the FPMM area have not been strongly rotated about a vertical axis.

The angular difference between the declination of a site mean and the declination for the average of reference sites for each unit is an estimate of the amount and sense of vertical-axis rotation to affect each site. Figure 5 graphically shows the sense and amount of vertical-axis rotation estimated for individual sites within the FPMM and southern Halfpint Range areas. Rotation values are +17° to -31° for the Ammonia Tanks (positive values are clockwise), +19° to -31° for the Rainier Mesa, and +22° to -43° for the Topopah Spring. This diagram further illustrates that there is little correspondence between the amount and sense of vertical-axis rotation estimated from the paleomagnetic data and the trend of structural features in the FPMM area.

Although angular discordances between individual site means of Figure 5 and the reference directions are not of sufficient magnitude and are often of incorrect sense to explain the pattern of arcuate structures in the FPMM area, they do merit attention. Three factors are probably responsible for the greater dispersion of paleomagnetic data from the FPMM area relative to data from the reference areas and the Halfpint Range: (1) errors arising from tilt corrections, (2) predeformation dispersion of remanent directions within units, and (3) true local-scale vertical-axis rotation.

Significant dispersion of site means from an individual unit may arise from errors associated with tilt corrections. Empirically, it is observed that dispersion of site means increases with structural diversity of the area sampled. Rocks sampled in the reference areas are nearly flat-lying and their site means display little dispersion. Rocks sampled in the FPMM area have the greatest variation in strike and dip and their site means show greatest dispersion. Declination errors arising from inaccurate tilt corrections are of greatest concern for units with steeply inclined magnetization, such as the Topopah Spring Member, because small solid-angle errors in tilt-corrected directions can produce relatively large differences in declination.

For the Rainier Mesa Member, the counterclockwise shift of declinations observed in lowest parts of the unit may be responsible for some dispersion of site means. The direction determined from reference sites in the Rainier Mesa Member is strongly biased toward the direction of magnetization carried by the middle and upper parts which comprise the greater volume of the unit. Therefore, means from sites restricted to the lowest Rainier Mesa in the FPMM area and Halfpint Range may show counterclockwise discordances of declination, with respect to the reference direction, that do not reflect true vertical-axis rotation of the rocks. Data from sites 7YF-6 and 7YF-9 are probably examples of this.

Finally, for some sites (e.g., 8YF-11, 8YF-31) the discordance of declinations is too great to be reasonably explained by tilt-correction errors or intra-unit dispersion, and thus, true vertical-axis rotation has probably occurred. However, such vertical-axis

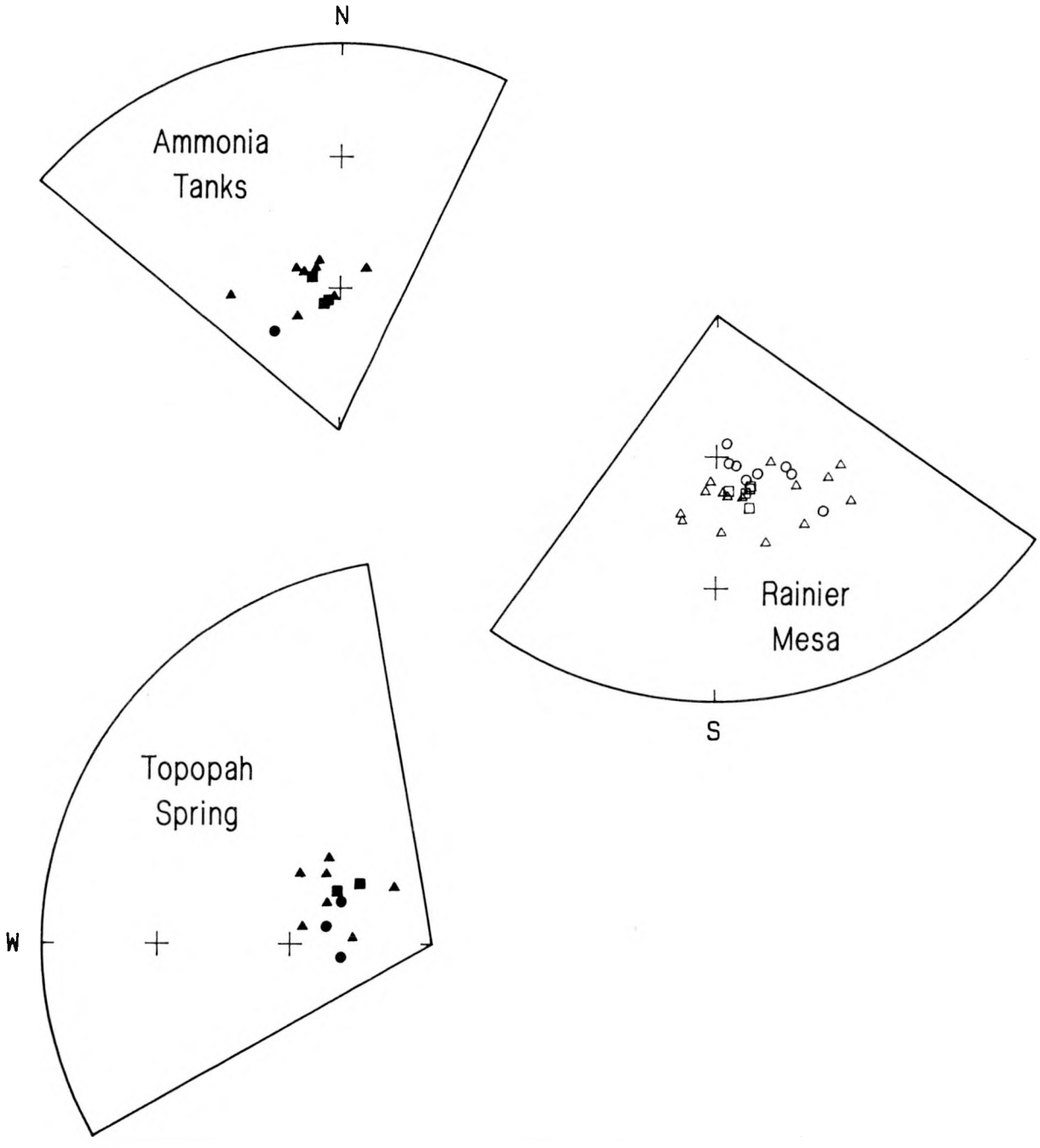


Figure 4. Equal-area projections showing tilt-corrected directions for site means of remanent magnetization from the Ammonia Tanks and Rainier Mesa Members of the Timber Mountain Tuff and the Topopah Spring Member of the Paintbrush Tuff. Sites from the FPMM area are shown as triangles. Symbols for sites are: FPMM area, triangles. Halfpint Range, circles. reference areas, squares. Solid and open symbols are projections on the lower and upper hemispheres, respectively.

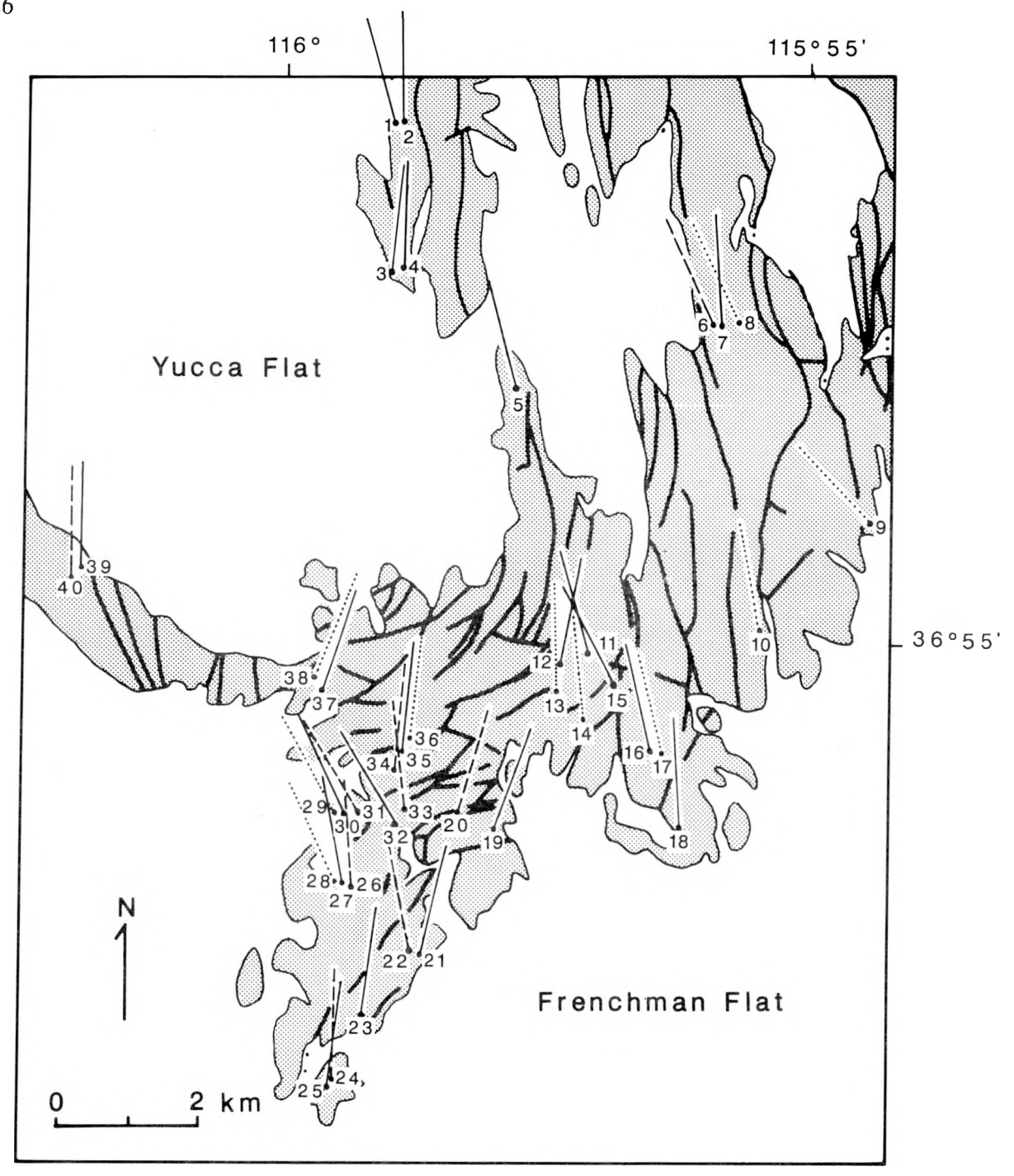


Figure 5. Estimates of vertical-axis rotation (angle between line and north) for individual sites (dots) from the FPMM and southern Halfpint Range areas. Amount of rotation is the angular difference between the declination of an individual site mean and the declination for the average of reference sites for each unit. Numbers by site locations are keyed to individual sites on table 1. Symbols for rotation estimates from the different units are: dashed lines, Ammonia Tanks Member. solid lines, Rainier Mesa Member. dotted lines, Topopah Spring Member. Heavy lines are faults.

rotation must be of local extent, and it is probably of both clockwise and counterclockwise sense.

TECTONIC IMPLICATIONS

The lack of regionally systematic clockwise rotation of rocks about a vertical axis in the FPMM area disproves the Yucca-Frenchman flexure model. As a result, evidence for the existence of the Yucca-Frenchman shear zone is lacking, inasmuch as the proposed clockwise flexure in the FPMM area was cited as the principal expression of right-lateral offset along the shear zone (Carr, 1984).

The lack of systematic vertical-axis rotation indicates that faults in the FPMM area originated with arcuate trends. This requires that the stress field within which the faults nucleated must have varied significantly over the relatively small FPMM area. For faults accommodating plane strain, the orientation of the principal stress axes controls the orientation in which faults nucleate (Anderson, 1951). For faults accommodating triaxial strain, both the orientation of the principal stress axes and, to a more poorly understood extent, the ratio of the principal stress magnitudes may control the orientation in which faults nucleate (Reches, 1983). Therefore, the pattern of arcuate structures in the FPMM area could reflect either a localized reorientation of the principal stress axes or a change in the relative magnitude of the principal stresses during growth of the faults.

To explain the pattern of arcuate structures in the FPMM area, I suggest that spatially offset fault zones north and south of the FPMM area simultaneously propagated into the zone between the two structural domains. As noted earlier, the FPMM area lies in an accommodation zone (fig. 1) between a northern structural domain (e.g., Halfpint Range, Yucca Flat) in which rocks in fault blocks dip west and a southern structural domain (e.g., southern Massachusetts Mountain, Frenchman Flat) in which rocks in fault blocks dip east. Interaction between local stress fields associated with the propagating tip of each fault zone (Pollard and others, 1982) may have caused reorientation of the stress field in the area between the overlapping fault segments, thereby allowing the arcuate structures to nucleate (fig. 6). In this context, the pattern of arcuate structures in the FPMM area is analogous to curved terminations observed in other tensile features such as joints (Pollard and others, 1982; Segall and Pollard, 1983), dikes (Delaney and Pollard, 1981), and oceanic spreading centers (MacDonald and Fox, 1983; Pollard and Aydin, 1984). The accommodation zone provided an area where tips of propagating fault zones could simultaneously overlap, thereby allowing reorientation of their local stress fields. Arcuate structural patterns are common within accommodation zones of other rifted areas (e.g., Rosendahl and others., 1986; Ebinger, 1989), and they have been produced in clay deformation models of accommodation zones (Serra and Nelson, 1988).

If the pattern of arcuate structures in the FPMM area does reflect interaction between two fault zones within an accommodation zone, the model may provide some insight into the structural development of the Yucca Flat and Frenchman Flat basins. To produce the clockwise curvature of structures in the FPMM area, the fault zone in the Halfpint Range (A, fig. 6) must have been located at longitudes east of the contemporary fault zone in the Massachusetts Mountain area (B, fig. 6). This is opposite to the present geographic offset of the Yucca Flat and Frenchman Flat basins. If structures observed in the Halfpint Range (northern domain) and Massachusetts Mountain area (southern domain) are representative of the style and episode of extension that led to development of Yucca Flat and Frenchman Flat basins, respectively, the present geographic offset of the basins suggests that the locus of extension within each domain migrated in the direction of fault block tilt (west for Yucca Flat, east for Frenchman Flat). This geometry of growth and tilting could be produced within each structural domain by sequential

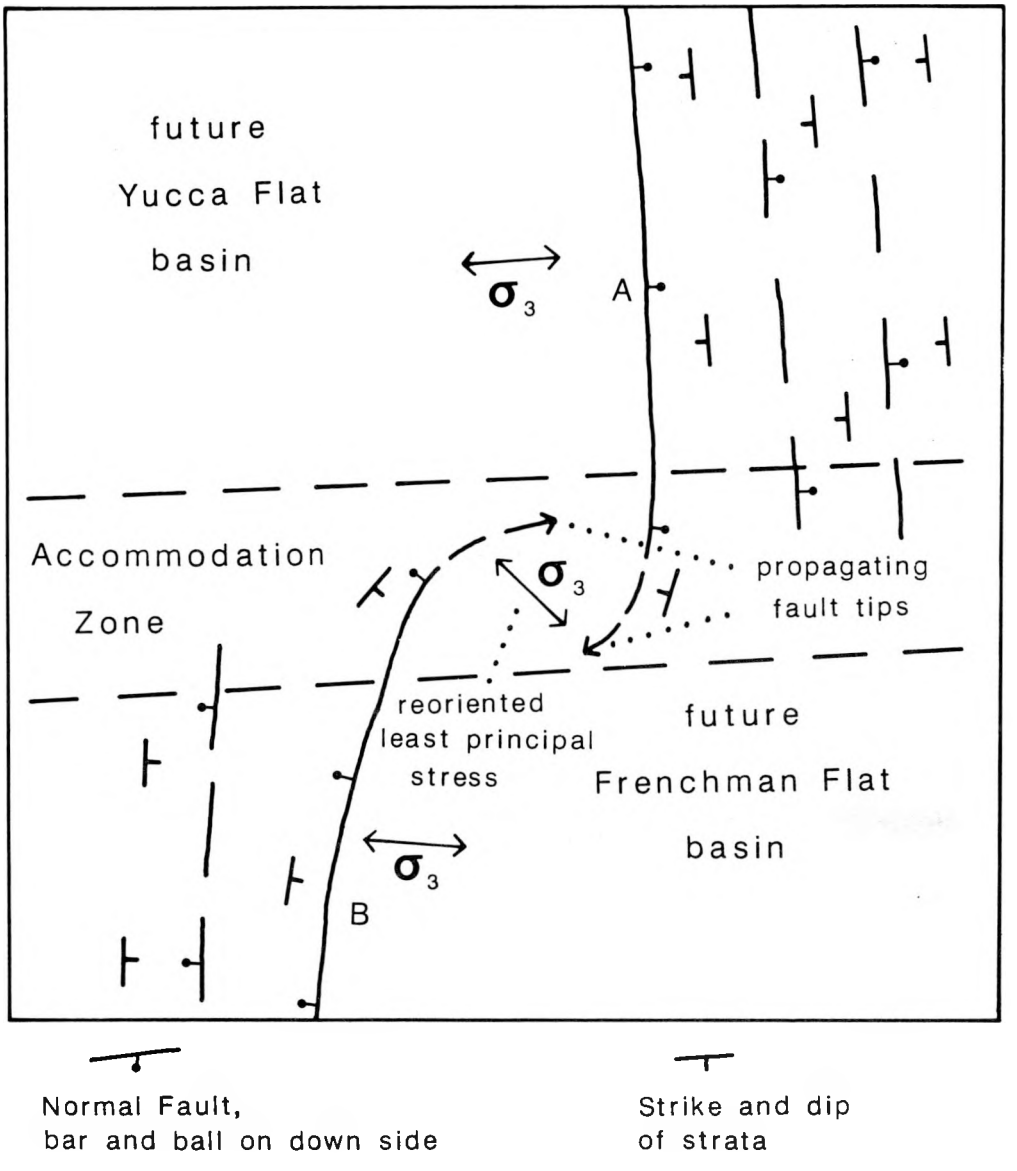


Figure 6. Schematic paleogeographic diagram showing development of arcuate structures in the FPMM area as the result of local reorientation of the stress field between overlapping segments of two fault zones that simultaneously propagated into an accommodation zone. Faults A and B depict positions of extensional zones that are inferred to have been active prior to development of the present Yucca Flat and Frenchman Flat basins.

incisement by normal faults into footwall rocks of previous fault blocks (e.g., Lister and Davis, 1989).

CONCLUSIONS

Paleomagnetic data obtained from the Ammonia Tanks and Rainier Mesa Members of the Timber Mountain Tuff and the Topopah Spring Member of the Paintbrush Tuff indicate that no regionally significant vertical-axis rotation has affected the French Peak-Massachusetts Mountain area. The pattern of arcuate structures observed in this area is not due to clockwise flexure along the previously proposed Yucca-Frenchman right-lateral shear zone of Carr (1984). The pattern of arcuate structures in the French Peak-Massachusetts Mountain area may reflect local reorientation of the stress field that occurred when fault zones simultaneously propagated into the accommodation zone that separates west-tilted fault blocks to the north from east-tilted fault blocks to the south.

ACKNOWLEDGMENTS

This investigation was conducted as part of an integrated series of studies by the U.S. Geological Survey to examine the structural framework of the Yucca Flat basin. This project is described under the annual work plan for Interagency Agreement DE-AI08-86NV10583 with the Department of Energy, Nevada Operations Office.

Special thanks go to W.C. Rivers for conducting much of the laboratory work. J.G. Rosenbaum kindly contributed data for three sites. R.L. Reynolds and K.F. Fox, Jr, provided helpful reviews of the manuscript.

REFERENCES

Anderson, E.M., 1951, The dynamics of faulting: Edinburg, Scotland, Oliver and Boyd, 2nd ed., 206 p.

Bosworth, William , Lambiase, J.J., and Keisler, R., 1986, A new look at Gregory's rift: The structural style of continental rifting: Eos, American Geophysical Union Transactions, v. 67, p. 577-583.

Carr, W.J., 1984, Regional structural setting of Yucca Mountain, southwestern Nevada, and late Cenozoic rates of tectonic activity in part of the southwestern Great Basin, Nevada and California: U.S. Geological Survey Open-File Report 84-854, 109 p.

Delaney, P.T., and Pollard, D.D., 1981, Deformation of host rocks and flow of magma during growth of minette dikes and breccia-bearing intrusions near Shiprock, New Mexico: U.S. Geological Survey Professional Paper 1201, 61 p.

Ebinger, C.J., 1989, Geometric and kinematic development of border faults and accommodation zones, Kivu-Rusizi rift, Africa: Tectonics, v. 8, p. 117-133.

Faulds, J.E., Hillmeyer, F.L., and Smith, E.I., 1988, Geometry and kinematics of a Miocene "accommodation zone" in the central Black and southern Eldorado Mountains, Arizona and Nevada, in Weide, D.L., and Faber, M.L., eds., This Extended Land, Geological Journeys in the Southern Basin and Range: Geological Society of America Field Trip Guidebook, Cordilleran Section, p. 293-310.

Fisher, R.A., 1953, Dispersion on a sphere: Royal Society of London Proceedings, v. A217. p. 295-305.

Hinrichs, E.N., and McKay, E.J., 1965, Geologic map of the Plutonium Valley quadrangle, Nye and Lincoln Counties, Nevada: U.S. Geological Survey Geologic Quadrangle Map GQ-384, scale 1:24,000.

Kirschvink, J.L., 1980, The least-squares line and plane and analysis of paleomagnetic data: Geophysical Journal of the Royal Astronomical Society, v. 62, p. 699-718.

Lister, G.S., and Davis, G.A., 1989, The origin of metamorphic core complexes and detachment faults formed during Tertiary continental extension in the northern Colorado River region, U.S.A.: Journal of Structural Geology, v. 11, p. 65-94.

MacDonald, K.C., and Fox, P.J., 1983, Overlapping spreading centers: New accretion geometry on the East Pacific Rise: Nature, v. 302, p. 55-58.

McKeown, F.A., Healy, D.L., and Miller, C.H., 1976, Geologic map of the Yucca Lake quadrangle, Nye County, Nevada: U.S. Geological Survey Geologic Quadrangle Map GQ-1327, scale 1:24,000.

Pollard, D.D., and Aydin, Atilla, 1984, Propagation and linkage of oceanic ridge segments: Journal of Geophysical Research, v. 89, p. 10,017-10,028.

Pollard, D.D., Segall, Paul, and Delaney, P.T., 1982, Formation and interpretation of dilatant echelon cracks: Geological Society of America Bulletin, v. 93, p. 1,291-1,303.

Poole, F.G., 1965, Geologic map of the Frenchman Flat quadrangle, Nye, Lincoln, and Clark Counties, Nevada: U.S. Geological Survey Geologic Quadrangle Map GQ-456, scale 1:24,000.

Poole, F.G., Elston, D.P., and Carr, W.J., 1965, Geologic map of the Cane Springs quadrangle, Nye County, Nevada: U.S. Geological Survey Geologic Quadrangle Map GQ-455, scale 1:24,000.

Reches, Zeev, 1983, Analysis of faulting in three-dimensional strain field: Tectonophysics, v. 47, p. 109-129.

Rosenbaum, J.G., 1986, Paleomagnetic directional dispersion produced by plastic deformation in a thick Miocene welded tuff, southern Nevada: Implications for welding temperatures: Journal of Geophysical Research, v. 91., p. 12,817-12,834.

Rosendahl, B.R., Reynolds, D.J., Lorber, P.M., Burgess, C.F., McGill, J., Scott, D., Lambiase, J.J., and Derksen, S.J., 1986, Structural expressions of rifting: Lessons from Lake Tanganyika, Africa, in Frostick, L.E., Renaut, R.W., Reid, I., and Tiercelin, J.J., eds., Sedimentation in the African rifts: Geological Society of London Special Publication 25, p. 29-44.

Segall, Paul, and Pollard, D.D., 1983, Joint formation in granitic rock of the Sierra Nevada: Geological Society of America Bulletin, v. 94, p. 563-575.

Serra, S, and Nelson, R.A., 1988, Clay modeling of rift asymmetry and associated structures: Tectonophysics, v. 153, p. 307-312.

STRUCTURAL RELATIONS WITHIN THE PALEOZOIC BASEMENT OF THE MINE MOUNTAIN BLOCK; IMPLICATIONS FOR INTERPRETATION OF GRAVITY DATA IN YUCCA FLAT, NEVADA TEST SITE

James C. Cole, Ronald R. Wahl, and Mark R. Hudson
U.S. Geological Survey,
Mail Stop 913, Denver CO 80225-0046

ABSTRACT

Detailed geological mapping in the Mine Mountain block between Yucca Flat and Mid Valley demonstrates that most of the low-angle fault contacts between various Paleozoic rock units are the result of Tertiary near-surface block sliding, contrary to the long-held notion that the principal structural control derives from late Mesozoic thrusting during the Sevier orogeny. When structural and stratigraphic features of the hangingwall rocks above these low-angle faults are compared to similar data for the footwall rocks beneath, no evidence is found for the systematic patterns and three-dimensional relationships that characterize thrusted terranes of the Sevier in southern Nevada.

The complex structure of the Mine Mountain block can be approximated as an irregular stack of east-tilted, tabular, fault-bounded sheets, composed of Silurian and Devonian carbonate rocks and less common Ordovician quartzite and Mississippian siltstone, that tectonically overlie clastic rocks of the Mississippian upper part of the Eleana Formation. Bedding and stratigraphic order within these sheets face either eastward or westward, and no simple relation describes the stratigraphic progression from structurally lower to structurally higher sheets. Intense shattering typifies the basal zone of each hangingwall block (severity diminishes structurally upward), whereas the tops of footwall blocks are commonly striated on large mullions, but little broken. Cleavage is absent.

The overall eastward slope of the Mine Mountain structure appears to result from major tilting on high-angle, down-to-the-west faults that were active during Redrock Valley Tuff time (ca. 16? Ma), based on stratigraphic and reconnaissance paleomagnetic data. The high-level block sliding is inferred to have taken place at about the same time, because a minor slide block is intercalated with coarse conglomerate that overlies the Redrock Valley at the north end of Mine Mountain. Data obtained from slickensided surfaces within the slide structure indicate the prevailing direction of tectonic transport was toward the west and southwest.

If the exposed relations at Mine Mountain are extrapolated as a general structural model for the Paleozoic rocks of the area, then the distribution of rock types in the subsurface is much less predictable than with the Mesozoic thrust model. Disconnected and stratigraphically unrelated sheets of diverse Paleozoic rocks may overlie the Eleana eastward to the Carpetbag fault, and possibly beyond. The traditional interpretation of Yucca Flat gravity data is that local gradients correspond to scarps (elevation discontinuities) in the buried top of the

Paleozoic basement. The conservative approach for containment considerations requires that these scarps be inferred to mark the traces of high-angle faults. The Mine Mountain model, however, allows that lateral gravity gradients may be due to lateral density variations in Paleozoic rocks (resulting from the mid-Tertiary sliding), and may have no tectonic significance for the overlying volcanic and alluvial materials. Model calculations show that realistic assumptions for slide-sheet thickness and density contrast can account for observed gravity gradients for a range of burial depths.

INTRODUCTION

Rocks exposed in the vicinity of Yucca Flat at the Nevada Test Site include the regional clastic and carbonate strata that range in age from latest Proterozoic through Pennsylvanian, Cretaceous granitic intrusions, and the blanketing cover of Oligocene(?) to Holocene volcanic and sedimentary units. These younger units largely represent the eruptive products of the southwestern Nevada volcanic field, and the post-volcanic detrital fill within the present structural basins. Most of the geologic and engineering studies through the years have concentrated on understanding these units and their physical properties because they have been the media for most underground nuclear testing.

Our interest in investigating the pre-Tertiary "basement" rocks that are widely exposed in the hills and ranges surrounding Yucca Flat was raised by four principal considerations: 1. the structural framework of the testing media is a product of the structural history of the area, and the Paleozoic and older basement rocks provide a record of the earliest phases of the regional deformation; 2. greater understanding of the distribution and physical properties of the basement rocks would be essential if experiments were ever to be conducted there; 3. realistic models of local and regional ground-water systems require credible structural models of the location and connectivity of permeable and impermeable strata; and 4. significant lateral density variations within the Paleozoic terrane are required to reconcile standard two-dimensional gravity calculations with borehole data for depth to basement, but no existing structural model accounts for these density variations.

Early studies in the Nevada Test Site region recognized the common occurrence of older Paleozoic units above sub-horizontal fault contacts with younger Paleozoic strata at the Mine Mountain, CP Hills, and Calico Hills areas (figs. 1, 2; for example, Johnson and Hibbard, 1957; Barnes and others, 1965; Hinrichs, 1968; and Carr, 1974). Most of these early interpretations of the pre-Tertiary structure required major, although unquantified, late Mesozoic displacements on a singular great sheet of the Sevier thrust system to explain the observed relations. Robinson (1985), however, pointed out that the structural and stratigraphic correlations required by the thrust sheet model were highly speculative because outcrop is sparse and discontinuous, and argued that interpretations based on gravity sliding may also be applicable. Carr (1984) and Dockery and others (1984) acknowledged the possibility that older-over-younger faults in the Calico Hills and Mine Mountain areas might be post-Mesozoic near-surface, gravity-driven block slides, but they fundamentally retained the thrust mechanism as the dominant control of Paleozoic rock distributions.

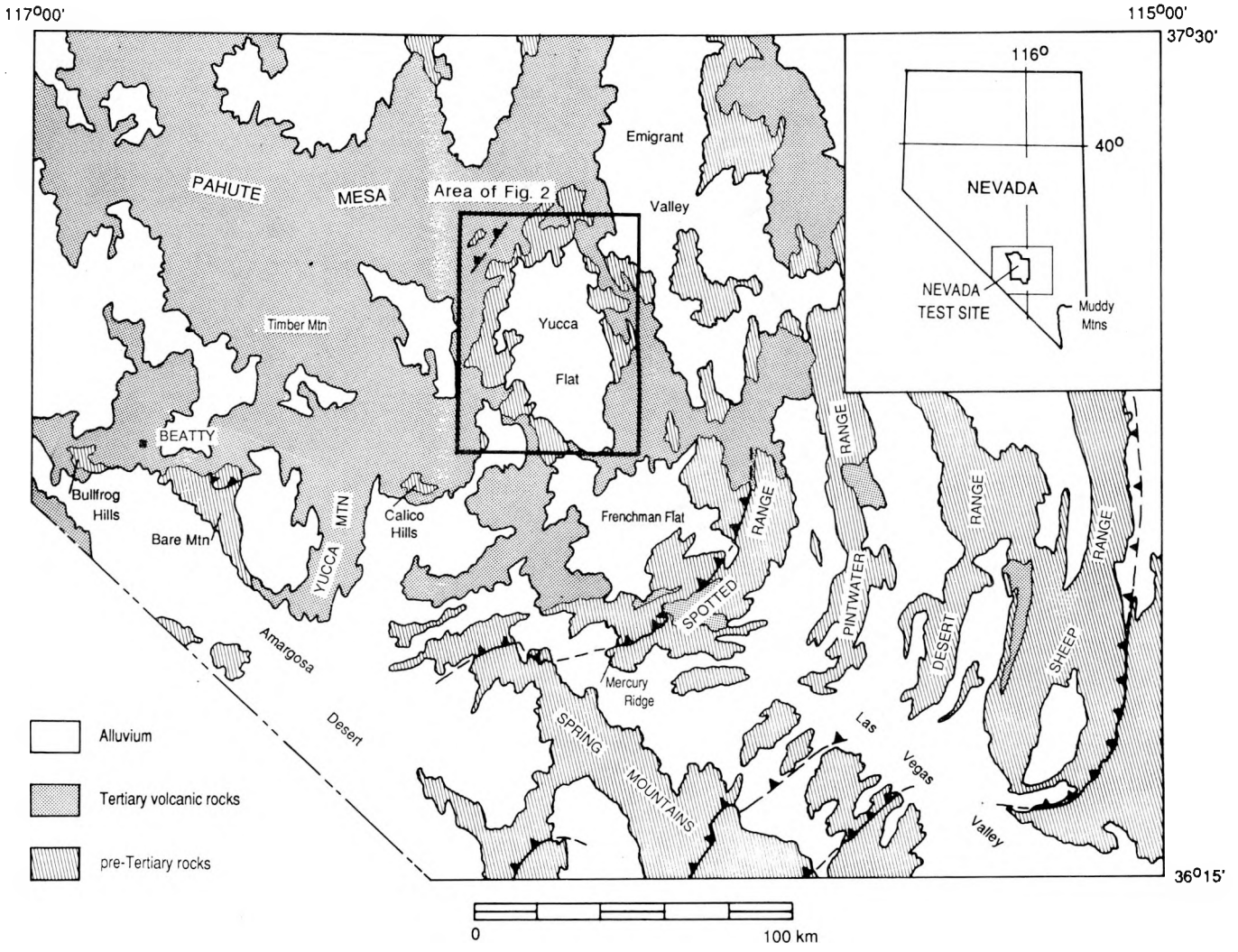


Figure 1. Regional geologic sketch map of southern Nevada in the area of the Nevada Test Site, showing the distribution of middle and upper Tertiary volcanic rocks and (pre-Tertiary) Paleozoic and Upper Proterozoic miogeoclinal sedimentary rocks. Major southeast-vergent thrusts of the Late Cretaceous Sevier orogenic belt are shown for reference (Guth, 1981; Wernicke and others, 1988).

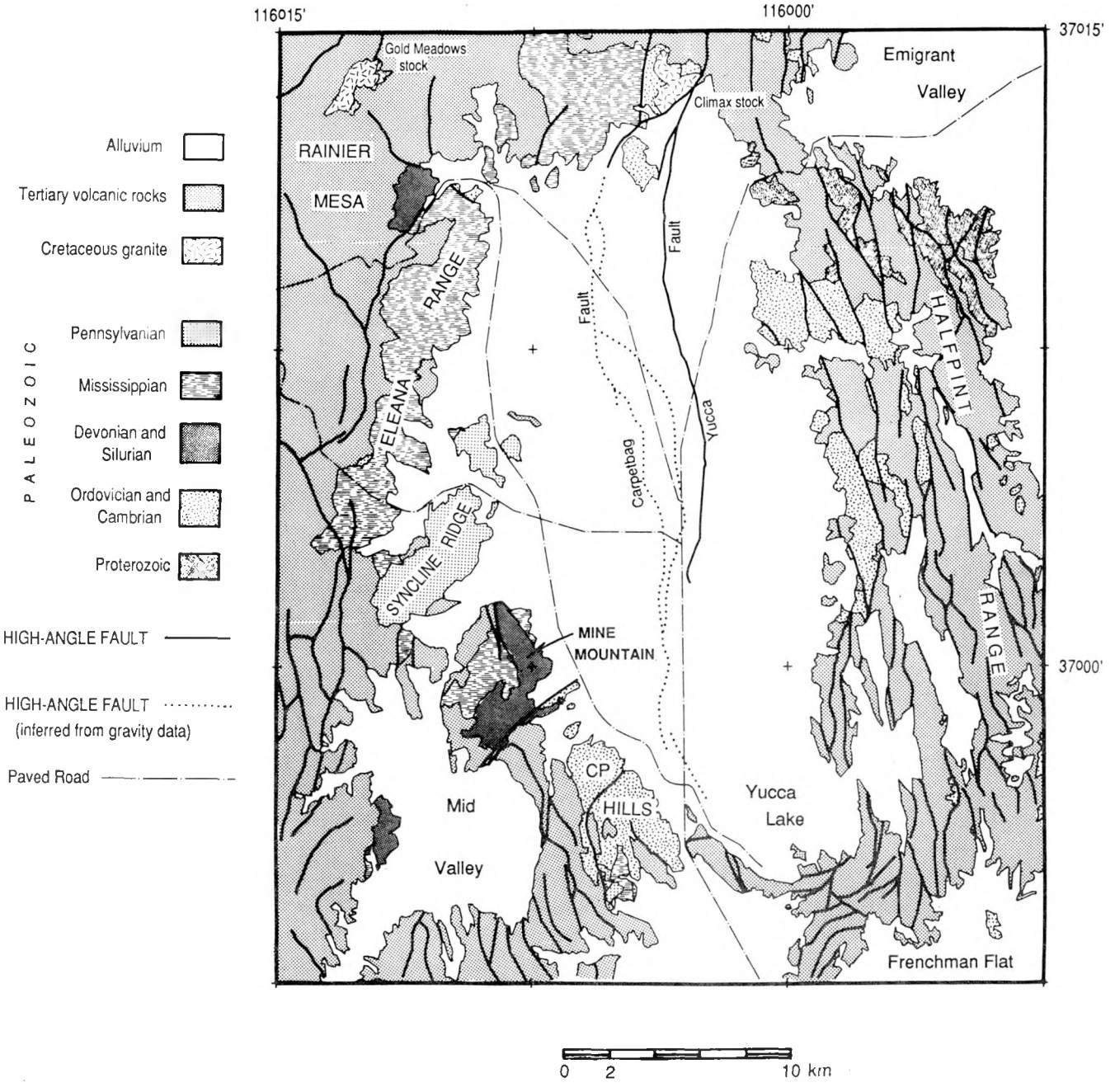


Figure 2. Geologic sketch map of the Yucca Flat area showing distribution of pre-Tertiary rock units (described in fig. 3).

This report is based on detailed mapping of the Mine Mountain area and describes the structures and stratigraphic relationships within the pre-Tertiary basement. The abundant information obtained to date is incompatible with the thrust-fault model, and rather demonstrates that all exposed low-angle tectonic contacts between Paleozoic rock units are normal faults that formed during an early to middle Miocene extensional event. The common (but not universal) stratigraphic inversion across these low-angle faults (older-over-younger) at Mine Mountain requires a prior event of crustal shortening (most likely the Sevier orogeny), but no structures have been recognized in the Mine Mountain or CP Hills areas that were clearly formed in that event.

ACKNOWLEDGMENTS

These investigations were conducted as part of an integrated study by the U.S. Geological Survey to examine the structural framework of the Yucca Flat basin. This project is described under the annual work plan for Interagency Agreement DE-AI08-86NV10583 with the U.S. Department of Energy, Nevada Operations Office.

We would especially like to acknowledge the input of P. L. Guth at the beginning of this program in 1987. Working as an unpaid volunteer, Guth helped recognize and define the more detailed stratigraphic elements (fig. 3) that were the tools needed to map out structures within the Paleozoic terrane. His work in the Sheep, Desert, and Pintwater Ranges to the southeast, where thrust-fault and normal-fault structures are preserved side by side, provided the basis to distinguish similar structures on the Nevada Test Site.

GEOLOGIC SETTING

In this part of the southern Great Basin, the late Mesozoic Sevier orogenic belt exerts considerable influence on the distribution and disposition of the Paleozoic rock units. This system of imbricate eastward-directed thrust sheets is well preserved to the south and east of the Nevada Test Site in the Spring Mountains and northeast of the Las Vegas Valley between the Spotted Range and the Muddy Mountains (fig. 1; Burchfiel and Davis, 1988; Wernicke and others, 1988). A review of the regional thrust system is beyond the scope of this paper, but it is important to note that the system is relatively simple in general. The Sevier belt involves a few major thrusts, most all plates were transported eastward, and the thrust surfaces are typically sharp, planar, and west-dipping (Guth, 1981, in press a, b; Wernicke and others, 1988). Thrust-related small-scale deformation in the hangingwall is commonly restricted to a zone within a few meters of the fault, but much greater footwall deformation is preserved in the form of overturned synclines, intense shearing, and cleavage development.

North and west of the Spotted Range thrust (Barnes and Poole, 1968; Barnes and others, 1982) within the Nevada Test Site area (fig. 1), recognition of Mesozoic thrust structures is much less certain because the Paleozoic rocks are discontinuously exposed beneath the Tertiary volcanic cover, and because Tertiary extensional deformation has altered the spatial relationships to a considerable degree. The Halfpint Range east of Yucca Flat exposes a disrupted but fairly regular west-facing section from the Late Proterozoic Johnnie Formation through the Ordovician Eureka Quartzite, whereas the western margin of Yucca Flat exposes a gener-

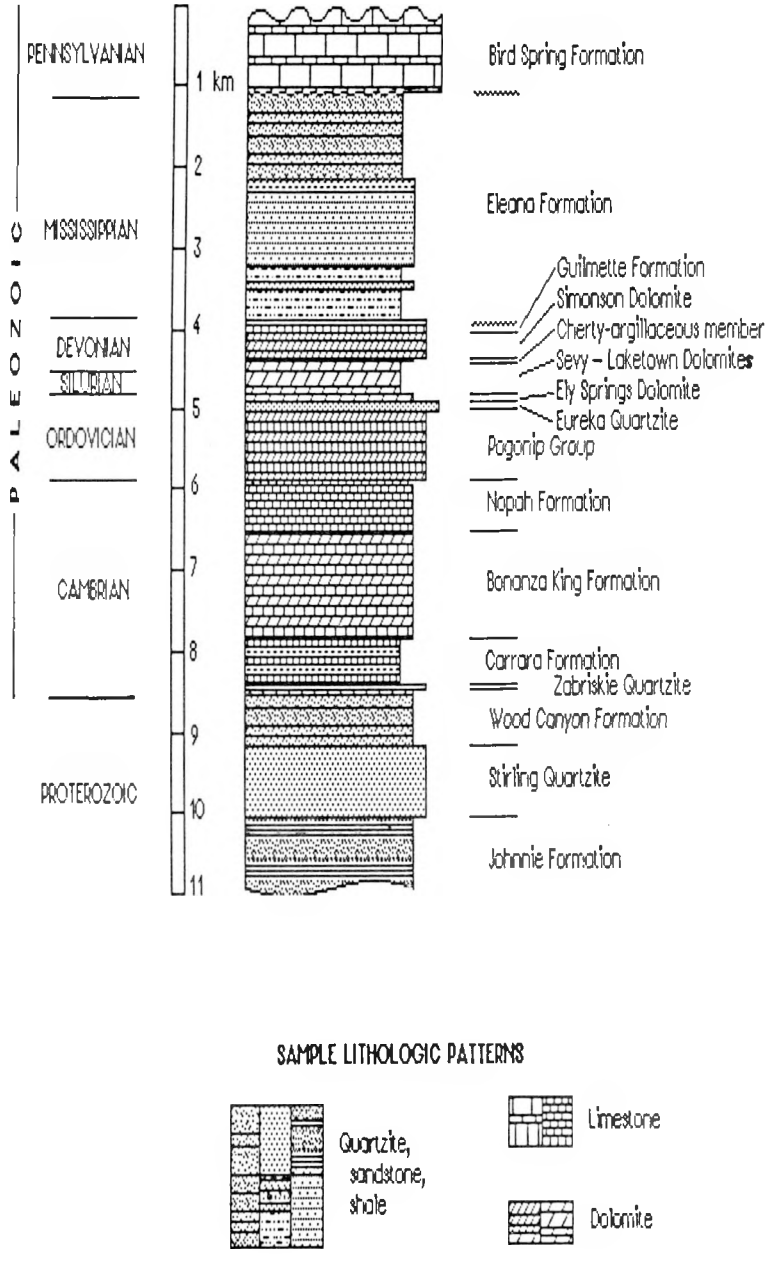


Figure 3. General stratigraphic column for the largely conformable Paleozoic and older sedimentary rocks exposed in the vicinity of Yucca Flat (P. L. Guth, written communication, 1988). Well defined paraconformable contacts are indicated at right by sawtooth line; minor diastems are probably present as well. Formation thicknesses are reasonably constant in the area, except for extreme variability within the Eleana Formation. The value shown here for the Eleana is probably maximum; informal units A through J of Poole and others (1961) not shown. The informal cherty-argillaceous member is provisionally assigned to the Simonson Dolomite. Laketown Dolomite has not been positively identified in Yucca Flat area outcrop because it is similar to the poorly bedded Sevy Dolomite and because of considerable structural complication, but may be present in areas mapped as Sevy-Laketown Dolomites.

ally south- and southeast-facing section from the Late Devonian at the base of the thick Eleana Formation through the Pennsylvanian Bird Spring Formation (figs. 2, 3). The intervening Silurian and Devonian dolomite and limestone units are chiefly preserved in a fault-bounded, west-facing section between the Eleana Range and the Tertiary cover of Rainier Mesa, and in the Mine Mountain area, as described in detail below.

Although it is the conclusion of this study that no Mesozoic thrusts are currently exposed at the Nevada Test Site north of Frenchman Flat, two features of the Paleozoic basement require that hinterland thrusting did occur west of the Spotted Range thrust (fig. 1). The entire Mississippian interval at Mercury Ridge is only about 300 m thick and consists chiefly of shelf limestone (Barnes and others, 1982), but the same interval west of Yucca Flat is more than 2300 m thick and consists of clastic debris that was shed eastward from the Antler orogenic belt into a subsiding basin (Poole and others, 1961). Because these two localities are currently about 80 km distant and must have been even closer prior to mid-Tertiary extension, the thickness and facies contrasts seem to require thrust convergence of the original basin (Guth, in press b). Similarly, the presence of Late Proterozoic and Early Cambrian Wood Canyon Formation at Gold Meadows west of the Eleana Range (fig. 2) indicates that the Cretaceous granite there was emplaced through a buried thrust that ramped Wood Canyon over the Mississippian Eleana Formation. West of the Nevada Test Site at the north end of Bare Mountain (fig. 1), Carr and Monsen (1988) mapped a disrupted fault complex with similar stratigraphic relationships that they interpreted as a southwest-vergent Mesozoic thrust.

Much recent structural work in the southern Great Basin has focused on defining the geometry and timing of major crustal distension which, at the latitude of the Nevada Test Site, has produced at least 100 percent extension of pre-Miocene features (Guth, 1981, in press b; Hamilton, 1988; Wernicke and others, 1988). The regularly tilted, fault-bounded ridges that are capped by Miocene volcanic rocks in the Nevada Test Site region attest to part of this extensional deformation and to the rotational style of faulting typical of higher crustal levels. However, the magnitude of this Miocene event and the characteristics of low-angle normal faults that were formed by it were not recognized at the time of initial quadrangle mapping in this area in the 1950's and 1960's, and so the thrust interpretations of that era do not reflect the current state of knowledge.

Our focus in the Mine Mountain area was to critically examine and evaluate detailed evidence for fault mechanisms that can produce older-over-younger stacking relations, and to compare them with features from neighboring thrusted terranes that have not been overprinted by younger extensional deformation.

GEOMETRIC CHARACTERISTICS OF THE MINE MOUNTAIN STRUCTURE

The main structural feature of the Mine Mountain area is the preservation of Silurian and Devonian carbonate rocks above low-angle fault contacts with Mississippian clastic rocks of the Eleana Formation (Orkild, 1968; fig. 4). The low-angle faults dip gently toward the east or east-northeast in the area north of the Mine Mountain Road, but are inclined toward the east-southeast, south, and locally toward the south-southwest in that area south of the road. As displayed at North Knob (fig. 5) and South Knob, vertical imbrication is typical of the overall Mine Mountain structure, and two or more major low-angle faults can be mapped

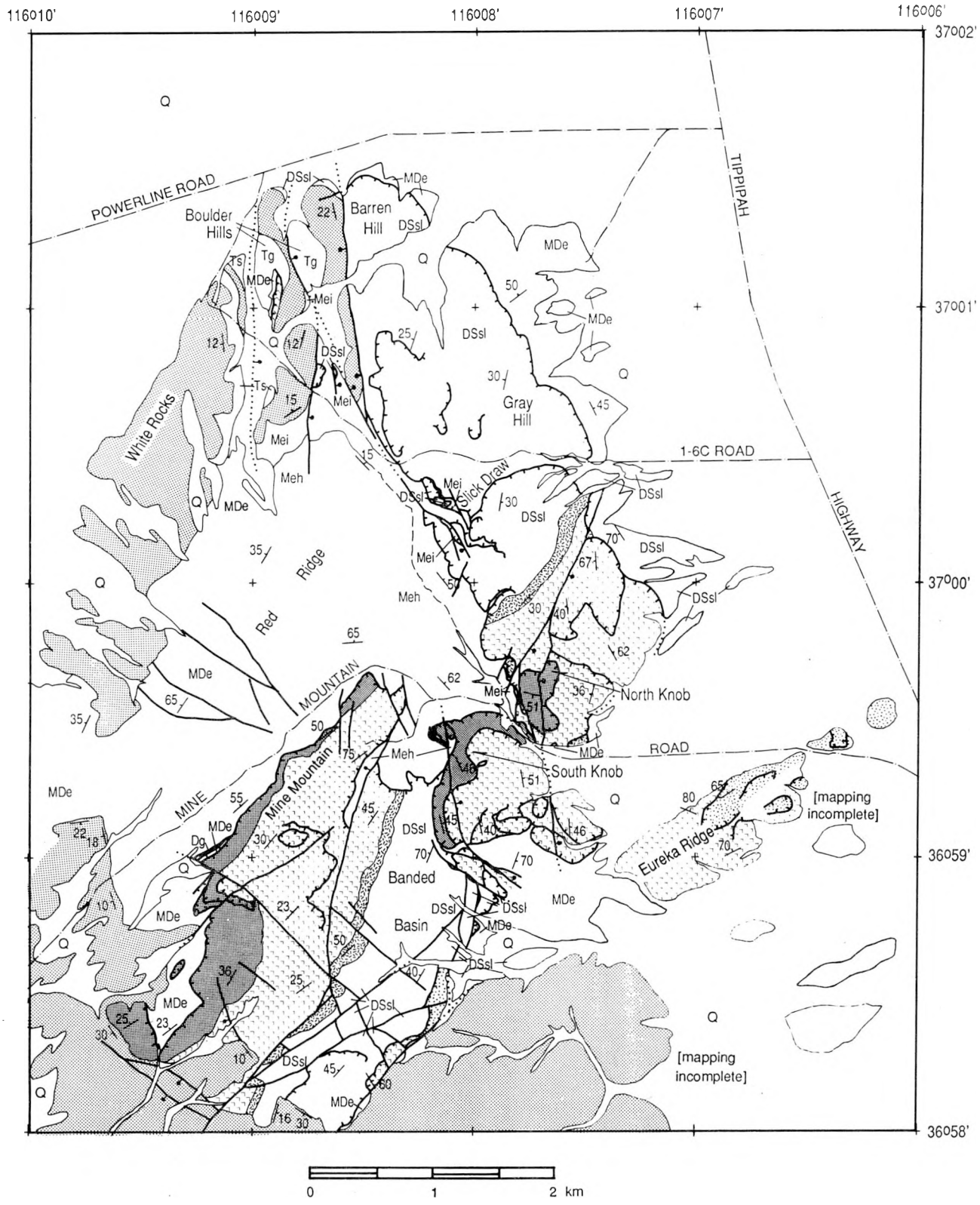


Figure 4. Geologic map of the Mine Mountain area, west of Yucca Flat, based on unpublished work by the senior author and P. L. Guth. Informal geographic place names are shown only as an aid to describe locations; ages of Paleozoic units are indicated on fig. 3.

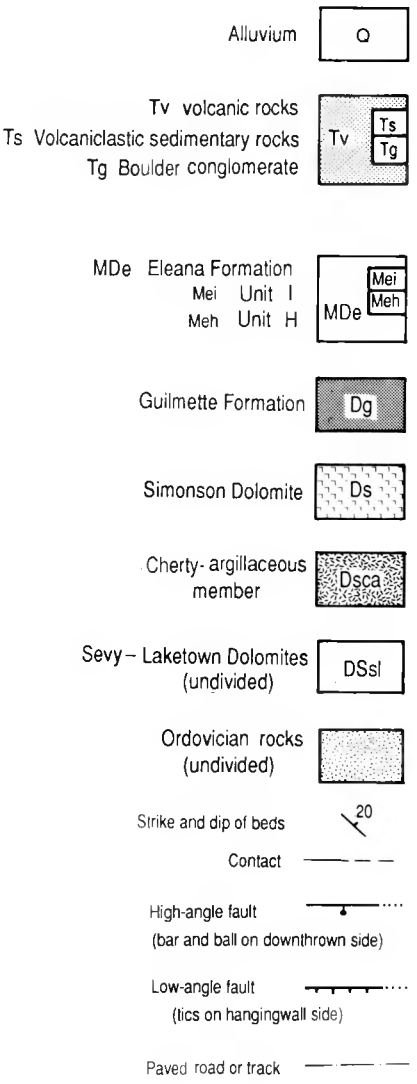


Figure 4. Continued.

within the Silurian-to-Mississippian rocks across any given east-west traverse. Thus, the structural units in this region may be thought of as sheetlike, with each sheet containing a fairly coherent stratigraphic slice, but bounded above and below by a low-angle fault.

The Eleana Formation, which forms the general substrate to this entire structure at the current level of exposure, appears to be little deformed internally (as described below) and bedding attitudes define a broad, open anticline that plunges gently toward the north (fig. 4). The contact between silty and limestone-bearing parts of the Eleana (informal units H and I of Poole and others, 1961) along the northeast limb of the anticline is broadly conformable to the base of the lowermost tectonic sheet in the area north of the Mine Mountain Road, but elsewhere the Eleana bedding is cleanly truncated upward and attitudes show no systematic relation to the low-angle faults.

One feature that emphasizes the complexity of these imbricated tectonic sheets is the internal stratigraphy of the Ordovician, Silurian, and Devonian units in the hangingwall blocks. Although all low-angle faults generally dip toward the east or south, the dip and stratigraphic-facing direction is eastward in some tectonic sheets and westward in others. For example, the main low-angle fault at Mine Mountain dips toward the southeast and cuts eastward downsection through an upright, west-tilted section from the Guilmette Formation, through the Simonson Dolomite, and into the Sevy-Laketown Dolomites (fig. 4). South of the 1-6C Road, another gently east-tilted low-angle fault cuts upsection toward the east through an east-tilted section from the Sevy-Laketown into the Simonson Dolomite. Immediately northeast of North Knob, a similar fault marks the contact between east-tilted Simonson in the footwall and west-tilted Simonson in the hangingwall.

In addition to these stratigraphic contrasts within sheets, relationships between sheets are also complex. At South Knob, the highest tectonic sheet carries east-tilted Simonson over a sheet of east-tilted (younger) Guilmette, and both tectonically overlie the lowermost sheet of (older) Sevy-Laketown. On Eureka Ridge (fig. 4), remnant slabs of Middle and Upper Ordovician Eureka Quartzite lie structurally above east-tilted Lower and Middle Ordovician Antelope Valley Limestone (Pogonip Group) as well as above west-tilted Devonian Simonson Dolomite.

In summary, the general geometric and stratigraphic relations in the Mine Mountain area describe a system of imbricated tectonic sheets that currently have a collective tilt direction toward the east and south. Although the oldest allochthonous units tend to form the lowermost sheets (and the youngest the highest), numerous exceptions are noted and the entire tectonic stack is largely chaotic.

The thickness of the major sheets is estimated to be about 75 to 100 m, but imbrications on a much finer scale have also been mapped. A traverse from the base to the summit on the west slope of South Knob begins in Eleana Formation footwall rocks and crosses a low-angle fault into a 10-m thick slab of Simonson Dolomite, and then crosses additional low-angle faults into Guilmette Formation (about 15 m thick), Eleana Formation (5 to 20 m thick), Simonson Dolomite (about 10 m thick), Eleana Formation (about 10 m thick), and finally into the uppermost sheet of Guilmette. An equally intricate pattern of imbrication is well displayed at

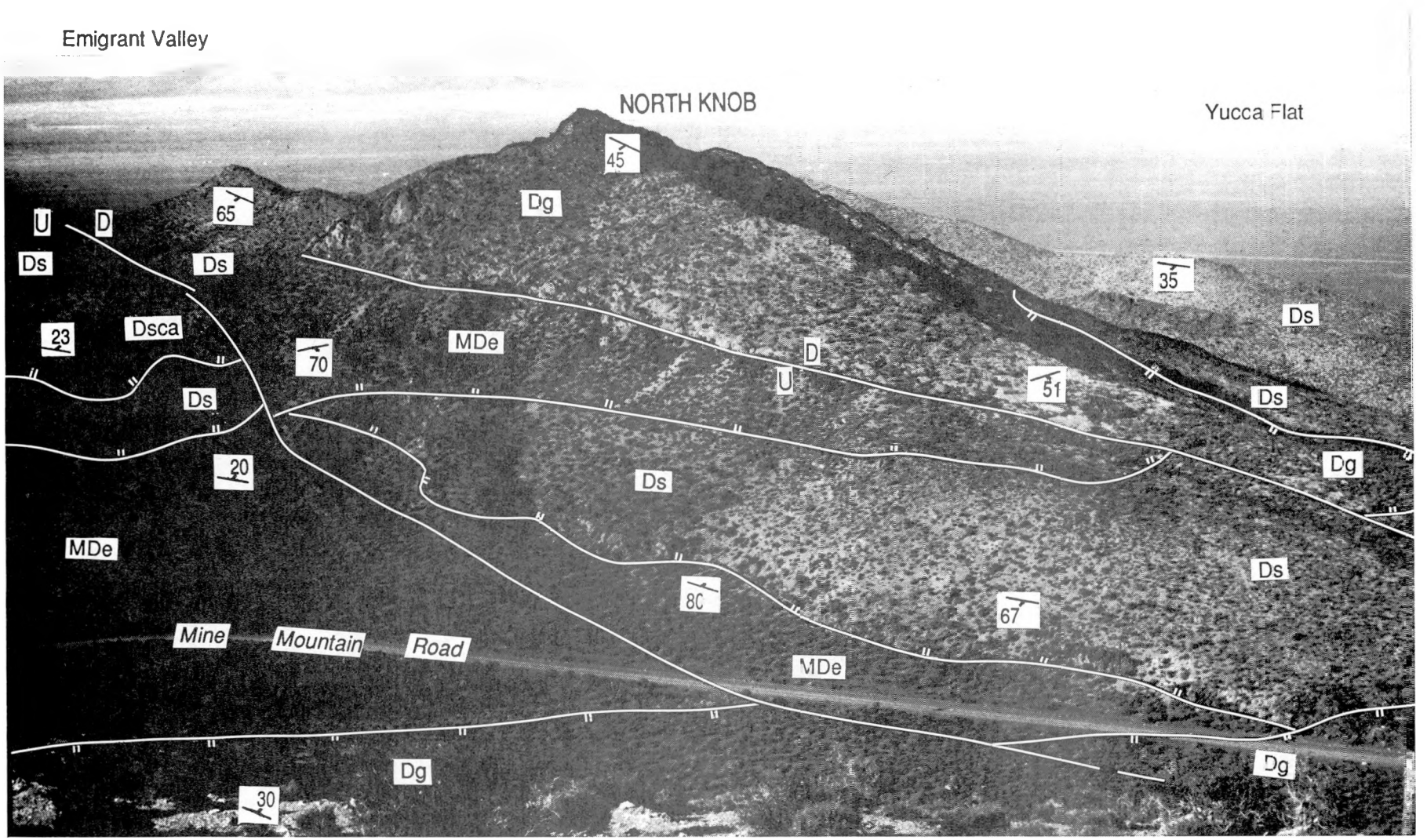


Figure 5. View toward the northeast from the slope of South Knob showing low-angle imbrications of tectonic sheets. Note that low-angle faults (shown with decoration on hangingwall block) cut obliquely across bedding both above and below, that each sheet has its own facing direction and that stratigraphic order is shuffled to a considerable extent. Two younger, high-angle faults cross the field of view from upper left to lower right (denoted by U/D symbols) and drop the imbricate sheets down toward the current structural basin of Yucca Flat. Refer to fig. 4 for explanation of symbols.

Slick Draw, south of the 1-6C Road (fig. 4). Here, the interleaved units consist of the Sevy-Laketown Dolomites and unit I of the Eleana Formation, which form a tectonically shuffled stack of no fewer than four identifiable sheets over a vertical distance of less than 75 m.

SMALL-SCALE FEATURES OF THE LOW-ANGLE FAULTS

The low-angle faults that bound these tectonic sheets in the Mine Mountain area are distinguishable from other types of faults on the basis of systematic characteristics of small-scale deformation features on the fault surface, within the hangingwall, and within the footwall rocks near the fault. The faults are most readily mapped where a significant stratigraphic or structural break occurs between hangingwall and footwall, but the distinctive fault zone structures described below can also be recognized within rather massive units like the Sevy-Laketown Dolomites, or between disjunct but well bedded stratigraphic pieces of a single formation (for example, the Simonson Dolomite).

Footwall rocks are characteristically little deformed at or near the fault, whether they consist of relatively incompetent siltstone and thin-bedded limestone of the Eleana Formation or brittle dolomite of one of the Silurian-Devonian units. Bedding attitude in the Eleana remains similar to local orientations up to the fault, regardless of the geometry of the fault-bedding intersection. Neither small-scale folds nor cleavage has been detected in these footwall rocks. Eleana limestone beds typically display irregular tension veins filled with recrystallized calcite within about one meter of the fault surface, but abundant disk-shaped crinoid fragments in the limestone show no sign of internal strain. Dolomitic footwall rocks tend to be somewhat more closely fractured within a few meters of low-angle faults, but they are otherwise undeformed.

In striking contrast to footwall behavior, the hangingwall rocks of these low-angle normal faults show characteristic intense brecciation and shattering. The style of deformation is best displayed by the brittle dolomites, but similar features are also identifiable within limestone and quartz-bearing rocks of various units. The brecciation results from numerous, random fractures that criss-cross the rock, but pieces are not significantly rotated or translated with respect to each other. Side-by-side breccia fragments, 1 to 3 cm in average diameter, can be closely matched across fracture surfaces, and fragments that contain traces of bedding show continuity from one to another (fig. 6). Comminuted rock matrix is not common between fragments because clast rotation, grinding, and milling were limited.

The intensity of brecciation diminishes systematically with distance above the fault surface. For dolomitic hangingwall rocks, pervasive shatter breccia (clasts less than about 5 cm) is common within 3 to 5 m of the fault; thin zones of more finely crushed rock are common and are variably oriented with respect to the overall fault surface. At greater distances, the average size of fragments is progressively larger, the brecciation is less pervasive, and the thin zones of intense crushing are less common. Fault-related fracturing is essentially indistinguishable from normal jointing at distances greater than about 15 m above the fault surface.

This intense fracture network at the base of the hangingwall block appears to have influenced ground-water circulation, because the breccias are densely recemented and are typically stained red, orange, and yellow with iron oxides



Figure 6. Detail photograph of outcrop east of Gray Hill (fig. 4), showing shattered Sevy-Laketown Dolomites in the hangingwall of a low-angle normal fault, located approximately 3 m below hammer. Color boundary within this breccia (at the midpoint of the hammer handle) marks an original bedding surface that is parallel to bedding in less disturbed rock 20 m above the fault. Brecciation was caused by intense fracturing (shatter) without much milling or rolling between fragments.



Figure 7. Photograph of outcrop in Slick Draw (fig. 4), showing large-scale fault mullions on the top of footwall dolomite that was overridden by Eleana Formation siltstone. These major striations plunge gently toward the northeast, which is also the tectonic transport direction at this site (deduced from slip-sense criteria; see text). Recurrent movement is indicated by younger, fine-scale scratches and striations (not shown) that have a more northerly trend in Slick Draw.

leached from the underlying Eleana Formation siltstone. The distinct hydrologic characteristic of the breccia zones persists even at present because the low-angle faults form prominent lineaments marked by hydrophilic plants.

The fault surfaces are best preserved where the footwall rock is dolomite, and these surfaces are typically marked by broad mullion grooves and ridges along the direction of dominant tectonic transport. Smaller-scale slickenside lineations are preserved, particularly in siliceous units of the Eleana Formation but also in some dolomites, and multiple sets of slickensides are not uncommon (kinematic significance of these features is described below). Rare lineations formed by fibrous growth of carbonate minerals, where present, also reflect the direction of tectonic transport.

The fault surfaces on dolomite (fig. 7) consist of a 1-cm-thick zone of intensely crushed and milled rock that is silicified, and recemented by dolomite. Iron-oxide staining is pervasive, and surfaces within this zone are commonly coated with fine crystalline aggregates of specular hematite. Highly polished surfaces preserve the fine-scale slickenside lineations as grooved scratches and as trails of silicified gouge in the lee of surface asperities. Fault surfaces in quartz-rich rocks (sandy carbonate beds, siliceous siltstone, quartzite) are generally well preserved, variably coated with iron oxides, and highly polished. Some of these faults are discrete curviplanar fractures through undisturbed rock, whereas others form subparallel networks within thin zones of crushed, silica-cemented quartzite.

FAULT KINEMATICS AND CONDITIONS OF DEFORMATION

Numerous subsidiary fault planes are observed in both hangingwall and footwall rocks, and many of these preserve slickenside lineations. Orientations of 389 faults and their associated striations were measured from 11 different sites across the entire Mine Mountain area in an attempt to document kinematic features of the system. Each site contained data collected within several tens of meters of the main low-angle fault, over an area of hundreds of square meters. The sense of offset was determinable on more than half of the slip planes from the geometry of secondary fault features (Riedel microfaults, tension fractures, offset markers, or asymmetric polish or gouge; Petit, 1987).

General patterns of subsidiary faults indicate a relatively simple movement history that is consistent with extensional normal faulting. High-angle dip-slip faults commonly truncate against or merge downward with low-angle dip-slip faults, and slip-sense criteria indicate that most of both are normal faults. Faults are diverse in terms of strike trend (fig. 8a) and rake angle (fig. 8c) and part of the diversity at some sites is due to multiple fault generations and (or) to reorientation by later tectonic rotations. However, most strike-slip and oblique-slip faults in the area form the bounding surfaces of scoop-shaped blocks that moved in concert with the more prevalent dip-slip faults.

These geometric relations indicate that the contact between Silurian-to-Devonian rocks and the underlying Eleana is largely a low-angle normal fault. The azimuthal trends for slickenside striations on all dip-slip faults, as well as for low-angle faults regardless of rake, show a strong bias toward southwest-directed transport directions (fig. 8d).

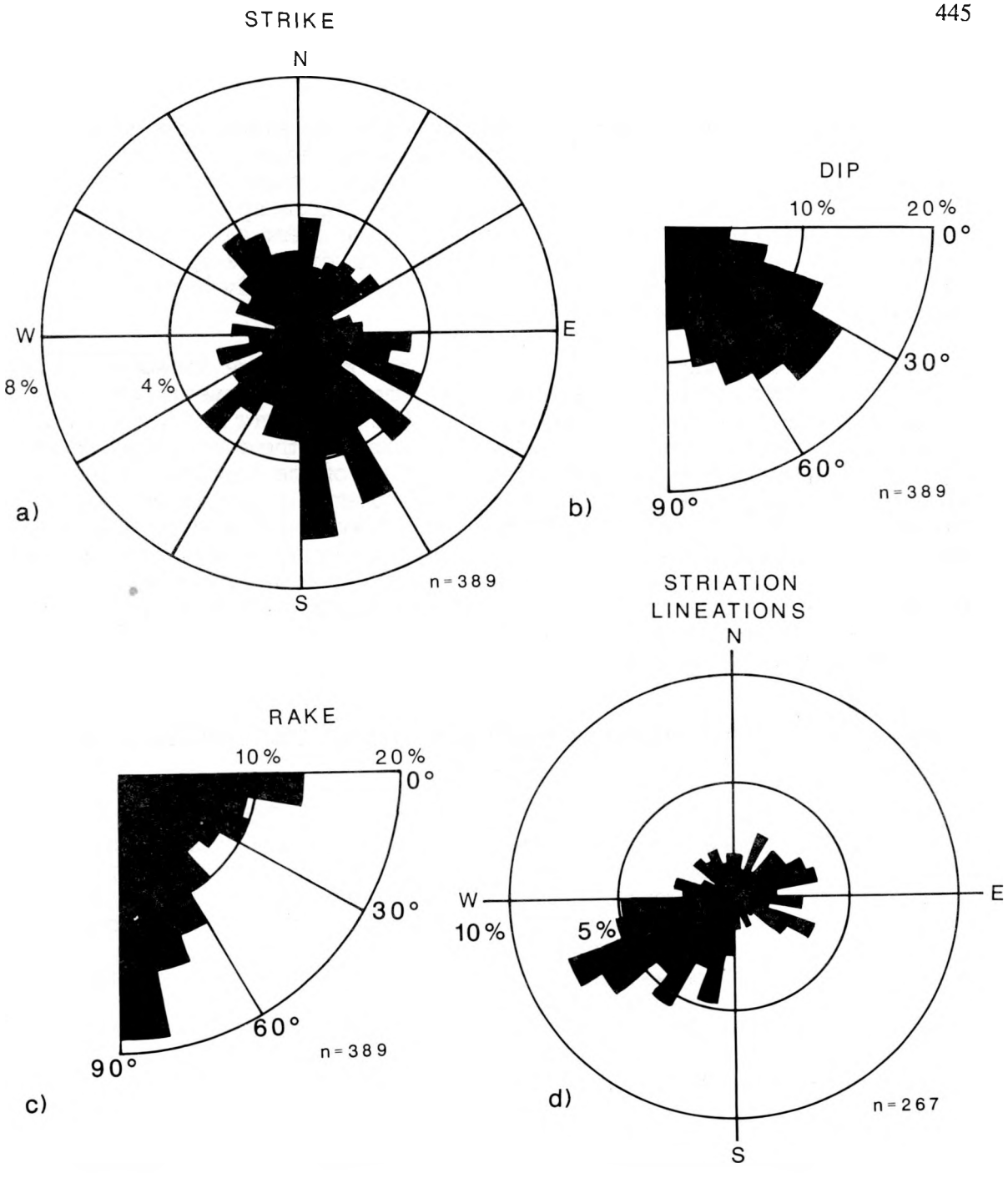


Figure 8. Structural data for small faults associated with the low-angle tectonic sheets in the Mine Mountain area. Rose diagrams show the distribution of: a) Strike azimuth (dip direction is 90° clockwise); b) Dip angle; and c) Rake of striations for 389 measured faults. For the subset (267 faults) that includes all gently inclined faults (less than 30° dip) and steeper faults that show dominantly dip-slip striations (rake greater than 45°), diagram d) shows the azimuth distribution of associated striations.

At a few sites in the central Mine Mountain area (for example, at Slick Draw, fig. 4), the main low-angle faults dip dominantly northeast. Slip-sense criteria indicate these are also normal faults whose striations imply northeast-directed tectonic transport (fig. 8d). The significance of opposing transport directions is not currently understood, but they might indicate concurrent deformation during northeast-southwest extension, sequential sliding on the same surface as its tilt direction reversed, or possibly that more than one structurally high source area was active in this area at the time of extension.

What was the overburden thickness at the time these low-angle faults slipped? No quantitative estimate is possible at present, but several factors seem to indicate at least a moderate depth of burial. The prominent mullion structures that are well preserved in Slick Draw (fig. 7) indicate that the overburden was sufficient to produce grinding, milling, and polishing of the footwall, rather than shattering and disaggregation. The overriding material at this locality was siltstone and limestone of the Eleana Formation, whose incompetence would also seem to require sufficient vertical load to cause scouring of the dolomitic footwall. The chemical activity recorded by the silicified and carbonate-cemented fault surfaces and by the precipitation of specular hematite suggest that ground water was heated above near-surface conditions, but temperatures were never high enough to convert clay minerals to mica.

RELATIONSHIP OF MINE MOUNTAIN STRUCTURE TO TERTIARY ROCKS

To a first-order approximation, the Tertiary rocks of the Nevada Test Site depositionally overlie all of the structures between Paleozoic units in the Mine Mountain area. None of the low-angle normal faults can be traced into the volcanic cover strata. The lowermost Tertiary unit is locally a thin colluvium or mudflow deposit (sedimentary breccia) that contains clasts of shattered dolomite similar to material in the low-angle fault zones. Elsewhere, airfall tuff beds, ashflow tuffs, or reworked tuffaceous sediments overlie the Paleozoic rocks and appear to fill depressions in an existing, erosional topographic surface. These Tertiary deposits are chiefly preserved on the northwest, west, and southwest flanks of the Mine Mountain structural block, and thickness patterns and onlap relations suggest that the northwestern flank was buried earlier and deeper by volcanic materials.

The youngest structures of the area are generally north-trending, steep, east-dipping normal faults that show as much as 100 m down-to-the-east displacement. They generally tilt the older Tertiary rocks 15° to 20° down toward the west (White Rocks; fig. 4) and are similar in geometry and offset pattern to the major post-11 Ma faults like the Carpetbag fault and the Yucca fault that control the Yucca Flat structural basin (fig. 2; Cole, 1987). Minor slip on conjugate northwest- to north-trending dextral faults and north- to northeast-trending sinistral faults (not shown at the scale of fig. 4) also postdate the low-angle normal faults of Mine Mountain. These younger features are not discussed further in this paper because our focus is on the older period of extension, but the westward tilt attributable to the younger period must be mentally removed in the following discussion in order to understand the earlier fault-bedding relationships.

Detailed mapping in the northern end of the Mine Mountain block, generally north of the 1-6C Road and east of White Rocks (fig. 9), defines structural and stratigraphic relations within the Tertiary section that imply some overlap in time between the low-angle faulting in the Paleozoic rocks and the earliest volcanic activity in the region, specifically the Redrock Valley Tuff (16.1 $\pm$ 0.6 Ma; Marvin and others, 1970). This Tuff is a moderately to densely welded ash flow that was chiefly erupted directly onto the eroded Paleozoic surface, although local thin deposits of biotite-hornblende-rich airfall tuff and (or) crudely stratified sedimentary breccia (Paleozoic rock clasts only) are also present. Thickness and degree of welding of the Redrock Valley are greatest in the easternmost fault block, and diminish progressively toward the west. At White Rocks, the Redrock Valley Tuff is nonwelded and less than a few meters thick, but to the east near Barren Hill (fig. 9), the Tuff is more than 60 m thick and welding is moderate in general and dense in the lowest part.

The correlation of thickness and welding intensity indicates the Redrock Valley was not differentially eroded, but rather deposited in a topographic trough that was deepest on the east. South of Barren Hill, a north-trending, high-angle, west-dipping fault cuts out a basal Tertiary biotite-hornblende-rich airfall tuff and part of the basal Redrock Valley. Abnormally steep welding foliation in the Tuff at this locality dips 65^{o} west, parallel to the fault, and preliminary paleomagnetic data confirm that little or none of that tilt can be attributed to primary dip. We conclude that this normal fault probably controlled the asymmetric half-graben into which the Redrock Valley was emplaced, and that subsequent movement (also down-to-the-west) rotated the welding fabric as much as an additional 40^{o} near the fault.

Recurrent movement must have sustained the topographic trough along its trend because the Redrock Valley Tuff is overlain in the Boulder Hills by a 50-m thick, laterally discontinuous well bedded unit of coarse conglomerate. Most of the detritus here consists of moderately rounded boulders and cobbles (as large as 1.5 m in diameter) of fossiliferous Bird Spring Formation limestone, limestone-cemented chert-pebble conglomerate of the Bird Spring, Eleana Formation quartzite and silica-cemented chert-pebble conglomerate, various Devonian and Silurian dolomites, fossiliferous Ordovician Antelope Valley Limestone (Pogonip Group), and Ordovician Eureka(?) Quartzite. This coarse debris must have been rapidly deposited in a subsiding trough because the conglomerate is not incised into the soft, non-welded top of the Redrock Valley Tuff.

The western of the two Boulder Hills (fig. 9) displays a large exotic block (approximately 400 m long parallel to strike, and 30 m thick) that is contained within the bedded boulder conglomerate. This block consists of siltstone and chert-granule sandstone (Eleana Formation) on its western margin and intensely brecciated, locally slickensided, gray and black, banded Simonson Dolomite along the entire eastern margin. We interpret this exotic block to be a fragment of the low-angle fault complex that was transported en masse down a slope (presumably from the east) and into the conglomerate depositional trough. Bedding in the conglomerate appears to be disturbed adjacent to the exotic slide block (probably due to localized soft-sediment deformation during sliding), but higher beds lap onto and cover it. Similar relationships have been described in detail in Tertiary syn-extensional basins in and around the Sheep Range to the southeast (Guth, 1981; Guth and others, 1988).

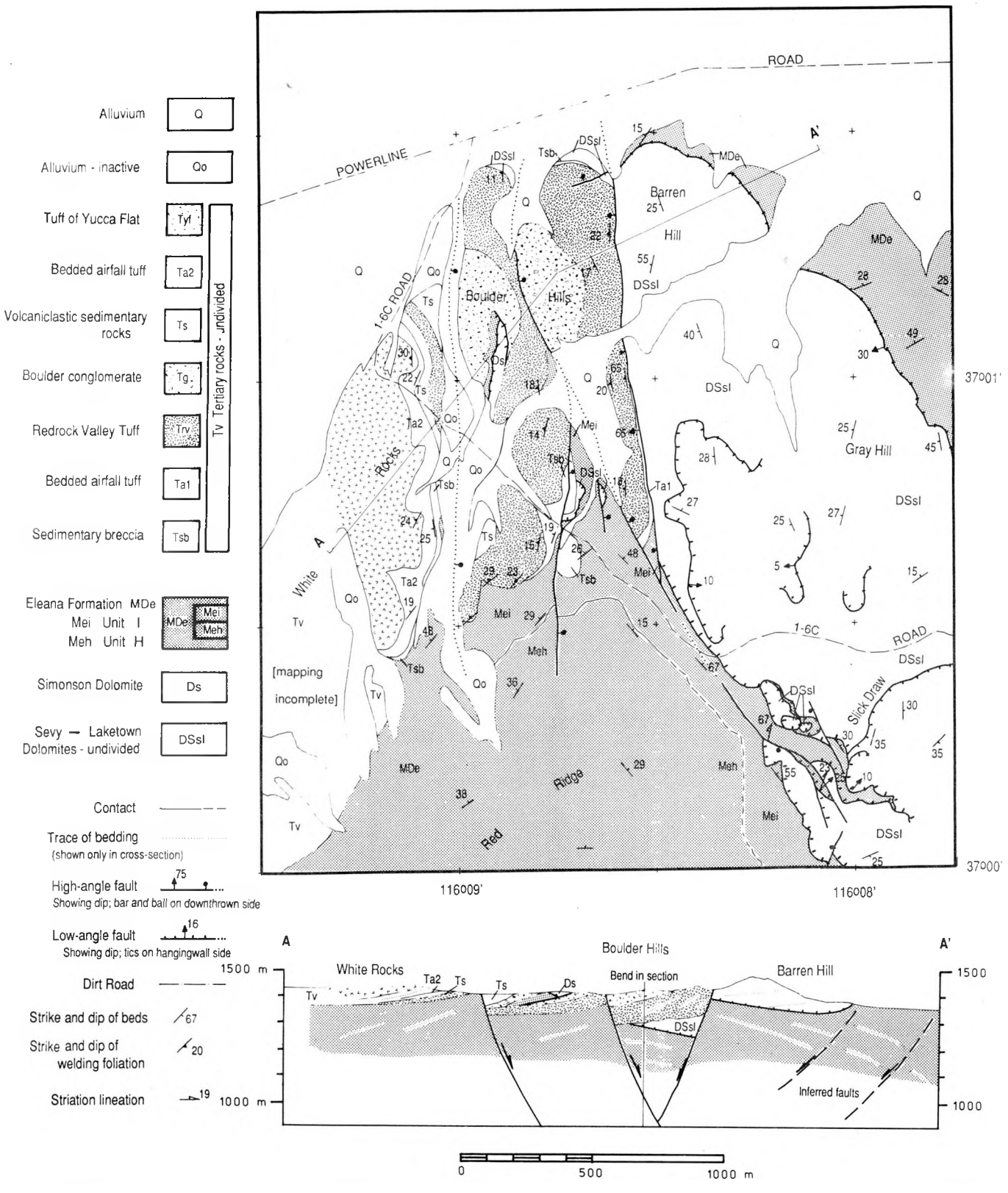


Figure 9. Detailed geologic map and cross-section for the northern Mine Mountain area. West-dipping normal faults controlled the extensional basin west of Barren Hill where the Redrock Valley Tuff and the boulder conglomerate were deposited. Subsequent antithetic tilting of approximately 20° toward the west is due to slip on post-11 Ma, east-dipping normal faults, similar to those that control the present structural basin of Yucca Flat. Ages of Paleozoic units are indicated on fig. 3.

The boulder conglomerate is itself conformably overlain by thin-bedded, tuffaceous sandstone, airfall tuff, and the moderately welded ash-flow tuff of Yucca Flat (about 14 Ma; Marvin and others, 1970), as shown in the White Rocks area (fig. 9). The continuity of bedding features in these post-Redrock Valley units suggests they are undisturbed (except for general post-11 Ma tilting) and, thus, largely postdate this early episode of major extensional deformation that gave rise to the low-angle fault complex and the depositional trough for the Redrock Valley Tuff. If the age of the tuff of Yucca Flat is sustained by geochronologic work in progress, then these observations would indicate that the early period of extension had mostly ceased by about 14 Ma.

DISCUSSION AND REGIONAL CONSIDERATIONS

The structural relations at Mine Mountain must be interpreted in the context of the regional deformational environment. The early to middle Miocene crust of the entire southern Great Basin province was extended by more than 100 percent (Guth, 1981; Wernicke and others, 1982, 1988), and the structures that formed during this extension are superimposed across the earlier tectonic fabric of late Mesozoic crustal shortening formed during the Sevier orogeny.

Extreme extension, as experienced by this broad province, produces a suite of characteristic structures at different levels of the crust (Lister and Davis, 1989). The geometry of the low-angle faults at Mine Mountain are consistent with the complex relationships to be expected in the middle and upper parts of an extended subregional hangingwall wedge, where mixed movement on steep rotational faults and low-angle normal faults may combine to tilt and excise various parts of the section. The intense shattering at the base of these tectonic sheets, and the contrasting lack of deformation in the adjoining footwall, show that overburden stress on the hangingwall was low. The fact that bedding orientation is preserved and that shatter fragments are not milled or strongly rotated suggest that differential lateral stresses were minimal as well. In terms of a conceptual model, these conclusions indicate that the hangingwall block breaks into fragments in brittle fashion as it slides passively down the slope of the low-angle normal fault.

As emphasized by Guth (1981; in press a), the footwall and hangingwall styles of deformation on these low-angle normal faults are substantially different from those associated with thrust faults. Footwall folds and cleavage, both well developed in the Sevier thrust systems of the region, are wholly lacking in the Mine Mountain area. Furthermore, the stratigraphic decollement zones that are characteristic of regional thrust systems (for example, the Late Proterozoic Johnnie Formation and the Cambrian Bonanza King Formation in the southern Sevier belt) exert no influence on the low-angle extensional faults in the Nevada Test Site area.

Previous studies have inferred that the structures within the Paleozoic rocks at CP Hills, located about 5 km to the southeast (fig. 2), are similar in origin to those at Mine Mountain (Johnson and Hibbard, 1957; Barnes and Poole, 1968; McKeown and others, 1976; Carr, 1984), and we concur. However, as at Mine Mountain, we interpret the low-angle structures in the CP Hills as extensional normal faults that formed during mid-Tertiary time. The same style of deformation that produces intensely brecciated hangingwall rocks above undisturbed but truncated footwall rocks is seen in the CP Hills, whether the age relationship is younger-over-older (Bonanza King Formation over Carrara Formation; fig. 3) or older-over-younger (Zabriskie Quartzite over Bird Spring Formation).

Current interpretations that require thrust solutions here, either east-vergent (Carr, 1984; Wernicke and others, 1988) or west-vergent (Caskey and Schweickert, 1989), are inconsistent with our observations, and with the absence of identifiable small-scale thrust features. In a broad sense, we agree with Robinson (1985) that the allochthonous structures within the Paleozoic at both CP Hills and Mine Mountain are disassociated from any regional systems that produced net crustal shortening. Current work in the Calico Hills area confirms similar structural relations and, thus, a similar extensional mechanism is inferred for the low-angle faults that carry Devonian dolomite and limestone over Mississippian Eleana Formation (Simonds and Scott, 1987; F. W. Simonds, oral communication, 1989).

We conclude that all these features were formed by the same process, and that they result from a time-transgressive extensional event that migrated from east (or southeast) toward the west (or northwest) during the middle to late Miocene, and which continues even at present in the Death Valley region (Hamilton, 1988). Regional structures of this time-and-space progression all possess the same "extensional polarity", in which formerly horizontal units were tilted toward the east on faults that dip west. By implication, the area of the regional crust was expanding westward relative to the stable craton at this time. Post-11 Ma extension in the Yucca Flat area shows the opposite polarity and the basin is presently expanding eastward on east-dipping normal faults.

Our constraints on the timing of low-angle normal faulting at Mine Mountain suggest that the main phase of extension began there somewhat prior to about 16 Ma, and was over prior to about 14 Ma. Similar timing is recorded to the south and east on the north side of the Las Vegas Valley in the Sheep Range detachment system (ca. 16 to 14 Ma; Guth and others, 1988). At Calico Hills and at Yucca Mountain, the main phase of extension occurred after about 13 Ma and prior to eruption of the 11.5 Ma Timber Mountain Tuff, although some tilting was later. In the Bullfrog Hills farther west near Beatty, Nevada, extreme extension took place chiefly between about 10 Ma and 8 Ma (Maldonado and Hausback, in press; Maldonado, in press).

If the style of deformation described above for the Mine Mountain area (and CP Hills) is extrapolated as a general model for at least the Yucca Flat region, then one may speculate about the distribution of rock units prior to the onset of major eruptions from the southwest Nevada volcanic field. Beneath the volcanic cover, we would expect to find isolated tectonic sheets and imbricate stacks of stratigraphically related sheets overlying a less disturbed footwall substrate, but pre-Tertiary stratigraphic order would generally be shuffled to a considerable degree.

The footwall block may contain a subregionally coherent stratigraphic sequence, which ought to reflect the general structural order following late Mesozoic thrusting of the Sevier orogeny. However, most likely the Eleana Formation, which comprises the footwall at Mine Mountain as well as in the CP Hills, is itself extended on deeper low-angle normal faults that were active at about the same time. Mapped relationships in the southern part of the Eleana Range (Orkild, 1963), for example, show low-angle faults within the Eleana Formation and between the Eleana and the Bird Spring Formation that cut bedding in both the hangingwall and footwall blocks. Hoover and Morrison (1980) described borehole evidence nearby at Syncline Ridge (fig. 2) that indicates both omission and repetition of parts of the Eleana and Bird Spring Formations across faults. These kinds of relations are better explained by low-angle normal faults than by thrusts.

It is most likely that this style of extensional deformation affects the entire Paleozoic section. We note that younger-over-older faults involve Cambrian units in the CP Hills, and numerous low-angle faults remove parts of the Cambrian and Proterozoic section in the northern Halfpint Range (fig. 2; Barnes and others, 1965). Shuffled stratigraphic relations and intense shattering were also mapped by Byers and Barnes (1967) between Cambrian and Ordovician units in the central Halfpint Range, east of Yucca Flat.

INTERPRETATION OF GRAVITY DATA IN THE YUCCA FLAT AREA

The foregoing observations and inferences provide a significantly different conceptual picture of the subsurface configuration of Paleozoic units than the previous thrust model (Carr, 1974, 1984). In the following section, we consider the consequences of the current extensional model on the assumptions that are used to calculate depth-to-basement from gravity observations.

Gravity data for the Nevada Test Site in general and the Yucca Flat area in particular are among the most comprehensive and detailed available for any region in the United States (Healey and others, 1987, and references therein). These data were collected in large part so that the depth to the top of the pre-Tertiary basement rocks could be estimated with confidence in areas where borehole intersections were lacking. By combining the borehole information with this very detailed gravity data set, two-dimensional model profiles are calculated that identify lateral steps in the depth of the Paleozoic-Tertiary contact. These steps are known to correspond to the positions of high-angle faults in many places, and thus the conservative assumption is generally made in the evaluation of containment design for an underground test that all calculated steps are fault-line scarps. The direct result of this assumption is that some sites for proposed tests are excluded from consideration because of presumed proximity to zones of fractured rock. However, we conclude below that not all scarps inferred from gravity data need be caused by fault offset and, thus, that the Cenozoic fill of the Yucca Flat basin may be less fractured than currently assumed.

The two-dimensional methods used to calculate the gravity-model sections have inherent limitations, chiefly the requirement that both the pre-Tertiary basement rocks and the Tertiary and Quaternary overburden be treated as media with uniform densities. Comparison of computed depths to basement with those measured in new drill holes regularly points out mismatches, and these discrepencies have been partially resolved over the years by making adjustments to the regional gradient correction. However, another portion of the mismatch can only be due to lateral variations in the density of either the basement or the overburden, and such variations routinely amount to 0.1 to 0.3 Mg/m^3 (that is, 10 to 40 percent of the average basement-overburden density contrast of 0.7 Mg/m^3).

The structural relations at Mine Mountain provide a realistic model for one major source of lateral density variation within the pre-Tertiary rocks. Transport of dense dolomite over less-dense limestone, quartzite, or siltstone on low-angle normal faults will introduce a density difference of about 0.2 Mg/m^3. Figure 10 illustrates the results of two sets of model calculations to evaluate the gravity effects of Mine Mountain-type structures beneath Yucca Flat. Figure 10a depicts the case of shallow burial (185 m) by Cenozoic deposits, and Figure 10b shows the equivalent model for deep burial (490 m). In both cases, a 130-m thick slab of

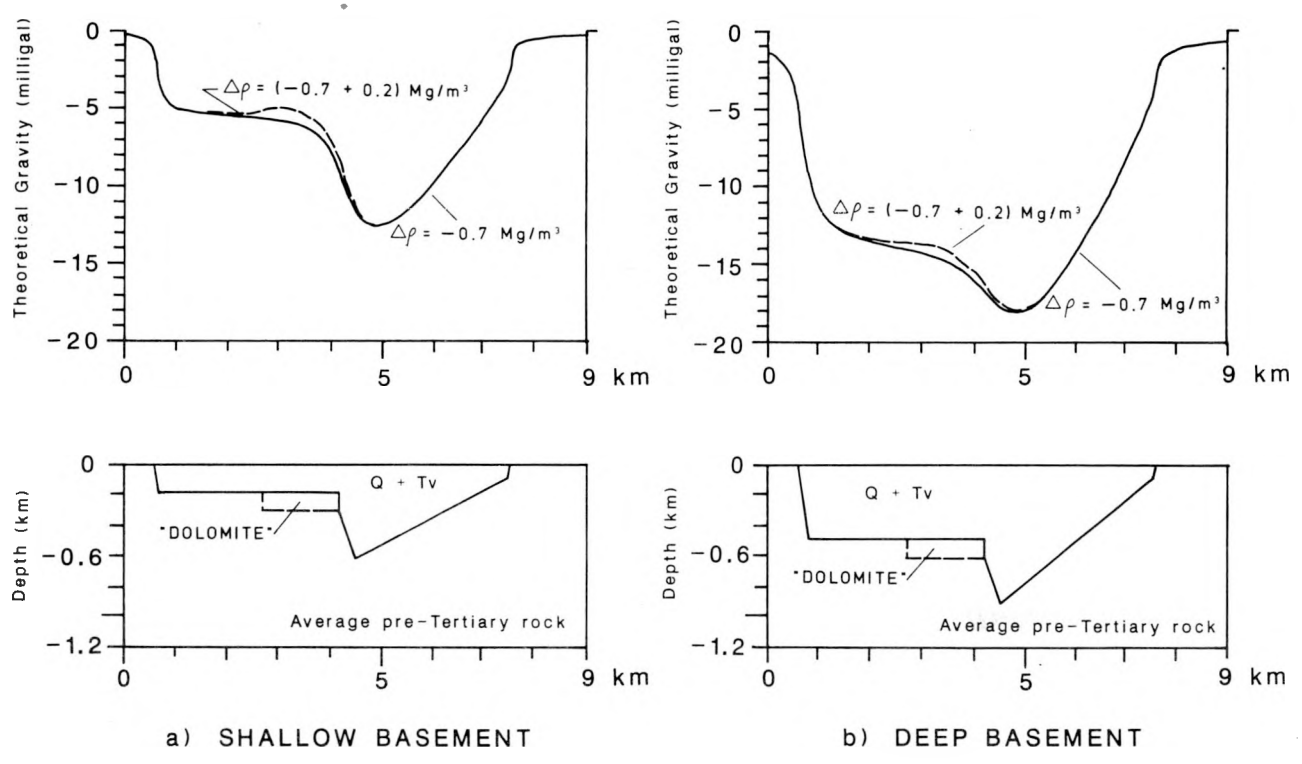


Figure 10. Calculated gravity profiles for simple models of pre-Tertiary basement configurations beneath low-density overburden of alluvium and volcanic rocks (Q + Tv); a) shallow burial (185 m), and b) deep burial (490 m) of a slab of dense rock ("dolomite") on top of "average pre-Tertiary rock" . In both configurations along a typical cross-section of Yucca Flat (see text), the solid curve shows the gravity effect of -0.7 Mg/m^3 density contrast ($\Delta\rho$) between overburden and "average pre-Tertiary rock", whereas the dashed curve shows the result of substituting denser dolomite for an equivalent volume of pre-Tertiary basement ($\Delta\rho$= -0.7 + 0.2 Mg/m^3; see text).

"dolomite" (representing the shattered hangingwall block of a low-angle normal fault) is substituted for an equivalent volume of "average pre-Tertiary rock" along a typical cross-section of Yucca Flat, and the gravity effects are compared.

As expected, the computed theoretical gravity field is most greatly affected by the thick wedge of low-density Cenozoic overburden east of a hypothetical "Carpetbag fault", whether in the case of 185-m burial (about 13 milligals) or 490-m burial (about 18 milligals). However, the effect of the dense dolomite slab is equally clear in both instances and results in a change of 1.4 and 0.9 milligals, respectively, amounts which can be routinely detected by present measurement techniques. The edge effect of this hypothetical dense slab produces the kind of local gradient in the measured gravity profile that would currently be interpreted as a scarp at the top of the basement, even though the elevation of the pre-Tertiary surface is constant.

These simple calculations demonstrate that low-angle imbrications of the pre-Tertiary sequence can produce gravity effects that are significant and detectable, and that previously would have been interpreted as high-angle fault scarps. The possibility must therefore be considered that some (perhaps many) of the smaller observed gravity gradients are not caused by scarps in the pre-Tertiary surface, and therefore imply no tectonic disruption of the Tertiary and Quaternary overburden.

We also caution that (two-dimensional) gravity data cannot be used alone to establish the continuity of apparent scarps throughout the Yucca Flat basin. If one attempts to connect apparently similar scarps across a north-south sequence of computed gravity-model sections, the impression is obtained that these scarps change strike direction markedly in some areas. We believe that these variations may simply indicate the edge effects of tectonic sheets of dissimilar density within the basement, and do not necessarily imply that the fault scarps are sinuous, nor that multiple, intersecting fault sets are required to explain the data.

In summary, the Mine Mountain model for the distribution of pre-Tertiary rocks beneath Yucca Flat has three important consequences for the underground testing program. First, Tertiary and younger faults may be less common than currently thought, and present interpretations may overestimate their total offset. Second, it is quite likely that carbonate rocks west of the Carpetbag fault are disconnected from any regional carbonate terrane and lie structurally isolated on top of the Eleana Formation. Third, the low-permeability Eleana Formation may be more extensive beneath Yucca Flat than previously thought and, thus, a more widespread hydrologic barrier may exist between testing environments and regional ground-water systems. These predictions can be inexpensively tested by suitable electrical resistivity surveys, but targeted drilling will be required to confirm the accuracy of the model.

REFERENCES CITED

Barnes, Harley, Christiansen, R. L., and Byers, F. M., Jr., 1965, Geologic map of the Jangle Ridge quadrangle, Nye and Lincoln Counties, Nevada: U.S. Geological Survey Geologic Quadrangle Map GQ-363, scale 1:24,000.

Barnes, Harley, Ekren, E. B., Rodgers, C. L., and Hedlund, D. C., 1982, Geologic and tectonic maps of the Mercury Quadrangle, Nye and Clark Counties, Nevada: U.S. Geological Survey Miscellaneous Investigations Map I-1197, scale 1:24,000.

Barnes, Harley, and Poole, F. G., 1968, Regional thrust-fault system in Nevada Test Site and vicinity, in Eckel, E. B., editor, Nevada Test Site: Geological Society of America Memoir 110, p. 233-238.

Burchfiel, B. C., and Davis, G. A., 1988, Mesozoic thrust faults and Cenozoic low-angle normal faults, eastern Spring Mountains, Nevada, and Clark Mountains thrust complex, California, in Weide, D. L., and Faber, M. L., editors, This Extended Land, Geological journeys in the southern Basin and Range: Geological Society of America Field Trip Guidebook, Cordilleran Section, p. 87-106.

Byers, F. M., Jr., and Barnes, Harley, 1967, Geologic map of the Paiute Ridge quadrangle, Nye and Lincoln Counties, Nevada: U.S. Geological Survey Geologic Quadrangle Map GQ-577, scale 1:24,000.

Carr, M. D., and Monsen, S. A., 1988, A field trip guide to the geology of Bare Mountain, in Weide, D. L., and Faber, M. L., editors, This Extended Land, Geological journeys in the southern Basin and Range: Geological Society of America Field Trip Guidebook, Cordilleran Section, p. 50-57.

Carr, W. J., 1974, Summary of tectonic and structural evidence for stress orientation at the Nevada Test Site: U.S. Geological Survey Open-File Report 74-176, 53 p.

_____ 1984, Regional structural setting of Yucca Mountain, southwestern Nevada, and late Cenozoic rates of tectonic activity in part of the southwestern Great Basin, Nevada and California: U.S. Geological Survey Open-File Report 84-854, 109 p.

Caskey, S. J., and Schweickert, R. A., 1989, Mesozoic west-vergent thrust in the CP Hills, Nevada Test Site, Nye County, Nevada [abs.]: Geological Society of America Abstracts with Programs, vol. 21, no. 5, p. 64.

Cole, J. C., 1987, Breakup of an allochthonous slab: Origin of the Yucca Flat basin, Nevada Test Site [abs.]: Geological Society of America Abstracts with Programs, vol. 19, no. 7, p. 623.

Dockery, H. A., Byers, F. M., Jr., and Orkild, P. P., editors, 1984, Nevada Test Site field trip guidebook 1984: Los Alamos National Laboratory Report LA-10428-MS, 49 p.

Guth, P. L., 1981, Tertiary extension north of the Las Vegas Valley shear zone, Sheep and Desert Ranges, Clark County, Nevada: Geological Society of America Bulletin, vol. 92, p. 763-771.

_____ [in press a], Bedrock geologic map of the Indian Springs quadrangle, Nevada: U.S. Geological Survey Open-File Map, scale 1:100,000.

_____ [in press b], Superposed Mesozoic and Cenozoic deformation, northwestern Clark County, Nevada, in Wernicke, B. P., editor, Extension at the latitude of Las Vegas: Geological Society of America Memoir 167.

Guth, P. L., Schmidt, D. L., Deibert, Jack, and Yount, J. C., 1988, Tertiary extensional basins of northwestern Clark County, Nevada, in Weide, D. L., and Faber, M. L., editors, This Extended Land, Geological journeys in the southern Basin and Range: Geological Society of America Field Trip Guidebook, Cordilleran Section, p. 239-254.

Hamilton, Warren, 1988, Detachment faulting in the Death Valley region, California and Nevada, in Carr, M. D., and Yount, J. C., editors, Geologic and hydrologic investigations of a potential nuclear waste disposal site at Yucca Mountain, southern Nevada: U.S. Geological Survey Bulletin 1790, p. 51-86.

Healey, D. L., Harris, R. N., Ponce, D. A., and Oliver, H. W., 1987, Complete Bouguer gravity map of the Nevada Test Site and vicinity, Nevada: U.S. Geological Survey Open-File Report 87-506, scale 1:100,000.

Hinrichs, E. N., 1968, Geologic structure of Yucca Flat area, Nevada, in Eckel, E. B., editor, Nevada Test Site: Geological Society of America Memoir 110, p. 239-246.

Hoover, D. L., and Morrison, J. N., 1980, Geology of the Syncline Ridge area related to nuclear waste disposal, Nevada Test Site, Nye County, Nevada: U.S. Geological Survey Open-File Report 80-942, 70 p.

Johnson, M. S., and Hibbard, D. E., 1957, Geology of the Atomic Energy Commission Nevada Proving Grounds area, Nevada: U.S. Geological Survey Bulletin 1021-K, p. 333-384.

Lister, G. S., and Davis, G. A., 1989, The origin of metamorphic core complexes and detachment faults formed during Tertiary continental extension in the northern Colorado River region, U.S.A.: Journal of Structural Geology, vol. 11, p. 65-94.

Maldonado, Florian, [in press], Detachment faulting and mineralization at Bullfrog Mountain, Bullfrog Hills area, in Mattson, S. R., Broxton, D. E., Crowe, B. M., Buono, Anthony, and Orkild, P. P., editors, Geology and hydrology of the proposed nuclear waste repository at Yucca Mountain, Nevada, and the surrounding area: Geological Society of America Field Trip guidebook, 1989 National Meeting.

Maldonado, Florian, and Hausback, B. P., [in press], Geologic map of the northeast quarter of the Bullfrog 15-minute quadrangle, Nye County, Nevada: U.S. Geological Survey Miscellaneous Investigations Map I-2049, scale 1:24,000.

Marvin, R. F., Byers, F. M., Jr., Mehnert, H. M., Orkild, P. P., and Stern, T. W., 1970, Radiometric ages and stratigraphic sequence of volcanic and plutonic rocks, southern Nye and western Lincoln Counties, Nevada: Geological Society of America Bulletin, vol. 81, p. 2657-2676.

McKeown, F. A., Healey, D. L., and Miller, C. H., 1976, Geologic map of the Yucca Lake quadrangle, Nye County, Nevada: U.S. Geological Survey Geologic Quadrangle Map GQ-1327, scale 1:24,000.

Orkild, P. P., 1963, Geologic map of the Tippipah Spring quadrangle, Nye County, Nevada: U.S. Geological Survey Geologic Quadrangle Map GQ-213, scale 1:24,000.

_____ 1968, Geologic map of the Mine Mountain quadrangle, Nye County, Nevada: U.S. Geological Survey Geologic Quadrangle Map GQ-746, scale 1:24,000.

Petit, J. P., 1987, Criteria for the sense of movement on fault surfaces in brittle rocks: Journal of Structural Geology, vol. 9, p. 597-608.

Poole, F. G., Houser, F. N., and Orkild, P. P., 1961, Eleana Formation of Nevada Test Site and vicinity, Nye Canyon, Nevada: U.S. Geological Survey Professional Paper 424-D, p. D104-D111.

Robinson, G. D., 1985, Structure of pre-Cenozoic rocks in the vicinity of Yucca Mountain, Nye County, Nevada--a potential nuclear-waste disposal site: U.S. Geological Survey Bulletin 1647, 22 p.

Simonds, F. W., and Scott, R. B., 1987, Detachment faulting and hydrothermal alteration in the Calico Hills, southwest Nevada [abs.]: Eos, Transactions of the American Geophysical Union, vol. 68, p. 1475.

Wernicke, Brian, Snow, J. K., and Walker, J. D., 1988, Correlation of early Mesozoic thrusts in the southern Great Basin and their possible indication of 250-300 km of Neogene crustal extension, in Weide, D. L., and Faber, M. L., editors, This Extended Land, Geological journeys in the southern Basin and Range: Geological Society of America Field Trip Guidebook, Cordilleran Section, p. 255-267.

Wernicke, Brian, Spencer, J. E., Burchfiel, B. C., and Guth, P. L., 1982, Magnitude of crustal extension in the southern Great Basin: Geology, vol. 10, no. 10, p. 499-503.

PALEOSTRESS INVESTIGATION NEAR RAINIER MESA, NEVADA TEST SITE

by
Scott A. Minor
U.S. Geological Survey
P.O. Box 25046, MS 913
Denver, CO 80225

ABSTRACT

Knowledge of the fault-kinematic and paleostress histories in the Rainier Mesa/Yucca Flat region can be beneficial to containment scientists in understanding the effects of natural faults on containment of nuclear detonations. Fault-slip data, consisting of fault and slickenside-striae orientations and slip-sense determinations, may be inverted to find best-fit orientations of principal stresses (σ_1, σ_2, and σ_3, where $\sigma_1 \geq \sigma_2 \geq \sigma_3$). The computed ratio $\Phi = (\sigma_2 - \sigma_3)/(\sigma_1 - \sigma_3)$ is indicative of the relative magnitudes and the degree of resolution of the principal stresses. An iterative cluster analysis may also be conducted to separate out of a heterogeneous data set two or more fault subsets compatible with unique stress solutions.

Fault-slip data were collected from 444 small-displacement (0.1-10 m) faults cutting 16-11 Ma tuffs and tuffaceous sedimentary rocks in nine areas mainly along the south, east, and northeast flanks of Rainier Mesa to investigate the faulting and paleostress history in the region. Two of the faults appear to have been test-reactivated as tension cracks and may have also experienced renewed shear displacement. One to three different stress solutions were computed from data collected in seven of the measurement areas. From cross-cutting relations of faults and faulted stratigraphic units, the relative age of many of the computed stress regimes and associated faults were determined. Using stratigraphic constraints and similarities in stress results, a relative stress-regime and faulting sequence was constructed for the study region.

Interpretation of these data and results give the following tectonic history. At about 16 Ma the region was subject to a normal-fault stress regime (σ_1 vertical and σ_2 and σ_3 horizontal) with σ_3 oriented northwest. Between 16 and 14 Ma the σ_3 axis gradually rotated about 70° counterclockwise to a west-southwest orientation. During this period the locus of faulting, primarily normal-slip in nature, migrated westward from the Whiterock Spring area to the east flank of Rainier Mesa. A fundamental but brief (<1 m.y.) change in the stress field to a strike-slip configuration (σ_1 and σ_3 horizontal) occurred at about 14 Ma and was characterized by a small (~10°) clockwise shift in σ_3 orientation. Faulting associated with this regime was mainly confined to a narrow zone in Stockade Wash characterized by dextral strike-slip faults and a broad zone on the northeast flank of Rainier Mesa characterized by dextral oblique-slip movement on earlier-formed faults. The stress field reverted back to a normal-fault configuration sometime after about 13 Ma and the σ_3 direction again rotated counterclockwise to the southwest. Northwest-striking normal faults formed in the Stockade Wash area after this change, which may have been due to stresses associated with the development of the nearby Timber Mountain caldera at about 11 Ma. After approximately 11 Ma the σ_3 axis rotated clockwise about 50° to a west-northwest direction after which north-northeast-striking faults formed near the top of Rainier Mesa. This clockwise rotation may have been the initial phase of an eventual shift of σ_3 to its present 310° position.

INTRODUCTION

The fault-kinematic and paleostress evolution of the Rainier Mesa/Yucca Flat region during the late Cenozoic is poorly understood. Information on the faulting and paleostress history of this region is valuable for assessing the tectonic development of the Yucca Flat basin. Fault-slip paleostress studies can indicate dominant modes of faulting (e.g., strike-slip vs normal), fault kinematics (e.g., extension directions), temporal and spatial changes in faulting modes and kinematics, and, by comparison with other studies, the regional tectonic significance of geologic structures present in the area investigated. This information can be beneficial to containment scientists in understanding the effects of natural faults on containment of underground nuclear detonations. Fracturing observed after nuclear explosions is influenced by the structural arrangement of pre-existing faults and joints and by the current regional stress field (e.g., Miller and Miller, 1977). Understanding how rocks in the region responded mechanically and kinematically to paleostress fields could be valuable for developing predictive models of rock failure due to underground nuclear explosions.

Previous Investigations

Carr (1974) compiled all available tectonic, structural, seismic, strain-gage, and drill-hole-elongation evidence of the orientations of the "present-day" maximum and minimum horizontal stress axes for the Nevada Test Site region. The results of Carr's compilation suggest that the orientation of the regional minimum horizontal stress axis is 310°. A paleostress study was conducted by Dockery (1984) using fault-slip data collected at or near "major fault zones" primarily in the southern Yucca Flat area. From her data and the results of Carr's and other workers' studies, she concluded that the horizontal least-principal stress axis has rotated clockwise from a more westerly orientation during the last 17 m.y. to its present 310° orientation.

The results of two other paleostress studies conducted west of Yucca Flat within the Nevada Test Site support this notion of a clockwise stress rotation. At Yucca Mountain, Scott and Hofland (1987), using fault-slip data, concluded that the minimum horizontal stress axis in the area trended 265° during faulting sometime after 13 Ma. Also using fault-slip data, Frizzel and Zoback (1987) reported a least-principal stress orientation of 300° during Quaternary(?) faulting in Hampel Wash (about 20 mi southwest of Yucca Flat).

Several investigators have made subsurface in-situ stress determinations near working points within the Rainier Mesa and Yucca Flat areas using, among others, overcore (e.g., Ellis and Magner, 1980) and hydrofracture techniques.

PALEOSTRESS INVESTIGATION

Numerous, locally well-exposed faults of small displacement cut upper Tertiary tuffs and tuffaceous sedimentary rocks near the southern and eastern flanks of Rainier Mesa, and provide an excellent opportunity to study the late Tertiary fault kinematic and paleostress history of the northwest margin of the Yucca Flat basin. In this study, fault-slip data, comprised of fault and slickenside-striae orientations and associated slip-sense, were systematically collected from 444 faults in this region.

Study Area Setting

Rainier Mesa is located in the northeast part of the Nevada Test Site and lies directly west of northwestern Yucca Flat. The area of study consists mainly of the south and east flanks of Rainier Mesa but also includes two small areas further northeast and southwest (fig. 1).

Pre-Tertiary rocks in the area consist of folded and complexly faulted middle Paleozoic carbonate rocks and younger Devonian and Mississippian clastic rocks of the Eleana Formation (fig. 2). Uncon-

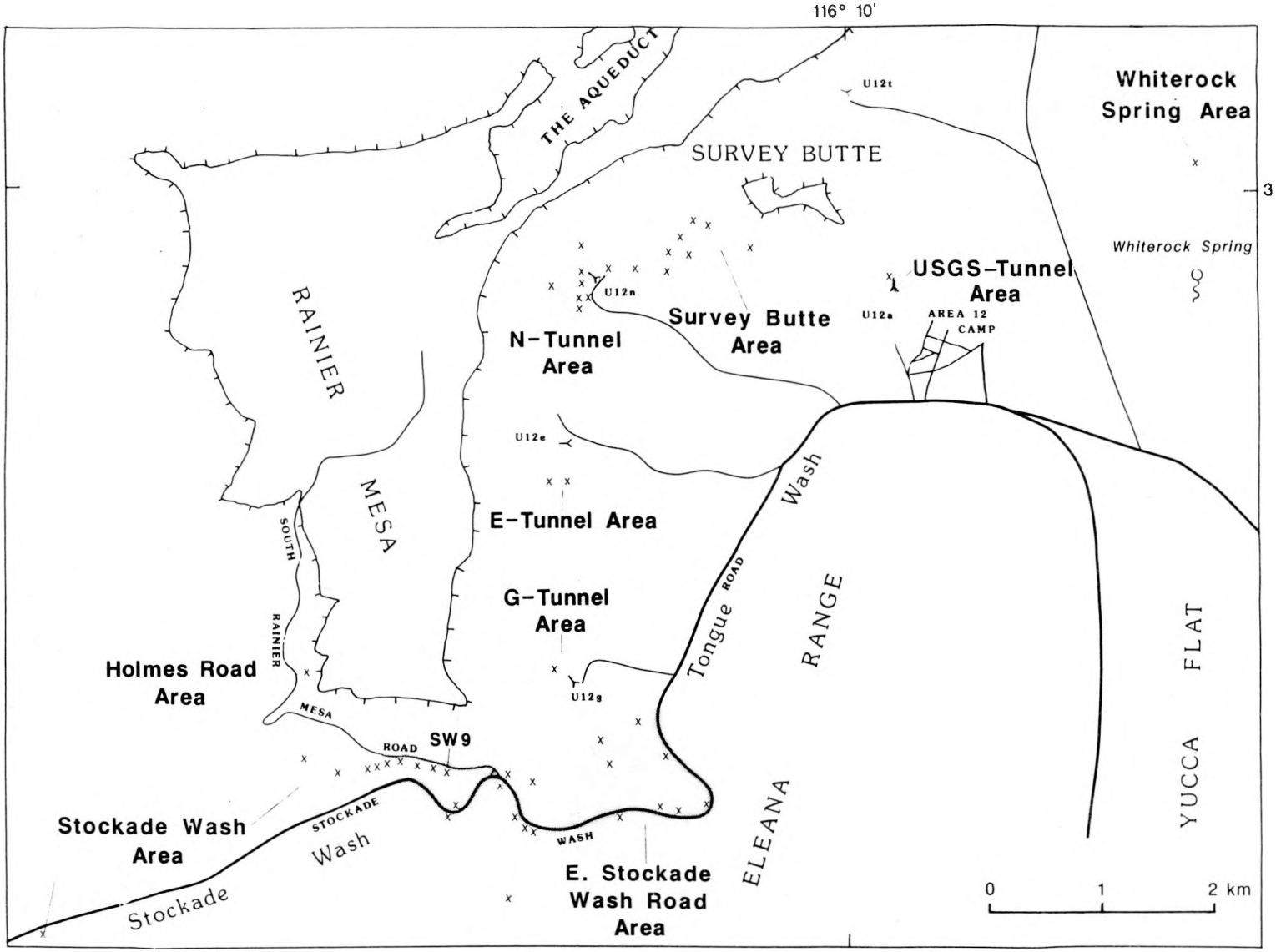


Figure 1. Map showing study-region measurement areas (stippled) and sites (x's), major physiographic features and roads, and tunnel-complex portals. Topographic rim of Rainier Mesa shown by hachured line.

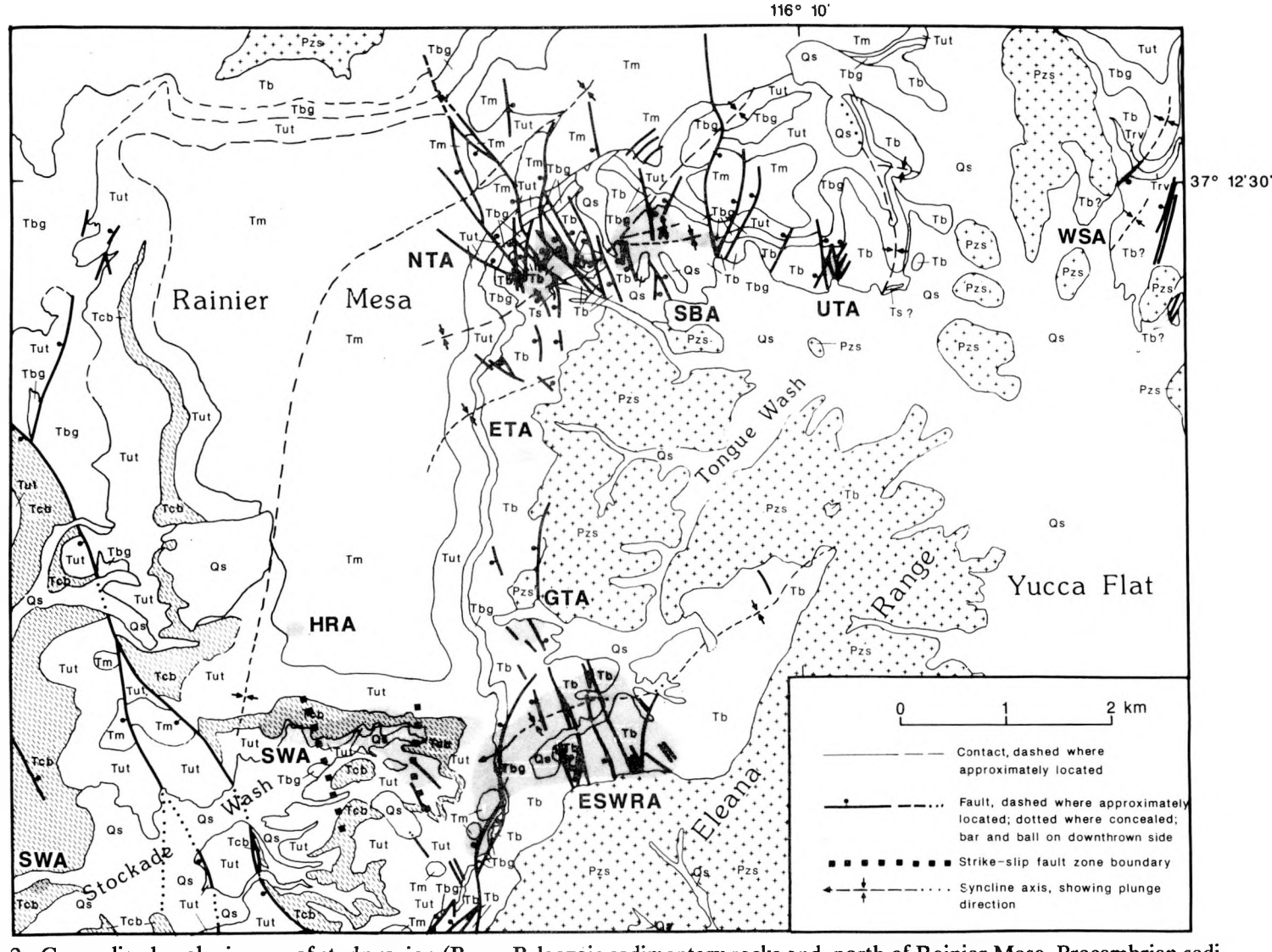


Figure 2. Generalized geologic map of study region (Pzs = Paleozoic sedimentary rocks and, north of Rainier Mesa, Precambrian sedimentary and Cretaceous intrusive rocks; Tertiary units: Tb = tunnel beds; Trv = Redrock Valley Tuff; Ts = Tub Spring Member of the Belted Range Tuff; Tbg = Grouse Canyon Member of the Belted Range Tuff; Tut = undifferentiated tuff and tuffaceous sedimentary rocks, including the Paintbrush Tuff; Tcb = ash-flow tuff unit possibly correlative with Bullfrog Member of the Crater Flat Tuff; Tm = Timber Mountain Tuff; Qs = Quaternary surficial deposits). Stipple pattern shows areas of fault-slip measurements (SWA = Stockade Wash area; HRA = Holmes road area; ESWRA = east Stockade Wash road area; GTA = G-tunnel area; ETA = E-tunnel area; NTA = N-tunnel area; SBA = Survey Butte area; UTA = USGS-tunnel area; WSA = Whiterock Spring area). Geology simplified and modified from Gibbons and others (1963).

formably overlying these rocks on an irregular paleotopographic surface is an approximately 400-m-thick upper Tertiary sequence of volcanic and volcaniclastic rocks. Near Rainier Mesa, this sequence consists, from the base upwards, of tuff and tuffaceous sedimentary rocks informally called the tunnel beds (Tb), welded and bedded tuff of the Grouse Canyon Member of the Belted Range Tuff (Tbg), undifferentiated tuff and tuffaceous sedimentary rocks (Tut) intercalated with ash-flow cooling units probably of the Crater Flat Tuff (Tcb) (D.A. Sawyer. U.S. Geological Survey, oral commun., 1989) and the overlying Paintbrush Tuff, and welded cooling units of the Timber Mountain Tuff (Tm) that form the mesa caprock (fig. 2). Lenses of the Tub Spring Member of the Belted Range Tuff (Ts) and Redrock Valley Tuff (Trv) occur locally within the lower part of the tunnel beds in troughs of large, open northeast-trending synclines that traverse the area (fig. 2). These structures have been interpreted to be primary "depositional" synclines that formed over paleocanyons on the pre-Tertiary surface (Hansen and others, 1963). Faults affecting the Tertiary rocks are discussed in detail below. Quaternary surficial deposits (Qs) in the region include basin-fill alluvium underlying Yucca Flat, landslide deposits, colluvium, and talus.

Field Methods

Outcrops of upper Tertiary rocks in the Stockade Wash area and along the east flank of Rainier Mesa were examined for exposed fault surfaces bearing slickenside striae. Faults cutting the underlying Paleozoic basement rocks were disregarded to eliminate possible bias from pre-Tertiary faulting events. Strike, dip, rake, and where possible, separation were measured on all suitable faults observed. Most measured faults have dip separations ranging from 1 cm to 10 m. The slip sense of each fault was evaluated using several criteria of Petit (1987); each slip-sense determination was assigned a definite, probable, or inferred certainty ranking, depending on the degree of confidence in the determination. Critical to this study were field observations that might reveal the relative age of faults, particularly cross-cutting relations of faults, slickenside striae, and stratigraphic units. Bedding attitudes of the faulted rocks were measured at each site to help assess the possibility of horizontal-axis rotations of the measured faults.

A total of nine fault-measurement areas in the vicinity of Rainier Mesa were designated on the basis of domains of concentrated, well-exposed faults and (or) distinctive faulting style (fig. 1). Each area contains 1 to 16 measurement sites at which 1 to 27 relatively closely spaced faults were measured.

Fault-Slip Data

Stockade Wash Area

The Stockade Wash measurement area (SWA) consists of two subareas--a main area in upper Stockade Wash containing 14 sites and a much smaller area consisting of one site (fig. 1). Most of the 112 faults measured from these two subareas are present in ash-flow tuff (Tcb) that forms prominent cliffs mostly along the north side of Stockade Wash (fig. 2). Although this faulted tuff was originally mapped as the Stockade Wash Member of the Paintbrush Tuff, it probably is equivalent to the Bullfrog Member of the Crater Flat Tuff (D.A. Sawyer, oral commun., 1989). A smaller proportion of the faults were measured in bedded tuff that underlies the ash-flow tuff and presumably overlies the Grouse Canyon Member.

A majority of the measured faults strike north-northwest and dip either to the west-southwest or east-northeast (fig. 3a-c). Most faults dip at high angles ($\geq 70°$), and a relatively large percentage dip within 5° of vertical (fig. 3d). The faults display a strong clustering of rakes within 5° of horizontal and mainly have a dextral sense of slip (fig. 3e,f). A less well-defined cluster of rake values occurs between about 50° and 90° on faults that exhibit primarily normal-dextral or normal-sinistral oblique slip. Thus, there is a strong bimodality to the data that appears to be due to a mixed population of similarly striking normal oblique-slip faults and dextral (and lesser sinistral), subvertical strike-slip faults. A similar distribution of fault-slip data collected at a single site (SW9) in upper Stockade Wash (fig. 4) illustrates

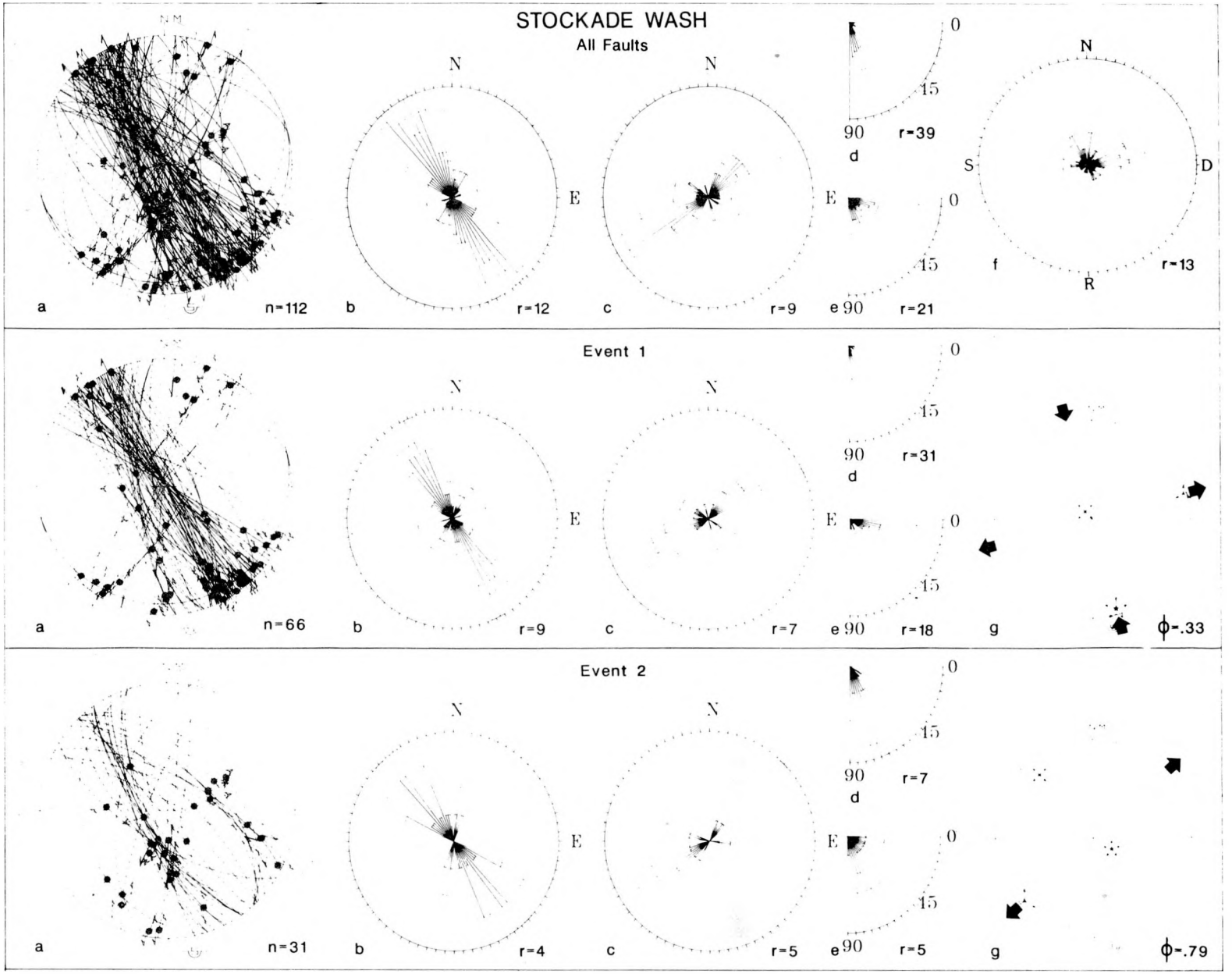

STOCKADE WASH
All Faults
N
E
S
D
R
0
15
90
a
n=112
b
r=12
c
r=9
d
r=39
e 90
r=21
f
r=13
Event 1
n=66
r=9
r=7
r=31
r=18
g
ϕ=.33
Event 2
n=31
r=4
r=5
r=7
r=5
ϕ=.79

Figure 3.

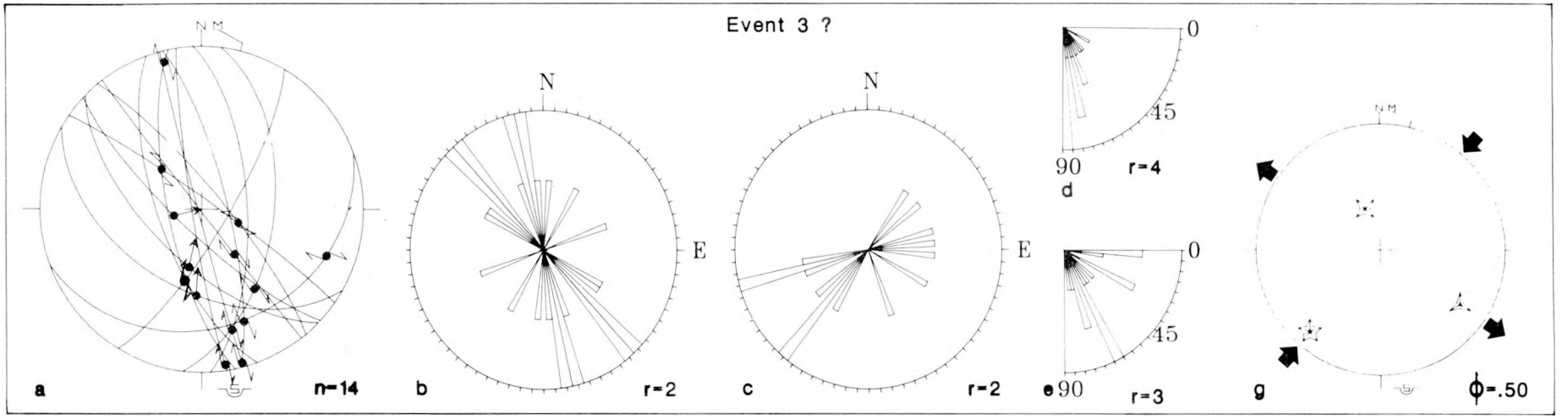


Figure 3 (continued). Fault-slip data summary plots and diagrams for all measurements in Stockade Wash area (first row) and for individual events. a) Lower hemisphere equal-area projection of fault planes (great circles) and striae (solid dots) showing slip sense (arrows--single arrow indicates hanging-wall slip sense; complete, partial, and missing arrowheads denote certain, probable, and inferred slip-sense determinations, respectively); N and M denote north and magnetic north, respectively; n indicates total number of measured faults), b) distribution of fault strikes (r indicates maximum diagram radius in terms of number of data), c) distribution of fault dip directions, d) distribution of fault dip angles, e) distribution of fault rake angles, f) distribution of fault rake angles relative to associated slip-sense (N, R, S, and D indicate normal-slip, reverse-slip, sinistral-slip, and dextral-slip, respectively), g) lower hemisphere equal-area projection of computed principal stress axes (three-, four-, and five-point symbols represent σ_3, σ_2, and σ_1, respectively; relative size of symbols related to Φ value); large solid arrows indicate inferred directions of extension (diverging arrows) and shortening(converging arrows).

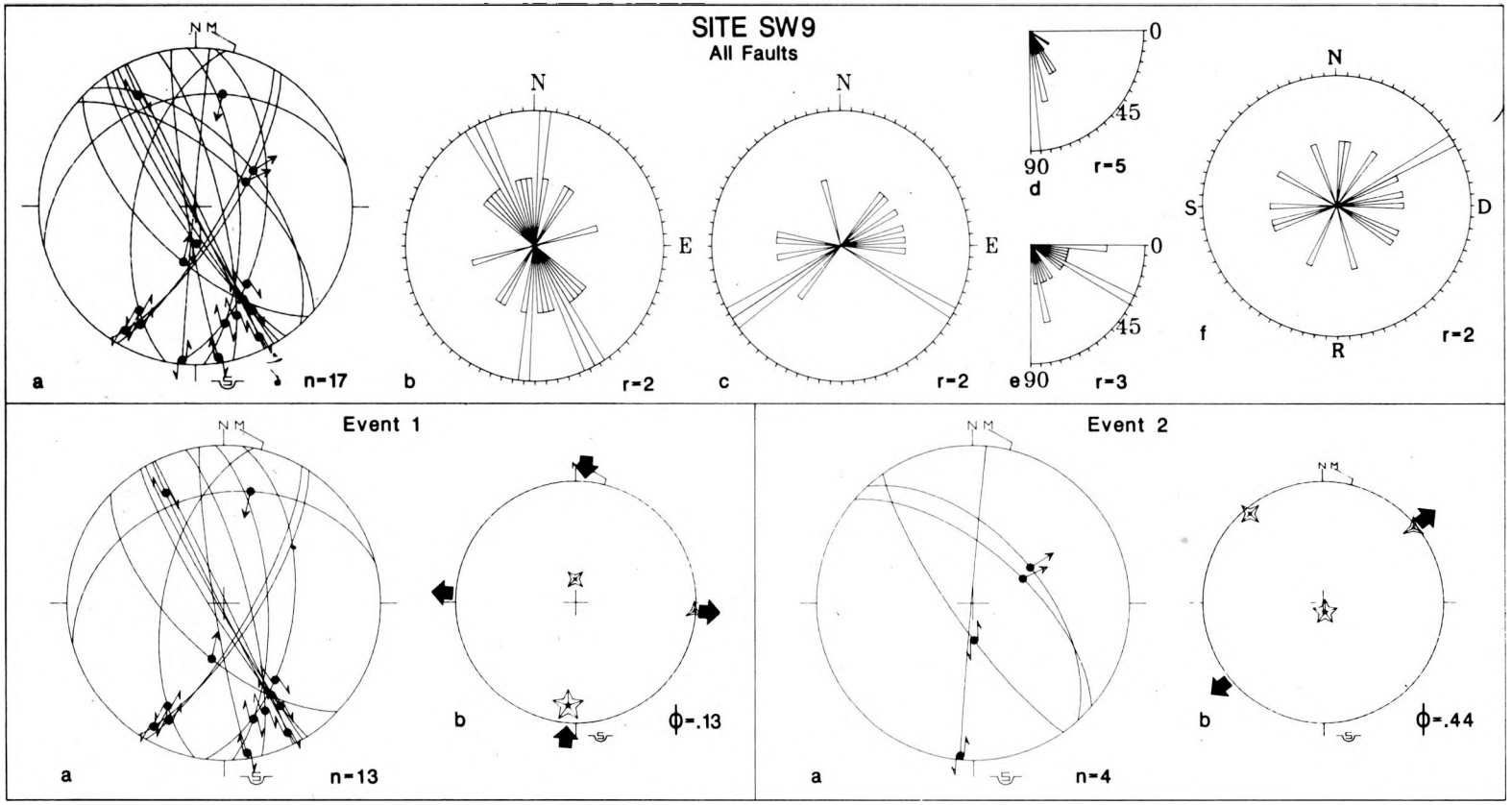


Figure 4. Fault-slip data summary plots and diagrams for all measurements at site SW9 (first row) and for individual events. See figure 3 for explanation of plots and diagrams.

that data collected at any given site or group of sites in an area are, in a general sense, representative of the entire data set for the area.

Few of the faults in the vicinity of the SWA have previously been mapped; a north-northwest-striking, large-displacement (~100 m), down-to-the-southwest fault and smaller branching faults are the only prominent structures shown on the map of Gibbons and others (1963) (fig. 2). These mapped faults appear to be concentric with and, thus, genetically related to the Timber Mountain caldera located a few kilometers to the southwest. The sparsity of large mapped faults in the SWA can be explained in part by the small-displacement, strike-slip nature of many of the mesoscopic faults, which do not generate significant stratigraphic separations of the nearly horizontal units. The larger part of the measurement area appears to span a dextral, north-northwest-trending strike-slip fault zone (fig. 2). The west and east borders of the zone are expressed by a generally sharp decrease in the frequency of strike-slip faults away from the zone. The main strike-slip zone appears to have a width of about 1 km but its extent along trend is unknown. A lack of north-northwest-striking strike-slip faults along the northern projection of the zone in exposures of rocks overlying the prominent ash-flow tuff suggests that the strike-slip faults formed soon after emplacement of the tuff, which is tentatively correlated with Bullfrog Member of the Crater Flat Tuff. Structures that accommodate local horizontal shortening were observed along the eastern edge of the main strike-slip zone at site SW9 (fig. 1) and at a site about 0.5 km to the south in a large pair of roadcuts along Stockade Wash road. At SW9, dextral and sinistral strike-slip faults abruptly or gently curve into one or more small-displacement, low-angle thrust faults (fig. 5). In the roadcuts to the south, a conspicuous faulted drag fold formed underneath a prominent apparent thrust sheet that was in turn complexly draped and faulted over the fold.

Numerous dextral northwest-striking strike-slip faults present in the isolated western subarea suggest that another similar strike-slip zone crosses Stockade Wash at that location. Accommodation faults very similar to those observed to the east are also present in this subarea.

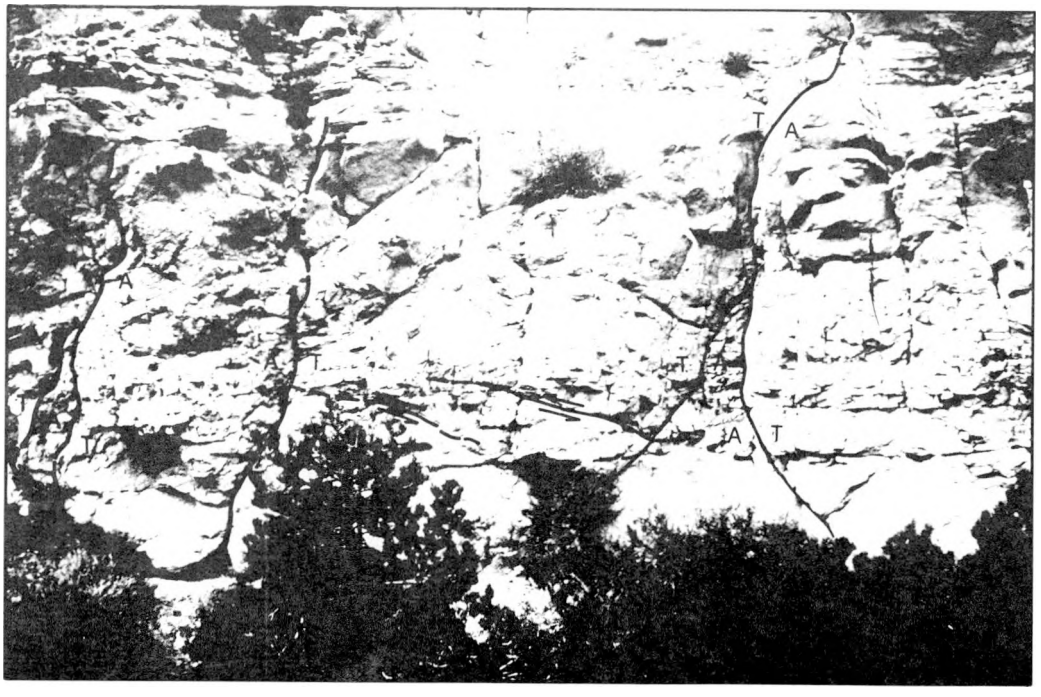


Figure 5. Photograph taken at site SW9 of faulted bedded tuff underlying ash-flow tuff sheet; looking north. Slip sense of faults (highlighted) indicated by arrows and letters (T = towards; A = away).

East Stockade Wash Road Area

The east Stockade Wash road measurement area (ESWRA) is east of the topographic divide, extending south from Rainier Mesa, that separates Stockade Wash from Tongue Wash (fig. 1). Eight of the 13 sites in the area are roadcuts along eastern Stockade Wash road that yield excellent exposures of 89 of the 115 faults measured. All but 12 faults were measured in probable equivalents of the lower tunnel beds (stratigraphically below the Grouse Canyon Member of the Belted Range Tuff) that form a large northeast-trending synclinal wedge extending obliquely across the northern Eleana Range (fig. 2); the other faults were measured in the Grouse Canyon Member or in overlying bedded tuff.
Most faults measured in the area strike between 330° and north and dip more commonly to the west-southwest than to the east-northeast (fig. 6a-c). Most faults dip more than 60° and are commonly near vertical (fig. 6d). Nearly all of the rake values exceed 50° and tend toward 90° (fig. 6e). Most of the faults exhibit normal to normal-oblique slip with a greater frequency of normal-dextral movement (fig. 6f). Several previously mapped (Gibbons and others, 1963) high-angle, relatively large-displacement, north-northwest-striking (~340°) normal(?) faults in the eastern part of the measurement area (fig. 2) were included in the measurements. These larger faults are typically surrounded by subparallel smaller displacement (mesoscopic) faults that decrease in frequency away from the main fault in such a manner as to define crude fault zones. Between these zones are areas devoid of or containing only a few faults. Thus, most of the measurement sites are along the fault zones. The western part of the area is structurally dominated by a conspicuous, large-displacement (~75 m), down-to-the-west fault zone that strikes anomalously north rather than north-northwest (fig. 2). In a large roadcut along Stockade Wash road, the zone is about 100 m wide and contains a central or main north-striking fault that is approximately vertical. Fault-slip data from smaller faults forming much of the zone are similar to that of the other measured faults in the area despite the difference in strike of the main controlling fault.

The virtual lack of strike-slip faults in the measurement area clearly distinguishes it from the SWA and suggests that a fault-domain partition exists between the two areas.

G-Tunnel and E-Tunnel Areas

The small G-tunnel (GTA) and E-tunnel (ETA) measurement areas cover 1 or 2 measurement sites and contain 10 and 6 measured faults, respectively. These fault occurrences are assigned to individual areas primarily because they are geographically isolated from neighboring areas. The G-tunnel area is located near the south end of the east flank of Rainier Mesa near the U12g portal, whereas the E-tunnel area is further north on the east flank near the U12e portal (fig. 1). Both measurement areas are entirely in the tunnel beds (fig. 2).

Measured faults in both areas generally strike north-northwest and are steeply dipping to subvertical (fig. 7a,b). Rake values are scattered, although there is a weak concentration of steep (80-90°) rakes, most of which are associated with normal-slip faults. Reverse-slip and dextral strike-slip faults are included in both data sets. In a general sense, the faults in both areas resemble those measured from the ESWRA. The GTA is along strike of some of the fault zones measured in the ESWRA and also contains mapped small north-northwest-striking faults (fig. 2). Tertiary rocks surrounding and within ETA contain few mesoscopic and mapped faults.

N-Tunnel and Survey Butte Areas

The N-tunnel measurement area (NTA) is located near the U12n portal, where the east flank of Rainier Mesa curves toward the northeast (fig. 1), and contains 9 sites at which 43 faults were measured. The Survey Butte measurement area (SBA), which is on the southwest flank of Survey Butte directly east of the NTA, contains 7 sites at which 39 faults were measured. The measured faults from both areas are in the tunnel beds with the exception of two faults at the easternmost site of the SBA that cut the Grouse Canyon Member of the Belted Range Tuff. The fault-slip data distribution plots and diagrams for the two areas are very similar and the areas are hereafter referred to as the composite N-tunnel/Survey Butte measurement area (NTSBA). However, data plots and diagrams are presented for both the NTSBA (fig. 8) and SBA (fig. 9) mainly to illustrate their close similarities.

Most of the measured faults strike 330-355° and dip nearly equally east and west; more westerly striking faults mainly belong to the NTA subset whereas the more northerly striking faults belong to the SBA subset (figs. 8 and 9, a,b). A smaller strike mode at 305° is entirely due to the NTA data. Faults dip almost exclusively 60-90° with the SBA faults skewed more toward a 60° value (fig. 8d). Most fault rakes are greater than 40°, and a broad mode in the rake distribution peaks at 90° (fig. 8e). Nearly all of the steep-rake faults exhibit normal or normal-oblique (both dextral and sinistral) slip (fig. 8f). The NTA faults diverge somewhat from this rake pattern in that the rake values are more evenly distributed between 0-90°; the shallow-rake faults are equally dextral and sinistral. Several low-angle, nearly bedding-parallel thrust faults measured in the NTA appear to be accommodation structures associated with adjoining shallow-rake high-angle faults. In the NTSBA the average strike of mapped faults changes from north in the SBA to north-northwest in the NTA (fig. 2). This east-to-west counterclockwise change is reflected somewhat in the slight discrepancy in strikes of mesoscopic faults in the two areas.

USGS-Tunnel Area

The small USGS-tunnel measurement area (UTA) consists of 1 site containing 27 faults near the U12a portal (commonly referred to as the USGS tunnel) on the southeast flank of Survey Butte near Area 12 Camp (fig. 1). The area, which is located within the tunnel beds, was previously studied by Hansen and others (1963), who mapped the local faults in considerable detail.

In contrast to the areas described above, the UTA faults consistently strike north-northeast (25° average) (fig. 10a,b). Faults typically dip $\geq 70°$ to the west, but their rakes are quite variable; the slip-sense of many of the faults ranges from normal through oblique to sinistral; several faults exhibit reverse-slip (fig. 10c-f). Concentrated north-northeast- and north-striking faults mapped in the area crudely define a broad fault zone (fig. 2); most of these faults apparently do not extend far to the north into the younger Grouse Canyon Member of the Belted Range Tuff, suggesting that the mapped (and measured) faults are overlapped by and predate the younger strata.

Whiterock Spring Area

The Whiterock Spring measurement area (WSA), northeast of the UTA (fig. 1), consists of 1 site containing 18 faults. The measured faults cut rocks as young as a partly welded ash-flow tuff mapped as Redrock Valley Tuff by Sargent and Orkild (1973). Structural relationships in the WSA indicate that all the faulting occurred prior to deposition of bedded tuff directly overlying the Redrock Valley Tuff. Essentially all the faults are steep-rake, normal-slip faults that strike northeast and dip 65-80° either northwest or southeast (fig. 11).

Holmes Road Area

The small Holmes road measurement area (HRA) is located along the base of a cliff below the southwest rim of Rainier Mesa just east of south Rainier Mesa road (informally called Holmes road) (fig. 1). The area consists of 1 site containing 8 measured faults. All measured faults cut the nonwelded base of the Rainier Mesa Member of the Timber Mountain Tuff. The faults are primarily north-northeast-trending, steeply dipping, normal oblique-slip faults with moderate to steep rakes ($>45°$) (fig. 12).

Test-induced Fault Reactivation

Evidence of faulting or fault reactivation due to post-1950's underground test explosions are rare. Only two faults measured in this study show evidence of test-induced refracturing, one in the ETA above the U12e tunnel complex and one in the UTA above the U12a complex. The ETA fault is in an area of extensive, variously oriented, wide (as much as 2 m), presumably test-induced tension cracks. The fault strikes northwest, dips steeply northeast, and has been dilated as much as 2.5 m orthogonal to its surface (fig. 7b, fault labeled "T"). The modern topographic surface has a maximum dip separation of about 1.5 m (down-to-the-northeast) across this normal-slip fault, suggesting that the fault experienced renewed shear displacement as well as tensional dilation. Nevertheless, no superposed striae were observed on the fault surface. The UTA fault, also in an area of local, probable test-induced fracturing

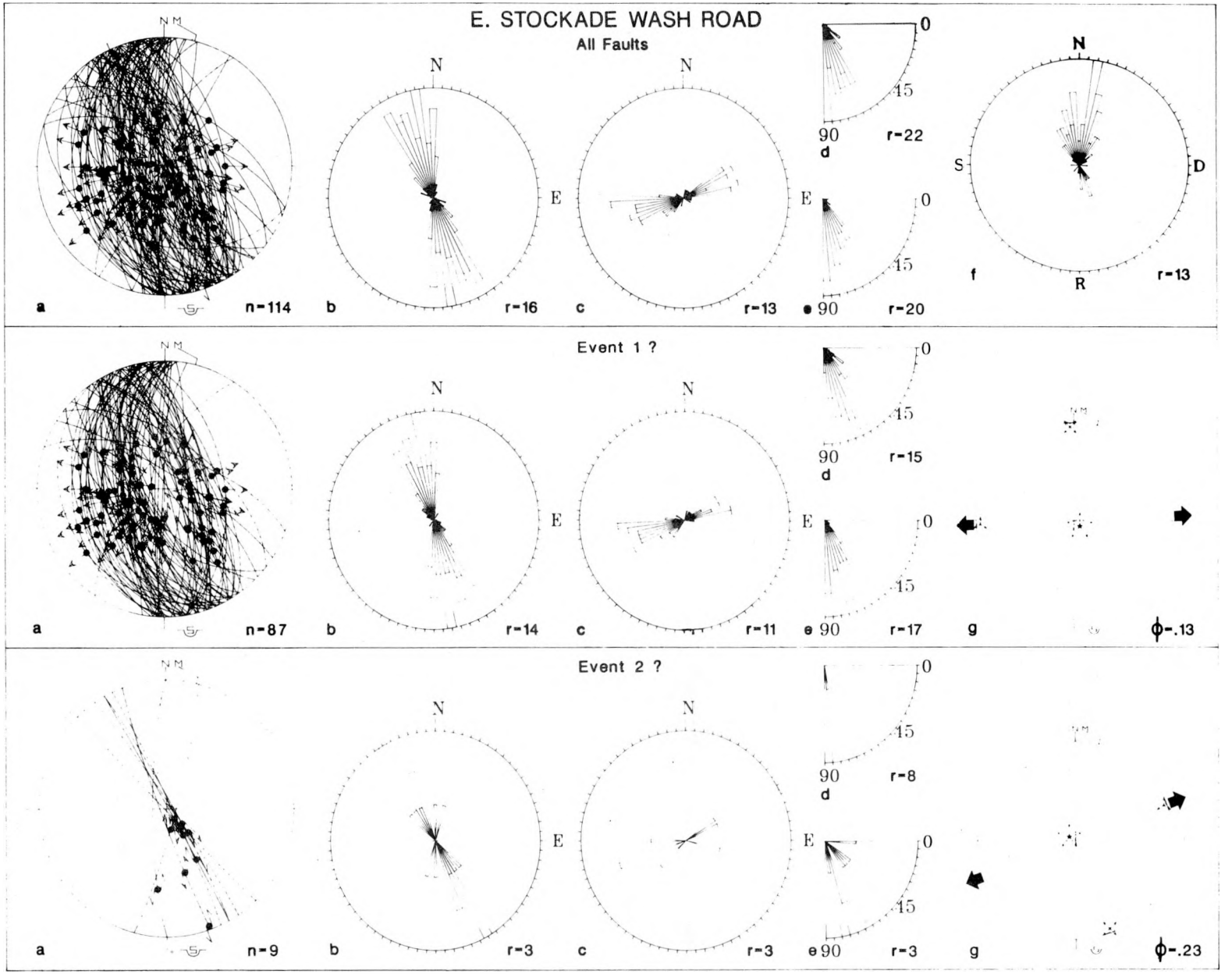

E. STOCKADE WASH ROAD
All Faults
N
E
S
D
R
0
15
90
a
n=114
b
r=16
c
r=13
d
r=22
e
r=20
f
r=13
Event 1 ?
n=87
r=14
r=11
r=15
r=17
g
ϕ=.13
Event 2 ?
n=9
r=3
r=3
r=8
r=3
ϕ=.23

Figure 6.

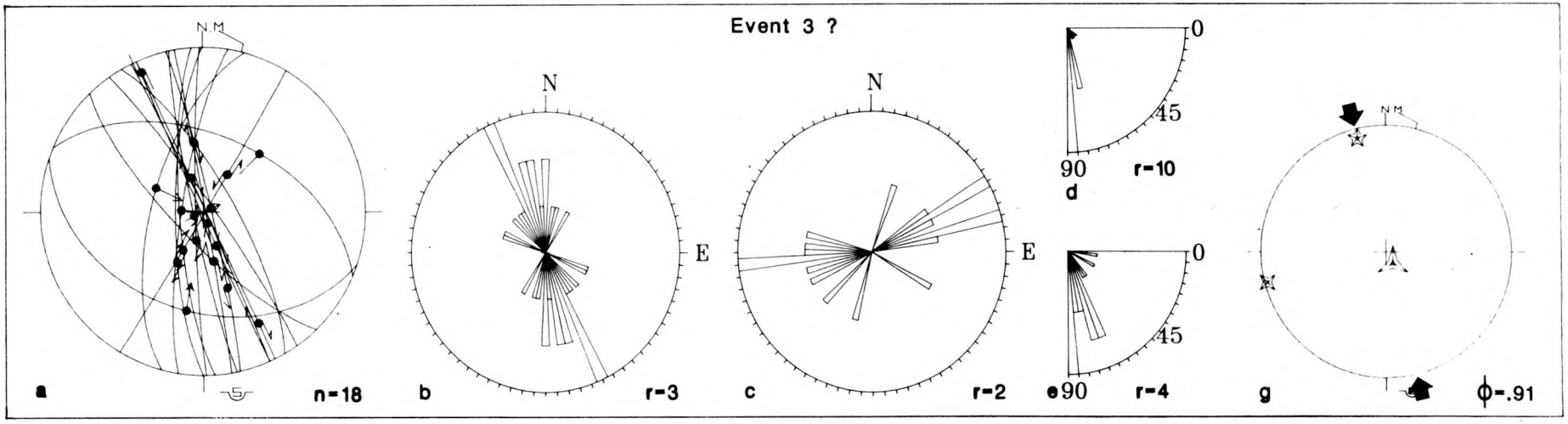


Figure 6 (continued). Fault-slip data summary plots and diagrams for all measurements at east Stockade Wash road area (first row) and for individual events. See figure 3 for explanation of plots and diagrams.

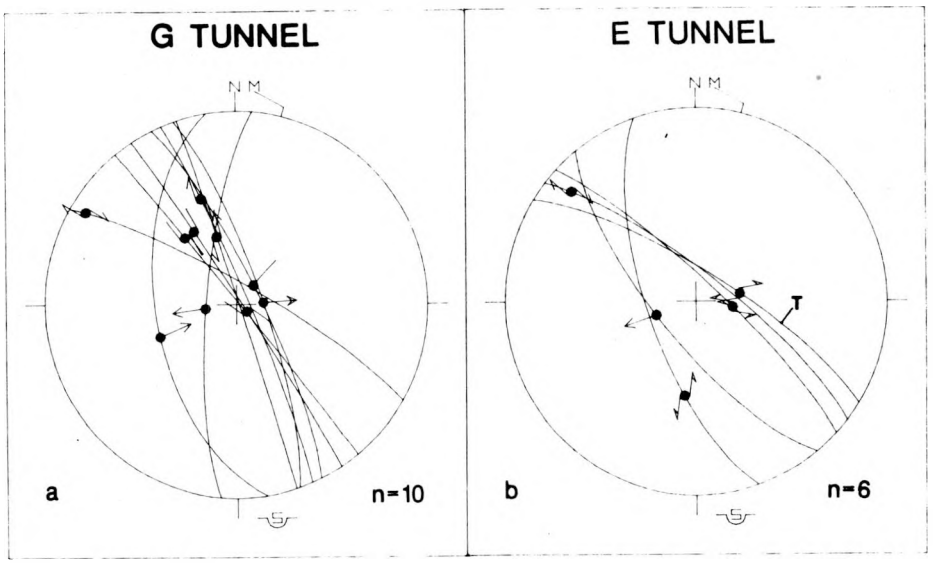


Figure 7. Fault-slip data summary plots for all measurements at G-tunnel (a) and E-tunnel (b) areas. See figure 3 for explanation of plots and diagrams. "T" in plot b) denotes probable test-reactivated fault.

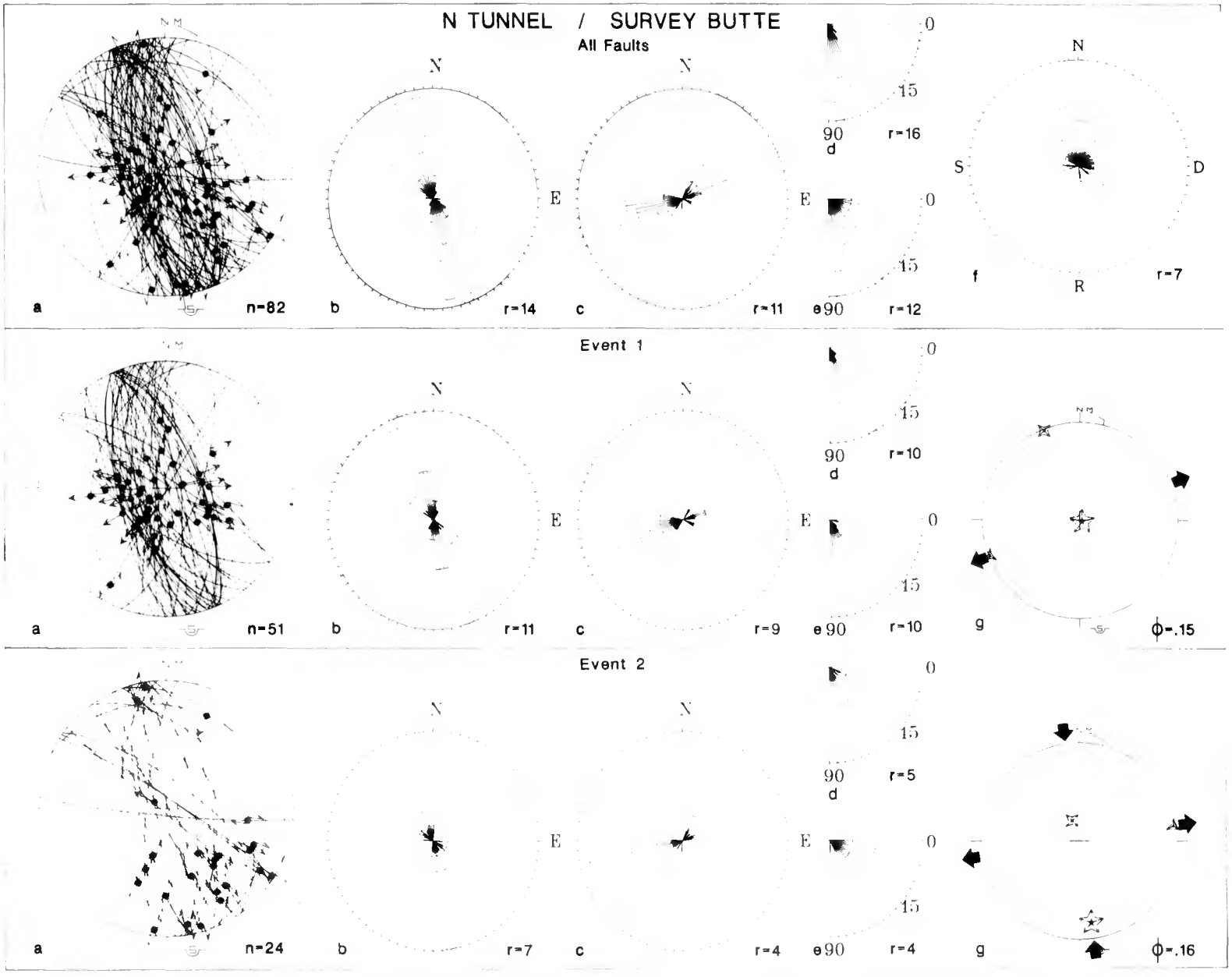


Figure 8. Composite fault-slip data summary plots and diagrams for all measurements at N-tunnel and Survey Butte areas (first row) and for individual events. See figure 3 for explanation of plots and diagrams.

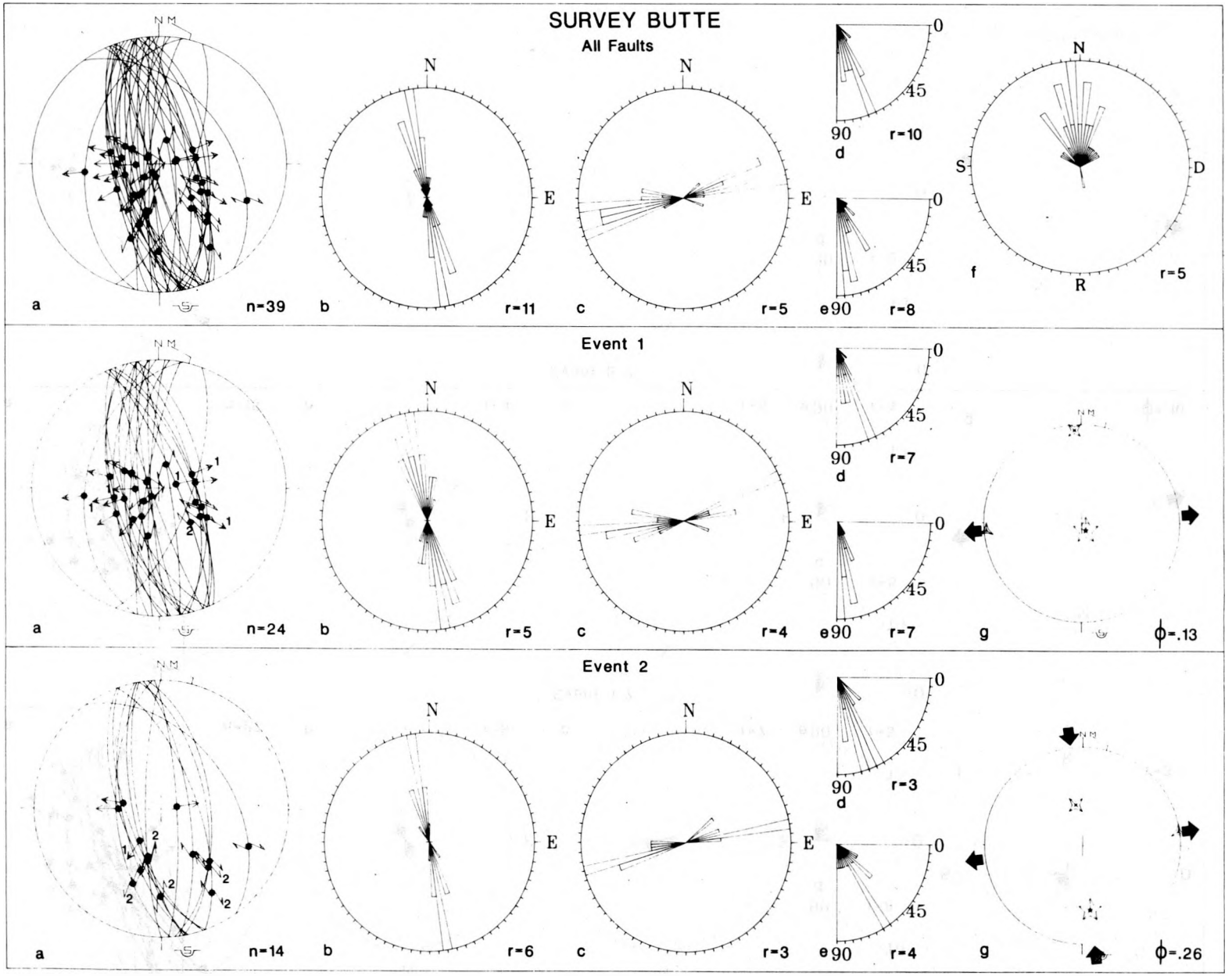


Figure 9. Fault-slip data summary plots and diagrams for all measurements at Survey Butte area (first row) and for individual events. See figure 3 for explanation of plots and diagrams.

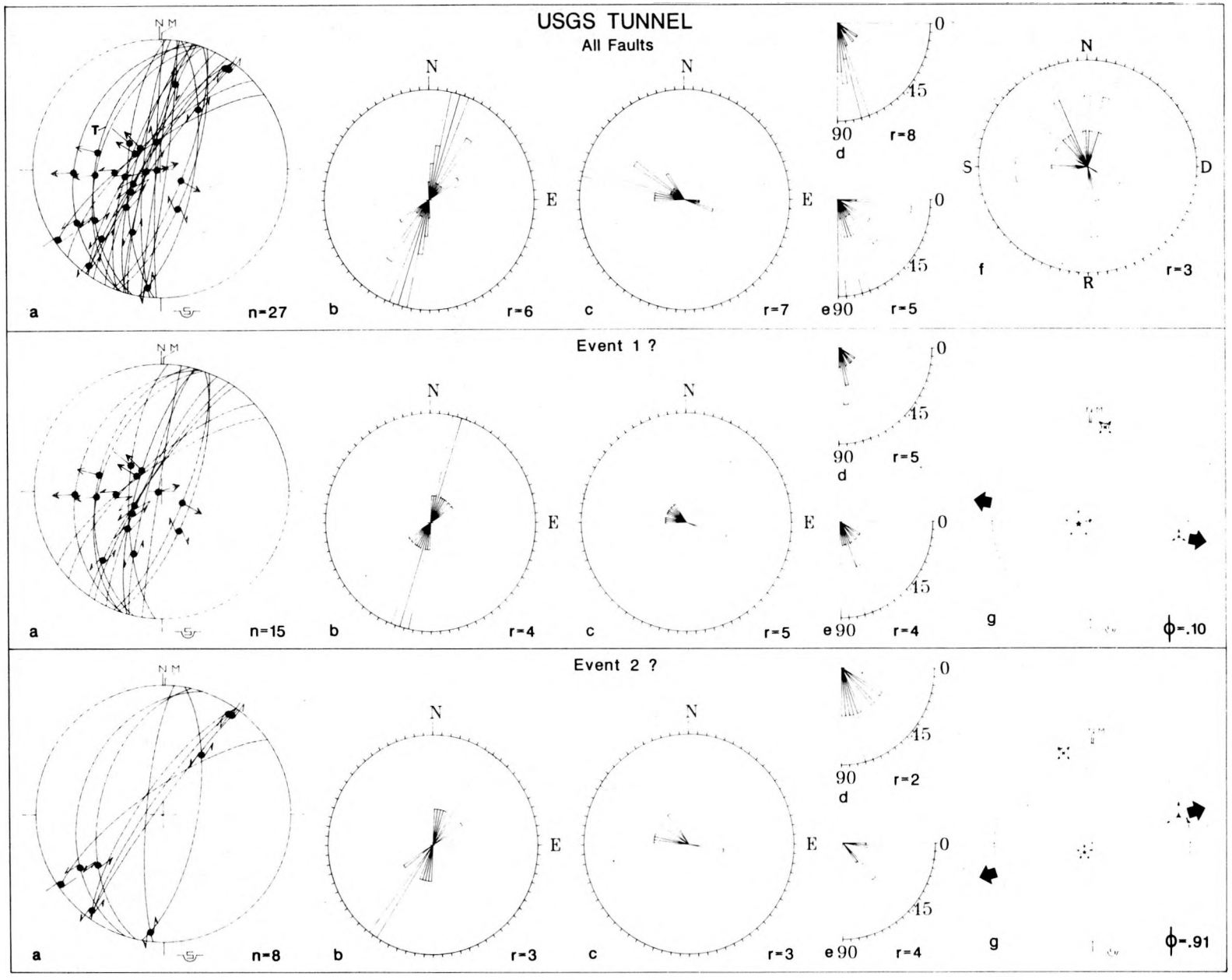


Figure 10. Fault-slip data summary plots and diagrams for all measurements at USGS-tunnel area (first row) and for individual events. See figure 3 for explanation of plots and diagrams. "T" in plot a) denotes probable test-reactivated fault.

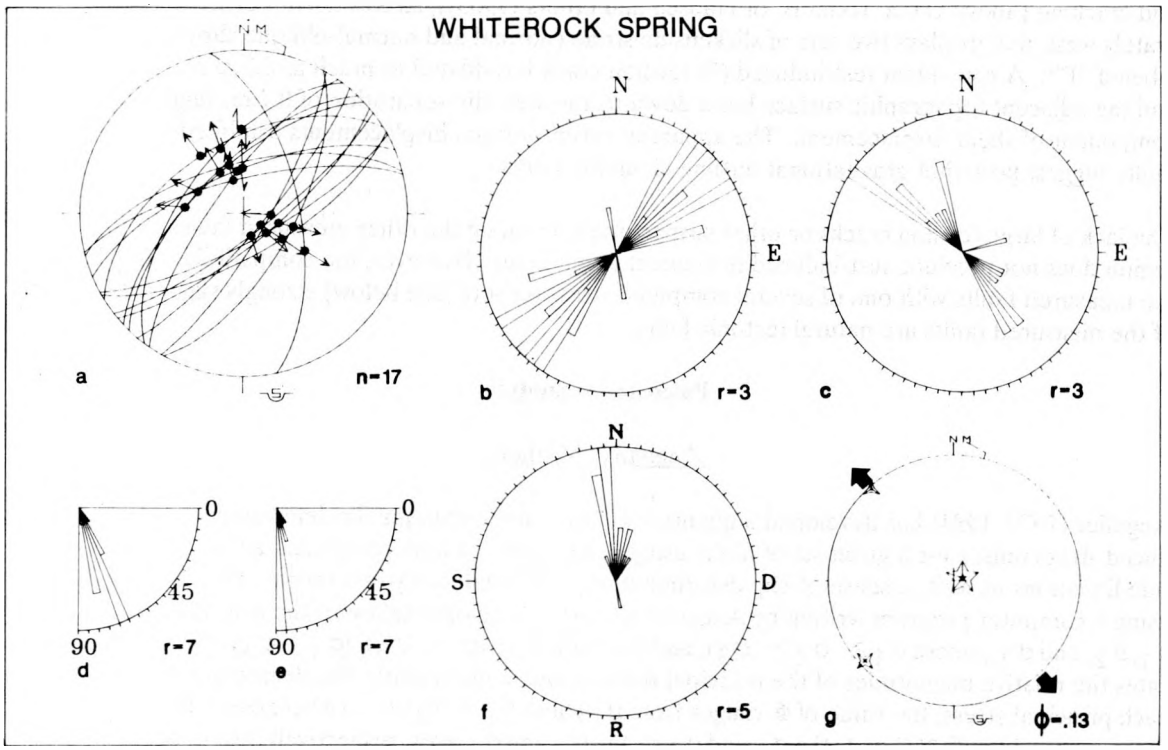


Figure 11. Fault-slip data summary plots and diagrams for all measurements at Whiterock Spring area. See figure 3 for explanation of plots and diagrams.

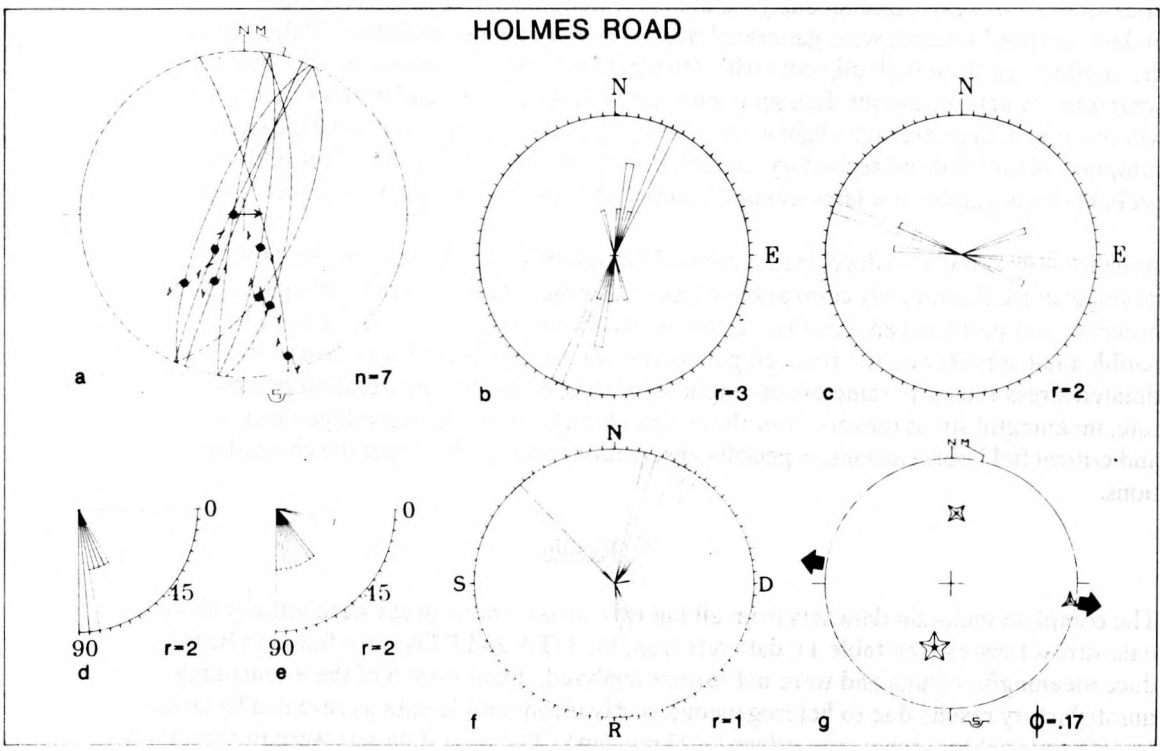


Figure 12. Fault-slip data summary plots and diagrams for all measurements at Holmes road area. See figure 3 for explanation of plots and diagrams.

and cracking (above U12a "room B" of Hansen and others (1963)), strikes north-northeast, dips moderately west, and displays two sets of slickenside striae (normal and normal-oblique slip) (fig. 10a, fault labeled "T"). A coincident test-induced (?) tension crack has dilated as much as 0.7 m along the fault and the adjacent topographic surface has a down-to-the-west dip separation of 0.7 m, suggesting a component of shear displacement. The apparent, recent normal displacements exhibited by these two faults suggest post-shot gravitational settling along the faults.

The lack of large tension cracks or other suspect features along the other measured faults in the study region does not preclude test-induced movement along them. However, the compatibility of most of the measured faults with one of several computed stress tensors (see below) strongly suggests that most of the measured faults are natural tectonic faults.

Paleostress Analysis

Analytical Methods

Angelier (1979, 1984) has developed a quantitative inversion technique for determining the best-fit, reduced stress tensor for a given set of faults using orientations of fault planes and accompanying slickenside lineations as well as sense-of-slip determinations. The reduced stress tensor, which is obtained using a computer program written by Angelier, consists of the orientation of the principal stress axes, σ_1, σ_2, and σ_3 (where $\sigma_1 \geq \sigma_2 \geq \sigma_3$), and the ratio $\Phi = (\sigma_2 - \sigma_3)/(\sigma_1 - \sigma_3)$. The Φ ratio indicates the relative magnitudes of the principal stresses and, consequently, the degree of resolution of each principal stress; the value of Φ ranges from 0 (where $\sigma_2 = \sigma_3$) to 1 (where $\sigma_2 = \sigma_1$) Thus in those cases where $\Phi \approx 0$ or 1, the σ_2 and σ_3 or the σ_2 and σ_1 axes, respectively, are poorly constrained. The computer program, using a least-squares iterative technique, minimizes the angular deviation (δ) between the computed resolved shear-stress vector on each fault plane and the actual striae directions. The analysis makes no assumptions concerning the orientations of fault planes relative to the stress axes, so that reactivated faults are given equal consideration with "new" ones. The technique does assume, however, that all analyzed faults formed under the same stress field and that no secondary localized stresses were generated near pre-existing discontinuities. Values of δ, which indicate the goodness of fit of fault-slip data with calculated paleostress tensors, are the best test of the first assumption. A heterogeneous data set composed of faults formed under more than one stress regime will result in a large average angular deviation (δ_{av}) and perhaps an unrealistic stress tensor. The assumption of no localized secondary stresses is probably invalid, but the effects of local stresses will probably be negligible if a large enough number of faults are analyzed (Angelier, 1984).

Angelier (1984) has also developed a method for subdividing a heterogeneous fault-slip data set into homogeneous, dynamically compatible subsets. A mixed data set is run through a separate computer program that performs an iterative, statistical clustering analysis to find the most homogeneous, compatible fault subsets and the reduced paleostress tensors associated with those subsets. Inferred or estimated stress-tensor parameters are input as starting points for the iteration process. Deriving accurate, meaningful stress tensors from these type of analyses are strongly dependent on making careful and critical field observations, especially observations that might reveal the chronology of fault dislocations.

Results

The complete fault-slip data sets from all but two measurement areas were initially analyzed for best-fit paleostress tensors (see table 1); data sets from the GTA and ETA were found to be too small to produce meaningful results and were not further analyzed. Data from 6 of the 8 remaining areas yielded unsatisfactory results due to heterogeneous, partly incompatible data as revealed by large δ_{av} values ($>15°$) and (or) low coherence values (<90 percent). These six data sets were further analyzed using the iterative clustering program to find two tensor solutions that better fit the data (table 1). The initial stress tensor solutions were generally entered into the program along with parameters for a second

TABLE 1. -- Paleostress analytical results

[All angles in degrees; σ_1, σ_2, σ_3 = principal stresses, where $\sigma_1 \geq \sigma_2 \geq \sigma_3$; $\Phi=(\sigma_2-\sigma_3)/(\sigma_1-\sigma_3)$; δ_{av} = average angular deviation between fault striae and computed maximum resolved shear stress; Coh = coherence; T = single tensor analysis of entire data set; C = cluster analysis; R = single tensor analysis using faults rejected by cluster method; Do. = same as above; querried events denote uncertain relative-age assignment]

Measurement area	Event	Sites	Faults	σ_1 axis trend	σ_1 axis plunge	σ_2 axis trend	σ_2 axis plunge	σ_3 axis trend	σ_3 axis plunge	Φ	δ_{av}	Coh (%)	Analyt method
SWA	all	15	112	166	8	330	81	75	2	0.34	12	70	T
Do.	1	Do.	66	165	7	315	82	75	4	.33	11	100	R
Do.	2	Do.	31	122	72	320	17	228	5	.79	9	100	C
Do.	3?	Do.	14	221	15	340	61	124	24	.50	19	93	C
ESWRA	all	13	115	187	84	1	6	91	1	.09	16	83	T
Do.	1?	Do.	87	135	83	358	5	267	5	.13	16	100	C
Do.	2?	Do.	9	301	84	159	5	69	4	.23	14	90	C
Do.	3?	Do.	18	346	8	256	3	149	81	.91	13	100	R
NTA	all	9	43	148	67	330	23	239	0	.47	20	70	T
Do.	1	Do.	23	156	73	339	17	248	1	.38	14	14	C
Do.	2	Do.	14	186	7	95	12	305	76	.02	11	100	C
SBA	all	7	39	163	72	352	18	261	3	.15	16	97	T
Do.	1	Do.	24	151	83	356	6	265	3	.13	11	100	C
Do.	2	Do.	14	173	34	350	56	82	1	.26	9	100	C
NTSBA	all	16	82	160	77	345	13	254	1	.19	17	78	T
Do.	1	Do.	51	133	88	338	2	248	1	.15	14	100	C
Do.	2	Do.	24	172	18	340	72	81	3	.16	17	100	C
UTA	all	1	27	235	76	11	10	103	9	.06	14	70	T
Do.	1?	Do.	15	255	80	10	4	100	9	.10	11	100	C
Do.	2?	Do.	8	218	80	342	6	73	8	.91	3	100	C
WSA	all	1	18	73	84	228	5	318	2	.13	9	94	T
HRA	all	1	8	194	46	4	43	99	5	.17	15	88	T

preliminary tensor estimated from the data distribution plots and diagrams in figures 3 through 12. In some cases, the clustering program was run a second time after more refined preliminary tensor values were added. The number of faults rejected by the two computed stress tensors for each of the areas varied from 1 to 15. The number of rejected faults from two of the areas (SWA and ESWRA) was large enough to analyze the faults in the single-tensor computation program. Both of these analyses yielded satisfactory results (table 1), allowing a third tensor to be defined for the areas. Assuming that each stress tensor from a given area represents a unique stress regime that existed for an interval of time, establishing a relative chronology of faults compatible with each paleostress tensor allows the relative stress-regime chronology to be determined for the area. Using the relative fault-age criteria described earlier, a tentative stress/fault regime or "event" chronology was established for each area. All of the paleostress results are summarized numerically in table 1 and graphically in lower parts of figures 3 through 12. The results from each measurement area are discussed below.

Stockade Wash Area

Over half of the faults (66) from the SWA are compatible with a well-constrained ($\Phi = 0.33$) strike-slip stress tensor solution (σ_2 subvertical) with σ_3 trending 255° (fig. 3, event 1). Nearly all the subvertical strike-slip faults measured in the area fit this solution. Although most of these shallow-rake faults strike north-northwest and are dextral, a small number are north-northeast-striking sinistral faults. Most relative age criteria are consistent with this stress regime being the oldest. The next apparent stress "event" had a normal-fault stress configuration (σ_1 subvertical) with σ_3 trending 228° and was also well defined ($\Phi = 0.79$) (fig. 3, event 2). Faults associated with this regime ($n = 31$) in general strike northwest, dip 60-80° either northeast or southwest, and have steep to moderate rakes associated with normal or normal-oblique slip. Thus, the previously mentioned bimodality in fault mode apparent from the overall data set can be clearly attributed to at least two distinct paleostress regimes that affected the area at different times.

Ninety-three percent (14) of the remaining faults marginally fit ($\delta_{av} = 19°$) a well-constrained ($\Phi = 0.50$) strike-slip stress tensor having a σ_3 trend of 304° (fig. 3, event 3?). Faults associated with this possible stress regime, which very questionably followed the other two, are quite variable in terms of strike, dip, rake, and slip sense. Nevertheless, most high-angle dextral strike-slip faults strike close to north and all reverse faults are moderately dipping and strike northwest.

Two stress tensors computed for the 17 faults measured at site SW9 in the SWA illustrate that generally similar tensor results are obtained from subsets of the data. As for the entire data set, an older strike-slip stress event was computed for most of the faults (13), which are mainly high-angle, north-northwest-striking dextral strike-slip faults (fig. 4). However, the trend of the σ_3 axis is shifted 19° clockwise relative to that computed for all the SWA event-1 data; this discrepancy may reflect local perturbations in the paleostress field or, alternatively, the relatively small number of measured faults at the site. Nevertheless the SW9 event-1 results indicate that both low-angle thrust faults and dextral oblique-slip faults measured at the site (figs. 4 and 5) are kinematically compatible with the strike-slip faults and associated stress tensor. Most likely there is a similar compatibility with the "accommodation" faults exposed in the roadcut 0.5 km to the south of SW9. The younger stress tensor computed for site SW9 is essentially identical to that for the entire data set even though only four faults were utilized; a normal-fault stress solution was obtained from mainly northwest-trending normal-slip faults.

East Stockade Wash Road Area

Seventy-six percent ($n = 87$) of the faults measured in the ESWRA are compatible with a normal-fault stress solution with σ_3 trending 267°, but somewhat weakly constrained ($\Phi = 0.13$) (fig. 6, event 1?). Nearly all these faults strike 330-360°, have steep dips (>60°) and rakes (>55°), and are normal-slip or normal-oblique-slip faults. Field criteria establishing the age of faults compatible with this tensor relative to those of the other two described below are sparse, but three clear cross-cutting relations of striae and faults suggest that it was the earliest of the three. The relative ages of the remaining two stress/fault regimes are less certain. One regime also has a well-constrained normal-fault stress con-

figuration with σ_3 oriented at 249° for which the 9 associated faults are all nearly vertical and strike mainly about 330° (fig. 6, event 2?). Essentially all remaining faults (18) are compatible with a reverse-fault stress regime with σ_3 vertical and σ_1 trending 346°, but poorly constrained ($\Phi = 0.91$) (fig. 8, event 3?). These faults also strike chiefly north-northwest, and their rakes and dips are generally very steep. The dominant fault mode is reverse slip.

N-Tunnel and Survey Butte Areas

The relative chronology of faulting in the combined NTSBA has been well established primarily due to excellent preservation of superposed slickenside striae on many of the fault surfaces. For most faults displaying dual striae, striae determined to be older are compatible with one stress solution, whereas those found to be younger fit with a second stress tensor. This relative-age pattern of fault striae is well displayed at two sites in the SBA, and is illustrated in figure 9a (events 1 and 2) where older striae are labeled "1" and younger striae are labeled "2".

The first event is characterized by a normal-fault stress configuration with σ_3 fairly well constrained ($\Phi = 0.15$) at 248° (fig. 8, event 1). Faults compatible with this stress regime primarily strike near 340° and dip $\geq 65°$ either northeast or southwest. These faults are mainly normal-slip faults with rakes rarely greater than 70°. Stress tensors for the older event obtained from separate cluster analyses of the individual NTA and SBA data subsets are very similar to that for the entire data set with the exception that the trend of σ_3 is rotated clockwise 15° for the SBA set (fig. 10g, event 1). This fact coupled with the observation that the SBA normal faults generally strike closer to north than the NTA faults suggest either that there was a slight spatial variation in the extension direction (and thus fault strike) during event 1 or that there was a temporal change in the extension direction and that the event 1 faults from the two areas are not coeval. This problem is further addressed below. Event 2 is characterized by a strike-slip stress configuration with σ_3 trending essentially 262° for both the NTSBA and the SBA subset (fig. 8, event 2). Faults fitting this solution are chiefly high-angle (>60°), moderate rake dextral and sinistral oblique-slip faults that strike north-northwest.

USGS-Tunnel Area

One of two events computed from the UTA data is characterized by a somewhat poorly constrained ($\Phi = 0.10$) normal-fault stress configuration with σ_3 trending 280° (fig. 10, event 1?). The 15 faults compatible with this tensor mainly strike north-northeast, dip 70-85° to the west, and have steep rakes (>65°) associated with normal or normal-sinistral-oblique slip. The other event also has a normal-fault stress solution although σ_3 is oriented differently (253°) (fig. 10, event 2?). Most of the eight faults associated with this event strike about 15° further northeast than those of event 1 and exhibit low-rake sinistral strike-slip displacement. The discrepancy between the strike-slip fault mode and normal-fault stress solution can be explained by the high Φ value (0.91) that indicates the stress tensor is very close to having a strike-slip configuration (i.e., σ_1 and σ_2 are nearly the same in magnitude). From a few limited and somewhat inconsistent relative-age observations and from similarities to the SBA results it is inferred that event 2 is younger than event 1.

Whiterock Spring Area

All but one of the measured faults in the UTA tightly fit ($\delta_{av} = 9°$) a normal-fault stress tensor solution. The σ_3 axis trends 318°.

Holmes Road Area

All but one of the measured faults are compatible with a poorly defined (σ_1 plunges 46°) normal-fault stress solution (fig. 12g). However, the σ_3 axis is fairly well constrained ($\Phi = 0.17$) at 279°.

DISCUSSION AND SUMMARY

Fault-slip data from each measurement area for which stress tensor analyses could be performed are compatible with one to three stress solutions. It should be possible to correlate solutions from differ-

ent areas if one assumes that for unspecified intervals of time in the geologic past the stress field acting on the rocks in the study region was spatially constant. In detail this assumption is probably invalid due to factors such as the local effects of irregular paleotopography and the depth dependence of the vertical component of stress. As a first order assumption, however, it is considered valid because of the similar geologic setting throughout the study region and the relatively close proximity of all measurement areas.

Correlation of stress events from different areas is based on stratigraphic age constraints and similarities among tensors. Stratigraphic control on ages of faulting is based on the principal that faults can not be older than rocks they cut or younger than rocks that truncate them. A general, coarse stratigraphy can be followed laterally across the study region, and is considered a valid correlation tool. Recognition of similar stress tensors, and especially a similar sequence of tensors computed from data collected in different areas is also a useful, though less reliable means of correlation. Caution must be exercised in correlating similar tensors because of the possibility of spatial changes in the regional stress field.

Consideration of the possibility of local rotations of rocks following faulting must be made before correlating and interpreting paleostress results. It is unlikely that horizontal-axis rotations have significantly influenced the orientation of paleostress axes because most rocks in the measurement areas dip shallowly. Limited paleomagnetic data (M.R. Hudson, U.S. Geological Survey, oral commun., 1989) from older tuffs in the study region preclude significant vertical-axis rotations.

The following correlations have been made to reconstruct a paleostress and faulting sequence for the study region (refer to fig. 13). Clearly the oldest faults measured are those in the WSA that do not cut rocks younger than the Redrock Valley Tuff (fig. 2). These normal-slip faults formed under a normal stress field with σ_3 oriented northwest (fig. 13, no. 1). Faults measured in each of the areas along the east flank of Rainier Mesa (all other areas except the SWA and HRA) (fig. 1) occur anywhere stratigraphically between the Tub Springs Member of the Belted Range Tuff (lower tunnel beds) and just above the Grouse Canyon Member (fig. 2). Therefore, only similarities in tensor configurations and "event" chronologies at individual measurement areas may be used to determine the sequence of events among those areas. Normal-fault paleostress configurations with σ_3 oriented west-northwest to west-southwest and low Φ values (0.18 average) characterize the first or inferred first events at each of the east-flank areas as well as the second event in the ESWRA (refer to fig. 6, events 1 and 2; figs. 7-10, event 1). In detail these first-event σ_3 directions swing 32° counterclockwise from the easternmost area (UTA) through the central area (SBA) to the westernmost areas (NTA and ESWRA) (fig. 13, nos. 2-4). This shift in σ_3 may have been due to a pronounced spatial change in the regional stress field during the time of faulting. Alternatively, the counterclockwise swing represents a regional temporal stress change that was accompanied by a westward shift in the locus of faulting. This latter explanation is strongly favored because of the known older age of the WSA stress configuration that defines a northwest starting reference direction for the σ_3 shift. Lending further support to this interpretation is the fact that the σ_3 direction associated with the probable second event at ESWRA is shifted 18° counterclockwise relative to that of the first event. This early normal-fault stress regime probably ended prior to deposition of Crater Flat rocks because compatible faults are not observed in the SWA.

The early normal-fault stress regime is followed by strike-slip stress configurations with σ_3 oriented west-southwest and low Φ values (0.21 average) (figs. 8 and 9, event 2). At the NTA the second event is characterized by a reverse-fault stress configuration (table 1), but the extremely low Φ value (0.02) indicates that the faults are essentially also compatible with a strike-slip solution (i.e., vertical σ_2 axis). In a similar manner, strike-slip faults associated with the second event at the UTA (fig. 10, event 2) are nearly as compatible with a strike-slip solution as they are with the computed normal-fault solution (Φ =0.91). Additionally, at SWA to the southwest the first event is associated with a strike-slip stress regime having a west-southwest oriented σ_3. All of these "local" strike-slip events are correlated with one another and collectively indicate that the region experienced a fundamental change from a normal

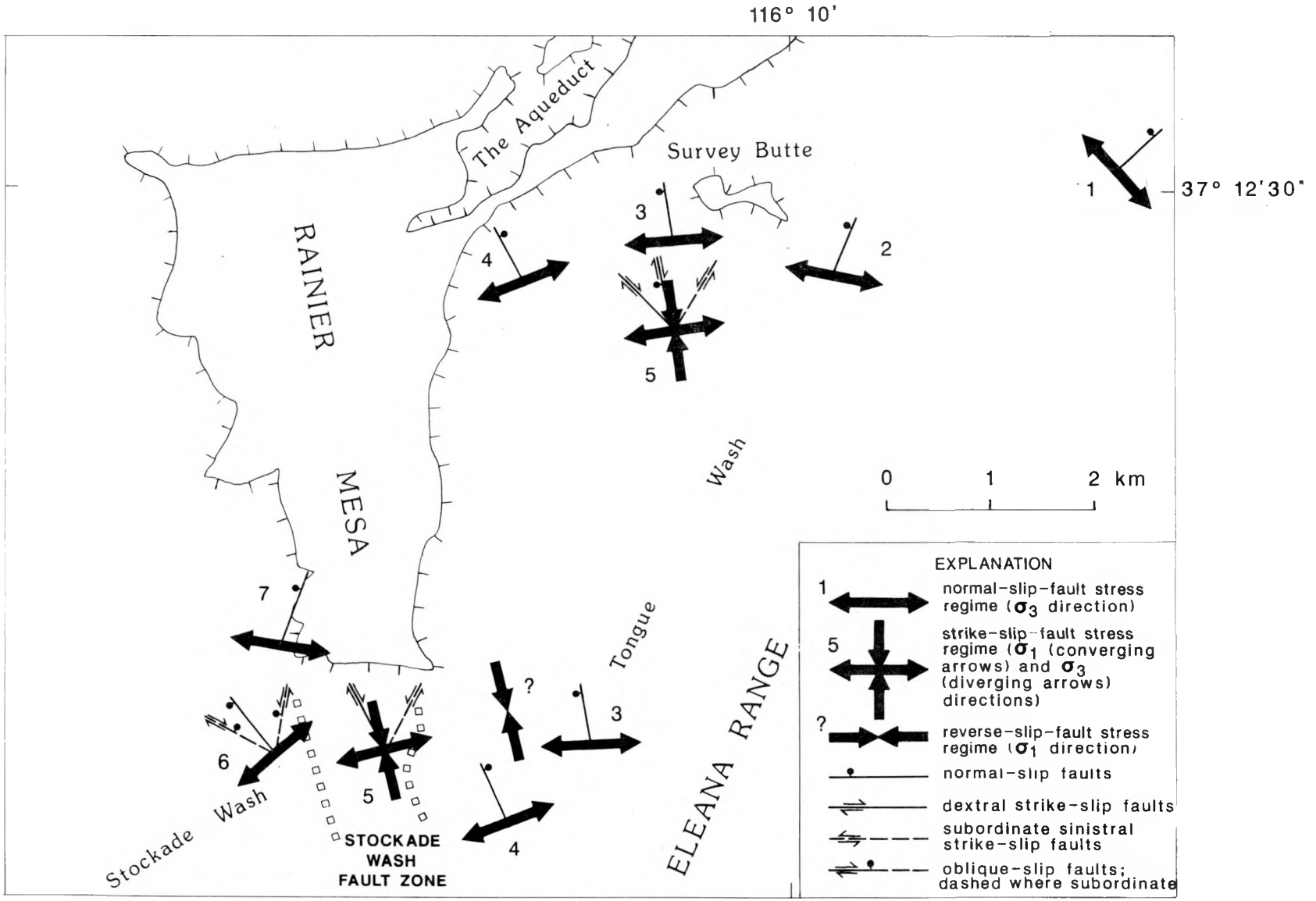


Figure 13. Map summarizing study-region stress-regime sequence (nos. 1 to 7) , principal-stress-axis directions, and location and mode of associated faulting. Stress regime labeled "?" has uncertain relative age.

to strike-slip stress regime that was possibly accompanied by a small (~10°) clockwise shift in the σ_3 direction (fig. 13, no. 5). Strike-slip faulting associated with this regime was principally confined to a broad zone along the northeast flank of Rainier Mesa and the more narrow Stockade Wash zone. The virtual absence of SWA-type strike-slip faults in overlying rocks exposed just north of SWA (partly Paintbrush Tuff rocks) suggests that the strike-slip regime was short lived.

The inferred final-event reverse-fault stress solution associated with the ESWRA (fig. 6, event 3?) may reflect a local perturbation in the stress field during the strike-slip regime, for the north-northwest σ_1 direction is essentially coincident with that of the computed strike-slip stress tensors (fig. 13, axis labeled "?"). Such a perturbation, involving a reversal of the σ_2 and σ_3 axes, could be explained by faulting at very shallow paleodepths, compression associated with formation of the large east-northeast-trending syncline traversing the ESWRA (fig. 2), or a combination of the above. However, faults in the area appear to extend undisturbed across the axial zone of the syncline, suggesting little or no relation of the stress configuration to folding.

A change back to a normal-fault stress regime was "recorded" only by "event 2" normal faults in the SWA (fig. 3, event 2). Accompanying this change was another counterclockwise shift of the σ_3 axis to the southwest (fig. 13, no. 6).

The few faults measured in the HRA cut the Timber Mountain Tuff, which overlies rocks exposed in the SWA, and thus, likely postdate the SWA strike-slip event. The weakly defined normal-fault stress solution compatible with these faults includes a west-northwest-directed σ_3 axis (fig. 12). This suggests that the σ_3 axis rotated clockwise about 50° from its earlier southwest direction sometime after deposition of Crater Flat Tuff (fig. 13, no. 7). The inferred third-event stress tensor computed from a small number of SWA faults (fig. 3, event 3?) may represent an additional 25° of clockwise rotation of the σ_3 axis although not much confidence is placed in the solution due to poor fit of the data (δ_{av}=19°).

The proposed paleostress evolution of the study region is summarized briefly below (refer to fig. 13). Prior to and probably just following deposition of the Redrock Valley Tuff at about 16 Ma the area was subject to a normal-fault stress regime (σ_1 vertical) with σ_3 oriented northwest (fig. 13, no. 1). Between 16 Ma and about 14 Ma (age of the Bullfrog Member of the Crater Flat Tuff), the study region experienced a progressive counterclockwise shift in the orientation of σ_3 from northwest to west-southwest (fig. 13, nos. 1-4). The locus of faulting during this shift in the normal-fault stress field migrated progressively westward from the Whiterock Spring area to the east flank of Rainier Mesa. Consequently, normal faults tended to form along strike directions that gradually changed from northeast in the east to north-northwest in the west. At about 14 Ma the regional stress field underwent a possibly brief (<1 m.y.) but fundamental change to a strike-slip regime (σ_2 vertical) that was possibly accompanied by a slight (~10°) clockwise shift of σ_3 (fig. 13, no. 5). Dextral-slip faults principally formed during this regime within a 1-km-wide northerly trending fault zone in upper Stockade Wash, whereas in a broad zone on the northeast flank of Rainier Mesa dextral oblique-slip movement chiefly occurred on older faults formed during the earlier regime. The stress field reverted back to a normal-fault configuration sometime after about 13 Ma and the σ_3 direction again rotated counterclockwise (~25°) to the southwest (fig. 13, no. 6). Northwest-striking normal-slip faults that formed in the Stockade Wash area after this change are very similar to the relatively large-displacement, apparently caldera-related normal faults mapped southwest of Rainier Mesa (fig. 2). This suggests that the southwest shift of the σ_3 axis reflects the development of σ_3 trajectories radial to the Timber Mountain caldera before and (or) during its collapse at about 11 Ma. Following emplacement of the Timber Mountain Tuff at approximately 11 Ma the σ_3 axis rotated clockwise about 50° to a west-northwest direction as recorded in north-northeast-striking faults near the southwest corner of Rainier Mesa. This clockwise rotation may have been the initial phase of an eventual shift of σ_3 to the present-day 310° orientation.

This study differs significantly from previous paleostress studies in the region in that the results indicate a major (90°) counterclockwise rotation of the σ_3 axis during Miocene time. Earlier studies conducted both in the Nevada Test Site region (e.g., Dockery, 1984) and elsewhere in southern Nevada (e.g.,

Angelier and others, 1985) lend support to only a clockwise rotation of σ_3 during Neogene and Quaternary time. This difference may be due to the absence in other studies of measured faults of the age span 16-11 Ma, the approximate age of the counterclockwise stress rotation. Considering the age uncertainty of the faults measured in this study, the counterclockwise rotation may have occurred in as short a time as about 2 m.y.--a stress change too brief, perhaps, to have been detected in other studies. Alternatively, the counterclockwise stress rotation may have been a local phenomenon, perhaps related to an overprint of the regional stress field by deviatoric stresses associated with the development of the Timber Mountain caldera.

This study also indicates that, in general, the orientations of faults cutting Neogene rocks in the region are not reliable indicators of the orientations of the modern, ambient principal stresses. The orientation of faults relative to the stress axes can be quite complex, in part, due to fault reactivation of fractures having less-than-favorable orientations. Furthermore, it is now clear that the regional stress field causing Neogene faulting near Rainier Mesa has undergone a complex evolution over millions of years, and therefore observed fault orientations are primarily associated with paleostress fields that are now extinct. Thus, determinations of the modern ambient stress field for radionuclide containment purposes are limited to precise in-situ stress techniques.

ACKNOWLEDGMENTS

The excellent field assistance of Gary D'Urso, F.W. Simonds, and T.G. Thompson of the U.S. Geological Survey and S.H. Leedom of the U.S. Department of Energy is greatly appreciated. Jacques Angelier of the Universit Pierre et Marie Curie, France, generously supplied copies of his paleostress analytical computer programs for the use of U.S. Geological Survey scientists. G.S. Hofland and T.P. Barnhard of the U.S. Geological Survey are acknowledged for their critical contributions towards the development of fault-slip-graphics computer programs used in this study.

REFERENCES CITED

Angelier, Jacques, 1979, Determination of the mean principal directions of stresses for a given fault population: Tectonophysics, v. 56, p. T17-T26.

_____1984, Tectonic analysis of fault slip data sets: Journal of Geophysical Research, v. 89, no. B7, p. 5835-5848.

Angelier, Jacques, Colletta, Bernard, and Anderson, R.E., 1985, Neogene paleostress changes in the Basin and Range: a case study at Hoover Dam, Nevada-Arizona: Geological Society of America Bulletin, v. 96, p. 347-361.

Carr, W.J., 1974, Summary of tectonic and structural evidence for stress orientation at the Nevada Test Site: U.S. Geological Survey Open-File Report 74-176, 53 p.

Dockery, Holly, 1984, Rotation of late Cenozoic extensional stresses, Yucca Flat region, Nevada Test Site, Nevada: Houston, Texas, Rice University, Ph.D. thesis, 77 p.

Ellis, W.L., and Magner, J.E., 1980, Compilation of results of three-dimensional stress determinations made in Rainier and Aqueduct Mesas, Nevada Test Site, Nevada: U.S. Geological Survey Open-File Report 80-1098, 27 p.

Frizzel, V.A., Jr., and Zoback, M.L., 1987, Stress orientation determined from fault slip data in Hampel Wash area, Nevada, and its relation to contemporary regional stress field: Tectonics, v. 6, no. 2, p. 89-98.

Gibbons, A.B., Hinrichs, E.N., Hansen, W.R., and Lemke, R.W., 1963, Geology of the Rainier Mesa quadrangle, Nye County, Nevada: U.S. Geological Survey Geologic Quadrangle Map GQ-215, scale 1:24,000.

Hansen, W.R., Lemke, R.W., Cattermole, J.M., and Gibbons, A.B., 1963, Stratigraphy and structure of the Rainier and USGS tunnel areas, Nevada Test Site: U.S. Geological Survey Professional Paper 382-A, p. A1-A49.

Miller, C.H. and Miller, D.R., 1977, Orientation of explosion-induced surface fractures estimated from pre-explosion fractures and in situ stress measurements: Bulletin of the Association of Engineering Geologists, v. XIV, no. 1, p. 27-37.

Petit, J.P., 1987, Criteria for the sense of movement on fault surfaces in brittle rocks: Journal of Structural Geology, v. 9, no. 5/6, p. 597-608.

Scott, R.B., and Hofland, G.S., 1987, Fault-slip paleostress analysis of Yucca Mountain, southern Nevada [abs.]: Eos, Transactions of the American Geophysical Union, v. 68, p. 1461.